

Springer Series in Computational Neuroscience

Antonio Di Ieva *Editor*

The Fractal Geometry of the Brain



Springer

Springer Series in Computational Neuroscience

Series Editor

Alain Destexhe

UNIC

Gif-sur-Yvette, France

Romain Brette

Institut de la Vision

Paris, France

Computational Neuroscience gathers monographs and edited volumes on all aspects of computational neuroscience, including theoretical and mathematical neuroscience, biophysics of the brain, models of neurons and neural networks, and methods of data analysis (e.g. information theory). The editors welcome suggestions and projects for inclusion in the series. About the Editors: Alain Destexhe is Research Director at the Centre National de la Recherche Scientifique (CNRS), France, and Romain Brette is Research Director at the Institut National de la Santé et de la Recherche Médicale (INSERM), France.

More information about this series at <http://www.springer.com/series/8164>

Antonio Di Ieva
Editor

The Fractal Geometry of the Brain

 Springer

Editor

Antonio Di Ieva, MD, PhD
Neurosurgery Unit, Faculty of Medicine and Health Sciences
Macquarie University
Sydney
New South Wales
Australia

Department of Neurosurgery
Royal North Shore Hospital
Sydney
Australia

Garvan Institute of Medical Research
Sydney
Australia

Medical University of Vienna
Vienna
Austria

University of Toronto
Toronto
Ontario
Canada

The original version of this book was revised.

An erratum to this chapter can be found at DOI [10.1007/978-1-4939-3995-4_37](https://doi.org/10.1007/978-1-4939-3995-4_37)

ISSN 2197-1900 ISSN 2197-1919 (electronic)
Springer Series in Computational Neuroscience
ISBN 978-1-4939-3993-0 ISBN 978-1-4939-3995-4 (eBook)
DOI 10.1007/978-1-4939-3995-4

Library of Congress Control Number: 2016948130

© Springer Science+Business Media New York 2016

This work is subject to copyright. All rights are reserved by the Publisher, whether the whole or part of the material is concerned, specifically the rights of translation, reprinting, reuse of illustrations, recitation, broadcasting, reproduction on microfilms or in any other physical way, and transmission or information storage and retrieval, electronic adaptation, computer software, or by similar or dissimilar methodology now known or hereafter developed.

The use of general descriptive names, registered names, trademarks, service marks, etc. in this publication does not imply, even in the absence of a specific statement, that such names are exempt from the relevant protective laws and regulations and therefore free for general use.

The publisher, the authors and the editors are safe to assume that the advice and information in this book are believed to be true and accurate at the date of publication. Neither the publisher nor the authors or the editors give a warranty, express or implied, with respect to the material contained herein or for any errors or omissions that may have been made.

Printed on acid-free paper

This Springer imprint is published by Springer Nature
The registered company is Springer Science+Business Media LLC New York

*To my father,
who introduced me to fractals as a young boy,
as well as to science, for science's sake.*

Foreword

The *Fractal Geometry of the Brain* adopts an encyclopedic view of the multiple ways the notion of fractal enters into the clinical, as well as scientific, understanding of the human brain, with multiple papers addressing the brain's form, function, and pathologies. This ambitious task is undertaken from the perspective of making available to the biomedical community a measure of complexity that can characterize both disease and wellness, a measure, the fractal dimension, which is fully consistent with the complexity of biomedical phenomena and with phenomena that have historically resisted being characterized by one or a few scales.

A fractal is a geometric concept used to describe the scaling of physical objects in space, which cannot be characterized by one or a few scales. This is not an esoteric mathematical concept, but is a concrete practical measure of variability in complex phenomena. Thus, the folds of the brain's surface, the regions of space that confine the flow of material through the brain, as well as tumor growth, are not described by smooth integer dimension paths, or surfaces, but have dimensions between the integers. These fractal dimensions entail a scaling across multiple scales, with the fractal dimension determining how the scales are tied together. This scaling gives rise to a self-similarity of the object in space, which like nested Russian dolls repeat the same structure at ever smaller scales. Multiple examples of such space-filling biomedical phenomena are presented throughout the book and used to explain how such scaling is related to robustness and its loss to disease.

A fractal can also describe a dynamic process, as observed in physiologic time series. Here again the variability cannot be determined by a given rate or any other characteristic scale determined by an average. The dynamic changes in physiologic time series are coupled across a wide range of time scales, with no one scale being dominant. A fractal dimension again determines how the slowest and the fastest changes are coupled together, even though one may be on the order of fractions of a second and the other on the order of days or even weeks. Such coupling gives rise to a self-similarity of the dynamic variability in time. The scale at which a physician ought to intervene, in order

to control the dynamics of the process, is often the crucial question. Here again a number of dynamic phenomena and their disruptions are described throughout the book.

Finally, there is the statistical fractal, where the self-similarity does not reside in the space or time variation of the variable of interest, but rather this fractal is contained in the scaling of the distribution describing the random fluctuations in physiological variables. But here, as in the cases of the two other kinds of fractals, it is not the mathematics that is emphasized; although the multiple ways the fractal dimension can be estimated from data is discussed, it is the biomedical implications of the self-similar statistics that is of most concern. How the scaling opens up a new way of understanding, of both the normal behavior and the multiple ways normality can be subverted, is of most importance to clinical medicine.

I have taken the space to distinguish the three manifestations of fractal used in the book for good reason. Each fractal form assists in understanding a different aspect of the brain. The phrase fractal geometry in the book's title is not geometry in the classical mathematical sense, but that should not be a surprise. Mathematicians have been arguing over the meaning (and existence) of fractals and fractal geometry, since Benoit Mandelbrot¹ introduced his idiosyncratic definitions into the scientific lexicon, over 40 years ago. Mandelbrot was more interested in understanding the complexity of natural and social phenomena, using relatively simple mathematical models, than he was in satisfying the scientific criteria in any given discipline, including those laid down by mathematicians.

The brain, with its rich complexity of neuronal interconnections, the broad spectrum of time scales in its dynamics, and its statistical variability in the performance of tasks, is a natural candidate for fractal modeling. The brain's complexity is defined by a balance between regularity and randomness as captured by its various fractal dimensions. The fractal dimension is ubiquitous in the various complex processes within the brain because fractal processes have been proven to have an evolutionary advantage over those that do not.

Mandelbrot recognized a number of ways that his fractal concept could be used to gain a deeper understanding of physiologic complexity¹, using what he candidly admitted were toy models. The handbook, *Fractal Physiology*,² extending his applications of the fractal concept to real-world physiological data, was introduced in 1994, but it took another 20 years for a journal of the same name to become available. Ewald Weibel, in the memorial volume dedicated to Mandelbrot,³ entitled his contribution: "How Benoit Mandelbrot Changed My Thinking About Biological Form." This remembrance details his personal, but not atypical, journey a number of biomedical scientists have taken, from the traditional perspective of biology and

¹B.B. Mandelbrot, *Fractals, Form, Chance and Dimension*, W.H. Freeman and Co., San Francisco, 1977.

²J.B. Bassingthwaighe, L.S. Liebovitch, and B.J. West, *Fractal Physiology*, Oxford University Press, NY, 1994.

³M. Frame and N. Cohen, Eds., *Benoit Mandelbrot; A Life in Many Dimensions*, World Scientific, NJ, 2015.

physiology to one encompassing the rich variability observed in the data and captured by the concept of fractal dimension. This book is in this tradition, with a focus on the human brain, and is remarkably successful in its undertaking.

March 2016

Bruce J. West, PhD
Fellow of APS, ARL, and AAAS
Information Science Directorate
US Army Research Office
Research Triangle Park, NC, USA

Preface

This book's title, *The Fractal Geometry of the Brain*, recalls Benoit Mandelbrot's famous book in which he described *the fractal geometry of nature* more than 30 years ago. Since then fractals have found application in many fields, especially in the biomedical sciences and, in particular, the neurosciences. In light of the hodological interconnection of ideas regarding the study of the amazing and complex system called the brain, it seems natural that neuroscientists also peered through the lens of fractal analysis to view the brain as fractal, self-similar in both neuroanatomical structures and neurophysiological time series. Nonetheless, in practice fractals – often deemed too exotic, esoteric, misunderstood, or simply not understood – do not yet have clearly defined roles in biomedical research and clinical neurosciences. With an aim of defining those roles, the scope of this book summarizes the state of the art of fractal analysis in neuroscience.

This book reviews the most intriguing applications of fractal analysis to the neurosciences with a focus on current applications and future perspectives, limits, advantages, and disadvantages. It is essentially for scientists, scholars, physicians, and students of different disciplines interested in applying fractal-based computational models to the study of the brain. This book is mainly clinically oriented, offering suggestions for applying fractals “from bench to bedside,” but also covers numerous research aspects. Thanks to the valuable inputs of 58 experts worldwide (physicians, basic and clinical neuroscientists, computer scientists, mathematicians, psychologists, biologists, physicists, and engineers, among others) from 19 different countries, who have made personal contributions in the field, this book is a holistic body of work on fractals and the brain that describes how fractal analysis can help analyze the marvelous and complex system called the brain in its entire physiopathological spectrum.

The book is organized into four parts, each introduced by a short chapter that summarizes the topics of its section:

Part I “Introduction to Fractal Geometry and Its Applications to the Neurosciences” (Chaps. 1, 2, 3, and 4) summarizes the “nuts and bolts” of fractal geometry and its applications to basic and clinical neurosciences.

Part II “Fractals in Neuroanatomy and Basic Neurosciences” (Chaps. 5, 6, 7, 8, 9, 10, and 11) investigates the brain as a fractal object in a hierarchical, multilevel analysis from neurons and microglia to the whole brain itself, with all its structural and functional complexity. A specific chapter is dedicated to the fractal geometry of cranial sutures, and the concluding chapter explores an evolutionary perspective on the fractal geometry of the human brain.

Part III “Fractals in Clinical Neurosciences” (Chaps. 12, 13, 14, 15, 16, 17, 18, 19, 20, 21, 22, 23, 24, 25, 26, 27, 28, 29, and 30) summarizes applications of computational fractal-based analysis to the clinical neurosciences, moving sequentially through the different disciplines. Chapters 13, 14, and 15 summarize applications of fractal analysis to neurological diseases and in particular neurodegenerative diseases. Chapters 16, 17, and 18 discuss cerebrovascular-related topics, and Chaps. 19 and 20 focus on neuroimaging. Chapter 21 bridges neuroimaging to the field of neuro-oncology, and Chaps. 22, 23, and 24 investigate brain tumors from neuropathological, neuroradiological, and oncological points of view. Next, Chaps 25, 26, and 27 cover fractal-based analysis of brain time series (i.e., EEG, EMG, and biosignals in Parkinsonian diseases). Chapter 28 focuses on applications of fractals to the sensory extension of the brain, the eye. Chapter 29 covers cognitive neurosciences and psychiatric diseases, and lastly in the section, Chap. 30 focuses on the relationships between fractals and visual experiences, including in the visual arts.

Part IV “Computational Fractal-Based Neurosciences” (Chaps. 31, 32, 33, 34, 35, and 36) illustrates applications of fractal analysis to neuroscience by means of software and computer science tools. Chapters 35 and 36 introduce some bioengineering-related aspects of fractal geometry, from fractal neuronal interfaces to future perspectives in artificial intelligence.

I hope that this book provides the stimulus to ignite new ideas in the open minds of out-of-the-box thinkers who are interested in the study and treatment of the brain from a novel and progressive perspective.

February 2016

Antonio Di Ieva
Sydney, Australia

Acknowledgments

First of all, I would like to acknowledge all of the contributors, without whose expertise and enthusiasm this comprehensive book would not have seen the light of day. Among them, a special thanks goes to Audrey Karperien, as she has not only written three extraordinary chapters but, despite her own duties, has also enthusiastically agreed to review chapters written by others (Preface, Chaps. 1, 3 and 31).

I would like to thank Jennilee Davidson for her lovable, continuous support in proofreading a great part of the book. Moreover, I'd like to acknowledge Timothy Lam for his help to draft Chap. 20 and Joseph Di Michele for Chap. 24. The great enthusiasm I have found in several of my students at the University of Toronto in performing fractal-based research in clinical neurosciences has been a source of great satisfaction, and I also thank Dr. Michael Cusimano for the great neurosurgery-based and scientific network we've shared.

In addition, I would like to thank the professors (who have become friends) who supervised my Ph.D. in clinical neurosciences at the Medical University of Vienna in the period of 2009–2011, supporting my research on the applications of computational fractal-based analyses into the fields of neurosurgery and neuroanatomy, neuropathology, and neuroradiology: Manfred Tschabitscher, Christian Matula, and Johannes Hainfellner.

Last but not least, a special thanks goes to two old friends of mine, Carlo Russo and Fabio Grizzi. Although not present among the contributors of this book, their presence is shadowed in every page of mine. I will not forget the endless discussions we have had (and still have) on the applications of fractals in biomedicine, in the lab of the Humanitas Institute in Milan and in Vienna and in Toronto and in Sydney as well as online almost on a daily basis, without any spatiotemporal barriers. Also unforgettable are the endless hours spent to run experiments during my on call nights, when, between an emergency in the operating theater and a case to manage in the ER, several computers were computing our calculations in parallel over nights and weekends. The indefatigable support by Carlo Russo, who has programmed the

requested software applications, and who has always been very keen to brainstorm “in real time,” is something more unique than rare!

A unified fractal model of the brain would not have been possible without this self-similar network of great friends and precious colleagues from all around the world.

Antonio Di Ieva

Contents

Part I Introduction to Fractal Geometry and Its Applications to Neurosciences

- 1 The Fractal Geometry of the Brain: An Overview** 3
Antonio Di Ieva
- 2 Box-Counting Fractal Analysis: A Primer for the Clinician** 13
Audrey L. Karperien and Herbert F. Jelinek
- 3 Tenets and Methods of Fractal Analysis ($1/f$ Noise)** 45
Tatjana Stadnitski
- 4 Tenets, Methods, and Applications of Multifractal Analysis in Neurosciences** 65
Renaud Lopes and Antoine Ayache

Part II Fractals in Neuroanatomy and Basic Neurosciences

- 5 Fractals in Neuroanatomy and Basic Neurosciences: An Overview** 83
Antonio Di Ieva
- 6 Morphology and Fractal-Based Classifications of Neurons and Microglia** 91
Audrey L. Karperien and Herbert F. Jelinek
- 7 The Morphology of the Brain Neurons: Box-Counting Method in Quantitative Analysis of 2D Image** 109
Nebojša Milošević
- 8 Neuronal Fractal Dynamics** 127
Małgorzata Kołodziej and Przemysław Waliszewski

9	Does a Self-Similarity Logic Shape the Organization of the Nervous System?	137
	Diego Guidolin, Cinzia Tortorella, Raffaele De Caro, and Luigi F. Agnati	
10	Fractality of Cranial Sutures	157
	Takashi Miura	
11	The Fractal Geometry of the Human Brain: An Evolutionary Perspective	169
	Michel A. Hofman	
 Part III Fractals in Clinical Neurosciences		
12	Fractal Analysis in Clinical Neurosciences: An Overview	189
	Antonio Di Ieva	
13	Fractal Analysis in Neurological Diseases	199
	Francisco J. Esteban, Leticia Díaz Beltrán, and Antonio Di Ieva	
14	Fractal Dimension Studies of the Brain Shape in Aging and Neurodegenerative Diseases	213
	Luduan Zhang and Guang H. Yue	
15	Fractal Analysis in Neurodegenerative Diseases	233
	Daniel Pirici, Laurentiu Mogoanta, Daniela Adriana Ion, and Samir Kumar-Singh	
16	Fractal Analysis of the Cerebrovascular System Physiopathology . .	251
	Martin Soehle	
17	Fractals and Chaos in the Hemodynamics of Intracranial Aneurysms	263
	Gábor Závodszy, György Károlyi, István Szikora, and György Paál	
18	Fractal-Based Analysis of Arteriovenous Malformations (AVMs) . .	279
	Antonio Di Ieva and Gernot Reishofer	
19	Fractals in Neuroimaging	295
	Salim Lahmiri, Mounir Boukadoum, and Antonio Di Ieva	
20	Computational Fractal-Based Analysis of MR Susceptibility-Weighted Imaging (SWI) in Neuro-oncology and Neurotraumatology	311
	Antonio Di Ieva	
21	Texture Estimation for Abnormal Tissue Segmentation in Brain MRI	333
	Syed M.S. Reza, Atiq Islam, and Khan M. Iftekharuddin	
22	Tumor Growth in the Brain: Complexity and Fractality	351
	Miguel Martín-Landrove, Antonio Brú, Antonio Rueda-Toicen, and Francisco Torres-Hoyos	

23 Histological Fractal-Based Classification of Brain Tumors 371
 Omar S. Al-Kadi and Antonio Di Ieva

24 Computational Fractal-Based Analysis of Brain Tumor Microvascular Networks 393
 Antonio Di Ieva and Omar S. Al-Kadi

25 Fractal Analysis of Electroencephalographic Time Series (EEG Signals) 413
 Wlodzimierz Klonowski

26 On Multiscaling of Parkinsonian Rest Tremor Signals and Their Classification 431
 Lorenzo Livi

27 Fractals and Electromyograms 445
 Sridhar Poosapadi Arjunan and Dinesh Kant Kumar

28 Fractal Analysis in Neuro-ophthalmology 457
 Giorgio Bianciardi, Maria Eugenia Latronico, and Claudio Traversi

29 Fractals in Affective and Anxiety Disorders 471
 Sergio Iglesias-Parro, Maria Felipa Soriano, and Antonio José Ibáñez-Molina

30 Fractal Fluency: An Intimate Relationship Between the Brain and Processing of Fractal Stimuli 485
 Richard P. Taylor and Branka Spehar

Part IV Computational Fractal-Based Neurosciences

31 Computational Fractal-Based Neurosciences: An Overview 499
 Antonio Di Ieva

32 *ImageJ* in Computational Fractal-Based Neuroscience: Pattern Extraction and Translational Research 503
 Audrey L. Karperien and Herbert F. Jelinek

33 Fractal Analysis in MATLAB: A Tutorial for Neuroscientists 523
 Juan Ruiz de Miras

34 Methodology to Increase the Computational Speed to Obtain the Fractal Dimension Using GPU Programming 533
 Juan Ruiz de Miras and Jesús Jiménez Ibáñez

35 Fractal Electronics as a Generic Interface to Neurons 553
 William J. Watterson, Saba M. Moslehi, Julian H. Smith, Rick D. Montgomery, and Richard P. Taylor

36 Fractal Geometry Meets Computational Intelligence: Future Perspectives 567
 Lorenzo Livi, Alireza Sadeghian, and Antonio Di Ieva

Erratum E1

Index 581

Contributors

Luigi F. Agnati, MD, PhD Department of Biomedical Sciences, University of Modena and Reggio Emilia, Modena, Italy

Omar S. Al-Kadi Institute of Bioengineering, Ecole Polytechnique Fédérale de Lausanne (EPFL), Lausanne, Switzerland
King Abdullah II School for IT, University of Jordan, Amman, Jordan

Sridhar Poosapadi Arjunan School of Engineering, RMIT University, Melbourne, Australia

Antoine Ayache CNRS 8524 UMR, Lille 1 University, Sciences and Technology, Villeneuve d'Ascq, France

Leticia Díaz Beltrán Department of Experimental Biology, School of Sciences, University of Jaén, Jaén, Spain

Giorgio Bianciardi, MS, MD, PhD Department of Medical Biotechnologies, University of Siena, Siena, Italy

Mounir Boukadoum, PhD. Department of Computer Science, University of Quebec at Montreal, Montreal, QC, Canada

Antonio Brú Department of Applied Mathematics, Universidad Complutense de Madrid, Madrid, Spain

Raffaele De Caro Department of Molecular Medicine, University of Padova, Padova, Italy

Juan Ruiz de Miras Computer Science Department, University of Jaén, Jaén, Spain

Antonio Di Ieva, MD, PhD Neurosurgery Unit, Faculty of Medicine and Health Sciences, Macquarie University, Sydney, NSW, Australia

Department of Neurosurgery, Royal North Shore Hospital, Sydney, Australia

Garvan Institute of Medical Research, Sydney, Australia

Medical University of Vienna, Vienna, Austria

University of Toronto, Toronto, ON, Canada

Francisco J. Esteban Department of Experimental Biology, School of Sciences, University of Jaén, Jaén, Spain

Diego Guidolin, PhD Department of Molecular Medicine, University of Padova, Padova, Italy

Michel A. Hofman, PhD Netherlands Institute for Neuroscience, Royal Netherlands Academy of Arts and Sciences, Amsterdam, The Netherlands

Jesús Jiménez Ibáñez Computer Science Department, University of Jaén, Jaén, Spain

Antonio Jose Ibáñez-Molina Department of Psychology, University of Jaén, Jaén, Spain

Khan M. Iftekharuddin Vision Lab, Department of Electrical and Computer Engineering, Old Dominion University, Norfolk, VA, USA

Sergio Iglesias-Parro Department of Psychology, University of Jaén, Jaén, Spain

Daniela Adriana Ion, MD, PhD Department of Physiopathology, University of Medicine and Pharmacy Carol Davila, Bucharest, Romania

Atiq Islam Applied Research, Ebay Inc., San Jose, CA, USA

Herbert F. Jelinek School of Community Health & Centre for Research in Complex Systems, Charles Sturt University, Albury, Australia

György Károlyi Institute of Nuclear Techniques, Budapest University of Technology and Economics, Budapest, Hungary

Audrey L. Karperien School of Community Health & Centre for Research in Complex Systems, Charles Sturt University, Albury, Australia

Włodzimierz Klonowski, PhD, DSc Nalecz Institute of Biocybernetics and Biomedical Engineering, Polish Academy of Sciences, Warsaw, Poland

Małgorzata Kołodziej, MD Department of Neurosurgery, Justus-Liebig University, Giessen, Germany

Dinesh Kant Kumar School of Engineering, RMIT University, Melbourne, Australia

Samir Kumar-Singh, MD, PhD Molecular Pathology Group, Faculty of Medicine and Health Sciences, Cell Biology & Histology and Translational Neuroscience Department, University of Antwerp, Antwerp, Belgium

Salim Lahmiri, PhD Faculty of Engineering, Centre for Pattern Recognition and Machine Intelligence, Concordia University, Montreal, QC, Canada

Maria Eugenia Latronico, MD Department of Medical Sciences, Surgery and Neurosciences, University of Siena, Siena, Italy

Lorenzo Livi Department of Computer Science, Ryerson University, Toronto, ON, Canada

Renaud Lopes Clinical Imaging Core Facility (CI2C), INSERM U1171, Lille University Hospital, Lille, France

Miguel Martín-Landrove Centre for Molecular and Medical Physics, Faculty of Science, Universidad Central de Venezuela, Caracas, Venezuela

Centre for Medical Visualization, National Institute for Bioengineering, Universidad Central de Venezuela, Caracas, Venezuela

Nebojša Milošević, PhD Department of Biophysics, School of Medicine, KCS-Institute of Biophysics, University of Belgrade, Belgrade, Serbia

Takashi Miura, MD, PhD Kyushu University, Graduate School of Medical Sciences, Fukuoka, Japan

Laurentiu Mogoanta, MD, PhD Department of Histology, University of Medicine and Pharmacy of Craiova, Craiova, Romania

Rick D. Montgomery, MD Physics Department, University of Oregon, Eugene, OR, USA

Saba M. Moslehi Physics Department, University of Oregon, Eugene, OR, USA

György Paál Department of Hydrodynamic Systems, Budapest University of Technology and Economics, Budapest, Hungary

Daniel Pirici, MD, PhD Department of Research Methodology, University of Medicine and Pharmacy of Craiova, Craiova, Romania

Gernot Reishofer, MD, PhD Department of Radiology, MR-Physics, Medical University of Graz, Graz, Austria

Syed M.S. Reza Vision Lab, Department of Electrical and Computer Engineering, Old Dominion University, Norfolk, VA, USA

Antonio Rueda-Toicen Centre for Medical Visualization, National Institute for Bioengineering, Universidad Central de Venezuela, Caracas, Venezuela

Algorithmic Nature Group, LABORES for the Natural and Digital Sciences, Paris, France

Alireza Sadeghian Department of Computer Science, Ryerson University, Toronto, ON, Canada

Julian H. Smith Physics Department, University of Oregon, Eugene, OR, USA

Martin Soehle, MD, PhD, MHBA Department of Anesthesiology and Intensive Care Medicine, University of Bonn, Bonn, Germany

Maria Felipa Soriano Department of Mental Health Service, Hospital San Agustín de Linares, Linares (Jaén), Spain

Branka Spehar School of Psychology, University of New South Wales, Sydney, NSW, Australia

Tatjana Stadnitski, MD, PD Institute of Psychology and Education, University of Ulm, Ulm, Germany

István Szikora, MD Department of Neurointerventions, National Institute of Clinical Neurosciences, Budapest, Hungary

Richard P. Taylor Department of Physics, University of Oregon, Eugene, OR, USA

Francisco Torres-Hoyos Physics Department, University of Córdoba, Córdoba, Colombia

Cinzia Tortorella Department of Molecular Medicine, University of Padova, Padova, Italy

Claudio Traversi, MD Department of Medical Sciences, Surgery and Neurosciences, University of Siena, Siena, Italy

Przemysław Waliszewski Department of Urology, Urological Unit, Hufeland Clinics GmbH, Bad Langensalza, Germany

The Będlewo Institute for Complexity Research, Poznań, Poland

William J. Watterson Physics Department, University of Oregon, Eugene, OR, USA

Guang H. Yue, PhD Human Performance and Engineering Research, Kessler Foundation, West Orange, NJ, USA

Department of Physical Medicine and Rehabilitation, Rutgers New Jersey Medical School, Rutgers, The State University of New Jersey, Newark, NJ, USA

Gábor Závodszyk Department of Hydrodynamic Systems, Budapest University of Technology and Economics, Budapest, Hungary

Luduan Zhang, PhD LZ Biomedical, LLC, Broomfield, CO, USA

Part I
Introduction to Fractal Geometry
and Its Applications to Neurosciences

Chapter 1

The Fractal Geometry of the Brain: An Overview

Antonio Di Ieva

Abstract The first chapter of this book introduces some history, philosophy, and basic concepts of fractal geometry and discusses how the neurosciences can benefit from applying computational fractal-based analyses. Further, it compares fractal with Euclidean approaches to analyzing and quantifying the brain in its entire physiopathological spectrum and presents an overview of the first section of the book as well.

Keywords Brain • Fractals • Fractal geometry • Fractal analysis • Multifractal • Neurosciences • Fractal dimension • Lacunarity • Self-similarity • Scaling

You cannot explain the third dimension to ones living in a 2D world.

Neither can you explain the fractal dimension to some counting only in integer numbers.

You cannot describe the light to people living in the darkness.

Or ask people to think out of the box, if they don't know anything else than the box itself.

Sharing knowledge is the final aim, teaching is an illusion.

You can just hope to ignite stimuli in the right minds.

(A.D.I., Caserta, Italy, March 2015)

A. Di Ieva, MD, PhD

Neurosurgery Unit, Faculty of Medicine and Health Sciences, Macquarie University,
Sydney, NSW, Australia

Garvan Institute of Medical Research, Sydney, NSW, Australia

Medical University of Vienna, Vienna, Austria

University of Toronto, Toronto, ON, Canada

e-mail: diieva@hotmail.com

© Springer Science+Business Media New York 2016

A. Di Ieva (ed.), *The Fractal Geometry of the Brain*, Springer Series in
Computational Neuroscience, DOI 10.1007/978-1-4939-3995-4_1

1.1 From the *Fractal Geometry of Nature* to Fractal Analysis in Biomedicine

Among the cycling trends characterizing how humans have built knowledge over time, relatively recent applications of the reductionist approach have allowed for great discoveries and paradigm shifts in several modern scientific disciplines. Even given the limits of reductionism, this approach has favored development of very specific individual topics and allowed for important advances as diverse as space exploration and the discovery of DNA. Ironically, though, the reductionist approach, encroaching on its own heels, has also ushered in a more holistic view of nature, while several disciplines focusing on the study of very specific and restricted topics have reemerged in the *omics* (a suffix referring to the concept of wholeness, or “completion”): genomics, metabolomics, proteomics, connectomics, etc. Genomics, for instance, in attempting to define and explain individual pathologies by analyzing the genome, spurred further need to analyze each gene product (the proteins), spawning the age of proteomics. Fortunately, the even more detailed view of the nature of things has still left space for the general idea that everything is interconnected.

Fractal geometry, even though it developed from a holistic view of nature, as theorized by fractal pioneer Benoit Mandelbrot (1924–2010), has had a similar destiny. As a field, it underwent rapid development of methods and ideas, culminating in the discipline of “fractalomics” [17], a view wherein everything is fractal, where *Fractals Everywhere* (to use the title of Michael Barnsley’s book [3]), where everything can be explained or at least described by means of fractal geometry. This view, however, is inadequate. As emphasized by Mandelbrot in his seminal *The Fractal Geometry of Nature* [23], fractals are not everywhere and are not really a panacea [21]. As happens with so many theories, the initial enthusiasm and explosion of scientific publications, conferences, and ideas has been scaled down, owing at least in part to intrinsic limitations of the methods and pitfalls described by both “fans” and critics of the latest fashion.

The application of fractalomics to biomedical science has followed essentially within this path. In the beginning, fractal analysis was applied to the study of histological and/or microscopic images [5, 6, 33], planting roots in several branches of biology and medicine. Yet substantial amounts of research and numerous publications regarding fractals in biomedicine notwithstanding, fractal geometry was not fully introduced into the lexicon of physicians, generally known as reluctant to accept paradigm shifts. In neuroscience in particular, as widely described in this book, several applications of “neuro-fractalomics” have been used to explain and quantify physiological and pathological phenomena, yet a common protocol, which might give fractal analysis the dignity of a consolidated scientific methodology, is still lacking.

One contributor to the slow transition to clinical application in biomedicine and neuroscience is a practical one. The substantial work on fractals noted above is not all readily accessible to the clinical world. This is evident when one crosses the

keywords “fractal” and “brain” on PubMed, which provides about 600 articles, or on PubMed Central, which yields a few thousand, neither of which gives sufficient merit to the real weight that fractal analysis has had in the field of neuroscience and its potential for further investigation [8, 9]. Fractal geometry is a relatively new paradigm and, like many new paradigms, has required, and still requires, a long time to be “metabolized,” to become accepted by the general audiences of physicians, scientists, and laypeople. Thus, this book links together several experts in the field to ignite new ideas and potential collaborations for a new perspective on the study of the human brain in its entire physiopathological spectrum. This first chapter introduces fractal geometry and fractal analysis and briefly outlines the contents of the book’s first section on the rudiments of fractal analysis in neuroscience.

1.2 From Euclid to the Fractal Metrology

Fractal geometry is a mathematical and philosophical model with strengths and weaknesses. Mandelbrot coined the word “fractal” from the Latin adjective *fractus* (meaning broken, or fractured), with the corresponding Latin verb *frangere* signifying “to break,” or to create irregular fragments [23]. As is well known to the readers of Mandelbrot’s works, fractal geometry was initially developed on the basis of what were considered “monsters” of Euclidean geometry: mathematical or natural phenomena not fully explicable or quantifiable by means of ideal, platonic, and/or Euclidean approaches. Mandelbrot “visited” galleries of such monsters, populated by bizarre mathematical creatures described by Cantor, Peano, Hausdorff, Sierpinski, and Urysohn, among several other mathematicians, and drafted a manifesto of fractal geometry based upon a body of well-defined laws and coherent principles, including those derived from chaos theory [32] “to bear resemblance to pathologic entities or mathematical monsters, [...] despite, or owing to, their beauty, richness and fascinating shapes” [20].

Similar to the way that music can be considered a universal language [7], fractal geometry can be seen as a universal language by which nature can be explained, or at least described and quantified. Expanding the music analogy, the “notes” of fractal geometry are fractal dimensions (denoted FD, D_F , or simply D , in this book) arrived at through fractal analysis. D can be considered a dimension, a quantifier, a parameter, an estimator, and so on, but is essentially a number that quantifies something. This “something” can be the “geometrical complexity” or the “space-filling property” of an object or a pattern, the roughness of a surface, or the variation of a time series, for instance, where the more irregular a phenomenon or the more an object or pattern fills the space in which it is embedded (e.g., the microvascular network in a tissue), the higher the D [23]. D is also a continuous variable, easy to use and compare by means of mathematical and statistical methods, and suited for describing the physiological gradualism of natural phenomena in a “non-saltatory” manner. There are different methods to compute D , the box-counting algorithm being the most basic and frequently used one (see Chaps. 2, 3, 7, and 32 among others).

In his milestone paper on Britain's coastline, published in the journal *Science* in 1967 [24], Mandelbrot defined the concepts of fractal dimension and self-similarity. According to Mandelbrot's definition, the topological dimension (D_T), which can be informally understood as the commonly known dimensions of typical (*Euclidean*) geometry, is always an integer, but D need not be an integer. Expanding further, a fractal is a set for which D (or more specifically, a measure known as the Hausdorff-Besicovitch dimension) strictly exceeds the topological dimension [23].

The value of D arrived at for a particular phenomenon is an intrinsic and unique value of that phenomenon itself, but represents an "averaging" of variation in data [28]. The fact that it is strictly linked to the geometrical complexity of an object does not mean that it is the object. Different objects can share the same D value, and a series of objects with the same D do not necessarily belong to the same class [34]. It should also be emphasized that owing to logarithmic calculations involved in determining a D value (see Chaps. 2 and 3, for details), small changes in D can correspond to big differences in the shape of an object. In sum, D describes the overall structure and complexity of an object, but does not tell the shape of the object (neither can a Euclidean dimension). In principle, this is similar to other metrics, such as the unit meter, for instance, which can quantify the height of objects or persons, where a chair and table can have the same height in meters but are not the same object, just as people are unique but may have the same height and weight values. These general principles apply to D determined for other phenomena such as time series as well as objects.

The universality of fractal geometry is shown by the fact that the same concepts or methods may be applied to completely different disciplines, from meteorology to medicine, from physics to biology. As an example, the box-counting method, despite having several intrinsic limitations, can be used to analyze the geometrical complexity of a microvascular network of a tumor as well as the distribution of trees in a forest, or the surface roughness of a cell as well as the coastline of an island.

Of course, as in every model, there are limitations. Despite being a "universal language," fractal geometry has not proposed or found any holy grails nor, as alluded to above, is it a cosmological constant able to describe and/or explain everything. The concepts and methods of fractal analysis applied to "biomedical fractalomics," for example, have neither explained nor defeated cancer, and "neuro-fractalomics" has not unveiled the great mysteries of the brain. A positivist view of fractal geometry might lead to its own failure as a model.

Moreover, mathematicians may argue that the existence of a fractal pattern is the *conditio sine qua non* for applying fractal analysis, and, from a strictly mathematical point of view, this is correct. Mathematical fractals are invariant under certain transformations of scale (self-similar) infinitely, whereas natural "fractals" are self-similar within limits [24]. To elaborate, it is not appropriate to extrapolate for biological systems (e.g., the brain) or features (e.g., cell morphology or event frequency) beyond certain limits of investigation; rather, natural fractal or fractal-like patterns can be considered statistically self-similar only within upper and lower limits (the scaling window), in which the relationship between the scale of observation and measured size or length can be established [19]. Indeed, it has been proposed that

biological fractality can only be considered to be supported by the evidence when the experimental scaling range covers at least two orders of magnitude [17, 38].

Despite the reality of limited or statistical self-similarity, however, fractal analysis of biological phenomena is viable. The box-counting method, for example, offers a quantitative parameter, the box-counting dimension, which is related to the space-filling property (or the “level of occupancy”) of an analyzed object regardless of whether the object is fractal, pseudo-fractal, quasi-fractal, semi-fractal, super-fractal, or any of the other definitions that have been proposed. In this respect, it is difficult to overemphasize that fractal geometry is a model that, like other models, can be an approximation. It is reasonable to use fractals as models of natural objects in the same way that a perfect circle is often used to represent the cross section of an artery, for example [2].

Focusing the interest on biomedicine, fractal geometry has dual usefulness: (1) providing a unique model of analysis to attempt to explain the peculiarity and singularity of phenomena and (2) proposing a system of universal quantification, a simple tool used to describe natural things in an appropriate and more realistic way.

These two points require some clarification. Every phenomenon has its peculiar features, its own “fingerprint” of features, which makes it unique or different from others. As described in Chap. 24, the pattern of distribution of microvessels in tumors, for example, is different from the one found in normal tissues. In the same way, neoplastic cells have different shapes and features in comparison to normal cells. Similarly, electroencephalographic records of healthy individuals have their own specific and unique features that are different from those of patients affected by epilepsy (see Chap. 25). In general, each phenomenon has its spatiotemporal peculiarity, which may be very difficult to describe in terms of Euclidean geometry or nonlinear mathematics but more readily described in terms of fractal geometry.

In such a view, fractal geometry indeed has a double role: on one hand, it aims to outline the “cutoff” which separates different phases of transition, from physiologic to pathological states for example, with an increase or decrease in geometrical complexity or space-filling properties. On the other hand, fractal analysis provides valid, objective, and more realistic tools of measurement.

The objectiveness of the parameters is of course related to the standardization of the methods of data acquisition (e.g., image resolution or scale window limits); otherwise, comparing outputs computed by means of a heterogeneous dataset may lead to various (and wrong) results (see the “black box” concept in Chap. 12). This has been (and still is) one of the most notorious pitfalls encountered in clinical applications of fractal analysis. But this problem is also quite “ancient”; indeed in the history of measurement, samples have always been collected or standardized in order to be used as a reference, such as the international prototype kilogram, deposited at the International Bureau of Weights and Measures, or, the second, defined as the *second* division of the hour by 60 (the first division being the minute) or, more precisely, the duration of 9,192,631,770 cycles of radiation corresponding to the transition between two energy levels of the caesium-133 atom at rest at a temperature of 0 K.

1.3 The Fractal Geometry of the Brain

The title of this book implicitly assumes that the brain is a fractal structure and that the fractal geometry of the brain exists. This might be wrong, or at least misleading, as several mathematicians do not consider fractal geometry as a formal geometry in the traditional sense. In general, geometry was developed for the measurement of the earth, as the Greek etymology of the word suggests, and is the branch of mathematics related to the analysis of shape, size, relative positions, and properties of objects. Although developed for practical purposes, traditional geometry is not sufficient to fully describe the complexity of physical phenomena. Regardless of the existing controversies on the nature of fractal geometry and the distinctions between fractal and formal Euclidean geometry, both serve practical purposes.

Whereas the concepts and rules of Euclidean geometry may be considered adequate for an ideal world [18], fractal geometry provides tools of analysis more appropriate for the real world. It searches for the generators, or common rules, that nature, for entropic economy, adopts for phenomena which can be otherwise apparently completely different and through fractal analysis provides valid, objective, and more realistic tools like the fractal dimension, to analyze shapes and properties of natural objects. As stated by Mandelbrot: “Many patterns of Nature are so irregular and fragmented, that, compared with Euclid—a term used in this work to denote all of standard geometry—Nature exhibits not simply just a higher degree but altogether a different level of complexity. The existence of these patterns challenges us to study those forms that Euclid leaves aside as being *formless*, to investigate the morphology of the *amorphous*” [23].

According to Mandelbrot, the fractal dimension has been “injected” into several different scientific fields [25], from physics to geomorphology and from economics to biology. Among a myriad of examples, fractals have been used to analyze Internet traffic [1], econometrics time series [22], DNA base sequences [31] and packing of chromatin in the human genome [16], recursive genome function [30], social networks [35], ecosystems [4], metabolite exchange [40], automatic keyword extraction in text [27], human gait [39], and even the architecture of Gothic cathedrals and the neurobiological mechanisms of human creativity [11]. The application of fractal geometry to the neurosciences has been the consequence of a new trend of research focused on the analysis of the intrinsic complexity of biological systems, which have, according to Ludwig von Bertalanffy’s *weltanschauung*, a tendency to form multilevel structures of “systems within systems,” each of which forms a “whole in relation to its parts and is simultaneously part of a larger whole” [12]. Fractal geometry represents a holistic framework to explain biological ontogenesis involving a fractal hierarchy, from a single cell to the function of the human brain [13, 37].

With the intention to avoid philosophical or mathematical diatribe on the meaning of fractal geometry or any speculations on the real fractal geometry of nature and of the brain, this book is essentially focused on the translational practical applications of fractal analysis to the neurosciences. Computational neuroscience is interdisciplinary, where different fields, such as cognitive science and computer science, mathematics and physics, psychology, and neurobiology, converge in the study of

the nervous system. Fractal analysis can be seen as a tool, or a methodology, of computational neuroscience. *Computational fractal-based analysis* is most likely the most correct term, considering that in this perspective fractals “simply” become a tool in the hands of the scientists dealing with biomedical sciences. Putting fractal analysis under the same umbrella as all the computational methods used to analyze the brain can be considered wrong, and the use of D as a universal quantifier to describe every natural object can be misleading. But it is true that fractal geometry offers powerful tools for an objective and more realistic description of complex systems, such as the brain, and that some estimators, such as the box-counting dimension, are robust quantitative parameters. Despite continuous debates about the use of the term fractal to describe natural objects, fractal geometry is still a useful *tool* to describe and quantify the inherent complexity of objects [23], including neurons and the brain itself. A tool is a tool, and as famously stated by Lars Leksell, the Swedish neurosurgeon who pioneered stereotaxis and radiosurgery, “A fool with a tool is still a fool.” It rests upon the operator how to use such a powerful tool to explain phenomena and quantify natural things.

Of course fractal analysis does not “simply” offer some quantitative parameters. D and related parameters obtained through fractal analysis, for example, with all their pros and cons, are powerful *geometrical* tools. But fractal geometry has something more than a *normal* geometry. The concept of self-similarity, the repetition of iterations generating natural patterns, the scale invariance, the multifractal scaling, the strange attractors, and the chaotic patterns are all concepts with much more intriguing roots. The elegant beauty of the Koch curve (the “snowflake”) and the sublime fascination of the Mandelbrot set evoke something more than mere rules and equations of other descriptive geometries. It is not by coincidence that fractal patterns have been found in music and visual arts, and computer graphics have offered a true exploitation of fractal art.

I have personally always been fascinated by Hofman’s concept that “the macroscopic organization of the brain in mammals is governed by a few simple generative rules and that these internal factors of brain design, bearing no relation to the selective reasons of initial enlargement, may be the primary determinants directing the evolution of the brain” [14]. The repetition of patterns to microscopic, mesoscopic, and macroscopic levels is a peculiarity of mathematical fractals, but natural objects own such a peculiarity in a finite range, and this cannot ever be emphasized enough. This resolution scaling effect applies to cell morphometry (including neuron morphometry) and overall brain morphometry. Convoluted brain tissue, tortuous brain vessels, ramified neural cells, and jagged electroencephalographic records, for instance, all resist description by Euclidean and other more traditional geometries, yet, within their respective limits, yield gracefully to the universal language of fractal analysis.

As the old adage goes, “not everything that matters can be measured and not everything that can be measured matters.” But it is also true that if it is worth doing, it is worth measuring. Fractal geometry offers a novel perspective on the description and measurement of nature. Nature shows complexity, roughness, apparent chaos and mystery, and beauty—the sublime. And what is there in nature more complex, apparently chaotic and mysterious, beautiful, and sublime than the human brain?

1.4 Fractal Dimension and Neurosciences

At this point it is clear that natural and especially biological morphologies are irregular, and, when we can assess them (using computers) as distributions of points in space and time, we can often describe and quantitate them rather compactly by the methods of fractal analysis [15, 29].

But how is fractal analysis performed? As expressed in the preface to this book, the first section offers one answer to this question by outlining key tenets of fractal analysis. In particular, Chaps. 2, 3, and 4 explain basic concepts of fractal geometry (fractal dimension, self-similarity, and scaling) and introduce specific methods and examples of practical applications of fractal analysis to neuroscience.

The fractal dimension is a powerful tool for characterizing features, but its meaning has to be fully understood in order to avoid misuse of fractal analysis in biomedicine [26]. Several important limitations, caveats, and recent methodological considerations are therefore also discussed in those chapters. In addition, supplementary methods of fractal analysis are discussed. In Chap. 2, for instance, *Audrey Karperien and Herbert Jelinek* discuss lacunarity, a measure that complements D . In box counting, D measures *how much* the object (or data) fills the space [10], but lacunarity measures *how* the data fill the space [23, 36]. Other fundamental parameters and concepts of fractal analysis, such as the Hurst coefficient (H), the scaling exponent (α), the power exponent (β), the fractional differencing parameter, and fractal noise, are discussed in Chap. 3 by *Tatjana Stadnitski*. While Chap. 2 focuses mainly on applications of fractal analysis to images, Chap. 3 is essentially dedicated to time series analysis. Finally, Chap. 4, by *Renaud Lopes and Antoine Ayache*, discusses limitations of the “mono-fractal” approach, which describes phenomena by means of a single D value, introducing multifractal behavior measured by a spectrum of D values.

The reader who is already an expert in fractal analysis, familiar with basic concepts, and up to date on methodological developments may jump directly to Section II of this book, but less versed readers can read the next three chapters in order to comprehensively understand the rest of the book wherein specific applications of fractals in basic and clinical neurosciences are discussed.

References

1. Abry P, Baraniuk R, Flandrin P, Riedi R, Veitch R, Veitch D. Multiscale nature of network traffic. *IEEE Signal Proc Mag.* 2002;3:28–46.
2. Baish JW, Jain RK. Fractals and cancer. *Cancer Res.* 2000;60:3683–8.
3. Barnsley MF. *Fractals everywhere*. New York: Academic Press; 1988.
4. Brown JH, Gupta VK, Li BL, Milne BT, Restrepo C, West GB. The fractal nature of nature: power laws, ecological complexity and biodiversity. *Philos Trans R Soc Lond B Biol Sci.* 2002;357:619–26.
5. Cross SS. Fractals in pathology. *J Pathol.* 1997;182:1–8.

6. Cross SS. The application of fractal geometric analysis to microscopic images. *Micron*. 1994;25:101–13.
7. Di Ieva A. Memetics in neurosurgery and neuroscience. *NeuroQuantology*. 2008;6:182–93.
8. Di Ieva A, Grizzi F, Jelinek H, Pellionisz AJ, Losa GA. Fractals in the neurosciences, part I: general principles and basic neurosciences. *Neuroscientist*. 2013;20:403–17.
9. Di Ieva A, Esteban FJ, Grizzi F, Klonowski W, Martin-Landrove M. Fractals in the neurosciences, part II: clinical applications and future perspectives. *Neuroscientist*. 2015;21:30–43.
10. Gazit Y, Berk DA, Leunig M, Baxter LT, Jain RK. Scale-invariant behavior and vascular network formation in normal and tumor tissue. *Phys Rev Lett*. 1995;75:2428–31.
11. Goldberger AL. Fractals and the birth of gothic: reflections on the biologic basis of creativity. *Mol Psychiatry*. 1996;1:99–104.
12. Grizzi F, Chiriva-Internati M. The complexity of anatomical systems. *Theor Biol Med Model*. 2005;2:26.
13. Hermansen TD, Ventegodt S, Rald E, Clausen B, Nielsen ML, Merrick J. Human development I: twenty fundamental problems of biology, medicine, and neuro-psychology related to biological information. *Sci World J*. 2006;6:747–59.
14. Hofman MA. The fractal geometry of convoluted brains. *J Hirnforsch*. 1991;32:103–11.
15. Keipes M, Ries F, Dicato M. Of the british coastline and the interest of fractals in medicine. *Biomed Pharmacother*. 1993;47:409–15.
16. Lieberman-Aiden E, van Berkum NL, Williams L, Imakaev M, Ragozcy T, Telling A, et al. Comprehensive mapping of long-range interactions reveals folding principles of the human genome. *Science*. 2009;326:289–93.
17. Losa GA. The fractal geometry of life. *Riv Biol*. 2009;102:29–59.
18. Losa GA. Fractal morphometry of cell complexity. *Riv Biol*. 2002;95:239–58.
19. Losa GA, Nonnenmacher TF. Self-similarity and fractal irregularity in pathologic tissues. *Mod Pathol*. 1996;9:174–82.
20. Mandelbrot BB. Les fractales, les monstres et la beauté. In: Balaubre G, editor. *L'irruption des géométries fractales dans les sciences*. Paris: Editions de l'Académie Européenne Interdisciplinaire des Sciences (AEIS); 2006. p. 317–41.
21. Mandelbrot BB. Is nature fractal? *Science*. 1998;279:783–4.
22. Mandelbrot BB. *Fractals and scaling in finance: discontinuity, concentration, risk*. New York: Springer; 1997.
23. Mandelbrot BB. *The fractal geometry of nature*. New York: W.H. Freeman; 1982.
24. Mandelbrot B. How long is the coast of Britain? Statistical self-similarity and fractional dimension. *Science*. 1967;156:636–8.
25. Mandelbrot BB. Stochastic models for the earth's relief, the shape and the fractal dimension of the coastlines, and the number-area rule for islands. *Proc Natl Acad Sci U S A*. 1975;72:3825–8.
26. Murray JD. Use and abuse of fractal theory in neuroscience. *J Comp Neurol*. 1995;361:369–71.
27. Najafi E, Darooneh AH. The fractal patterns of words in a text: a method for automatic keyword extraction. *PLoS One*. 2015;10:e0130617.
28. Normant F, Tricot C. Method for evaluating the fractal dimension of curves using convex hulls. *Phys Rev A*. 1991;43:6518–25.
29. Peitgen HO, Richter PH. *The beauty of fractals: images of complex dynamical systems*. Berlin: Springer; 1986.
30. Pellionisz AJ. The principle of recursive genome function. *Cerebellum*. 2008;7:348–59.
31. Peng CK, Buldyrev SV, Goldberger AL, Havlin S, Mantegna RN, Simons M, et al. Statistical properties of DNA sequences. *Phys A*. 1995;221:180–92.
32. Prigogine I. *Les lois du chaos*. Paris: Flammarion; 1997.
33. Rigaut JP. An empirical formulation relating boundary lengths to resolution in specimens showing “non-ideally fractal” dimensions. *J Microsc*. 1984;133:41–54.

34. Sernetz M, Gelleri B, Hofmann J. The organism as bioreactor. Interpretation of the reduction law of metabolism in terms of heterogeneous catalysis and fractal structure. *J Theor Biol.* 1985;117:209–30.
35. Strogatz SH. Exploring complex networks. *Nature.* 2001;410:268–76.
36. Tolle CR, McJunkin TR, Rohrbaugh DT, LaViolette RA. Lacunarity definition for ramified data sets based on optimal cover. *Phys A.* 2003;179:129–52.
37. Ventegodt S, Hermansen TD, Nielsen ML, Clausen B, Merrick J. Human development II: we need an integrated theory for matter, life and consciousness to understand life and healing. *Sci World J.* 2006;6:760–6.
38. Weibel ER. Design of biological organisms and fractal geometry. In: Nonnenmacher TF, Losa GA, Weibel ER, editors. *Fractals in biology and medicine*, vol. I. Basel: Birkhäuser Press; 1994.
39. West BJ, Scafetta N. Nonlinear dynamical model of human gait. *Phys Rev E Stat Nonlin Soft Matter Phys.* 2003;67:051917.
40. West GB, Brown JH, Enquist BJ. The fourth dimension of life: fractal geometry and allometric scaling of organisms. *Science.* 1999;284:1677–9.

Chapter 2

Box-Counting Fractal Analysis: A Primer for the Clinician

Audrey L. Karperien and Herbert F. Jelinek

Abstract This chapter lays out elementary principles of fractal geometry underpinning much of the rest of this book. It assumes minimal mathematical background, defines key principles and terms in context, and outlines the basics of a fractal analysis method known as box counting and how it is used to do fractal, lacunarity, and multifractal analyses. As a standalone reference, the chapter grounds the reader to be able to understand, evaluate, and apply essential methods to appreciate the exquisitely detailed fractal geometry of the brain.

Keywords Box-counting • Fractals • Fractal analysis • Lacunarity • Multifractal • FracLac • Theoretical Models

2.1 Fractal Analysis: What Does It Measure?

Fractal analysis is a way of measuring phenomena when the details of design are as important as gross morphology. It has been applied to fields as diverse as music [75], finance [10], space science [3], urban development [25], materials technology [5], geology [2], epidemiology [30, 31], and search and rescue [79], in addition to topics in this book such as signal processing (EEG/ECG) [16, 17, 41, 46], diagnostic imaging [103, 104], histology [45], tumor morphology [22], vasculature [34, 55], and overall brain structure [70]. A common thread narrows the field to a focus: the need to measure peculiar phenomena that are difficult to describe other than by noting that they tend to repeat themselves at different scales or have the property of being “self-similar.”

A.L. Karperien (✉) • H.F. Jelinek (✉)
School of Community Health & Centre for Research in Complex Systems,
Charles Sturt University, Albury, NSW, Australia
e-mail: akarperien@yahoo.com; hjelinek@csu.edu.au

Self-Similar

Being a whole that resembles a part of itself; *similar* in this term connotes similitude as in the usual definition of the word but can also mean “identical to” (i.e., a self-similar pattern may be approximately like or identical to a part of itself).

In the parlance of fractal analysis, this property is often called *complexity*, and its value in neuroscience is the remarkable feature that it can be assigned a number called a *fractal dimension* (D_F). Whereas the concept of a D_F applies to both temporal and spatial patterns, we introduce it here in terms of spatial patterns only, specifically what one can observe with one’s eyes, using the analogy of zooming in on a slide under a microscope or a digital image on a computer. In particular, this chapter is primarily about fractal analysis of digital images. In that context, for this practical, non-mathematically oriented chapter, the working definition of complexity or a D_F is a *change in detail* with *change in resolution* [66]:

Fractal Dimension (D_F)

A unitless number to measure fractal scaling as a *change in detail* with *change in scale*; strictly speaking, the number conveys that a pattern scales as a fractal if it both has meaningful detail and repeats that detail at all levels of magnification or resolution. (Section 2.3.1 explains how to quantify the *change in detail* and the *change in scale*.)

To appreciate why “detail” is emphasized in this definition of a D_F , imagine first a pattern with no detail, such as a simple line, upon which one zooms in many times to always see the same simple line—this is trivial, not fractal, scaling and what is commonly referred to as Euclidean geometry. In contrast, now imagine always seeing the same intricate pattern reproduced at every level of resolution—that is fractal scaling [23, 24]. Figure 2.1 illustrates this distinction as well as differences between theoretical and practical self-similar scaling.

Supplementary Measures in Fractal Analysis The self-similarly detailed phenomena typically quantified with fractal analysis are also often investigated using measures that complement D_F s, such as *lacunarity* and *multifractality*. Lacunarity, at the other end of the spectrum to self-similarity, measures heterogeneity, and multifractality identifies certain patterns of complexity not identifiable with the single D_F . The rest of this chapter explains the basics of how to calculate and critically evaluate all three, D_{FS} (Sect. 2.2), lacunarity (Sect. 2.4), and multifractality (Sect. 2.6), in neuroscience.

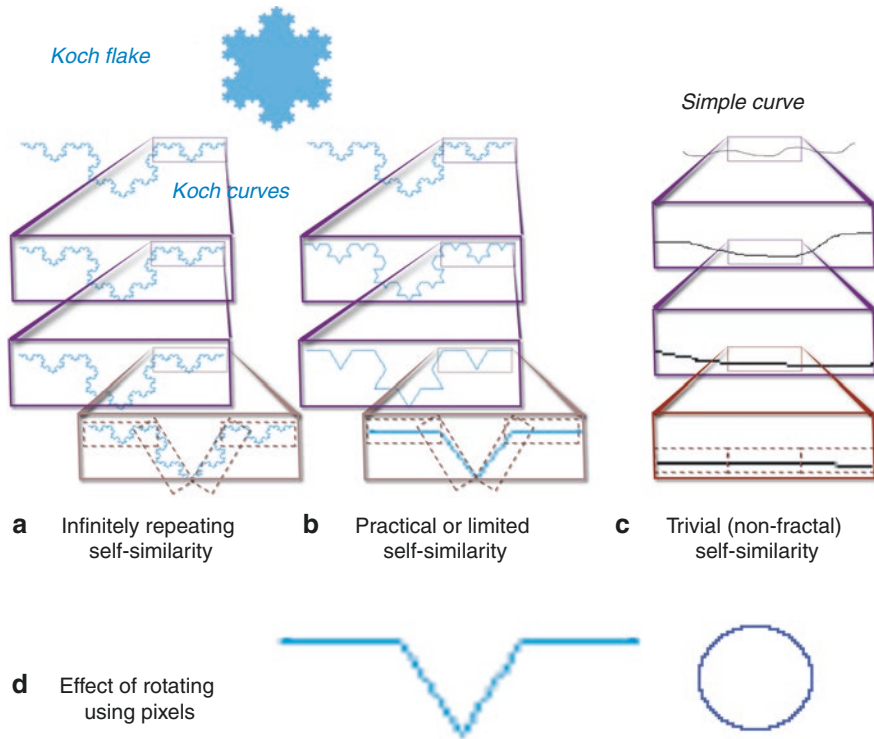


Fig. 2.1 Infinite, practical, and trivial self-similar scaling (a) Each row shows the *top image* scaled by magnifying 1/3 of the pattern to the parent size successively. The Koch Flake and Koch Curve (a side of the flake) in *a* and *b* are canonical fractals. Fractal curves, in theory, are scale independent, infinitely reproducing the same starting pattern or *unit of detail* regardless of the resolution used to inspect them. (b) The *bottom* frame shows that each scaling reproduces a defining unit of detail four times. The *bottom* frame in *b* shows the smallest unit of detail that a theoretical Koch fractal is based on, although by definition no amount of magnification would make a theoretical fractal resolve into its basic unit of detail. In contrast to a theoretical fractal, a pixel- or print-based image of a Koch fractal eventually resolves into straight-line segments. Whereas dynamic computer graphics can be made to simulate infinite scaling, fixed pixel-based digital and printed images repeat only to the practical minimum element size (pixels or printer resolution) used to render them. (c) A simple line may scale self-similarly and, in theory, infinitely, but the scaling is trivial, lacking detail, ever resolving into virtually straight segments. In contrast, fractal patterns never resolve into undetailed, smooth segments. (d) Another limitation of pixel-based images is fidelity. *Lines* in digital images differ with the angle of rotation and arcs are approximated by “steps,” because they are represented using an array of fixed pixels (fractal images generated with the ImageJ *Fractal-Generator* plugin available from <http://imagej.nih.gov/ij/plugins/fractal-generator.html>)

2.2 How Is a D_F Calculated?

One of the simplest ways to calculate a D_F is as the logarithmic ratio of *change in detail* (N) to *change in scale* (S) (Eq. 2.1):

$$D_F = \frac{\log N}{\log S} \tag{2.1}$$

A D_f relates these features to each other somewhat like “narrowness” relates length to width, or “circularity” relates circumference to diameter, but whereas people can decide how relatively narrow or circular something is by looking at it, most people cannot so easily gauge how relatively complex something is by looking at it (at least not at this point in history).

Despite not being intuitive, the change in detail with change in scale is explainable in a straightforward way. First, to understand what the change in scale, S , refers to, imagine, for example, measuring the length of a DNA strand or tortuous blood vessel, or the circumference of a crenelated plasma membrane in a digital image. Depending on the reason for measuring any of these structures, one might be interested in the net distance covered from one point to another, or, alternatively, the unraveled length. Likewise, depending on how we expect to use the measurement, we might measure the Koch Curve in Fig. 2.1 as either as long as the box enclosing it in the second row in Fig. 2.1a, or as long as the sum of all the steps along its winding path. S in Eq. 2.1 is based on the first measure, the net length:

Change in Scale (S in Eq. 2.1)

The relative change in magnification or resolution used to determine a D_f ; the reciprocal of the ratio that is multiplied by an original net size to get a new size when scaling a pattern to calculate a D_f . As an example, in Fig. 2.1a, the enclosing box’s net length is multiplied by $1/3$ in each successive row so $S=3$. The numerator in this example is 1 but this is not a restriction— S for scaling a geometric pattern into, for example, 4 pieces each $3/8$ the original size, is $8/3$.

The *change in detail*, N , for Eq. 2.1, is based on the second measure of a structure, that found by unravelling the twists or more generally, counting the details. The bottom of Fig. 2.1b shows the basic *unit of detail* that is reproduced in the Koch curve. The relationship between this detailed size and the net size is the key to understanding fractal scaling [66]:

Change in Detail (N in Eq. 2.1)

The number of times a starting pattern or unit of detail repeats at each scaling; the number of new parts in each scaled piece when S is the change in scale for calculating a D_f . In terms of the Koch Curve in Fig. 2.1(a and b), for instance, the pattern resolves into four new parts when scaled by $1/3$ the length of the parent box. In other words, when this fractal pattern is magnified by a factor of 3, the number of new parts is not the more intuitive 3 but 4.

Substituting the values for N and S for the Koch Curve into Eq. 2.1 yields a $D_f = \log 4 / \log 3 = 1.26$. Although the arrangement of the new parts is important to a pattern per se, at this point in the discussion, the number of new parts sufficiently

represents the change in detail for calculating a D_f (see Sects. 2.2.1.1, 2.3.1, and 2.4.2.1 for further discussion of the pattern itself) [23, 49].

2.2.1 Practical Points

2.2.1.1 Statistical Self-Similarity

Equation 2.1 and the definition of a D_f (Sect. 2.1) suggest that self-similar fractal scaling must be infinite and exact, but this is not the case in nature. Infinite theoretical fractals differ from finite manifestations of them. The lower limit illustrated in Fig. 2.1b, for instance, is a case of the broad rule that practical bounds generally limit fractal scaling in not just digital images but nature as well. Moreover, in addition to having limiting physical bounds, scaling in nature is typically statistical, as illustrated in Fig. 2.2, which shows three branching structures generated using the same scaling ratio applied as both exact and averaged patterns [62].

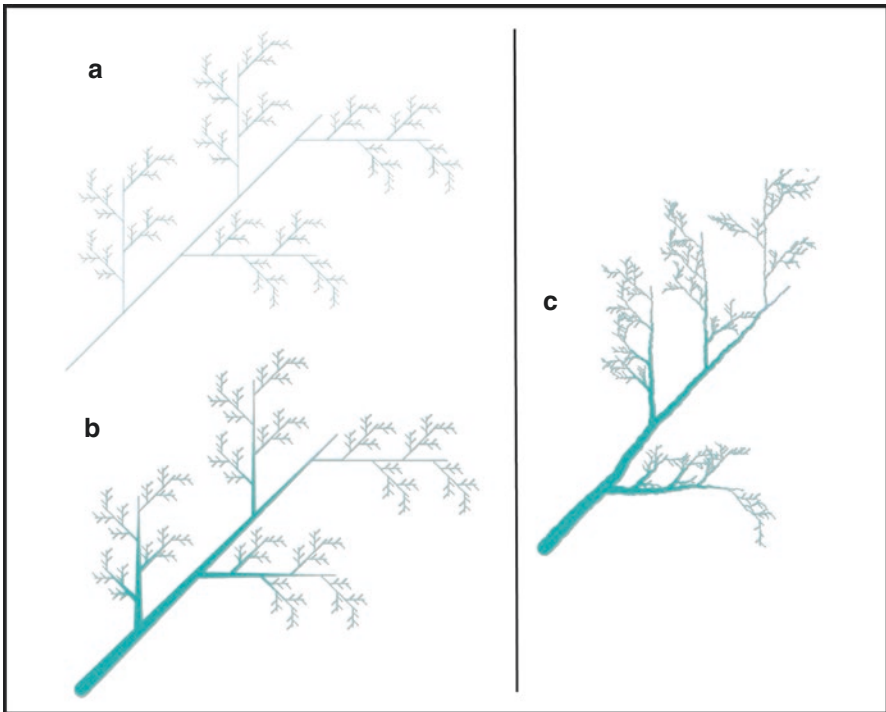


Fig. 2.2 Exactly and statistically self-similar branching. **(a)** An exactly self-similar, skeletonized, branching pattern reproducing a defining unit of detail by generating 4 new branches each $3/8$ the length of the parent, with a theoretical $D_f = \log 4 / \log (8/3) = 1.41$. **(b)** The same fundamental branching pattern as in **(a)** but represented as a silhouette; although branch diameter changes as well as length, the branching D_f based on branch length and number is the same as for **(a)**. **(c)** A statistically self-similar pattern having the same theoretical D_f as **(a)** and **(b)** that reproduces itself by generating, on average, 4 new branches $3/8$ the length of the parent (images generated using the fractal biomodeling tool *MicroMod for ImageJ*)

Statistical Self-Similarity or Scale Invariance

Self-similar scaling that resembles fractal scaling but is not necessarily infinite or not necessarily exact (or both); the type of scaling typically seen in nature; a statistically self-similar pattern, for example, may be composed of units that are similar but not necessarily identical to the whole and that repeat in a regular but not necessarily strictly defined scaling pattern.

2.2.1.2 D_F and Density

Another practical point to be aware of is how the D_F relates to density. Generally, the closer a geometric form comes to filling the space it is embedded in, the higher the D_F . To elaborate, the line in Fig. 2.1c, when scaled by 1/3, resolves into three new parts each 1/3 the length of the original enclosing box, so has a $D_F = \log 3 / \log 3 = 1.00$. Similarly, a filled plane scaled by 1/3 would have nine new parts, and $D_F = \log 9 / \log 3 = 2.00$. The Koch Curve, with a D_F of 1.26, lies between these limits. The principle that the D_F approaches the dimension of the space a pattern is embedded in holds for many fractal patterns, but does not mean the D_F measures merely density; rather, a D_F measures additional features and is not necessarily strictly correlated with density (see Sect. 2.4.2.1) [23, 65, 66].

2.2.1.3 The D_F in Neuroscience

Many phenomena in neuroscience scale statistically self-similarly or scale invariantly, with structural and functional implications on many levels. The complexity in the contour of the Koch Curve, for instance, is reminiscent of the complexity in the borders of tumor masses, the plasma membranes of individual tumor cells, and the membranes of cell parts such as nuclei within a tumor cell as observed on histopathology slides [69]. Fractal scaling also resides in tortuous and branching nervous system structures that scale into *scale-invariant parts* (e.g., neurons and other branching brain cells, tracts, and vessels) [19, 76].

Scale invariance in the nervous system sometimes extends beyond the level of discrete structures. $D_{F,S}$ for cultured rat oligodendrocytes, for instance, have been shown to be consistent over a tenfold range of magnification when comparing portions of cells, whole cells, and entire fields of cells [7]. At the same time, this is not to suggest that all ways of inspecting a phenomenon will necessarily converge on a single D_F . They may or they may not. In contrast to the consistency in cultured rat oligodendrocytes, the D_F in living organisms may vary with the level of magnification or resolution from the tissue level to the cellular level (where the cell membrane boundaries dictate the D_F) to the subcellular and molecular levels [6, 59, 61, 82]. It may also vary with the particular part of a brain structure being investigated, where there may exist several pertinent $D_{F,S}$ (e.g., different layers of newborn rat retina have distinct $D_{F,S}$ and altered oxygen exposure leads to histo-architectural

changes characterized by in some layers increased but in other layers decreased D_{FS} [87, 88]).

Whereas in the examples of Figs. 2.1 and 2.2 the scaling was known and easy to identify, in practice, scaling in biological phenomena is usually not so readily measured. Emphasizing this point, Fig. 2.3 illustrates statistical scale invariance in membrane detail and branching patterns for two brain cells.

As might be inferred from Fig. 2.3, one reason natural fractal scaling is typically not easily measured on inspection is sheer practicality. It would be tedious and time consuming to manually trace, unravel, determine the angles of, and measure the lengths and widths of parts of patterns, then identify and count them as units of

Hypertrophied
astrocyte

Hypertrophied
microglial cell

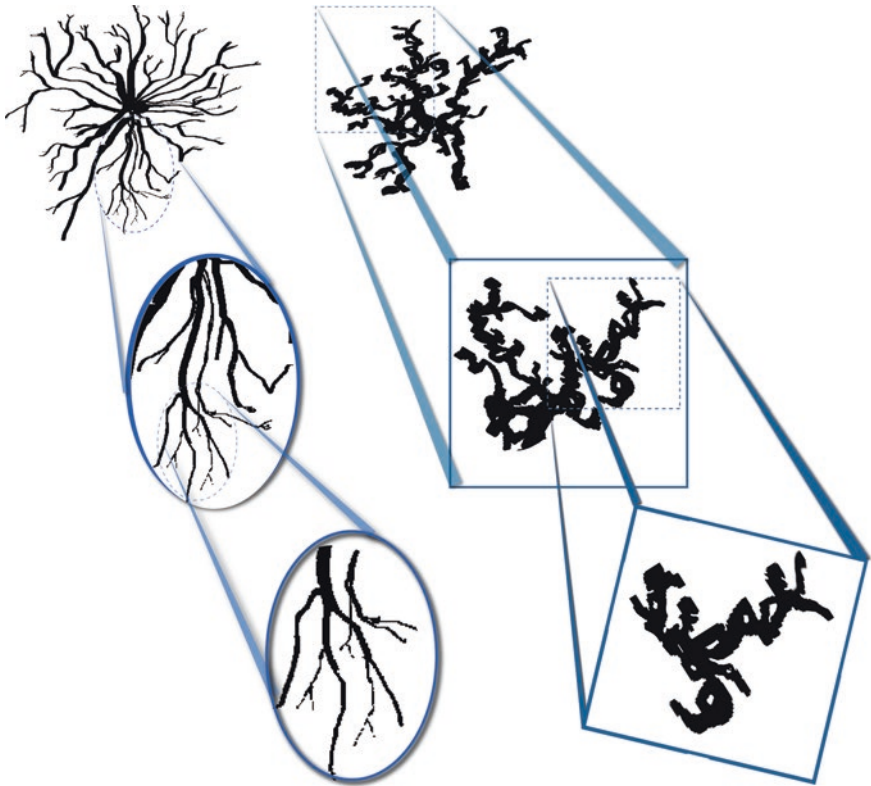


Fig. 2.3 Two types of brain cell showing statistical self-similarity as is typically found in nature. Insets highlight detail roughly repeated at each scaling. *Hypertrophied* refers to morphological changes after brain trauma compared to in normal tissue. These cell morphologies were deliberately selected to illustrate fractal scaling; in reality, both astrocytes and microglia comprise morphologically and functionally heterogeneous groups of which the cells depicted are but one type [6, 59, 91]

detail, and then further analyze the measurements to find scaling trends [37]. This applies to finding the basic unit of detail in everything within the purview of digital image analysis in fractal-based neuroscience, meaning anatomical subjects ranging from gross overall CNS structure [70] to the most tortuous of vessels, great and small [19, 76], to tracts and functional circuitry [28], and further to the finest levels within cells and the extracellular milieu [92], all represented by a variety of imaging modalities including retinal photography, radiography, histopathology, electron microscopy, etc. [20, 33, 34].

Fortunately, the tedium of finding units of detail and scaling rules can be left to software, and the joy of discovery to the analyst. Without manually measuring any part of the cells in Fig. 2.3, one can estimate their $D_{F,S}$ using any of several accessible software packages. From the freeware *FracLac for ImageJ* [50], for instance, the measured D_F of the astrocyte in Fig. 2.3 is 1.58 and the microglial cell 1.59. These values are not theoretically but empirically determined D_F s called box-counting dimensions (D_B).

Box-Counting Dimension (D_B)

A type of empirically determined, averaged D_F typically calculated using software implementing *box-counting* methods that measure proxies for the change in detail and the change in scale (see Eq. 2.1); a D_B does not identify or depend on identifying the actual unit of detail and its corresponding scaling ratio but is usually determined from the regression line for $\log N$ vs $\log S$ in Eq. 2.1.

One can analyze the fractal geometry of the brain using any of several $D_{F,S}$ (e.g., dilation, mass vs. radius [50], or local connected $D_{F,S}$ [55, 58]), but the D_B stands out as an elegant, robust, easily implemented, and often used measure; therefore, it is the chief D_F discussed in the rest of this chapter [11, 40, 42, 52, 53, 56, 76, 94].

2.3 Box Counting

What exactly does the D_B measure for the cells in Fig. 2.3? It measures the usual ratio of change in detail with change in scale, $\log N/\log S$ from Eq. 2.1, with a slight twist to measure detail indirectly. The basic method of box counting is to examine images at increasing levels of resolution by using a series of smaller and smaller sampling elements and then determine the scaling ratio from the data for the series. This is similar to how the Koch Curve in Fig. 2.1 was scaled and magnified, except that in box counting the actual scale and unit of detail are unknown, so the image is sampled using arbitrary values of S and the unit of detail is inferred from the data after the fact. Figure 2.4 illustrates the essential process for a binary image of a Koch Curve.

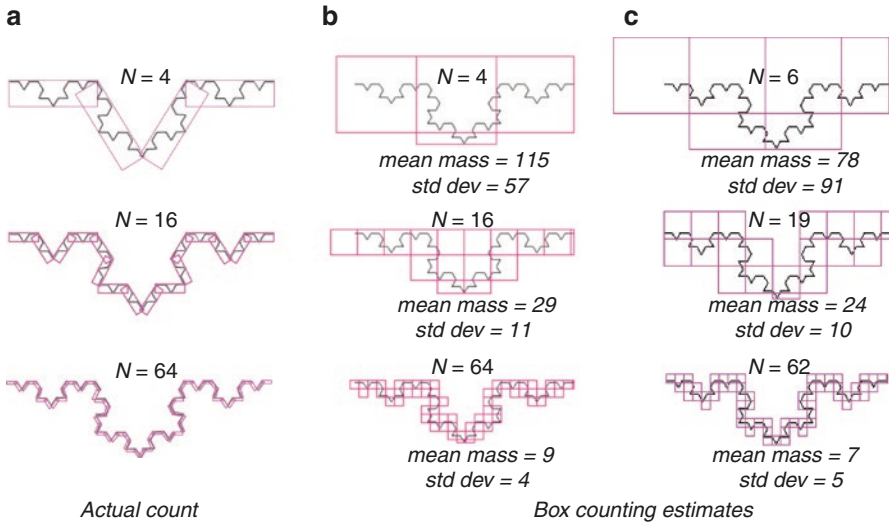


Fig. 2.4 Measuring the change in detail by box counting compared to actual counting. **(a)** A Koch Curve measured precisely by breaking it up using its known scaling (i.e., 4 new parts each enclosed in a rectangular space $1/3$ the net length of the parent). Box-counting algorithms implemented in the software (e.g., **b**, **c**) approximate this process. **(b)** Box counting based on a priori knowledge of the scaling ratio and unit of detail. **(c)** Box counting based on a guess at the scaling pattern. In the fixed grid box-counting method shown in **b** and **c** images are broken into evenly spaced *square boxes*, and N (Eq. 2.1) is the number of boxes containing foreground pixels (edge blocks in the figure are truncated for display but are counted as an entire box if they contain any foreground pixels). Another quantity, the *mass*, is the number of foreground pixels per box. N is identical for **a** and **b** at each level because **b** was set up using the Koch Curve's known scaling ratio (\log_4/\log_3) and the sample closest to ideal was selected out of many attempts at positioning the boxes. In practice, scaling features are usually unknown, and N corresponds to theoretical only in an average sense (explained in Sect. 2.3.2.1). Similarly, for mass, in **a**, the proportion of the pattern in every box is equal at any particular scale, but in typical box counting, it varies by box so that the overall mass for any box size is found by averaging. (**b** and **c** generated in *FracLac for ImageJ* using the “draw grids” option)

Binary Image

Binary in the context of fractal analysis usually refers to digital images having only two possible pixel values (usually black and white), one of which is deemed *foreground* and the other *background*. Binary images are the usual input for binary box-counting fractal analysis; binary patterns are usually extracted from original color or grayscale (Sect. 2.5) digital images. There are three basic types: *binary silhouettes* are filled patterns, *binary contours* are unfilled outlines, and *binary skeletons* are tracings of a pattern without regard for diameter (such as the branching pattern in Fig. 2.2a). Importantly, all of these binary pattern types can generally be extracted from the same image (see Sect. 2.4.2.1 for discussion of pattern type and D_B).

2.3.1 Sampling, S , and N in Box Counting

The method is called “box” counting because the sample elements are usually conceptually boxes, meaning square arrays of pixel points; however, the sampling elements can also be ovals, hexagons, rectangles, or even virtual volumes instead of areas, providing the possibility of analyzing three-dimensional (3D) images. Most box-counting algorithms do not overlap sampling elements, placing them in a “tight” or “fixed grid” pattern, but one type, sliding-box algorithms, does overlap samples. Moreover, box-counting algorithms usually sample images exhaustively but can also sample randomly, for another case in which samples may overlap [51, 84].

In all types of sampling, S for Eq. 2.1 relates to the sampling element’s size; for 2-dimensional (2D) images, S approximates the sampling unit’s length, such as the side of the square or diameter of the hexagon or oval. As an example, if the top image in Fig. 2.4a is 1 arbitrary unit, at a $1/3$ scale, the box size would be $(1 \times 1/3) = 1/3$ with S its reciprocal, 3 (see Table 2.1a) [23, 50].

N for Eq. 2.1 relates to the content of each sampling element and depends on the type of analysis being done. For fixed grid binary box counting, N is the number of boxes containing any foreground pixels, as was illustrated in Fig. 2.4b, c. For *binary mass box counting*, N is based on the average foreground pixels per box or “mass” and is used to determine fractal metrics other than the D_B , including mass dimensions, mass lacunarity (explained in Sect. 2.4), and mass multifractal spectra (explained in Sect. 2.6). For grayscale analysis, N is based on a projected volume (explained in Sect. 2.5) [14, 23, 66, 72, 73, 85].

Table 2.1 Using different box sizes and regression lines to calculate the D_B for a Koch Curve

Box counting	Box size	S	N	$\log N/\log S$	D_B
(a) Idealized	Relative ^a				
Figure 2.4a–b	$(1/3) \times 1 = 1/3$	3	4	1.26	Log
	$(1/3)^2 \times 1 = 1/9$	9	16	1.26	1.26
	$(1/3)^3 \times 1 = 1/27$	27	64	1.26	
(b) Idealized	Pixels				
Figure 2.4a, b	$(1/3) \times 81 = 27$	1/27	4	0.42	Reg
	$(1/3)^2 \times 81 = 9$	1/9	16	1.26	1.26
	$(1/3)^3 \times 81 = 3$	1/3	64	3.79	
(c) Actual	Pixels				
Figure 2.4c	27	1/27	6	0.54	Reg
Same sizes as b	9	1/9	19	1.34	1.06
Different locations than b	3	1/3	62	3.76	
(d) Actual	Pixels				
Not shown	40	1/40	5	0.44	Reg
Different sizes than Fig. 2.4	20	1/20	15	0.90	1.22
Different locations than Fig. 2.4	5	1/5	67	2.61	

Log log-log calculation, *Reg* regression line slope

^aOriginal image size = 81 pixels

2.3.2 Methodological Issues in Box Counting

Unlike in the idealized box counting with known scaling shown in Fig. 2.4a, b, in practical box counting, how a unit of detail is arranged and scales are not usually known ahead of time. As Fig. 2.4c illustrates, this is problematic because N determined with box counting varies with box size and position.

2.3.2.1 Regression Lines

To address in part the lack of knowledge of scaling ahead of time, box-counting software implementations typically apply a series of sizes and then extract a single value for the D_B through regression analysis. This is done by applying several decremented scales, counting the respective N s, and finding the D_B as the limit of the ratio for Eq. 2.1 as size gets smaller and smaller, calculated as the slope of the regression line for $\log N$ vs. $\log S$ (see Table 2.1b–d). Because the starting image size is the same for all sample sizes, S can be determined from the reciprocal of each box size (Table 2.1b–d) [23, 60, 66].

High Correlation Coefficients: Necessary but Not Sufficient By the properties of regression lines, if the relationship between $\log N$ and $\log S$ is linear for a large proportion of the sizes, the correlation coefficient (r^2) is high. However, a valid linear relationship, a high r^2 , does not validate a D_B . Indeed, several regression lines with r^2 greater than 0.99 (1.00 being perfect correlation) but widely differing slopes ($D_{B,S}$) can be found for the same control image by manipulating both the scaling between and the range of sizes [8, 49, 52, 69]. Therefore, a high r^2 is necessary for but does not guarantee high validity.

2.3.2.2 Sampling Size, Location, and Rotational Orientation Bias

To obtain a valid regression line slope, box-counting implementations have to address several factors inherent to the method itself. These include determining the smallest and largest valid sizes, the method of scaling sizes between them, and the positioning of boxes [8, 36, 69]. Figure 2.4b, c illustrated that an image can be sampled in different ways using just one gauge of sampling element, resulting in the ambiguous situation of there being many N s for one size, substantially influencing the resulting $D_{B,S}$ and mass-related measures (e.g., compare the $D_{B,S}$ from Table 2.1a–d) [26, 47, 49, 64, 80].

Related to grid location, the rotational orientation of a pattern, or from an alternative perspective, the rotational orientation of the sampling grid, can also affect the D_B [48]. As was illustrated in Fig. 2.1d, this is because pixels are arranged in 2D arrays, such that rotating an image through an arc digitally requires making approximations that can change the primary data—in sum, it can create a new pattern. The various arcs that make up a simple circle, for instance, can be shown to have different

empirical $D_{B,S}$ owing to the arrangement of pixels to emulate roundness (e.g., enlarging a single pixel wide circle reveals horizontal portions at the top and bottom and vertical portions on the sides) [48]. Note that this is a digital image-rendering phenomenon and is not the same as the feature known as *rotational invariance* measured by lacunarity (see Sect. 2.4).

Table 2.2 quantitates the phenomenon from two perspectives in the standard deviation (σ) columns. The σ - r column shows the variation comparing rotations as individual images, each rotation scanned at 12 grid locations, and σ shows the overall variation for an image considering all rotations and locations. The computational difference is evident in the first entry (*b-Koch Curve-o*), which has different ranges and standard deviations for each but the same mean. In general, the range of $D_{B,S}$ can be broad despite the variability not being correspondingly high if a small part of the arc yields a markedly different value than the rest (see *b-Koch Flake-o*, for instance).

Also, the table shows that different patterns are affected to different degrees; for example, the D_B for the filled rectangle is considerably more affected by rotation than that for the outlined, and the round (*-c*) texture samples depend less on rotation (lower standard deviation) than do square samples from the same areas on the same images. Two factors influencing variation with digital rotation are the overall shape and the density of pixels. Figure 2.5 shows the dependency on the ratio of the

Table 2.2 Effect on the D_B of rotating 800×800 pixel digital images by 30° increments (rotate function in FracLac using 12 locations × 12 rotations = 144 samples per image)

Image	μ - r	$D_{B,R}$			$D_{B,T}$		
		Min- r	Max- r	σ - r	Min	Max	σ
b-Koch Curve-o	1.25	1.24	1.26	0.005	1.22	1.29	0.022
b-Koch Flake-o	1.27	1.22	1.29	0.001	1.21	1.30	0.020
b-Rectangle-o	1.02	1.02	1.02	0.001	0.99	1.04	0.019
b-Rectangle-f	1.85	1.74	1.85	0.048	1.72	1.91	0.055
b-Mic-o	1.52	1.52	1.52	0.002	1.50	1.57	0.022
b-Mic-f	1.59	1.58	1.60	0.003	1.57	1.63	0.021
b-Ast-o	1.59	1.57	1.59	0.009	1.55	1.62	0.021
b-Ast-o	1.58	1.58	1.60	0.008	1.56	1.61	0.020
g-TEM-s	1.61	1.58	1.67	0.046	1.56	1.72	0.051
g-TEM-c	1.62	1.61	1.62	0.000	1.60	1.66	0.021
g-Retina-s	1.25	1.21	1.31	0.043	1.18	1.34	0.045
g-Retina-c	1.28	1.28	1.28	0.002	1.26	1.30	0.009

$D_{B,R}$ average box-counting dimension per rotation (from an image rotated in 30° increments to make 12 rotated images each scanned at 12 locations), $D_{B,T}$ average box-counting dimension for all (144) scans, μ - r mean $D_{B,R}$ (also equals mean $D_{B,T}$), Min - r $D_{B,R}$ for rotation image with lowest $D_{B,R}$, Max - r $D_{B,R}$ for rotation image with highest $D_{B,R}$, σ - r standard deviation for μ - r , Min and Max lowest and highest $D_{B,T}$, respectively, σ standard deviation for $D_{B,T}$, *b* binary, *g* grayscale, *-o* outlined, *-f* filled, *-s* square sample, *-c* circular sample, *Mic* microglia (Fig. 2.3), *Ast* astrocyte (Fig. 2.3), *TEM* transmission electron micrograph of mouse cerebellum (see Fig. 2.11), *Retina* retinal fundus photograph (see Fig. 2.8)

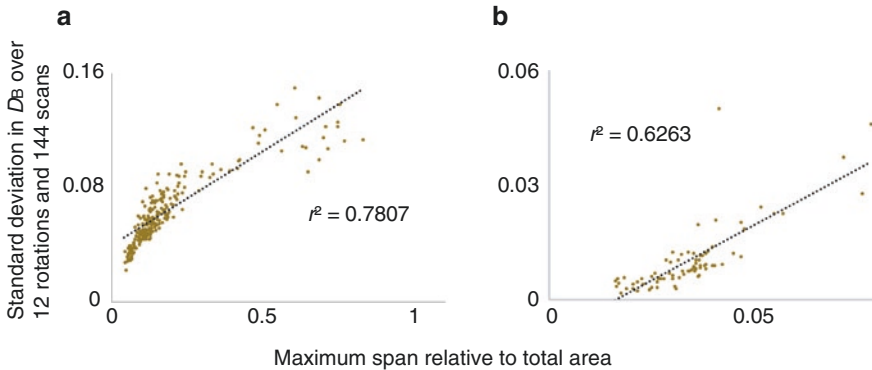


Fig. 2.5 Positive correlation between variation in the D_B with digital rotation and ratio of maximum span to total area. **(a)** 310 binary outlines of astrocytoma nuclei. **(b)** 79 binary outlines of microglia Both samples were also positively correlated with pixel density (not shown: astrocytoma $r^2=0.7119$ and microglia $r^2=0.5831$) but not circularity (astrocytoma $r^2=0.0427$ and microglia $r^2=0.0253$)

maximum span across a pattern to the total area of the pattern for two samples (binary contours, one of whole microglia and one of astrocytoma nuclei). In addition, it is known that digital images of non-stellate are more affected than digital images of stellate neurons [77].

2.3.2.3 Box-Counting Solutions

All of the above suggests a paradox—that accurate and valid results require knowledge beforehand of the optimal series of sizes, orientation, and box placement for each image [45, 49, 51]. Manifold solutions are available in box-counting software to address the problem, including sampling over multiple orientations and rotations and providing D_B s for average, minimum, and maximum covers, controlling for density differences, empirically determining optimizing solutions, etc. [26, 47, 49, 64, 80]. The particular method to select depends on the research need. For instance, to generate a series of sizes, if the scaling is known ahead of time, a custom series can be calculated, as was done for Fig. 2.4a. For the more general case when scaling is not known, other strategies available in software include applying an arbitrary pattern such as a simple linear decrease (e.g., subtracting 1 from each size), rational scaling (e.g., scaling by any fraction, such as $1/2$ or $8/3$), and power increments (i.e., going upward, $size_{(n+1)} = (size_n)^x$). For all of these, the minimum and maximum sizes can be specified in pixels or as a percent of image size (e.g., empirically, for control images, results tend to fail as box sizes exceed roughly 45% of the image size).

Optimizing solutions targeting bias with box position in *FracLac*, for example, oversample an image by selecting different grid locations and rotating the image, then extract an optimized grid series using methods to select minimum covers and

smoothest scaling patterns, including methods for automatically optimizing minimum and maximum box sizes (see also Chap. 32). These methods generally yield accuracy from 0.00% to 3.00% from theoretical for certain fractals, non-fractals, and in silico biological models. Such outcomes notwithstanding, variation in box-counting results depends on the pattern and the method, so prudent application requires some preliminary work to establish the particulars for specific research questions [45, 47, 49].

2.4 Lacunarity

Lacunarity, complementary to the D_B , is based on data that can normally be gathered during typical box counting [85].

Lacunarity

A measure of heterogeneity in patterns; characterized variously as “gappiness,” rotational invariance, and visual impressions of patchiness in texture; typically calculated during box counting based on mass measures (i.e., the relative content of each sampling unit of a particular size) (see *mass* in Fig. 2.4).

2.4.1 Calculating Lacunarity

Like the D_B , lacunarity comes in various types that depend on the box-counting sampling method (e.g., “sliding box” and “fixed box” lacunarities) [54, 72]. Lacunarities calculated during box counting are often based on the mean mass per box at each sampling size, which results in a series of values, one for each size. Various strategies reduce this data to a single measure describing an entire pattern, such as taking the mean of the mean for all sizes, and further selecting a representative value for an image if multiple sampling positions are used. The type we discuss here, fixed grid, mass-based lacunarity (Λ) is based on the mean of all squared *coefficients of variation* (standard deviation divided by the mean) [23, 66, 72, 73, 85]. Some ways to calculate lacunarity are redundant with the calculated D_F because both depend on the same data; however, this is not the case with Λ and the D_B because the mass from which Λ is calculated is independent of the count from which the D_B is calculated [49, 54, 73, 85].

Lacunarity has been applied in several contexts in neuroscience [49, 54, 73, 85]. As one example, Λ based on binary patterns extracted from dynamic contrast-enhanced computed tomography of head and neck tumors, images that reflect both tumor blood supply and capillary permeability, has been used to answer questions about how blood flow patterns in tumors relate to patient outcomes, showing that lower Λ of the overall vascularization pattern is associated with better outcomes, suggesting a more heterogeneous tumor blood supply predicts worse outcomes [1].

2.4.2 Understanding the D_B and Λ

The D_B and Λ work together to objectively quantify subtle differences in various phenomena, where patterns indistinguishable by their D_B are often distinguishable by their mass-related Λ and vice versa [6, 29, 39, 40, 49, 52, 54, 73, 78, 85, 86, 91]. Both, for instance, are sensitive to subtle changes in branching brain cell morphology that are not visually detectable yet have significant functional implications, but whereas the D_B is more sensitive for branching, Λ is superior for particular features such as soma size relative to process length [6, 40, 52].

Section 2.4.1 outlined the computational basis of this complementary relationship; Fig. 2.6 illustrates it. What the D_B measures increases left to right, and Λ from bottom to top in the figure. To understand Λ , consider the column near 1.26, which has two images with similar calculated D_B s but drastically differing Λ s. Rotating the Koch Flake (*KF*), which has low Λ , affects it little; but rotating the Henon Map (*HM*), a canonical multifractal with higher Λ , affects that image markedly—it has a distinct orientation relative to its surroundings. In terms of gaps, *KF* has one large gap, but *HM* has many irregular gaps. Similarly, for *QC* and *Mrf* in the column from 1.50 to 1.51, moving up (i.e., as Λ increases) *Mrf* depends more on orientation and is more heterogeneous in its gaps [49, 54, 73, 85].

2.4.2.1 Pattern Idiosyncrasies

The type of pattern selected can affect the results of box-counting fractal analysis. In particular, binary silhouettes typically have higher D_B s and Λ than do either outlined or skeletonized counterparts of the same image. For a typical branching structure, for instance, filled silhouettes and outlined contours bear information about changing branch diameter, but skeletonized patterns generally use a consistent (usually single pixel) diameter line so lose that information. The higher D_B of filled patterns can be understood as the filled state resembling a filled plane (which has a theoretical $D_F=2$ as was noted in Sect. 2.2.1.2) more than does its outlined or skeletonized state. The higher Λ can be understood by considering silhouettes, contours, and skeletons as the same collection of containers in different states (e.g., the outlined circle in the lower left of Fig. 2.6 has one container and it is empty) where the outlined and skeletonized states have only empty or mostly identical containers but the silhouette has some filled and some empty, making it the more heterogeneous. In this regard, similar to the D_B (see Sect. 2.2.1.2), Λ is moderately correlated, but not redundant, with density [49, 95, 96].

These trends are not strict rules. The astrocyte in Fig. 2.6 (*Aho* and *Ahf*), for instance, defies the trend; Λ is lower in the outlined state, *Aho*, as expected, but the D_B is essentially the same in both. This relates to the containers (branches in this case) being narrow so that filling them does not substantially change the number of groups of pixels but does change the distribution, the variation in gap

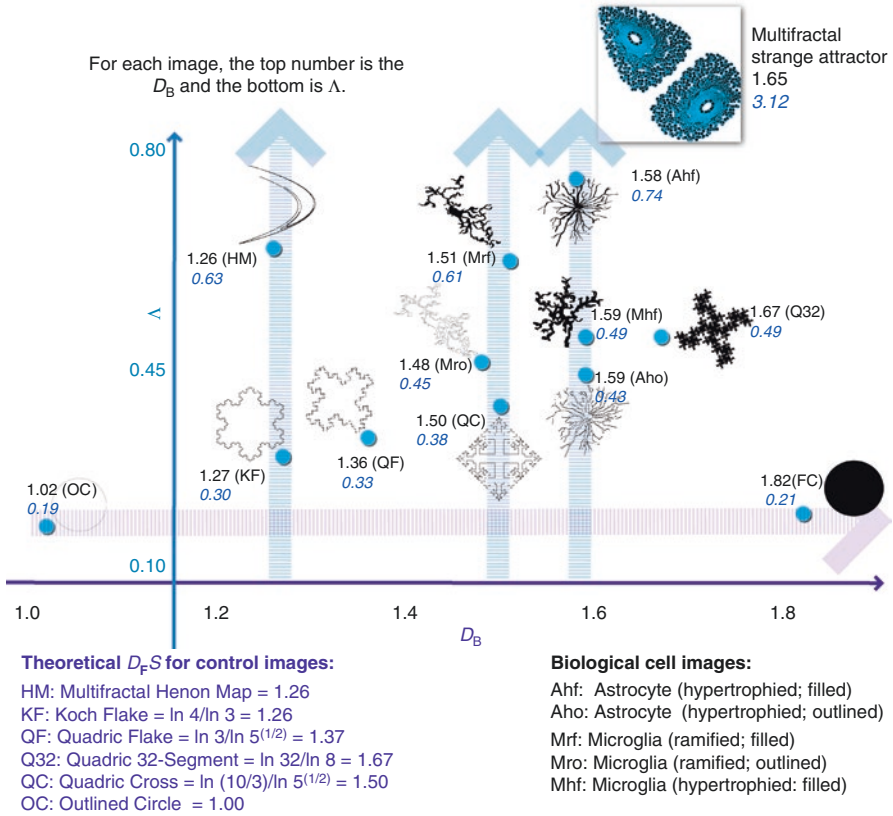


Fig. 2.6 Λ vs. D_B for selected binary images of theoretical fractals and brain cells The vertical axis's range is a limitation of the dataset, not of Λ per se, as indicated by the much higher Λ of the strange attractor at the top of the figure; that image is colored to emphasize the pattern, but the D_B and Λ are for its binary silhouette. The biological cells shown are drawn at roughly the same size because D_B s are scale independent, but in reality, the astrocyte (Ahf and Aho) spans a broader area than both microglia and the ramified microglia (Mrf and Mro) a broader area than the hypertrophied microglia (Mhf). (D_B s and Λ calculated using *FracLac for ImageJ* [50]. QF generated with the Fractal Generator available from <http://rsb.info.nih.gov/ij/plugins/fractal-generator.html>; Multifractals generated with the *Fractal Growth Models* plugin available from <http://rsb.info.nih.gov/ij/plugins/fgm/index.html>.)

size. The circle in Fig. 2.6 also challenges the trend; the filled state, FC, has a much higher calculated D_B than the unfilled, OC, but barely higher calculated Λ . This is understandable when one considers that both are round, rotationally invariant containers each with only one container state therefore similar Λ s, but the filled state is markedly closer to filling the plane therefore has a higher D_B [23, 62]. Overall, the fractal analyst evaluating results or deciding what type of pattern to assess needs to be aware that these trends exist but cannot assume they are pertinent without investigating to what extent they actually affect results [43].

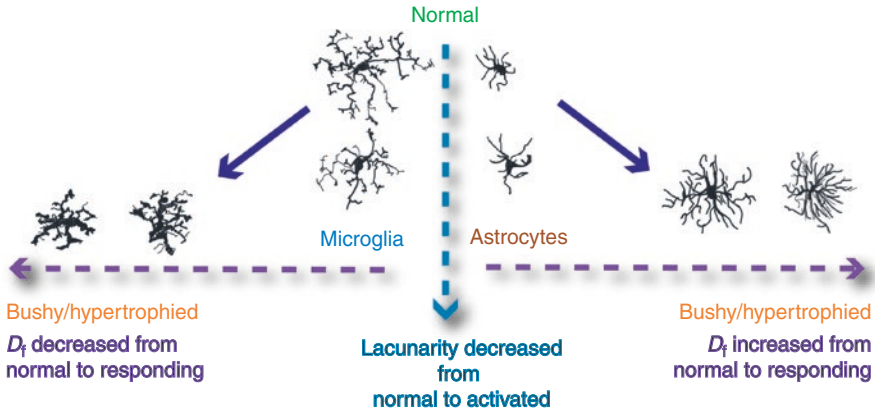


Fig. 2.7 As microglia hypertrophy, they typically decrease in complexity overall, after potentially a brief increase (not shown); astrocytes, in contrast, increase. Both generally decrease in lacunarity (see Chapter 6 for a more detailed discussion of nuances in the trends in microglial morphology)

2.4.2.2 Applying Lacunarity

A practical example of the complementary relationship between the D_B and Λ is found in work by Barreto et al. [6], who measured binary outlines of astrocytes to study how complexity and heterogeneity changed over the hours and weeks after ischemia induced by surgical middle cerebral artery occlusion in mice. Astrocyte complexity increased soon after injury, then slowly dropped back, whereas Λ generally decreased, but along a different schedule than the increase. Moreover, a neuroprotective (heat shock protein 72) genotype decreased the effect on complexity, but not Λ [6, 54]. Barreto et al. attributed the difference in D_B at least in part to redistribution of normally varied morphologies astrocytes adopt even within one region, with a shift away from cells with lower complexity [6, 78]. They assumed Λ quantified initially large, irregular vacant spaces between processes (higher Λ) becoming filled more homogeneously with increasing numbers of radial processes (lower Λ).

These trends for astrocytes are intriguing when compared to what is known for microglia, which are pertinent to compare to astrocytes, both being peppered throughout the CNS, sharing the same basic microenvironment in time and space, thus potentially relevant to fractal analysis of that environment as a whole. Figure 2.7 compares trends for astrocytes and microglia (the illustration does not compare them along the same time scale).

2.5 Grayscale Volumes and Box Counting

So far, this chapter has discussed box-counting analysis of binary images, but there are some differences that apply to analysis of grayscale images. In particular, the detail, N , for Eq. 2.1 measured in grayscale box-counting analysis is neither count nor mass related,

but pixel intensity based. This is because the restriction that limits pixel values to either foreground or background in binary images does not apply to grayscale images; rather, pixel values cover a range (e.g., from 0 to 255 in 8-bit grayscale images) [4, 12, 13, 51].

Grayscale analysis is generally pertinent when the questions are about texture rather than structure. Grayscale box counting has been used to investigate textures such as the fractal nature of whole brain structures, electron microscopy images [21], whole histological images where the environment cells are embedded in is important, and intracellular structures including nuclei [22]. Both texture and structure can be analyzed by either binary [71, 88] or grayscale methods, but, as illustrated in Fig. 2.8, each method is more suited to certain types of questions [22].

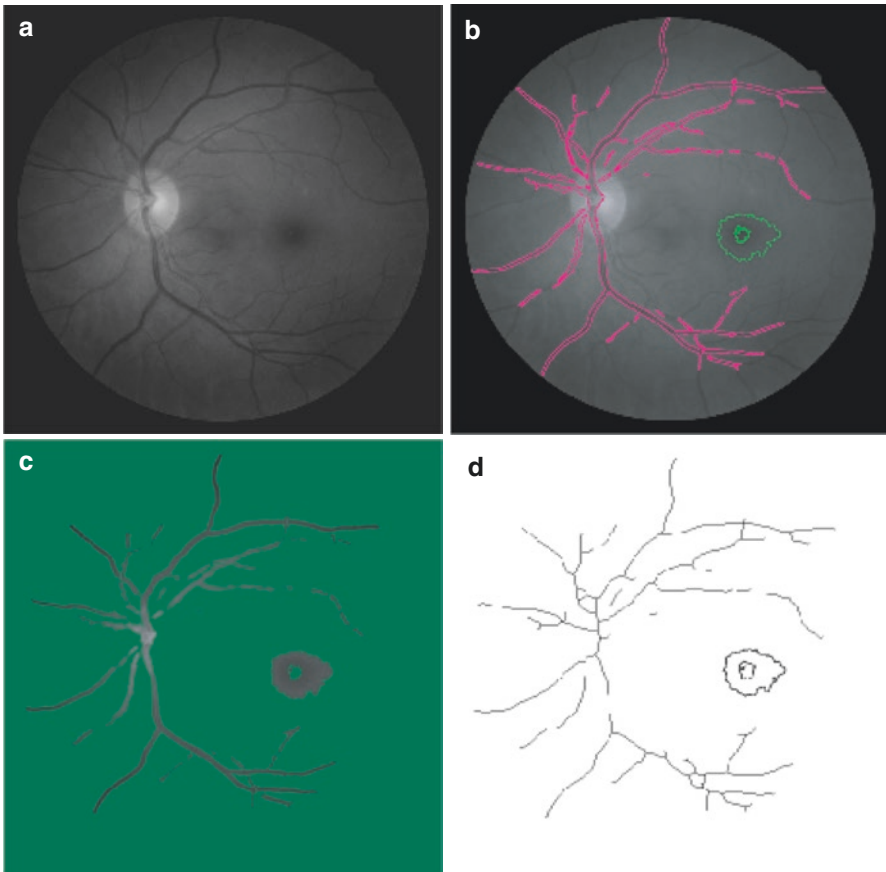


Fig. 2.8 Grayscale vs. binary analysis of a retinal fundus photo. (a) The entire retinal fundus photo. (b) ROIs (region of interest: a selection that isolates parts of an image) selecting vessels and part of the macular area. (c) The ROI from *b* extracted as grayscale information; the green background would not be processed when calculating the grayscale D_B . (d) The ROI from *c*, with retinal vessels converted to a binary skeleton and the macular area to a binary contour. In *grayscale* analysis, images are analyzed as textures over an entire image (*a*) or ROI (*b*, *c*). In both methods, all of the pixels within the image or ROI contribute to the grayscale D_B . In binary analysis, in contrast, only the pixels of the extracted pattern (*d*) contribute

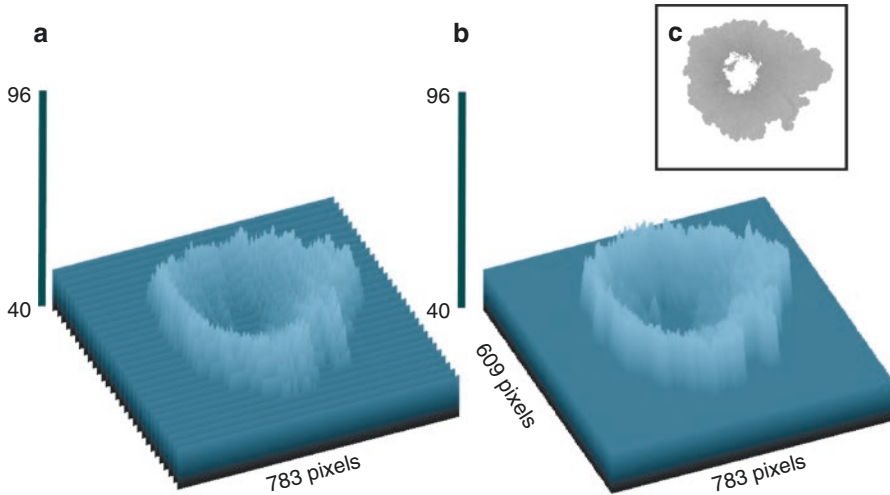


Fig. 2.9 Grayscale surface plots illustrating the general idea of converting 2D grayscale images into 3D information, showing the same image partitioned using two different resolutions. (a) Higher resolution. (b) Lower resolution (larger and fewer slices). These simplified plots show rectangular slices across the image, but the partitions are usually symmetrical (e.g., arrays of square or cylindrical columns). (c) The inset shows the selection on the image from Fig. 2.8, from which the surface plots were made (surface plots generated in *Fiji*)

One way box counting is implemented for grayscale images is by projecting the image into volumes after partitioning it into areas. Images are partitioned into 3D columns having a base determined the same as in binary box counting (i.e., a square or other shape with length S) and height determined as the difference, d , between the maximum and minimum pixel intensity (e.g., scaled to between 0 and 255) within the area (A) at the base of the column (see Fig. 2.9) [4, 51]. The measure of detail, N , is then based on the mean *volume*, which, depending on the method being used, is usually calculated as one of (i) $d \times A$, (ii) $(d+1) \times A$, or (iii) $(d+1)$ [4, 12, 51]. Then, as usual, the D_B is calculated from the slope of the regression line for the log-log ratio of N vs. S [12, 50].

2.6 Multifractal Analysis

The fractal analysis described thus far here is sometimes called *monofractal analysis*, to distinguish it from *multifractal analysis*, which identifies patterns characterized better by a spectrum of D_F s than a single D_F . The multifractal analysis process is analogous to applying warping filters to an image to exaggerate features that might otherwise be unnoticeable. Mono- and non-fractals are little or not affected by the distortions, but multifractals are affected in characteristic ways that are used to distinguish them from mono- and non-fractals.

The warp filters are a set of arbitrary exponents traditionally denoted by the symbol Q . In fractal analysis software, the Q set is something the user typically manipulates from a starting default set (e.g., bracketing 0 symmetrically such as -5 to 5) [14]. A generalized dimension (D_Q) is determined for each Q , based on the mass dimension (D_M). N from Eq. 2.1 for the D_M is the mean of the probability distribution of all masses at one size, reflecting the density over the image (mass for binary box counting was illustrated in Fig. 2.4) [14]. For the D_Q , each mass is distorted by being raised to Q , then N_Q is the mean for this distorted density distribution for a size. Graphs are generated based on this data, having predictable features that distinguish amongst non-, mono-, and multi-fractal scaling and also quantify multifractal features. Figure 2.10 shows two such graphs, the graph of D_Q vs. Q and $f(\alpha_Q)$ vs. α_Q , that are commonly used in multifractal analysis [14, 23, 66, 93, 101]. See also Chap. 4.

2.6.1 Reading the D_Q Curve

The generalized dimension curve (D_Q vs. Q) is typically decreasing, sigmoidally around $Q=0$ for multifractals, but much flatter for mono- and non-fractals. Indeed, if it has essentially one value for all Q_s , the pattern is not multifractal. As explained in Fig. 2.10a, at any scale, negative Q_s amplify and positive shrink the pattern, affecting different densities nonlinearly. If distortion over all scales reveals noticeable differences (i.e., the pattern has a set of unique D_{Q_s}), then the scaling is considered multifractal. The curve is measured objectively using a characteristic known as “dimensional ordering,” whereby $D_{(0)} \geq D_{(1)} \geq D_{(2)}$, which defines an interval used to assess the spectrum’s amplitude [23, 66, 93, 101].

As mentioned, software may let the researcher select values for Q , but it also often ensures that the Q set includes integer values for 0, 1, and 2 in order to assess the amplitude; however, there are some points to be aware of when interpreting those values. To elaborate, in multifractal analysis in general, $D_{(0)}$, $D_{(1)}$, and $D_{(2)}$ generally correspond to quantities known as, respectively, the “capacity dimension” (closely related to the D_B), the “information dimension” (analogous to a quantity known as the Shannon entropy), and the “correlation dimension,” which can be calculated for different types of fractal patterns (i.e., including temporal) using different methods of fractal analysis. But there are practical issues affecting the actual values obtained for these by box counting. For example, in practice, the D_B obtained from optimized box counting (Sect. 2.3.2.3) differs from $D_{(0)}$ obtained from optimized multifractal analysis, owing to differences in optimizing methods. Similarly, the Shannon entropy for $D_{(1)}$ cannot be determined directly using standard box counting [18, 32].

Applying the basic rules for reading the D_Q curve to Fig. 2.10a, one can see that the curve for the Henon multifractal is a typical multifractal curve showing considerable heterogeneity in scaling, in contrast with the curve for the circle, which is flat, as is typical of homogeneous non-fractals. In keeping with the trends shown earlier in Fig. 2.6, increased heterogeneity with multifractal scaling is complementary with the heterogeneity of different types of lacunarity [40, 49].

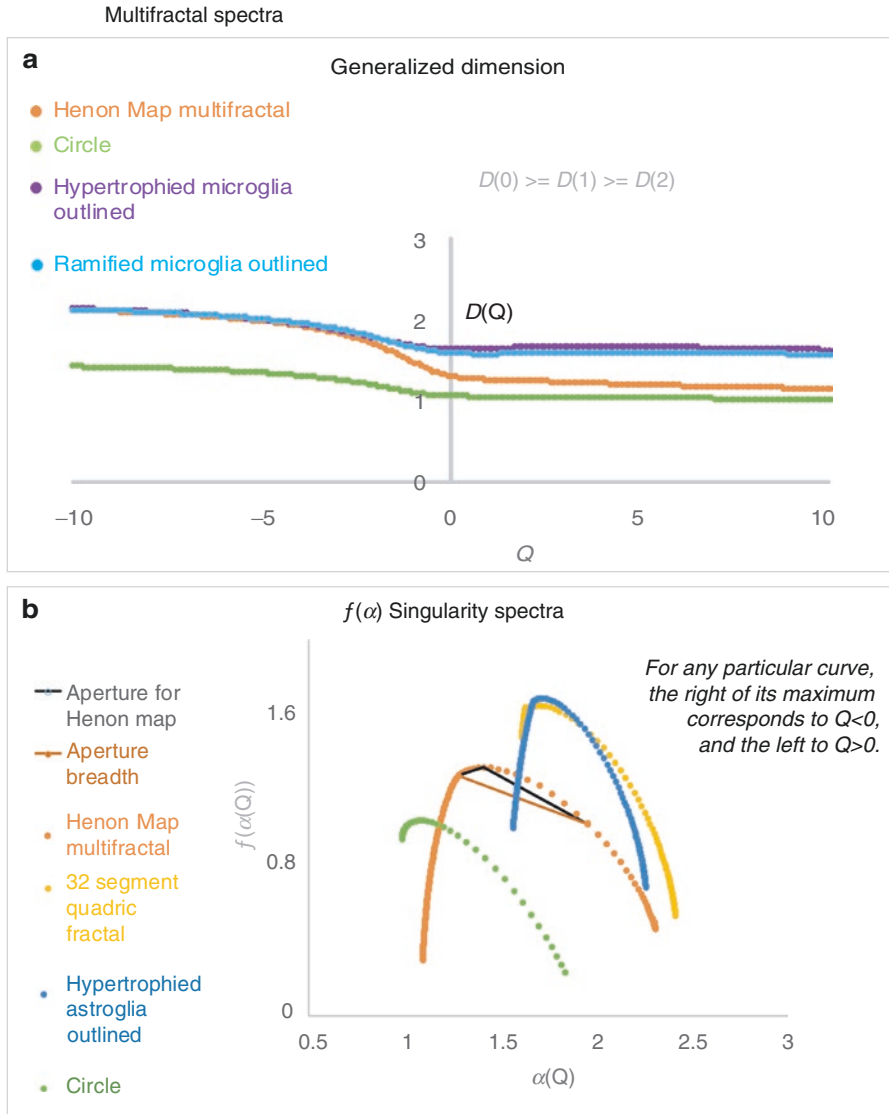


Fig. 2.10 Two graphs frequently used for multifractal analysis. **(a)** Generalized dimensions. The horizontal axis, Q , is an exponent and the vertical a probability-based D_F that varies with Q . Being exponents applied to probabilities (i.e., between 0 and 1), negative Q s, amplify and positive Q s, shrink the value on the vertical axis, as is most clearly seen in the curve for the multifractal. Multifractals are characterized by generally steeper slopes around $Q=0$. The flatter mono- and non-fractal curves stay close to one value for all Q . **(b)** $f(\alpha)$ Multifractal spectra. The horizontal axis, $\alpha(Q)$, is a D_F based on Q and the vertical a D_F dependent on $\alpha(Q)$, and further modified by Q . Compared to mono- and non-fractals, multifractals are characterized by broader $f(\alpha)$ spectra, which can be measured by their apertures (see legend) (graphs generated for Fig. 2.6's images using *FracLac*)

One can also apply the rules for reading multifractal curves to interpret the curves in Fig. 2.10 for microglia at different activation levels. The results shown are for two outlined patterns extracted from, respectively, the unactivated microglial cell with $D_B = 1.48$ from Fig. 2.6 (*Mro*) and the more activated microglial cell from Fig. 2.6 (*Mhf*) (for the outlined version of *Mhf*, not shown in Fig. 2.6, the calculated $D_B = 1.54$). That the hypertrophied cell had a higher D_B is evident from the portion of its curve slightly above that for the ramified cell. Their curves are both flat, neither suggesting multifractal scaling. These curves are similar to curves from images of comparable monofractals. The curve (not shown) for the 32 segment quadric fractal from Fig. 2.6 (*Q32*), for instance, has a similar slope near $Q=0$ but lies slightly above the cells (i.e., it is a monofractal with higher $D_B = 1.67$) [14, 23, 50].

2.6.2 Reading the $f(\alpha)$ Curve

The second commonly used graph discussed here, the $f(\alpha)$ spectrum, is a typically convex curve opening downward as shown in Fig. 2.10b. Again, the shape distinguishes multifractals from other patterns, being (1) broader and (2) less convergent particularly on the left for multifractals than for mono- and non-fractals. One feature used to quantify $f(\alpha)$ spectra is the *aperture* (illustrated for the Henon Map in Fig. 2.10b), defined by lines from $Q=1$ to 0 to -1 , and the total breadth from $Q=1$ to -1 . The slopes and lengths of the aperture lines quantify the scaling regardless of any other values of Q used. Defining the aperture interval as from 1 to -1 seems reversed but can be understood knowing the variable along the horizontal axis, $\alpha_{(Q)}$, itself decreases with Q [14, 23, 50].

2.6.3 Applying Multifractal Analysis

Multifractal analysis has been applied in novel ways in neuroscience. It has been used in hemodynamics, for example, showing in arteriovenous malformations correlations of size and flow with $D_{(0)}$, $D_{(1)}$, and $D_{(2)}$ (these correlations are similar to although weaker than correlations of size and flow with the D_B) [20, 27, 76, 90]. It has also revealed postmortem capillary distribution differences in Alzheimer's disease, small vessel disease dementia, and control from three different brain regions [15]. In retinal pathology, it has been used to differentiate normal from pathological retina, D_Q curves for binary vessel tracings extracted from normal retinal fundus photographs showing smaller amplitudes than those from pathological (diabetic macular edema), and $f(\alpha)$ spectra showing distinctively different shapes and asymmetry. Also of general import for the multifractal analyst, similar to the trends noted in Sect. 2.4.2.1, it has been shown that skeletonized retinal patterns have lower D_Q spectra than filled [20, 27, 76, 90, 95].

The sampling location bias discussed in Sect. 2.3.2.2 can invalidate multifractal analysis results in particular. A common problem in multifractal analysis is anomalous spectra created from inappropriate sampling. Signs of this include that the left ($Q > 0$) and right ($Q < 0$) portions of the $f(\alpha)$ spectra (Fig. 2.10b) fail to meet in a continuous curve, flip upwards, or cross over. This often means that an image has a density distribution with very small probabilities taking on inappropriately greater significance in some, but not all, grid positions [14, 47, 100].

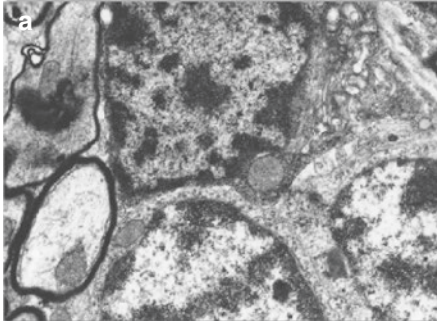
Values of $Q < 0$ are most relevant to this problem, so sometimes using a different range of Q s can fix the problem; similarly, sampling only above a certain density or limiting the smallest size can also sometimes fix this problem. If different settings are used for different samples within a dataset, these arbitrary solutions can alter the results in unexpected ways or make comparisons difficult, so a preferred alternative is to use the same density, Q , etc. but increase the sampling locations and rotation until normal results are obtained. As a practical illustration, the multifractal spectra in Fig. 2.10 were generated for the set of images from Fig. 2.6, using *FracLac* implementing the solutions suggested above including multiple grid locations. For most of the control images, normal multifractal curves appeared by 12 runs, but for the astrocytes and microglia, results could be read only after running 500 different sampling locations (taking roughly 1 min more per image) [14, 47, 100].

This has practical implications for fractal analysis in neuroscience. As an example, microglia are known to scale as multifractals, but relatively rarely, less than 10% of cells, when in a hyper-ramified or transitional state between their normal/ramified and pathological/hypertrophied states, and more often, for example, in elderly human brain [29, 49, 52]. An investigator formulating a question about hyper-ramification and multifractality then analyzing a sample using too few locations might see only unreadable multifractal spectra and consequently abandon their questions about multifractal scaling in these cells. Alternatively, being aware of what inadequate sampling looks like and that an extra minute of processing might solve the problem could inspire further curiosity.

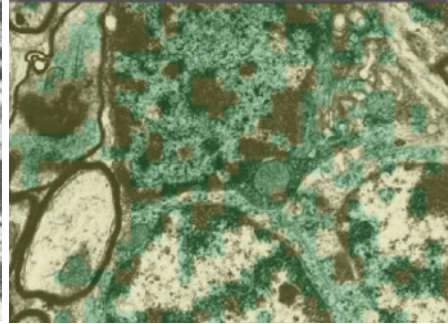
2.7 Subscanning

Another method the prudent interpreter of box-counting fractal analysis should understand is subscanning analysis, used to investigate variation over space. Subscanning analyzes several independent domains that may or may not overlap in one image [50, 82]. Subscanning and multifractal analysis both reveal variation over a single information set; but multifractal analysis investigates one pattern as a whole and subscanning investigates local areas on one image independently of other areas and then presents the results so that the variation in the local D_B can be compared and assessed. Figure 2.11 illustrates how subscanning using color coding can be used in general to investigate variation in the local D_B .

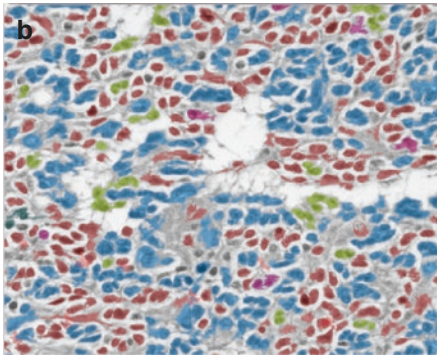
The variation revealed by subscanning can be used to assess the process of box counting itself (e.g., applying it to a circle that yields a global D_B of 1.04 identifies



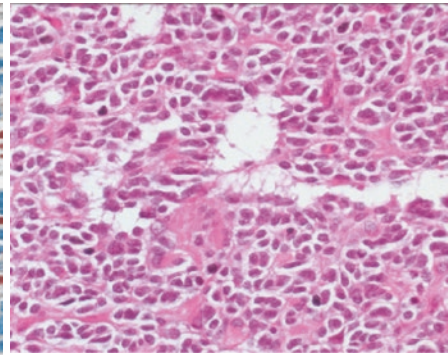
Transmission Electron Micrograph of Mouse Cerebellum; Post fixed in osmium tetroxide, stained with lead and uranyl acetate; original magnification 12,000x.



Scanned as grayscale in *ImageJ*:
 1) `FracLac>Sub>ImageType>Gray1`
 2) `Method>Rectangles`
 3) `Subscan size = 4%>OK`
 4) `FracLac>Scan`



Human Astrocytoma; H&E stained; original magnification 40x.



Scanned as grayscale., nuclei auto-segmented in *ImageJ*:
 1) `Process>Binary>MakeBinary`
 2) `Analyze>Analyze Particles >Add to Manager`
 3) `File>Revert (back to grayscale)`
 4) `FracLac>BC>ImageType>Gray1>OK`
 5) `FracLac>ROIs`

Fig. 2.11 Subscanning identifies local variation in the D_B using color coding. (a) Structures within an area of mouse cerebellum differentiated by differences in the local D_B (green vs yellow areas). (b) Variation in the local D_B among several of the same structure (i.e., different colors of nuclei in a histopathology slide of astrocytoma)

areas ranging from 0.99 to 1.09, reflecting pixel effects as discussed in Sect. 2.3.2.2). In one study of astrocytes, subscanning showed that the D_B was consistent (around 1.7) from the perisomatic area to the most peripheral extent of a branch's territory faithfully revealed by light microscopy, but rapidly dropped off at the tips of the processes. The variation, however, was attributable to the inability of light microscopy to resolve the finest processes at the ends, because when astrocytes were reconstructed via 3D modeling, the branching pattern at the ends was the same as everywhere else [82].

2.8 The Validity of 2D Patterns from 4-Dimensional Reality

An overarching issue anyone using or interpreting fractal analysis should become familiar with is the validity of 2D patterns. The images used for Figs. 2.3, 2.6, and 2.10 are all 2D. Yet, biology is not. Microglia, for instance, play active roles in brain structure and function, in development, normal cognition, alcoholism, autism, chronic stress, pain mediation, Alzheimer's disease, aging, etc. [9, 29, 44, 57, 63, 68, 74, 81, 83, 91, 97–99, 102]. They are dynamic in space and time, in living, normal brains waving and winding their processes around neurons at speeds of roughly $1.5 \mu\text{m}/\text{min}$, and in pathological or developing tissue, in vivo and in vitro, rapidly or sometimes more slowly migrating and phagocytosing [9, 29, 68, 89, 98]. When examining microglia intertwined and interacting with neurons within the CNS or even alone in a dish, the microgliologist realizes these are 3D biological phenomena, indeed, four-dimensional phenomena changing over time, as are virtually all phenomena in neuroscience. Nonetheless, we have discussed here fractal analysis of 2D, still images. A question often asked is how to resolve the discrepancy in dimensions.

One way is by appealing to an analogy in facial recognition software. To elaborate, given an image, facial recognition software uses many features to identify a face within the image. Intriguingly, one such feature is the simple isosceles triangle that can be drawn on an image across the eyebrows with its vertex at the mouth [67]. Like cell profiles or black and white images of any structure, such drawings are 2D. That is, a 2D pattern (the triangle) extracted from an image of a face serves to meaningfully identify an originally 3D biological structure that changes in space and time (the actual face).

A similar principle applies to fractal analysis of 2D patterns extracted from images representing 3D structures such as dynamic cells existing in the 3D space of the CNS or cell culture over the fourth dimension of time. In the same way that the triangle on the face is not the face, and the face is not a triangle, yet still the triangle is vital to recognizing the face within the software, the patterns extracted from images of cells are not the cells but hold the descriptors we are concerned with in fractal analysis. Indeed, in some cases, 2D representations convey 3D information that may be integral to a pattern, such as when vessel diameter or length is smaller for vessels farther away from the image plane, and this relative distance is itself what is being investigated. As such, a discerning approach acknowledges that 2D images are reasonable proxies for 3D phenomena, subject to the limits that they are investigated within.

A further implication of this is that the D_B calculated for a digital image is not necessarily the D_F of the phenomenon as a whole; rather, it is always the D_B of the pattern the researcher is interested in. Choosing a pattern type (e.g., grayscale area or binary silhouette, contour, or skeleton) and a method of extracting it depends on several factors, one of the foremost being the research question itself. Thus, it is important to be aware that different patterns may or may not generate different D_B s even when extracted from the same image. This should be liberating to the concerned researcher, who can be reassured that he or she is free to investigate fractal scaling in any phenomenon without having to first determine if the phenomenon itself is a “legitimate” fractal [35].

2.8.1 Control and Calibration

Another issue to be aware of in box-counting fractal analysis is verifying the results. When possible, fractal analysis software should be calibrated using controls, such as the control images from Fig. 2.6. It is important to match benchmark images to the images being investigated (e.g., in size and number of foreground pixels) and to the goals of the research (e.g., mono- vs. multifractal images or in silico cell models created using known scaling parameters) and note deviations from theoretical and potential influences like rotation (Sect. 2.3.2.2) [38, 39, 76]. In multifractal analysis, control images are particularly useful for establishing parameters for dimensional ordering and the $f(\alpha)$ aperture (see Sects. 2.6.1 and 2.6.2) [35].

2.9 Conclusion

In summary, this chapter has laid out elementary principles of fractal geometry and explained fractal analysis as a way of measuring phenomena when the details of design are as important as gross morphology. The chapter outlined how the details change with scale in theoretical and natural fractal patterns. It also grounded the reader in the basics of binary and grayscale box counting and explained trends and complementary relationships among the D_B , Λ , and multifractal spectra with application to topics in neuroscience in particular. It illustrated that although the tedium of fractal analysis can be left to the click of a button, prudent and defensible interpretation of it needs some regard for common pitfalls. Accordingly, it reviewed several methodological considerations, such as different types of pattern idiosyncrasies and sampling issues, and discussed practical methods of addressing them. Overall, this chapter prepares the fractal analyst to conscientiously and confidently use the elegant, robust techniques of box counting to measure and interpret the D_B , lacunarity, and multifractality of the exquisitely detailed fractal geometry of the brain.

References

1. Abramyuk A, Wolf G, Shakirin G, Haberland U, Tokalov S, Koch A, Appold S, Zöphel K, Abolmaali N. Preliminary assessment of dynamic contrast-enhanced CT implementation in pretreatment FDG-PET/CT for outcome prediction in head and neck tumors. *Acta Radiol.* 2010;51(7):793–9.
2. Aguado PL, Del Monte JP, Moratitel R, Tarquis AM. Spatial characterization of landscapes through multifractal analysis of DEM. *Sci World J.* 2014;2014:563038.
3. Agui JH. Lunar dust characterization for exploration life support systems. 2007. Paper presented at the 45th AIAA aerospace sciences meeting and exhibit, NASA Goddard Space Flight Center, Greenbelt.
4. Bache-Wiig PCHaJ. Fractal count. 2012.
5. Barille R, LaPenna P. Multifractality of laser beam spatial intensity in a turbulent medium. *Appl Opt.* 2006;45(14):3331–9.

6. Barreto GE, White RE, Xu L, Palm CJ, Giffard RG. Effects of heat shock protein 72 (Hsp72) on evolution of astrocyte activation following stroke in the mouse. *Exp Neurol.* 2012;238(2):284–96.
7. Behar TN. Analysis of fractal dimension of O2A glial cells differentiating in vitro. *Methods.* 2001;24(4):331–9.
8. Bisoi AK, Mishra J. On calculation of fractal dimension of images. *Pattern Recogn Lett.* 2001;22(6–7):631–7.
9. Blank T, Prinz M. Microglia as modulators of cognition and neuropsychiatric disorders. *Glia.* 2013;61(1):62–70.
10. Bogachev MI, Bunde A. Improved risk estimation in multifractal records: application to the value at risk in finance. *Phys Rev E Stat Nonlin Soft Matter Phys.* 2009;80(2 Pt 2):026131.
11. Cavallari M, Falco T, Frontali M, Romano S, Bagnato F, Orzi F. Fractal analysis reveals reduced complexity of retinal vessels in CADASIL. *PLoS One.* 2011;6(4):e19150.
12. Chaudhuri B, Sarkar N. Texture segmentation using fractal dimension. *Pattern analysis and machine intelligence.* IEEE Trans. 1995;17(1):72–7.
13. Chen W-S, Yuan S-Y, Hsieh C-M. Two algorithms to estimate fractal dimension of gray-level images. *OPTICE.* 2003;42(8):2452–64.
14. Chhabra A, Jensen RV. Direct determination of the $f(\alpha)$ singularity spectrum. *Phys Rev Lett.* 1989;62(12):1327–30.
15. Cornforth D, Jelinek H. Automated classification of dementia subtypes from post-mortem cortex images. In: Zhang S, Jarvis R, editors. *AI 2005: advances in artificial intelligence*, Lecture Notes in Computer Science, vol. 3809. Berlin: Springer; 2005. p. 1285–8.
16. Cornforth DJ, Tarvainen MP, Jelinek HF. Using Renyi entropy to detect early cardiac autonomic neuropathy. *Conf Proc IEEE Eng Med Biol Soc.* 2013;2013:5562–5.
17. Cornforth DJ, Tarvainen MP, Jelinek HF. How to calculate Renyi entropy from heart rate variability, and why it matters for detecting cardiac autonomic neuropathy. *Front Bioeng Biotechnol.* 2014;2:34.
18. De Bartolo S, Gabriele S, Gaudio R, et al. Multifractal behaviour of river networks. *Hydrol Earth Syst Sci Discuss.* 2000;4(1):105–12.
19. Di Ieva A, Boukadoum M, Lahmiri S, Cusimano MD. Computational analyses of arteriovenous malformations in neuroimaging. *J Neuroimaging.* 2015;25(3):354–60.
20. Doubal FN, MacGillivray TJ, Patton N, Dhillon B, Dennis MS, Wardlaw JM. Fractal analysis of retinal vessels suggests that a distinct vasculopathy causes lacunar stroke. *Neurology.* 2010;74(14):1102–7.
21. Égerházi L, Smausz T, Bari F. Inverted fractal analysis of TiOx thin layers grown by inverse pulsed laser deposition. *Appl Surf Sci.* 2013;278(0):106–10.
22. Fabrizii M, Moïnfar F, Jelinek HF, Karperien A, Ahammer H. Fractal analysis of cervical intraepithelial neoplasia. *PLoS One.* 2014;9(10):e108457.
23. Falconer K. *Fractal geometry: mathematical foundations and applications.* Hoboken: Wiley; 2014.
24. Fernandez E, Jelinek HF. Use of fractal theory in neuroscience: methods, advantages, and potential problems. *Methods.* 2001;24(4):309–21.
25. Filho MNB, Sobreira FJA. Accuracy of lacunarity algorithms in texture classification of high spatial resolution images from urban areas. In: Jun C, Jie J, Förstner W, editors. *XXIst ISPRS Congress, Beijing, July 3–11, 2008. The International Archives of the Photogrammetry, Remote Sensing and Spatial Information Science*, vol WG III/4: Automatic Image Interpretation for City-Modeling. International Society for Photogrammetry and Remote Sensing, p. 6.
26. Goni J, Sporns O, Cheng H, Aznárez-Sanado M, Wang Y, Josa S, Arrondo G, Mathews VP, Hummer TA, Kronenberger WG, Avena-Koenigsberger A, Saykin AJ, Pastor MA. Robust estimation of fractal measures for characterizing the structural complexity of the human brain: optimization and reproducibility. *Neuroimage.* 2013;83:646–57.
27. Gould DJ, Vadakkan TJ, Poché, Ross A, Dickinson ME. Multifractal and lacunarity analysis of microvascular morphology and remodeling. *Microcirculation.* 2011;18(2):136–51.

28. Gutierrez RC, Hung J, Zhang Y, Kertesz AC, Espina FJ, Colicos MA. Altered synchrony and connectivity in neuronal networks expressing an autism-related mutation of neuroligin 3. *Neuroscience*. 2009;162(1):208–21.
29. Hinwood M, Tynan RJ, Charnley JL, Beynon SB, Day TA, Walker FR. Chronic stress induced remodeling of the prefrontal cortex: structural re-organization of microglia and the inhibitory effect of minocycline. *Cereb Cortex*. 2013;23(8):1784–97.
30. Holdsworth AM, Kevlahan NK-R, Earn DJD. Multifractal signatures of infectious diseases. *J R Soc Interface*. 2012;9(74):2167–80.
31. Jelinek HF, Cornforth D. Fractal analysis in clinical screening and investigation. In: Classification and application of fractals. Nova Science Publishers; 2012. p. 277–301.
32. Jelinek HF, Cornforth DJ, Roberts T, Landini G, Bourke P, Bossomaier T. Image processing of finite size rat retinal ganglion cells using multifractal and local connected fractal analysis. In: Yu GIWaX editor. AI 2004: advances in artificial intelligence: 17th Australian Joint Conference on Artificial Intelligence, Cairns, Australia, 2005. Lecture Notes in Artificial Intelligence. Springer Verlag. p. 961–6.
33. Jelinek HF, Cree MJ, Leandro JGG, Soares JA, Cesar J, Roberto M, Luckie A. Automated segmentation of retinal blood vessels and identification of proliferative diabetic retinopathy. *J Opt Soc Am A Opt Image Sci Vis*. 2007;24(5):1448–56.
34. Jelinek HF, de Mendonça MBM, Fernando O, Garcia CAA, Nogueira RA, Soares JVB, Marcondes RC. Fractal analysis of the normal human retinal vasculature. *Internet J Ophthalmol Vis Sci*. 2010;8:2.
35. Jelinek HF, Elston N, Zietsch B. Fractal analysis: pitfalls and revelations in neuroscience. In: Losa GA, Merlini D, Nonnenmacher TF, Weibel ER, editors. Fractals in biology and medicine, vol IV, Mathematics and biosciences in interaction, vol VII. Basel: Birkhäuser Verlag; 2005. p. 85–94.
36. Jelinek HF, Fernandez E. Neurons and fractals: how reliable and useful are calculations of fractal dimensions? *J Neurosci Methods*. 1998;81(1–2):9–18.
37. Jelinek HF GNE. Pyramidal neurons in macaque visual cortex: interareal phenotypic variation of dendritic branching pattern. *Fractals*. 2001;09(03):287–95.
38. Jelinek HF, Karperien A. Microglia modelling and analysis using L-systems grammar. In: Encarnação P, Veloso A, editors. BIOSTEC 2008 International Joint Conference on Biomedical Engineering Systems and Technologies, Funchal, Madeira, 28–31 Jan 2008. BIOSIGNALS 2008 International Conference on Bio-inspired Systems and Signal Processing. Springer. p. 289–94.
39. Jelinek HF, Karperien A, Cornforth D, Cesar RMJ, Leandro J. MicroMod—an L-systems approach to neuron modelling. In: Sarker R, McKay B, Gen M, Namatame A, editors. Sixth Australia-Japan Joint Workshop on Intelligent and Evolutionary Systems, Canberra, Nov 30–Dec 1 2002. AJJWIES'02. Australian National University, Canberra.
40. Jelinek HF, Karperien A, Milosevic NT. Lacunarity analysis and classification of microglia in neuroscience. In: Proceedings of the 8th European Conference on Mathematical and Theoretical Biology, Cracow, 2011. European Society for Mathematical and Theoretical Biology (ESMTB).
41. Jelinek HF, Md Imam H, Al-Aubaidy H, Khandoker AH. Association of cardiovascular risk using non-linear heart rate variability measures with the framingham risk score in a rural population. *Front Physiol*. 2013;4:186.
42. Jelinek HF, Milošević NT, Karperien A, Krstonošić B. Box-counting and multifractal analysis in neuronal and glial classification. In: Dumitrache I, editor. Advances in intelligent control systems and computer science, Advances in Intelligent Systems and Computing, vol. 187. Berlin: Springer; 2013. p. 177–89.
43. Jelinek HF, Milosevic NT, Ristanovic D. The morphology of alpha ganglion cells in mammalian species: a fractal analysis study. *CEAI*. 2010;12(1):3–9.
44. Jinno S, Yamada J. Using comparative anatomy in the axotomy model to identify distinct roles for microglia and astrocytes in synaptic stripping. *Neuron Glia Biol*. 2011;7(1):55–66.
45. Kam Y, Karperien A, Weidow B, Estrada L, Anderson AR, Quaranta V. Nest expansion assay: a cancer systems biology approach to in vitro invasion measurements. *BMC Res Notes*. 2009;2:130.

46. Karmakar C, Jelinek H, Khandoker A, Tulppo M, Makikallio T, Kiviniemi A, Huikuri H, Palaniswami M. Identifying increased risk of post-infarct people with diabetes using multi-lag Tone-Entropy analysis. *Conf Proc IEEE Eng Med Biol Soc.* 2012;2012:25–8.
47. Karperien A. FracLac user's guide. <http://rsbweb.nih.gov/ij/plugins/fraclac/FLHelp/Introduction.htm>. 2012.
48. Karperien A. Defining microglial morphology: form, function, and fractal dimension. Australia: Charles Sturt University; 2004.
49. Karperien A. Defining microglial morphology: form, function, and fractal dimension. Thesis, Charles Sturt University, Australia. 2004.
50. Karperien A. FracLac for Image J. Charles Sturt University. 2013.
51. Karperien A. FracLac2015 for ImageJ: JavaDoc, source code, and jar. vol 7, 201501 edn. National Institutes of Health ImageJ Plugins. 2015.
52. Karperien A, Ahammer H, Jelinek HF. Quantitating the subtleties of microglial morphology with fractal analysis. *Front Cell Neurosci.* 2013;7:3.
53. Karperien A, Jelinek H. Fractal, multifractal, and lacunarity analysis of microglia in tissue engineering. *Front Bioeng Biotechnol.* 2015;3.
54. Karperien A, Jelinek H, Milošević N. Reviewing lacunarity analysis and classification of microglia in neuroscience. Paper presented at the 8th European Conference on Mathematical and Theoretical Biology, Poland. 2011.
55. Karperien A, Jelinek HF, Leandro JJG, Soares JVB, Cesar J, Roberto M, Luckie A. Automated detection of proliferative retinopathy in clinical practice. *Clin Ophthalmol.* 2008;2(1):109–22.
56. Karperien A, Jelinek HF, Milošević NT. Multifractals: a review with an application in neuroscience. In: CSCS18-18th International Conference on Control Systems and Computer Science: Fifth Symposium on Interdisciplinary Approaches in Fractal Analysis Bucharest, 2011. Politehnica press, pp 888–93.
57. Kreutzberg GW. Microglia, the first line of defence in brain pathologies. *Arzneimittelforschung.* 1995;45(3A):357–60.
58. Landini G, Murray PI, Misson GP. Local connected fractal dimensions and lacunarity analyses of 60 degrees fluorescein angiograms. *Invest Ophthalmol Vis Sci.* 1995;36(13):2749–55.
59. Liu S, Li ZW, Weinreb RN, Xu G, Lindsey JD, Ye C, Yung WH, Pang CP, Lam DS, Leung CK. Tracking retinal microgliosis in models of retinal ganglion cell damage. *Invest Ophthalmol Vis Sci.* 2012;53(10):6254–62.
60. Losa GA. Fractals in biology and medicine. In: Meyers R, editor. *Encyclopedia of Molecular Cell Biology and Molecular Medicine*, Wiley-VCH Verlag, Berlin, 2011;1–25.
61. Losa GA, Baumann G, Nonnenmacher TF. Fractal dimension of pericellular membranes in human lymphocytes and lymphoblastic leukemia cells. *Pathol Res Pract.* 1992;188(4–5):680–6.
62. Losa GN, Theo F, Merlini D, Weibel ER, editors. *Fractals in biology and medicine, Mathematics and Biosciences in Interaction*, vol. II. Basel: Birkhauser; 1997.
63. Maezawa I, Calafiore M, Wulff H, Jin LW. Does microglial dysfunction play a role in autism and Rett syndrome? *Neuron Glia Biol.* 2011;7(1):85–97.
64. Mancardi D, Varetto G, Bucci E, Maniero F, Guiot C. Fractal parameters and vascular networks: facts & artifacts. *Theor Biol Med Model.* 2008;5:12.
65. Mandelbrot, Evertsz, Hayakawa. Exactly self-similar left-sided multifractal measures. *Phys Rev A.* 1990;42(8):4528–36.
66. Mandelbrot BB. The fractal geometry of nature. Updated and augmented. In: Freeman WH editor. *W.H. Freeman and Company*, New York; 1983.
67. Mittal R, Srivastava P, Mukherjee A, others. Autonomous robot control using facial expressions. *Int J Comp Theory.* 2012;4(4):633.
68. Nimmerjahn A, Kirchhoff F, Helmchen F. Resting microglial cells are highly dynamic surveillants of brain parenchyma in vivo. *Science.* 2005;308(5726):1314–8.
69. Nonnenmacher TF, Baumann G, Barth A, Losa GA. Digital image analysis of self-similar cell profiles. *Int J Biomed Comput.* 1994;37(2):131–8.

70. Pantic I, Dacic S, Brkic P, Lavrnja I, Pantic S, Jovanovic T, Pekovic S. Application of fractal and grey level co-occurrence matrix analysis in evaluation of brain corpus callosum and cingulum architecture. *Microsc Microanal.* 2014;20(5):1373–81.
71. Pantic I, Nestic D, Stevanovic D, Starcevic V, Pantic S, Trajkovic V. Effects of ghrelin on the structural complexity of exocrine pancreas tissue architecture. *Microsc Microanal.* 2013;19(3):553–8.
72. Plotnick R, Gardner R, O'Neill R. Lacunarity indices as measures of landscape texture. *Landsc Ecol.* 1993;8(3):201–11.
73. Plotnick RE, Gardner RH, Hargrove WW, Prestegard K, Perlmutter M. Lacunarity analysis: a general technique for the analysis of spatial patterns. *Phys Rev E Stat Phys Plasmas Fluids Relat Interdiscip Topics.* 1996;53(5):5461–8.
74. Polito A, Brouland JP, Porcher R, Sonnevile R, Siami S, Stevens RD, Guidoux C, Maxime V, de la Grandmaison GL, Chretien FC, Gray F, Annane D, Sharshar T. Hyperglycaemia and apoptosis of microglial cells in human septic shock. *Crit Care.* 2011;15(3):R131.
75. Rankin SK, Fink PW, Large EW. Fractal structure enables temporal prediction in music. *J Acoust Soc Am.* 2014;136(4):EL256–62.
76. Reishofer G, Koschutnig K, Enzinger C, Ebner F, Ahammer H. Fractal dimension and vessel complexity in patients with cerebral arteriovenous malformations. *PLoS One.* 2012;7(7):e41148.
77. Ristanovic D, Stefanovic BD, Puskas N. Fractal analysis of dendrite morphology of rotated neuronal pictures: the modified box counting method. *Theor Biol Forum.* 2014;107(1–2):109–21.
78. Rozovsky I, Finch CE, Morgan TE. Age-related activation of microglia and astrocytes: in vitro studies show persistent phenotypes of aging, increased proliferation, and resistance to down-regulation. *Neurobiol Aging.* 1998;19(1):97–103.
79. Saeedi P. Self-organised multi agent system for search and rescue operations. University College London. 2010.
80. Schulze MM, Hutchings N, Simpson TL. The use of fractal analysis and photometry to estimate the accuracy of bulbar redness grading scales. *Invest Ophthalmol Vis Sci.* 2008;49(4):1398–406.
81. Sheets KG, Jun B, Zhou Y, Zhu M, Petasis NA, Gordon WC, Bazan NG. Microglial ramification and redistribution concomitant with the attenuation of choroidal neovascularization by neuroprotectin D1. *Mol Vis.* 2013;19:1747–59.
82. Shigetomi E, Bushong EA, Hausteine MD, Tong X, Jackson-Weaver O, Kracun S, Xu J, Sofroniew MV, Ellisman MH, Khakh BS. Imaging calcium microdomains within entire astrocyte territories and endfeet with GCaMPs expressed using adeno-associated viruses. *J Gen Physiol.* 2013;141(5):633–47.
83. Sierra A, Tremblay M-E, Wake H. Never-resting microglia: physiological roles in the healthy brain and pathological implications. *Front Cell Neurosci.* 2014;8:240.
84. Smith AR. A pixel is not a little square and a voxel is not a little cube. *Microsoft Technol Memo.* 6.
85. Smith Jr TG, Lange GD, Marks WB. Fractal methods and results in cellular morphology – dimensions, lacunarity and multifractals. *J Neurosci Methods.* 1996;69(2):123–36.
86. Soltys Z, Ziaja M, Pawliński R, Setkowicz Z, Janeczko K. Morphology of reactive microglia in the injured cerebral cortex. Fractal analysis and complementary quantitative methods. *J Neurosci Res.* 2001;63(1):90–7.
87. Ștefănuț AC, Țălu Ș, Miclăuș V, Mureșan A, Moldovan R, Szabo B. Postnatal development of the retina in rats exposed to hyperoxia: a fractal analysis. *ISRN Biomed Imaging.* 2013;2013:1–6.
88. Ștefănuț AC, Țălu Ș, Miclăuș V, Mureșan A, Szabo B. A Fractal analysis study of retinal development in rats exposed to the alternating hyperoxia-hypoxia. *Annals of RSCB.* 2013;XVIII(Issue 1/2013):8.

89. Stence N, Waite M, Dailey ME. Dynamics of microglial activation: a confocal time-lapse analysis in hippocampal slices. *Glia*. 2001;33(3):256–66.
90. Stosić T, Stosić BD. Multifractal analysis of human retinal vessels. *IEEE Trans Med Imaging*. 2006;25(8):1101–7.
91. Streit WJ, Walter SA, Pennell NA. Reactive microgliosis. *Prog Neurobiol*. 1999;57(6):563–81.
92. Szymanski JJ, Jamison JT, DeGracia DJ. Texture analysis of poly-adenylated mRNA staining following global brain ischemia and reperfusion. *Comput Methods Programs Biomed*. 2012;105(1):81–94.
93. Takayasu H. *Fractals in the physical sciences: nonlinear science: theory and applications*. Manchester: St. Martin's Press; 1990.
94. Tălu S. Multifractal characterisation of human retinal blood vessels. *Oftalmologia*. 2012;56(2):63–71.
95. Tălu S. Multifractal geometry in analysis and processing of digital retinal photographs for early diagnosis of human diabetic macular edema. *Curr Eye Res*. 2013;38(7):781–92.
96. Țălu Ș, Giovanzana S. Image analysis of the normal human retinal vasculature using fractal geometry. *Int J Bioflux Soc*. 2012;4(1):5.
97. Todd K, Butterworth RF. Mechanisms of selective neuronal cell death due to thiamine deficiency. *Ann N Y Acad Sci*. 1999;893:404–11.
98. Tremblay ME, Stevens B, Sierra A, Wake H, Bessis A, Nimmerjahn A. The role of microglia in the healthy brain. *J Neurosci*. 2011;31(45):16064–9.
99. Tremblay S, Miloudi K, Chaychi S, Favret S, Binet F, Polosa A, Lachapelle P, Chemtob S, Sapiéha P. Systemic inflammation perturbs developmental retinal angiogenesis and neuroretinal function. *Invest Ophthalmol Vis Sci*. 2013;54(13):8125–39.
100. Trevino J, Liew SF, Noh H, Cao H, Dal Negro L. Geometrical structure, multifractal spectra and localized optical modes of aperiodic Vogel spirals. *Opt Express*. 2012;20(3):3015–33.
101. Vicsek T. *Fractal growth phenomena*. 2nd ed. Singapore: World Scientific; 1992.
102. Wen YR, Tan PH, Cheng JK, Liu YC, Ji RR. Microglia: a promising target for treating neuropathic and postoperative pain, and morphine tolerance. *J Formos Med Assoc*. 2011;110(8):487–94.
103. Yasar F, Akgunlu F. Fractal dimension and lacunarity analysis of dental radiographs. *Dentomaxillofac Radiol*. 2005;34(5):261–7.
104. Yasar F, Yesilova E, Akgunlu F. Alveolar bone changes under overhanging restorations. *Clin Oral Investig*. 2010;14(5):543–9.

Chapter 3

Tenets and Methods of Fractal Analysis (1/f Noise)

Tatjana Stadnitski

Abstract This chapter deals with methodical challenges confronting researchers of the fractal phenomenon known as pink or 1/f noise. This chapter introduces concepts and statistical techniques for identifying fractal patterns in empirical time series. It defines some basic statistical terms, describes two essential characteristics of pink noise (self-similarity and long memory), and outlines four parameters representing theoretical properties of fractal processes: the Hurst coefficient (H), the scaling exponent (α), the power exponent (β), and the fractional differencing parameter (d) of the ARFIMA (autoregressive fractionally integrated moving average) method. Then, it compares and evaluates different approaches to estimating fractal parameters from observed data and outlines advantages, disadvantages, and constraints of some popular estimators. The final section of this chapter answers the questions: Which strategy is appropriate for the identification of fractal noise in empirical settings and how can it be applied to the data?

Keywords 1/f noise • Fractal parameters • ARFIMA • Long memory

3.1 Tenets and Methods of Fractal Analysis (1/f Noise)

Pink or *1/f noise* is a well-studied fractal (i.e., self-similar) phenomenon. As will be explained here, the word “pink” in the name arises from its characteristically long “memory” being intermediate between that of *white noise* (no memory) and *red* or *Brown noise* (infinite memory). Pink noise serves as an adequate model for many biological processes because it exhibits both stability and adaptability, two properties typical of healthy complex systems [4]. Highly correlated fluctuations of pink noise are typical for neural dynamics. For instance, cognitive reactions generated in psychological experiments including mental rotation, lexical decision, shape and

T. Stadnitski, MD, PD
Institute of Psychology and Education, University of Ulm, Ulm, Germany
e-mail: tatjana.stadnitski@uni-ulm.de

color discrimination, and word naming demonstrated a $1/f$ noise character [17, 41, 42]. Pink noise was also detected in visual perception [3], in rhythmic tasks requiring coordination of motor and cognitive activities [8, 10], and in brain dynamics of electroencephalogram records [1, 2, 7, 24]. The oscillatory neural synchronization [29], the spontaneous phase-transition process of many interacting neurons [5], and the fit between the phase-transition conjecture and the criticality condition [43, 44] have been discussed as the cause for these observations in the recent neurophysiologic literature. Some researchers view $1/f$ noise as a communication channel for complex networks through which the brain influences complex processes and is influenced by them [e.g., 1]. Generally, it is thought that $1/f$ noise reflects the coordinative, metastable basis of cognition [e.g., 22]. Brain dynamics have been investigated statistically either by monofractal methods or by studying autocorrelation functions of the related time series. Another alternative for the statistical analysis of brain dynamics is to examine their spectral density functions and periodograms obtained by the Fast Fourier Transform algorithm. Different methodological approaches for the detection of $1/f$ noise and interrelations between them will be discussed in the following subchapters.

3.2 Statistical Terms: Parameter, Estimator, Estimate

To understand how pink noise is evaluated in fractal analysis, one should first know the differences among the following statistical concepts: “parameter,” “estimator,” and “estimate.” A *parameter* is a quantity that defines a particular system, such as the mean of the normal distribution. Strictly speaking, to obtain a population parameter, one must measure an entire population, which is mostly infeasible, so instead one generally uses *estimators* (rules or formulae) to infer population parameters from observed samples. For any parameter, there are usually multiple estimators with diverse statistical properties. As an example, suppose we have n observations of some phenomenon X ; then we can estimate the population mean (μ) using two

well-known estimators, the sample mean, $\hat{\mu}_1 = \frac{1}{n} \sum_{i=1}^n X_i$, and the median, $\hat{\mu}_2 = X_{0.5}$.

In contrast to parameters, estimators are not numbers but functions characterized by their distributions, expectancy values, and variances, where the quantity to be estimated generally differs from its estimation. Thus, because every estimation method involves some estimation error, the investigator must choose which method best suits the task at hand. Based on the above example, for instance, μ may differ from both $\hat{\mu}_1$ and $\hat{\mu}_2$, and an investigator might choose the former as the better estimator of μ if the phenomenon being investigated is better understood using a smaller variance and narrower confidence intervals. In fractal analysis, one way to decide which estimator to use is by means of *Monte Carlo simulations*. For instance, computational algorithms can generate a population with a known parameter value, and repeated samples of the same size can be drawn from this population, e.g., 1,000 time series with $T=500$, and then different estimators can be applied to the series,

yielding 1,000 estimates of the parameter per method. An *estimate* is a particular numerical value obtained by applying an estimator. Good estimators are unbiased, i.e., their means equal the true parameter value, and have small variability, i.e., their estimates do not differ strongly. Considering that just one estimate per method is available in a typical research situation, an estimator with a narrow range is usually better than one with a broad range.

3.3 Properties of 1/f Noise: Self-Similarity and Long Memory

Fractals are *self-similar structures or processes* where the whole has the same shape as its parts. The concept of self-similarity, as well as examples such as the Koch snowflake or the Sierpinski triangle, is covered in Chap. 2. To summarize here, there are two types of self-similarity: strict and statistical. Strictly self-similar geometrical objects like the Koch snowflake are composed of exact copies of the whole object. Statistical fractals like Romanesco broccoli consist of sub-pieces that closely replicate the whole structure. Pink noise is statistically self-similar, meaning its smaller segments look like its larger segments, and all exhibit the same statistical properties as the overall process. It is also *scale invariant*, meaning its characteristics remain similar when viewed at different scales of time or space.

These properties, self-similarity and scale invariance, can be modeled mathematically by *power laws*. A power law is a functional relationship between two quantities, where one quantity varies as a power of another. For instance, the relation between external stimuli and internal sensation can be described by a power law proposed by the American psychologist Stevens: $S = cI^b$, where S is sensation magnitude, I is stimulus intensity, c is an arbitrary constant to determine the scale unit, and b is the power exponent, which depends on the type of stimulation. This *exponential function* states that the perceived strength of subjective sensation increases proportionally with the intensity of the physical stimulus. Assuming c is positive, if the exponent b is zero, the graph of the function is a horizontal line; if b is one, the graph is a line of slope c ; if b is greater than one, the line curves upward; and if b is between 1 and 0, it curves downward. Most relevant here, when the log is taken of both sides, power functions have the convenient feature of becoming linear, with a slope equal to the value of the exponent. For instance, the logarithmic form of Stevens' power law is $\log(S) = \log(c) + b\log(I)$, i.e., a straight line with slope of b (Fig. 3.1). In general, multiplying the argument I of the Stevens' or similar functions by a constant k causes *proportional scaling* of the function itself: $f(kI) = c(kI)^b = k^b f(I) \propto f(I)$. Therefore, the slope of the straight line on the log-log plot can be viewed as the signature of a power law, or, in fractal analysis parlance, a measure of fractality.

Power laws express self-similarity in fractal processes by demonstrating that the same principles hold for all segments of the process and on all scales. For instance, fractals are often described by a power law stating that the frequency of occurrence

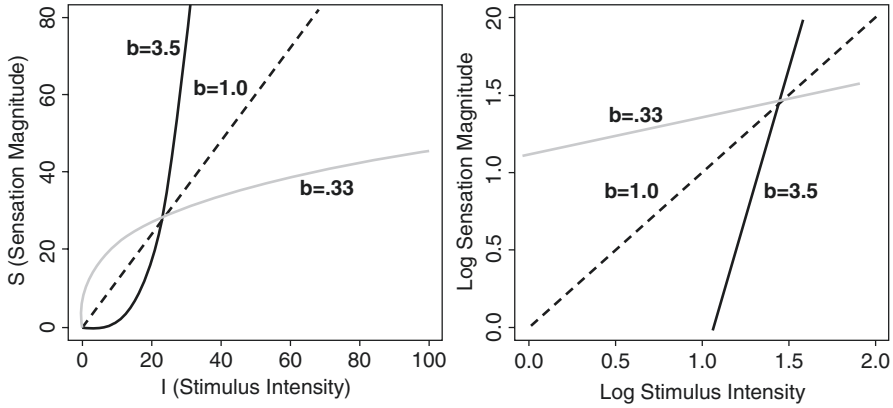


Fig. 3.1 Stevens' power law functions

(F) of an element of a given size is inversely proportional to some power of its size ($F_s \propto 1/\text{size}^{\text{power}}$). Dividing a process into intervals of equal length n allows viewing it on different scales. Fluctuations (F) of fractal processes are proportional to n , i.e., they increase with growing interval length ($F_n \propto n^{\text{power}}$). Another power law assumes that the variance of fractal processes (S) is inversely proportional to their frequency (f) ($S_f \propto 1/f^{\text{power}}$).

3.3.1 Memory

Pink noise is generally measured as a time series (i.e., as successive measurements made over a time interval). Self-similarity within a time series can be modeled by the *autocorrelation function* (ACF). The autocorrelation function describes the correlation of a signal with itself at different lags. In other words, it reflects the similarity between observations in reference to the amount of time between them. Informally, this relates to the notion of the “memory” of a process, which can range from no memory to infinite memory. To elaborate, white noise is a sequence of time-ordered, uncorrelated, random variables, sometimes called random shocks or innovations, and therefore is considered to have “no memory.” A process that can be predicted by its immediate past, although the autocorrelations decay quickly as the number of intervening observations increases, is considered to have a “short memory.” On the other end of the spectrum, red noise results from integrating white noise, so can be represented as the sum of random shocks such that the impact of a particular innovation never dissipates, which implies no decay in autocorrelation and infinite memory.

As was mentioned earlier, pink noise is intermediate between white and red. The self-similarity of pink noise manifests in a power-like decaying autocorrelation function. Pink noise possesses very slowly decaying autocorrelations reflecting statistical dependence between observations separated by a large number of time units.

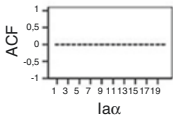
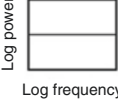
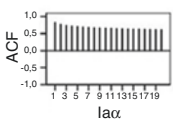
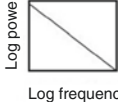
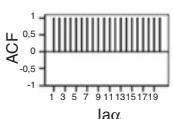
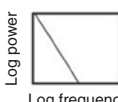
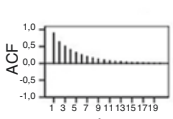

	MEMORY	ACF	POWER SPECTRUM	FRACTAL PARAMETERS
WHITE NOISE	NO			$H=0.5$ $\alpha=0.5$ $\beta=0$ $d=0$
PINK NOISE	LONG			$H=1$ $\alpha=1$ $\beta=1$ $d=0.5$
RED NOISE	INFINITE			$H=0.5$ $\alpha=1.5$ $\beta=2$ $d=1$
AUTOREGRESSIVE PROCESS	SHORT			No power low $d=0$

Fig. 3.2 Theoretical autocorrelation functions, logarithmic power spectra, and parameter values of pink noise compared with non-fractal patterns. (Note: white, pink, and red noises are self-similar processes.) Pink noise is intermediate between white and red. Autoregressive processes are not self-similar

This explains why pink noise can be viewed as intermediate between white noise with no correlation in time and red noise with no correlation between increments. Due to persistence of its autocorrelations, $1/f$ noise is also called a *long-memory process* or *long-range-dependent process*. The ACF of processes with different memory characteristics is compared in Fig. 3.2.

3.3.2 Stationarity

One of the most important concepts of time series analysis is stationarity. A process is said to be stationary if its mean, variance, and autocorrelations do not change over time; otherwise, it is non-stationary. Non-stationary behaviors can evolve from cycles and stochastic or deterministic trends. Changing data, as a rule, are unpredictable and cannot be modeled or forecasted unless stabilized; therefore, non-stationary time series are usually transformed to make them stationary. White noise, also called *Gaussian noise*, is stationary with constant mean and variance, whereas red noise, also called *Brownian motion*, is non-stationary. Because summing

Gaussian noise produces Brownian motion, differencing Brownian motion creates Gaussian noise, which means that increments of red noise are stationary. For this reason, red noise is sometimes termed difference stationary. As an intermediate between white and red noise, pink noise is both stationary and non-stationary, with slow fluctuations of its parameters. Due to this property, the $1/f$ process becomes both stable and adaptive.

Generally, there are two different classes of long-memory processes in fractal analysis: *non-stationary fractional Brownian motions* (fBm) and *stationary fractional Gaussian noises* (fGn) [26, 27]. Mandelbrot and van Ness [26] introduced fBm as Brownian motion with correlated increments. A positive correlation implies that an increasing trend in the past is expected to be followed by an increasing trend in the future. Therefore, fBm with positive correlations of increments are called *persistent*. Fractional Brownian motions with negative correlations of increments are called *anti-persistent* because an increasing trend here is likely to be followed by a decrease in the future. Mandelbrot and Wallis [27] defined fractional Gaussian noise as a series of successive increments in an fBm. This means that each fBm is related to a specific fGn, and both are characterized by the same fractal dimension [25].

A *fractal dimension* (D) is an index of complexity of self-similar objects describing how details in a pattern change with the scale at which it is measured. Euclidean geometry is three dimensional: The dimension of a line is 1, of a square is 2, and of a cube is 3. According to the following power law $NR \propto R^D$, the number of self-similar pieces into which the object may be broken (N) is proportional to some scaling factor (R). Hence, the fractal dimension can be calculated as $D = (\log N)/(\log R)$. For example, a line is one dimensional because we can break it into N self-similar pieces, each is $1/N$ the length of the original (i.e., $N=R$). A square is two-dimensional because it consists of N^2 self-similar copies of itself, each of which must be magnified by a factor of N to yield the original figure (i.e., $N=R^2$). For instance, we can decompose a square into 4 self-similar sub-squares with the scaling factor 2, or 9 self-similar pieces with the scaling factor 3, or 16 self-similar pieces with the scaling factor 4. For description of fractal images like the Koch snowflake, the Sierpinski triangle, or a piece of broccoli, the spaces of integer dimension are not enough. Figure 3.3 visualizes that the Koch snowflake is constructed by iteratively scaling a starting segment into four new pieces with the scaling factor 3: All original line segments are replaced with four, each a self-similar copy that is $1/3$ the length of the original (i.e., $N=4$, $R=3$). In contrast to a line or a square, the Koch snowflake has non-integer dimension: $D = (\log 4)/(\log 3) \approx 1.26$. Similarly, the Sierpinski triangle breaks into three self-similar pieces with the scaling factor 2 resulting in the non-integer dimension $D = (\log 3)/(\log 2) \approx 1.58$. Fractal dimension can also be understood as a measure of the space-filling capacity of an object. Hence, a square is larger than a line, while the Koch snowflake and the Sierpinski triangle take a position between these two sets: The Koch snowflake is closer to a line and the Sierpinski triangle is closer to a square. For the same reason, jagged and irregular patterns of white and red noise yield a fractal dimension of 1.5. Successive observations of white noise and increments of red noise are independent of each other, so $D=1.5$ describes a random independent system. By contrast, fGn and fBm are correlated noises. The course of persistent series is smoother and closer to a line implying

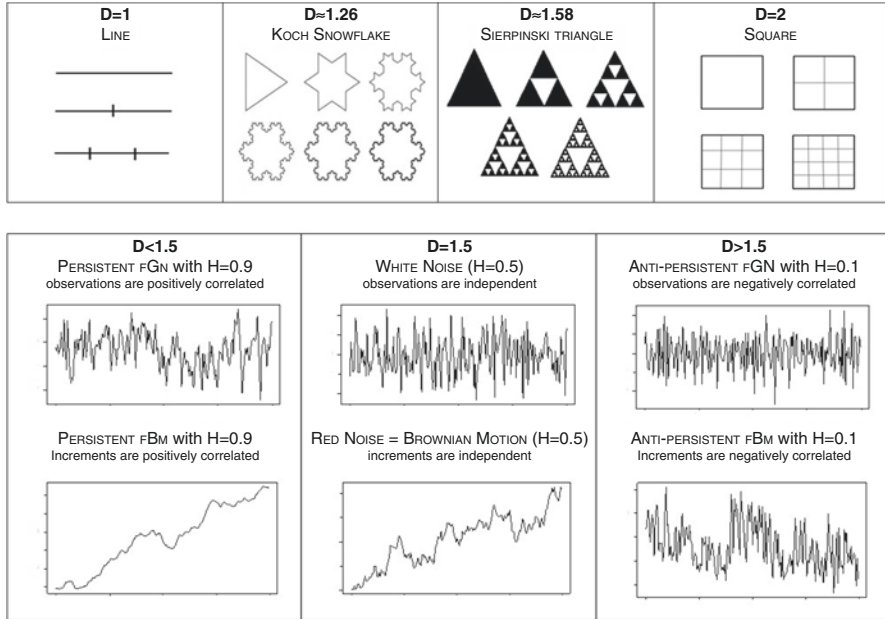


Fig. 3.3 Geometric objects and time series with different dimensions

lower fractal dimensions than that of uncorrelated noises. Being more jagged, anti-persistent series occupy more space and have therefore higher fractal dimensions closer to $D=2$ (Fig. 3.3). Stationary fractional Gaussian noises and non-stationary fractional Brownian motions represent a continuum; pink noise marks the boundary between fGn and fBm. Successive observations of pink noise time series are positively correlated resulting in fractal dimensions near $D=1$

3.4 Fractal Parameters

The extent of self-similarity and the memory properties of a process are often described using four fractal parameters: the Hurst coefficient (H), the scaling exponent (α), the power exponent (β), and the fractional differencing parameter (d).

3.4.1 Hurst Coefficient

H expresses the probability that an event in a process is followed by a similar event. Investigating the behavior of the Nile River, Hurst [21] observed that wet years were often followed by wet years resulting in wet periods and dry years by dry producing droughts. This tendency to self-similarity, which is typical of many climatic

processes, is known as the Hurst phenomenon or Joseph effect [28]. As a probability measure, the Hurst coefficient ranges between 0 and 1, which corresponds to a fractal dimension between 1 and 2 ($D=2-H$). $H=0.5$ for both white and red noise, because white noise is a sequence of independent innovations and red noise consists of uncorrelated increments. The Hurst coefficient of fractal processes deviates from 0.5, whereby $H<0.5$ denotes anti-persistent and $H>0.5$ positively persistent processes. Anti-persistence implies negative correlations between successive increments. Pink noise is characterized by $H=1$. Recall that differencing Brownian motion creates Gaussian noise and summing Gaussian noise produces Brownian motion. Thus, related fGn and fBm are characterized by the same Hurst exponent (Fig. 3.3).

3.4.2 Scaling Exponent (α)

As described above, self-similarity can be modeled mathematically by power laws. If we divide a process into segments of equal length, n , we can effectively view it on different scales. The *Detrended Fluctuation Analysis* (DFA) proposed by Peng et al. [30] demonstrates that fluctuations (F) of fractal signals are related to the interval size (n) by the following power law:

$$F(n) \propto n^\alpha$$

For white noise, $\alpha=0.5$, and for red, $\alpha=1.5$ (Fig. 3.2). Fluctuations of pink noise are proportional to n , i.e., they increase with growing interval length which implies that $\alpha=1$. For stationary fractional Gaussian noises, $\alpha < 1$, and for non-stationary fractional Brownian motions, $\alpha > 1$.

3.4.3 Power Spectra

For studying discrete-time processes, there are two major approaches: *time-domain* and *frequency-domain analysis*. Although time and frequency domains are mathematically equivalent, they examine data from different perspectives and pursue different goals. In time domain analysis, the central concept is the memory of the process: To what extent is its present state predictable from its past? Therefore, statistical assessments are mostly based on autocorrelations. The main goal of frequency-domain analysis is to detect cycles in the data by identifying frequencies that explain variance in a time series. Here, the power spectrum and spectral density function serve as the most important statistical tools.

The power spectrum determines how much power (i.e., variance or amplitude) is accounted for by each frequency in a series. The term “frequency” describes how rapidly things repeat themselves. Thus, there exist fast and slow frequencies. For instance, a time series with $T=100$ observations can be reconstructed by 50 periodic

or cyclic components ($T/1, T/2, T/3, \dots, 2$). The frequency is the reciprocal of the period and can be expressed in terms of number of cycles per observation. $f=0$ implies no repetition, $f=1/T$ the slowest, and $f=0.5$ the fastest frequency. The *spectral density function* gives the amount of variance accounted for by each frequency measured. Spectral analysis represents a special type of variance analysis (ANOVA) where the overall process variance is divided into components of independent cycles with different lengths. For nonperiodic processes like white noise, the variance is equally distributed across all possible frequencies. For cyclic processes, a few so-called major frequencies explain a great amount of the series' variance (i.e., all of the series' power is concentrated at one or a few frequencies).

3.4.4 Power Exponent

β quantifies the extent of self-similarity. Fractal processes have self-similar power spectra with a spectral density that is proportional to the reciprocal of the frequency and can be expressed by the following power law:

$$S(f) \propto 1/f^\beta.$$

For white noise, the variance is distributed equally over the frequencies; thus $\beta=0$ and the logarithmic power spectrum has a slope of 0. For red noise, power falls off rapidly with increasing frequency, i.e., low-frequency components predominate, $\beta=2$, and the power spectrum has a slope of -2 . For pink noise, $\beta=1$ implying that its variance is inversely proportional to its frequency, and the power spectrum is a straight line with slope -1 . This property becomes more vivid in the logarithmic expression: $\log(S)=-\beta\log(f)$. The power exponent of stationary fractional Gaussian noises can be any real value in the range $[-1; 1]$ with $-1 < \beta < 0$ for anti-persistent and $0 < \beta < 1$ for positively persistent signals. For non-stationary fractional Brownian motions, $1 < \beta < 2$ means anti-persistent and $2 < \beta < 3$ positively persistent series. These power laws do not hold for short-memory autoregressive processes, the spectra of which are not straight lines. The linear relation between the power and the frequency of such processes breaks down at the low frequencies where random variation appears. As a result, a flat plateau (the zero slope of white noise) dominates low frequencies in spectral plots. Figure 3.2 shows the power spectra of the discussed processes.

3.4.5 Differencing Parameter (d)

As described previously, one of the typical characteristics of pink noise is a power-like decaying autocorrelation function with a long memory. Granger et al. [18] and Hosking [20] demonstrated that memory properties of fractal time series can be parsimoniously modeled by the *differencing parameter* d of the Box-Jenkins

ARIMA (autoregressive integrated moving average) methodology [6] allowing it to take on continuous values.

In the time domain, each time series can be described by three types of mathematical models: autoregressive (AR), moving average (MA), and integrated (I). In an AR model, the value of the current observation depends on the values of the previous observations,

$$Y_t = \phi_1 Y_{t-1} + \dots + \phi_p Y_{t-p} + u_t,$$

where ϕ quantifies the magnitude of the dependence, p specifies the order of the dependence, and u_t is a sequence of purely independent and identically distributed innovations or white noise.

An MA process is described by:

$$Y_t = u_t - \theta_1 u_{t-1} - \dots - \theta_q u_{t-q}.$$

Here performance at time t depends on both the current and past error terms. A process containing both autoregressive and moving average components is called mixed. An integrated process is represented by the equation

$$Y_t = Y_{t-1} + a_t,$$

where the random part a_t can be generated by any ARMA process. Red noise is an integrated process with $a_t = u_t$; therefore, it can be expressed as the sum of white noise. The term “integrated” implies that the impact of the random component in the series does not dissipate over time. As a result, integrated processes are non-stationary and show instability in level. That is why red noise is also called *random walk*. Differencing red noise produces stationary white noise:

$$\Delta Y_t = Y_t - Y_{t-1} = u_t.$$

The equation demonstrates that increments of red noise, ΔY_t , are stationary. Integrated models are also known in the time series literature as *unit root processes*. A situation of non-stationarity is called the unit root problem when the regression coefficient of a first-order autoregressive model equals one. The name unit root is due to the fact that $\phi = 1$. In this case, the autoregressive model can be written as $(1-L)Y_t = u_t$, where L is the lag operator: $LY_t = Y_{t-1}$, $L^2 Y_t = Y_{t-2}$ and so on. The term unit root refers to the root of the polynomial in the lag operator. If $(1-L)=0$, we obtain $L=1$.

The autoregressive integrated moving average (ARIMA) method describes processes through the three parameters p , d , and q . For example, the following process

$$Y_t = \phi_1 Y_{t-1} + u_t + \theta_1 u_{t-1}$$

is called ARMA (1, 1) because it contains one autoregressive (Y_{t-1}) and one moving average term (u_{t-1}). Therefore, the value of the autoregressive parameter p reflects

how many preceding observations influence the current observation. The value of the moving average term q describes how many previous random shocks must be taken into account when describing the dependency present in the time series. Within the Box-Jenkins ARIMA framework, d is a whole number and refers to the order of differencing that is necessary to make a process stationary ($d=0$). Thus, the ARMA (1, 1) process can also be written as ARIMA (1, 0, 1). White noise is ARIMA (0, 0, 0). Models with $d=1$ are called integrated of order 1. Red noise is ARIMA (0, 1, 0). Autoregressive fractionally integrated moving average (ARFIMA) modeling extends the traditional Box-Jenkins approach by allowing the differencing parameter d to take on non-integer values. This enables ARFIMA models to give parsimonious descriptions of any long-range dependencies in time series. Pink noise has a d of 0.5. Stationary fractal noises can be modeled with $-0.5 < d < 0.5$. Values of d in the interval $[-0.5; 0]$ suggest anti-persistence. Processes with $d > 0$ are long-term persistent. Therefore, finite long memory can be modeled with $0 < d < 0.5$. For $0.5 \leq d \leq 1.5$, the process is non-stationary.

To summarize, there are different mathematical methods to express self-similar power law organization of fractal structures. Since fractal signals can be analyzed in both time and frequency domains, there are different fractal parameters like the Hurst coefficient, the scaling exponent α , the power exponent β of spectral analysis, or the differencing statistic d of the ARFIMA framework. It is crucial to understand that these parameters express exactly the same characteristics, which implies that each quantity can be converted to the other. For instance, interrelations between the parameters for stationary processes are $H = (\beta + 1)/2$, $\alpha = H = d + 0.5$, and $\beta = 2d$. The expected theoretical values for 1/f noise are $H = 1$, $\alpha = 1$, $\beta = 1$, and $d = 0.5$. Table 3.1 outlines the relationship between the parameters and demonstrates how one quantity can be transformed into the other (Table 3.1).

Table 3.1 Fractal parameters and relations between them

	H	α	β	d
White noise	0.5	0.5	0	0
Pink noise	1	1	1	0.5
Red noise	0.5	1.5	2	1
Stationary fGn anti-persistent positively persistent	[0; 1]	[0; 1]	[-1; 1]	[-0.5; 0.5]
	<0.5	<0.5	<0	<0
	>0.5	>0.5	>0	>0
Non-stationary fBm anti-persistent positively persistent	[0; 1]	[1; 2]	[1; 3]	[0.5; 1.5]
	<0.5	<1.5	<2	<1
	>0.5	<1.5	>2	>1
Relation to other parameters for fGn	$H = \alpha$	$\alpha = H$	$\beta = 2H - 1$	$d = H - 0.5$
	$H = (\beta + 1)/2$	$\alpha = (\beta + 1)/2$	$\beta = 2\alpha - 1$	$d = \alpha - 0.5$
	$H = d + 0.5$	$\alpha = d + 0.5$	$\beta = 2d$	$d = \beta/2$
Relation to other parameters for fBm	$H = \alpha - 1$	$\alpha = H + 1$	$\beta = 2H + 1$	$d = H + 0.5$
	$H = (\beta - 1)/2$	$\alpha = (\beta - 1)/2 + 1$	$\beta = 2(\alpha - 1) + 1$	$d = \alpha - 0.5$
	$H = d - 0.5$	$\alpha = d + 0.5$	$\beta = 2d$	$d = \beta/2$

3.5 Estimators of Fractal Parameters

As noted previously, parameters are descriptive measures of a population that are usually unknown and therefore estimated from a sample. A sample is a limited subset of a population, which can present a distorted image of the whole. Thus, the quality of inference depends on the properties of the observed sample. Fractal parameters are inferred from empirical time series, their autocorrelations, and estimates of the spectral density function like a *periodogram*. Figure 3.4 demonstrates that independent samples (three time series with $T=200$ observations) derived from the same pink noise population can produce rather different ACFs and periodograms (Fig. 3.4). Furthermore, it illustrates that empirical power spectra and estimated autocorrelation functions can deviate substantially from the theoretical pattern of the generating process depicted in Fig. 3.2.

Slow decaying autocorrelations and the straight line on the log-log periodogram plot are necessary but not sufficient conditions for fractal time series. In fact, there

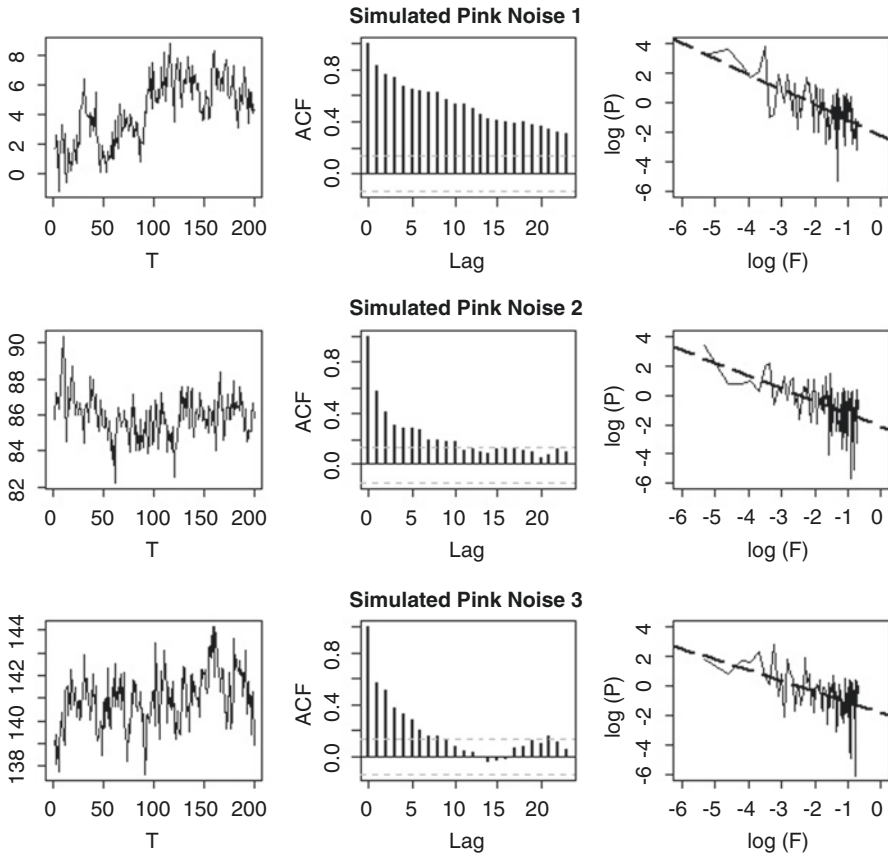


Fig. 3.4 Simulated empirical pink noise time series with their ACFs and log-log pots

are many ways to generate finite amounts of data that mimic the pink noise behavior. For instance, it is known that a combination of non-fractal signals like white noise and random walk can produce patterns similar to $1/f$ noise. Figure 3.5 shows that autoregressive ($p \neq 0, d=0, q=0$) and integrated ($p \neq 0, d=1, q \neq 0$) ARIMA models can imitate fractal structures. Thus, accurately inferring fractal parameters from empirical data is a challenging statistical issue. Estimating methods must be able to discern fractal behavior in the presence of non-fractal noise and to reliably distinguish between genuine fractals and fractal-like signals (Fig. 3.5).

Numerous procedures for measuring the fractal parameters $\beta, \alpha, H,$ and d have been developed in recent years. Generally, the estimation methods can be assigned to three categories: (1) exact or approximate maximum-likelihood or conditional sum of squares ARFIMA estimation of d like the exact method proposed by Sowell [32], the approximate algorithm (fracdiff) of Haslett et al. [19], and the conditional sum of squares approach introduced by Chung [9]; (2) fractal methods predicated on the relationship $F(n) \propto n^\alpha$ such as Detrended Fluctuation Analysis (DFA) of Peng

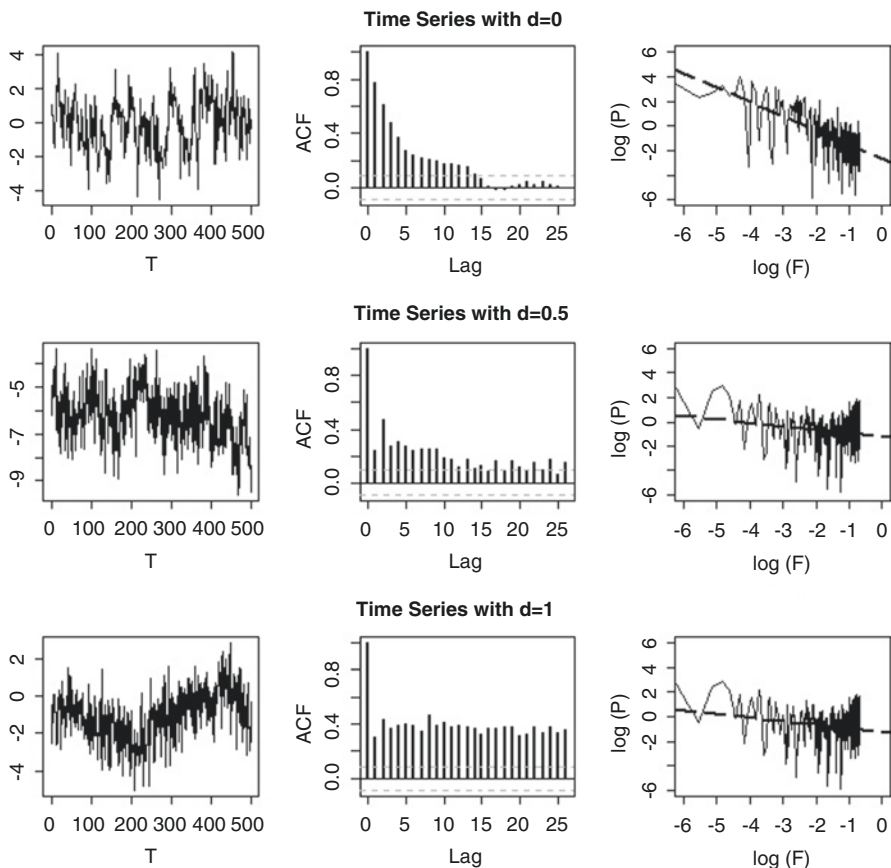


Fig. 3.5 Simulated empirical fractal and non-fractal time series with their ACFs and log-log pots

Table 3.2 Estimators of fractal parameters available in the software package R

Procedure	Outputs estimates of	Can be applied to	Available
DFA	α	fGn and fBm	Library <i>fractal</i>
SSC	α	fGn and fBm	[21] ^a
PSD	β	fGn and fBm	[22]
^{low} PSD _{we}	β	fGn and fBm	[22] ^a
HurstSpec	α	fGn and fBm	Library <i>fractal</i>
fdGPH	d	fGn and fBm	Library <i>fracdiff</i>
fdSperio	d	fGn and fBm	Library <i>fracdiff</i>
FDWhittle	d	fGn and fBm	Library <i>fractal</i>
fracdiff approximate ML	d	Only fGn	Library <i>fracdiff</i>

^aR-Codes for SSC und ^{low}PSW_{we} estimations are available at http://www.psychologie.uni-heidelberg.de/projekte/zeitreihen/R_Code_Data_Files.html

et al. [30] and Signal Summation Conversion (SSC) developed by Eke et al. [14]; (3) periodogram-based procedures like Power Spectral Density (PSD) method (e.g., [15]), Whittle (FDWhittle) [39], Sperio (fdSperio) [31], and Geweke-Porter-Hudak (fdGPH) [16]. Recall that a periodogram is an estimate of the spectral density function and the following power law relation is expected for fractal processes: $S(f) \propto 1/f^\beta$. Table 3.2 contains estimators of the fractal parameters from the open source *statistical software R* (www.r-project.org). Because of its availability, *R* is increasingly used in the neurosciences. As compared with other software tools, *R* has many further advantages: It provides a variety of statistical and graphical techniques and is highly extensible, allowing users to develop new computational routines by combining the existing functions. Various packages are under constant development for *R* and cover a wide range of modern statistics (Table 3.2).

Due to the complexity of the fractal methods, it is not possible to compare them mathematically. Therefore, their properties (e.g., accuracy, variability) are examined by means of a Monte Carlo method. Figure 3.6 demonstrates findings obtained in one simulation study. The estimators are compared and evaluated using bias moduli ($|\text{mean of estimates} - \text{true parameter}|$), standard errors of estimates, as well as the percentage of signal misclassifications employing the following rules: $\beta < 1 \rightarrow$ fGn and $\beta > 1 \rightarrow$ fBm, $\alpha < 1 \rightarrow$ fGn and $\alpha > 1 \rightarrow$ fBm, and $d < 0.5 \rightarrow$ fGn and $d > 0.5 \rightarrow$ fBm. Estimations are averaged for different sample sizes (128, 512, 1,024, 2,048) and parameterizations (e.g., H variations from 0.1 to 0.9) (Fig. 3.6).

ARFIMA algorithms were evaluated thoroughly by Stadnyska et al. [37] and Torre et al. [40]. The main advantage of the ARFIMA methods is the possibility of the joint estimation of the short-memory and long-memory parameters. This solves a potential finite-sample problem of biased overestimation of fractality in time series that contain both long-range and short-range components. Moreover, goodness of fit statistics based on the likelihood function, like the Akaike information criterion (AIC) or the Bayesian Information Criterion (BIC), allow determining the amount of “short-term contamination” and enabling a reliable discrimination between short- and long-memory processes. The greatest problem with ARFIMA

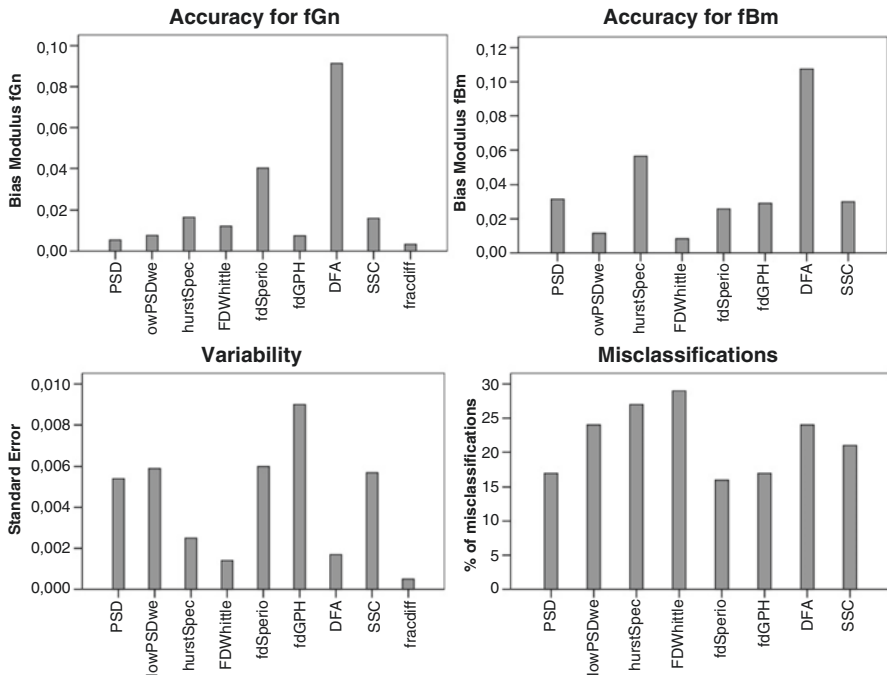


Fig. 3.6 Evaluation of the fractal methods implemented in R by means of a Monte Carlo method

estimators is that they only work for stationary series because their range is confined to $[0; 0.5]$. As a result, non-stationary fractional Brownian motions ($0.5 \leq d \leq 1.5$) tend to receive estimates of d close to 0.5. Consequently, such empirical series can easily be misclassified as $1/f$ noise. Hence, checking for stationarity is a necessary precondition for ARFIMA estimation which can be done using special procedures called *unit root tests* (see [35], for a comprehensive overview). The Augmented Dickey-Fuller test (ADF) [12], the most popular method, checks the null hypothesis “ $H_0: d=1$, series has a unit root”; thus, the rejection of H_0 implies that the series under study is probably stationary. Dolado et al. [13] developed a procedure that extends the Dickey-Fuller approach to fractionally integrated processes: Fractional Dickey-Fuller (FDF) test. In contrast, the Kwiatkowski-Phillips-Schmidt-Shin (KPSS) test [23] assumes that processes are stationary ($H_0: d=0$). Therefore, the properties of the series under study can be determined using a combination of both procedures: (1) if the ADF is significant and the KPSS is not, then the data are probably stationary with $d \in [0; 0.5]$; (2) in the Brown noise case, an insignificant ADF and a significant KPSS results are expected; (3) $d \in]0; 1[$, if both tests are significant.

Eke et al. [14], Delignières et al. [11], Stroe-Kunold et al. [38], Stadnytska et al. [36], and Stadnitski [33] systematically analyzed different power law-based methods. In contrast to ARFIMA procedures, these estimators can be applied directly to different classes of time series. Consequently, they represent adequate tools for

distinguishing fGn and fBm signals. However, due to considerably larger biases and more pronounced standard errors, the precision of fractal and periodogram – based methods is distinctly inferior to that of the ARFIMA approaches. Moreover, algorithms like PSD, DFA, or SSC use different data transformations like detrending or filtering. As a result, the performance of estimators strongly depends on the manipulations employed. For instance, numerous modifications have been suggested to improve the PSD estimation. The method $^{\text{low}}\text{PSD}_{\text{we}}$ consists of the following operations: (1) subtracting the mean of the series from each value, (2) applying a parabolic window to the data $[w]$, (3) performing a bridge detrending $[e]$, and (4) estimating β excluding 7/8 of high-frequency power estimates $[low]$. The estimator PSD is constructed without transformations. Simulation studies demonstrated that PSDs were more accurate for fGn noises, whereas $^{\text{low}}\text{PSD}_{\text{we}}$ were accurate for fBm signals. The greatest disadvantage of fractal and periodogram-based methods is their poor performance for complex processes that combine long- and short-term components. For example, simulation studies demonstrated that FDWhittle, the best procedure for pure noises, showed the worst accuracy in complex cases.

3.6 Identification of Fractal Noise in Empirical Settings

The most important findings from the reported evaluations for researchers studying fractality can be summarized as follows. First, all estimators require at least 500 observations for acceptable measurement accuracy. Further, it is essential to know that there exist different procedures with diverging characteristics. The central difficulty is that there is no clear winner among them: None of the procedures is superior to the other. As a result, the choice of the measurement method determines the outcome of fractal analyses. The performance of the methods strongly depends on aspects like the properties of the underlying process (e.g., stationary vs. non-stationary) or empirical context. For instance, Maximum Likelihood algorithms, the most accurate estimation techniques of the time domain, can only handle stationary data. Most estimators from the frequency domain can be applied to stationary and non-stationary time series directly; however, they are less precise than ARFIMA methods. Moreover, they tend to fail in empirical series that combine fractal and non-fractal dynamics. Hence, the key finding from simulation studies is that fractal estimators can produce erroneous results under disadvantageous conditions. Further, estimates from the same time series obtained from different methods can vary considerably. Consequently, comparisons of results from studies in which fractality was determined with different measurement instruments are problematic and must be interpreted cautiously.

To emphasize the importance of the last conclusion, fractal parameters of the simulated time series presented in Fig. 3.5 are estimated with different methods. Table 3.3 shows the obtained point estimates. To make the comparisons more convenient, all measures are converted to d . The demonstration aims to point out that non-fractal series could be easily misclassified as fractal noises. It is even possible

Table 3.3 Point estimates of the fractal parameters obtained from different fractal methods

Procedure	Autoregressive process ($d_{\text{true}} = 0$)	Pink noise process ($d_{\text{true}} = 0.5$)	Integrated process ($d_{\text{true}} = 1$)
DFA	0.65	0.43	0.33
SSC	0.40	0.36	0.61
PSD	0.64	0.21	0.05
HurstSpec	0.66	0.44	0.24
fdGPH	0.37	0.36	0.77
fdSperio	0.24	0.37	0.80
FDWhittle	0.71	0.24	0.24
fracdiff	0.50	0.24	0.23
Approximate ML	(0) ^a	(0.46) ^a	(0.46) ^a

To make the comparisons more convenient, all measures are transformed to d

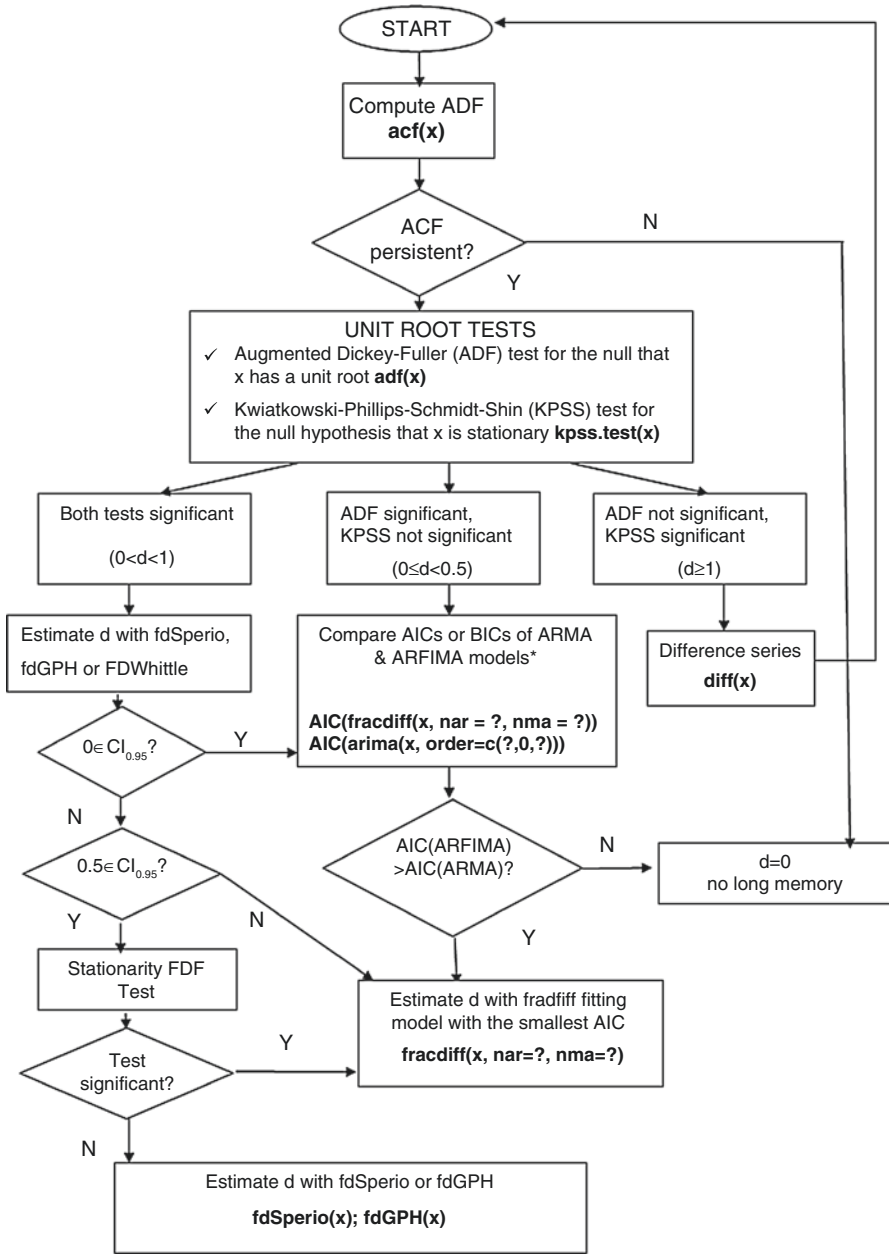
^aJoint estimation of long- and short-memory components

to erroneously attribute the $1/f$ properties to autoregressive or integrated processes (Table 3.3).

Depending on the hypotheses of the research, diverse objectives of fractal time series analyses can be distinguished: to discriminate between fractal and non-fractal patterns for diagnostic purposes, to test for the effective presence of genuine persistent correlations in the series, to provide an accurate estimation of the strength of these long-range dependencies, or to identify the short-term process that accompanies a fractal pattern. Simulation studies demonstrated that the performance of fractal methods strongly depends on aspects like the complexity of the underlying process or parameterizations. As a result, strategic approaches are necessary when analyzing fractals. Moreover, different objectives require distinct strategies. An example of such a strategic approach is described by Stadnytska et al. [36]. The algorithm presented in Fig. 3.7 allows an accurate estimate of the fractional differencing parameter d by combining different tests and statistical techniques. Furthermore, it distinguishes between fractal and non-fractal empirical time series. For instance, the procedure will probably debunk autoregressive or integrated time series from Fig. 3.5 as non-fractal. Stadnitski [34] demonstrated the application of this strategy to an empirical time series using R (Fig. 3.7).

3.7 Summary

Self-similarity and long memory are essential characteristics of a fractal pattern. Slowly decaying autocorrelations and power laws reflect these properties in the parameters H , α , β , and d . These fractal parameters express exactly the same statistical characteristics; thus, each quantity can be converted to the other. The expected theoretical values of pink noise are $H=1$, $\alpha=1$, $\beta=1$, and $d=0.5$. There are two major types of estimators for these parameters: ARFIMA algorithms and procedures searching for power laws. The former are very accurate methods capable of



* To obtain BIC instead of AIC use $AIC(arima(x, order=c(?,0,?)), k=\log(n))$, $AIC(fraddiff(x, nar = ?, nma = 1?), k=\log(n))$, n is the number of observations.

Fig. 3.7 Strategy for estimating d proposed by Stadnytska et al. [36]

measuring both long- and short-term dependencies, but they can only handle stationary processes. The latter are adequate for stationary and non-stationary data; their precision, however, is distinctly inferior to that of the ARFIMA methods and they tend to overrate fractal parameters in series containing short-memory components. The greatest problem is that no estimator is superior for a majority of theoretical series. Moreover, in a typical research situation, it is usually unclear what kind of process generated empirical data. Consequently, the estimation of fractality requires elaborate strategies. The estimation method proposed by Stadnytska et al. [36] represents an example of such a strategic approach.

References

1. Allegrini P, Menicucci D, Bedini R, Fronzoni L, Gemignani A, Grigolini P, et al. Spontaneous brain activity as a source of ideal $1/f$ noise. *Phys Rev E*. 2009;80:061914-1-13.
2. Allegrini P, Paradisi P, Menicucci D, Gemignani A. Fractal complexity in spontaneous EEG metastable-state transitions: new vistas on integrated neural dynamics. *Front Physiol*. 2010;1(128):1-9.
3. Aks DJ, Sprott JC. The role of depth and $1/f$ dynamics in perceiving reversible figures. *Nonlinear Dynamics Psychol Life Sci*. 2003;7:161-80.
4. Bak P, Tang C, Wiesenfeld K. Self-organized criticality: an explanation of $1/f$ noise. *Phys Rev Lett*. 1987;59:381-4.
5. Bianco S, Geneston E, Grigolini P, Ignaccolo M. Renewal aging as emerging property of phase synchronization. *Phys A: Stat Mech Appl*. 2008;387:1387-92.
6. Box GEP, Jenkins GM. *Time series analysis, forecasting and control*. San Francisco: Holden Day; 1970.
7. Buiatti M, Papo D, Baudonnière PM, van Vreeswijk C. Feedback modulates the temporal scale-free dynamics of brain electrical activity in a hypothesis testing task. *Neuroscience*. 2007;146:1400-12.
8. Chen Y, Ding M, Kelso JAS. Origins of time errors in human sensorimotor coordination. *J Mot Behav*. 2001;33:3-8.
9. Chung CF. A generalized fractionally integrated ARMA process. *J Time Ser Anal*. 1996;2:111-40.
10. Delignières D, Lemoine L, Torre K. Time intervals production in tapping oscillatory motion. *Hum Mov Sci*. 2004;23:87-103.
11. Delignières D, Ramdani S, Lemoine L, Torre K. Fractal analyses for short time series: a re-assessment of classical methods. *J Math Psychol*. 2006;50:525-44.
12. Dickey D, Fuller WA. Likelihood ratio statistics for autoregressive time series with a unit root. *Econometrica*. 1981;49:1057-72.
13. Dolado JJ, Gonzalo J, Mayoral L. A fractional Dickey-Fuller test for unit roots. *Econometrica*. 2002;70:1963-2006.
14. Eke A, Herman P, Bassingthwaighte JB, Raymond G, Percival D, Cannon MJ, et al. Physiological time series: distinguishing fractal noises from motions. *Pflügers Arch*. 2000;439:403-15.
15. Eke A, Herman P, Kocsis L, Kozak LR. Fractal characterization of complexity in temporal physiological signals. *Physiol Meas*. 2002;23:1-38.
16. Geweke J, Porter-Hudak S. The estimation and application of long memory time series models. *J Time Ser Anal*. 1983;4:221-38.
17. Gilden DL, Thornton T, Mallon MW. $1/f$ noise in human cognition. *Science*. 1995;267:1837-9.
18. Granger CWJ, Joyeux R. An introduction to long-range time series models and fractional differencing. *J Time Ser Anal*. 1980;1:15-30.

19. Haslett J, Raftery AE. Space-time modeling with long-memory dependence: assessing Ireland's wind power resource. *Appl Stat.* 1989;38:1–50.
20. Hosking JRM. Fractional differencing. *Biometrika.* 1981;68:165–76.
21. Hurst HE. Long-term storage: an experimental study. London: Constable; 1965.
22. Kello CT, Beltz BC, Holden JG, Van Orden GC. The emergent coordination of cognitive function. *J Exp Psychol: Gen.* 2007;136:551–68.
23. Kwiatkowski D, Phillips PCB, Schmidt P, Shin Y. Testing the null hypothesis of stationarity against the alternative of a unit root. *J Econ.* 1992;54:159–78.
24. Linkenkaer-Hansen K, Nikouline VV, Palva JM, Ilmoniemi RJ. Long-range temporal correlations and scaling behavior in human brain oscillations. *J Neurosci.* 2001;21:1370–7.
25. Mandelbrot BB. How long is the coast of Britain? Statistical self-similarity and fractional dimension. *Science.* 1967;156:636–8.
26. Mandelbrot BB, van Ness JW. Fractional Brownian motions, fractional noises and applications. *SIAM Rev.* 1968;10:422–37.
27. Mandelbrot BB, Wallis JR. Computer experiments with fractional Gaussian noises. *Water Resour Res.* 1969;5:228–67.
28. Mandelbrot BB. *The fractal geometry of the nature.* New York: Freeman; 1977.
29. Medina JM. $1/f^\alpha$ noise in reaction times: a proposed model based on Pieron's law and information processing. *Phys Rev E.* 2009;79:011902.
30. Peng CK, Mietus J, Hausdorff JM, Havlin S, Stanley HE, Goldberger AL. Long-range anticorrelations and non-Gaussian behavior of the heartbeat. *Phys Rev Lett.* 1993;70:1343–6.
31. Reisen VA. Estimation of the fractional difference parameter in the ARFIMA (p, d, q) model using the smoothed periodogram. *J Time Ser Anal.* 1994;15:335–50.
32. Sowell F. Maximum likelihood estimation of stationary univariate fractionally integrated time series models. *J Econ.* 1992;53:165–88.
33. Stadnitski T. Some critical aspects of fractality research. *Nonlinear Dynamics Psychol Life Sci.* 2012;16:137–58.
34. Stadnitski T. Measuring fractality. *Front Physiol.* 2012;3(127):1–13.
35. Stadnitska T. Deterministic or stochastic trend: decision on the basis of the augmented Dickey-Fuller test. *Methodology.* 2010;6:83–92.
36. Stadnitska T, Braun S, Werner J. Analyzing fractal dynamics employing R. *Nonlinear Dynamics Psychol Life Sci.* 2010;14:117–44.
37. Stadnitska T, Werner J. Sample size and accuracy of estimation of the fractional differencing parameter. *Methodology.* 2006;4:135–44.
38. Stroe-Kunold E, Stadnitska T, Werner J, Braun S. Estimating long-range dependence in time series: an evaluation of estimators implemented in R. *Behav Res Methods.* 2009;41:909–23.
39. Taqqu MS, Teverovsky V. On estimating the intensity of long-range dependence in finite and infinite variance time series. In: Adler R, Feldman R, Taddqu MS, editors. *A practical guide to heavy tails: statistical techniques and applications.* Boston: Birkhauser; 1998. p. 177–217.
40. Torre K, Delignières D, Lemoine L. Detection of long-range dependence and estimation of fractal exponents through ARFIMA modeling. *Br J Math Stat Psychol.* 2007;60:85–106.
41. Van Orden GC, Holden JG, Turvey MT. Self-organization of cognitive performance. *J Exp Psychol.* 2003;3:331–50.
42. Ward M. *Dynamical cognitive science.* Cambridge: MIT Press; 2002.
43. Werner G. Viewing brain processes as critical state transitions across levels of organization: neural events in cognition and consciousness, and general principles. *Biosystems.* 2009;96:114–9.
44. Werner G. Fractals in the nervous system: conceptual implication for theoretical neurosciences. *Front Physiol.* 2010;1:1–28.

Chapter 4

Tenets, Methods, and Applications of Multifractal Analysis in Neurosciences

Renaud Lopes and Antoine Ayache

Abstract The characteristics of biomedical signals are not captured by conventional measures like the average amplitude of the signal. The methodologies derived from fractal geometry have been a very useful approach to study the degree of irregularity of a signal. The monofractal analysis of a signal is defined by a single power-law exponent in assuming a scale invariance in time and space. However, temporal and spatial variation in scale invariant structure of the biomedical signal often appears. In this case, the multifractal analysis is well suited because it is defined by a multifractal spectrum of power-law exponents. There are several approaches to the implementation of this analysis and there are numerous ways to present these.

In this chapter, we review the use of multifractal analysis for the purpose of characterizing signals in neurosciences. After describing the tenets of multifractal analysis, we present the several approaches to the estimation of the multifractal spectrum. Finally, we describe the application of this spectrum on biomedical signals in the characterization of several diseases in neurosciences.

Keywords Multifractal analysis • Multifractal spectrum • Electroencephalogram • Brain imaging • Neurological diseases

R. Lopes (✉)
Clinical Imaging Core Facility (CI2C), INSERM U1171, Lille University Hospital,
Lille, France
e-mail: renaud.lopes@gmail.com

A. Ayache
CNRS 8524 UMR, Lille 1 University – Sciences and Technology, Villeneuve d’Ascq, France

4.1 Introduction

The methodologies derived from fractal geometry have been a very useful approach to study the degree of fragmentation (or irregularity) in natural, artificial, and statistical structures or processes [27]. Fractal structures are characterized by self-similarity, scaling independence, and a fractal dimension, an exponent obtained from a power or scaling law.

However, due to the complexity of some processes, one exponent may not be enough to characterize a complex phenomenon. Multifractal formalism allows using more exponents. In this case, the object of analysis is divided into several fractal sets, each generating a fractal dimension that is then translated into a continuous spectrum of exponents (the so-called spectrum of singularities or multifractal spectrum). Figure 4.1 shows an example of multifractal spectra for monofractal, multifractal, and white noise signals. The multifractality degree (MD) obtained from this continuous spectrum allows measuring the information content. Multifractal systems are common in nature, especially in geophysics. They include fully developed turbulence, stock market time series, heartbeat dynamics, human gait, and natural luminosity time series, among others.

In neurosciences, multifractal analysis has been a very useful approach to studying problems related with neurodegenerative disease, epilepsy, schizophrenia, brain tumors, among others.

This chapter reports tenets, methods, and applications of multifractal analysis in neurosciences. The purpose of this chapter is to provide a survey of multifractal analysis approaches and to discuss the main results in neurosciences. It is organized as follows: in the next section, we introduce more formally the tenets of multifractal analysis; Sect. 4.3 gives the survey of multifractal analysis

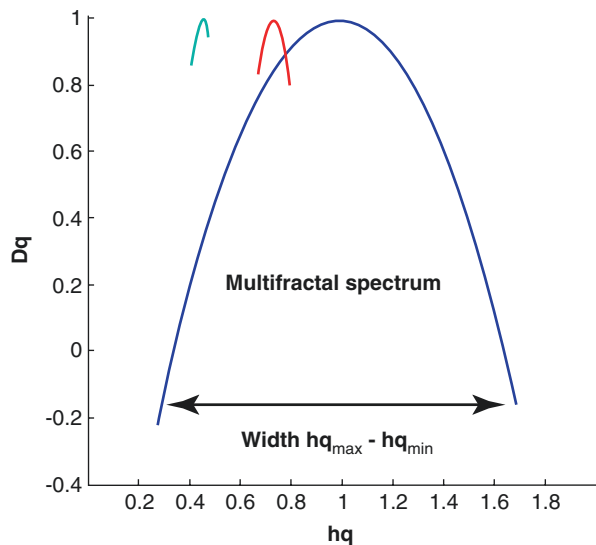


Fig. 4.1 An example of multifractal spectra for monofractal, multifractal, and white noise signals

approaches, their principles, and limitations. Section 4.4 discusses the main applications of multifractals in the neurosciences applications and the methods used.

4.2 Tenets of Multifractal Analysis

Many signals, recorded from real data, exhibit a very irregular behavior (see, e.g., [23, 29, 31, 34]). They are rapidly varying on small intervals and display oscillations of different sizes. For instance, they can be time series of prices of financial assets, they can also be heartbeat time series, and so on. In the sequel, we denote by f one of these signals. Roughly speaking, the local roughness of f at some place, in other words the “typical” size of its oscillations in a neighborhood of some fixed point t_0 , provides relevant information on the signal f at this place. Also, it is crucial to wonder whether local roughness of f changes from place to place and in that situation to have a global and synthetic description of all of its values. This is the keystone of multifractal analysis (see, e.g., [23, 31]).

The main goal of this section is to explain some important notions, which formalize the ideas presented in the first paragraph.

First we define the notion of *pointwise Hölder exponent*, which provides a precise measure of the local roughness of a signal f at an arbitrary fixed point t_0 . Let α be any given nonnegative number; one says that f satisfies a *Hölder condition of order α at t_0* , whenever there exists a polynomial P of degree less α , and there is a constant c , such that, for any t in the neighborhood of t_0 (in other words, $|t-t_0|$, the distance between t and t_0 is small) one has

$$|f(t) - P(t-t_0)| \leq c|t-t_0|^\alpha \quad (4.1)$$

Observe that P and c depend a priori on t_0 ; in other words, one should expect that they change if t_0 is replaced by another point t_1 . Also, observe that when α lies between 0 and 1, then P is always the constant polynomial equals to $f(t_0)$; thus, in this case, the inequality (4.1) reduces to $|f(t) - f(t_0)| \leq c|t-t_0|^\alpha$. The pointwise Hölder exponent of f at t_0 is denoted by $\alpha_f(t_0)$ and defined as the supremum of the numbers α satisfying (4.1).

The well-known *Brownian motion* and its most natural generalization called the *fractional Brownian motion* have traditionally been used in order to model rough signals. Maybe one can say that the Brownian motion is the keystone of classical mathematical finance; among many other things, the Brownian motion plays a key role in the very famous Black-Scholes model for pricing options on risky financial assets [4]. As regards the fractional Brownian motion, this self-similar Gaussian process with stationary increments was first introduced in 1941 by Kolmogorov [22] in order to model velocity of turbulence at intermediate scales (the inertial zone). Yet, its denomination “fractional Brownian motion” (fBm) only goes back to

the late sixties and was first used in the seminal article [29] by Mandelbrot and Van Ness. We mention that the fBm has been made to be known and adopted by a large audience, thanks to this seminal article and to several other works by Mandelbrot, which have followed it (see [27, 28]). The fBm is denoted by B_H , since it mainly depends on the *Hurst parameter* H , which belongs to the interval $(0,1)$. Up to a renormalization factor, B_H can be defined as the centered Gaussian stochastic process with covariance satisfying, for all t and s ,

$$E[B_H(t), B_H(s)] = \frac{1}{2}(|t|^{2H} + |s|^{2H} - |s-t|^{2H})$$

Observe that the fBm reduces to the Brownian motion in the particular case where $H=1/2$. In all the other cases (that is $H \neq 1/2$), the increments of B_H are correlated, and they even display long-range dependence when $H > 1/2$. Surely, the additional degree of freedom provided by the Hurst parameter makes the fBm to be a considerable more flexible model than the Brownian motion. Yet, the fBm has to be abandoned as a model for velocity of turbulence. It is important for us to precisely explain the reasons for this abandonment. Indeed, by this way, we can clarify the differences between the so-called monofractal and multifractal signals.

Assume that f is an arbitrary rough signal. The so-called *structure function of f* is denoted by I_f , and defined, for all h and positive p , as

$$I_f(h,p) = \int |f(t+h) - f(t)|^p dt \quad (4.2)$$

We mention, in passing, that some important variants of the structure function can be defined in terms of wavelet coefficients, continuous wavelet transforms, and the so-called wavelet leaders (see, e.g., [23, 31]). Generally speaking (except in pathological cases), if $|h|$ is small, then the quantity $I_f(h,p)$ behaves approximately as

$$I_f(h,p) \sim |h|^{\zeta_f(p)} \quad (4.3)$$

When f is a signal issued from velocity of a turbulent flow, various experiments, based on wind-tunnels measurements, have shown that *there is no linear dependence between p and the exponent $\zeta_f(p)$* . The situation is very different in the case where f is the fBm B_H , because it can then be shown that the exponent $\zeta_{B_H}(p)$ satisfies $\zeta_{B_H}(p) = Hp$, which clearly means that $\zeta_{B_H}(p)$ linearly depends on p . This linear dependence can be partially explained by the fact that the pointwise Hölder exponent of the fBm B_H remains the same all along its sample path; more precisely, for all t , one has $\alpha_{B_H}(t) = H$. In sharp contrast, for a signal f issued from velocity of a turbulent flow, the pointwise Hölder exponent $\alpha_f(t)$ keeps changing from point to point in an unpredictable and chaotic way. What are then the values that $\alpha_f(t)$ is most likely to have? In order to answer to this question, it is useful to introduce the notions of *iso-Hölder sets* and of *spectrum of singularities*. To each fixed nonnegative number,

ρ is associated an iso-Hölder set $S_f(\rho)$, defined as the set of all the points t such that $\alpha_f(t) = \rho$. The Hausdorff dimension of $S_f(\rho)$ is denoted by $D_f(\rho)$. The spectrum of singularities of f is defined as the whole collection of the values taken by $D_f(\rho)$, when ρ runs through the set of all the nonnegative numbers; therefore, this spectrum is denoted by D_f . Observe that in the case of the fBM B_H , the spectrum D_{B_H} is *trivial*, since it only consists in two values. It is for that reason that the fBm is called a *monofractal signal*. In sharp contrast, when a spectrum D_f contains infinitely many different values (i.e., in practice, a great number of different values), then the corresponding f is called a *multifractal signal*. Notice that models for such signals can be obtained through multiplicative cascades (see, e.g., [23, 31]). We end this paragraph by emphasizing the fact that the spectrum of singularities D_f provides a global and synthetic geometrical description of all the values of the pointwise Hölder exponent of a multifractal signal f . Thus, D_f contains relevant and useful information related with the roughness of f to which it is important to access. This leads us to *the natural question on how the spectrum of singularities D_f can be explicitly obtained and determined in practice*.

Trying to compute D_f by using its very definition is definitively an impossible task, even to the most powerful computer. The first obstruction is that this task requires the calculation of the pointwise Hölder exponents of f at infinitely many points. The second obstruction is that calculating the Hausdorff dimension of a set, by using the very definition of this dimension, can very hardly be done in practice. Thus, it is a challenging issue to provide satisfactory answers to the fundamental question raised at the end of the last paragraph. In order to deal with this issue, multifractal analysis, and more particularly the so-called *multifractal formalism*, was introduced by the physicians Parisi and Frisch in [34]. Since almost three decades, multifractal analysis is a very active interdisciplinary research area where mathematicians, physicians, and other scientists interact. It is worth mentioning that the main idea of the multifractal formalism, due to Parisi and Frisch, is that the exponent $\zeta_f(p)$, governing the local asymptotic behavior of the structure function (see (4.3) and (4.2)), can be obtained *as the Legendre transform of the spectrum of singularities D_f* . That is one has

$$\zeta_f(p) = \inf_{\rho} \{p\rho + 1 - D_f(\rho)\} \quad (4.4)$$

As a consequence, $D_f(\rho)$ can be recovered through *the Legendre inversion formula*:

$$D_f(\rho) = \inf_p \{p\rho + 1 - \zeta_f(p)\} \quad (4.5)$$

We conclude this section by stressing that the two crucial formulas (4.4) and (4.5) are among other things very useful for clinicians who want to obtain multifractal spectra through computations. Yet these two formulas are not always satisfied. The main preoccupation of multifractal analysis is to determine the weakest possible conditions under which these they are valid (see, e.g., [23, 31]).

4.3 Methods of Multifractal Analysis

The multifractal spectrum (also called spectrum of singularities) D_f of a signal f can be estimated by two families of methods. The first one uses the “box-counting” approach, which is only based on time (for 1D signal) and space (for n D signal, $n > 1$) domain. The term “box counting” is used because the signal f is divided into boxes or segments in the computation of D_f . The procedure is repeated with different sizes of boxes. The second one uses time-frequency decomposition of the signal f for the estimation of D_f . The wavelet theory is commonly used for the decomposition. In this case, the scale of the wavelet decomposition can be compared as the size of boxes in the first family of methods. The methods and their benefits and drawbacks are summarized in Table 4.1.

4.3.1 Time Domain Methods

4.3.1.1 Generalized Fractal Dimensions and Multifractal Spectrum

Standard box-counting techniques are used to analyze point’s sets. Each set is described by an infinite number of generalized dimensions, D_q , also called “Renyi’s dimension,” and by the multifractal spectrum (or spectrum of singularities) D_f . The generalized dimensions D_q are computed as a function of the order of the probability moment q and then the multifractal spectrum can be obtained by Legendre transform.

The Legendre transform could lead to some errors [39]. In 1989, Chhabra and Jensen defined a method for the direct estimation of the multifractal spectrum [8]. This method is widely used [11, 41] but has the drawbacks of the box-counting methods.

Besides problems arising when the boxes contain few points, the algorithms are characterized by low statistics, emphasized by the negative exponents ($q < 0$); this, in turn, makes the measure to diverge exponentially [14].

4.3.1.2 The “Sandbox” or Cumulative Mass Method

The sandbox method, developed by [40], is useful for the assessment of the generalized fractal dimensions for both positive and negative moment orders, q , permitting the reconstruction of the complete multifractal spectrum.

This method consists in randomly selecting N points belonging to the structure and then counting, for each point i , the number of pixels $M_i(r)$ that belong to the structure inside a disk of diameter r centered at this point. The generalized dimensions D_q are obtained using the mean of $M_i(r)$ for various r .

The advantage of this method is that the boxes are centered on the structure, so there are no boxes with too few elements (i.e., pixels) inside. Indeed, for $q < 0$, boxes that contain a small number of elements (because they barely overlap with the cluster) give anomalously large contributions.

Table 4.1 Review of approaches to the estimation of multifractal spectrum

Name	Pros	Cons
Time domain methods		
Generalized fractal dimensions and multifractal spectrum	Easy implementation	Highly dependent to the box sizes
	Development to 1D, 2D, or 3D signals	Problems arising when the boxes contain few points
Sandbox method	Easy implementation	Dependent to the box sizes
	Development to 1D, 2D, or 3D signals	Only for binarized signals in the case of 2D or 3D signals
	Boxes centered on the structure	
The large-deviation multifractal spectrum	Not always a concave spectrum	High computation cost
		Difficult to apply in 2D and 3D
Multifractal detrended fluctuation analysis or multifractal detrended moving average	Easy implementation	Dependent to the box sizes
	Development to 1D, 2D, or 3D signals	Only for binarized signals in the case of 2D or 3D signals
	Use of the “profile” of the signal	
	Robust even for signals of small lengths	
Time-frequency domain methods		
Wavelet transform modulus maxima	Less dependent to the wavelet and number of scales than “box-counting” methods	High computation cost
	Development to 1D, 2D, or 3D signals	The continuous wavelet transform introduced some discontinuities at the endpoints of the signal
		No mathematical background
Wavelet leaders-based multifractal analysis	Less dependent to the wavelet and number of scales than “box-counting” methods	Need large signals
	Development to 1D, 2D, or 3D signals	
	Mathematical background	
	Robust to the estimation of the right part of spectrum	
Multifractional Brownian motion	Estimation of the Hölder exponent to each point of the signal	Very few applications
	Development to 1D, 2D, or 3D signals	Need large signals

The sandbox procedure represents a solution to the border effect problem (i.e., the presence of almost empty cells containing few points not centered in them), permitting the reconstruction of the multifractal spectrum also for negative q [12].

Finally, we can quote that this method has just been developed for binarized signals.

4.3.1.3 The Large-Deviation Multifractal Spectrum

When the multifractal spectrum is estimated using the abovementioned methods, its shape is always concave. The advantage of the large-deviation multifractal spectrum is that it will not always be concave and so less information loss will occur. However, much more numerical computation is required and the method becomes difficult to apply in two and three dimensions. Indeed, the algorithm necessitates the calculation of two limits, instead of just one as for the two previous methods.

In view of the high computation cost, this method is primarily used for 1D signals [6, 38]. This spectrum can also be applied to image segmentation [1].

4.3.1.4 Multifractal Detrended Fluctuation Analysis: MDFA

The detrended fluctuation analysis (DFA) method is a widely used technique for the quantification of monofractal properties. This method has the advantage to avoid spurious detection of correlations that are artifacts of nonstationarities in the time series and has successfully been applied in several fields such as neuron spiking [5] and DNA sequences [7]. In 2002, Kantelhardt et al. [18] proposed a generalization of the DFA method for the multifractal characterization of nonstationary time series and called it the multifractal detrended fluctuation analysis (MDFA) procedure. It consists of three main steps. Briefly, the first one is to construct the “profile” of the signal. The second one is to divide the profile into non-overlapping segments of equal length, and the third one is to calculate the local trend for each segment by a least-square fit of the data and calculate the variance. For more details of the MDFA method, see in Kantelhardt et al. [18].

This method is sensitive to the length of segments.

4.3.1.5 Multifractal Detrended Moving Average: MDMA

In 2010, Gu and Zhou [16] developed a similar approach than the MDFA procedure based on the moving average technique. They called it the multifractal detrended moving average (MDMA). Both methods rely on a measure of fluctuations but differ in calculating the moments of the fluctuation function. Indeed, in the MDMA approach, the signal is divided into segments after the calculation of the profile and the detrending step. For more details of the MDMA method, see in Gu and Zhou [16].

It has been shown that MDMA outperformed the MDFA in the estimation of scaling exponents [16].

4.3.2 Time-Frequency Domain Methods

The second class of methods is defined in time-frequency domain. All of the next approaches for the estimation of multifractal spectrum are based on the wavelet transform. The wavelet transform of a signal is used like an “oscillating” box to

represent its components. Some methods use the discrete wavelet transform and others are based on the continuous wavelet transform.

4.3.2.1 Wavelet Transform Modulus Maxima: WTMM

The wavelet transform modulus maxima (WTMM) method, originally developed by Muzy et al. [32], is based on the concept of wavelets in general and the use of the continuous wavelet transform in particular. It has been developed and used in one and two dimensions in several fields [3, 20, 21]. In [19], the method was applied in 3D and the authors showed its robustness using simulated 3D multifractal models. In the WTMM method, the wavelet transform maxima are used to define a partition function whose power-law behavior is used for an estimation of the local exponents and to assess the dimension of the detected exponents. A matching set of fractal exponents and dimensions is used to obtain the multifractal spectrum.

The method presents some limits. It is more difficult to implement than the previous methods. It has some freedom degrees, like the wavelet choice and the scales number. Also, the continuous wavelet transform introduced some discontinuities at the endpoints of the signal, due to zero padding. It is necessary to define a cone of influence for the analysis and it is defined as the region of the wavelet spectrum, in which the decrease of the wavelet amplitude near the edges becomes significant. However, Kestener et al. [19] showed that it is more effective than the “box-counting” methods.

4.3.2.2 Wavelet Leaders-Based Multifractal Analysis: WLMA

The wavelet leaders-based multifractal analysis (WLMA) computes the scaling exponents by measuring how the absolute value of the wavelet coefficients changes as a function of scale. The data are transformed to the wavelet domain with a discrete wavelet transform, and the wavelet leaders are calculated by finding the maximum wavelet coefficient among the adjacent wavelet coefficients for the current scale and all smaller scales. The estimated multifractal formalism has a mathematical validity and the right part of spectrum is valid ($q < 0$), meaning that the partition function (obtained by wavelet leaders) is also valid when $q < 0$ [43]. For more details of the WLMA, see in Wendt et al. [43].

4.3.2.3 Multifractal Brownian Motion: mBm

Based on multifractal modeling, Lopes et al. [25] introduced an extension of the fBm which overcomes some of its limitations. The proposed model is based on multifractional Brownian motion (mBm). The intuitive idea which leads to mBm consists in replacing the fBm Hurst parameter by a smooth function depending on the space variable t . Briefly, a signal is modeled by a mBm. The estimation procedure of the Hölder exponent at each t was inspired both by the variance method and

by a method called the localized generalized quadratic variations method [2]. The novelty of the procedure is that the estimator was obtained through its wavelet coefficients. The advantage in using wavelet coefficients is that they offer more numerical stability than sampled values; wavelet coefficients are less sensitive to perturbations by white noise than sampled values. For more details of the mBm procedure, see in Lopes et al. [25].

4.4 Applications of Multifractal Analysis

Over the last years, multifractal analysis has been applied extensively in neurosciences. In this section, the applications are grouped into three main domains: electroencephalogram (EEG) signal, blood oxygen level-dependent (BOLD) signal, and brain imaging. The methods and their applications are summarized in Table 4.2.

4.4.1 Electroencephalogram Signal: EEG

The electroencephalogram (EEG) is a recording of the electrical activity of the brain from the scalp (see also Chap. 25). The recorded waveforms reflect the cortical electrical activity. Many studies in neuroscience have converged to raise the hypothesis that the underlying pattern of neuronal activation from the EEG signals is non-linear, with self-affine dynamics, while EEG signals themselves are nonstationary. Therefore, fractal analysis of EEG signals has shown scaling behaviors that may not be consistent with monofractal process. These signals may be better modeled as an underlying multifractal process. Several studies confirmed this hypothesis and are summarized below.

Gadhoumi et al. [15] used the WLMA approach for the prediction of seizure onset in epilepsy patients. The method was able to differentiate between the preictal and the interictal states with a sensitivity of 80 % and a specificity of 25 %.

Table 4.2 The methods for the estimation of multifractal spectrum and their applications in neurosciences

Methods	Applications		
	EEG	fMRI	Brain imaging
Fractal dimensions	[35, 42]	[33]	[26, 37]
Sandbox			
Large-deviation spectrum			
MDFA or MDMA	[24, 30, 45]		
WTMM	[45]	[44]	
WLMA	[15]	[9, 10]	
mBm			

Liang et al. [24] showed that MDFA indices could track the changes in EEG pattern during different anesthesia states. However, they compared these indices with other indices of entropy measures, and they found that some entropy features can obtain better performance.

Matic et al. [30] used MDFA metrics to distinguish different grades of abnormality in the background EEG activity in neonates after perinatal asphyxia.

Plonnikov et al. [35] analyzed normal and abnormal EEG development by means of measures regarding the EEG as a multifractal structure. Their goal was to check the stated hypothesis that during the brain maturation, the EEG signal goes over the stages of some types of noise not only in healthy subjects but also in patients with cerebral pathology. They used a different approach to measure the multifractal properties of the EEG signal, known as fractal dynamics. They divided the EEG signal into 1-s time segments and computed some fractal measures on each segment. They showed that during the brain maturation, the EEG signal goes over the stages of some types of noise.

Weiss et al. [42] used the range of multifractal spectrum, computed by the generalized fractal dimensions, to characterize the topography and the sleep stages on EEG recordings. They showed that brain EEG signals are more complex than they could be fully described by a single monofractal exponent, and therefore, a multifractal approach may be more appropriate for modeling the fractal properties of brain dynamics. Moreover, the multifractal measure outperformed the relative band powers and the monofractal exponent in the overall sleep stage discrimination.

Zorick et al. [45] used MDFA approach to classify EEG signals from waking and different sleep stages and demonstrate its potential utility for automatic classification of different states of consciousness. Also, they showed that MDFA approach had lower indices of variability when applied on EEG signals than WTMM approach.

4.4.2 Brain Imaging

Most of research protocols in neurosciences used brain imaging informations, such as magnetic resonance imaging (MRI), positron emission tomography (PET), or single-photon emission computed tomography (SPECT) (see also Chaps. 19, 20, and 21).

Functional MRI measures brain activity by detecting associated changes in blood flow through the BOLD signal. Several studies of the temporal scale free or fractal property in fMRI have demonstrated that this constitutes an intrinsic feature of ongoing brain activity [9, 17]. It was shown that the Hurst coefficient decreases during task in activating and deactivating brain regions. However, using one scaling exponent assumes Gaussianity and self-similarity, while fMRI signals may significantly depart from those either of those two assumptions [9]. To address this issue, the scaling properties of fMRI signals can be investigated using multifractal analysis, thus measuring a collection of scaling exponents. Evidence for the presence of

multifractality in both resting-state and task-related fMRI signals has been demonstrated in almost the whole brain. The studies reported below are the most recent publications in the field of multifractal analysis applied to fMRI signals.

Wink et al. [44] conducted multifractal analysis using WTMM on resting-state fMRI signals in the right inferior frontal cortex and revealed that the faster responding participants had wider multifractal spectrum.

Shimizu et al. [36] found multifractal structures in white and gray matter, and the significant differences in the singularity spectra between the activated and the non-activated brain regions. They used WTMM approach to extract multifractal properties of fMRI signals.

Ciuciu et al. [10] studied the multifractal time dynamics of fMRI signals during rest and task. They used the WLMA approach to measure a collection of scaling exponents. They showed that most fMRI signals appear multifractal at rest except in non-cortical regions. Task-related modulation of multifractality appears only significant in functional networks compared to artifacts.

The multifractal analysis can be used for the applications in control group versus patient group characterization. Ni et al. [33] studied the discriminating power of multifractal properties to detect Alzheimer disease patients from healthy volunteers, especially when combining with the traditional resting-state fMRI features.

There are fewer published works on multifractal analysis in other brain imaging modalities. Takahashi et al. [37] used the multifractal spectrum to quantitatively evaluate white matter hyperintensity on MR images. Lopes et al. [26] used a 3D adaptation of multifractal spectrum to characterize the local changes in homogeneity in brain SPECT images. There was a statistically significant difference between the control group and the pathological group.

4.5 Conclusion

A limitation with fractal analysis is to describe objects by a single fractal value, whereas they exhibit a multifractal behavior. Multifractal analysis is a response to this limit. It allows computing a spectrum or a set of fractal dimensions. Many algorithms exist to evaluate the spectrum of singularities D_f (the so-called multifractal spectrum) of a signal f and numerical differences between the methods appear. The choice of the method is not a trivial task because no “gold standard” approach exists. However, the advantages and limitations of each method have to be known in relation to input data.

About time domain approaches, MDFA and MDMA methods are computationally more stable than others methods in terms of boxes (or segments) size. Moreover, they are the most used in the last studies. The choice between MDFA and MDMA is not trivial. Eke et al. [13] showed that MDFA is applicable for more types of signals than MDMA.

About time-frequency domain approaches, the WTMM method is the most used in the literature. However, WLMA overcomes major difficulties partially

solved by WTMM such as no mathematical results are expected to hold for the WTMM method, the high computational cost of WTMM, and the easily theoretically and practically generalization to higher dimensions of WLMA [43]. For the mBm method, its low number of studies does not allow to conclude about its robustness.

There is no consensus on the choice between time or time-frequency domains approaches. The only strong result is that MDFA is more consistent than WTMM and WLMA methods for shorter signals (less than 7500 time points) [33, 45].

Most of applications of multifractal analysis in neurosciences are interested in 1D signals, such as EEG and functional MRI signals. Evidence for the presence of multifractality in both EEG and fMRI signals has been largely demonstrated. The multifractal analysis is also able to discriminate two or more states in a signal or to characterize patients from healthy volunteers. Few studies are interested in the use of multifractal analysis in 2D or 3D brain images. First works were interesting, but they used “box-counting” methods; it will be interesting to see the influence of more robust methods, such as wavelet-based methods.

References

1. Abadi M, Grandchamp E. Texture features and segmentation based on multifractal approach. *Prog Pattern Recog Image Anal Appl Proc.* 2006;4225:297–305.
2. Benassi A, Cohen S, Istas J. Identifying the multifractional function of a Gaussian process. *Stat Probab Lett.* 1998;39(4):337–45.
3. Bhatti A, Nahavandi S, Frayman Y. 3D depth estimation for visual inspection using in wavelet transform modulus maxima. *Comput Electr Eng.* 2007;33(1):48–57.
4. Black F, Scholes M. The pricing of options and corporate liabilities. *J Polit Econ.* 1973;81(3):637–54.
5. Blesic S, Milosevic S, Stratimirovic D, Ljubisavljevic M. Detrended fluctuation analysis of time series of a firing fusimotor neuron. *Phys A.* 1999;268(3–4):275–82.
6. Broniatowski M, Mignot P. A self-adaptive technique for the estimation of the multifractal spectrum. *Stat Probab Lett.* 2001;54(2):125–35.
7. Buldyrev SV, Dokholyan NV, Havlin S, Stanley HE, Stanley RHR. Expansion of tandem repeats and oligomer clustering in coding and noncoding DNA sequences. *Phys A.* 1999;273(1–2):19–32.
8. Chhabra A, Jensen R. Direct determination of the $f(\alpha)$ singularity spectrum. *Phys Rev Lett.* 1989;62(2):1327–30.
9. Ciuciu P, Abry P, Rabrait C, Wendt H. Log wavelet leaders cumulant based multifractal analysis of EVI fMRI time series: evidence of scaling in ongoing and evoked brain activity. *IEEE J-Stsp.* 2008;2(6):929–43.
10. Ciuciu P, Varoquaux G, Abry P, Sadaghiani S, Kleinschmidt A. Scale-free and multifractal time dynamics of fMRI signals during rest and task. *Front Physiol.* 2012;3:186.
11. Cuevas E. $f(\alpha)$ multifractal spectrum at strong and weak disorder. *Phys Rev B.* 2003;68(2).
12. De Bartolo SG, Gaudio R, Gabriele S. Multifractal analysis of river networks: sandbox approach. *Water Resour Res.* 2004;40(2).
13. Eke A, Herman P, Sanganahalli BG, Hyder F, Mukli P, Nagy Z. Pitfalls in fractal time series analysis: fMRI BOLD as an exemplary case. *Front Physiol.* 2012;3:417.
14. Feeny BF. Fast multifractal analysis by recursive box covering. *Int J Bifurcat Chaos.* 2000;10(9):2277–87.

15. Gadhouri K, Gotman J, Lina JM. Scale invariance properties of intracerebral EEG improve seizure prediction in mesial temporal lobe epilepsy. *PLoS One*. 2015;10(4):e0121182.
16. Gu GF, Zhou WX. Detrending moving average algorithm for multifractals. *Phys Rev E*. 2010;82(1).
17. He BJ. Scale-free properties of the functional magnetic resonance imaging signal during rest and task. *J Neurosci: Off J Soc Neurosci*. 2011;31(39):13786–95.
18. Kantelhardt JW, Zschiegner SA, Koscielny-Bunde E, Havlin S, Bunde A, Stanley HE. Multifractal detrended fluctuation analysis of nonstationary time series. *Phys Stat Mech Appl*. 2002;316(1–4):87–114.
19. Kestener P, Arneodo A. Three-dimensional wavelet-based multifractal method: the need for revisiting the multifractal description of turbulence dissipation data. *Phys Rev Lett*. 2003;91(19).
20. Kestener P, Arneodo A. Generalizing the wavelet-based multifractal formalism to random vector fields: application to three-dimensional turbulence velocity and vorticity data. *Phys Rev Lett*. 2004;93(4).
21. Khalil A, Joncas G, Nekka F, Kestener P, Arneodo A. Morphological analysis of H I features. II. Wavelet-based multifractal formalism. *Astrophys J Suppl Ser*. 2006;165(2):512–50.
22. Kolmogorov AN. The local structure of turbulence in incompressible viscous fluid for very large Reynolds numbers. *Doklady Akademia Nauk SSSR*. 1941;30:301–5.
23. Lapidus ML, van Frankenhuijsen M. Fractality, self-similarity and complex dimensions. *P Symp Pure Math*. 2004;72:349–72.
24. Liang Z, Wang Y, Sun X, Li D, Voss LJ, Sleight JW, Hagihira S, Li X. EEG entropy measures in anesthesia. *Front Comput Neurosci*. 2015;9:16.
25. Lopes R, Ayache A, Makni N, Puech P, Villers A, Mordon S, Betrouni N. Prostate cancer characterization on MR images using fractal features. *Med Phys*. 2011;38(1):83–95.
26. Lopes R, Steinling M, Szurhaj W, Maouche S, Dubois P, Betrouni N. Fractal features for localization of temporal lobe epileptic foci using SPECT imaging. *Comput Biol Med*. 2010;40(5):469–77.
27. Mandelbrot B. *The fractal geometry of nature*. San Francisco: Freeman; 1983.
28. Mandelbrot B. *Fractals and scaling in finance: discontinuity, concentration, risk*. New York: Springer; 1997.
29. Mandelbrot BB, Van Ness JW. Fractional Brownian motions, fractional noises and applications. *SIAM Rev*. 1968;10:422–37.
30. Matic V, Cherian PJ, Koolen N, Ansari AH, Naulaers G, Govaert P, Van Huffel S, De Vos M, Vanhatalo S. Objective differentiation of neonatal EEG background grades using detrended fluctuation analysis. *Front Hum Neurosci*. 2015;9:189.
31. Meyer Y. *Wavelets: algorithms and applications*. SIAM Press: Philadelphia; 1993.
32. Muzy JF, Bacry E, Arneodo A. Wavelets and multifractal formalism for singular signals – application to turbulence data. *Phys Rev Lett*. 1991;67(25):3515–8.
33. Ni H, Zhou L, Ning X, Wang L, Alzheimer’s Disease Neuroimaging I. Exploring multifractal-based features for mild Alzheimer’s disease classification. *Magn Reson Med: Off J Soc Magn Reson Med/Soc Magn Reson Med*. 2015.
34. Parisi G, Frisch U. On the singularity structure of fully developed turbulence. In: Ghil RBR, Parisi G, editors. *Turbulence and predictability in geophysical fluid dynamics*. Proceedings International School of Physics “E. Fermi”, Amsterdam; 1985.
35. Polonnikov RI, Wasserman EL, Kartashev NK. Regular developmental changes in EEG multifractal characteristics. *Int J Neurosci*. 2003;113(11):1615–39.
36. Shimizu Y, Barth M, Windischberger C, Moser E, Thurner S. Wavelet-based multifractal analysis of fMRI time series. *Neuroimage*. 2004;22(3):1195–202.
37. Takahashi T, Murata T, Narita K, Hamada T, Kosaka H, Omori M, Takahashi K, Kimura H, Yoshida H, Wada Y. Multifractal analysis of deep white matter microstructural changes on MRI in relation to early-stage atherosclerosis. *Neuroimage*. 2006;32(3):1158–66.
38. Touchette H, Beck C. Nonconcave entropies in multifractals and the thermodynamic formalism. *J Stat Phys*. 2005;125:455–71.

39. Veneziano D, Moglen GE, Bras RL. Multifractal analysis – pitfalls of standard procedures and alternatives. *Phys Rev E*. 1995;52(2):1387–98.
40. Vicsek T. Mass multifractals. *Phys A*. 1990;168:490–7.
41. Wang J, Ning XB, Ma QL, Bian CH, Xu YL, Chen Y. Multiscale multifractality analysis of a 12-lead electrocardiogram. *Phys Rev E*. 2005;71(6).
42. Weiss B, Clemens Z, Bodizs R, Vago Z, Halasz P. Spatio-temporal analysis of monofractal and multifractal properties of the human sleep EEG. *J Neurosci Methods*. 2009;185(1):116–24.
43. Wendt H, Abry P, Jaffard S. Bootstrap for empirical multifractal analysis. *IEEE Signal Proc Mag*. 2007;24(4):38–48.
44. Wink AM, Bullmore E, Barnes A, Bernard F, Suckling J. Monofractal and multifractal dynamics of low frequency endogenous brain oscillations in functional MRI. *Hum Brain Mapp*. 2008;29(7):791–801.
45. Zorick T, Mandelkern MA. Multifractal detrended fluctuation analysis of human EEG: preliminary investigation and comparison with the wavelet transform modulus maxima technique. *PLoS One*. 2013;8(7), e68360.

Part II
Fractals in Neuroanatomy
and Basic Neurosciences

Chapter 5

Fractals in Neuroanatomy and Basic Neurosciences: An Overview

Antonio Di Ieva

Abstract The introduction of fractal geometry in the neurosciences has been a major paradigm shift over the last decades as it has helped overcome approximations and limitations that occur when Euclidean and reductionist approaches are used to analyze neurons or the entire brain. Fractal geometry allows for quantitative analysis and description of the geometric complexity of the brain, from its single units to the neuronal networks.

As illustrated in the second section of this book, fractal analysis provides a quantitative tool for the study of morphology of brain cells (i.e., neurons and microglia) and its components (e.g., dendritic trees, synapses) as well as the brain structure itself (cortex, functional modules, neuronal networks). The self-similar logic which generates and shapes the different hierarchical systems of the brain and even some structures related to its “container,” that is, the cranial sutures on the skull, is widely discussed in the following chapters, with a link between the applications of fractal analysis to the neuroanatomy and basic neurosciences to the clinical applications discussed in the third section.

Keywords Brain • Microglia • Neuroanatomy • Neuron • Fractal • Self-similarity • Neuronal networks

A. Di Ieva, MD, PhD
Neurosurgery Unit, Faculty of Medicine and Health Sciences, Macquarie University,
Sydney, NSW, Australia

Garvan Institute of Medical Research, Sydney, NSW, Australia

Medical University of Vienna, Vienna, Austria

University of Toronto, Toronto, ON, Canada

e-mail: diieva@hotmail.com

By echoing some concepts expressed by the seventeenth-century English scholar Richard Bentley, Benoit Mandelbrot expressed that “Clouds are not spheres, mountains are not cones, coastlines are not circles, and bark is not smooth, nor does lightning travel in a straight line” [17].

5.1 What About the Brain?

Although Mandelbrot’s fractal geometry has often been seen as “mathematical esoterica,” candidly confessed by himself, the new model has been applied in the biomedical domain, including the neurosciences [6, 7, 15]. The natural complexity of the brain, its hierarchical structure, and the sophisticated topological architecture of the neurons organized in micro- and macro-networks can only roughly be described by means of Euclidean geometry and linear dynamics approaches [7].

Regardless of the mathematical meaning of fractal geometry, it should be emphasized that in the context of neuroscience (and all the biomedical sciences), fractal geometry should not really be considered as a model or a theory but rather as a framework. It is a useful framework to describe the complexity of the brain functional networks, in both its physiological and pathological states, in all its hierarchical structure, from protein/synapses networks to macroscopic organizations of neurons and other cells, as confirmed by the small-world topologies seen in cellular as well as large-scale neuronal networks [9, 10].

5.2 Fractals, Neurons, and Microglia

The adult human brain contains about 86 billion neurons and 85 billion nonneuronal cells (adult male with an average brain of 1.5 kg) [12]. It is now known that the complexity of brain function is not strictly related to such a high number of cells but rather to its network connectivity.

Fractal analysis provides a quantitative tool for the study of morphology of brain cells and its components (i.e., dendritic trees, synapses, etc.) as well as the brain structure itself as summarized below and in the entire second section of the book.

Fractal analysis has been proven to be useful in quantifying the cytoneuroarchitecture, by providing a global estimate of axonal and dendritic branching, in discriminating between certain functionally different neuronal types that are visually similar [3–5, 14, 18, 20, 21, 23, 24], as well as in following the change of dendritic complexity induced by drugs [1]. The fractal dimension of a neuron increases with the ruggedness of the cellular border, the degree and pattern of branching, and the space-filling capacity. The fractal-based neuronal and nonneuronal morphometry even allows the characterization of cells in pathological conditions, as demonstrated, for example, by a lower complexity of the astrocytic cells’ borders in the brain cortex of babies, which becomes higher in healthy adults, and then again

smaller in aged subjects, and is significantly reduced in subjects affected by dementia [22]. Inversely to the FD, lacunarity has been shown to increase with age, and the relationship between FD and lacunarity can be used for a holistic and dynamic representation of the neuroglial network over time, from the process of differentiation to the senescence of cells. As elucidated in Chap. 6 by *Audrey Karperien* and *Herbert Jelinek*, together microglia and neurons contribute to the fractal topology of the brain that defines its computational capabilities. Methods, aims, and results to compute the fractal dimension of neurons are presented in Chap. 6, as well as in Chap. 7 by *Nebojša Milošević*. The fractal dynamics of the synapse formation process are illustrated by *Małgorzata Kołodziej* and *Przemysław Waliszewski* in Chap. 8.

5.3 Brains and Trees

It is not necessary to be a botanist to be able to distinguish a weeping willow from a pine. How? Both have a trunk, roots, and branches, but nonetheless they look very different. They share many specific qualities of trees; however, among other characteristics, they each have a different geometrical shape, which is one reason why it is not difficult to distinguish them: the romantic weeping willow, with its crying leaves vs. the austere shape of a Scots pine! These two trees have different geometrical shapes, or better, they each fill the space differently. Considering that they could have the same Euclidean measures (e.g., height, width, and number of branches), they each own a distinctive fractal dimension for their peculiar geometrical complexity in the three-dimensional space.

A systematic and exhaustive research about the specific fractal geometry of all trees has not been published yet, in spite of this simple and intuitive idea.

However, the literature is full of evidence about the existence of a geometrical fingerprint found in many biological systems: bronchial trees, vascular trees, neuronal trees, and so on. Clearly nature follows specific rules, which are common for several distinct systems, and some morphological *generators* generate different hierarchical levels of anatomical systems. The use and abuse of the word “tree” in biomedical sciences are not a coincidence. Botanic and vascular trees have branches, bifurcations, and trunks, something that, in short, can be only roughly estimated by means of Euclidean approaches. Are trees fractal structures? The answer is controversial; however, regardless of the fractal or quasi-fractal or semi-fractal nature of the trees, what is sure is that fractal analysis can help describe and quantify their geometrical complexity. The brain also shows many fractal treelike structures. Not by coincidence, the old anatomical books mention the *arbor vitae* (Latin word meaning “tree of life”), for example, in reference to the white matter of the cerebellum; some researchers have confirmed its fractal nature or at least used fractal analysis to differentiate some brain and cerebellar diseases. Fractal analysis has been used to successfully distinguish between the shapes of different classes of neurons with their specific dendritic arborizations, as previously written. Moreover, peculiar

vascular and microvascular networks characterize the brain and its pathological counterparts (e.g., brain tumors or cerebrovascular malformations, as discussed in the third section of this book).

5.4 Increase of the Fractal Dimension from “Too Smooth to Too Folded” Human Brains

In 1991, Hofman showed that the whole brain cortex has a fractal structure [13], as confirmed in following studies [8, 16], although, from the mathematical point of view, the brain is not strictly self-similar [26]. The fractality of the convoluted brain is based on the hypothesis that the convolutions are result of fractal folding and compartmentalization of neurons into modular circuits, governed by simple generative rules to generate the brain design [13]. The cerebral cortex is characterized “by the hierarchical organization of groups of neurons or, in terms of fractal geometry, infinitely nesting clusters of neurons” [13]. Comparing several species and performing allometric analysis, Hofman showed that among mammals, there are two major groups: (1) species with smooth, non-convoluted brains where the cortical surface area increases as the two third power of brain volume; (2) species with convoluted brain, where the cortical morphology is described by more complex mathematical models, with a cutoff from the transition of a lissencephalic brain to a gyrencephalic one, as illustrated below. The FD of the human brain was computed to 2.70 ± 0.07 , and the folding of the cortical surface to such a value and the compartmentalization of neurons into modular circuits were suggested to be the architectural reason of the high degree of parallel processing occurring in the cerebral cortex to maximize the processing of transfer of information [13]. The relationship between cortical surface and the square root of cortical thickness has implications regarding the origin of folding in evolutionary and developmental perspective, as well as in pathologies such as human lissencephaly, as recently reconfirmed [19]. The calculated ~ 2.5 fractal dimension value of gyrencephalic brains has intriguingly been found remarkably close to the value of crumpled sheets of paper [19].

In human pathology, the term lissencephaly refers to “smooth brain” phenotypes present in a wide spectrum of malformations of the normal cortical folding, caused by dysfunction in the migration of neurons during the process of corticogenesis. The terms used for a complete lack of the gyri (agyria) or broad gyri (pachygyria) add a qualitative element to the description of the lissencephalic patterns, although no objective quantitative indexes are in clinical use. On the other side of the spectrum of the abnormal cerebral gyrogenesis (process of formation of the gyri) and sulcogenesis (formation of the grooves) are lesions characterized by the brain cortex being “hyperfolded,” and/or more gyri are present (polymicrogyria).

Computational fractal-based analyses have proposed FD and further complementary indexes as objective parameters to estimate the topological complexity of natural objects, such as the brain cortex, as well as imaging markers of normal vs.

diseased human brains in a very wide range of neurological diseases (see third section). In an unpublished exploratory analysis, we computed the folding of a few human lissencephalic vs. polymicrogyric brains, finding an average FD value of 2.15 vs. 2.85, respectively. It is interesting to note that these values are at the extreme wings of a normal distribution of the patterns according to the increasing complexity of the brain folding. Computational fractal-based analyses can add a computer-aided quantitative parameter to the qualitative (and often subjective) description of the brain structure performed by morphologists (e.g., neuroradiologists or neuroanatomists/pathologists).

5.5 Neuronal Networks

The functional modularity of the brain shows self-similar features at each level of analysis, although such self-similarity is statistical rather than exact, like in many other biological systems. The fractal dimension has been shown as a valid parameter to characterize the topological structure and space-filling properties of networks [11], including the neuronal ones [9].

The brain and neuronal networks “self-similarity logic” is intriguingly introduced by *Diego Guidolin, Cinzia Tortorella, Raffaele De Caro, and Luigi Agnati* in Chap. 9. Interestingly enough, such logic can also be applied to the analysis of cranial sutures, as covered in Chap. 10 by *Takashi Miura*. By means of a multifractal approach, it has been shown that the brain maintains a state of self-organized criticality [25]. Neural networks have been shown to use a self-similar branching structure of dendrites and downstream networks in interconnected reciprocal feedback loops: output from outer branch nodes of the network tree enters inner branch nodes of the dendritic tree in single neurons [2]. The recurrent fractal neural networks theory has been suggested to provide a strategy to understand the exchange of global and local information processing, in a holistic view of the translation from neuronal computation into conscious experience [2]. The topological concept of self-similar networks of the brain seems to reconcile the reductionistic approach to dissect the brain into single units (neurons, columns, modules, nuclei, and so on) in a broad highly connected network which gives the mind its unity. Small-world networks and scale-free topologies, observed on a subcellular, cellular, and in large-scale brain networks (as seen in functional magnetic resonance imaging, fMRI) [9], may be the anatomical and functional basis of the high efficiency of information flow in the brain as well as of the emergence of consciousness.

In conclusion, the analysis of the self-similar patterns can suggest some operational modes and principles on which the brain architecture is shaped, from its anatomical (i.e., brain design) to functional (i.e., information processing) spectrum; In this context, an evolutionary and comparative anatomy perspective is intriguingly and brightly presented by *Michel Hofman* in Chap. 11. This holistic chapter on the fractal geometry of the brain links the section two to the next more clinically oriented section of the book.

References

1. Alvarez DN, De Simoni A, Velzing EH, Bracey E, Joëls M, Edwards FA, et al. Corticosterone reduces dendritic complexity in developing hippocampal CA1 neurons. *Hippocampus*. 2009;19:828–36.
2. Bieberich E. Recurrent fractal neural networks: a strategy for the exchange of local and global information processing in the brain. *Biosystems*. 2002;66:145–64.
3. Cannon RC, Wheal HV, Turner DA. Dendrites of classes of hippocampal neurons differ in structural complexity and branching patterns. *J Comp Neurol*. 1999;413:619–33.
4. Caserta F, Eldred WD, Fernandez E, Hausman RE, Stanford LR, Bulderez SV, et al. Determination of fractal dimension of physiologically characterized neurons in two and three dimensions. *J Neurosci Methods*. 1995;56:133–44.
5. Caserta F, Stanley HE, Eldred WD, Daccord G, Hausman RE, Nittmann J. Physical mechanisms underlying neurite outgrowth: a quantitative analysis of neuronal shape. *Phys Rev Lett*. 1990;64:95–8.
6. Di Ieva A, Esteban FJ, Grizzi F, Klonowski W, Martin-Landrove M. Fractals in the neurosciences, part II: clinical applications and future perspectives. *Neuroscientist*. 2015;21:30–43.
7. Di Ieva A, Grizzi F, Jelinek H, Pellionisz AJ, Losa GA. Fractals in the neurosciences, part I: general principles and basic neurosciences. *Neuroscientist*. 2013;20:403–17.
8. Free SL, Sisodiya SM, Cook MJ, Fish DR, Shorvon SD. Three-dimensional fractal analysis of the white matter surface from magnetic resonance images of the human brain. *Cereb Cortex*. 1996;6:830–6.
9. Gallos LK, Makse HA, Sigman M. A small world of weak ties provides optimal global integration of self-similar modules in functional brain networks. *Proc Natl Acad Sci U S A*. 2012;109:2825–30.
10. Gallos LK, Sigman M, Makse HA. The conundrum of functional brain networks: small-world efficiency or fractal modularity. *Front Physiol*. 2012;3:123.
11. Gou L, Wei B, Sadiq R, Sadiq Y, Deng Y. Topological vulnerability evaluation model based on fractal dimension of complex networks. *PLoS One*. 2016;11:e0146896.
12. Azevedo FA, Carvalho LR, Grinberg LT, Farfel JM, Ferretti RE, Leite RE, Jacob Filho W, Lent R, Herculano-Houzel S. Equal numbers of neuronal and nonneuronal cells make the human brain an isometrically scaled-up primate brain. *J Comp Neurol*. 2009;513:532–41.
13. Hofman MA. The fractal geometry of convoluted brains. *J Hirnforsch*. 1991;32:103–11.
14. Jelinek HF EG. Dendritic branching patterns of pyramidal cells in the visual cortex of the nocturnal owl monkey: a fractal analysis. *Fractals*. 2003;9:297–303.
15. John AM, Elfanagely O, Ayala CA, Cohen M, Prestigiacomo CJ. The utility of fractal analysis in clinical neuroscience. *Rev Neurosci*. 2015;26:633–45.
16. Kiselev VG, Hahn KR, Auer DP. Is the brain cortex a fractal? *Neuroimage*. 2003;20:1765–74.
17. Mandelbrot BB. *The fractal geometry of nature*. New York: W.H. Freeman; 1982.
18. Milošević NT, Ristanović D, Gudović R, Rajković K, Marić D. Application of fractal analysis to neuronal dendritic arborisation patterns of the monkey dentate nucleus. *Neurosci Lett*. 2007;425:23–7.
19. Mota B, Herculano-Houzel S. Brain Structure. Cortical folding scales universally with surface area and thickness, not number of neurons. *Science*. 2015;349:74–7.
20. Porter R, Ghosh S, Lange GD, Smith TG. A fractal analysis of pyramidal neurons in mammalian motor cortex. *Neurosci Lett*. 1991;130:112–6.
21. Ristanović D, Nedeljkov V, Stefanović BD, Milošević NT, Grgurević M, štulić V. Fractal and nonfractal analysis of cell images: comparison and application to neuronal dendritic arborization. *Biol Cybern*. 2002;87:278–88.
22. Senitz D, Reichenbach A, Smith TG. Surface complexity of human neocortical astrocytic cells: changes with development, aging, and dementia. *J Hirnforsch*. 1995;36:531–7.

23. Skrzat J, Usarz M, Trabka J, Goncerz G. Differentiation of neurons populations based on fractal dimension. *Folia Morphol (Warsz)*. 1996;55:444–6.
24. Smith TG, Marks WB, Lange GD, Sheriff WH, Neale EA. A fractal analysis of cell images. *J Neurosci Methods*. 1989;27:173–80.
25. Suckling J, Wink AM, Bernard FA, Barnes A, Bullmore E. Endogenous multifractal brain dynamics are modulated by age, cholinergic blockade and cognitive performance. *J Neurosci Methods*. 2008;174:292–300.
26. Zhang L, Liu JZ, Dean D, Sahgal V, Yue GH. A three-dimensional fractal analysis method for quantifying white matter structure in human brain. *J Neurosci Methods*. 2006;150:242–53.

Chapter 6

Morphology and Fractal-Based Classifications of Neurons and Microglia

Audrey L. Karperien and Herbert F. Jelinek

Abstract Microglia and neurons live physically intertwined, intimately related structurally and functionally in a dynamic relationship in which microglia change continuously over a much shorter timescale than neurons. Although microglia may unwind and depart from the neurons they attend under certain circumstances, in general, together both contribute to the fractal topology of the brain that defines its computational capabilities. Both neuronal and microglial morphologies are well described using fractal analysis complementary to more traditional measures. For neurons, the fractal dimension has proved valuable for classifying dendritic branching and other neuronal features relevant to pathology and development. For microglia, fractal geometry has contributed substantially to classifying functional categories, where in general, the more pathological the biological status, the lower the fractal dimension for individual cells, with some exceptions including hyper-ramification. Here we briefly review the intimate relationships between neurons and microglia, and survey work applying fractal analysis to their respective morphologies, summarizing key results and highlighting methodological issues.

Keywords Fractals • Fractal analysis • Microglia • Neuron • Theoretical Models • Box-counting • Dendritic spines

6.1 A Brief Introduction to Neurons and Microglia

One can tell much from observing the general profile of a cell under a microscope. Students of both neuroscience and hematology, for instance, are taught to predict the function, age, and location of a cell based on general morphological characteristics [22, 82]. Indeed, cell shape is a well-known feature upon which to make diagnostic and clinical decisions [15, 32, 36, 101]. Sometimes criteria that decisions can be

A.L. Karperien (✉) • H.F. Jelinek (✉)
School of Community Health & Centre for Research in Complex Systems,
Charles Sturt University, Albury, Australia
e-mail: akarperien@yahoo.com; hjelinek@csu.edu.au

based on are readily apparent and easily quantified, such as when the three-dimensional (3D) radius or two-dimensional (2D) diameter is used to classify red blood cells, but other times objectively measurable criteria are elusive. This is largely the case with the two brain cells this chapter focuses on, neurons, the relatively stable structural and functional units of physiological signaling, and neuroinflammatory microglia, the more dynamic attendants of those units.

6.1.1 Neuronal and Microglial Morphology in Context

Microglia live closely intertwined with neurons in the complex 3D environment of the central nervous system (CNS). Both have characteristically radial structures with multiple ramified processes. In both cells, the processes are usually relatively long compared to their essentially central cell bodies but come in varieties having specialized form and function [56, 65, 73, 74].

Neuronal design includes centralizing somata of varying size and shape, richly branching, spine-encrusted dendritic arbors that bring in and integrate signals, and generally less branched and sometimes much longer axons that decide to send signals along to target tissues. Depending on where a neuron is and what its role is, its fundamental features are formed and arranged differently. Indeed, morphology is often all the information required to classify neurons, even deduce their location and function [1, 10, 11].

Similar to neurons, microglia normally have a central although often elongated soma, highly ramified processes specialized for such tasks as tending to dendritic spines and (at least in mice) a dedicated process that extends along the initial axon segment [3] (a neuronal part responsible for action potential initiation) [76–78, 84, 87, 88, 90, 92]. One key difference between the morphologies of these interlinked cells is that in normal adult humans, microglia are usually considerably smaller than the neurons they attend, the total cell spanning an area comparable to the neuron's soma. They are motile and distributed unevenly throughout the CNS, hovering nearer somata more in gray than white matter, generally inclined to stay near neuronal processes, constantly and rapidly moving and waving their own processes in close proximity to the neuronal processes they attend [76–78, 84, 87, 88, 90, 92]. Another important morphological difference is that microglia periodically adopt a wholly unbranched morphology to perform some of their duties. Whereas they are capable of and perform phagocytosis in all their guises (e.g., in spine pruning), for mass phagocytosis and waste disposal, they can fully wind in their processes to adopt an amoeboid form able to migrate to sites of trauma [49, 76–78, 87–94].

Like neuronal morphology, microglial morphology tells much about what a cell does, and many of the same factors that influence the changes in neuronal morphology also affect microglial morphology at the same time that microglia are influencing neuronal morphology [3, 76–78, 88, 92]. An important difference, however, is that microglia change form and position much more quickly and dramatically in real time with important consequences. In normal adult brain, the microglial soma is essentially stationary, but processes move to contact both axonal boutons and dendritic spines in patterns that include distinct contact and rest intervals [95]. In

traumatized brain, the microglial process that contacts the initial axon segment, for instance, loses contact when microglia retract processes and adopt their amoeboid form [3, 76–78, 84, 87, 88, 90, 92].

Being able to quantitatively assess these physically and functionally interlinked brain cell types is vital to many of the goals of neuroscience. But just what should one measure about a neuron with a dense dendritic arbor on one end and a relatively sparse but extremely much longer axon on the other? And how might one characterize and compare the multiple personalities of an individual microglial cell? Further, how might one quantitate the 3D intimacy between neurons and microglia? Neuroanatomical examples are many wherein traditional measures such as total cell area, branch length, number of branch points, and angle of branching could not differentiate between visually subtle but important differences in populations of both cell types yet introducing fractal measures, alone or in conjunction with other measures, made it possible to draw distinctions [21, 26, 41].

Thus, this chapter broadly surveys fractal approaches to classifying neurons and microglia and discusses interpretations and implications of such work for understanding the fractal geometry of the brain. This chapter reviews these topics separately, reflecting the current dearth of studies comparing and assimilating results of fractal analysis of both. This chapter draws on key definitions, terminology, and methodological considerations explained in the introductory chapters of this book.

6.2 Fractal Analysis of Neurons

Table 6.1 lists a sample (from studies cited in the US National Institutes of Health's PubMed database) of the methods and approaches that have contributed to the state of the art of neuronal classification by fractal measures. To sum up the field, the fractal dimension (D_F) characterizes very well neuronal structure in terms of the dendritic arbor (see Sect. 6.2.1) and offers a basis for objectively distinguishing among several accepted neuroanatomical and functional categories of neuron. As Table 6.1 indicates, the D_F has further been used to draw distinctions between neurons in pathological and nonpathological scenarios and has shown promise for gauging developmental stages. Whereas there is in place a solid basis for objectively quantifying several neuron types to sort and compare them using the D_F , direct correlations between the D_F and neurophysiological events or overall function remain in the theoretical domain [4, 53].

6.2.1 Fractal Analysis of Dendritic Arbors

The 3D topology of the CNS underlies its computational capabilities, and evidence indicates that its functioning has fractal components [4, 12, 17, 19, 24, 51, 71, 75, 85, 97, 98, 103]. Dendritic arbors are chiefly the local signal-integrating wiring of that topology, and much of the work published classifying neurons using fractal

Table 6.1 Selected sample of fractal analysis approaches to neuronal morphology cited in PubMed (August 2015; search terms “neuron” and “fractal”)

Topic and summary	Model	References	Analysis method
Neuroanatomy			
(a) Higher D_F for apical dendritic branching pattern in superficial than deep pyramidal neurons	Rat	[102]	Modified Richardson’s (1.030±0.004 vs. 1.010±0.005; $p<0.008$)
	Cerebral cortex		
	2D binary skeletonized images		Box counting (1.129±0.014 vs. 1.085±0.012; $p<0.029$)
	Multiplane microphotography		10 vs. 10 cells
	Superficial pyramidal = soma in lamina II–III, apical dendrites terminating in layer I; deep = soma in lamina V–VI, apical dendrites terminating in layers III–IV	[57]	Box counting (1.33±0.06 vs. 1.24±0.04; $p<0.001$) 15 vs. 15 cells
(b) Different D_{BS} between dendritic arbor of inner and outer sublaminae as four classes: simple inner and outer and complex inner and outer	Adult rat; both genders	[34]	Box counting
	Retinal ganglion cells		Simple <1.39< complex
	2D binary skeletons		27 vs. 32 cells
	Scanned camera lucida		
Pathology			
(c) Lower D_F of Purkinje cell dendritic arbors in pathological model	Mouse (reeler mutation)	[45]	3D box counting and Sholl
	Cerebellar cortex		
	3D images; synchrotron X-ray microscopy of Golgi staining		1.71±0.03 vs. 1.25±0.02
	Gait, posture, balance, tremor disorders		
(d) Lower D_F of corneal nerve fibers (also decreased length and increased tortuosity) in corneal small fiber sensory neuropathy	Human	[16]	Box counting
	Corneal small sensory fibers		
	In vivo observation with corneal confocal microscopy		
	Amyotrophic lateral sclerosis (ALS)		
Development			
(e) D_F positively correlated with neuronal size and developmental changes in mathematical model of human fetal development	Human	[64]	Box counting and Sholl
	Fetal dentate nucleus		
	Scanned camera lucida drawings of Golgi-impregnated neurons		

methods focuses on their D_F (i.e., a D_F for which somata and axons are ignored). This is not to say that the evidence for fractal scaling implicates the dendritic arbor to the exclusion of a neuron's other parts or collections of other parts or that there is reason to reject the possibility of fractal scaling in the gross or fine structure of axons and somata. Indeed, there are specific reasons to explore those topics such as the intimate physical arrangement of axonal terminals relative to dendrites, spontaneous neurotransmitter release that has been shown to occur on a fractal schedule [51], and fractal features of axonal networks [19] and gross brain matter [14, 24, 46, 61, 99].

Rather, the reasons for classifying neurons based on their dendritic arbors are practical. At the tissue level, the different parts of a neuron often comprise seemingly distinct compartments. For example, axons form tracts and local collections of somata or dendritic arbors form defining layers in various brain structures. Soma shape and branching within the dendritic arbor in particular are usually seen more completely under a microscope than are typically longer axons and are readily captured in the visual field of imaging systems. On the basis of individual cells, the richly branching, signal-integrating dendritic arbor is visually suggestive of fractal scaling and itself comes in many morphological arrangements that have been used to characterize neurons descriptively and functionally [17, 32, 51, 60]. As Table 6.1 illustrates, characterizing neurons by the D_F for dendritic branching alone has demonstrated practical utility in objectively quantitating several heuristically defined functional and morphological categories of neuron.

That success notwithstanding, there are some key issues to note with respect to classifying neurons based on the D_F of the dendritic arbor. One general point is that there are differences among species in the D_F for dendritic branching in at least some categories of neuron [33]. This is especially important to bear in mind when applying fractal results based on animal models of disease such as the studies listed in Table 6.1 under *Pathology*.

Another point to be aware of is what is meant by the dendritic arbor per se. Many studies calculate a D_F for binary skeletonized, single pixel wide patterns extracted from digital images, but this is not the only pattern that could be assessed; binary silhouettes, for instance, can also be extracted and assessed and for some fractal analysis methods; silhouettes tend to have higher D_F s than skeletons (see Chaps. 2 and 32). Moreover, the level of resolution and the extent to which dendritic branching is captured can influence the result, reflecting not differences in fundamental branching per se but methodological matters [27].

Furthermore, the general dendritic branching pattern investigated by fractal analysis often discounts dendritic spines, as was done in the work listed in items *a* and *b* in Table 6.1, for instance, which used binary skeletons devoid of spines and reduced to single pixel wide strands. In this respect, as explained in Fig. 6.1, for in silico stellate neuron models, binary silhouettes extracted from models with spines have a higher average D_F than those without. The D_F used for measuring the modeled spines was the box-counting dimension (D_B), demonstrated to be robust and sensitive to neuronal and other cell morphology, including microglial (see Sect. 6.3) [32, 34, 68, 69].

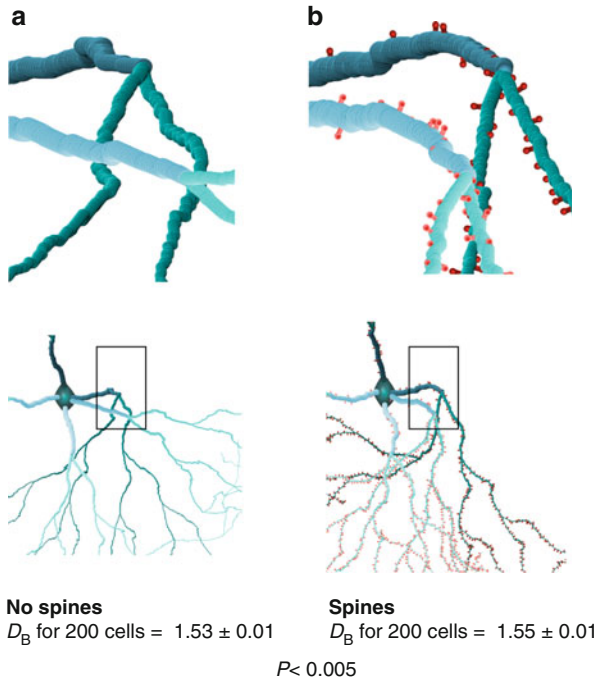


Fig. 6.1 Greater D_B for simulated planar stellate dendritic arbor neurons with spines (200 cells modeled with and 200 without dendritic spines). **(a)** An example of the original model with no spines. **(b)** An example of the original model with spines modeled as “mushroom” shaped at a rate of 0.014, length = $2 \times$ terminal diameter, spine diameter = $0.5 \times$ terminal diameter, head diameter = $3 \times$ spine diameter, spine angle = 90° . The examples are representative of each set, both modeled using one set of base parameters with random variation to simulate natural variation (binary patterns generated in *MicroMod2015* [40] based on built-in *Stellate* model)

The overall branching pattern defines one feature of the dendritic arbor, but spines are a morphological and functional feature that defines another element of neurophysiological significance. Spines play important roles in both increasing the available surface area for and integrating information in neuron signaling. Moreover, from a structural perspective, they change over time. In addition to being modified with learning and experience in general, they have been shown to retract and swell with experimental temperature manipulation and in rodent pyramidal cells to be lost toward distal aspects of the apical dendrite with chronic stress [1, 13, 47, 63, 81].

6.2.2 Methodological Issues

That spines affect the D_B for models is just one part of the general consideration that method matters in fractal classification of neurons. Methodological considerations include, in addition to the choice of which parts of a neuron to measure, the D_F type

and technique of determining it. Table 6.1 lists a representative but not comprehensive selection of approaches and methods that have been used (e.g., other methods not listed include multifractal [32], local connected fractal dimension [25], and wavelet-based [35, 55] analysis).

That each method has its strengths and weaknesses can be appreciated by considering the studies in item *a* in Table 6.1. Those studies compared cortical pyramidal neurons (a broad category having distinct apical and basal dendrites and branching axons) based on binary, skeletonized patterns derived from digital images of only the signature apical dendrites. Both studies showed that two subtypes, superficial and deep pyramidal cells, differed significantly in the D_F , yet from one study to the next, the actual values differed substantially for the same neuroanatomical subcategory of neuron. The important point to discern here is that this reflects methodological differences, and the result to focus on is the relative difference when the same method is applied [27].

With neurons in particular, the method matters. The first study in item *a* in Table 6.1 used two types of D_F , one from a modified Richardson's method (D_R) and one a type of D_B . As noted, both successfully differentiated between superficial and deep pyramidal cells, but the actual values obtained were notably higher for the D_B .

This is probably attributable to fundamental differences between these methods that can affect results for neurons. In essence, the D_R method uses a caliper to directly measure branching in radial patterns and as such would be expected to be very sensitive to the patterns assessed in the study. In contrast, box counting uses grid-based sampling to estimate scaling and does not necessarily measure the same feature the D_R measures, even from the same pattern. The more general D_B is not restricted to nor specialized for skeletonized radial patterns in the way that the modified D_R is, but the D_B has been used to successfully classify such patterns (e.g., see $p < 0.001$ in item *a* in Table 6.1.) as well as space filling patterns such as detailed membrane features and mass distributions including branching cell processes where intracellular contents are relevant (e.g., the spines in the models in Fig. 6.1) [1, 11, 50].

Even within a method, issues particularly relevant to neurons may be important. Digital rotation, for instance, is a known issue that affects box counting and is especially pertinent if not addressed for patterns with the generally elongated shape spanned by the apical dendrite of pyramidal cells (reviewed in Chap. 32) [11]. One strategy (e.g., in item *a* in Table 6.1) partially addresses digital rotation effects by aligning the main trunk of each dendrite in the same orientation for all images being compared, but this strategy leaves the part of the pattern representing all subbranches uncompensated for. This is because subbranches in the dendritic arbor are not oriented in space the same as the main branch so neither is their pixel-related orientation in a digital image. As such, this type of correction renders comparisons of the main trunk, but not of subbranches more valid from one image to the next, leaving open the possibility of considerable inherent variation not being addressed if assessed using only one orientation. This sort of correction also ignores the broader issue of sampling location bias in general that affects box counting as explained in Chaps. 2 and 32.

An alternative that addresses both digital rotation and sampling location bias more comprehensively is to sample a broad range of digital rotations using multiple sampling locations. Figure 6.2 illustrates the effect of digital rotation for a set of 200 branching structures modeled on manual measurements from digital images of pyramidal cells. The set models statistically equivalent versions of an apical dendrite based on the fractal parameters listed in Fig. 6.2b. The figure suggests that variation in the D_B by digital rotation can be notable for structures such as apical dendrites but can be controlled by appropriate sampling. In general, the choice of method and the details of its implementation are relevant when interpreting D_F s but also when planning large-scale studies in particular (e.g., calculating a D_R is tedious, whereas validated free, open source box-counting software that automatically deals with digital rotation and sampling bias is currently available) [39].

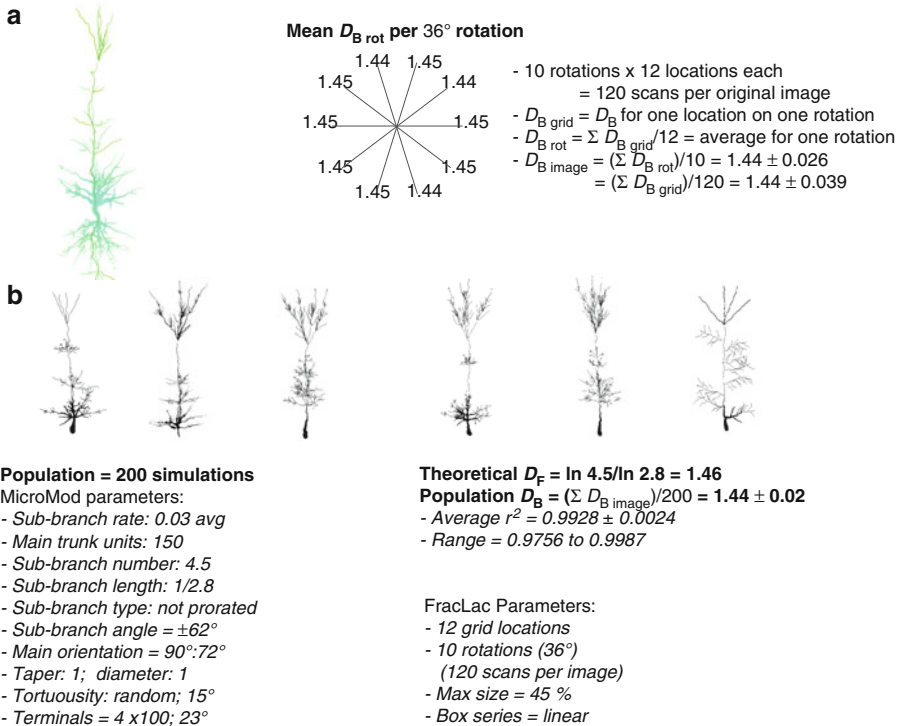


Fig. 6.2 Box-counting dimension for simulated branching pattern for pyramidal cell apical dendrites. (a) The clocklike figure shows the variation in the D_B with digital rotation for one sample model rotated in 36° increments (rotated each time from the starting orientation rather than by accumulating distortions) and how the D_B was calculated for each model, using 12 grid locations and 10 rotations for each. (b) A sample of binary contours from 200 simulations made using one set of parameters with average branching and random variation. Similar results were obtained for binary skeletons (not shown) (simulated using *MicroMod2015* for ImageJ; D_B determined using *FracLac2015* [40])

6.2.2.1 Complementary Methods

Fractal analysis can be a key part of broader characterizations of neuronal morphology. The work on human fetuses listed in Table 6.1e emphasizes this. The researchers in that study combined fractal analysis with other measures including another type of analysis called Sholl analysis. They measured several parameters and found that three were positively correlated with the growing size of neurons but at different rates over the gestational period in humans. The parameters were the global D_F and radius of the arbor and another measure of branching, the number of dendritic intersections. The researchers combined these parameters to develop a mathematical model describing prenatal development of the dendritic arbor of neurons in the dentate nucleus, with potential for developing methods of monitoring developmental abnormalities [8, 64].

6.2.2.2 3D Analysis

A final issue to discuss before moving on to the topic of microglia is 3D analysis of neurons. In many neurons, the dendritic arbor is relatively symmetrical or essentially “flat” (contained within a relatively planar volume within the CNS), which is related to laminar organization at the tissue level and makes it possible to capture relevant detail in digital images from histological preparations. In the study listed in item *c* in Table 6.1, researchers found that although the dendritic arbors of cerebellar Purkinje neurons in normal mice were essentially planar and arranged parallel to each other, arbors in the mutated model depended on the visualizing orientation (i.e., were larger perpendicular to the sagittal plane and smaller in the same plane) [45]. The differences presumably relate to disrupted laminar organization seen at the tissue level in the mutation mouse model. Whether the D_F differed by plane was not specified.

This approach is applicable to the assumption of 2D analysis that 2D representations adequately represent 3D structures. This means not that a 2D D_F is equivalent to a 3D D_F , similar to the way an area is not equivalent to a volume, but that it will consistently describe the part of the scaling in the underlying 3D structure that is being observed. The assumption is explained in detail in Chaps. 2 and 32. The crux of the matter is that it is assumed that the salient scaling features of a dendrite are consistent thus will be captured in unbiased samples. The assumption is borne out for neurons in a general sense by findings in the literature of reasonably small standard deviations in the D_F within populations of neurons, suggesting that, insofar as the plane for imaging has been varied in the published literature, plane does not affect the fractal dimension [32]. Such circumstantial evidence notwithstanding, it is important to be aware that D_F s calculated for dendritic arbors might differ by plane especially in pathological circumstances and may provide a means to quantify features of structural abnormalities.

6.3 Microglia

As with neurons, for microglia work has been published using fractal analysis to study and classify microglial morphology in neuroanatomy, pathology, and development. Table 6.2 lists samples of that work in normal and pathological models, in 2D and 3D, and using individual cellular branching patterns and other features.

One difference between the two fields of fractal analysis of neurons and of microglia is that the D_F for microglia has been more clearly correlated with function. Using box counting, it has been shown that, basically, microglia in normal, healthy brain are highly ramified with a relatively high D_B and that in response to certain stimuli such as chronic stress [20], they may hyper-ramify to a state with a slightly higher D_B , but when responding to fully noxious pathological events such as brain trauma, enter a cycle of deramification with concomitantly decreasing D_B , to a rounded, amoeboid form with a very low D_B , and then return through a cycle of increasing re-ramification and increasing D_B when resuming normal activity (see Fig. 6.3) [6, 29, 31, 38, 41, 43, 44, 58, 72, 92]. Different stages within the cycle shown in Fig. 6.3 are often classified using categories that describe both form and function, and the D_F has been shown to objectively quantify these categories [41].

Much of the fractal analysis work published for microglia has used box counting based on binary silhouettes or contours, a strong point being that this methodology is robust for all of the general morphological types, branched and unbranched, facilitating comparisons such as in Fig. 6.3.

Similar to what has been seen for neurons, the D_F is typically positively correlated with increasing size of the span covered by a cell but measures features in addition to size. It has been shown to delineate microglia based on other categories such as age (see Table 6.2f, g). Also similar to what has been found for neurons, the D_F for microglia objectively distinguishes cells in different pathological states (e.g., Alzheimer's). One strength of this approach is that it differentiates differences that can reflect important pathological events or other activities that are subtle or undetectable visually [41, 44, 80]. In the work listed in Table 6.2d, for instance, the D_F was useful for quantitating not only gross pathological responses but also less easily observable responses over different brain regions after transient global ischemia [79, 80].

This general capacity for quantifying subtleties of microglial morphology has important implications, because microglia are immunoinflammatory cells but also much more, having multiple roles in maintaining normal brain structure and function, interacting with all parts of the neuron [58, 88, 92]. They are involved in pruning spines, facilitating synaptic transmission, interacting with extracellular matrix, and axonal excitability [3, 87]. They secrete growth factors and inflammatory mediators and play major roles in dealing with stress at all levels from sleep deprivation [100] to subtle cognitive experience [21] to pain modulation [23] and severe trauma [2, 49, 62, 66, 83, 84]. In this respect, many roles of microglia in normal brain function and subtler dysfunction are currently being investigated suggesting the D_F of microglia will have potential application in many fields (e.g., drug

Table 6.2 Selected sample of fractal analysis approaches to microglial morphology cited in PubMed (August 2015; search terms “microglia” and “fractal”)

Topic and summary of classification criterion	Model	References	Analysis method
Neuroanatomy			
(a) Consistent D_B by location but substantial variability in hull size correlated with process size and complexity	Healthy adult rat	[48]	Box counting and Sholl
	Prefrontal cortex		Convex hull
Pathology			
(b) D_B defines activation-based cycle with two sides (higher D_B = lower activation except transient peak of hyper-ramification)	Multiple models	[41]	Box counting, lacunarity, and multifractal
(c) Hyper-ramification in chronic stress increases D_B (peak of cycle before decrease to full activation); minocycline decreases D_B ; larger cells affected more than smaller	Adult male rats	[20]	Box counting, Sholl, and other morphometrics
	Chronic stress induces hyper-ramification coincident with increase in depression-like behaviors		
	Attenuated by minocycline		
(d) D_F correlates with course and intensity of pyramidal cell degeneration but different dynamics in different brain regions	Adult (3 month) female rats	[79, 80]	Mass radius, dilation, and other morphometrics
	Global ischemia (cardiac arrest)		
	Upper layer cerebral cortex, stratum radiatum of CA1, and hilus of dentate; no visible neurodegeneration but microglial reaction in upper layer of cerebral cortex, weak relative to hippocampal areas		
(e) Decreased D_B (higher activation) with pathology and increased D_F (lower activation) with neuroprotectin D1	Mice	[72]	2D and 3D box counting
	Laser-induced choroidal neovascularization		
	Attenuated by neuroprotectin D1 eye drops		
Development			
(f) Higher D_B (less activated) in young adult microglia compared to middle aged	Rats 3–5 and 15–19 months	[18]	Box counting
	Dorsal root ganglia and lumbar spinal cord		
(g) D_F increased over time but with different dynamics by brain region	Rat	[59]	Dilation
	Developing cerebral hemisphere		

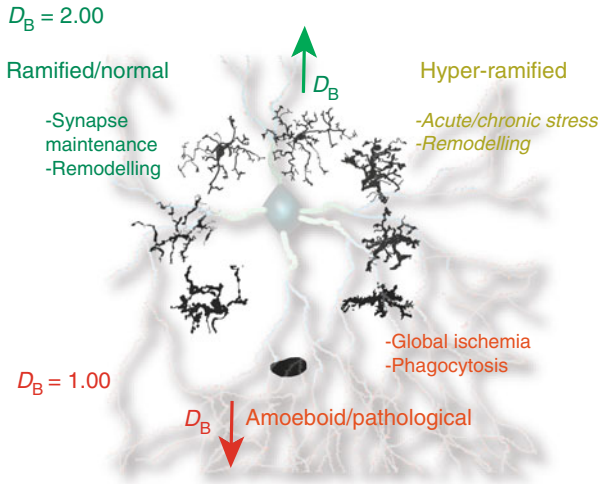


Fig. 6.3 Schematic showing cycle of microglial morphology, activation level, and D_B . Microglial complexity is highest in the ramified (*top cells*) and lowest in the amoeboid (*bottom cell*) forms responding to severe compromise, where the D_B is close to 1.00 (*bottom red arrow*). The D_B generally corresponds to the level of re-ramification or de-ramification between the peak values. The D_B objectively differentiates between gross differences separating morphological/functional categories but also between subtle differences within the cycle to quantitate subtle differences in activity. Using cell span, lacunarity, and multifractality (not shown) further differentiates between cells with similar D_B s

monitoring, learning [76], stress [20], alcoholism [37], and schizophrenia [5]; see Table 6.2c, e).

Along with the D_F , lacunarity and multifractal analysis have been used to classify microglial morphology. In particular, lacunarity has been used to objectively discern among very similar looking microglial morphologies within an activation category and having the same D_B (e.g., more “rodlike” have higher Λ than more radial cells; rodlike forms appear when reacting microglia fuse but could also reflect physical confines or active migration) [41, 42, 80, 84]. In silico modeling has shown that the D_B is more sensitive for branching structures, but lacunarity is for particular features that are not always visually recognized such as soma size relative to process length [30, 31, 38, 41]. Multifractal analysis has shown promise for identifying microglia particularly in transitional states [32, 41, 43].

6.4 Future Directions

Whereas neurons are the critical structural and functional basis of signaling, microglia are their dynamic, constant attendants, physicians, and undertakers. Being able to quantitatively assess both of these brain cell types is vital to the overall science of understanding, monitoring, and modifying nervous system function. This chapter

has outlined ways the D_F has been used to describe and categorize these two cell types in normal and pathological models, in 2 and 3 dimensions, using individual cellular branching patterns [25, 32, 52, 67], but also other features [28, 32, 35]. This chapter also explained that there are a variety of approaches, each with its strengths and weaknesses, making some preferred over others depending on the application. Box counting of silhouettes has particular promise for comparisons of neurons and microglia, in being able to capture features relevant to studies of both cell types in all potential forms.

The detailed designs of neurons and microglia are inherently related. The topological structure of neurons dictates the brain's computational capacity, and also interacts reciprocally with the topological structure of microglia, in normal but also pathological states. Moreover, the fundamental features of neuronal morphology change. Being part of a living system, neuronal morphology is reciprocally and profoundly influenced by the system it provides central communication and control for, and microglia are a major part of that plasticity [76–78, 84, 87, 88, 90, 92]. In both cells, branching and other features of morphology change with experience and in the long term over time, with age, alcohol exposure, etc. [7, 47, 63, 76, 86, 96].

It is intriguing in this regard that despite such lifelong plasticity, the D_F s for neurons based on dendritic arbors and for microglia are stable for different neuro-anatomical/functional categories. This brings up questions about the normal variety in the D_F that should be expected within a category and how that variety itself might be related to cognitive capacities, etc. In particular, it brings up questions about the D_F of neurons where spines are included and how studying microglial and neuronal function together including this feature might bring valuable insight.

In conclusion, the stage is set to draw these two fields closer, to use fractal measures of neuronal and microglial categories to investigate complex features and interactions such as signal integration, spine morphology, chemical mediators, network effects, 3D orientation, etc. [9, 19, 54, 60, 61]. Classifying tissue using this type of approach offers a perspective on connectivity and synchronicity complementing the perspective afforded by studying dendritic branching or microglial morphology alone [9, 70].

References

1. Alvarez DN, De Simoni A, Velzing EH, Bracey E, Joels M, Edwards FA, Krugers HJ. Corticosterone reduces dendritic complexity in developing hippocampal CA1 neurons. *Hippocampus*. 2009;19(9):828–36.
2. Alliot F, Godin I, Pessac B. Microglia derive from progenitors, originating from the yolk sac, and which proliferate in the brain. *Brain Res Dev Brain Res*. 1999;117(2):145–52.
3. Baalman K, Marin MA, Ho TS, Godoy M, Cherian L, Robertson C, Rasband MN. Axon initial segment-associated microglia. *J Neurosci*. 2015;35(5):2283–92.
4. Bhattacharya J, Edwards J, Mamelak A, Schuam EM. Ongoing hippocampal neuronal activity in human: is it noise or correlated fractal process? In: Losa GA, Merlini D, Nonnenmacher TF, Weibel ER, editors. *Fractals in biology and medicine*, vol IV, vol. VII. Basel: Birkhäuser Verlag Basel; 2005. p. 95–106.

5. Blank T, Prinz M. Microglia as modulators of cognition and neuropsychiatric disorders. *Glia*. 2013;61(1):62–70.
6. Bohatschek M, Kloss CU, Kalla R, Raivich G. In vitro model of microglial deramification: ramified microglia transform into amoeboid phagocytes following addition of brain cell membranes to microglia-astrocyte cocultures. *J Neurosci Res*. 2001;64(5):508–22.
7. Bose M, Muñoz-Llanca P, Roychowdhury S, Nichols JA, Jakkamsetti V, Porter B, Byrapureddy R, Salgado H, Kilgard MP, Aboitiz F, Dagnino-Subiabre A, Atzori M. Effect of the environment on the dendritic morphology of the rat auditory cortex. *Synapse (New York NY)*. 2010;64(2):97–110.
8. Cerbai F, Lana D, Nosi D, Petkova-Kirova P, Zecchi S, Brothers HM, Wenk GL, Giovannini MG. The neuron-astrocyte-microglia triad in normal brain ageing and in a model of neuroinflammation in the rat hippocampus. *PLoS ONE*. 2012;7(9):e45250.
9. Cornforth D, Jelinek HF. Automated classification of dementia subtypes from post-mortem cortex images. In: Zhang S, Jarvis R, editors. *AI 2005: advances in artificial intelligence*, Lecture Notes in Computer Science, vol. 3809. Berlin: Springer; 2005. p. 1285–8.
10. De Simoni A, Edwards FA. Pathway specificity of dendritic spine morphology in identified synapses onto rat hippocampal CA1 neurons in organotypic slices. *Hippocampus*. 2006;16(12):1111–24.
11. De Simoni A, Griesinger CB, Edwards FA. Development of rat CA1 neurones in acute versus organotypic slices: role of experience in synaptic morphology and activity. *J Physiol*. 2003;550(Pt 1):135–47.
12. Djamgoz MB, Krasowska M, Martinoli O, Sericano M, Vallerga S, Grzywna ZJ. Structure-function correlation in transient amacrine cells of goldfish retina: basic and multifractal analyses of dendritic trees in distinct synaptic layers. *J Neurosci Res*. 2001;66(6):1208–16.
13. Edwards FA. Dancing dendrites. *Nature*. 1998;394(6689):129–30.
14. Esteban FJ, Sepulcre J, de Mendizabal NV, Goni J, Navas J, de Miras JR, Bejarano B, Masdeu JC, Villoslada P. Fractal dimension and white matter changes in multiple sclerosis. *Neuroimage*. 2007;36(3):543–9.
15. Fabrizii M, Moifar F, Jelinek HF, Karperien A, Ahammer H. Fractal analysis of cervical intraepithelial neoplasia. *PLoS ONE*. 2014;9(10):e108457.
16. Ferrari G, Grisan E, Scarpa F, Fazio R, Comola M, Quattrini A, Comi G, Rama P, Riva N. Corneal confocal microscopy reveals trigeminal small sensory fiber neuropathy in amyotrophic lateral sclerosis. *Front Aging Neurosci*. 2014;6:278.
17. Fetterhoff D, Opris I, Simpson SL, Deadwyler SA, Hampson RE, Kraft RA. Multifractal analysis of information processing in hippocampal neural ensembles during working memory under $\Delta(9)$ -tetrahydrocannabinol administration. *J Neurosci Methods*. 2015;244:136–53.
18. Galbavy W, Kaczocha M, Puopolo M, Liu L, Rebecchi MJ. Neuroimmune and neuropathic responses of spinal cord and dorsal root ganglia in middle age. *PLoS ONE*. 2015;10(8):e0134394.
19. Gutierrez RC, Hung J, Zhang Y, Kertesz AC, Espina FJ, Colicos MA. Altered synchrony and connectivity in neuronal networks expressing an autism-related mutation of neuroligin 3. *Neuroscience*. 2009;162(1):208–21.
20. Hinwood M, Tynan RJ, Charnley JL, Beynon SB, Day TA, Walker FR. Chronic stress induced remodeling of the prefrontal cortex: structural re-organization of microglia and the inhibitory effect of minocycline. *Cereb Cortex*. 2012.
21. Hinwood M, Tynan RJ, Charnley JL, Beynon SB, Day TA, Walker FR. Chronic stress induced remodeling of the prefrontal cortex: structural re-organization of microglia and the inhibitory effect of minocycline. *Cereb Cortex*. 2013;23(8):1784–97.
22. Hoffbrand AV, Moss PAH, Pettit JE. *Essential haematology*. 6th ed. Malden: Wiley-Blackwell; 2011.
23. Huang CY, Chen YL, Li AH, Lu JC, Wang HL. Minocycline, a microglial inhibitor, blocks spinal CCL2-induced heat hyperalgesia and augmentation of glutamatergic transmission in substantia gelatinosa neurons. *J Neuroinflammation*. 2014;11:7.

24. Ivanov PC, Ma QDY, Bartsch RP, Hausdorff JM, Nunes Amaral L, Schulte-Frohlinde V, Stanley HE, Yoneyama M. Levels of complexity in scale-invariant neural signals. *Phys Rev E Stat Nonlinear Soft Matter Phys.* 2009;79(4 Pt 1):041920.
25. Jelinek HF, Cornforth DJ, Roberts T, Landini G, Bourke P, Bossomaier T. Image processing of finite size rat retinal ganglion cells using multifractal and local connected fractal analysis. In: Yu GIWaX (ed) *AI 2004: advances in artificial intelligence. 17th Australian Joint Conference on Artificial Intelligence*, Cairns, Australia, 2005. *Lecture Notes in Artificial Intelligence*. Springer Verlag, p. 961–6.
26. Jelinek HF, Elston GN. Pyramidal neurons in macaque visual cortex: interareal phenotypic variation of dendritic branching pattern. *Fractals.* 2001;09(03):287–95.
27. Jelinek HF, Elston NZ, Zietch B. Fractal analysis: pitfalls and revelations in neuroscience. In: Losa GA, Merlini D, Nonnenmacher TF, Weibel ER, editors. *Fractals in biology and medicine, Mathematics and Biosciences in Interaction*, vol. VII. IVth ed. Basel: Birkhäuser Verlag Basel; 2005. p. 85–94.
28. Jelinek HF, Fernandez E. Neurons and fractals: how reliable and useful are calculations of fractal dimensions? *J Neurosci Methods.* 1998;81(1–2):9–18.
29. Jelinek HF, Karperien A, Buchan A, Bossomaier T. Differentiating grades of microglia activation with fractal analysis. *Complex Int.* 2008;1–12.
30. Jelinek HF, Karperien A, Cornforth D, Cesar RMJ, Leandro J. MicroMod—an L-systems approach to neuron modelling. In: Sarker R, McKay B, Gen M, Namatame A, editors. *Sixth Australia-Japan joint workshop on intelligent and evolutionary systems*, Canberra, Australia, November 30-December 1, 2002. *AJJWIES'02*. Australian National University, Canberra. 2002.
31. Jelinek HF, Karperien A, Milošević NT. Lacunarity analysis and classification of microglia in neuroscience. In: *Proceedings of the 8th European conference on mathematical and theoretical biology*, Cracow, Poland, 2011. *European Society for Mathematical and Theoretical Biology (ESMTB)*. 2011.
32. Jelinek HF, Milošević NT, Karperien A, Krstonošić B. Box-counting and multifractal analysis in neuronal and glial classification. In: Dumitrache I, editor. *Advances in intelligent control systems and computer science, Advances in Intelligent Systems and Computing*, vol. 187. Berlin: Springer; 2013. p. 177–89.
33. Jelinek HF, Milošević NT, Ristanović D. The morphology of alpha ganglion cells in mammalian species: a fractal analysis study. *CEAI.* 2010;12(1):3–9.
34. Jelinek HF, Ristanović D, Milošević NT. The morphology and classification of alpha ganglion cells in the rat retinae: a fractal analysis study. *J Neurosci Methods.* 2011;201(1):281–7.
35. Jones CL, Jelinek HF. Wavelet packet fractal analysis of neuronal morphology. *Methods.* 2001;24(4):347–58.
36. Kam Y, Karperien A, Weidow B, Estrada L, Anderson AR, Quaranta V. Nest expansion assay: a cancer systems biology approach to in vitro invasion measurements. *BMC Res Notes.* 2009;2:130.
37. Kane CJ, Phelan KD, Han L, Smith RR, Xie J, Douglas JC, Drew PD. Protection of neurons and microglia against ethanol in a mouse model of fetal alcohol spectrum disorders by peroxisome proliferator-activated receptor-gamma agonists. *Brain Behav Immun.* 2011;25 Suppl 1:S137–45.
38. Karperien A. Defining microglial morphology: form, function, and fractal dimension. Thesis, Charles Sturt University, Australia. 2004.
39. Karperien A. *FracLac2015 for ImageJ: JavaDoc, source code, and jar.* vol 7, 201501 edn. National Institutes of Health ImageJ Plugins. 2015.
40. Karperien A. *MicroMod 2015 for ImageJ: fractal branching Bio-modelling tool* vol 1, 2015 edn. Natl Inst Health Image J Plugins. 2015.
41. Karperien A, Ahammer H, Jelinek HF. Quantitating the subtleties of microglial morphology with fractal analysis. *Front Cell Neurosci.* 2013;7:3.

42. Karperien A, Jelinek H, Milošević N. Reviewing lacunarity analysis and classification of microglia in neuroscience. Paper presented at the 8th European Conference on Mathematical and Theoretical Biology, Poland. 2011.
43. Karperien A, Jelinek HF, Milošević NT. Multifractals: a review with an application in neuroscience. In: CSCS18-18th international conference on control systems and computer science: fifth symposium on interdisciplinary approaches in fractal analysis bucharest, Romania, 2011. Politehnica Press; pp. 888–3.
44. Karperien AL, Jelinek HF, Buchan AM. Box-counting analysis of microglia form in schizophrenia, Alzheimer's disease and affective disorder. *Fractals*. 2008;16(02):103–7.
45. Kim J, Kwon N, Chang S, Kim K-T, Lee D, Kim S, Yun SJ, Hwang D, Kim JW, Hwu Y, Margaritondo G, Je JH, Rhyu IJ. Altered branching patterns of Purkinje cells in mouse model for cortical development disorder. *Sci Rep*. 2011;1:122.
46. King RD, Brown B, Hwang M, Jeon T, George AT, AsDNI. Fractal dimension analysis of the cortical ribbon in mild Alzheimer's disease. *Neuroimage*. 2010;53(2):471–9.
47. Kirov SA, Petrak LJ, Fiala JC, Harris KM. Dendritic spines disappear with chilling but proliferate excessively upon rewarming of mature hippocampus. *Neuroscience*. 2004;127(1):69–80.
48. Kongsui R, Beynon SB, Johnson SJ, Walker FR. Quantitative assessment of microglial morphology and density reveals remarkable consistency in the distribution and morphology of cells within the healthy prefrontal cortex of the rat. *J Neuroinflammation*. 2014;11:182.
49. Kreutzberg GW. Microglia, the first line of defence in brain pathologies. *Arzneimittelforschung*. 1995;45(3A):357–60.
50. Kuwajima M, Spacek J, Harris KM. Beyond counts and shapes: studying pathology of dendritic spines in the context of the surrounding neuropil through serial section electron microscopy. *Neuroscience*. 2013;251:75–89.
51. Lamanna J, Esposti F, Malgaroli A, Signorini MG. Fractal behavior of spontaneous neurotransmitter release: from single-synapse to whole-cell recordings. *Conf Proc IEEE Eng Med Biol Soc*. 2011;2011:3346–9.
52. Li Z, Da F, Costa L. Investigating shape and function relationship in retinal ganglion cells. *J Integr Neurosci*. 2002;1(2):195–215.
53. Losa GA. Fractals in biology and medicine. In: Meyers R, editor. *Encyclopedia of Molecular Cell Biology and Molecular Medicine*, Wiley-VCH Verlag, Berlin. 2011:1–25.
54. Meijering E. Neuron tracing in perspective. *Cytom Part A J Int Soc Anal Cytol*. 2010;77(7):693–704.
55. Misiak D, Posch S, Lederer M, Reinke C, Huttelmaier S, Moller B. Extraction of protein profiles from primary neurons using active contour models and wavelets. *J Neurosci Methods*. 2014;225:1–12.
56. Mittelbronn M, Dietz K, Schluesener HJ, Meyermann R. Local distribution of microglia in the normal adult human central nervous system differs by up to one order of magnitude. *Acta Neuropathol*. 2001;101(3):249–55.
57. Puškaš N, Zaletel I, Stefanovic BD, Ristanović D. Fractal dimension of apical dendritic arborization differs in the superficial and the deep pyramidal neurons of the rat cerebral neocortex. *Neurosci Lett*. 2015;589:88–91.
58. Nimmerjahn A, Kirchhoff F, Helmchen F. Resting microglial cells are highly dynamic surveillants of brain parenchyma in vivo. *Science*. 2005;308(5726):1314–8.
59. Orłowski D, Soltys Z, Janeczko K. Morphological development of microglia in the postnatal rat brain. A quantitative study. *Int J Dev Neurosci*. 2003;21(8):445–50.
60. Pani G, De Vos WH, Samari N, de Saint-Georges L, Baatout S, Van Oostveldt P, Benotmane MA. MorphoNeuroNet: an automated method for dense neurite network analysis. *Cytom Part A J Int Soc Anal Cytol*. 2014;85(2):188–99.
61. Pantic I, Dacic S, Brkic P, Lavrnja I, Pantic S, Jovanovic T, Pekovic S. Application of fractal and grey level co-occurrence matrix analysis in evaluation of brain corpus callosum and cingulum architecture. *Microsc Microanal*. 2014;20(5):1373–81.
62. Radewicz K, Garey LJ, Gentleman SM, Reynolds R. Increase in HLA-DR immunoreactive microglia in frontal and temporal cortex of chronic schizophrenics. *J Neuropathol Exp Neurol*. 2000;59(2):137–50.

63. Radley JJ, Anderson RM, Hamilton BA, Alcock JA, Romig-Martin SA. Chronic stress-induced alterations of dendritic spine subtypes predict functional decrements in an hypothalamo-pituitary-adrenal-inhibitory prefrontal circuit. *J Neurosci*. 2013;33(36):14379–91.
64. Rajkovic K, Bacic G, Ristanović D, Milošević NT. Mathematical model of neuronal morphology: prenatal development of the human dentate nucleus. *Biomed Res Int*. 2014;2014:812351.
65. Ren L, Lubrich B, Biber K, Gebicke-Haerter PJ. Differential expression of inflammatory mediators in rat microglia cultured from different brain regions. *Brain Res Mol Brain Res*. 1999;65(2):198–205.
66. Rezaie P, Cairns NJ, Male DK. Expression of adhesion molecules on human fetal cerebral vessels: relationship to microglial colonisation during development. *Brain Res Dev Brain Res*. 1997;104(1–2):175–89.
67. Ristanović D, Milošević NT, Jelinek HF, Stefanovic IB. The mathematical modelling of neuronal dendritic branching patterns in two dimensions: application to retinal ganglion cells in the cat and rat. *Biol Cybern*. 2009;100:97–108.
68. Ristanović D, Stefanovic BD, Puškaš N. Fractal analysis of dendrite morphology of rotated neuronal pictures: the modified box counting method. *Theor Biol Forum*. 2014;107(1–2):109–21.
69. Ristanović D, Stefanovic BD, Puškaš N. Fractal analysis of dendrite morphology using modified box-counting method. *Neurosci Res*. 2014;84:64–7.
70. Sandu A-L, Rasmussen Jr I-A, Lundervold A, Kreuder F, Neckelmann G, Hugdahl K, Specht K. Fractal dimension analysis of MR images reveals grey matter structure irregularities in schizophrenia. *Comput Med Imaging Graph*. 2008;32(2):150–8.
71. Serletis D, Bardakjian BL, Valiante TA, Carlen PL. Complexity and multifractality of neuronal noise in mouse and human hippocampal epileptiform dynamics. *J Neural Eng*. 2012;9(5):056008.
72. Sheets KG, Jun B, Zhou Y, Zhu M, Petasis NA, Gordon WC, Bazan NG. Microglial ramification and redistribution concomitant with the attenuation of choroidal neovascularization by neuroprotectin D1. *Mol Vis*. 2013;19:1747–59.
73. Sheffield LG, Berman NE. Microglial expression of MHC class II increases in normal aging of nonhuman primates. *Neurobiol Aging*. 1998;19(1):47–55.
74. Sheffield LG, Marquis JG, Berman NE. Regional distribution of cortical microglia parallels that of neurofibrillary tangles in Alzheimer's disease. *Neurosci Lett*. 2000;285(3):165–8.
75. Shimizu Y, Umeda M, Mano H, Aoki I, Higuchi T, Tanaka C. Neuronal response to Shepard's tones: an auditory fMRI study using multifractal analysis. *Brain Res*. 2007;1186:113–23.
76. Sierra A, Beccari S, Diaz-Aparicio I, Encinas JM, Comeau S, Tremblay M-E. Surveillance, phagocytosis, and inflammation: how never-resting microglia influence adult hippocampal neurogenesis. *Neural Plast*. 2014;2014:610343.
77. Sierra A, Tremblay M-E, Wake H. Never-resting microglia: physiological roles in the healthy brain and pathological implications. *Front Cell Neurosci*. 2014;8:240.
78. Siskova Z, Tremblay M-E. Microglia and synapse: interactions in health and neurodegeneration. *Neural Plast*. 2013;2013:425845.
79. Soltys Z, Orzylowska-Sliwinska O, Zaremba M, Orlowski D, Piechota M, Fiedorowicz A, Janeczko K, Oderfeld-Nowak B. Quantitative morphological study of microglial cells in the ischemic rat brain using principal component analysis. *J Neurosci Methods*. 2005;146(1):50–60.
80. Soltys Z, Ziaja M, Pawlinski R, Setkowicz Z, Janeczko K. Morphology of reactive microglia in the injured cerebral cortex. Fractal analysis and complementary quantitative methods. *J Neurosci Res*. 2001;63(1):90–7.
81. Spruston N, Kath WL. Dendritic arithmetic. *Nat Neurosci*. 2004;7(6):567–9.
82. Squire LR. *Fundamental neuroscience*. 4th ed. Amsterdam: Elsevier/Academic; 2013.
83. Stoll G, Jander S. The role of microglia and macrophages in the pathophysiology of the CNS. *Prog Neurobiol*. 1999;58(3):233–47.
84. Streit WJ, Walter SA, Pennell NA. Reactive microgliosis. *Prog Neurobiol*. 1999;57(6):563–81.
85. Suckling J, Wink AM, Bernard FA, Barnes A, Bullmore E. Endogenous multifractal brain dynamics are modulated by age, cholinergic blockade and cognitive performance. *J Neurosci Methods*. 2008;174(2):292–300.

86. Taylor AM, Castonguay A, Taylor AJ, Murphy NP, Ghogha A, Cook C, Xue L, Olmstead MC, De Koninck Y, Evans CJ, Cahill CM. Microglia disrupt mesolimbic reward circuitry in chronic pain. *J Neurosci*. 2015;35(22):8442–50.
87. Tremblay M-E. The role of microglia at synapses in the healthy CNS: novel insights from recent imaging studies. *Neuron Glia Biol*. 2011;7(1):67–76.
88. Tremblay M-E, Lowery RL, Majewska AK. Microglial interactions with synapses are modulated by visual experience. *PLoS Biol*. 2010;8(11):e1000527.
89. Tremblay M-E, Majewska AK. A role for microglia in synaptic plasticity? *Commun Integr Biol*. 2011;4(2):220–2.
90. Tremblay M-E, Marker DF, Puccini JM, Muly EC, Lu S-M, Gelbard HA. Ultrastructure of microglia-synapse interactions in the HIV-1 Tat-injected murine central nervous system. *Commun Integr Biol*. 2013;6(6):e27670.
91. Tremblay M-E, Riad M, Majewska A. Preparation of mouse brain tissue for immunoelectron microscopy. *J Vis Exp*. 2010;(41):1–5.
92. Tremblay M-E, Stevens B, Sierra A, Wake H, Bessis A, Nimmerjahn A. The role of microglia in the healthy brain. *J Neurosci*. 2011;31(45):16064–9.
93. Tremblay M-E, Zettel ML, Ison JR, Allen PD, Majewska AK. Effects of aging and sensory loss on glial cells in mouse visual and auditory cortices. *Glia*. 2012;60(4):541–58.
94. Tremblay S, Miloudi K, Chaychi S, Favret S, Binet F, Polosa A, Lachapelle P, Chemtob S, Sapiéha P. Systemic inflammation perturbs developmental retinal angiogenesis and neuroretinal function. *Invest Ophthalmol Vis Sci*. 2013;54(13):8125–39.
95. Wake H, Moorhouse AJ, Jinno S, Kohsaka S, Nabekura J. Resting microglia directly monitor the functional state of synapses in vivo and determine the fate of ischemic terminals. *J Neurosci*. 2009;29(13):3974–80.
96. Wang J, Cheng Y, Wang X, Roltsch Hellard E, Ma T, Gil H, Ben Hamida S, Ron D. Alcohol elicits functional and structural plasticity selectively in dopamine D1 receptor-expressing neurons of the dorsomedial striatum. *J Neurosci*. 2015;35(33):11634–43.
97. Warsi MA, Molloy W, Noseworthy MD. Correlating brain blood oxygenation level dependent (BOLD) fractal dimension mapping with magnetic resonance spectroscopy (MRS) in Alzheimer's disease. *MAGMA*. 2012;25(5):335–44.
98. Weiss B, Clemens Z, Bódizs R, Vágó Z, Halász P. Spatio-temporal analysis of monofractal and multifractal properties of the human sleep EEG. *J Neurosci Methods*. 2009;185(1):116–24.
99. West BJ, Scafetta N. A multifractal dynamical model of human gait. In: *Fractals in biology and medicine*. Springer, Basel, Switzerland; 2005. p. 131–40.
100. Wisor JP, Schmidt MA, Clegern WC. Evidence for neuroinflammatory and microglial changes in the cerebral response to sleep loss. *Sleep*. 2011;34(3):261–72.
101. Young B. *Wheater's functional histology: a text and colour atlas*. 5th ed. Edinburgh: Churchill Livingstone/Elsevier; 2006.
102. Zaletel I, Ristanović D, Stefanović BD, Puškaš N. Modified Richardson's method versus the box-counting method in neuroscience. *J Neurosci Methods*. 2015;242:93–6.
103. Zorick T, Mandelkern MA. Multifractal detrended fluctuation analysis of human EEG: preliminary investigation and comparison with the wavelet transform modulus maxima technique. *PLoS ONE*. 2013;8(7):e68360.

Chapter 7

The Morphology of the Brain Neurons: Box-Counting Method in Quantitative Analysis of 2D Image

Nebojša Milošević

Abstract This chapter calls attention to the difference among basic terms of fractal geometry and fractal analysis presented on 2D images of neurons from the human dentate nuclei. In further quantitative estimation, the most popular technique of fractal analysis, i.e., the “box-counting method,” was used. Image preprocessing was investigated, precisely how images at different sizes, resolutions, and rotation angles could influence in the magnitude of the box dimension. All preprocessing tasks were evaluated on 17 standardized images from the dentate nuclei, classified into three groups due to their width and height.

In addition, box-counting methodology was investigated to show how box dimension could estimate the shape of the neuron image, space-filling property, and the degree of dendrite aberrations, by using different processed images of the neuron. As the results show difference image presentation between images of neurons with sparse or dense dendritic tree, along with small or large cell bodies, this chapter sums up investigation of 76 images from the adult human dentate nucleus quantifying their three morphological properties, previously mentioned.

Keywords Box dimension • Fractal geometry • Fractal analysis • Image preprocessing • Neuronal morphology • Self-similarity • Two-dimensional images

7.1 Introduction

Although standard quantitative methods in science are based on classical Euclidean geometry [15], fractal geometry is developed as a new geometry of nature [32]. Early investigations showed that the most common biological patterns can be characterized by fractal geometry [7], and thus, concepts of fractal geometry are being

N. Milošević, PhD

Department of Biophysics, School of Medicine, KCS-Institute of Biophysics,
University of Belgrade, Belgrade 11129, Serbia

e-mail: mtn@med.bg.ac.rs

used in diverse research areas [7, 32], particularly are proven to be an increasingly useful tool in quantitative image analysis in medical science [21].

The fractal analysis is derived from fractal geometry [17], as a modern mathematical method of measuring complexity of patterns in geometry and nature [32], using simple parameter [15]: the fractal dimension (FD). For example, FD is larger if the object's border is more rugged, the branching pattern more abundant and lines more irregular and twisted [7, 17]. Generally, there is a link between FD and the *topological dimension* (D_T)¹: while D_T is always an integer (two for object in plane and three for object in space), FD is decimal number [15], between one and two (for object in plane) or between two and three (for object in space).

The aim of this chapter is to explore the concept of fractal analysis and its application on 2D images of neurons from the human dentate nuclei, using the most popular technique of fractal analysis: the “box-counting method” (BC). As such images can be characterized with global FD, or images can be termed as “monofractals” [25], the BC methodology and image preprocessing are presented and investigated.

7.2 Starting from the Fractal Geometry Toward the Fractal Analysis

7.2.1 Fractal Geometry in 2D Space

The basic idea (i.e., the starting point) of fractal geometry is the term *fractal* [17], which can be comprehended as a theoretical abstraction that cannot be defined analytically [15]. Two types of fractals are being used in quite different fields (a) *mathematical* (or *geometrical* in 2D space) and (b) *natural* (or *statistical*, *empirical*, etc.) [17]. The first group of fractals is mathematical constructions characterized by never-ending cascades of similar structural details [15], while the other group is more restricted. Thus, each geometrical fractal should be considered as an infinite ordered set of fractal objects defined on a metric space, with four features [17]: (a) *starting object* (or the *initiator*), (b) *recursion algorithm*, (c) *geometrical self-similarity*, and (d) *fractal dimension*. Every single fractal starts with *initiator* [7, 17] and ends with the *limit fractal* [28]. Incomplete fractal constructs are called *prefractals* [7, 17, 28]. All of them represent the *geometrical fractal set* [17].

7.2.2 Self-Similarity and Scaling

Fractals, in general, possess two important properties – *self-similarity* and *scaling* [15]. As reported previously [20], there are strong equivalence between these two properties for mathematical fractals, particularly for geometrical fractals [28]. The

¹Topological dimension of a space (or object) is the minimum number of coordinates needed to specify a position of any point within it.

pieces of mathematical fractal are exact duplication of the whole object, and therefore it is commonly said that mathematical fractal is *geometrically self-similar* [15]. On the other hand, this definition has to be quantified when dealing with natural objects, because their pieces are rarely identical copies of the whole object [17].

Measuring a property on a piece of a natural object using high resolution usually shows that small portion of the object quantitatively resembles the whole object. This resemblance means that, for instance, the part fills space in the same way as the whole [20]. A more exact interpretation of this condition has been offered in [28] introducing a *generating element* of a generator, which is usually made up of straight-line segments. For example, two generating elements of two generators of a fractal set can be geometrically similar or not [28]. The segments of natural objects [23] are rarely exact reduced copies of the whole object; rather than being geometrically self-similar, they are *statistically self-similar* [17]. One reason for the occurrence of statistical self-similarity is that computer reconstructions of geometrical objects are restricted to a set of scaling steps due to the resolution and size of the screen, whereas biological objects are self-limited in their scaling due to their functional requirements [17].

Statistical self-similarity implies that the measured property depends on the size (or resolution) of the scale which is used [2], i.e., the property *scales* with the measure. The self-similarity and scaling can be quantitatively estimated by the fractal dimension, as this measure describes the complexity of form and space-filling property of an object. The rule that shows how the measured value depends on the resolution of measurement is called the *scaling relationship* and the simplest relationship is given by *power law scaling* [2]:

$$A(r) = B \cdot r^{\alpha(D)}, \quad (7.1)$$

where A is a measured property of the object (such as length, area, or volume), B is a factor for the power law, r is the scale (resolution) at which it is measured, and $\alpha(D)$ is the scaling exponent, representing a simple function of the fractal dimension D of the object.² Taking the logarithms of both sides of Eq. 7.1 yields

$$\log A(r) = \alpha(D) \cdot \log r + \log B. \quad (7.2)$$

Thus, power law scaling is revealed as a straight line when the logarithm of the measured property (A) is plotted against the logarithm of the scale (r) at which it is measured.

7.2.3 Fractal Analysis

Consequently to the fractal theory, *fractal analysis* could be thought as an experimental technique which uses methodology of Mandelbrot's fractal geometry and Euclid's traditional geometry to investigate several properties of real objects [17].

²This function depends of the Euclidean dimension (E) of the object embedded in space and is accepted to be $\alpha(D) = E - D$.

Previous work on fractal analysis represented traditionally a 2D analysis [4] focused mainly to the analysis of border's outlines of natural objects [32]. These papers investigate mainly the object border, its complexity (or, simply, object's structure) and function [32]. The problem is guided to the calculation of the *fractal dimension* and analysis of the meaning of the parameter value to the considered object [27].

By analogy with the investigation of a geometrical fractal set, the use of fractal analysis postulates the following attributes: (a) *shape* of a starting object (which corresponds to the *initiator* in fractal geometry), (b) *algorithm* (enabling its successive application to the starting object), (c) *scaling* (or *statistical self-similarity*), and (d) *fractal dimension*. The *limit generator* is the same as the starting object, while it was not changed during repeated application of the algorithm [7].

In fractal analysis there are two basic approaches to measure the fractal dimension of objects in a plane [32]. The first and most commonly used is *length-related method* comprising the classical Richardson's coastline method [14], box-counting method [33], and dilation method [4]. The second method is *mass-related method* [32]. Using a different method of fractal analysis has led to difficulties in comparing the results, because each method of determination of the fractal dimension gives slightly different results when analyzing the same structure [4, 7]. It should be noted that the coastline method is equivalent to the box-counting method, only when one analyzes the border of a system [7]. There is still a problem to present, analyze, and compare different methods of measuring the fractal dimension [27].

7.3 Box-Counting Method

Segment-counting method [31], a version of Richardson's method for measuring the length of any unformed line [26] and a type of fractal analysis methods, is robust (with very high correlation coefficients) but it is tedious and time consuming [27]. Thus, the need for more handsome methods emerges, and conventional *box-counting* [32] appears to be the method which suitably measures fractal dimensions of real objects [3, 7, 9, 13, 22, 27, 32, 36]. This is very similar (someone would say equal) to the idea from traditional calculus, when the area of plane region within any closed unformed boundaries has to be measured [26]. Briefly, the area of such region is superimposed with a net of equivalent squares, or "boxes," over this region [34].

Conventional box-counting method "covers" the object with rectangular coordinate grid [32]. In the plane, image of the object is overlaid with a grid, and the number of boxes (intersected by the pattern and within it) is counted [21]. Each set of boxes is characterized by the square side r . The corresponding number of squares N necessary to cover the pattern is presented as a function of r . Fractal dimension (in further text, box dimension, D_B) is determined as the slope of the log-log relationship between N and r . Strictly mathematically "speaking," the lower and upper box dimensions of a subset $F \subset R^n$ are, respectively, defined by

$$\underline{\dim}_B(F) = \lim_{\delta \rightarrow 0} \frac{\log N_\delta(F)}{-\log \delta}, \quad \overline{\dim}_B(F) = \lim_{\delta \rightarrow 0} \frac{\log N_\delta(F)}{-\log \delta}, \quad (7.3)$$

and if lower and upper values are equal, then the common value is referred to as the box-counting dimension of F and is denoted by

$$\dim_B(F) = \lim_{\delta \rightarrow 0} \frac{\log N_\delta(F)}{-\log \delta}, \quad (7.4)$$

where $N_\delta(F)$ can be the smallest number of cubes of side δ (naturally, in 3D) that covers F or the largest number of disjoint cubes of side δ with centers in F [6].

7.3.1 Application on 2D Digital Image

When the box-counting method is applied on digitized images, it covers the image with a grid of square cells (with cell size r), where for binary images, the cell size is expressed as the number of pixels. The number of squares $N(r)$ needed to cover the image is given by a power law:

$$N(r) = \text{const} \cdot r^{-D_B}, \quad (7.5)$$

where D_B is the box dimension, obtained as an absolute value of the slope of the log–log relationship between $N(r)$ and r [18]. Figure 7.1 shows this procedure on 2D neuronal image from the monkey dentate nucleus. The box size is progressively smaller (i.e., using geometric progression) where the sequence of box sizes is reduced by a factor $1/2^n$ ($n=1, 2, 3 \dots$) from one grid to the next. It is important to state here that the scaling factor is not known a priori and the choice of scaling factor can have a dramatic impact on the results. Thus, a scaling factor of 2 is appropriate for box-counting procedure (Fig. 7.1).

Regardless from the fact that mathematical fractal requires infinite orders of magnitude of power law scaling and therefore is fractal over all scales, physical, biological, and other structures in nature have a finite number of decades between a high and a low cutoff scale. The scaling ranges of experimentally declared fractals are limited, often to five orders of magnitude or more [14]. Neuroscience shows an even more negative situation, as images span over a relatively small scaling range, mainly between 0.5 and 2 order of magnitude [7].

A previous research [20] promotes a hypothesis that the 2D neuronal images could be considered fractal over several decades of scale, if the box sizes are scaled as a power of 2. This sequence represents a finite increasing geometric progression $\{r_n\}$, and, by definition, $r_{n+1}/r_n = q$ for every n , where q is the constant common ratio [20]. As previous studies present results of box-counting method, using arithmetical, geometrical, and random progression of box sizes, applied on various images of cells

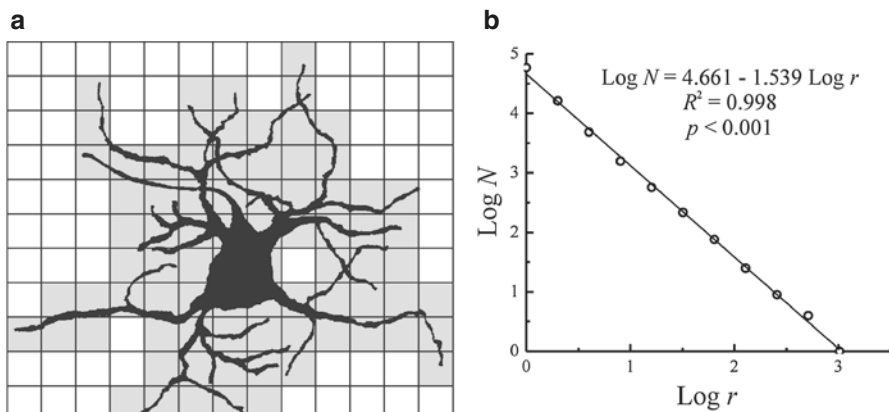


Fig. 7.1 Application of the box-counting method to “black-and-white” image of a neuron from the monkey dentate nucleus: (a) the whole image is covered with a set of squares and squares in which cover dendrites (light gray color) are counted. (b) Log–log plot between numbers of squares (N) and square size (r) is fitted by a straight line. R is the corresponding correlation coefficient. The fractal dimension D is the negative value of the slope of fitted line (in this case 1.539)

from the rat spinal cord [20] and monkey cerebellum [17, 20], statistical evaluation of the correlation coefficient of fitted line has shown that it is different from zero with a very high significance ($p < 0.0001$). However, choosing the size of boxes as a finite increasing geometric progression represents better solution of fitting problem, because in this case, the starting object will fulfill all conditions of fractal analysis [17].

Finally, in performing box-counting method, the box sizes should be taken from 2^0 to 2^k pixel, where k is the value for which N is equal to one. In that case the relationship between $\log N$ and $\log r$ was linear on more than two decades of the range [17], when correlation coefficient of fitted line was statistically evaluated.

7.3.2 The Software for Box-Counting

At the time of writing this chapter (August 2015), a search on “fractal analysis software” throughout World Wide Web yielded more than 600,000 results. Among them, there are three main programs (*Benoit*, *Fractal.yse*, and *FracLab*) which use box-counting, along with other fractal methods. In addition, there is a program which uses box-counting method only (*Fractal Dimension Estimator*), or there are appropriate plug-ins in main programs for image and signal analysis (*MathLab*, *Image J*, *Fiji*, etc.). Our further investigation will be restricted on *Image J* software (www.imagej.nih.gov/ij/) and appropriate plug-in (Analyze→Tools→Fractal Box Count) which emerge in *FracLac* (www.imagej.nih.gov/ij/plugins/fraclac/fraclac.html), developed by Audrey Karperien [12].

This plug-in was initially developed as a part of a master’s at Charles Sturt University (Australia) and code from Thomas R. Roy, University of Alberta

(Canada). As the first version was introduced in 2002, it continues to develop in response to many suggestions from users and includes inputs from the Image J, neuroscience, engineering, programming, etc. communities [12]. FracLac scans images with a shifting grid algorithm that can do multiple scans from different locations on each image, using either a nonoverlapping or an overlapping sliding box method. For details, see Chap. 32.

7.4 Material

A total of 77 Golgi-impregnated multipolar neurons of the rhesus monkey (*M. mulatta*) dentate nucleus have been analyzed. The drawings of these neurons have been taken from the experimental data published in an original book [5]. Information and detailed description of the histological procedures can be found here [5, 20].

In order to standardize the sample, four morphological parameters were calculated: the number of primary dendrites (N_{pd}), area of the neuron (A), length of skeletonized image of the neuron (L), and the density of dendrites (N_m). Bearing in mind the width and height of the image, 17 images were selected for further analysis (Table 7.1). They were classified in such a way that five neurons were of type A (i.e., the central neurons, width \approx height), six neurons of type B (i.e., asymmetrical neuron-type 1, width $>$ height), and six neurons of type C (i.e., asymmetrical neuron-type 2, width $<$ height). Their schematic representations are shown in Fig. 7.2.

7.5 Box-Counting Methodology

As biological image (i.e., image of neuron) does not reflect fractal, in theoretical or ideal sense, then interpreting the image using FD is meaningless [10]. But FD may still be useful as a quantitative parameter of neuronal images, since it indicates complexity or the scale dependence of a pattern [1]. In addition, fractal analysis of biological images (particularly, images of neuron) is not intended to indicate that the

Table 7.1 Morphological parameters of 17 multipolar neurons from the monkey dentate neurons, scanned at resolution of 100 dpi

Cell type	A	B	C
Number of cells	5	6	6
Width (px)	340–470	520–700	400–430
Height (px)	320–460	250–520	550–610
Number of primary dendrites N_{pd}	7.2 ± 0.8	6.6 ± 0.5	7.0 ± 0.6
Area of the neuron A (μm^2)	$3,165 \pm 200$	$3,550 \pm 300$	$4,310 \pm 200$
Total length L (μm)	$1,250 \pm 90$	$1,473 \pm 100$	$1,783 \pm 200$
Dendritic density N_m	16.6 ± 0.4	16.5 ± 0.3	15.2 ± 0.3

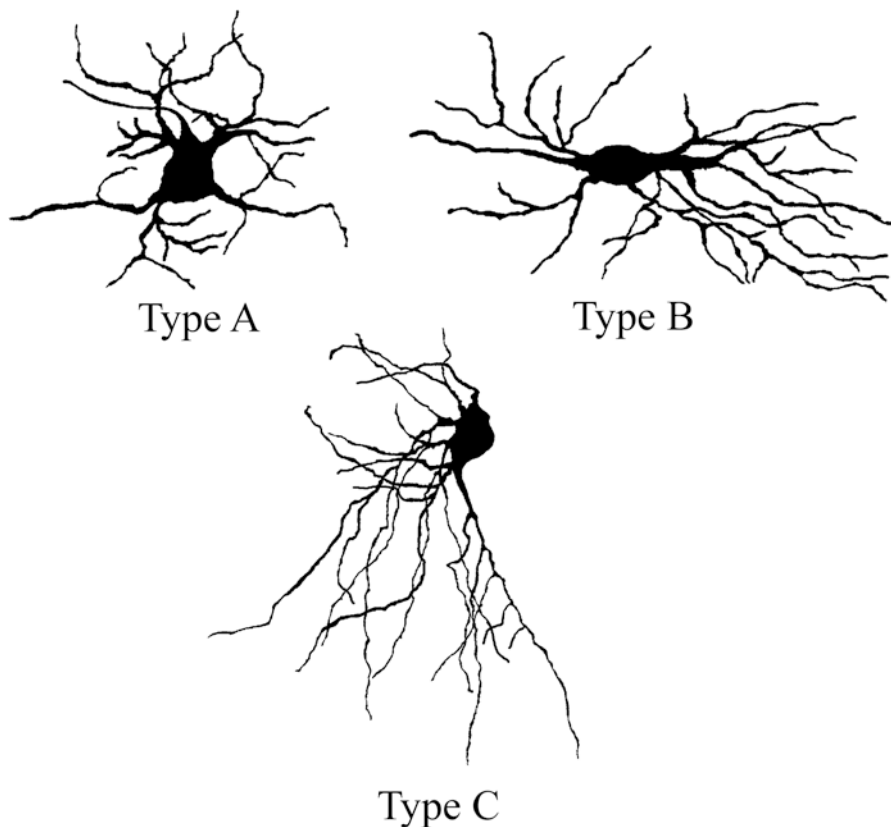


Fig. 7.2 Illustration of three groups of neurons from the monkey dentate nucleus: (a) width is approximately equal to the height, (b) width is higher than the height, and (c) width is lower than height (Original images can be found in Chan-Palay [5])

object is fractal [27]. Results have suggested that variations in sampling and preparing images for analysis, as well as analysis itself, can have nontrivial effects on the estimation and interpretation of FD [10].

7.5.1 Image Size and Resolution

Theoretically, images of identical objects at different sizes and same resolution should not influence the magnitude of FD, in this case the BD [10]. Following this idea, we analyzed three groups of neurons (A, B, and C) at three resolutions (300 dpi, 600 dpi, and 900 dpi). Thus, the size of the image was changed, while resolution was kept the same. Particularly, one primary distance was increased (width for groups A and B, and height for group C) through five values: from 300 pixels (px) to 1,500 px (300 dpi), from 500 to 3,000 px (600 dpi), and from 1,000 to

5,000 px (900 dpi). Finally, the Spearman rank correlation analysis was used to investigate whether there was an influence in the BDs of each group of neuron images with the image size. Results are summarized in Table 7.2.

As can be seen, there was an increase in BD with the size of the neuronal image. Particularly, BDs of group A neuronal images statistically increase with the size (Table 7.2), as the level of significance increases with resolution (from $p < 0.05$ for 300 dpi to $p < 0.001$ for 900 dpi). In contrast, BDs of group C neuronal images were not influenced with the size of the image. Finally, BDs of group B neuronal images significantly increase with the size only for 300 dpi. Bearing in mind the parameter a (i.e., the slope of the straight line), actually its minor value (for all groups this value is between 10^{-4} and 10^{-5}), it could be stated that the size of the image does not influence BD value of the image.

Results of this analysis suggested that for our sample of images (particularly images with same width and height, group A) there was an increase in BDs with size, in strong mathematical sense, but in real situation, it could be stated that BD remains the same value, while the size of the image increases. In addition it has to be noted that the effect on FD associated with the resizing may not be related to the size per se but rather to the computer processing. As such, increasing the size of an image leads to insertion of interpolated (Euclidean) information along the boundaries and therefore changes the value of FD [10].

Scanning the same cells at different resolutions returned different FD values, even when all other parameters are kept constant [7]. In their previous work, Jelinek et al. [10] have analyzed the FD at two different resolutions (72 dpi and 150 dpi) of a neuronal image. They concluded that cells scanned at low resolution had higher values of FD than those obtained at high resolution [10]. In order to test this hypothesis, we printed our sample of cells on A4 paper, keeping their size to A5 format, and each cell was scanned from resolution of 100 to 1,100 dpi. The choice of final resolution (1,100 dpi) was restricted by scanner (Mustek 1,200, Mustek Systems Inc., Taiwan). For each group of neurons, BD was calculated and their mean values were plotted against the resolution. The Spearman rank correlation was applied for each group in order to investigate the influence of image resolution on BDs. Plots of each group, along with results of correlation analysis, are presented on Fig. 7.3.

As it can be seen, there was an increase in BD with the resolution, in each group of neurons. Particularly, this trend of increasing BD was statistically very significant, at least for $p < 0.01$ (Fig. 7.3). For all groups of neuronal images, the higher value of BDs was obtained using final resolution, what suggested that maximal resolution would maximize the resemblance between the digital and original drawings. It seems likely that such images retain most of the neuronal details, enabling reduction of experimental errors in the fractal measurements [20].

Then again, the values of the slope (parameter a) suggest low increase of BD with resolution, and someone could state that *the resolution does not influence on BD value of the image*. This conclusion is very challenging, as it needs more data (higher resolution and/or other images) but another (maybe opposite) conclusion can be shown: for our sample of images, in order to calculate precise BD, more important is that all images are at the same resolution than the level of resolution per se.

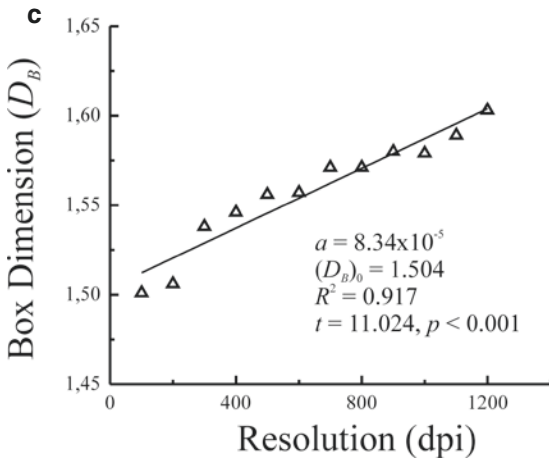
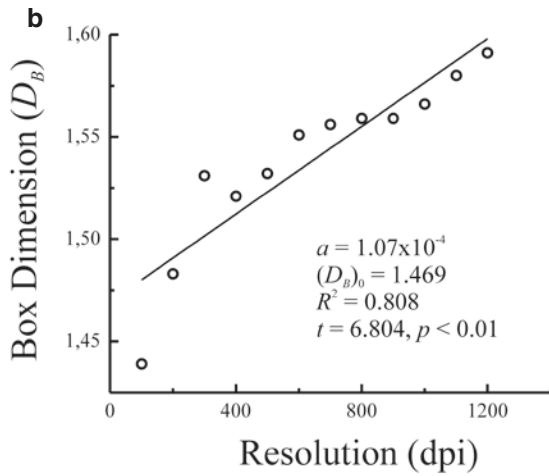
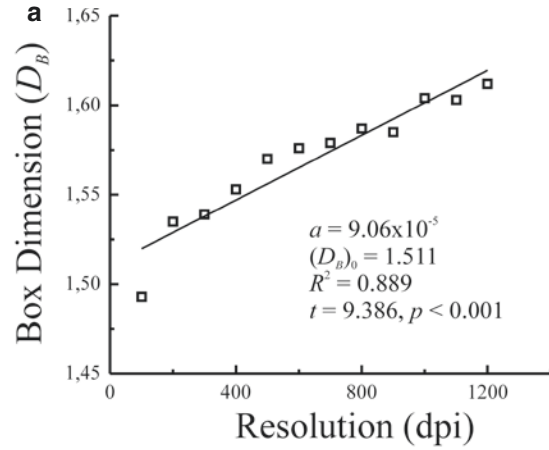
Table 7.2. Results of the Spearman rank correlation analysis of three groups of neurons of the monkey dentate nucleus at three different resolutions (300, 600, and 900 dpi)

Cell type	Group A	Group B	Group C	Group A	Group B	Group C	Group A	Group B	Group C
Parameters									
a	$8.08 \cdot 10^{-5}$	$8.20 \cdot 10^{-5}$	$2.98 \cdot 10^{-5}$	$3.39 \cdot 10^{-5}$	$2.18 \cdot 10^{-5}$	$1.91 \cdot 10^{-5}$	$1.91 \cdot 10^{-5}$	$1.46 \cdot 10^{-5}$	$1.19 \cdot 10^{-5}$
$(D_B)_0$	1.404	1.400	1.433	1.460	1.472	1.470	1.494	1.498	1.502
R^2	0.700	0.696	0.334	0.852	0.444	0.274	0.912	0.600	0.299
t	3.416	3.706	1.584	5.365	2.189	1.374	7.198	3.000	1.460
Resolution	300			600			900		

$N = 5$, $p_{0.05} = 3.182$

BDs in each group were fitted with straight line ($D_B = (D_{B,0}) + a \cdot x$, where x is the size of the cell). R^2 is the coefficient of determination and t is calculated t -value

Fig. 7.3 Plots of mean BDs against the resolution for central (a), type 1 (b), and type 2 (c) asymmetrical neurons from the dentate nucleus. The mean BDs in each group was fitted with straight line ($D_B = (D_B)_0 + a \cdot r$, where r is the resolution). R^2 is the coefficient of determination, t is calculated t -value, and p is level of significance



7.5.2 Image Rotation

It is well known that a picture exhibits *rotational symmetry* if rotation by a specific angle around some central axis point can return the picture to its original configuration [29]. For instance, squares and hexagonal snowflakes are common examples of “ideal symmetry,” and it is reasonable to imagine that the BDs of such picture in these positions have the same value. The neurons which are homogeneously filling a spherical volume are termed *stellate* [8]: as their dendrites radiate in all directions from the cell bodies [29]. In contrast, neurons lacking strong radial symmetry can be termed *non-stellate* (such as, for instance, pyramidal, Purkinje, those with fusiform bodies, etc.). Thus, this section explores how the BD changes in the course of continuous rotation of non-stellate neurons between such extreme positions and offers a possible explanation for these findings.

In digital imaging a pixel is a physical point in a raster image, being the smallest controllable element of a picture on the screen. In computational methods, an image composed of many pixels is known as a *bitmapped* image [29]. A *binary* (or the “black-and-white”) image is a digital image that has only two possible values for each pixel. A special kind of binary pictures is a “binary-skeletonized” picture. This picture consists of one-pixel-wide lines. In a skeletonized line, on a screen, two adjacent pixels can be in touch either by their sides or by their vertices [30]. In the first case, the pixels can form horizontal or vertical lines, while in the second case, they form an oblique straight line with the angle between the horizontal and oblique line being 45° . Thus, it is acceptable that the BD of an asymmetrical oblique object is smaller than that of a horizontal or vertical object. For more details on this subject, the reader is referred to [29].

To demonstrate this effect on the BD, a sample of 17 images was continuously rotated from 0 to 360° , increasing the angle by 15° . The axis of rotation was created connecting two distant points of dendritic field area around the neuron [18]: briefly, after the convex polygon was formed by connecting the tips of the longest dendrites (Fig. 7.4a). The BD either increases or decreases (Fig. 7.4b) from 0 to 45° and after that angle BD decreases (i.e., increases) to 90° . The same procedure was repeated in the following intervals, 90 – 180° , 180 – 270° , and 270 – 360° , with the small deviations, possibly as a consequence of the secondary branches which emanate from the longest primary dendrite [29]. The maximal (or minimal) BD was noticed in 45° , 135° , 225° , and 315° (Fig. 7.4b), and final BD was calculated as the mean of these four values (Fig. 7.4).

To conclude, in order to apply this effect on the calculation, each image should be analyzed for symmetry: the axis should be constructed and the image should be rotated by four angles ($45^\circ + k\pi/2$, where $k=0, 1, 2$, and 3) and apparent BD should be recorded. Accurate BD will be the mean of these values. Our sample of neurons has showed difference in BDs without and after rotation: the BD of initial image was either higher or lower than the same value after the image was rotated. The BDs of type B (Fig. 7.4c, right) and type C (Fig. 7.4c, left) neuronal images (a type of asymmetrical cells) were different than the initial value, from -6 to 6% .

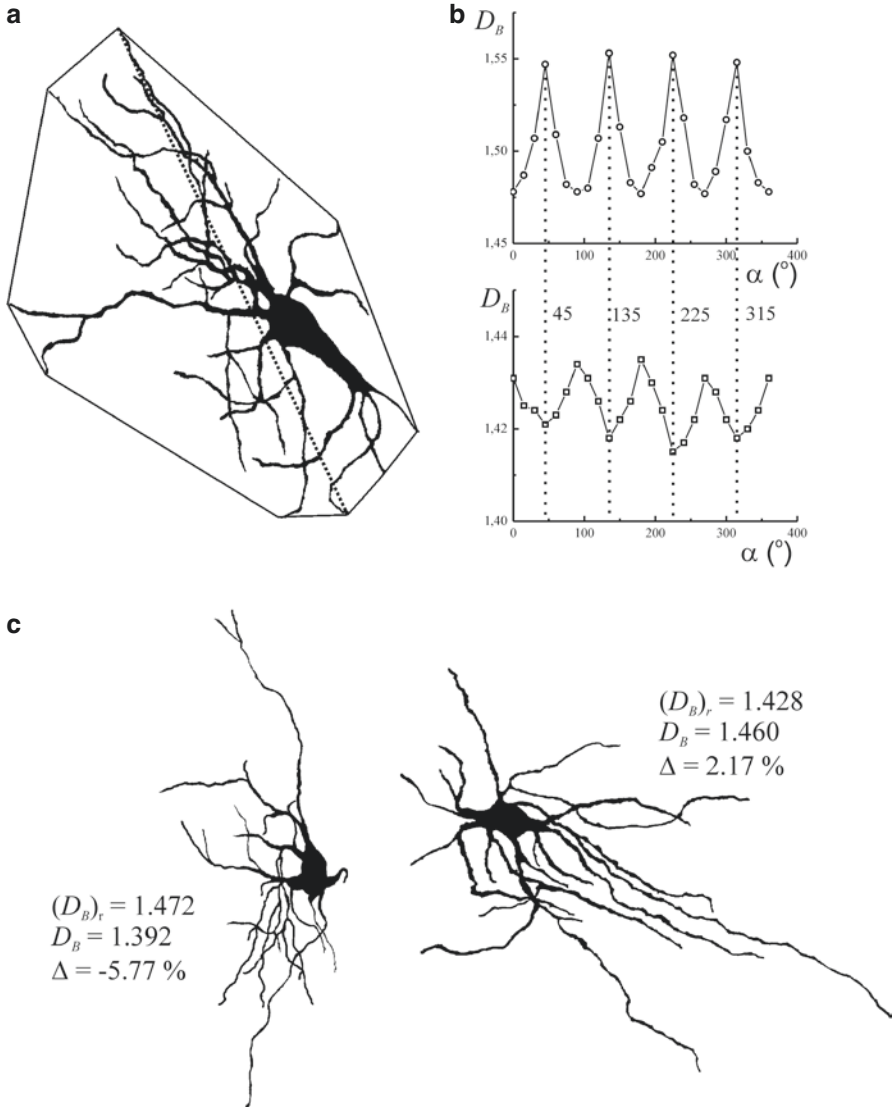


Fig. 7.4 (a) The illustration of the dendritic field area and axis of rotation on the image of asymmetrical neuron. (b) Plots of the BD against the angle when 17 images of the monkey dentate nucleus were continuously rotated from 0 to 360° and (c) two types of asymmetrical neurons from the monkey dentate nucleus. Initial value of the BD, $(D_B)_0$, the same value after rotation, (D_B) , and their difference (Δ) are shown for each type of cells

7.5.3 Image Representation

When the box-counting method is applied to 2D image of the object, the FD depends on image presentation [7]. For instance, it has been reported previously that the box-counting method, applied to “binary-skeletonized” images of neurons, represents a robust technique for quantifying both the complexity of the neuronal dendritic tree and straightness of individual dendrites [17]. However, many researches use different processed images [24, 33], including *binary silhouettes* [10] or “binary-outline” images [21]. In addition, Jelinek and Fernández investigated the effect of image presentation, and they concluded that “black-and-white” images [21] have showed higher values than outlined and skeletonized images [11]. Thus, when calculating FD using complete “black-and-white” images, there may be a space-filling effect that can lead to a higher value of the FD (or $D=2$), depending on the relationship between the internal area and the contour [35].

Also this could be true for the box-counting method, as Fig. 7.5 provides an explanation how this method can estimate object’s projection in plane. Theoretically speaking, when filled square encompasses the image of the object and its size (r) is reduced by two (Fig. 7.5a), the number of boxes increases, concretely multiplying previous number by 4. Therefore, the slope of log–log relationship between N and r was equal to 2 with coefficient of determination (R^2) equal to one (Fig. 7.5b). Thus, the slope of the relationship $\log(N)$ vs. $\log(r)$ could represent BD of the area [19], if the object is in 2D. It might be accurate to say that BD, in this case, estimates the *space-filling* property of object. Figure 7.5b, also, presents the value of BD and R^2 for irregular object, as shown in Fig. 7.5a, obtained in *Image J*.

Consequently, the command (*Process*→*Binary*→*Outline*) in *Image J* creates the border of “black-and-white” image, as shown in Fig. 5.3a, and another command (*Process*→*Binary*→*Skeletonize*) creates one-pixel-wide boundary. Such procedure creates “binary-outline” image of the object and calculated BD (i.e., the $(D_B)_{out}$) evaluates the irregularity in the shape of the image, or precisely the value of $(D_B)_{out}$ shows how this value deviates from values of classic geometric figures (Fig. 7.5c).

In previous study [17], the difference between “black-and-white” and “binary-outline” images from Artiodactyla and mammalian spinal cords has been investigated. Neuronal images from Artiodactyla spinal cord are examples of neurons with thin dendrites, sparsely covered with spines and small cell bodies. Hence, these images (and such type of cells) should be analyzed either as “black-and-white” or “binary-outline” images in order to calculate statistically the same box dimension [17]. On the other hand, neuronal images from rat’s and cat’s spinal cords represent neurons with thick dendrites and/or large cell bodies. For these images, results undoubtedly show that they should be investigated as “black-and-white” or “binary-outline” images in order to quantify their space filling or the shape [17].

Another study sums up investigation of 76 images from the adult human dentate nucleus using the box-counting method [16], which was used to quantify the space-filling property, shape, and dendritic irregularity of the neurons. Each of these properties are described with the corresponding quantity: BD of the “black-and-white”

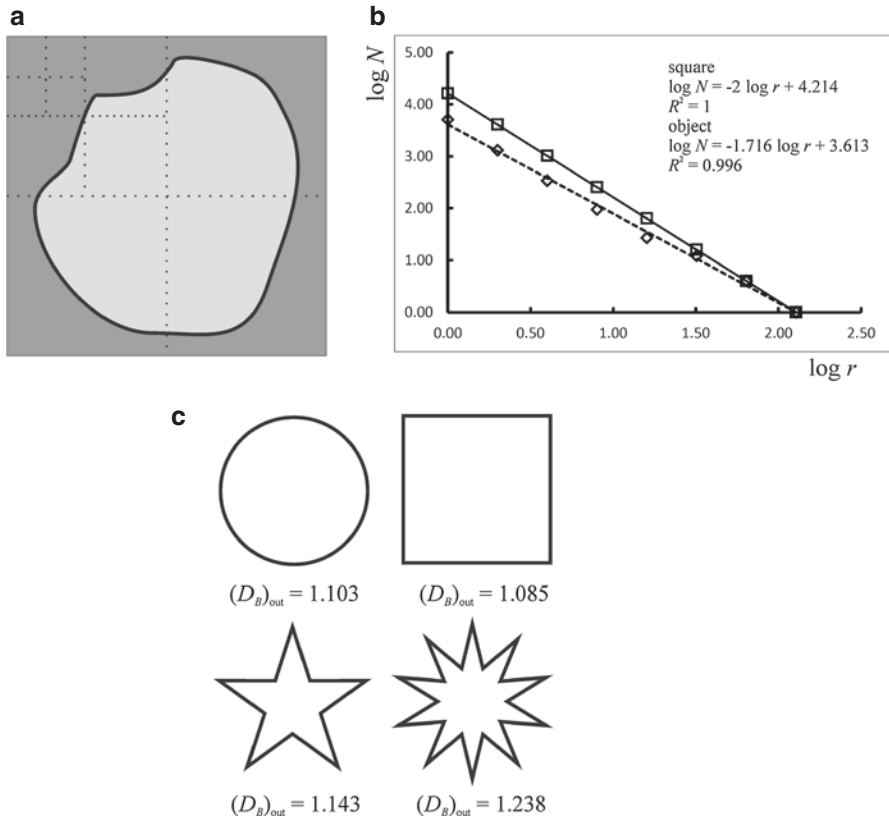


Fig. 7.5 (a) The image of the object (light gray color) encompassed by square (dark gray color) with demonstration the halving of the box sizes that overlay the image and square. (b) Log–log plot between numbers of squares (N) and square size (r) for the square (square points and straight line) and previous object (diamond points and dashed line). The D_B is the absolute value of the slope of the regression line and R^2 is the corresponding coefficient of determination. (c) Outline images of the circle, square, simple, and complex star (For qualitative presentation, the width of border was three pixels and value for the $(D_B)_{out}$ is inscribed below the image)

image $(D_B)_{bin}$, BD of the “binary-outline” image $(D_B)_{out}$, and BD of the “binary-skeleton” image $(D_B)_{skel}$. The $(D_B)_{bin}$ was subjected to the size of the dendritic field (A_{DF}) in order to resolve doubt that these parameters quantify the same property of neuronal morphology (Fig. 7.6). Consequently, the $(D_B)_{out}$ was subjected to the circularity ratio (M) to make evident how these parameters quantify the same property of the neuron but using different methods (Fig. 7.6b). The results are consistent with previous data and improve them, having in mind the size of the sample (i.e., number of neurons) and the fact that box-counting parameters are more sensitive than the size of dendritic field and circularity ratio. Finally, authors claim that this study is the first that quantified the shape of the neuron using box-counting method of fractal analysis [16].

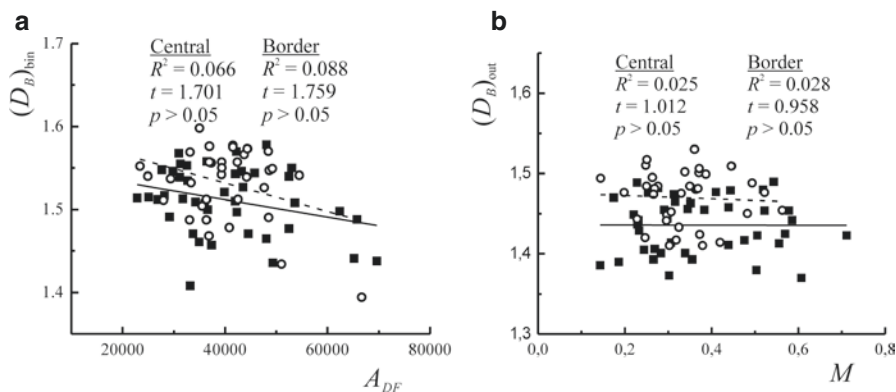


Fig. 7.6 (a) Plots of binary box dimension $(D_B)_{\text{bin}}$ versus dendritic field area A_{DF} for central (filled squares, straight line) and border (empty circles, dashed line) neurons. (b) Plots of outline box dimension $(D_B)_{\text{out}}$ versus circularity ratio M for central (filled squares, straight line) and border (empty circles, dashed line) neurons. The coefficient of determination (R^2), calculated t -value, and level of significance (p) are inscribed in upper side of the plot

7.6 Discussion

The extension of the concepts of fractal geometry toward the biomedical sciences has led to significant progress in understanding complex functional properties and structural features [2]. Generally, various systems in nature, if they accomplish four properties (Sects. 2.1 and 2.3) during their construction or formation, can be thought either ideal or natural fractal objects [17]. On the other hand, fractal analysis is the estimation of fractal characteristics of data [7, 32]. It consists of several methods to assign a fractal dimension and other fractal characteristics to a dataset. According to the numerous authors, fractal analysis is derived from the fractal geometry [7], and it is used to describe the organization of objects found in nature, quantifying their complexity with a value of the fractal dimension [17].

In terms of fractal geometry, the simplest scaling relationship describing a property of an object is an inverse power law scaling [17]. Generally, for real objects this law of scaling can be regarded as the *polynomial scaling law* [16], as it is characteristic of geometrical and real objects in fractal analysis. In addition, in fractal analysis, the measurement of the FD is usually not intended to indicate whether an object is a fractal or not but rather provides a measure of the complexity of scaling inherent in the object [7].

Once fractal geometry was formulated, many neuroscientists adopted fractal analysis as an appropriate method for objective quantitative analysis of neuronal structures. One of the advantages of using fractal analysis (i.e., fractal dimension) is its capacity to differentiate between neurons that differ in the complexity of their dendritic and axonal branching patterns [32]. This text calls attention to the methodology issues of the most popular technique of fractal analysis, the box-counting method. Besides preprocessing tasks, such as image size, resolution, and rotation, this text shows significance of the BD calculated for different presentations of the

same neuronal image from the adult human dentate nuclei: precisely the space-filling property, perimeter of the neuron shape, and irregularity of dendrites.

In conclusion, to calculate the FD of an object, it is not necessary to investigate its main fractal properties (such as, the self-similarity, scaling, scale invariance, and space filling). Investigation of these properties is the main subject of the fractal geometry. The chief aim of the fractal analysis is to calculate the FD of an object and to ascertain the significance of the obtained value in terms of the complexity of the object.

Acknowledgment This work was supported by the Ministry of Education and Science Republic of Serbia, contract no. III 41031. Assistance with all question/problems/ideas and solutions concerning fractal theory, fractal geometry, fractal analysis, and box-counting method by Professor Dušan Ristanović (Department of Biophysics, Medical School, University of Belgrade) and Herbert Jelinek (Charles Sturt University, Albury, Australia) is gratefully acknowledged.

References

1. Barnsley MF. *Fractals everywhere*. Boston: Academic; 1988.
2. Bassingthwaite JB, Liebovitch LS, West BJ. *Fractal physiology*. New York: Oxford University Press; 1994.
3. Bizzarri M, Giuliani A, Cucina A, Anselmi FD, Soto MA, Sonnenschein C. Fractal analysis in a system biology approach to cancer. *Semin Cancer Biol*. 2011;21(3):175–2.
4. Caserta F, Eldred WD, Fernández E, Hausman RE, Stanford LR, Buldyrev SV, et al. Determination of fractal dimension of physiologically characterized neurons in two and three dimensions. *J Neurosci Methods*. 1995;56:133–44.
5. Chan-Palay V. *Cerebellar dentate nucleus: organization, cytology and transmitters*. Berlin: Springer; 1977. p. 548.
6. Falconer K. *Fractal geometry: mathematical foundation and applications*. 2nd ed. England: Wiley; 2003.
7. Fernández E, Jelinek HF. Use of fractal theory in neuroscience: methods, advantages, and potential problems. *Methods*. 2001;24:309–21.
8. Fiala JC, Harris KM. Dendrite structure. In: Stuar G, Spruston N, Häustorn M, editors. *Dendrites*. Oxford: Oxford Univ Press; 2002. p. 1–34.
9. Hoop B, Kazemi H, Liebovitch L. Rescaled range analysis of resting respiration. *Chaos*. 1993;3:27–9.
10. Jelinek HF, Elston GN, Zietsch B. Fractal analysis: pitfalls and revelations in neuroscience. In: Losa GA, Merlini D, Nonnenmacher TF, Weibel ER, editors. *Fractals in biology and medicine IV*. Basel: Birkhäuser; 2005. p. 85–94.
11. Jelinek HF, Fernández E. Neurons and fractals: how reliable and useful are calculations of fractal dimension? *J Neurosci Methods*. 1998;81:9–18.
12. Karperien A. FracLac for ImageJ, version 2.5. <http://rsb.info.nih.gov/ij/fractalac/FLHelp/Introduction.htm>. 1999–2007.
13. Losa GA. The fractal geometry of life. *Riv Biol*. 2009;102(1):29–59.
14. Mandelbrot BB. *The fractal geometry of nature*. 20th ed. New York: NW Freeman and Co; 2004.
15. Mandelbrot BB. *The fractal geometry of nature*. New York: WH Freeman and Co.; 1983.
16. Marić DL, Milošević NT, Jelinek HF, Rajković K. Neurons of the human dentate nucleus: box-count method in the quantitative analysis of cell morphology. In: Dumitrache I, Magda Florea A, Pop F, editors. *Proceedings of 19th International Conference on Control Systems and Computer Science, Vol. 2: interdisciplinary approaches in fractal analysis IAFA 2013*. Los Alamitos: The Institute of Electrical and Electronics Engineers; 2013. p. 319–24.

17. Milošević NT, Rajković N, Jelinek HF, Ristanović D. Richardson's method of segment counting versus box-counting. In: Dumitrache I, Magda Florea A, Pop F, editors. Proceedings of 19th International Conference on Control Systems and Computer Science, Interdisciplinary approaches in fractal analysis IAFA 2013, vol. 2. Los Alamitos: The Institute of Electrical and Electronics Engineers; 2013. p. 299–305.
18. Milošević NT, Ristanović D, Marić D, Rajković K. Morphology and cell classification of large neurons in the adult human dentate nucleus: a quantitative study. *Neurosci Lett.* 2010;468:59–63.
19. Milošević NT, Ristanović D, Rajković K. Mathematical model of box-counting analysis in the human dentate nucleus during development. In: Banaszak G, Waliszewski P, editors. *Fractals and complexity.* Poland: Cracow; 2012. p. 46–0.
20. Milošević NT, Ristanović D. Fractality of dendritic arborization of spinal cord neurons. *Neurosci Lett.* 2006;396:172–6.
21. Milošević NT. Fractal analysis of two dimensional images: parameters of the space-filling and shape. In: Dumitrache I, Magda Florea A, Pop F, Dumitrascu A, editors. Proceedings of 20th International Conference on Control Systems and Computer Science, IAFA: fractal analysis of medical images, vol. 2. Los Alamitos: The Institute of Electrical and Electronics Engineers; 2015. p. 539–44.
22. Neale EA, Bowers LM, Smith TG. Early dendrite development in spinal cord cell cultures: a quantitative study. *J Neurosci Res.* 1993;34:54–66.
23. Panico J, Sterling P. Retinal neurons and vessels are not fractal but space-filling. *J Comp Neurol.* 1995;36:479–90.
24. Porter R, Ghosh S, Lange GD, Smith TG. A fractal analysis of pyramidal neurons in mammalian motor cortex. *Neurosci Lett.* 1991;130:112–6.
25. Rajković N, Stojadinović B, Radulović M, Milošević NT. Histological images of malignant breast tumor: mono and multifractal analysis. In: Dumitrache I, Magda Florea A, Pop F, Dumitrascu A, editors. Proceedings of 20th International Conference on Control Systems and Computer Science, IAFA: fractal analysis of medical images, vol. 2. Los Alamitos: The Institute of Electrical and Electronics Engineers; 2015. p. 531–8.
26. Ristanović D, Milošević NT, Stefanović IB, Marić D, Popov I. Cell image area as a tool for neuronal classification. *J Neurosci Methods.* 2009;182:272–8.
27. Ristanović D, Milošević NT. Fractal analysis: methodologies for biomedical researches. *Theor Biol Forum.* 2012;105(2):99–118.
28. Ristanović D, Nedeljkov V, Stefanović DB, Milošević NT, Grgurević M, Štulić V. Fractal and nonfractal analysis of cell images: comparison and application to neuronal dendritic arborization. *Biol Cybern.* 2002;87:278–88.
29. Ristanović D, Stefanović B, Puškaš N. Fractal analysis of dendrite morphology of rotated neuronal pictures: the modified box counting method. *Theor Biol Forum.* 2014;107(1–2):109–21.
30. Ristanović D, Stefanović B, Puškaš N. Fractal analysis of dendrites morphology using modified Richardson's and box counting method. *Theor Biol Forum.* 2013;106(1–2):157–68.
31. Ristanović D, Stefanović BD, Milošević NT, Grgurević M, Stanković JB. Mathematical modeling and computational analysis of neuronal cell images: application to dendritic arborization of golgi-impregnated neurons in dorsal horns of the rat spinal cord. *Neurocomputing.* 2006;69:403–23.
32. Smith TG, Lange DG, Marks WB. Fractal methods and results in cellular morphology – dimensions, lacunarity and multifractals. *J Neurosci Meth.* 1996;69:123–36.
33. Smith TG, Lange GD. Fractal studies of neuronal and glial cellular morphology. In: Iannaccone PM, Khokha M, editors. *Fractal geometry in biological systems: an analytical approach.* New York: CRC Press; 1995. p. 173–86.
34. Taylor HE, Wade TL. *University calculus.* New York: Wiley; 1962. p. 765.
35. Vicsek T. *Book fractal growth phenomena.* Singapore: World Scientific; 1992.
36. West BJ, Deering W. Fractal physiology for physicists: Levi statistics. *Phys Rep.* 1994;246:1–100.

Chapter 8

Neuronal Fractal Dynamics

Małgorzata Kołodziej and Przemysław Waliszewski

Abstract Synapse formation is a unique biological phenomenon. The molecular biological perspective of this phenomenon is different from the fractal geometrical one. However, those perspectives are not mutually exclusive and supplement each other. A cornerstone of the first one is a chain of biochemical reactions with the Markov property, that is, a deterministic, conditional, memoryless process ordered in time and in space, in which the consecutive stages are determined by expression of some regulatory proteins. The coordination of molecular and cellular events leading to the synapse formation occurs in fractal time-space, that is, the time-space that is not only the arena of events but also influences those events actively. That time-space emerges owing to coupling of time and space through nonlinear dynamics. The process of synapse formation possesses fractal dynamics with non-Gaussian distribution of probability and a reduced number of molecular Markov chains ready for transfer of biologically relevant information.

Keywords Neurons • Synapse • Differentiation • Dynamics • Gompertz growth • Fractal • Fractal time-space • Complexity

8.1 Synapse Formation from the Perspective of Molecular and Cellular Biology

The word synapse originates from the Greek words “συν” (together) and “ἄπτειν” (to fasten). Indeed, a synapse enables a transfer of electrical or chemical impulses between neurons within the nervous system or from neurons to target cells, such as

M. Kołodziej
Department of Neurosurgery, Justus-Liebig University,
Rudolf-Buchheim-Strasse 3, 35392 Giessen, Germany

P. Waliszewski (✉)
Department of Urology, Urological Unit, Hufeland Clinics GmbH, Rudolph-Weiss Strasse 1-5,
99947 Bad Langensalza, Germany

The Będlewo Institute for Complexity Research, Poznań, Poland
e-mail: complexityresearch@yahoo.com

muscle cells. The synapse is a complex molecular structure composed of an axon and the dendrites of an adjacent neuron. It possesses both a presynaptic and a postsynaptic membrane. There is a synaptic cleft between them. In the fast electrical synapses, the presynaptic and postsynaptic membranes are connected by special molecular channels called gap junctions. Those channels enable a direct flow of electric current from the presynaptic membrane to the postsynaptic one. The slower chemical synapses use a number of neurotransmitters to regulate the function of the postsynaptic neurons. Those relatively simple chemical compounds are released from the axon membrane and bind to the specialized receptors in the postsynaptic membrane. In consequence, the postsynaptic neuron may change immediately its potential and initiate an electrical response. It may also activate some secondary molecular signaling pathways that inhibit or excite the postsynaptic neuron.

A neuromuscular junction is an example of a specialized synapse that not only transfers electrochemical impulses but also activates some molecular events leading to the muscle contraction. The neuromuscular junction consists of a motor neuron, a myofiber, and a Schwann cell. In this kind of a synapse, the impulse depolarizes the motor neuron by releasing the neurotransmitter, acetylcholine. Acetylcholine voyages crossways through the synaptic cleft and docks to its receptors in the sarcolemma. The muscle contraction begins after opening of the receptor ion channels. The entire synapse is covered by a myelin sheath provided by the Schwann cell that protects the junction [12].

The formation of synapses is a complex process that starts during embryogenesis and continues in a lifetime. Cell types involved in the synapse formation originate from different regions of the growing embryo. The myoblasts originating from the mesoderm form a multinucleated myotube. During the myotube formation, motoneurons from the neural tube initiate preliminary contacts with the myotube. The Schwann cells that originate from the neural apex are directed by the axons to their targets. After the contact between Schwann cell and axon is established, both cells create a loose, unmyelinated covering over the axons [15].

In the central nervous system, astrocytes are nonneural cells that regulate a number of activities in the brain, such as synaptic transmission, neurometabolism, plasticity of synapses, and cerebrovascular tone [15]. In particular, astrocytes secrete two protein factors that regulate the process of synapse formation [5]. The first one is known as thrombospondin (TSP). This factor determines the formation of morphologically normal but functionally silent synapses. The second factor, which has not been isolated yet, converts those silent synapses into the fully functional ones [5]. In addition, the functional maturation of synapses is regulated directly by glia as “support cells.” TSP is also expressed in glia as extracellular matrix protein that binds heparin. It was also demonstrated that TSP affects the relocation of synaptic proteins to new synapses rather than induces their expression over there [5].

The specific patterning of synapse development at the neuromuscular junction shows that the majority of muscles are innervated at their centers. Although it may seem that the axons specifically target the midpoint of the myotube, a number of observations suggest that this is not a valid supposition. After the initial axonal contact, the newly formed myotube gates grow symmetrically from the point of

innervation. In combination with the fact that receptor mass is the result of axonal contact in its place of origin, the structural patterns of muscle fibers can be classified as both myotatic development and axonal innervation [15].

The first contact between motoneuron and myotube generates synaptic transmission but the signal is very weak. One week later, the fully functional synapse is formed. This synapse plays a role in the development of new axons [7]. To form a presynaptic terminal, molecular signaling must go through a number of subcellular sections. In the soma, presynaptic proteins need to be synthesized, packaged together, and attached to microtubule motors for delivery through the axon. Within the axon, transport of presynaptic packages is controlled to confirm that developing synapses achieve a sufficient volume of factors. At individual axonal sites, extracellular interactions must be translated into intracellular signals that can incorporate mobile transport vesicles into the nascent presynaptic terminal. Even once the initial recruitment process is complete, the components and subsequent functionality of the presynaptic terminals are constantly altered. For example, the axon of motoneuron releases arginine that binds to a muscle-specific kinase receptor in the postsynaptic membrane. This binding induces the downstream activation of the cytoplasmic protein rapsyn. Rapsyn contains a domain that is responsible for clustering of acetylcholine receptors in the postsynaptic membrane [12]. The coordination of all those processes in time and in space is the most mysterious part of the process of synapse formation [3].

The competition between axons is an activity-dependent process. It is based on the synaptic pruning or synapse elimination. It has been suggested that a strong synapse, which produces enough action potential or exhibits strong activity to depolarize the postsynaptic membrane, wards off the weaker axons [12]. The most important consequence of synaptogenesis is the ability of the motoneuron to discriminate between fast- and slow-twitch muscle fibers; fast-twitch muscle fibers are innervated by “fast” motoneurons, and slow-twitch muscle fibers are innervated by “slow” motoneurons. Here is to suppose that nonselective pathways indicate that the axons are led to their targets by the matrix through which they travel. Finally, the axons may innervate muscle fibers nonspecifically and cause that the muscles gain the characteristics of the axon that innervates them. In this path, a “fast” motoneuron can convert any muscle fiber into a fast-twitch muscle fiber [12]. Those changes in receptor subunits lead to the growth of the postsynaptic cluster size and cluster development [1].

The main transmitter in the peripheral synapses is acetylcholine. A counterpart of it in the central nervous system is glutamate and its receptors, especially the NMDA (N-methyl-D-aspartate) receptor. The activation of NMDA receptor induces synaptogenesis over the activation of downstream products. The most important messenger in the brain and the spinal cord is glycine, which docks on glycine receptors. Glycine receptors play an important role in the excitability of the spinal cord and brain stem neurons [1]. Because of embryo development, some of receptor attributes undergo important modifications resulting in main variation of their physiological function like switching of receptor structures. The previous data have shown that the development is associated with the changes of the monomeric alpha or heteromeric alpha 2 beta receptors in immature neurons to the alpha 1 beta receptors in mature neurons.

Together with those changes, the apparent receptor correspondence to glycine and strychnine, as well as that of Zn(2+) and ethanol, increases during the development process. The established receptor shows a slow desensitizing current and high sensitivity to modulation by protein kinase C. The high level of glycinergic transmission in juvenile spinal neurons modulates neuronal excitability initiating membrane depolarization and alterations in intracellular calcium, which leads to chronic inhibition of glycinergic transmission, initiate neurite outgrowth, and changes in the level of synaptic transmission induced by GABA(A) and AMPA receptors. The plasticity of juvenile glycerine receptors is associated with cytoskeleton dynamics [1].

The environment, in which the neurons are located, plays an important role during the synaptogenesis. Brain-derived neurotrophic factor (BDNF), which is produced by the brain, regulates the process of synapse development, including synthesis of a transmitter, concentration of the transmitter in vesicles, and cholesterol biosynthesis, which is important for the synaptogenesis. Indeed, the BDNF-null mutants show a defect in neuronal growth and formation of synapse [13]. The second important molecule is neuroligin, which plays a role in cell adhesion in the postsynaptic membrane. A defect in genes encoding neuroligin leads to mental retardation and autism [20]. However, many of the signaling processes regulating synaptogenesis in the central nervous system can also be regulated by matrix metalloproteinases (MMPs) [4]. An important component for the controlled actin assembly, Abelson interacting protein-1 (Abi-1), was identified as a binding partner for the postsynaptic density (PSD) protein ProSAP2/Shank3. The dynamic and locally specific regulation of actin in cytoskeleton is critical for the emergence of synaptic plasticity [11]. It was demonstrated that the downregulation of Abi-1 by small interfering RNA leads to the excessive dendrite branching and a reduction in a number of synapses. The overexpression of Abi-1 has the opposite consequence. Abi-1 can play a role as a specific synapto-nuclear messenger and is involved in dendrite and synapse formation [11]. Furthermore, filopodia (dendritic spines morphology) play a role in synaptogenesis by initiating of contact between axons of other neurons. It was reported that new neurons were contacted by axosomatic, axodendritic, and axospinous synapses. Dendritic spines primarily synapsed on multiple-synapse boutons already present in the synapse. The connectivity of new neurons continued to change until at least 2 months, long after the formation of the first dendritic protrusions [14]. The brain stimulation following birth or after weaning or during adulthood leads to formation of numerous synapses [2]. It was also demonstrated that subcellular anatomical characteristics of astrocytes in the brain enabled them both identification and a response to changes in neuronal and synaptic activity [9].

8.2 Fractal Time-Space in the Dynamic Process of Synapse Formation

The explanation how all the above-outlined molecular and cellular phenomena spanning different levels of the complex, hierarchical, dynamic cellular system are coordinated in time and in space is one of the greatest challenges of modern biological

sciences. The process of synapse formation is here an interesting experimental model that may also stimulate theoretical research [5]. Molecular biological models depict synapse formation as a kind of a Markov process, that is, a deterministic, conditional, memoryless process ordered in time and in space, in which the consecutive stages occur owing to a transition rule that depends only on the current state. Although those models are static, they suggest some important molecular events occur in neurons in a collective manner, that is, a manner marked by similarity among or with the neurons of a given anatomical region.

The application of fractal calculus and principles of fractal geometry brings utterly different perspective. Cells represent supramolecular dynamic systems that grow and interact in both space and time [17–19]. Neuroanatomists found that morphological irregularities in both neuron and neural network structure resulting from those interactions can be measured by the spatial fractal dimension [10]. The existence of the spatial fractal dimension indicates the existence of some underlying emergent molecular and electrochemical processes in neural tissue. In addition, experimental data obtained from the study of cellular system P19/RAC 65 show that dynamics of synapse formation *in vitro* can be described by a family of the sigmoidal curves, such as the Gompertz one that is one of the solutions of Eq. (8.2) (see Appendix) [19]. This equation suggests that the process of synapse formation is a cooperative phenomenon, that is, the events occur not only in conjunction with others but also facilitate the further evolution of the process. In this equation, dynamics of synapse formation, the function of probability distribution, and the anharmonic potential are coupled to each other. In the background, there is coupling of two fundamental dimensions that define time and space in which all events occur (see Appendix, Eqs. 8.1 and 8.6). It is worth to notice that the emerging time-space is not just an arena for events and processes. This time-space influences them actively. This fact is reflected by the presence of both temporal and spatial fractal dimensions in Eq. (8.6) (see Appendix).

Indeed, synapse formation requires long-range interactions and diffusion of some important gene products between neural cells. The interacting cells create first a dynamic system with its own attractor, i.e., a fragment of time and space where the dynamic processes occur and where no further evolution of the system is possible at all owing to the action of the intrasystemic forces (drift) unless some extrasystemic forces (diffusion) act upon it. The extrasystemic impulses and their interaction with a network of neurons assume further control of the process. In addition, cells differentiate into neurons and create synapses with a conjugated probability and non-Gaussian distribution rather than with the classical probability and the Gaussian distribution (see Appendix, Eqs. 8.11, 8.12, 8.13, 8.14, and 8.15) [16]. In consequence of the Markovian nature of the molecular circuits, entropy of such chain of the coupled molecular reactions is always lower than entropy of the set of random and independent biochemical reactions (see Appendix, Eqs. 8.7, 8.8, 8.9, and 8.10). Also, a number of the molecular circuits that can transfer actively biologically relevant information in a given time are much lower than the total number of such circuits (Appendix, Eq. 8.16).

Benoit Mandelbrot was one of the first researchers who noticed that the random walk model can describe a wide range of neuronal activity in terms of two

parameters [6]. Furthermore, the analysis of the inter-spike intervals of the firing cortex neurons reveals different non-Gaussian probability distributions, such as exponential, gamma, lognormal, and power-law one. The coexistence of so different probability distributions unveils different stochastic processes including molecular ones that stand behind those distributions. Fractal scaling in dynamics of those intervals is correlated with the coupling between neuron firing and movement of muscle groups. Those neuron firings reveal long-range temporal correlations. The correlations are missing if the firings are not associated with some movements [8]. Fractal time-space is a prerequisite condition for the phenomenon of dynamic coalition of neurons. This coalition is based on the collective behavior of neurons that participate in generating of some muscular movements by entering the coalition and forming a network of firing neurons or leaving it for some time. In other words, the existence of fractal time-space enables both plasticity and adaptation of the neuronal network to different situations.

Appendix

If one assumes that the spatial variable x and the temporal variable t are coupled to each other in a linear manner into a single, complex spatiotemporal variable θ

$$\theta = \mu x + t, \quad (8.1)$$

then the Gompertz function, the function of probability distribution $P(\theta)$, the anharmonic potential $U(\theta)$, and the diffusion coefficient D are related each other through the one-dimensional differential operator (8.2). This operator contains the function of probability distribution [19]:

$$-\frac{1}{D} \frac{\partial^2 P(\theta)}{\partial \theta^2} + \frac{D}{4} P(\theta) + U(\theta) P(\theta) = 0 \quad (8.2)$$

This linear coupling of variables can also be defined as a function with both spatial and temporal fractal dimension. It is known from experimental data from the in vitro cellular system of P19/RAC 65 that the number of cells (or their volume) also changes in time t according to the Gompertz function $f(t)$ [17]. A volume of the spheroid V is given by equation:

$$V = V_k F(t_0) e^{a(1-e^{-bt})} = V_k f(t_0) a t^{b_i} = V_0 a t^{b_i} \quad (8.3)$$

in which V_k is a mean volume of a single cell, n stands for a number of cells in the spheroid, and the Gompertz function can be fitted with the fractal function $f(t) = at^b$ with very high accuracy, a coefficient of nonlinear regression $R \gg 0.95$ for $n \geq 100$ pairs of coordinates, in which a stands for a scaling coefficient, b_i is a temporal fractal dimension, and t is scalar time.

The volume V of the spheroid can also be expressed as a function of scalar geometrical variable x (i.e., a radius of a family of the concentric spheres covering the entire spheroid) by Eq. (8.4):

$$V = a_1 x^{b_s} \quad (8.4)$$

in which a_1 stands for a scaling coefficient, b_s is a spatial fractal dimension after scalar time t_1 , and x is a scalar, geometrical variable, which locates an effect in space.

Hence, we get Eq. (8.5):

$$V = a_1 x^{b_s} = V_0 a t^{b_t} = a_0 x^{b_{s_0}} a t^{b_t} \quad (8.5)$$

in which a , a_0 , and a_1 stand for the scaling coefficients, b_t is the temporal fractal dimension, b_{s_0} and b_s are the spatial fractal dimensions after time t_0 and t , respectively, and x is a geometrical variable.

Finally, Eq. (8.6) relates space and time in which proliferation, differentiation, and synapse formation occurs. This equation defines the geometrical variable x as a function of the scalar time t and both temporal and spatial fractal dimension:

$$\ln x = \frac{1}{b_s - b_{s_0}} \ln \frac{a_0 a}{a_1} + \frac{b_t}{b_s - b_{s_0}} \ln t \quad (8.6)$$

in which t stands for scalar time, x is geometrical variable, b_s is the spatial fractal dimension, and b_t is the temporal fractal dimension.

8.2.1 Entropy and Dynamics of Synapse Formation in Fractal Time-Space

It is worth to notice that the assumed Markov model of molecular interactions within differentiating neurons implies at least three important consequences. First, entropy (i.e., missing information) H_M of such the Markov chain of the coupled molecular reactions is always lower than entropy of the set of random and independent biochemical reactions H_R . Indeed, entropy is defined as the expected value of missing information H_p :

$$H_p = H(X) = -\sum_{j=1}^N p_j \log p_j \quad (8.7)$$

in which $p = (p_1, p_2, \dots, p_j)$, $j \in N$, is a probability density function over a generic variable X , and if $p_j = 0$, then $H_p = 0$, \log is a natural logarithm, providing a unit of measure.

Hence, the conditional entropy $H(X_k|Y_{k-1})$ of the X_k reaction stands for which conditional information is determined when the state $Y_{k-1} = i$ is given by the following equation:

$$H(X_k | Y_{k-1} = i) = -\sum_j p_{ij} \log p_{ij} \quad (8.8)$$

The conditional entropy of the Markov chain H_C is given by (8.9):

$$H_C = H(X_k | X_{k-1}) = -\sum_i p_i \sum_j p_{ij} \log p_{ij} \quad (8.9)$$

Finally, we get Eq. (8.10) for the n first steps of the Markov chain X_1, X_2, \dots, X_n from (8.7), (8.8), and (8.9), the principle of additivity of independent random events, and from the analog principle for the conditional probabilities:

$$\begin{aligned} H_M &= H(X_1) + \sum_{k=2}^{k=n} H(X_k | X_{k-1}) = -\sum_j p_j \log p_j + (n-1)H_C < nH_p \\ &= -\sum_j p_j \log p_j = H_R \end{aligned} \quad (8.10)$$

Second, Gompertz dynamics of molecular cellular growth can be normalized, i.e., growth dynamics of various tissue systems can be described by a single normalized Gompertz function $f_N(t)$ (8.11). In fact, this normalized Gompertz function is both a dynamics function $f_N(t)$ and a probability function $p_N(t)$ (see for details [17]):

$$f_N(t) = e^{-e^{-bt}} = p_N(t) \quad (8.11)$$

Consider a coupling of probability function $p_N(t)$ and antiprobability function $-\log p_N(t)$, in which $r=b$:

$$\frac{dp_N(t)}{dt} = -r p_N(t) \log p_N(t) \quad (8.12)$$

This equation defines a relationship between entropy $H(t)$ and the normalized Gompertz dynamics of growth $p_N(t)$:

$$p_N(t) = \int \frac{\partial p_N(t)}{\partial t} dt = -r \int p_N(t) \log p_N(t) dt = rH(t) \quad (8.13)$$

Finally, from (8.11) and (8.12), we get (8.14):

$$H(t)_{\text{Gompertz}} = \frac{1}{b} e^{-e^{-bt}} \quad (8.14)$$

According to Shannon theorem, of all the continuous distribution densities for which the standard deviation exists and is fixed, the Gaussian (i.e., normal) distribution has the maximum value of entropy H :

$$H_{\text{Gauss}} = - \int_{-\infty}^{\infty} \frac{e^{-\frac{t^2}{2\sigma^2}}}{\sqrt{2\pi\sigma^2}} \log \frac{e^{-\frac{t^2}{2\sigma^2}}}{\sqrt{2\pi\sigma^2}} dt = \frac{1}{2} \log(2\pi e\sigma^2) \quad (8.15)$$

In the case of growing supramolecular cellular system such as neuron, entropy, or missing information, $H(t)$ is a function of time related with dynamic function of growth in fractal space-time. For $b = 1$ both the normalized Gompertz function (8.11) and the entropy function (8.14) overlap each other. However, $b < 1$ for the majority of cellular systems. The distribution of probability is in those cases non-Gaussian.

Third, there is a relationship between the number of elements in the Markov chain and entropy. If $M_p(n)$ stands for a number of the Markov chains of the length n with the total probability p , $0 < p < 1$, there exists the same limit for each probability p that equals entropy H :

$$\lim_{n \rightarrow \infty} \frac{\log M_p(n)}{n} = H \quad (8.16)$$

If a total number of states of the supramolecular cellular system equal 2^m , then the number of molecular reactions interconnected in the Markov chains of the length n is 2^{nm} . It is clear from (8.16) that only 2^{nH} molecular Markov chains with probability $1 - \varepsilon$, $\varepsilon > 0$ will be involved in transfer of biologically relevant information.

References

1. Aguayo LG, van Zundert B, Tapia JC, Carrasco MA, Alvarez FJ. Changes on the properties of glycine receptors during neuronal development. *Brain Res Rev.* 2004;47(1-3):33-45.
2. Briones TL, Klintsova AY, Greenough WT. Stability of synaptic plasticity in the adult rat visual cortex induced by complex environment exposure. *Brain Res.* 2004;1018(1):130-5.
3. Bury LA, Sabo SL. Building a terminal: mechanisms of presynaptic development in the CNS. *Neuroscientist.* 2016;22(4):372-91.
4. Ethell IM, Ethell DW. Matrix metalloproteinases in brain development and remodeling: synaptic functions and targets. *J Neurosci Res.* 2007;85(13):2813-23.
5. Freeman MR. Glial control of synaptogenesis. *Cell.* 2005;120(3):292-3.
6. Gerstein GL, Mandelbrot B. Random walk models for the spike activity of a single neuron. *Biophys J.* 1964;4:41-68.
7. Guan C, Chien-Ping K. Schwann cell-derived factors modulate synaptic activities at developing neuromuscular synapses. *J Neurosci.* 2007;27(25):6712-22.
8. Hu J, Zheng Y, Gao J. Long-range temporal correlations, multifractality, and the causal relation between neural inputs and movements. *Frontiers Neurol.* 2013;4(158):1-11.
9. Kacerovsky JB, Murai KK. Stargazing: monitoring subcellular dynamics of brain astrocytes. *J Neurosci.* 2015;323:84-95.

10. Karperien A, Jelinek HF, Milosevic NT. Reviewing lacunarity analysis and classification of microglia in neuroscience. In: Waliszewski P, editor. *Fractals and complexity*. Wrocław: Format; 2013. p. 50–5.
11. Proepper C, Johannsen S, Liebau S, Dahl J, Vaida B, Bockmann J, Kreutz MR, Gundelfinger ED, Boeckers TM. Abelson interacting protein 1 (Abi-1) is essential for dendrite morphogenesis and synapse formation. *EMBO J*. 2007;26(5):1397–409.
12. Sanes JR, Lichtman JW. Development of the vertebrate neuromuscular junction. *Annu Rev Neurosci*. 1999;22:389–442.
13. Suzuki S, Kiyosue K, Hazama S, Ogura A, Kashihara M, Hara T, Koshimizu H, Kojima M. Brain-derived neurotrophic factor regulates cholesterol metabolism for synapse development. *J Neurosci*. 2007;27(24):6417–27.
14. Toni N, Teng EM, Bushong EA, Aimone JB, Zhao C, Consiglio A, van Praag H, Martone ME, Ellisman MH, Gage FH. Synapse formation on neurons born in the adult hippocampus. *Nat Neurosci*. 2007;10(6):727–34.
15. Ullian EM, Christopherson KS, Barres BA. Role for glia in synaptogenesis. *Glia*. 2004;47(3):209–16.
16. Waliszewski P, Konarski J. Neuronal differentiation and synapse formation occur in space and time with fractal dimension. *Synapse*. 2002;43(4):252–8.
17. Waliszewski P. A principle of fractal-stochastic dualism and Gompertzian dynamics of growth and self-organization. *Biosystems*. 2005;82(1):61–73.
18. Waliszewski P, Konarski J. On time-space of nonlinear phenomena with Gompertzian dynamics. *Biosystems*. 2005;80:91–7.
19. Waliszewski P. A principle of fractal-stochastic dualism, couplings, complementarity and growth. *Contr Eng Appl Informatics*. 2009;11(4):45–52.
20. Zeng X, Sun M, Liu L, Chen F, Wei L, Xie W. Neurexin-1 is required for synapse formation and larvae associative learning in *Drosophila*. *FEBS Lett*. 2007;581(13):2509–16.

Chapter 9

Does a Self-Similarity Logic Shape the Organization of the Nervous System?

Diego Guidolin, Cinzia Tortorella, Raffaele De Caro, and Luigi F. Agnati

Abstract From the morphological point of view, the nervous system exhibits a fractal, self-similar geometry at various levels of observations, from single cells up to cell networks. From the functional point of view, it is characterized by a hierarchical organization in which self-similar structures (networks) of different miniaturizations are nested within each other. In particular, neuronal networks, interconnected to form neuronal systems, are formed by neurons, which operate thanks to their molecular networks, mainly having proteins as components that via protein–protein interactions can be assembled in multimeric complexes working as micro-devices. On this basis, the term “self-similarity logic” was introduced to describe a nested organization where at the various levels almost the same rules (logic) to perform operations are used. Self-similarity and self-similarity logic appear intimately linked to the biophysical evidence for the nervous system being a pattern-forming system that can switch flexibly from one coherent state to another. Thus, they can represent key concepts to describe its complexity and its concerted, holistic behavior.

Keywords Fractal geometry • Cell networks • Molecular networks • Neuroanatomy • Neurodynamics

D. Guidolin, PhD (✉) • C. Tortorella • R. De Caro
Department of Molecular Medicine, University of Padova,
via Gabelli 65, 35121 Padova, Italy
e-mail: diego.guidolin@unipd.it

L.F. Agnati
Department of Biomedical Sciences, University of Modena and Reggio Emilia,
via Campi 287, 41100 Modena, Italy

9.1 Introduction

According to Jacob [64], from a structural standpoint, living systems are characterized by a hierarchical pattern of organization in which structures are nested within one another. It has been also pointed out that this conceptual proposal by Jacob can be applied not only to the living individual but also, in a complex organism, to its main organs [2, 5]. In fact, as stated by Grizzi and Chiriva-Internati [47], all anatomic systems exhibit the pivotal property to form multilevel structures each of which forms “a whole in relation to its parts and is simultaneously part of a larger whole” [47]. A key morphological consequence of this feature is that irregular and complex shapes in which structural detail increases (at least for a quite wide range of scales) with increasing magnification or resolution [18] characterize biological structures (but, more in general, the majority of natural objects). Thus, the conventional (Euclidean) view that natural structures have a well-defined form, which can be determined at some characteristic scale, appears just an approximation of the reality. The two related problems of defining the concept of “form” of a particular biological structure and that of providing its description in quantitative terms were deeply debated among morphologists since the classic work of Thompson [102] and are still under careful scrutiny. A breakthrough in this field occurred with the development of the “fractal geometry” by Benoit Mandelbrot [79, 80], based on previous mathematical achievements by Poincaré and Cantor. From a mathematical point of view, fractal objects are the result of iterative processes, a complex irregular shape characterizes them, and their measured properties depend on the scale at which they are measured. The most important and characterizing feature of fractal objects, however, is “self-similarity,” a term indicating that they are composed of parts that are smaller, exact duplications of the whole object over infinity of length scales. In other words, geometrical configurations characterizing a fractal object can be found again and again as far as magnification is increased (Fig. 9.1a). For what it concerns biological morphology, this mathematical framework was of key importance for two reasons. From one side it provided a conceptual support to describe the complexity of form exhibited by the biological objects. Of course, natural objects can at best be a quasi-fractal, exhibiting self-similarity only within a limited scale range and only statistically, since small details of a given anatomical system are rarely identical copies of the whole system. Nevertheless, they are often characterized by the same architectural scheme with the same structural complexity (Fig. 9.1b). Examples include the bronchial tree, the ductal system of glands, the biliary tree of the liver, and the vascular system [28, 29, 54, 77]. From the other side, fractal geometry also led to the definition of parameters allowing a quantitative characterization of complex shapes (see [37, 58, 94]). “Fractal dimension” (D), for instance, measures the rate of addition of structural details with increasing magnification, scale, or resolution [32]. Thus, it represents an estimator of morphological complexity: the more irregular an object, the higher its D value [80]. It can be quite easily evaluated by a variety of methods, the “box-counting method” (see [17, 94]) being the most widely used in biological applications. The information provided by D is often

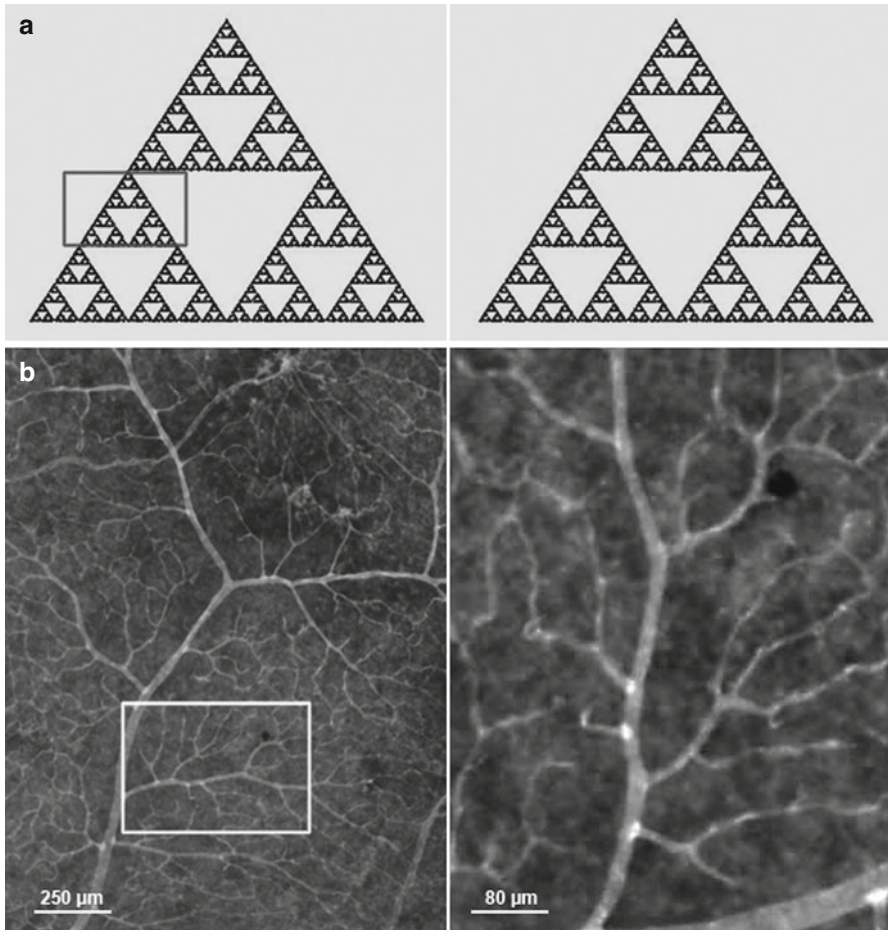


Fig. 9.1 (a) A classical mathematical fractal, the Sierpinski triangle. As illustrated each part is the exact duplication of the whole object over infinity of length scales. (b) A natural structure, the vascular network of the retina, exhibiting self-similarity. It can be considered a quasi-fractal: self-similarity only occurs within a limited scale range and only statistically since structural details are not identical copies of the whole system. Nevertheless, they are characterized by the same architectural scheme

complemented by the measurement of another fractal parameter, called “lacunarity.” In a general sense, this parameter can be considered as a measure of the non-uniformity (heterogeneity) of a structure, potentially useful to characterize how it fills the available space [94]. Roughly speaking, lacunarity exhibits higher values when the analyzed structure has large gaps. Several further methods and parameters based on fractal geometry (such as Hurst coefficient and detrended fluctuation analysis) have been proposed for the analysis of natural objects (see [40, 99]), and in the last decade, the use of fractal geometry-based tools has significantly expanded to

describe the morphology of the biological structures and the changes they undergo under physiological or pathological processes. Examples include, among others, the application of fractal principles to measure irregular and complex membrane ultrastructure of cells at specific functional and pathological stages [76, 78], the changes of the self-organization of endothelial cells *in vitro* induced by anti- or pro-angiogenic factors [50], the characterization of alveolar shape in normal lung and in emphysema [14], processes of vascular remodeling [49, 54], changes in the morphology and spatial distribution of the connective tissue in human carotid body during aging [55], chromatin architecture [74], and the consequences of its changes in terms of chromosome alterations [41].

Not only the morphology of living organisms, however, follows a nested organization, since a hierarchical scheme can also be recognized at the functional level, being each physiological function the combined result of processes occurring at system, tissue, cell, and molecular levels. In this respect, it has also been proposed that some auto similarity could prevail at each nested level [4], meaning that the different involved elements can interact, whatever their degree of miniaturization, according to similar rules. A well-known example is the feedback mechanism found in metabolic molecular networks where the amount of the final product inhibits its further production by acting directly upon a certain rate-limiting step. Feedback, however, is also found at organ and system level, e.g., in the circuits which maintain muscle length, or in arterial blood pressure control. For this reason, the term “self-similarity logic” has been suggested to convey the concept of a multilevel structural organization in which very similar functional rules (logic) apply at each level [8]. This view is in agreement with the statement of Russell and Aloy [91] that a key concept in biological system design is modularity: Nature duplicates and reuses existing parts and design principles again and again.

The present essay illustrates the hypothesis that both the structural (geometrical) “self-similarity” concept and the broader “self-similarity logic” principle are particularly apparent in the nervous system, likely providing a unitary conceptual scheme to describe many aspects of its morphological and functional organization.

9.2 Structural Self-Similarity of the Nervous System

As recently pointed out by Di Ieva et al. [34], the application of Euclidean geometry to neuroanatomy is strongly limited by several factors, such as the natural complexity of the brain, its hierarchical structure, and the sophisticated topological architecture of the neurons organized in micro and macro networks. For this reason, the introduction of new geometrical frameworks, such as the fractal geometry, and the tools they provided to quantitatively characterize the shape of the nervous structures led to a rapid increase of the amount of data supporting the prevalence of properties such as self-similarity in the brain at various levels of observation. They will be briefly reviewed in the sections that follow.

9.2.1 Cell Level: Complex Geometry of Neurons and Glial Cells

As illustrated in Fig. 9.2a, neurons are characterized by a quite complex morphology. In its foundational work *The Fractal Geometry of Nature*, Mandelbrot [80] specifically mentioned the Purkinje neurons of the cerebellum and wrote “it would be nice if neurons turned out to be fractal.” Studies undertaken to test this hypothesis were in general supportive (see [34, 109] for more comprehensive reviews, as well as Chaps. 6 and 7). Fractal shapes in the branching patterns of dendritic trees were identified in retina neurons [25] and in thalamic neurons [70]. Fractal analysis allowed a distinct differentiation of neuron types in the different laminae [83] of the dorsal horn of the spinal cord, and variations in the fractal structure of the pyramidal neuron dendrite branching resulted associated with differences in functional capacity among regions of the visual cortex [113]. Wen et al. [107] provided a clear-cut indication of self-similarity in neurons by examining the connectivity repertoire of basal dendrite arbors of more than 2000 pyramidal neurons. This study identified a universal statistical process underlying the construction of dendrite arbors, which led to structures in which fragments of the arbor were statistically similar to the entire arbor, thus displaying self-similarity. Additional evidence came from image analysis and in particular from 3D reconstruction techniques using scanning electron microscopy or confocal microscopy [92].

A morphology characterized by self-similarity properties, however, is not limited to neurons. Various mammalian astroglial cell types have been classified by means of fractal analysis [87], and lacunarity and fractal dimension have been used to show the physiological changes of neuronal and astroglial structures in the process of aging, whereby the fractal dimension decreases and lacunarity increases in neurons, while the contrary occurs for astrocytes [52, 100]. As far as other glial cell types are concerned, the sequence of oligodendrocyte developmental stages parallels changes in fractal dimension [20], and fractal analysis of cell ramification and space filling patterns differentiate microglia cells into two categories, depending on whether their fractal dimension did or did not increase after brain injury [95].

9.2.2 Tissue Level

9.2.2.1 Central Nervous System

The central nervous system (CNS) can be described as a huge network of cells interacting through communication pathways. It has been proposed that two main modes (see [9] for a review) of communication (wiring transmission (WT) and volume transmission (VT)) could be distinguished in the CNS. The first is characterized by a physical “wire” connecting the nodes of the network (as in the synaptic transmission between neurons), while the second concerns the three-dimensional

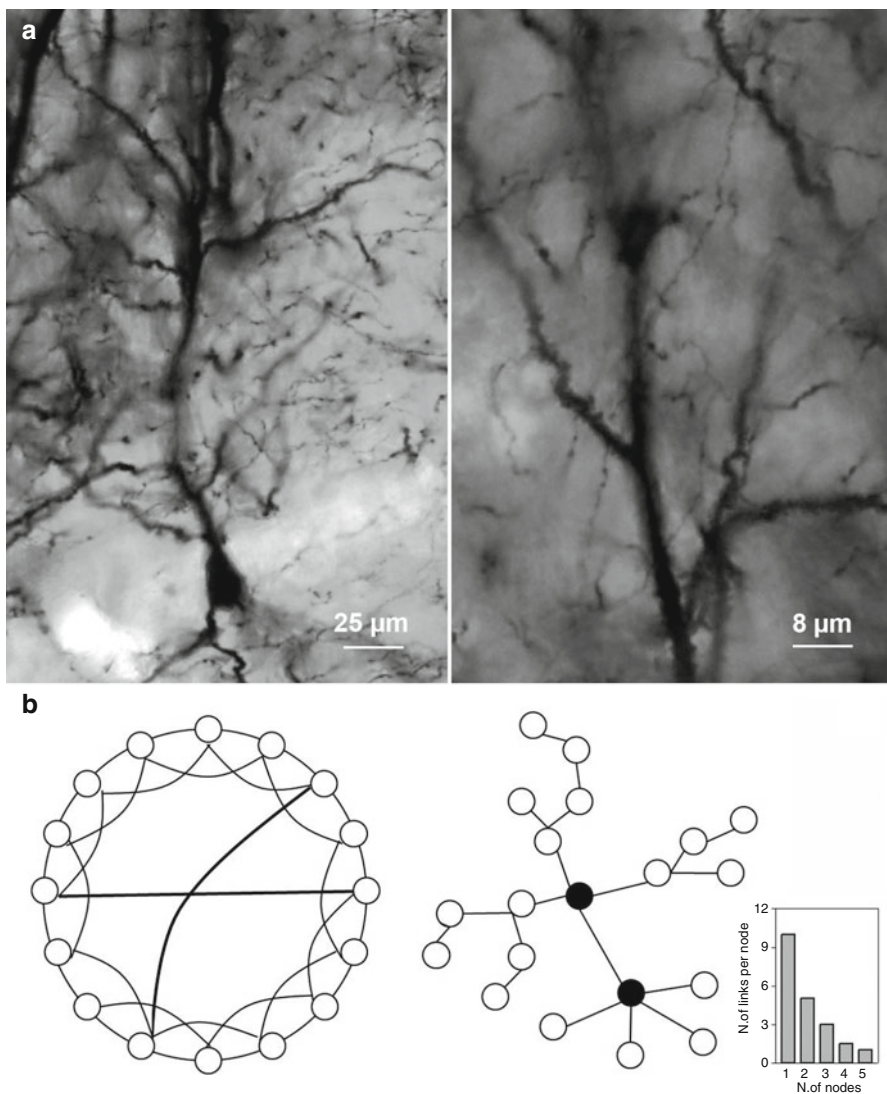


Fig. 9.2 (a) Golgi-stained hippocampal pyramidal neuron. As illustrated in the *right* panel, fragments of the dendritic arbor are statistically similar to the entire arbor, thus displaying self-similarity. (b) Schematic representation of the two network architectures identified in the CNS (see text). *Left* panel illustrates a “small-world network” and the *right* panel a “scale-free network.” In the latter some nodes (hubs of connectivity) have a high number of connections to other nodes, whereas most nodes have just few connections. More specifically, the distribution of the links among the nodes of the network follows a power law (shown in the *inset*)

diffusion of signals in the extracellular space for a distance greater than the synaptic cleft. VT is characterized by a very high divergence, since one source usually gives signals to a great many targets, including not only neurons but also other types of cells in the CNS, such as astrocytes [101] and microglial cells [38]. This

leads to the formation of “complex cellular networks,” exchanging signals in a certain volume of brain tissue and, due to this cross talk, integrating their activity [3]. In this context, the relationship between neurons and astrocytes is the best studied (see [39]), and recent findings highlighted the involvement of “neuron–astroglial interactions” in the higher brain functions. As a matter of fact, it has been introduced the concept of *tripartite synapse*, since in most glutamatergic central synapses, the extremity of a protoplasmic astrocyte process wraps the synaptic cleft. It should be noted that astrocytes express membrane receptors to neurotransmitters and can release their own chemical messengers (gliotransmitters). Thus, they establish a cross talk with both pre- and postsynaptic neurons. Several astrocytes participate in this functional organization, coupled with each other by gap junctions (see [24]) and communicating by “calcium waves” [85]. Thus, neuroastroglial networks do exist controlling not only dynamic glucose delivery [89] but also participating in cognitive functions [88].

The architecture of the CNS extends over a range of up to five orders of magnitude of scales: from microns for cell structures at one end to centimeters for interareal neuronal connections at the other. From the morphological point of view, the CNS appears strictly self-similar (i.e., a quasi-fractal) at low scale, as shown by studies on the shape of neuronal and glial elements (see Sect. 9.2.1). As far as the neuronal networks are concerned, the connections between different cortical areas were shown to possess an organization in the form of “small-world networks” [105], forming clusters of nearby cortical areas with short links, which in turn have long-range connections to other clusters [97, 98]. Within clusters, functional magnetic imaging identified a network topology of the type called “scale-free” [35], in which some nodes (hubs of connectivity) have a high number of connections to other nodes, whereas most nodes have just a handful. Both these types of network organization (see Fig. 9.2b) display a quite high level of geometrical self-similarity [96], suggesting that the CNS (at least for its neural component) can be considered self-similar over all its length scales.

9.2.2.2 Peripheral Nervous System

No studies specifically aimed at analyzing the overall architecture of the peripheral nervous system (PNS) in terms of self-similarity and fractal properties are currently available. It should be outlined, however, that quite recent studies have highlighted a close structural and developmental relationship between blood vessels and nerves [23, 36, 65, 73]. This association seems of particular relevance in patterning the peripheral nervous system. The molecular mechanisms regulating common wiring of nerves and blood vessels have attracted considerable interest over the past decade. Some common morphogenic signals and mechanisms have been recognized that direct formation of either structures. Indeed, axon guidance molecules, such as semaphorins, ephrins, slits, and netrins, function also as angiogenic and vessel-guiding factors. Angiogenic growth factors, such as VEGF, express neurogenic potential as well. This assumption may explain why in peripheral tissues, blood

vessels are often aligned with nerves and display similar branching pattern [84]. On the one hand, endothelial cells produce signals, such as endothelin-3, artemin, and neurotrophin-3, which guide axons to track alongside developing vessels [62, 72]. On the other hand, nerves may also produce signals such as VEGF-A to attract blood vessels and stimulate endothelial cell surviving.

This mutual structural relationship between the two systems is of particular importance for our discussion. In fact, the question about whether vascular networks could be considered structures strictly self-similar was addressed by a quite large number of studies (see [54]). Recently, Lorthois and Cassot [75] provided a review of the published results, together with a new multi-scale analysis performed on high-resolution image data sets of vascular networks [26]. The work demonstrated that the healthy vascular structures are a superposition of two components: at low scale, a non-fractal “mesh-like” capillary network which becomes homogeneous and space filling over a cutoff length of the order of its characteristic length (25–75 μm) and a “treelike” distribution network which can be demonstrated to be quasi-fractal (i.e., strictly auto-similar) for a quite wide range of length scales. Thus, the observed structural association between peripheral nerves and the “treelike” component of the vascular system legitimates the hypothesis of a self-similar architecture for the PNS as well.

9.3 A Self-Similarity Logic Drives the Functional Features of the CNS

From a functional point of view, it has been observed that the CNS parenchyma self-organizes in functional units. The best-known examples are the cortical columns (see [86]) consisting of an array of cooperating neuronal groups extending radially across the cortical cellular layers and representing units of operation. As far as the anatomical boundaries of these units are concerned, they appear loosely delimited in morphological terms, since they are dynamic entities changing according to functional needs. A role in delimiting them is probably played by astrocytes, since the astroglial cells, especially in mammalian brains, define the microarchitecture of the parenchyma by dividing the gray matter into relatively independent structural units through the process known as “tiling” [22].

A further characteristic of these basic units, important for our discussion, is suggested by a very simple observation. CNS functions (as, for instance, motor control) can indeed be studied either as the output of the entire system (e.g., by means of studies on reflex responses) or of some of its regions (e.g., by extracellular electrophysiological recordings from the motor areas) or even at the level of single neurons (e.g., by intracellular electrophysiological recordings from spinal motor neurons). These different approaches are not simply a consequence of the increased analytical power of the experimental tools employed, but rather they depend on an intrinsic characteristic of the system. In fact, the CNS is the holistic assembly of a

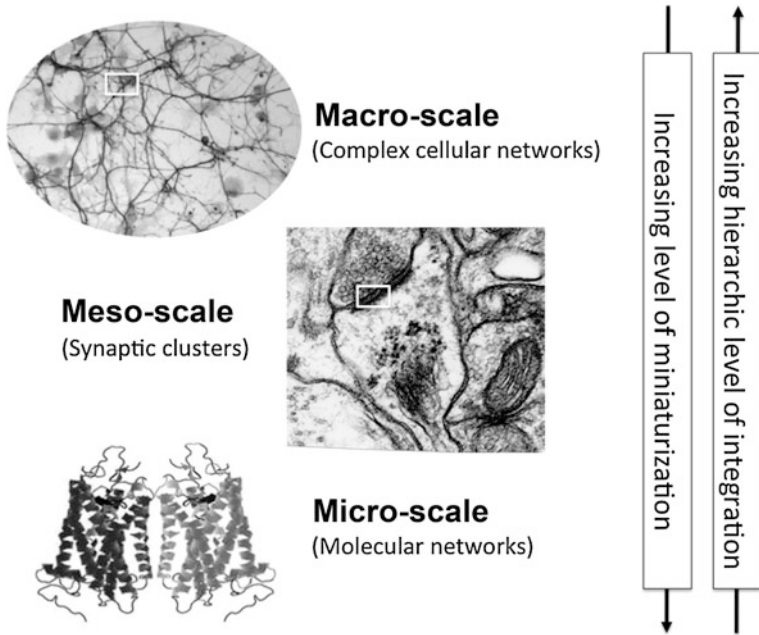


Fig. 9.3 Schematic representation of the hierarchic organization of the nervous system. The three main miniaturization levels, i.e., the macro-, meso-, and microscale, are illustrated

multilevel functional organization. In other words, a hierarchic criterion holds meaning that system components of different miniaturizations not only can be arranged to work together either in parallel or in series but also nested within each other [30]. For this reason, a structure of multiple layers that encased one within the other like a “Russian doll” has been argued for the basic functional units, and the term “functional module” (FM) has been proposed to indicate them [8].

In particular, it has been suggested [4, 104] that in each FM, at least macro-, meso- and microscale levels could be recognized (see Fig. 9.3):

- The macroscale level, in which it is possible to recognize neuronal networks and complex cellular networks [3].
- The mesoscale level is the level of single neurons and, in particular, of the so-called synaptic clusters (SC), in which multiple synapses act cooperatively to modulate their strength [46, 93]. SC are often organized around the dendritic spines and partially isolated from the surrounding environment by glial cells [31, 46].
- At the microscale level are the molecular networks, made by molecules that function as a metabolic and/or regulatory signaling pathway in a cell [21]. Of particular interest are the “receptor mosaics,” i.e., macromolecular complexes formed at the membrane level by G protein-coupled receptors [42] as a consequence of direct allosteric receptor–receptor interactions (see [56] for a review).

As pointed out by some authors, the same principles could be applied across the different levels of organization to account for the flux of dynamically emergent macrostate brain configurations [8, 108]. More specifically, processes resulting in a “network dynamics” [66, 81] among interacting elements are operating at each level of organization, leading to the emergence of “self-similarity logic” as a characteristic functional feature of the CNS. Furthermore, it is noteworthy that a common rule also seems to exist at all levels for what it concerns the remodeling processes in the CNS. It appears mainly based on the self-organization of the existing components to form a new complex capable of new “emergent” properties. These aspects will be discussed in the sections that follow.

9.3.1 Interaction-Dominant Dynamics in the CNS

From a general point of view, the types of dynamics a biological system exhibits can be classified into two broad classes [16]. In component-dominant dynamics, behavior is the product of a rigidly delineated architecture of modules, each with predetermined functions. On the contrary, interaction-dominant dynamics is crucially based on the plasticity of the system components and on the network of communication processes among these components. The nervous system can be better described as an interaction-dominant dynamics system where interaction processes alter the integrative action of the single components and where it is difficult, and sometimes impossible, to assign tightly defined and unique roles to each specific component.

For what it concerns such a complex dynamics of the CNS, the best investigated level is the neural network level. Information handling by neural networks has a long story behind it. In this regard, it is enough to cite the classical article by McCulloch and Pitts [81] and the further development that followed (see [59] for a historical review), which established that from networks of abstract models of neurons as switching devices, quite complex behavior can emerge.

In a network processing is carried out by a usually large number of simple processing elements (called nodes), having a nonlinear response function [63]. Each node receives input (excitatory or inhibitory) from some number of other nodes, responds to that input according to its response function, and in turn excites or inhibits other nodes to which it is connected. Thus, every input to the network will result in a flow of collective configurations of the nodes often converging to some stable pattern (also called “attractor”) that represents the response of the network. There are some key characteristics worth noting. First, what such a system “knows” is essentially captured by the pattern of connections and the efficiency associated with each of them [71]. Second, rather than using symbolic representations, the “vocabulary” of such a system consists of patterns of activation across different units. Furthermore, what made this type of dynamics so intriguing was the possibility of “learning procedures” [90], by which the network would adjust the connection efficiencies in small incremental steps (for instance, based on examples of a target behavior) in such a way that over time the network’s response accuracy would

improve. Thus, the behavior emerging in a network relies on a distributed rather than a centralized control.

It has to be pointed out that the identification of different classes of VT signals (see [9] for a review) including chemicals (such as neurotransmitters, ions, gases, and enzymes), as well as physical signals (such as electrotonic currents, temperature gradients, and pressure waves generated by arterial pulses), opens the possibility that the above described dynamics could not be limited to neural networks, but could also drive the behavior of the “complex cellular networks” (see Sect. 9.2.2.1) and, in particular, of the neuroastroglial networks [53]. In this context an organizational aspect deserving consideration concerns the possibility (see [3]) that the communication pathway between a signal source and its targets could be modulated by a “modifier” responding to teaching signals that could originate, for instance, from environmental inputs. Such a modifier could be spatially situated along a VT diffusion pathway and/or an astrocyte network [45].

A network dynamics, however, also appears to characterize the meso- and microscale levels of brain organization. At the mesoscale level, the abovementioned synaptic clusters represent the functional bridge between the cellular networks and the molecular level. They have been shown to be very plastic entities from both the structural [61] and the functional [106] point of view. Notably, it has been reported that plastic changes induced by long-term potentiation (LTP) at one synaptic contact lower the threshold for the induction of LTP at neighboring synapses at a stimulation strength that did not cause any plastic changes under control conditions [46]. Gally et al. [43] described a simple mechanism allowing such a temporal correlation between synaptic sites (see also [51]). It was based on a simple network dynamics in which the release from the depolarized postsynaptic spine of a diffusible substance (such as NO) was capable of acting as a signal returning from postsynaptic to both presynaptic and postsynaptic sites within some volume of tissue. The production of the diffusible substance at a particular time was a function of its activity at that time, and the movement of the substance by diffusion provided the possibility to establish temporal correlations between the activities of neighboring sites. For what it concerns the microscale level, in recent years, increasing experimental evidence supported the hypothesis that G protein-coupled receptors can form high-order receptor oligomers at the cell membrane (see [56] for a review). The existence of these supramolecular complexes is considered of particular importance because it allows the emergence of integrative functions performed by a protein aggregate as a whole. In fact, owing to receptor–receptor interactions in a suitable network dynamics, a configuration change of a given receptor will transform the probability of changing the configuration for the adjacent receptors, and the effect will propagate throughout the cluster, leading to a complex collective behavior and to an integrated regulation of multiple effectors [6]. It was suggested that this molecular mechanism might also lead to a transient and/or permanent change of the synaptic efficacy and then contribute to memory storage and engram formation (see [51] for a review).

Thus, network dynamics appears a characterizing feature of almost all the levels of the functional organization of the nervous system, providing a first key element

of the “self-similarity logic” that shapes its design from the functional point of view. This point will be further illustrated in the next sections by taking into consideration some basic operations performed by CNS networks according to Charles Sherrington’s studies (see [7] for a review) and that can be realized at different miniaturization levels.

9.3.1.1 The Concept of “Fringe”

A fringe is an area of overlap between two networks and can lead to facilitation. As shown in Fig. 9.4a, if neuron B has a low discharge rate, neuron B1 does not fire, but if neuron A is firing at high frequency, neuron B1 excitability becomes increased, and it is easier for the activity of neuron B to excite B1. Neuron B1 is said to be in the subliminal facilitation fringe of A.

As illustrated in Fig. 9.4b for receptor complexes, the concept of fringe (as other classical types of controls such as feedback or feed-forward and spatial or temporal summation) can also be used to describe some significant behavior of molecular networks. The concept of fringe is of particular importance since it can suggest mechanisms that at molecular network level regulate the cross talk between pathways allowing the production of complex cellular responses [3].

9.3.1.2 The Concept of “Lateral Inhibition”

Figure 9.4c illustrates a classical representation of lateral inhibition for neural circuits (see [19]) that can be transferred (Fig. 9.4d) to molecular networks. Thus, beside “physical compartmentalization” that allows a very efficient spatial segregation of signaling pathways, also a functional segregation, via lateral inhibition, can produce a similar effect.

The fact that a similar organization of the circuit, as in the case of fringe, can be recognized for lateral inhibition at neural network level as well as at molecular network level underlines once again the potential heuristic value of “self-similarity logic.”

9.3.2 *Remodeling Processes in the Nervous System*

The experience-based reshaping of the brain structures [82] is another general feature that deeply characterizes the nervous system, and a “self-similarity logic” principle appears a useful descriptive concept for this aspect as well.

Cell networks can be redeployed (or reused) for multiple functions, as recently shown by Anderson [15] following a careful survey of neuroimaging data. In this context, it was pointed out, for instance, that the Broca area is involved in multiple functional cognitive tasks besides containing FM involved in the control of speech

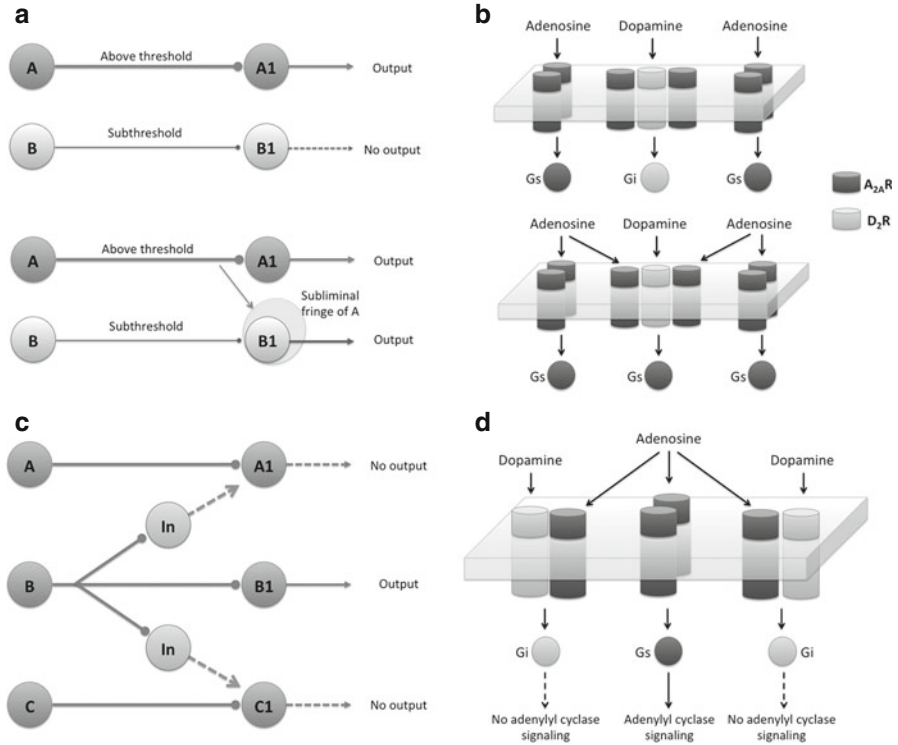


Fig. 9.4 (a) Schematic representation of the concept of fringe. Two input neurons, *A* and *B*, directly acting on two output neurons (*A1* and *B1*) are considered. It is surmised that only *A* gives an above threshold input to its target neuron (*upper panel*). However, if it fires at a high frequency, it can lower the threshold for the firing of *B1* (*lower panel*). (b) The same basic scheme is applied at microscale to receptor mosaics formed by *A₂A* and *D₂R* receptors with reciprocal inhibitory activity (see [56]). A low concentration of adenosine can activate only Gs-mediated signaling from *A₂A* homodimers (*upper panel*). However, high concentrations of adenosine can induce, via receptor–receptor interactions, an inhibition of the *D₂* receptor in the heterotrimer and its shift from Gi- to Gs-mediated signaling (*lower panel*). (c) Lateral inhibition mediated by interneurons (*In*) leads to focus the activity of a neural circuit in selected groups of neurons. (d) Possible lateral inhibition process at microscale level in a system involving *A₂A* and *D₂R* heterodimers and *A₂A* homodimers. Activation of *D₂* receptors by dopamine leads to a reduction in the affinity of *A₂A* receptors in the heterodimers, hence in a sharpening of the Gs-mediated signaling

[48]. Changes in connectivity between neurons can be obtained not only by establishing new connections (see, for instance, the neural circuitry responsible for seasonal breeding in several species [1]) but also by reactivating “silent” synapses when needed [68]. At the molecular level, the existence of receptor–receptor interactions [10] can lead to the assembly of oligomeric receptor complexes with different properties even if formed by the same types of monomers [11].

It is noteworthy that a common rule seems to exist at all levels. It is mainly based on the self-organization of existing components to form a new complex capable of

“emergent” properties. “Proliferation” (production, generation) of new system components seems to play a minor role in the remodeling processes occurring in the CNS. In this respect, the “self-similarity logic” driving the remodeling of the CNS appears to significantly differ from that operating in other plastic systems, as, for instance, the vascular system (see [54]). To illustrate the concept, the sprouting phenomenon (occurring in both systems) can be considered. Sprouting of capillaries involves the recruitment of many endothelial cells and the production of specialized endothelial cells called tip cells, which extending and retracting filopodia define the direction in which the new vascular sprout grows. Thus, these cells perform an analogous function to growth cones of neurons [44]. The latter, however, are dynamic, actin-supported extensions of single developing axons.

By using a metaphor originally proposed by Agnati et al. [8], the “self-similarity logic” emerging in the CNS remodeling processes can be illustrated with the term “mosaic” as it is defined in figurative art, i.e., as the process of making pictures by inlaying small bits of colored stones (*tesserae*). Thus the term indicates how from a given set of elements it is possible to achieve different patterns endowed with different emergent properties.

9.4 Concluding Remarks: A Place for Self-Similarity in a Global Model of the Nervous System?

A quite large body of presently available data identified self-similar structures at all levels of both the morphological and the functional organization of the nervous system. They appear almost embedded within one another, recalling the image of the Russian Matryoshka dolls [4, 8], with a “self-similarity logic” (i.e., a set of almost identical rules) operating at the successive levels of such a nested system. As pointed out by Werner [109], however, these observations remained largely islands in the otherwise rapidly advancing theoretical neuroscience with different priorities. Thus, a better integration of self-similarity with other insights into brain organization and complexity would be needed.

In this respect, of substantial interest is the biophysical evidence for the brain being a complex system in a regime of criticality, as understood in statistical physics (see [27] and [109] for a review). In statistical physics, systems operating at the critical point of transition between ordered and random behavior are metastable with respect to a set of control parameters and are capable of rapid qualitative change in response to fluctuations of external input. The important feature of the system organization following the critical transition is the formation of new objects with distinct properties. Typical physical examples are phase transitions, as, for instance, that from water to ice or from ferro- to paramagnetism.

For what it concerns the nervous system, criticality has a distinguished history. As early as 1950, Turing [103] postulated that the brain as a dynamical system would operate near a critical state as the prerequisite for instantaneous reaction to

novelty. A quite large body of experimental observations of sudden transitions between stable states was subsequently accumulated. Illustrative examples include the motor behavior [57, 67] and the visual system [60]. They were considered evidence for the brain being a pattern-forming system that can switch flexibly from one coherent state to another.

As far as the significance of criticality is concerned, three attributes deserve consideration [109]. The first is the just mentioned characteristic of critical transitions making them a universal mechanism for rapid switching between different cooperative patterns of neuronal behavior. Furthermore, excitable systems at criticality were shown to exhibit an optimal dynamical range for information processing [69]. Finally, a model that reproduces the typical features of systems at a critical point can learn and remember complex logical rules [33]. According to Werner [109], these intriguing features of critical systems are at the basis of their current appeal as a general theoretical framework to describe the nervous system.

An important question for our discussion can now be raised. Is there any relation between the just briefly summarized biophysical features of the nervous system and the self-similar organization it exhibits? Also documented by Aguirre et al. [13], the intimate relation between self-similar structures and nonlinear dynamics in dissipative systems is evident and well-substantiated, self-similarity, and self-similarity logic appearing basic design principles for complex systems. Two aspects, in particular, can be here emphasized. The first point is of morphological nature. A self-similar structure, such as a network (see Sect. 9.2.2), is likely the most economic architecture supporting dynamic transitions associated with the formation and dissolution of attractors (see [112]). In addition, the fractal morphology of the elements forming the cell networks in the nervous system is consistent with the constraint that the time for propagating signals as well as the length of distribution pathways should be minimized [110]. The second point concerns dynamics. In fact, at critical transitions, a reordering process of a system is needed in which events at many scales make contributions of equal importance [111]. A hierarchical nesting of self-similar structures operating according to similar rules (“self-similarity logic”) could, therefore, well support a process of this type, representing a compact format to store a range of temporal and/or spatial stimulus parameters: the metaphor of a set of strings resonating to specific frequencies has been proposed [109] to illustrate this concept. Also from the point of view of the computational tasks the nervous system can perform [53], it is possible to appreciate the relevance of this “vertical” morphofunctional organization, since it allows an enormous number of possible configurations for each FM, providing it with an extraordinary potential capability to process and store information [12].

In conclusion, although a great many questions concerning the dynamical properties of the nervous system as a hierarchic system of networks are still open, the self-similarity characterizing its structural and functional organization appears not only an efficient design principle but also a unifying concept to describe its complexity and its concerted, holistic behavior.

References

1. Adams VL, Goodman RL, Salm AK, Coolen LM, Karsch FJ, Lehman MN. Morphological plasticity in the neural circuitry responsible for seasonal breeding in the ewe. *Endocrinology*. 2006;147:4843–51.
2. Agnati LF, Fuxe K. New concepts on the structure of the neural networks: the miniaturization and hierarchical organization of the central nervous system. *Biosci Reports*. 1984;4:93–8.
3. Agnati LF, Fuxe K. Volume transmission as a key feature of information handling in the central nervous system: possible new interpretative value of the Turing's B-type machine. *Prog Brain Res*. 2000;125:3–19.
4. Agnati LF, Santarossa L, Genedani S, Canela EI, Leo G, Franco R, et al. On the nested hierarchical organization of CNS: basic characteristics of neural molecular networks. In: Erdi P, Esposito A, Marinaro M, Scarpetta S, editors. *Computational neuroscience: cortical dynamics, lecture notes in computer sciences*. Berlin/Heidelberg/New York: Springer; 2004. p. 24–54.
5. Agnati LF, Guidolin D, Fuxe K. The brain as a system of nested but partially overlapping networks. Heuristic relevance of the model for brain physiology and pathology. *J Neural Transm*. 2007;114:3–19.
6. Agnati LF, Guidolin D, Leo G, Fuxe K. A Boolean network modeling of receptor mosaics: relevance of topology and cooperativity. *J Neural Transm*. 2007;114:77–92.
7. Agnati LF, Guidolin D, Carone C, Dam M, Genedani S, Fuxe K. Understanding molecular networks builds on neuronal cellular network architecture. *Brain Res Rev*. 2008;58:379–99.
8. Agnati LF, Baluška F, Barlow PW, Guidolin D. 'Mosaic', 'self-similarity logic', and 'biological attraction' principles: three explanatory instruments in biology. *Commun Integr Biol*. 2009;2:552–63.
9. Agnati LF, Guidolin D, Guescini M, Genedani S, Fuxe K. Understanding wiring and volume transmission. *Brain Res Rev*. 2010;64:137–59.
10. Agnati LF, Guidolin D, Leo G, Carone C, Genedani S, Fuxe K. Receptor-receptor interactions: a novel concept in brain integration. *Prog Neurobiol*. 2010;90:157–75.
11. Agnati LF, Guidolin D, Vilardaga JP, Ciruela F, Fuxe K. On the expanding terminology in the GPCR field: the meaning of receptor mosaics and receptor heteromers. *J F Recept Sig Transduct Res*. 2010;30:287–303.
12. Agnati LF, Guidolin D, Cortelli P, Genedani S, Cela-Conde C, Fuxe K. Neuronal correlates to consciousness. The "Hall of mirrors" metaphor describing consciousness as an epiphenomenon of multiple dynamic mosaics of cortical functional modules. *Brain Res*. 2012;1476:3–21.
13. Aguirre J, Viana RL, Sanjuan MAF. Fractal structures in nonlinear dynamics. *Rev Mod Phys*. 2009;81:333–86.
14. Andersen MP, Parham AR, Waldrep JC, McKenzie WN, Dhand R. Alveolar fractal box dimension inversely correlates with mean linear intercept in mice with elastase-induced emphysema. *Int J Chron Obstruct Pulmon Dis*. 2012;7:235–43.
15. Anderson ML. Neural reuse: a fundamental organizational principle of the brain. *Behav Brain Sci*. 2010;33:245–313.
16. Anderson ML, Richardson MJ, Chemero A. Eroding the boundary of cognition: implications of embodiment (1). *Top Cogn Sci*. 2012;4:717–30.
17. Barnsley MF. *Fractals everywhere*. Burlington: Morgan Kaufmann Publishers; 1988.
18. Bassingthwaighe JB, Liebovitch LS, West BJ. *Fractal physiology*. Oxford: Oxford University Press; 1984.
19. Bear MF, Connors BW, Paradiso MA. *Neuroscience: exploring the brain*. New York: Lippincott Williams & Wilkins; 2006.
20. Bernard F, Bossu JL, Gaillard S. Identification of living oligodendrocyte developmental stages by fractal analysis of cell morphology. *J Neurosci Res*. 2001;65:439–45.

21. Bhalla US, Iyengar R. Emergent properties of networks of biological signaling pathways. *Science*. 1999;283:381–7.
22. Bushong EA, Martone ME, Ellisman MH. Maturation of astrocyte morphology and the establishment of astrocyte domains during postnatal hippocampal development. *Int J Dev Neurosci*. 2004;22:73–86.
23. Carmeliet P, Tessier-Lavigne M. Common mechanisms of nerve and blood vessel wiring. *Nature*. 2005;436:193–200.
24. Carmignoto G. Reciprocal communication systems between astrocytes and neurones. *Progr Neurobiol*. 2000;62:561–81.
25. Caserta F, Stanley HE, Eldred WD, Daccord G, Hausman RE, Nittman J. Physical mechanisms underlying neurite outgrowth: a quantitative analysis of neuronal shape. *Phys Rev Lett*. 1990;64:95–8.
26. Cassot F, Lauwers F, Fouard C, Prohaska S, Lauwers-Cances V. A novel three-dimensional computer-assisted method for a quantitative study of microvascular networks of the human cerebral cortex. *Microcirculation*. 2006;13:1–18.
27. Chialvo DR. Critical brain networks. *Physica A*. 2004;340:756–65.
28. Cross SS. Fractals in pathology. *J Pathol*. 1987;182:1–8.
29. Cross SS. The application of fractal geometric analysis to microscopic images. *Micron*. 1994;25:101–13.
30. Csete ME, Doyle JC. Reverse engineering of biological complexity. *Science*. 2002;295:1664–9.
31. Cutsuridis V, Wennekers T, Graham BP, Vida I, Taylor JG. Microcircuits: their structure, dynamics and role for brain function. *Neural Netw*. 2009;22:1037–8.
32. Cutting JE, Garvin JJ. Fractal curves and complexity. *Percept Psychophysiol*. 1987;42:365–70.
33. de Arcangelis L, Herrmann HJ. Learning as a phenomenon occurring in a critical state. *Proc Natl Acad Sci U S A*. 2010;107:3977–81.
34. Di Ieva A, Grizzi F, Jelinek H, Pellionisz AJ, Losa GA. Fractals in the neurosciences, Part I: general principles and basic neurosciences. *Neuroscientist*. 2013;20:403–17.
35. Eguiluz VM, Chialvo DR, Cecchi GA, Baliki M, Apkarian AV. Scale-free brain functional networks. *Phys Rev Lett*. 2005;94:018102.
36. Eichmann A, Makinen T, Alitalo K. Neural guidance molecules regulate vascular remodeling and vessel navigation. *Genes Dev*. 2005;19:1013–21.
37. Falconer K. *Fractal geometry: mathematical foundations and applications*. Hoboken: Wiley; 2003.
38. Färber K, Kettenmann H. Physiology of microglial cells. *Brain Res Rev*. 2005;48:133–43.
39. Fellin T, Carmignoto G. Neurone-to-astrocyte signaling in the brain represents a distinct multifunctional unit. *J Physiol*. 2004;559:3–15.
40. Fernandez E, Jelinek HF. Use of fractal theory in neuroscience: methods, advantages, and potential problems. *Methods*. 2001;24:309–21.
41. Fudenberg G, Getz G, Meyerson M, Mirny L. High order chromatin architecture shapes the landscape of chromosomal alterations in cancer. *Nat Biotechnol*. 2011;29:1109–13.
42. Fuxe K, Agnati LF, Benfenati F, Celani M, Zini I, Zoli M, Mutt V. Evidence for the existence of receptor–receptor interactions in the central nervous system. Studies on the regulation of monoamine receptors by neuropeptides. *J Neural Transm*. 1983;S18:165–79.
43. Gally JA, Montague PR, Reeke GN, Edelman GM. The NO hypothesis: possible effects of a short-lived, rapidly diffusible signal in the development and function of the nervous system. *Proc Natl Acad Sci U S A*. 1990;87:3547–51.
44. Gerhardt H, Golding M, Fruttiger M, Ruhrberg C, Lundkvist A, Abramsson A, et al. VEGF guides angiogenic sprouting utilizing endothelial tip cell filopodia. *J Cell Biol*. 2003;161:1163–77.
45. Giaume C. Astroglial wiring is adding complexity to neuroglial networking. *Front Neuroenerg*. 2010;2:129.

46. Golding NL, Staff NP, Spruston N. Dendritic spikes as a mechanism for cooperative long-term potentiation. *Nature*. 2002;418:326–31.
47. Grizzi F, Chiriva-Internati M. The complexity of anatomical systems. *Theor Biol Med Model*. 2005;2:26.
48. Grodzinsky Y, Santi A. The battle for Broca's region. *Trends Cogn Sci*. 2008;12:474–80.
49. Guidolin D, Nico B, Mazzocchi G, Vacca A, Nussdorfer GG, Ribatti D. Order and disorder in the vascular network. *Leukemia*. 2004;18:1745–50.
50. Guidolin D, Vacca A, Nussdorfer GG, Ribatti D. A new image analysis method based on topological and fractal parameters to evaluate the angiostatic activity of docexatel by using the Matrigel assay in vitro. *Microvasc Res*. 2004;67:117–24.
51. Guidolin D, Fuxe K, Neri G, Nussdorfer GG, Agnati LF. On the role of receptor-receptor interactions and volume transmission in learning and memory. *Brain Res Rev*. 2007;55:119–33.
52. Guidolin D, Zunarelli E, Genedani S, Trentini GP, De Gaetani C, Fuxe K, Benegiamo C, Agnati LF. Opposite patterns of age-associated changes in neurons and glial cells of the thalamus of human brain. *Neurobiol Aging*. 2008;29:926–36.
53. Guidolin D, Albertin G, Guescini M, Fuxe K, Agnati LF. Central nervous system and computation. *Q Rev Biol*. 2011;86:265–85.
54. Guidolin D, Crivellato E, Ribatti D. The “self-similarity logic” applied to the development of the vascular system. *Dev Biol*. 2011;351:156–62.
55. Guidolin D, Porzionato A, Tortorella C, Macchi V, De Caro R. Fractal analysis of the structural complexity of the connective tissue in human carotid bodies. *Front Physiol*. 2014;5:432.
56. Guidolin D, Agnati LF, Marcoli M, Borroto-Escuela DO, Fuxe K. G protein-coupled receptor type A heteromers as an emerging therapeutic target. *Expert Opin Ther Targets*. 2015;19:265–83.
57. Haken H, Kelso JA, Bunz H. A theoretical model of phase transitions in human hand movements. *Biol Cybern*. 1985;51:347–56.
58. Hastings HM, Sugihara G. *Fractals: a user's guide for the natural sciences*. Oxford: Oxford University Press; 1993.
59. Heims SJ. *The cybernetics group*. Cambridge, MA: MIT Press; 1991.
60. Hennig MH, Adams C, Willshaw D, Sernagor E. Early-stage waves in the retinal network emerge close to a critical phase transition between local and global functional connectivity. *J Neurosci*. 2009;29:1077–86.
61. Holtmaat AJ, Trachtenberg JT, Wilbrecht L, Shepherd GM, Zhang X, Knott GW, et al. Transient and persistent dendritic spines in the neocortex in vivo. *Neuron*. 2005;45:279–91.
62. Honma Y, Araki T, Gianino S, Bruce A, Heuckeroth R, Johnson E, et al. Artemin is a vascular-derived neurotrophic factor for developing sympathetic neurons. *Neuron*. 2002;35:267–82.
63. Hopfield JJ. Neurons with graded response have collective computational properties like those of two-state neurons. *Proc Natl Acad Sci U S A*. 1984;81:3088–92.
64. Jacob F. *La logique du vivant. Une histoire de l'hérédité*. Paris: Editions Gallimard; 1970.
65. Jones CA, Li DY. Common cues regulate neural and vascular patterning. *Curr Opin Genet Dev*. 2007;17:332–6.
66. Kauffman SA. *The origins of order*. New York: Oxford University Press; 1993.
67. Kelso JAS. *Dynamic patterns: the self organization of brain and behavior*. Cambridge, MA: MIT Press; 1995.
68. Kerchner GA, Nicoll RA. Silent synapses and the emergence of a postsynaptic mechanism for LTP. *Nat Rev Neurosci*. 2008;9:813–25.
69. Kinouchi O, Copelli C. Optimal dynamical range of excitable networks at criticality. *Nat Phys*. 2006;2:348–52.
70. Kniffki KD, Pawlak M, Vahle-Hinz C. Fractal dimension and dendritic branching of neurons in the somatosensory thalamus. In: Nonnenmacher TF, Losa G, Weibel ER, editors. *Fractals in biology and medicine*. Basel: Birkhauser Verlag; 1994. p. 221–9.

71. Knoblauch A, Palm G, Sommer FT. Memory capacities for synaptic and structural plasticity. *Neural Comp.* 2010;22:289–341.
72. Kuruvilla R, Zweifel LS, Glebova NO, Lonze BE, Valdez G, Ye H, et al. A neurotrophin signaling cascade coordinates sympathetic neuron development through differential control of TrkA trafficking and retrograde signaling. *Cell.* 2004;118:243–55.
73. Larrivé B, Freitas C, Suchting S, Brunet I, Eichmann A. Guidance of vascular development. Lessons from the nervous system. *Circ Res.* 2009;104:428–41.
74. Lieberman-Aiden E, van Berkum NL, Williams L, Imakaev M, Ragozcy T, Telling A, et al. Comprehensive mapping of long-range interactions reveals folding principles of the human genome. *Science.* 2009;326:289–93.
75. Lorthois S, Cassot F. Fractal analysis of vascular networks: insights from morphogenesis. *J Theor Biol.* 2010;262:614–33.
76. Losa GA. Fractal morphometry of cell complexity. *Riv Biol.* 2002;95:239–58.
77. Losa GA. The fractal geometry of life. *Riv Biol.* 2009;102:29–59.
78. Losa GA, Baumann G, Nonnenmacher TF. Fractal dimension of pericellular membranes in human lymphocytes and lymphoblastic leukemia cells. *Pathol Res Pract.* 1992;188:680–6.
79. Mandelbrot BB. *Les objets fractals: forme, hasard et dimension.* Paris: Flammarion; 1975.
80. Mandelbrot BB. *The fractal geometry of nature.* New York: W.H. Freeman & Co.; 1983.
81. McCulloch WS, Pitts WH. A logical calculus of the ideas immanent in nervous activity. *Bull Math Biophys.* 1943;5:115–3.
82. McEwen BS. Stress, sex, and neural adaptation to a changing environment: mechanisms of neural remodeling. *Ann NY Acad Sci.* 2010;1204:38–59.
83. Milosevic NT, Ristanovic D, Stankovic JB. Fractal analysis of laminar organization in spinal cord. *J Neurosci Methods.* 2005;146:198–204.
84. Mukoyama YS, Shin D, Britsch S, Taniguchi M, Anderson DJ. Sensory nerves determines the pattern of arterial differentiation and blood vessel branching in the skin. *Cell.* 2002;109:693–705.
85. Pereira A, Furlan FA. Astrocytes and human cognition: modeling information integration and modulation of neuronal activity. *Progr Neurobiol.* 2010;92:405–20.
86. Rakic P. Confusing cortical columns. *Proc Natl Acad Sci U S A.* 2008;105:12099–100.
87. Reichenbach A, Siegel A, Senitz D, Smith Jr TG. A comparative fractal analysis of various mammalian astroglial cell types. *Neuroimage.* 1992;1:69–77.
88. Robertson JM. The astrocentric hypothesis: proposed role of astrocytes in consciousness and memory formation. *J Physiol Paris.* 2002;96:251–5.
89. Rouach N, Koulikoff A, Abudara V, Willecke K, Glaume C. Astroglial metabolic networks sustain hippocampal synaptic transmission. *Science.* 2008;322:1551–5.
90. Rumelhart DE, Hinton GE, Williams RJ. Learning representations by back-propagating errors. *Nature.* 1986;323:533–6.
91. Russell RB, Aloy P. Targeting and tinkering with interaction networks. *Nat Chem Biol.* 2008;4:666–73.
92. Schierwagen A, Costa LF, Alpar A, Gartner U. Multiscale fractal analysis of cortical pyramidal neurons. In: Horsch A, Deserno TM, Handels H, Meinzer HP, Tolxdorff T, editors. *Bildverarbeitung für die Medizin 2007: informatik aktuell.* Berlin: Springer; 2007. p. 424–8.
93. Shepherd GM. *The synaptic organization of the brain.* New York: Oxford University Press; 1979.
94. Smith TG, Lange GD, Marks WB. Fractal methods and results in cellular morphology-dimensions, lacunarity and multifractals. *J Neurosci Methods.* 1996;69:123–36.
95. Soltys Z, Ziaja M, Pawlinski R, Setkowicz Z, Janeczko K. Morphology of reactive microglia in the injured cerebral cortex, fractal analysis and complementary quantitative methods. *J Neurosci Res.* 2001;63:90–7.
96. Song C, Havlin S, Makse HA. Self-similarity of complex networks. *Nature.* 2005;433:392–5.

97. Sporns O, Zwi JD. The small world of the cerebral cortex. *Neuroinformatics*. 2004;2:145–62.
98. Stam CJ, Reijneveld JC. Graph theoretical analysis of complex networks in the brain. *Nonlinear Biomed Phys*. 2007;1:3.
99. Stadnitski T. Measuring fractality. *Front Physiol*. 2012;3:127.
100. Suckling J, Wink AM, Bernard FA, Barnes A, Bullmore E. Endogenous multifractal brain dynamics are modulated by age, cholinergic blockade and cognitive performance. *J Neurosci Methods*. 2008;174:292–300.
101. Syková E, Chvátal A. Glial cells and volume transmission in the CNS. *Neurochem Int*. 2000;36:397–409.
102. Thompson DW. On growth and form. Cambridge: Cambridge University Press; 1917.
103. Turing AM. Computing machinery and intelligence. *Mind*. 1950;59:433–60.
104. Varela F, Lachaux JP, Rodriguez E, Martinerie J. The brainweb: phase synchronization and large-scale integration. *Nat Rev Neurosci*. 2001;2:229–39.
105. Watts D, Strogatz S. Collective dynamics of small world networks. *Nature*. 1998;393:440–2.
106. Welzel O, Tischbirek CH, Jung J, Kohler EM, Svetlitchny A, Henkel AW, et al. Synapse clusters are preferentially formed by synapses with large recycling pool sizes. *PLoS One*. 2010;5:e13514.
107. Wen Q, Stepanyants A, Elston GN, Grosberg AY, Chklovskii DB. Maximization of the connectivity repertoire as a statistical principle governing the shape of dendritic arbors. *Proc Natl Acad Sci U S A*. 2009;106:12536–41.
108. Werner G. Viewing brain processes as critical state transitions across levels of organization: neural events in cognition and consciousness, and general principles. *Biosystems*. 2009;96:114–9.
109. Werner G. Fractals in the nervous system: conceptual implications for theoretical neuroscience. *Front Physiol*. 2010;1:15.
110. West GB, Brown GH, Enquist BJ. The fourth dimension of life: fractal geometry and allometric scaling of organisms. *Science*. 1999;284:1677–9.
111. Wilson KG. Problems in physics with many scales of length. *Sci Am*. 1979;241:158–79.
112. Wuensche A, Lesser M. The global dynamics of cellular automata – an atlas of basin of attraction fields of one-dimensional cellular automata. Reading: Addison Wesley; 1992.
113. Zietsch B, Elston GN. Fractal analysis of pyramidal cells in the visual cortex of the Galago (*Otolemur Garnetti*): regional variations in dendritic branching patterns between visual areas. *Fractals*. 2005;13:83–90.

Chapter 10

Fractality of Cranial Sutures

Takashi Miura

Abstract It has long been known that skull suture has a typical fractal structure. Although the fractal dimensions have been measured, the generation mechanism of the fractal structure remains to be elucidated. Recent advances in the mathematical modeling of biological pattern formation have provided useful frameworks for understanding this mechanism. Applying a simple fractal principle, which the same rule appears on different scales, this chapter shows how various mechanisms lead to the formation of fractal structures in cranial sutures.

Keywords Suture fractal • Eden • Diffusion-limited aggregation

10.1 Biology of Skull Suture Development

Skull sutures, the structures between the several bones that make up the skull, are a well-known biological example of a fractal structure. At birth, sutures are relatively wide and straight (Fig. 10.1a, [40]). During development, they gradually wind and develop interdigitating patterns without changing their width (Fig. 10.1b, [7]). This winding structure sometimes becomes very complex and exhibits self-similarity (Fig. 10.1c, [9, 10, 17–20, 44]). After adolescence, the suture tissue gradually disappears and the skull bones become fused [5].

Skull suture biology is an interdisciplinary field [5, 6]. The timing of skull fusion is clinically important because premature fusion of the skull causes a pathological state called craniosynostosis [15], which leads to a deformed skull. Several candidate genes for craniosynostosis, such as fibroblast growth factor receptors [42], transcription factor twist [14], and ephrins [41], have been cloned from craniosynostosis patients [5]. Developmental biology of the suture has been classically studied by morphometry and surgical operation [23–30]. Recent advances in transgenic technology enable us to assay the functions of various genes involved in suture

T. Miura

Department of Anatomy and Cell Biology, Kyushu University Graduate School of Medical Sciences, 3-1-1 Maidashi Higashi-ku, Fukuoka 812-0054, Japan
e-mail: miura_t@anat1.med.kyushu-u.ac.jp

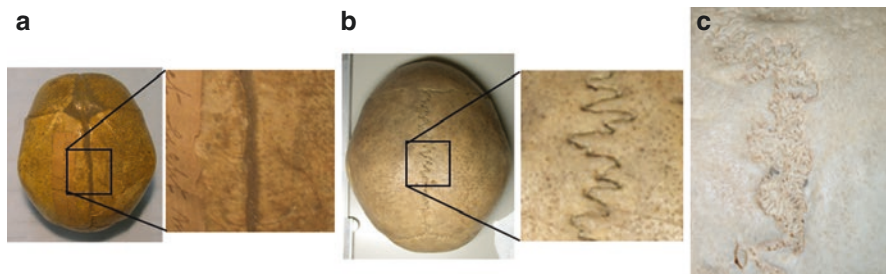


Fig. 10.1 Suture development. (a) Newborn suture is straight and relatively wide. (b) Adult suture is thin and interdigitated. (c) A lambda suture of the human skull. The suture can develop complex fractal patterns (From Miura et al. [22], reproduced with permission of the publisher)

development. Suture development involves several transcription factors (TWIST [3], MSX2 [37], Alx4 [2], Foxc1 [38], RUNX2 [36], Dlx5 [11]), extracellular signaling molecules (TGF betas [39], FGFs and their receptors [12, 21], BMPs, and hedgehog family [16]), and extracellular matrices [35]. Anthropologists are more interested in the mechanical aspects of suturing. Suture interdigitation is thought to strengthen the mechanical connection between bones; this idea has been mechanically tested [13]. The effect of external forces has also been investigated in artificially deformed skulls [1].

10.2 Fundamental Principle of Fractal Structure Formation: “The Same Rule Appears on Different Scales”

Models that generate fractal structures are based on a simple principle – “the same rule appears on different scales.” Fractal structures characteristically exhibit self-similarity, in which the same structure appears at different spatial scales. A structure generated by this principle is self-similar because the same structures on various spatial scales are simultaneously generated by the same rule.

A classic example of a fractal structure is the Koch curve (Fig. 10.2a). This structure is generated by repeated application of a specific rule to line segments at different spatial scales. Initially, the line segment is divided into three subsegments, and the middle segment is reformed into an equilateral triangle. Repetition of this process results in the Koch curve, a complex structure that is clearly self-similar, and obeys the above principle, *the same rule appears on different scales*.

Another class of models that generate fractal structure is the Eden front (Fig. 10.2b). Random addition of a lattice to the interface results in a rugged surface, which is regarded as a fractal structure. This scheme was first proposed as a general growth model of cell colonies [8]. The model begins with an array of occupied (black) and unoccupied (white) sites on a rectangular lattice. In each time step, a site adjacent to the preexisting occupied site (gray) is randomly chosen and converted to an occupied site (Fig. 10.2b). Repetition of this process results establishes

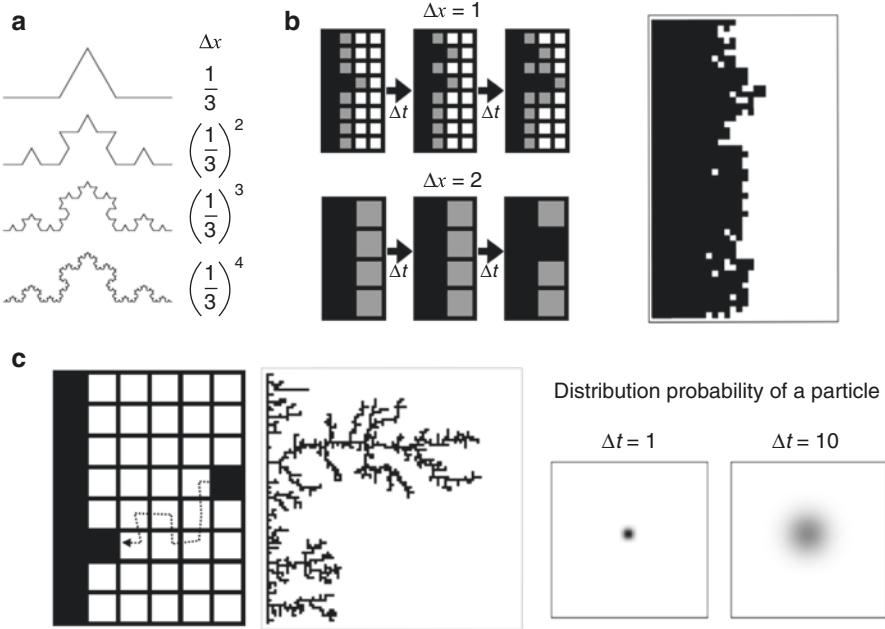


Fig. 10.2 Three models that generate fractal geometry. **(a)** Koch curve. A small structure is repeatedly added to the larger structure with spatial scale Δx . The same rule is applied on different spatial scales Δx . **(b)** Eden front. We define occupied sites (black) and unoccupied sites (*gray* and *white*) on a rectangular lattice. On the smaller spatial scale at $\Delta t=1$, an interface (*gray*) site is randomly chosen at each time step Δt and turned black. Applying the same rule on a larger spatial scale $\Delta x=2$, the timescale is extended to $2\Delta t$. **(c)** Diffusion-limited aggregation (DLA). In this model, the aggregation of randomly moving particles results in a ragged surface. The size of the generated structure is comparable to the diffusion length of the particles, that is, to the distribution probability of the particles, which depends on the timescale of diffusion Δt

the characteristic ragged surface. The perimeter of the structure is proportional to the cluster size on a log-log plot (i.e., is a power-law function of the cluster size). Like the Koch curve, this system typifies a fractal structure, and if we change the measurement length, a similar rule appears on different scales. To demonstrate this, we double the lattice size to $\Delta x = 2$ in Fig. 10.2b. The conversion rule is that if any of the four small sites constituting a larger site is occupied, the large site is labeled as occupied. The larger system qualitatively displays the same rule on a longer timescale, that is, one of the neighboring sites eventually becomes an occupied lattice. Therefore, this model also exemplifies the principle “the same rule appears on different scales.”

Diffusion-limited aggregation (DLA) is another class of models that generates fractal structures (Fig. 10.2c). In DLA, the original shape of the occupied region is defined on a square lattice. A particle is then released far from the edge of the region and moves randomly until it hits the occupied region. Here, we suppose that the occupied region is a bone structure. When the free particle encounters the bone, it is converted to bone, and another particle is released far from the bone-mesenchyme

boundary. Eventually, this process forms a ragged surface (Fig. 10.2c). Intuitively, this pattern formation can be understood from the protruded areas, which are more likely to capture moving particles (and hence expand) than the enclosed areas. The wavelength of the generated structure at a certain timescale Δt depends on the diffusion length of the particles, which is determined by their diffusion coefficient d_u and timescale Δt (Fig. 10.2c). Therefore, the size of the pattern changes over different timescales by the same principle, namely, “the same rule appears in different scales.”

10.3 Models of Skull Suture Development

10.3.1 Eden Collision Model

To our knowledge, the first attempt to explain fractality in fractal sutures was the Eden-based model. Prof Miyajima of Chubu University [33, 34] modeled the suture pattern as two confronting Eden fronts (Fig. 10.3). These fronts proceed and collide, forming the ragged interfaces of two bones. Although Miyajima’s model is a pioneering work in fractal suturing, it has several shortcomings. First, the time course of suture interdigitation development appears to differ from experimental observation. Real sutures become interdigitated *after* the approach of two osteogenic fronts (Fig. 10.1). In the Eden collision model, the two osteogenic fronts are ragged from the beginning, and the fractal dimension reduces after the collision. Second, the model cannot reproduce the maintenance of thin narrow suture tissue. This characteristic is clinically important for elucidating the mechanism of craniosynostosis. Third, known molecular interactions are difficult to incorporate in this system. The model assumes stochastic growth of the front, that is, the probability of growth is invariant along the osteogenic front and independent of the cell cycle. Whether the system actually obeys this rule is difficult to verify in experiments.

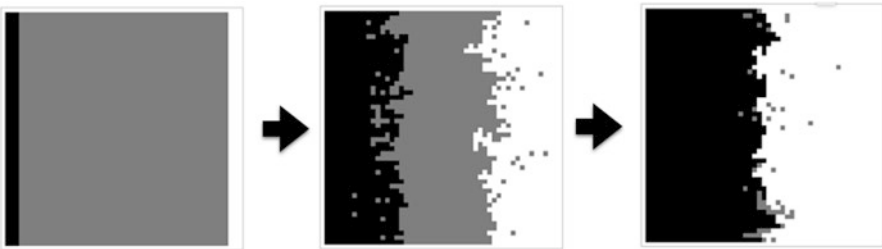


Fig. 10.3 Eden collision model of suture development [33, 34]. The model consists of two confronting Eden fronts. The originally straight interface roughens to form the Eden front and two interfaces collide to form the interdigitated boundary of the bones

10.3.2 Partial Differential Equation (PDE)-Based Model and the Koch Curve

Another class of models, based on partial differential equations (PDEs), was proposed in 2009 [22]. The Miura model proposes two variables: the tissue differentiation state $u(x,y,t)$ and distribution of the substrate factor molecules $v(x,y,t)$. The tissue differentiation state represents each point (x,y) at time t as bone ($u=1$) or mesenchyme ($u=-1$). The tissue differentiation state influences the generation of substrate factors, which are diffusible signaling molecules (such as FGF18 and BMP4) produced by the mesenchyme. The substrate molecule v promotes osteogenic differentiation (Fig. 10.4a).

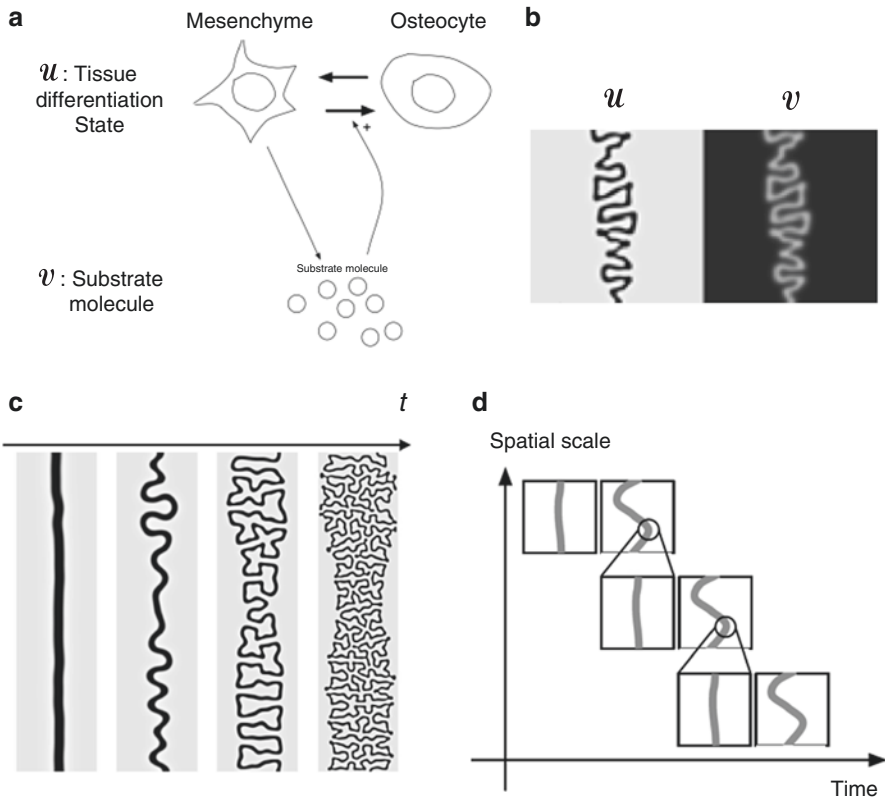


Fig. 10.4 PDE-based model of fractal structure generation. (a) Model definition. The model has two variables: the tissue differentiation state $u(x,y,t)$ and the substrate molecule distribution $v(x,y,t)$. u has two stable states, bone ($u=1$) and mesenchyme ($u=-1$). Substrate molecules passively diffuse from the mesenchyme tissue, promoting osteogenic differentiation. (b, c) Numerical simulation results of the model. Although interdigitation develops in (b), we observe only two characteristic lengths (the width and curvature of the suture). Fractal structures are established in (c). (d) Intuitive explanation of fractal pattern formation. The pattern is formed similarly to the Koch curve (From Miura et al. [22], reproduced with permission of the publisher)

By combining these two effects, this model reproduces the maintenance of narrow suture tissue and formation of interdigitation (Fig. 10.4a, b).

These behaviors are intuitively explained as follows: by default, the osteogenic front proceeds under the effect of substrate factors from the suture tissue. When two osteogenic fronts approach, the concentrations of the substrate factors decrease because their source (the mesenchyme tissue) is narrowed. Eventually, the osteogenic front progression is halted. If the suture tissue becomes too narrow, the substrate factor becomes so low that the osteogenic fronts retract. Consequently, this mechanism establishes an optimal width, maintaining a band-like region of mesenchyme. The optimal width of the suture tissue depends on the diffusion length of the substrate molecules.

We now consider the two-dimensional situation. When the band-like solution is slightly winding, the osteogenic front becomes slightly convex because the surrounding region contains more mesenchyme tissue, and the local concentration of substrate molecules is high. Therefore, any initial slight perturbation is amplified, causing interdigitation of the narrow band-like structure. In a mathematical analysis of this system Ohta et al. [32], derived the wavelength of the interdigitation.

The above-described system has only two fixed characteristic lengths and cannot replicate the scaling behavior observed in fractal structures. However, the system is well understood, and the width of the suture tissue and characteristic length of the interdigitation can be mathematically determined [32]. To obtain fractal structures, we need an additional mechanism. We assume that the spatial effect (governed by the diffusion coefficients) in the system is gradually decreased. After implementing the time-dependent effect (Fig. 10.4c), the system tends to generate smaller structures at later time points. This process is qualitatively similar to the procedure that generates the Koch curve and exhibits similar scaling behavior under an appropriately chosen growth function.

The Miura model has two major advantages. First, it includes a known molecular network; therefore, we can predict the effects of modifying a specific gene. Second, the model incorporates the maintenance of tissue width and thus handles the distinction between normal and craniosynostosis suture. However, the model does not seem to replicate the observed suture development, in which the rapid generation of larger structures is followed by the emergence of smaller structures [22].

10.3.3 *Mechanics-Based Model and DLA*

Another model [45] generates suture fractal patterns by mechanistic principles (Fig. 10.5). Zollikofer's model first defines the boundary of two bones and then calculates the mechanical stress distribution φ inside the bone, assuming that this stress is balanced and static. Under such conditions, φ satisfies Laplace's equation $\Delta\varphi=0$. Next, the boundary is iteratively grown by a stochastic process. The probability of growth depends on φ . In addition, the boundary is smoothed by a surface tension term. This model reproduces the formation of interdigitated patterns (Fig. 10.5b).

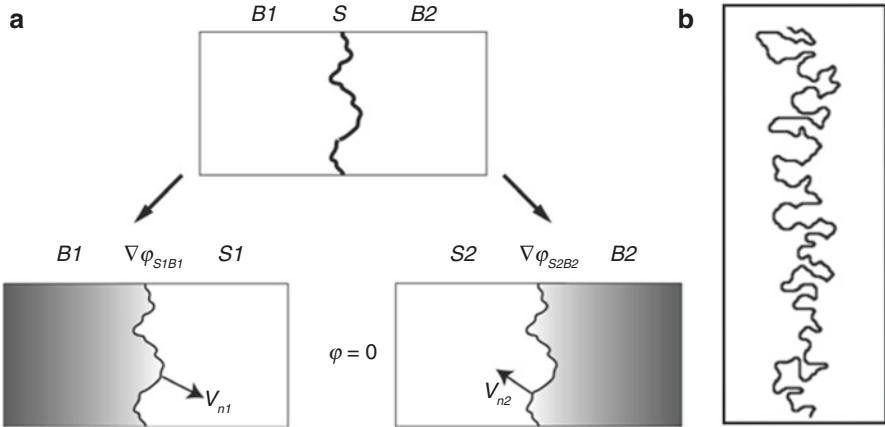


Fig. 10.5 Mechanics-based model of suture interdigitation formation. (a) The model defines two bones B1 and B2 with boundary S. The interface iteratively grows from both sides according to the stress distribution ϕ . (b) Suture pattern generated by the model (From [45], reproduced with permission of the publisher)

In fact, the mechanics-based and DLA models are equivalent. The distribution probability of randomly moving particles obeys Laplace’s equation. Therefore, the stochastic addition of particles to the interface is equivalent to DLA, which has a fractal dimension as discussed in the previous section.

Zollikofer’s model directly incorporates the mechanical aspect of bone growth. Mechanics is an important component of anthropological research, and this predicts the enhanced interdigitated structure under increased mechanical load [4]. However, the stable suture width does not naturally emerge from the model; instead, the width of the suture tissue is assumed a priori.

10.4 Future Directions

10.4.1 Other Classes of Models That Generate Fractal Structures

Fractal structures may form by mechanisms other than those discussed above. True fractal structures may require anomalous diffusion or stochasticity.

Anomalous diffusion is governed by the typical equation of fluid flow in porous media. Specifically, the distribution v of diffusible signaling molecules in a porous media obeys the equation $\frac{\partial v}{\partial t} = d_v \frac{\partial^2 v^m}{\partial x^2}$ ($m > 1$), which also follows the “the same rule appears on different scales” principle. Scale changes of concentration, time, and distance, such as nM to μM , centimeters to meters, and minutes to hours, can be

mathematically expressed as $u \rightarrow \lambda^\alpha u, t \rightarrow \lambda^\beta t, x \rightarrow \lambda^\gamma x$. When the scaling parameters α ; β , and γ are related through $\alpha - \beta = \alpha m - 2\gamma$, the system generates fractal structures because the governing equation is unaltered by the scale change, hence satisfying our fundamental principle: *the same rule appears on different scales*.

White noise added to a system also exhibits fractal behavior (Fig. 10.6). In our preliminary results, adding white noise (random noise) to the PDE system increased the complexity of the fractal structure, probably because white noise is itself a fractal phenomenon. Coarsening the white noise on spatial scale $\Delta x=1$ is equivalent to generating white noise on a larger spatial scale $\Delta x=2$ (Fig. 10.6b). Again, we find that *the same rule appears on different scales*.

10.4.2 Experimental Verification of Theoretical Models

These theoretical models must be verified in carefully designed experiments. In the model of [45], mechanical stress performs a similar role to the substrate factor in [22]. The stress distributions in an elastic body and the distribution of diffusible substances in an equilibrated solution both obey Laplace's equation ($\Delta u = 0$); therefore, we cannot distinguish these two mechanisms by their model behaviors alone. In addition, the chemical and mechanical factors are interdependent in actual suturing; for instance, mechanical stress can alter the gene expression in suture tissue [43] and ongoing differentiation obviously affects the mechanical property of bone [4].

The measurement of model parameters remains technically challenging. The diffusion coefficients of specific morphogens in the PDE model can be measured by

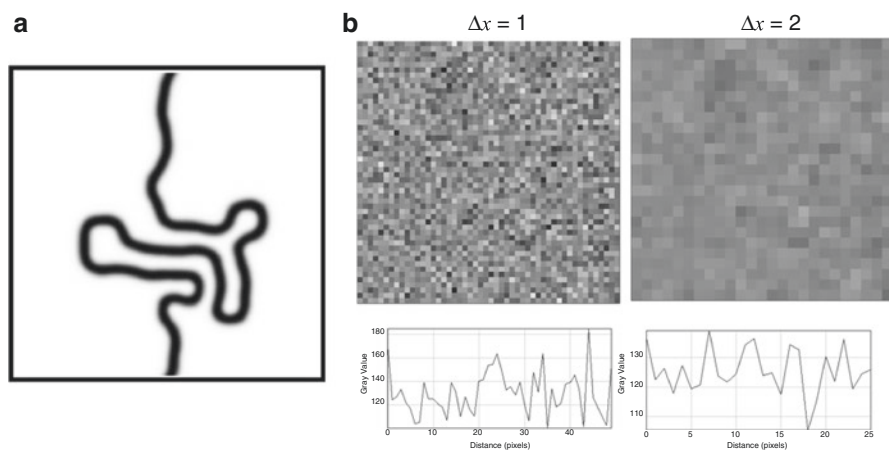


Fig. 10.6 White noise is a special type of fractal structure. (a) Addition of white noise to the PDE system results in a complex fractal structure. (b) If a white noise of small spatial scale ($\Delta x=1$) is observed on a larger spatial scale ($\Delta x=2$) by coarsening, we again obtain a white noise pattern

imaging techniques such as fluorescence recovery after photobleaching and fluorescence correlation spectroscopy [31]. Unfortunately, we lack consensus on the single most important molecule in this system, so diffusible signaling molecules are treated collectively. New molecules that are crucial for pattern formation may be identified in the future. The mechanics model [45] requires the mechanical properties of suture tissue, which may be measurable using atomic force microscopy. At present, the mechanism of fractal pattern formation remains unclear and must be elucidated in further experimental study.

10.4.3 Fractal Suture Analysis and Craniosynostosis in a Clinical Setting

The relationship between fractal dimension and craniosynostosis can be determined in a PDE framework. In general, lowering the effect of the signaling molecule v promotes curvature in the PDE model. Conversely, increasing the effect of the signaling molecule in the PDE model should induce craniosynostosis. Therefore, craniosynostosis development may be negatively correlated with the degree of curvature. The degree of interdigitation can be estimated from the amplitude of the winding pattern. However, an easier approach is to measure the fractal dimension using the box count method. Therefore, the fractal dimension provides a simple diagnostic tool for craniosynostosis.

References

1. Anton SC, Jaslow CR, Swartz SM. Sutural complexity in artificially deformed human (*Homo sapiens*) crania. *J Morphol*. 1992;214(3):321–32.
2. Antonopoulou I, Mavrogiannis LA, Wilkie AOM, Morriss-Kay GM. *Alx4* and *Msx2* play phenotypically similar and additive roles in skull vault differentiation. *J Anat*. 2004;204(6):487–99.
3. Bialek P, Kern B, Yang X, Schrock M, Sosic D, Hong N, Wu H, Yu K, Ornitz DM, Olson EN, Justice MJ, Karsenty G. A twist code determines the onset of osteoblast differentiation. *Dev Cell*. 2004;6(3):423–35.
4. Byron CD, Borke J, Yu J, Pashley D, Wingard CJ, Hamrick M. Effects of increased muscle mass on mouse sagittal suture morphology and mechanics. *Anat Rec A Discov Mol Cell Evol Biol*. 2004;279A(1):676–84.
5. Cohen MM, MacLean RE. Craniosynostosis. Diagnosis, evaluation, and management. Oxford University Press, Oxford. 2000.
6. Di Ieva A, Bruner E, Davidson J, Pisano P, Haider T, Stone SS, Cusimano MD, Tschabitscher M, Grizzi F. Cranial sutures: a multidisciplinary review. *Childs Nerv Syst*. 2013;29(6):893–905.
7. Drake R, Vogl W, Mitchell A. Gray's anatomy for students. Churchill Livingstone, Elsevier, Philadelphia, PA. 2014.
8. Eden M. A two-dimensional growth process. *Proc Fourth Berkeley Symp on Math Statist and Prob*. 1961;4:223–39.
9. Gibert J, Palmqvist P. Fractal analysis of the Orce skull sutures. *J Hum Evol*. 1995;28(6):561–75.

10. G'orski AZ, Skrzat J. Error estimation of the fractal dimension measurements of cranial sutures. *J Anat.* 2006;208(3):353–9.
11. Holleville N, Quilhac A, Bontoux M, Monsoro-Burq AH. BMP signals regulate *Dlx5* during early avian skull development. *Dev Biol.* 2003;257(1):177–89.
12. Iseki S, Wilkie AO, Morriss-Kay GM. *Fgfr1* and *Fgfr2* have distinct differentiation- and proliferation-related roles in the developing mouse skull vault. *Development.* 1999;126(24):5611–20.
13. Jaslow CR. Mechanical properties of cranial sutures. *J Biomech.* 1990;23(4):313–21.
14. Johnson D, Horsley SW, Moloney DM, Oldridge M, Twigg SR, Walsh S, Barrow M, Njølstad PR, Kunz J, Ashworth GJ, Wall SA, Kearney L, Wilkie AO. A comprehensive screen for TWIST mutations in patients with craniosynostosis identifies a new microdeletion syndrome of chromosome band 7p21.1. *Am J Hum Genet.* 1998;63(5):1282–93.
15. Johnson D, Wilkie AOM. Craniosynostosis. *Eur J Hum Genet.* 2011;19(4):369–76.
16. Kim HJ, Rice DP, Kettunen PJ, Thesleff I. FGF-, BMP- and Shh-mediated signaling pathways in the regulation of cranial suture morphogenesis and calvarial bone development. *Development.* 1998;125(7):1241–51.
17. Long CA. Intricate sutures as fractal curves. *J Morphol.* 1985;185(3):285–95.
18. Long CA, Long JE. Fractal dimensions of cranial sutures and waveforms. *Cells Tissues Organs.* 1992;145(3):201–6.
19. Lynnerup N, Jacobsen JCB. Brief communication: age and fractal dimensions of human sagittal and coronal sutures. *Am J Phys Anthropol.* 2003;121(4):332–6.
20. Masuda Y, Yohro T. Are there any regularities in cranial sutures? *Okajimas Folia Anat Jpn.* 1987;64(1):39.
21. Mehrara BJ, Mackool RJ, McCarthy JG, Gittes GK, Longaker MT. Immunolocalization of basic fibroblast growth factor and fibroblast growth factor receptor-1 and receptor-2 in rat cranial sutures. *Plast Reconstr Surg.* 1998;102(6):1805–17; discussion 1818–20.
22. Miura T, Perlyn CA, Kinboshi M, Ogihara N, Kobayashi-Miura M, Morriss-Kay GM, Shiota K. Mechanism of skull suture maintenance and interdigitation. *J Anat.* 2009;215(6):642–55.
23. Moss ML. Growth of the calvaria in the rat. *Determination Osseous Morph Am J Anat.* 1954;94(3):333–61.
24. Moss ML. Relative growth of the human fetal skeleton, cranial and postcranial. *Ann N Y Acad Sci.* 1955;63:528–36.
25. Moss ML. Experimental alteration of sutural area morphology. *Anat Rec A Discov Mol Cell Evol Biol.* 1957;127(3):569–89.
26. Moss ML. Fusion of the frontal suture in the rat. *Am J Anat.* 1958;102(1):141–65.
27. Moss ML. Rotations of the cranial components in the growing rat and their experimental alteration. *Acta Anat.* 1958;32(1–2):65–86.
28. Moss ML. The pathogenesis of premature cranial synostosis in man. *Acta Anat.* 1959;37:351.
29. Moss ML. Inhibition and stimulation of sutural fusion in the rat calvaria. *Anat Rec A Discov Mol Cell Evol Biol.* 1960;136(4):457–67.
30. Moss ML. Extrinsic determination of sutural area morphology in the rat calvaria. *Acta Anat.* 1961;44(3):263–72.
31. Muller P, Rogers KW, Jordan BM, Lee JS, Robson D, Ramanathan S, Schier AF. Differential diffusivity of nodal and lefty underlies a reaction-diffusion patterning system. *Science (New York, NY).* 2012;336(6082):721–4.
32. Ohta T, Mimura M, Kobayashi R. Higher-dimensional localized patterns in excitable media. *Physica D: Nonlinear Phenomena.* 1989;34(1–2):115–44.
33. Oota Y, Nagamine T, Ono K, Miyazima S. A two-dimensional model for sagittal suture of cranium. *Forma.* 2004;19:197–205.
34. Oota Y, Ono K, Miyazima S. 3D modeling for sagittal suture. *Physica A: Stat Mech Appl.* 2006;359:538–46.
35. Opperman LA, Chhabra A, Nolen AA, Bao Y, Ogle RC. Dura mater maintains rat cranial sutures in vitro by regulating suture cell proliferation and collagen production. *J Craniofac Genet Dev Biol.* 1998;18(3):150–8.

36. Park MH, Shin HI, Choi JY, Nam SH, Kim YJ, Kim HJ, Ryoo HM. Differential expression patterns of Runx2 isoforms in cranial suture morphogenesis. *J Bone Miner Res.* 2001; 16(5):885–92.
37. Rice R, Rice DPC, Olsen BR, Thesleff I. Progression of calvarial bone development requires Foxc1 regulation of Msx2 and Alx4. *Dev Biol.* 2003;262(1):75–87.
38. Rice R, Rice DPC, Thesleff I. Foxc1 integrates Fgf and Bmp signalling independently of twist or noggin during calvarial bone development. *Dev Dyn.* 2005;233(3):847–52.
39. Roth DA, Longaker MT, McCarthy JG, Rosen DM, McMullen HF, Levine JP, Sung J, Gold LI. Studies in cranial suture biology: part I. Increased immunoreactivity for TGF- β isoforms (β 1, β 2, and β 3) during rat cranial suture fusion. *J Bone Miner Res.* 1997;12(3):311–21.
40. Sadler TW. Langman's medical embryology. Baltimore: Lippincott Williams & Wilkins; 2006.
41. Twigg SRF. Mutations of ephrin-B1 (EFNB1), a marker of tissue boundary formation, cause craniofrontonasal syndrome. *Proc Natl Acad Sci U S A.* 2004;101(23):8652–7.
42. Wilkie AO, Slaney SF, Oldridge M, Poole MD, Ashworth GJ, Hockley AD, Hayward RD, David DJ, Pulleyn LJ, Rutland P. Apert syndrome results from localized mutations of FGFR2 and is allelic with crouzon syndrome. *Nat Genet.* 1995;9(2):165–72.
43. Yu JC, Lucas JH, Fryberg K, Borke JL. Extrinsic tension results in FGF-2 release, membrane permeability change, and intracellular Ca⁺⁺ increase in immature cranial sutures. *J Craniofacial Surg.* 2001;12(4):391.
44. Yu JC, Wright RL, Williamson MA, Braselton JP, Abell ML. A fractal analysis of human cranial sutures. *Cleft Palate-Craniofacial J: Off Publ Am Cleft Palate-Craniofac Association.* 2003;40(4):409–15.
45. Zollikofer CPE, Weissmann JD. A bidirectional interface growth model for cranial interosseous suture morphogenesis. *J Anat.* 2011;219(2):100–14.

Chapter 11

The Fractal Geometry of the Human Brain: An Evolutionary Perspective

Michel A. Hofman

Abstract The evolution of the brain in mammals is characterized by changes in size, architecture, and internal organization. Consequently, the geometry of the brain, and especially the size and shape of the cerebral cortex, has changed notably during evolution. Comparative studies of the cerebral cortex suggest that there are general architectural principles governing its growth and evolutionary development. In this chapter some of the design principles and operational modes that underlie the fractal geometry and information processing capacity of the cerebral cortex in primates, including humans, will be explored. It is shown that the development of the cortex coordinates folding with connectivity in a way that produces smaller and faster brains.

Keywords Brain design • Brain evolution • Cerebral cortex • Cortical folding • Fractal geometry • Human brain • Information processing • Primate neocortex • Neural wiring • Neural networks • Primates • Scaling

11.1 Introduction

During the past decades, considerable progress has been made in explaining the evolution of brain size in mammals in terms of physical and adaptive principles (see, e.g., [36, 47, 51, 61, 82]). In addition, a quantitative approach to the comparative morphology of the brain has made it possible to identify and formalize empirical regularities in the diversity of brain design, especially in the geometry of the cerebral cortex (e.g., [12, 13, 32, 35]). Though many aspects of brain evolution still remain unexplained, these comparative investigations, using scaling methods and mathematical models, have provided new insights into the

M.A. Hofman, PhD
Netherlands Institute for Neuroscience, Royal Netherlands Academy of Arts and Sciences,
Meibergdreef 47, Amsterdam 1105 BA, The Netherlands
e-mail: M.Hofman@nin.knaw.nl

evolutionary dynamics of the brain and its morphological constraints. The object of this chapter is to examine some of the design principles and operational modes that underlie the fractal geometry of the cerebral cortex in primates, including humans. It is shown that the development of the cortex coordinates folding with connectivity in a way that produces smaller and faster brains, and it will be argued that there are limits to information processing in a neuron-based system.

11.2 Principles of Brain Evolution

The evolution of the brain in mammals has been accompanied by an internal reorganization as a result of differential growth of its major parts. Consequently, the geometry of the brain, and especially the size and shape of the cerebral cortex, has changed notably since the late Cretaceous [40]. The evolutionary expansion of the cerebral cortex, indeed, is among the most distinctive morphological features of mammalian brains. Particularly in species with large brains, and most notably in great apes and marine mammals, the brain becomes disproportionately composed of neocortex [1, 66, 67, 73] (see Fig. 11.1). The volume of cortical gray matter, for example, expressed as a percentage of total brain volume increases from about 25 % for insectivores to 50 % for humans [23, 31], whereas the relative size of the entire cerebral cortex (including white matter) goes from 40 % in mice to about 80 % in humans [2, 25, 26, 31]. The relative size of the cerebellum, on the other hand, remains constant across phylogenetic groups, occupying about 10–15 % of the total brain mass in different orders [29, 50, 71].

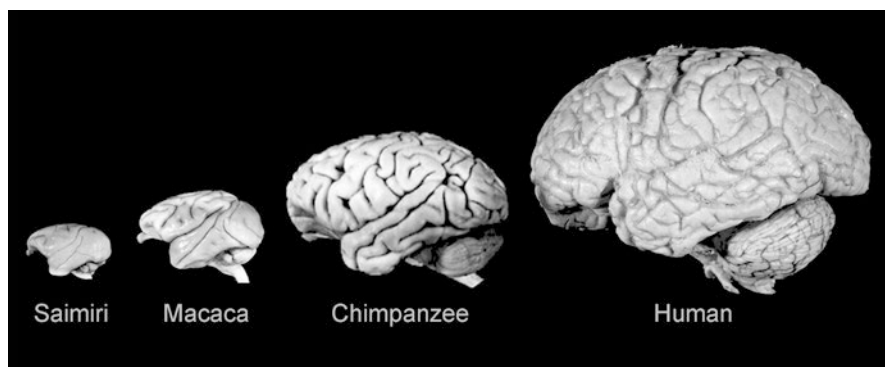


Fig. 11.1 Lateral views of the brains of some anthropoid primates showing the evolutionary expansion of the neocortex. Note the diverse configurations and gyral and sulcal patterns. *Saimiri sciureus*: $E=22$ g; *Macaca mulatta*: $E=95$ g; *Pan troglodytes*: $E=420$ g; *Homo sapiens*: $E=1,350$ g (Reproduced with permission from Hofman [36])

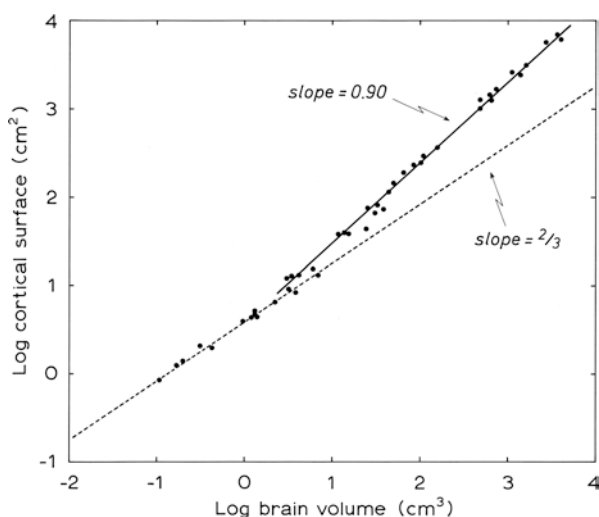
11.2.1 Evolution of the Cerebral Cortex

It is now well established that the cerebral cortex forms as a smooth sheet populated by neurons that proliferate at the ventricular surface and migrate outwards along radial glial fibers (for reviews, see [16, 57]). Differences in the duration of neurogenesis, which increases more rapidly with brain size for the cerebral cortex than for subcortical areas [15, 22, 48], lead to a systematic increase in the ratio of the cortical to subcortical regions. Whereas in small-brained species, the cortical volume expands by virtue of a combined increase in surface area and cortical thickness; the increase of the cortical volume in species with a brain size of more than 3–4 cm³ is almost entirely due to a disproportionate expansion of the cortical surface area [32]. It is the increase of the cortical surface area beyond that expected for geometrically similar objects of different volumes which creates the need to cortical folding [32, 35].

Consequently, the brains of larger species, like primates, are not well described by the ideal constructs of Euclidean geometry. Mandelbrot [52] coined the word “fractal” to identify complex geometric forms and developed the concept of fractal scaling to describe their organized variability. An important feature of fractal objects is that they are invariant, in a statistical sense, over a wide range of scales, a property that is known as scaling (for a review, see [35]).

In mammals with convoluted brains, among which are almost all primates, the cortical surface area, rather than being proportional to the 2/3 power of geometric similarity, is nearly a linear function of brain volume [30, 31] (Fig. 11.2). It means that if a mouse brain (volume = 0.5 cm³) were scaled up as the 2/3 power to the size of the human brain (volume = 1,400 cm³) it would have a cortical surface of only about 480 cm². The actual surface area of the human cortex, however, is about 2,000 cm², which is more than four times larger than would be predicted assuming

Fig. 11.2 Total cortical surface area as a function of brain volume in terrestrial mammals. Logarithmic scale. The slope of the regression line is 0.90 ± 0.012 , representing the surface-volume relationship for convoluted brains. Note that the cortical surface area of species with convoluted brains (area >10 cm²) is nearly a linear function of brain volume, rather than being proportional to the 2/3 power of geometric similarity (Modified with permission from Hofman [33])



geometric similarity, indicating that mammalian brains change their shape by becoming folded as they increase in size.

11.2.2 Mechanisms of Cortical Folding

Bok [5] was among the first comparative neuroanatomists who carefully observed and measured the folding of the human cortex. He cataloged possible geometrical deformations that could emerge in the folding of a layered system, having a radial structure which retained a constant volume during the folding process (Fig. 11.3). Since then several hypotheses about cortical folding have been developed, mainly emphasizing mechanisms *intrinsic* to the cortical gray matter (for reviews, see [3, 32]). Later studies suggest that *extrinsic* factors are more important and that tension along axons in the white matter is the primary driving force for cortical folding [76].

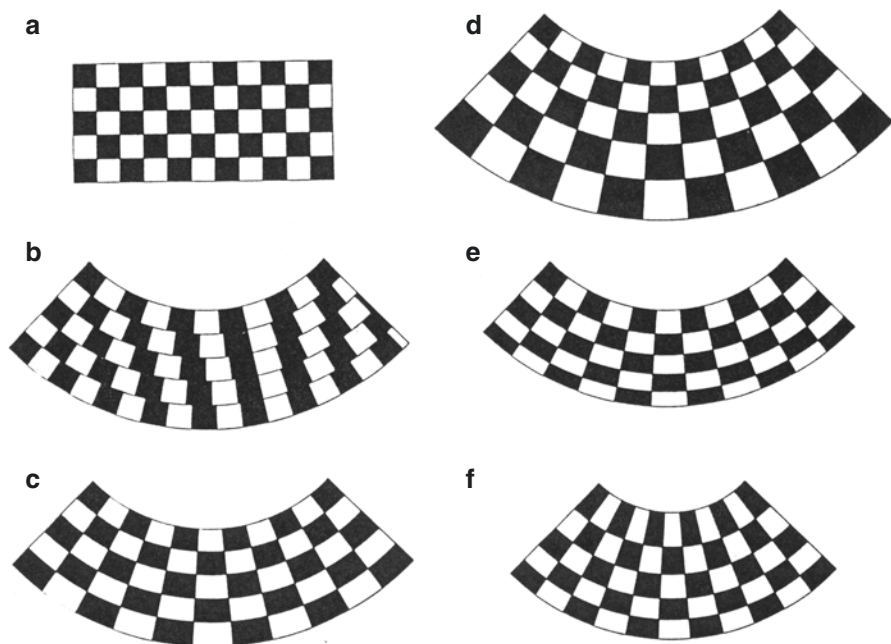


Fig. 11.3 Several ways for a simple pattern to change its intrinsic curvature, in which in each case different properties are maintained (after Bok 1929). In (b) the elements have kept their original form and surface area, in (c) their original arrangement and height, in (d) their original arrangement and form, and in (e) their original arrangement and surface area. In (f), here added to Bok's original series, the elements have kept their original arrangement and surface area, as in figure (e), but here the elements of the center row, instead of those of the inner row, have kept their original form. Although none of the patterns are found in the mammalian cortex *sensu stricto*, the pattern of (f) corresponds most with the transformations found in the geometry of the cerebral cortex during folding (Reproduced with permission from Hofman [32])

By keeping the aggregate length of axonal and dendritic wiring low, tension should contribute to the compactness of neural circuitry throughout the cortex.

Herculano-Houzel and colleagues have found that connectivity and cortical folding are directly related across species and that a simple model based on a white matter-based mechanism may account for increased cortical folding in the primate cerebral cortex [27, 28, 53, 58]. They argue that the mechanical tension generated by the pattern of connectivity of fiber bundles traveling through white matter may account for the observed pattern of cortical surface convolutions. The authors propose the degree of tension, taken as directly proportional to the morphological characteristics of the fiber bundle (i.e., axonal length and average cross-sectional area, and the proportion of efferent neurons), determines how much the cortical surface folds inwards.

This model is used to explain how surface convolutions vary with brain size and how gray matter thickness varies. Thus, the local wiring and cortical folding is a simple strategy that helps to fit the large sheetlike cortex into a compact space and keeps cortical connections short. An important evolutionary advantage of this design principle is that it enables brains to be more compact and faster with increasing size [24, 42].

Although the buckling and folding of curved multilayered surfaces, such as the cortical surface in mammals, has been characterized experimentally, the transitions in folding pattern cannot be reliably predicted by current theoretical models, owing to the nonlinearity of the underlying stretching and bending forces. Recently, Stoop and colleagues [72] presented a theory that builds on general differential-geometry principles and that describes the wrinkling morphology and pattern selection in curved multilayered surfaces. The framework developed in that study enables a systematic classification of wrinkling phenomena in complex geometries, by examining the symmetry properties of effective higher-order differential operators built from the surface metric and film-substrate coupling forces. A comparison to earlier experiments suggests that the theory is universally applicable to microscopic and macroscopic systems, and it therefore may help to contribute to a better understanding of tissue mechanics and morphogenesis of multilayered tissues, including the development of brain convolutions.

11.2.3 Scaling of the Primate Neocortex

Analysis of the cerebral cortex in anthropoid primates revealed that the volume of the neocortex is highly predictable from absolute brain size [32, 35, 83]. The volume of the cortical gray matter, containing local networks of neurons that are wired by dendrites and mostly nonmyelinated axons, is basically a linear function of brain volume, whereas the mass of long-range axons, forming the underlying white matter volume, increases disproportionately with brain size (Fig. 11.4). As a result, the volume of gray matter expressed as a percentage of total brain volume is about the same for all anthropoid primates. The relative white matter volume, on the other

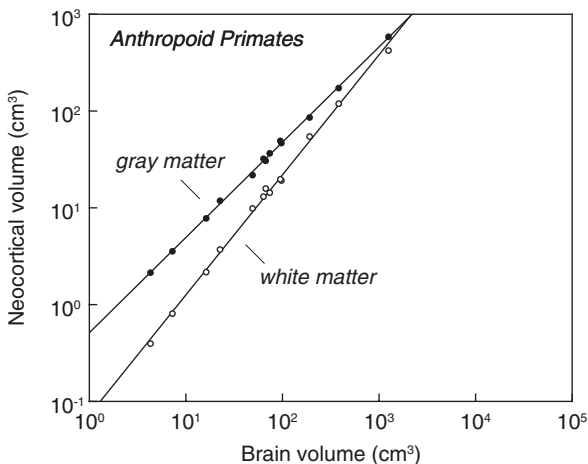


Fig. 11.4 Volumes of cerebral gray and white matter as a function of brain volume in anthropoid primates, including humans. Logarithmic scale. The slopes of the regression lines are 0.985 ± 0.009 (*gray matter*) and 1.241 ± 0.020 (*white matter*). Note the difference in the rate of change between gray matter (neural elements) and white matter (neural connections) as brain size increases (Reproduced with permission from Hofman [34])

hand, increases with brain size, from 9% in pygmy marmosets (*Cebuella pygmaea*) to about 35% in humans, the highest value in primates [32, 36].

Volumetric measurements of gray and white matter in the neocortex of anthropoid primates, furthermore, have shown that the “universal scaling law” of neocortical gray to white matter applies separately for frontal and non-frontal lobes and that changes in the frontal (but not non-frontal) white matter volume are associated with changes in other parts of the brain, including the basal ganglia, a group of subcortical nuclei functionally linked to executive control [65, 68]. These comparative analyses indicate that the evolutionary process of neocorticalization in primates is mainly due to the progressive expansion of the axonal mass that implement global communication, rather than to the increase in the number of cortical neurons and the importance of high neural connectivity in the evolution of brain size in anthropoid primates.

11.3 Fractal Geometry of Convolved Brains

The principal idea underlying scaling is that, although biological systems may evolve by rules distinct from those governing the development of a physical system, they cannot violate basic physical principles. One of the standard problems of classical scaling is that for any series of similar objects the surface area is proportional to the square of a length dimension, whereas the volume is proportional to the cube. According to this geometric principle, also known as Galileo’s principle of

“similitude,” surface area is proportional to the 2/3 power of volume, or in its generalized form

$$\text{Area} = k (\text{Volume})^{D/3} \tag{11.1}$$

where k is a scaling constant and $D=2$, the topological or Euclidean dimension of geometric similarity.

To determine the surface dimension D for mammalian brains, the empirical exponents were related to the generalized surface-volume relation (Eq. 11.1). The allometric equations are given in Table 11.1. The surface dimension of nonconvoluted brains coincides with the Euclidean dimension [30], indicating that mammals with a smooth cerebral cortex satisfy the geometric scaling model, very similar to the spherical surface area of an Euclidean hemisphere, where $\text{area} = 3.84 (\text{volume})^{2/3}$. Convoluted brains, on the other hand, with their surface dimension of $D=2.70 \pm 0.07$, have a fractal dimension far above the expected value of standard dimensional analysis (Table 11.2; see also [19, 20, 33, 35]).

Most studies of the fractal properties of the cerebral cortex have focused on computing whole-brain measures. Recently, King [43] was able to compute the local fractal dimension of the human cortex as extracted from high-resolution MRI scans. It turns out that the local fractal dimension values of the cerebral cortex vary roughly between 2.5 and 3.0, depending on the size of the region over which the counting was performed.

Table 11.1 Allometric scaling of the cerebral cortex against brain volume in mammals with convoluted brains

Covariate	(Sub) orders	Species	Intercept, b	Standard major axis, α (\pm SD)	r
Outer cortical surface area (cm ²)	7	18	4.47	0.726 \pm 0.021	0.994
Total cortical surface area (cm ²)	9	23	3.77	0.901 \pm 0.022	0.994
Mean cortical thickness (cm)	7	16	0.106	0.129 \pm 0.019	0.832
Cortical volume (gray matter, cm ³)	7	16	0.520	0.982 \pm 0.017	0.998
Cortical volume (white matter, cm ³)	7	16	0.046	1.280 \pm 0.045	0.991
Cortical volume (total, cm ³)	9	21	0.396	1.099 \pm 0.028	0.994

Reproduced with permission from Hofman [33]

The model is $\log y = \log b + \alpha \log x$, where x is the variate (i.e., brain volume in cubic centimeters), y is the covariate in centimeter units, $\log b$ is the log-y intercept at $\log x=0$, and α is the slope of the standard major axis. The strength of the relationship is reflected by Pearson’s correlation coefficient, r

Table 11.2 The fractal geometry of convoluted brains

Cortical parameter	Topological dimension	Empirical dimension	Difference (p-value)
Cortical thickness	1	0.39±0.057	<0.001
Outer cortical surface	2	2.18±0.062	<0.02
Total cortical surface	2	2.70±0.065	<0.001
Cortical gray matter	3	2.95±0.050	NS
Cortical white matter	3	3.84±0.134	<0.001
Total cortical volume	3	3.30±0.084	<0.01

Reproduced with permission from Hofman [33]

The model is based on the equation: $y = bx^{D/3}$, where y is the cortical structure, x is brain volume, b is an allometric constant, and D is the topological (Euclidean), respectively, empirical (fractal) dimension of the structure. The fractal dimensions are given as mean ± standard deviation

NS not significant

By Mandelbrot's definition, a fractal is any object or process of which the dimension, given by the equation

$$D = \log N / \log (1/r) \quad (11.2)$$

strictly exceeds its topological or Euclidean dimension. It means that every set with a non-integer D , as in convoluted brains, is a fractal. To derive this formula for dimension, consider a straight line of unit length divided into N segments of length r (r = ratio vector). By definition, $N \times r = 1$ and so $r = 1/N$. Analogously, a unit square contains N pieces of edge length r in an area of 1, so $r = 1/(N^{1/2})$ and a unit cube N pieces of edge length r in a volume of 1, so $r = 1/(N^{1/3})$. Denoting dimension by D , the relationship can be generalized to $r = 1/(N^{1/D})$, and the equation can be solved for the fractal dimension D . Dimension D is called the fractal dimension because it is not necessarily an integer.

In general, D is the number that tells us something about the overall structure and complexity of an object. The empirical area-volume relation, for example, found for convoluted brains indicates that the cortical surface is partly space filling and that its surface area fractally evolves into a volume, or that its volume, by fractal folding, attains the properties of an area [33].

11.3.1 Principles of Scaling

The central idea of the scaling principle is that many fractal forms can be generated by a procedure that replicates the same geometric configuration on every hierarchical level, a property that is known as self-similarity. In order for the exponent of self-similarity to have formal meaning, the sole requirement is that the shape be self-similar, i.e., the whole may be split up into N parts, obtainable from it by a similarity of ratio r (cf. Eq. 11.2).

A number of linear fractals can be represented by an initial polygon (the initiator) and a polygon (the generator), which replaces the sides of the initiator. Thus, a fractal structure could be generated, having the form and fractal dimension of a convoluted brain, by dividing the sides of a regular hexagon into $N=3$ segments of length $r=4/9$ (Fig. 11.5). The resulting similarity dimension, applying Eq. 11.2 gives $D = \log 3 / \log(4/9)^{-1}$, or a number equal to 1.3548. A similar procedure in 3D space, with a decahedron as initiator, yields a fractal dimension of the surface area of 2.7095, a value which is almost identical to the empirical dimension, $D=2.70$, for convoluted brains (see also [19, 32, 44]).

It is clear that specific geometric production rules may lead to the generation of “objects” which show a high resemblance with natural phenomena. However, one cannot conclude that a series of objects with the same fractal dimension belongs to the same class, since several sets of instructions can lead to the same numerical value. In other words, many different objects may have an equal D , but have a completely different appearance. In the next section, some organizing principles will be presented that may account for the fractal geometry of the mammalian brain.

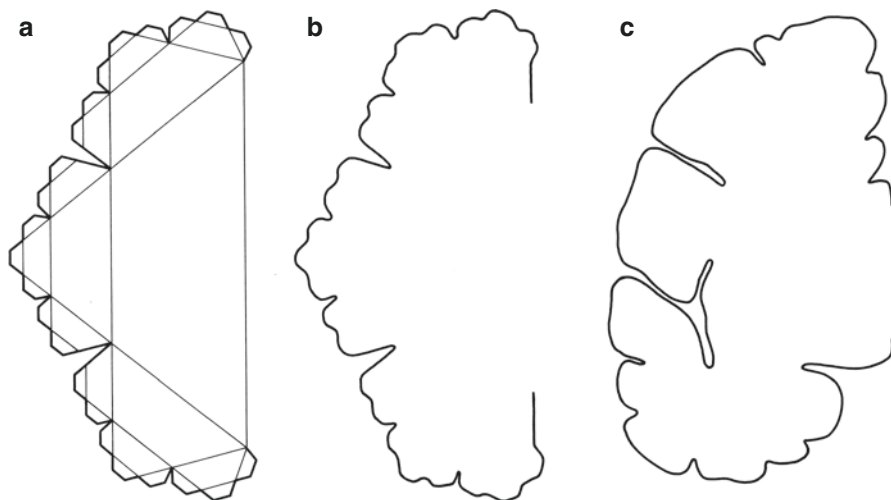


Fig. 11.5 Fractal model of the mammalian cerebral cortex. (a) The form and fractal dimension of a convoluted brain can be generated by dividing the sides of a regular hexagon (initiator) into three segments of length $r=4/9$. Continuing this procedure ad infinitum, it is obvious that the perimeter grows without bound. The resulting similarity dimension is not an integer but a number equal to 1.3548. For further details, see text. (b) The ultimate form cannot, of course, be depicted, but the smoothed third or fourth stage is a good approximation of the form of a highly convoluted brain with its rich pattern of gyri and sulci. (c) Cortical surface of a human hemisphere as seen in a frontal section at the level of the anterior commissure (Reproduced with permission from Hofman [33])

11.3.2 Fractal Scaling of the Neocortex

From anatomical studies we know that the primate neocortex is made up of distinct neural networks, which are organized in columnar arrays stretched out through the depth of the cortex [8, 11, 18, 38, 54, 55]. These modules, in turn, are linked together into larger neural networks by coalescing adjacent sets of columnar units. These networks, which also have a columnar arrangement, are found through the cerebral cortex [48, 57], so that we may consider columnar arrangements of neural elements as a general organizational framework of the primate cortex.

The arrangements of these clusters of neurons in vertical columns perpendicular to the pial surface, however, leads to a geometric dilemma with the evolutionary expansion of the brain. It is this dilemma – the requirement of the cortical surface area to keep abreast with the volumetric growth of the brain itself – which creates the need for cortical folding. Studies in mammals have shown that in species with convoluted brains the mass of interconnective nerve fibers, forming the underlying white matter, is proportional to the 1.28 power of brain volume [31, 33] (see also Table 11.1), meaning that the cortical white matter is a fractal system. As a result, the total cortical surface area (S_{cortex}), including all gyri and sulci, scales approximately as the 2/3 power of the white matter volume (V_{white}) or

$$S_{\text{cortex}} = 36.4 (V_{\text{white}})^{2/3} \quad (11.3)$$

In other words, the surface area of the cerebral cortex, and with that the total number of neuronal columns, is geometrically similar with the amount of white matter, i.e., with the number and length of the interconnective nerve fibers. In small species with nonconvoluted brains, a similar relationship was found between the cortical surface area and the mass of myelinated nerve fibers [33].

Apparently, the fractal geometry of the mammalian brain is a consequence of the design of the cerebral cortex, in which each cortical module, containing a large number of neurons, is connected to its environment by a specific number of axons. Here we have an analogy to Rent's rule for computer geometry [45], which says that the number of components (C) in each module of complex computer circuits is related to the number of terminals (T) according to $T \sim C^{D/D_T}$, where D is the fractal dimension and D_T is the Euclidean dimension. In a spatial circuit, where the components are organized in columnar units, while they are in contact with the outside by their surfaces, as in the cortex, $D_T=3$ and D is somewhere between 2 and 3. The ratio D/D_T increases with the degree of parallelism that is present in the design [45, 52].

Therefore, a fractal dimension of $D=2.70$, as found for convoluted brains, suggests a high degree of parallel processing to take place in the cerebral cortex, especially in highly corticalized mammals, such as monkeys and apes. To reach the state of integral parallelism in which each neural component has its own terminal, the length and number of the interconnective axons must be reduced in order to set limits to the axonal mass.

11.4 Fractal Principles of Neural Wiring

The most obvious problem imposed by large brains is increasing distances among the neuronal somata of functionally related regions and the inevitable lengthening of their essential communication lines, the axons. Importantly, the axonal length and volume increase much more rapidly than the number of neurons. Furthermore, a proportional increase of neurons and connections would inevitably lead to a rapid increase of synaptic path length, defined as the average number of monosynaptic connections in the shortest path between two neurons [9, 69, 79]. To limit the path length with increasing brain size shortcut connections can be inserted, resulting in small-world- and scale-free-type networks [7, 70].

Although such a solution can effectively decrease path length within the neocortex, the increased lengths of the axons and the associated increased travel time of the action potentials still pose serious problems. As compensation for these excessive delays, axon caliber and myelination should be increased [39]. An indication that larger brains deploy both more shortcuts (long-range connections) and larger-caliber axons is that the volume of the white matter increased at $4/3$ power of the volume of gray matter during the course of evolution.

Wen and Chklovskii [81] have shown that the competing requirements for high connectivity and short conduction delay may lead naturally to the observed architecture of the mammalian neocortex. Obviously, the brain functionally benefits from high synaptic connectivity and short conduction delays. A magnetic resonance imaging study, furthermore, focusing specifically on the prefrontal cortex, has shown that the volume of the white matter underlying prefrontal areas is disproportionately larger in humans than in other primates [63]. It suggests that the connective elaboration of the prefrontal cortex, which mediates such important behavioral domains as planning, aspects of language, attention, and social and temporal information processing, has played a key role in human brain evolution.

Although the frontal lobe as a whole has not been differentially enlarged throughout human evolution [64], there is increasing evidence for its reorganization, as some regions with known functional correlates are either bigger or smaller in the human brain than expected when compared with the same region in great apes. Comparative studies, for example, suggest that the human prefrontal cortex differs from that of closely related primate species less in relative size than it does in organization (for a review, see [74]).

Specific reorganizational events in neural circuitry may have taken place either as a consequence of adjusting to increases in size or as adaptive responses to specific selection pressures. It appears that the evolution of the human brain was accompanied by discrete modifications in local circuitry and interconnectivity of selected parts of the brain and that these species-specific adaptations may affect these parts differently [36, 37, 62, 73]. But the similarity in brain design among primates, including humans, indicates that brain systems among related species are internally constrained and that the primate brain could only evolve within the context of a limited number of potential forms.

11.4.1 Neocortical Wiring

In the neocortex, billions of neurons are interconnected via a massive yet highly organized network of axonal and dendritic wiring. This wiring enables both near and distant neurons to coordinate their responses to external stimulation. Specific patterns of cortical activity generated within this network have been found to correlate with cognitive and perceptual functions [77, 78]. Understanding the organizing principles of cortical wiring, therefore, represents a central goal toward explaining human cognition and perception in health and disease. Despite more than a century of endeavor, however, the organizing principles and function of cortical connectivity are still not well understood (see e.g., [4, 6, 21]).

Recent network studies, using diffusion tensor imaging (DTI), have demonstrated that not only the neurons in the neocortex are structurally and functionally highly organized, but that it also holds for the wiring of the entire brain [75, 80]. The interconnecting white matter axonal pathways are not a mass of tangled wires, as thought for a long time, but they form a rectilinear three-dimensional grid continuous with the three principal axes of development. The topology of the brain's long-range communication network looks like a 3D chessboard with a number of highly connected neocortical and subcortical hub regions. Structural connectivity networks, as defined by DTI, have identified a common hub in the medial parietal cortex of humans, chimpanzees, and macaque monkeys. However, the apparent lack of medial prefrontal hubs in humans that are present in chimpanzees and macaque monkeys, coupled with evidence of increased gyrification in human prefrontal cortex, suggests important evolutionary changes in the connectivity of human prefrontal cortex ([49, 56], for a review, see [59]).

The competing requirements for high connectivity and short conduction delay may lead naturally to the observed architecture of the human neocortex. Obviously, the brain functionally benefits from high synaptic connectivity and short conduction delays. The design of the primate brain is such that it may perform a great number of complex functions with a minimum expenditure of energy and material both in the performance of the functions and in the construction of the system. In general, there will be a number of adequate designs for an object, which, for practical purposes, will all be equivalent.

11.4.2 Neural Network Communication

We have shown that in species with convoluted brains, the fraction of mass devoted to wiring seems to increase much slower than that needed to maintain a high degree of connectivity between the neural networks [35]. These findings are in line with a model of neuronal connectivity, which says that as brain size increases there must be a corresponding fall in the fraction of neurons with which any neuron communicates directly. The reason for this is that if a fixed percentage of interconnections is

maintained in the face of increased neuron number, then a large fraction of any brain size increase would be spent maintaining such degree of wiring, while the increasing axon length would reduce neural computational speed [60]. The human brain, for example, has an estimated interconnectivity of the order of 10^3 , based on data about the number of modular units and myelinated nerve fibers [35]. This implies that, on average, each cortical module is connected to a thousand other modules, and that the mean number of processing steps, or synapses, in the path interconnecting these modules, is about two.

In a binary system, with an interconnectivity of $I=1$, the growth of connections (C) is a linear function of the number of units (U), and in a fully connected network, where $I=U$, both variables are related according to the equation: $C=U(U-1)$, which is nearly equivalent to $C=U^2$. In such a system, the number of connections increases much faster than the number of units (Fig. 11.6). Generally, the growth of connections to units is a factorial function of the number of units in a fully connected network and a linear function of the number of units in a minimally connected network. The human cerebral cortex, with an estimated interconnectivity of about 10^3 , lies somewhere between these extremes, and close to the line for $I=U^{0.5}$. It implies that in humans the number of myelinated axons scales to the 1.5 power of

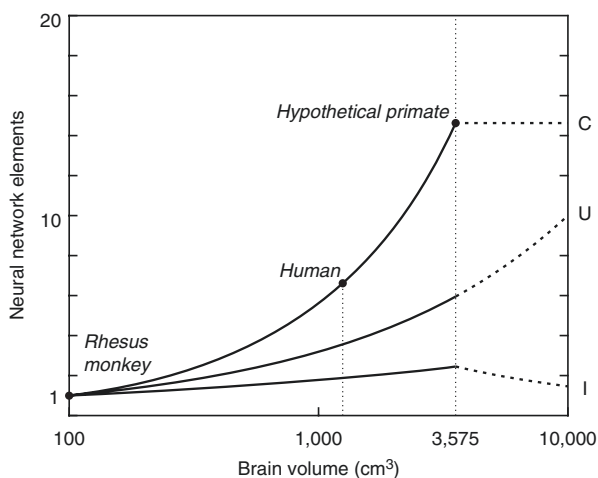


Fig. 11.6 The number of connections (C), cortical processing units (U), and level of interconnectivity (I) in the primate neocortex as a function of brain size. Semilogarithmic scale. Values are normalized to one at a brain volume of 100 cm^3 , the size of a monkey brain. Note that the number of myelinated axons increases much faster than the number of cortical processing units. The human cerebrum, for example, contains six times more myelinated axons than that of a rhesus monkey, whereas the number of cortical processing units is only three times larger. Dashed lines show the potential evolutionary pathway of these neural network elements in primates with very large brains, i.e., beyond the hypothetical upper limit of the brain’s processing power (see text and Hofman [34, 35]). Note that a further exponential growth in the number of cortical processing units, without an increase in the number of connections, will lead to a decrease in connectivity between these units and thus to more local wiring (Reproduced with permission from Hofman [35])

the number of modular processing units, that is, a fourfold increase in modular units requires an eightfold increase in the number of nerve fibers [34, 35].

Herculano-Houzel et al. [28], furthermore, have shown that in primates the mass of the white matter scales linearly across species with its number of nonneuronal cells, which is expected to be proportional to the total length of myelinated axons in the white matter. Decreased connectivity in the brain is compatible with previous suggestions that neurons in the cerebral cortex are connected as small-world and scale-free networks which slow down the increase in global conduction delay in cortices with larger numbers of neurons [4, 69, 70, 78].

11.4.3 *Limits to Information Processing*

The primate cortex, as we have seen, has evolved from a set of underlying structures that constrain its size and the amount of information it can store and process. Therefore, the functional capacity of a neuronal structure is inherently limited by its neural architecture and signal processing time (see e.g., [14, 35, 46]).

The processing or transfer of information across cortical regions, rather than within regions, in large-brained species can be only achieved by reducing the length and number of the interconnective axons in order to set limits to the axonal mass. The *number* of fibers can be reduced by compartmentalization of neurons into modular circuits in which each module, containing a large number of neurons, is connected to its neural environment by a small number of axons. The *length* of the fibers can be reduced by folding the cortical surface and thus shortening the radial and tangential distances between brain regions. Local wiring – preferential connectivity between nearby areas of the cortex – is a simple strategy that helps keep cortical connections short. In principle, efficient cortical folding could further reduce connection length, in turn, reducing white matter volume and conduction times [9, 10, 17, 35]. Thus, the development of the cortex does seem to coordinate folding with connectivity in a way that could produce smaller and faster brains.

Once the brain has grown to a point where the bulk of its mass is in the form of connections, then further increases (as long as the same ratio in interconnectivity is maintained) will be unproductive. Increases in number of units will be balanced by decreased performance of those units due to the increased conduction time. Model studies of the neocortex growth in primates at different brain sizes, using a conservative scenario, revealed that with a brain size of about 3,500 cm³ the total volume of the subcortical areas (i.e., cerebellum, brain stem, diencephalon, etc.) reaches a maximum value [34, 36]. Increasing the size of the brain beyond that point, following the same design principle, would lead to a further increase in the size of the neocortex, but to a reduction of the subcortical volume. Consequently, primates with very large brains (e.g., over 5 kg) may have a declining capability for neuronal integration despite their larger number of cortical neurons.

This architectural dilemma explains why large-brained primates, in order to maintain processing capacity, tend to show more specialization in the neocortex.

Indeed, an increase in the number of distinct cortical areas with increasing brain size has been reported [41, 73]. It may also explain why large-brained species may develop some degree of brain lateralization as a direct consequence of size. If there is evolutionary pressure on certain functions that require a high degree of local processing and sequential control, such as linguistic communication in human brains, these will have a strong tendency to develop in one hemisphere.

11.5 Concluding Remarks

The evolution of the cerebral cortex in mammals is mainly characterized by the development and multiplication of clusters of neurons which are strongly interconnected and in physical proximity. Since these clusters of neurons are organized in vertical columns, an increase in the number and complexity of these neuronal networks will be reflected by an expansion of the cortical surface area beyond that expected for geometric similar brains. As a result, the cortical surface area fractally evolves into a volume with increasing brain size.

It appears that the potential for brain evolution results from the self-similar compartmentalization and hierarchical organization of neural circuits and from the invention of fractal folding, which reduces the interconnective axonal distances. The competing requirements for high connectivity and short conduction delay may lead naturally to the observed architecture of the brain. The similarity in brain design among mammals furthermore indicates that brain systems among related species are internally constrained and that the brain could only evolve within the context of a limited number of potential forms.

References

1. Aboitiz F, Montiel JF. From tetrapods to primates: conserved developmental mechanisms in diverging ecological adaptations. *Prog Brain Res.* 2012;195:3–24.
2. Azevedo FAC, Carvalho LRB, Grinberg LT, Farfel JM, Ferretti REI, Leite REP, Filho WJ, Lent R, Herculano-Houzel S. Equal numbers of neuronal and nonneuronal cells make the human brain an isometrically scaled-up primate brain. *J Comp Neurol.* 2009;513:532–41.
3. Bayly PV, Taber LA, Kroenke CD. Mechanical forces in the cerebral cortical folding: a review of measurements and models. *J Mech Behav Biomed Mater.* 2014;29:568–81.
4. Bohland JW, Wu C, Barbas H, Bokil H, Bota M, Breiter HC et al. A proposal for a coordinated effort for the determination of brainwide neuroanatomical connectivity in model organisms at a mesoscopic scale. *PLoS Comput Biol.* 2009;5:e1000334.
5. Bok ST. Der Einfluss der in den Furchen und Windungen auftretenden Krümmungen der Grosshirnrinde auf die Rindenarchitektur. *Z Ges Neurol Psychiat.* 1929;121:682–750.
6. Budd J, Kisvárdy ZF. How do you wire a brain? *Front Neuroanat.* 2013;7:14.
7. Bullmore E, Sporns O. The economy of brain network organization. *Nat Rev Neurosci.* 2012;13:336–49.
8. Buxhoeveden DP. Minicolumn size and human cortex. *Prog Brain Res.* 2012;195:219–35.

9. Buzsáki G, Logothetis N, Singer W. Scaling brain size, keeping time: evolutionary preservation of brain rhythms. *Neuron*. 2013;80:751–64.
10. Casanova MF. White matter volume increase and minicolumns in autism. *Ann Neurol*. 2004;56:453.
11. Casanova MF. Cortical organization: a description and interpretation of anatomical findings based on systems theory. *Transl Neurosci*. 2010;1:62–71.
12. Changizi MA. Principles underlying mammalian neocortical scaling. *Biol Cybern*. 2001;84:207–15.
13. Changizi MA. Scaling the brain and its connections. In: Kaas JH, editor. *Evolution of nervous systems*, vol. 3. New York: Academic; 2007. p. 167–80.
14. Changizi MA, Shimojo S. Parcellation and area-area connectivity as a function of neocortex size. *Brain Behav Evol*. 2005;66:88–98.
15. Charvet CJ, Finlay B. Embracing covariation in brain evolution: large brains, extended development, and flexible primate social systems. *Prog Brain Res*. 2012;195:71–87.
16. Cheung AF, Pollen AA, Tavare A, DeProto J, Molnár Z. Comparative aspects of cortical neurogenesis in vertebrates. *J Anat*. 2007;211:164–76.
17. Chklovskii DB, Mel BW, Svoboda K. Cortical rewiring and information storage. *Nature*. 2004;431:782–8.
18. Da Costa NM, Martin KAC. Whose cortical column would that be? *Front Neuroanat*. 2010;4:16.
19. Di Ieva A, Grizzi F, Jelinek H, Pellionisz AJ, Losa GA. Fractals in the neurosciences, part I: general principles and basic neurosciences. *Neuroscientist*. 2013;20:403–17.
20. Di Ieva A, Esteban FJ, Grizzi F, Klonowski W, Martín-Landrove M. Fractals in the neurosciences, part II: clinical applications and future perspectives. *Neuroscientist*. 2015;21:30–43.
21. Douglas RJ, Martin KA. Neuronal circuits of the neocortex. *Ann Rev Neurosci*. 2004;27:419–51.
22. Finlay BL, Uchiyama R. Developmental mechanisms channeling cortical evolution. *Trends Neurosci*. 2015;38:69–76.
23. Frahm HD, Stephan H, Stephan M. Comparison of brain structure volumes in Insectivora and Primates. Part I. Neocortex. *J Hirnforsch*. 1982;23:375–89.
24. Harrison KH, Hof PR, Wang SS-H. Scaling laws in the mammalian neocortex: does form provide clues to function? *J Neurocytol*. 2002;31:289–98.
25. Herculano-Houzel S. The human brain in numbers: a linearly scaled-up primate brain. *Front Hum Neurosci*. 2009;3:31.
26. Herculano-Houzel S. Neuronal scaling rules for primate brains: the primate advantage. *Prog Brain Res*. 2012;195:325–40.
27. Herculano-Houzel S, Collins CE, Wong P, Kaas JH, Lent R. The basic nonuniformity of the cerebral cortex. *Proc Natl Acad Sci U S A*. 2008;105:12593–8.
28. Herculano-Houzel S, Mota B, Wong P, Kaas JH. Connectivity-driven white matter scaling and folding in primate cerebral cortex. *Proc Natl Acad Sci U S A*. 2010;107:19008–13.
29. Herculano-Houzel S, Manger PR, Kaas JH. Brain scaling in mammalian evolution as a consequence of concerted and mosaic changes in numbers of neurons and average neuronal cell size. *Front Neuroanat*. 2014;8:77.
30. Hofman MA. Size and shape of the cerebral cortex in mammals. Part I. The cortical surface. *Brain Behav Evol*. 1985;27:28–40.
31. Hofman MA. Size and shape of the cerebral cortex in mammals. Part II. The cortical volume. *Brain Behav Evol*. 1988;32:17–26.
32. Hofman MA. On the evolution and geometry of the brain in mammals. *Prog Neurobiol*. 1989;32:137–58.
33. Hofman MA. The fractal geometry of convoluted brains. *J Hirnforsch*. 1991;32:103–11.
34. Hofman MA. Brain evolution in hominids: are we at the end of the road. In: Falk D, Gibson KR, editors. *Evolutionary anatomy of the primate cerebral cortex*. Cambridge: Cambridge University Press; 2001. p. 113–27.

35. Hofman MA. Design principles of the human brain: an evolutionary perspective. *Prog Brain Res.* 2012;195:373–90.
36. Hofman MA. Evolution of the human brain: when bigger is better. *Front Neuroanat.* 2014;8:15.
37. Hofman MA. Evolution of the human brain and intelligence: from matter to mind. In: Goldstein S, Naglieri JA, Princiotta D, editors. *Handbook of intelligence: evolutionary theory, historical perspective and current concepts.* Berlin: Springer; 2015. p. 65–82.
38. Innocenti GM, Vercelli A. Dendritic bundles, minicolumns, columns, and cortical output units. *Front Neuroanat.* 2010;4:11.
39. Innocenti GM, Vercelli A, Caminiti R. The diameter of cortical axons depends both on the area of origin and target. *Cereb Cortex.* 2013;24:2178–88.
40. Jerison HJ. *Evolution of the brain and intelligence.* New York: Academic; 1973.
41. Kaas JH. The evolution of neocortex in primates. *Prog Brain Res.* 2012;195:91–102.
42. Karbowski J. How does connectivity between cortical areas depend on brain size? Implications for efficient computation. *J Comput Neurosci.* 2003;15:347–56.
43. King RD. Computation of local fractal dimension values of the human cerebral cortex. *Appl Math.* 2014;5:1733–40.
44. Kiselev VG, Hahn KR, Auer DP. Is the brain cortex a fractal? *Neuroimage.* 2003;20:1765–74.
45. Landman BS, Russo RL. On a pin versus block relationship for partitions of logic graphs. *IEEE Trends Comput.* 1971;20:1469–79.
46. Laughlin SB, Sejnowski TJ. Communication in neural networks. *Science.* 2003;301:1870–4.
47. Lefebvre L. Primate encephalization. *Prog Brain Res.* 2012;195:393–412.
48. Lewitus E, Keleva I, Kalinka AT, Tomancak, Huttner WB. An adaptive threshold in mammalian neocortical evolution. *PLoS Biol.* 2014;12:e1002000, 1–15.
49. Li L, Hu X, Preuss TM, Glasser MF, Damen FW, Qiu Y, Rilling JK. Mapping putative hubs in human, chimpanzee and rhesus macaque connectomes via diffusion tractography. *Neuroimage.* 2013;80:462–74.
50. MacLeod C. The missing link: evolution of the primate cerebellum. *Prog Brain Res.* 2012;195:165–87.
51. Macphail EM, Bolhuis JJ. The evolution of intelligence: adaptive specializations versus general process. *Biol Rev.* 2001;76:341–64.
52. Mandelbrot BB. *The fractal geometry of nature.* San Francisco: Freeman; 1982.
53. Mota B, Herculano-Houzel S. How the cortex gets its folds: an inside-out, connectivity-driven model for the scaling of mammalian cortical folding. *Front Neuroanat.* 2012;6:3.
54. Mountcastle VB. The columnar organization of the brain. *Brain.* 1997;120:701–22.
55. Opris I, Casanova MF. Prefrontal cortical minicolumn: from executive control to disrupted cognitive processing. *Brain.* 2014;137:1863–75.
56. Preuss TM. The human brain: rewired and running hot. *Ann NY Acad Sci.* 2011;1125(S1):E183–91.
57. Rakic P. Evolution of the neocortex: a perspective from developmental biology. *Nat Rev Neurosci.* 2009;10:724–35.
58. Ribeiro PFM, Ventura-Antunes L, Gabi M, Mota B, Grinberg LT, Farfel JM, et al. The human cerebral cortex is neither one nor many: neuronal distribution reveals two quantitative different zones in the gray matter, three in the white matter, and explains local variations in cortical folding. *Front Neuroanat.* 2013;7:28.
59. Rilling JK. Comparative primate neuroimaging: insights into human brain evolution. *Trends Cogn Sci.* 2014;18:45–55.
60. Ringo JL, Doty RW, Demeter S, Simard PY. Time is of the essence: a conjecture that hemispheric specialization arises from interhemispheric conduction delay. *Cereb Cortex.* 1994;4:331–43.
61. Roth G, Dicke U. Evolution of the brain and intelligence in primates. *Prog Brain Res.* 2012;195:413–30.

62. Schoenemann PT. Evolution of the size and functional areas of the human brain. *Ann Rev Anthropol.* 2006;35:379–406.
63. Schoenemann PT, Sheehan MJ, Glotzer ID. Prefrontal white matter volume is disproportionately larger in humans than in other primates. *Nat Neurosci.* 2005;8:242–52.
64. Semendeferi K, Damasio H. The brain and its main anatomical subdivisions in living hominoids using magnetic resonance imaging. *J Hum Evol.* 2000;38:317–32.
65. Sherwood CC, Smaers J. What's the fuss over human frontal lobe evolution? *Trends Cogn Sci.* 2013;17:432–3.
66. Sherwood CC, Bauernfeind AL, Bianchi S, Raghanti MA, Hof PR. Human brain evolution writ large and small. *Prog Brain Res.* 2012;195:237–54.
67. Smaers JB, Soligo C. Brain reorganization, not relative brain size, primarily characterizes anthropoid brain evolution. *Proc R Soc B.* 2013;280:20130269.
68. Smaers JB, Schleicher A, Zilles K, Vinicius L. Frontal white matter volume in anthropoid primates. *PLoS One.* 2010;5:e9123.
69. Sporns O, Chilavo DR, Kaiser M, Hilgetag CC. Organization, development and function of complex brain networks. *Trends Cogn Sci.* 2004;8:418–25.
70. Sporns O, Honey CJ, Kötter R. Identification and classification of hubs in brain networks. *PLoS One.* 2007;2:e1049, 1–14.
71. Stephan H, Frahm HD, Baron G. New and revised data on volumes of brain structures in insectivores and primates. *Folia Primatol.* 1981;35:1–29.
72. Stoop N, Lagrange R, Terwage D, Reis PM, Dunkel J. Curvature-induced symmetry breaking determines elastic surface patterns. *Nat Mater.* 2015;14:337–42.
73. Striedter GF. *Principles of brain evolution.* Sunderland: Sinauer Associates; 2004.
74. Teffer K, Semendeferi K. Human prefrontal cortex: evolution, development, and pathology. *Prog Brain Res.* 2012;195:191–218.
75. Van den Heuvel MP, Sporns O. Rich-club organization of the human connectome. *J Neurosci.* 2011;31:15775–86.
76. Van Essen DC. A tension-based theory of morphogenesis and compact wiring in the central nervous system. *Nature.* 1997;385:313–8.
77. Wang SS-H, Shultz JR, Burish MJ, Harrison KH, Hof PR, Towns LC, Wagers MW, Wyatt KD. Functional trade-offs in white matter axonal scaling. *J Neurosci.* 2008;28:4047–56.
78. Wang X-J. Neurophysiological and computational principles of cortical rhythms in cognition. *Physiol Rev.* 2010;90:1195–268.
79. Watts DJ, Strogatz SH. Collective dynamics of 'small-world' networks. *Nature.* 1998;393:440–2.
80. Wedeen VJ, Rosene DL, Wang R, Dai G, Mortazavi F, Hagmann P, Kaas JH, Tseng WY. The geometric structure of the brain fiber pathway. *Science.* 2012;335:1628–38.
81. Wen Q, Chklovskii DB. Segregation of the brain into gray and white matter: a design minimizing conduction delays. *PLoS Comp Biol.* 2005;1:e78:617–630.
82. Willemet R. Reconsidering the evolution of brain, cognition, and behavior in birds and mammals. *Front Psychol.* 2013;4:396.
83. Zhang K, Sejnowski TJ. A universal scaling law between gray matter and white matter of cerebral cortex. *Proc Natl Acad Sci U S A.* 2000;97:5621–6.

Part III
Fractals in Clinical Neurosciences

Chapter 12

Fractal Analysis in Clinical Neurosciences: An Overview

Antonio Di Ieva

Abstract Over the last years, fractals have entered into the realms of clinical neurosciences. The whole brain and its components (i.e., neurons and microglia) have been studied as fractal objects, and even more relevant, the fractal-based quantification of the geometrical complexity of histopathological and neuroradiological images as well as neurophysiopathological time series has suggested the existence of a gradient in the patterns representation of neurological diseases. Computational fractal-based parameters have been suggested as potential diagnostic and prognostic biomarkers in different brain diseases, including brain tumors, neurodegeneration, epilepsy, demyelinating diseases, cerebrovascular malformations, and psychiatric disorders as well. This chapter and the entire third section of this book are focused on practical applications of computational fractal-based analysis into the clinical neurosciences, namely, neurology and neuropsychiatry, neuroradiology and neurosurgery, neuropathology, neuro-oncology and neurorehabilitation, and neuro-ophthalmology and cognitive neurosciences, with special emphasis on the translation of the fractal dimension as clinical biomarker useful from bench to bedside.

Keywords Biomarker • Classifier • Fractal analysis • Fractal dimension • Brain tumor • Epilepsy • Neurodegeneration • Aneurysm • Arteriovenous malformation • Electroencephalography • Neuroimaging • Neurology • Neuro-ophthalmology • Cognitive neurosciences • Psychiatry

A. Di Ieva, MD, PhD
Neurosurgery Unit, Faculty of Medicine and Health Sciences, Macquarie University,
Sydney, NSW, Australia

Garvan Institute of Medical Research, Sydney, NSW, Australia

Medical University of Vienna, Vienna, Austria

University of Toronto, Toronto, ON, Canada

e-mail: diieva@hotmail.com

To see is to believe

Data on the specific fractal characteristics of distinct biological systems (in both physiological and pathological states) accumulate daily. The researches in the field have two specific aims: (1) finding the geometrical fingerprint which characterizes each physical and biological system and (2) looking for the quantitative parameters which could be helpful to distinguish different physiopathological states (e.g., normal tissue versus cancer).

The greatest promise of fractal analysis is that it offers objective measures of seemingly random structures, and it is a tool for examining the mechanistic origins of pathological forms [1].

Since the first applications of fractal analysis to biological images [5, 6], it has been clear that such a computational-based method can help recognize and quantify patterns to suggest potential diagnostic and prognostic biomarkers. Fractal analysis has been shown to be able to characterize the complexity of images, or “more precisely their texture composition” [19]. The quantification of the geometrical complexity of histopathological and neuroradiological images as well as neurophysiopathological time series suggests the existence of a gradient in the pattern’s representation and networks from those in the normal brain to those affected by pathologies (e.g., brain tumors, epilepsy, dementia). For such a reason, fractal analysis has found large applications in the clinical neurosciences, as briefly summarized in this chapter and illustrated in the following chapters of the third section of this book. Limitations of the translational applications of fractals into clinical practice are discussed at the end of this chapter.

12.1 Clinical Neurology and Cerebrovascular System

The fractal dimension (FD) and other complementary parameters have been investigated to characterize the topological complexity of the brain in its entire physiopathological spectrum.

In Chap. 13, *Francisco Esteban, Leticia Beltrán, and Antonio Di Ieva* review the main applications of the computational fractal-based analysis for the study of several neurological conditions, with special emphasis on the diagnostic precision of the FD. In consideration of the close relationship of the eye to the brain and neurological diseases, a specific chapter is focused on the application of fractal analysis into neuro-ophthalmology (Chap. 28 by *Giorgio Bianciardi, Maria Latronico, and Claudio Traversi*).

The fractal dimension has been proposed as a potential surrogate biomarker of the degree of brain damage in neurodegenerative diseases, and even in the normal cerebral aging process [7], as widely illustrated from the neuroimaging point of view by *Luduan Zhang and Guang Yue* in Chap. 14 and more from the neuropathology perspective by *Daniel Pirici, Laurentiu Mogoanta, Daniela Ion, and Samir Kumar-Singh* in Chap. 15.

The vascular tree of the brain has also been characterized by means of its fractal features, not only from its angiostructural point of view but also in its functionality. The spatiotemporal complexity of cerebral hemodynamics has in fact been studied by means of fractal characterization [4, 15, 20, 26, 28, 34]. Although there is speculation about the fractality, pseudo-fractality, or multifractality of vascular trees [31, 35–37], the fractal-based morphometrics of the vascular and microvascular networks of the brain has been used to find morphometric image markers. The fractal-based analyses of the cerebrovascular system physiopathology are discussed by *Martin Soehle* in Chap. 16, with special emphasis on the subarachnoid hemorrhage. In regard to cerebrovascular pathologies, *Gábor Závodszy*, *György Károlyi*, *István Szikora*, and *György Paál* illustrate their intriguing researches on the fractality and chaotic patterns in the hemodynamics of intracranial aneurysms in Chap. 17, while *Antonio Di Ieva* and *Gernot Reishofer* apply computational fractal-based modeling to the analysis of the brain arteriovenous malformations in Chap. 18, proposing new image and prognostic biomarkers of such pathologies.

12.2 Neuroimaging

Brain imaging was first revolutionized by the clinical application of angiograms, ultrasound, and computed tomography (CT) followed by magnetic resonance imaging (MRI), positron emission tomography (PET), and single-photon emission computed tomography (SPECT) later on. MRI is the most widely used technique in neuroimaging to characterize the structure (structural imaging) and even the function (functional imaging, by means of functional MRI, fMRI) of the nervous system, which completely revolutionized the clinical neurosciences (e.g., neurology, psychiatry, and neurosurgery) for patient management. Different MR images can be obtained by selecting the pulse sequences (e.g., T1, T2, and proton density images), used to differentiate gray matter, white matter, and cerebrospinal fluid, as well as the different pathological conditions. Fractal analysis has been shown to be appropriate for the analysis of MR images, including fMRI biosignals. Functional MRI allows for investigation of the amplitude of activation in neural networks of brain, and the fractal-based time-series analysis is successfully used to identify the process of dysregulation of dynamic interactions between different brain regions in healthy adults versus pathological states [3, 25].

In Chap. 19, *Salim Lahmiri*, *Mounir Boukadoum*, and *Antonio Di Ieva* offer an excursus on the use of the fractal dimension and the related Hurst exponent in the characterization of several pathologies in neuroimaging, with special emphasis on the MR image classification. The application of a relatively novel MR imaging sequence, the susceptibility-weighted imaging (SWI) into neuro-oncology (also with some perspectives in neurotraumatology), is then presented by *Antonio Di Ieva* in Chap. 20. The chapters regarding neuroimaging bridge the discussion toward the application of fractals to the analysis of brain tumors, as illustrated by *Syed Reza*, *Atiq Islam*, and *Khan Iftekharuddin* in Chap. 21, in which the fractal-based classification and texture estimation for MRI brain tumors features are presented.

12.3 Neurohistology, Neuropathology, and Neuro-oncology

As stated by Baish and Jain in 2000, “By focusing on the irregularity of tumor growth rather than on a single measure of size such as diameter or volume, fractal geometry is well suited to quantify those morphological characteristics that pathologists have long used in a qualitative sense to describe malignancies – their ragged border with the host tissue and their seemingly random patterns of vascular growth” [1]. Cancer has been often described as a complex, chaotic, and heterogeneous system, emerging from the disruption of tissue architecture, which begs the question “If heterogeneous, how much?”; Fractal analysis responds by offering some parameters for the patterns quantification.

The existence of a gradient in the geometrical complexity of histological texture or microvascular networks from those in the normal brain to those in malignant brain tumors has been speculated upon. The complex network dynamics and fractality of brain oncogenesis (i.e., development of brain tumors) are discussed by *Miguel Martín-Landrove, Antonio Brú, Antonio Rueda-Toicen, and Francisco Torres-Hoyos* in Chap. 22. The texture analysis of histological features of brain tumors (mainly meningiomas) is the topic of Chap. 23 by *Omar Al-Kadi and Antonio Di Ieva*, while in Chap. 24, the same authors present their findings on the analysis of the geometrical complexity of brain tumors’ (mainly gliomas) microvascular networks. Although translation of the concepts of “fractal tumors” or “fractal microvascularity” into clinical practice (“from bench to bedside”) still has some difficulties to overcome, future research in neuro-oncology should focus on finding new and reliable parameters correlated with biological and epidemiological characteristics. From this perspective, fractals and multi-parameter morphometric computer-aided analyses could be of benefit in translational research and in the medical armamentarium as a conventional procedure to improve diagnostic capacity and accuracy.

Experimental studies have not only been focused on the geometrical complexity of the neoplastic cells but also on the fractal structure of the environment surrounding such cells [33].

In summary, in histology and pathology, fractal analysis is used to quantitatively and objectively characterize cancer tissues in order to overcome the operator-dependent bias of classification and categorization [1, 6, 9, 13, 16, 18, 21, 29]. Moreover, the fractal dimension has also been shown useful to quantify the response for cancer treatment, in animal models [32], as well as in neuroimaging of patients affected by brain tumors [8].

Following the new paradigm which has shifted the reductionist approach to a systems biology approach [12, 24], cancer has been interpreted in its multilevel hierarchical system. Using an “ecological approach” [23], it has been shown that the spread of cancer cells (human glioma cells), like the spread of a specific tree species in a forest, have a specific “spatiotemporal signature,” characterized by a particular fractal geometry and scale invariance of the boundaries of the patterns generated in

the different physiopathological states [22]. Fractal analysis offers a common language for the identification of such spatiotemporal fingerprinting in different natural systems.

12.4 Fractal-Based Time-Series Analysis in Neurosciences

As discussed in the first section of this book, fractal and multifractal analysis can be applied to the study of the time-series biosignals. Examples of neurophysiological time series are the electroencephalographic (EEG), magnetoencephalographic (MEG), or electromyographic (EMG) records, and intracranial pressure (ICP) curves as well [11].

According to the latest discoveries regarding the network connectivity of the human brain, it is very intriguing to note that brain function depends upon adaptive self-organization of large neural assemblies, and that the brain functional networks are characterized by small-world properties, implying a scale-invariant or fractal small-world topological organization [2] (see also Chap. 9). The fractal small-world connectivity of the brain, based on the connectivity of hubs and topologically pivotal nodes, is the anatomical and functional background of its architecture, in physiological as well as pathological states [2, 27, 30]. EEG, MEG, fMRI, and other methods offer valid tools of analysis of such networks.

In Chap. 25, *Włodzimierz Klonowski* provides answers for “everything you wanted to ask about fractals and EEG” [17]. Other types of time-series analyses are offered by *Lorenzo Livi*, who in Chap. 26 discusses the multifractal detrended fluctuation analysis and multiscaling features found in patients affected by Parkinson’s disease, whereas in Chap. 27 *Sridhar Arjunan* and *Dinesh Kumar* illustrate fractal approaches for extracting information from surface electromyograms, with applications in patients’ rehabilitation and monitoring of the age-related changes in the muscles’ properties.

12.5 Cognitive Sciences, Neuropsychology, and Psychiatry

Abnormal fractal dynamics have been observed in several behavioral and psychological conditions as well as neuropsychiatric diseases, opening the venues to the applications of computational fractal-based analysis into the cognitive neurosciences, neuropsychology, and psychiatry.

In Chap. 29, *Sergio Iglesias-Parro*, *Maria Soriano*, and *Antonio Ibáñez-Molina* provide a panoramic view on the application of nonlinear approaches to the study of mental disorders, including affective and anxiety disorders.

A complementary approach is intriguingly suggested in Chap. 30 by *Richard Taylor* and *Branka Spehar* who investigate the significance of fractals for the human visual system and the clinical applications of such findings in addressing

stress-related illnesses, as well as introduce the topics related to the fascinating field of neuroesthetics.

12.6 Limitations of Application of Fractal Analysis into Clinical Neurosciences

The translation of fractal analysis into clinical practice still has some obstacles.

The fractal dimension is a geometrical feature of irregularly shaped objects, but it is not a magic number. It is a dimension, and as two different objects can have the same size (the same three different Euclidean dimensions of length, width, and height), two very different patterns can share the same fractal dimension, as discussed in Chap. 1. This means that FD should be considered as a complementary method along with other parameters.

The fractal-based morphometric approach does not necessarily constitute a superior tool in comparison to other approaches. Different types of nonlinear analyses can be performed along and integrated into other approaches in order to achieve a holistic view of the same problem.

Despite of the difficulty to discriminate between fractality and “apparent fractality originating from underlying randomness” [14], fractal analysis does not offer a mere mathematical theoretical model, because in clinical medicine it is aimed to find reliable parameters such as diagnostic, prognostic, and therapeutic biomarkers. Although the universality of the fractal language, fractal geometry cannot be considered as a Rosetta stone for the interpretation of every phenomenon; this has to be clear to the clinician and neuroscientist applying computational models for the translation of data into clinical applications.

12.6.1 *The “Black Box”*

Clinicians are not required to fully understand how fractal analysis and other computational methods work, just as a person using a computer for various tasks does not necessarily have to understand how the computer works. Clinicians should rather understand the proper way to use computational methods, address a problem, understand the inputs which could be analyzed by means of different and less conventional approaches, and correlate such findings to clinical findings, in order to make them useful in clinical perspective.

As discussed in several chapters, the computation and use of FD has pros and cons, and it should be understood that different values may be the result of “true differences in image texture or a result of certain arbitrary decisions made during the estimation process” [19]. The standardization of the technique as well as the delineation of the outcome assessment has to be clearly defined in order to guarantee an internal and external validation of the method and to avoid the bias of operator-dependent variability.

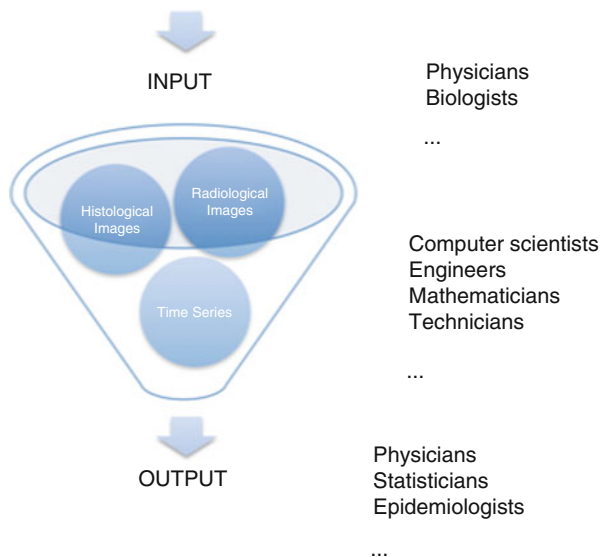


Fig. 12.1 The diagram shows the concept of the “black box” [38]. The black box is here represented by a funnel, where the data processing, by means of fractal analysis or other computational methods, occurs. The spheres are the data input to processing, which can be histological images (e.g., stained brain tumors, immunostained microvessels), radiological images (e.g., region of interests of brain tumors in MR or CT imaging) or times series (e.g., EEG, MEG, or intracranial pressure signals). The data are processed in the black box by means of standardized methods (e.g., box-counting method). The outputs are the results of the analysis, which are values useful for statistical analyses and epidemiological correlations, for example, or that can be validated as potential morphometric markers and/or diagnostic/prognostic biomarkers. The different professional figures involved in the process may be the ones quoted on the right of the figure

By using a concept from the artificial intelligence language, the concept of the black box will be used to explain this [9] (Fig. 12.1). The black box is substantially the machine, the computing algorithm. Although its way to function is not obscure to computer scientists and engineers, it may be “black” to clinicians, who eventually do not understand exactly what is happening inside of the machine. For example, clinicians and sometimes even radiologists do not fully understand the physics background of computed tomography and magnetic resonance imaging, but when specific algorithms transform the raw data into images they can interpret the meaning of such images very well. In such example, the hardware and software transforming the raw data into images are the “black box.” Different algorithms may run in the black box, e.g., the Fourier transform of the raw magnetic resonance signals, or the box-counting method for computing the fractal dimension of an image like a histological slide, the detrended fluctuation analysis of a time series, etc. A specific task of the black box can be requested by a clinician for a specific application, but the competence to work “inside the black box” is still left to other kinds of specialists and technicians.

The role of clinician is then to understand how that black box can be used, selecting the proper inputs to be analyzed. Examples of inputs could be microvessels or

other features in histological samples, or specific radiological sequences. The clinician, we define here as the “operator”, has to choose not only the inputs, but also the methods to identify them (e.g., which kind of immunohistochemistry to detect endothelium, the threshold to extract binarized images, the selection of region of interests in histological or radiological images, etc.). This is an essential task, because the lack of standardization of such a step would introduce a heterogeneous cohort of data into the black box, and the outputs, although computed in the same way, will be very heterogeneous as well (and therefore, useless). Therefore the operator provides the inputs to the black box, but he/she is still required for the interpretation of the outputs. The outputs are the data generated by the computational method working in the black box, and can be expressed in terms of morphometric parameters of angioarchitecture, for example, or the index of complexity of a radiological image. These data have to be analyzed by the clinician again to be correlated to epidemiological findings, for example, or clinical features, in order to be demonstrated as potential biomarkers, which might be useful in clinical practice. Although the different steps can be performed by different operators, the entire procedure should be carefully orchestrated, otherwise the translation of results into clinical practice might be misleading. The literature is full of controversial results on the same topics, e.g., researches finding higher or lower values of FD in the same tissues. The heterogeneity of the results has likely been the main reason for the failure of widespread use of fractal geometry into biomedicine. For example, in a review we compared the results of the morphometrics of the microvascularization in different subtypes of pituitary adenomas, finding completely different and noncomparable results [10]. By analyzing the reason of such discrepancies, it turned out that all of the authors chose different analytic methods and different antigens, which gave rise to a plethora of incomparable results due to their heterogeneity. The different inputs and outputs in the “black box” inevitably outputted completely different results, giving wrong and naïve conclusions on the role of the microvascularization of the pituitary tumors. The comparison of oranges and apples may lead to wrong conclusions. Every computational method applied into the biomedical sciences, and therefore into the clinical neurosciences, should be standardized and verified in order to offer meaningful and useful results. This is essential to avoid the rejection a priori of a useful model!

References

1. Baish JW, Jain RK. Fractals and cancer. *Cancer Res.* 2000;60:3683–8.
2. Bassett DS, Meyer-Lindenberg A, Achard S, Duke T, Bullmore E. Adaptive reconfiguration of fractal small-world human brain functional networks. *Proc Natl Acad Sci U S A.* 2006;103:19518–23.
3. Bullmore E, Fadili J, Maxim V, Sendur L, Whitcher B, Suckling J, et al. Wavelets and functional magnetic resonance imaging of the human brain. *Neuroimage.* 2004;23 Suppl 1:S234–49.
4. Cassot F, Lauwers F, Fouard C, Prohaska S, Lauwers-Cances V. A novel three-dimensional computer-assisted method for a quantitative study of microvascular networks of the human cerebral cortex. *Microcirculation (New York, NY 1994).* 2006;13:1–18.

5. Cross SS. Fractals in pathology. *J Pathol.* 1997;182:1–8.
6. Cross SS. The application of fractal geometric analysis to microscopic images. *Micron.* 1994;25:101–13.
7. Di Ieva A, Esteban FJ, Grizzi F, Klonowski W, Martin-Landrove M. Fractals in the neurosciences. Part II: clinical applications and future perspectives. *Neuroscientist.* 2015;21:30–43.
8. Di Ieva A, Matula C, Grizzi F, Grabner G, Trattnig S, Tschabitscher M. Fractal analysis of the susceptibility-weighted imaging patterns in malignant brain tumors during antiangiogenic treatment: technical report on four cases serially imaged by 7T magnetic resonance during a period of four weeks. *World Neurosurg.* 2012;77:785.e11–21.
9. Di Ieva A, Tschabitscher M. Fractal-based classification of brain tumors angioarchitecture. In: Mitchell EW, Murray SR (Eds). *Classification and applications of fractals: new research.* New York: Nova Science Publishers; 2012. p. 205–16.
10. Di Ieva A, Grizzi F, Gaetani P, Goglia U, Tschabitscher M, Mortini P, et al. Euclidean and fractal geometry of microvascular networks in normal and neoplastic pituitary tissue. *Neurosurg Rev.* 2008;31:271–80.
11. Di Ieva A, Schmitz EM, Cusimano MD. Analysis of intracranial pressure: past, present, and future. *Neuroscientist.* 2013;19:592–603.
12. Dinicola S, D’Anselmi F, Pasqualato A, Proietti S, Lisi E, Cucina A, et al. A systems biology approach to cancer: fractals, attractors, and nonlinear dynamics. *OMICS.* 2011;15:93–104.
13. Goldberger AL, West BJ. Fractals in physiology and medicine. *Yale J Biol Med.* 1987;60:421–35.
14. Hamburger D, Biham O, Avnir D. Apparent fractality emerging from models of random distributions. *Phys Rev E Stat Phys Plasmas Fluids Relat Interdiscip Topics.* 1996;53:3342–58.
15. Herman P, Kocsis L, Eke A. Fractal branching pattern in the pial vasculature in the cat. *J Cereb Blood Flow Metab.* 2001;21:741–53.
16. Di Ieva A. Fractal analysis of microvascular networks in malignant brain tumors. *Clin Neuropathol.* 2012;31:342–51.
17. Klonowski W. Everything you wanted to ask about EEG but were afraid to get the right answer. *Nonlinear Biomed Phys.* 2009;3:2.
18. Landini G. Fractals in microscopy. *J Microsc.* 2011;241:1–8.
19. Lopes R, Betrouni N. Fractal and multifractal analysis: a review. *Med Image Anal.* 2009;13:634–49.
20. Lorthois S, Cassot F. Fractal analysis of vascular networks: insights from morphogenesis. *J Theor Biol.* 2010;262:614–33.
21. Losa GA, Nonnenmacher TF. Self-similarity and fractal irregularity in pathologic tissues. *Mod Pathol.* 1996;9:174–82.
22. Marco DE, Cannas SA, Montemurro MA, Hu B, Cheng S-Y. Comparable ecological dynamics underlie early cancer invasion and species dispersal, involving self-organizing processes. *J Theor Biol.* 2009;256:65–75.
23. Merlo LMF, Pepper JW, Reid BJ, Maley CC. Cancer as an evolutionary and ecological process. *Nat Rev Cancer.* 2006;6:924–35.
24. Noble D. Biophysics and systems biology. *Philos Trans A Math Phys Eng Sci.* 2010;368:1125–39.
25. Olejarczyk E. Application of fractal dimension method of functional MRI time-series to limbic dysregulation in anxiety study. *Conf Proc Annu Int Conf IEEE Eng Med Biol Soc.* 2007;2007:3408–10.
26. Panerai RB. Complexity of the human cerebral circulation. *Philos Trans A Math Phys Eng Sci.* 2009;367:1319–36.
27. Plenz D, Thiagarajan TC. The organizing principles of neuronal avalanches: cell assemblies in the cortex? *Trends Neurosci.* 2007;30:101–10.
28. Risser L, Plouraboue F, Steyer A, Cloetens P, Le Duc G, Fonta C. From homogeneous to fractal normal and tumorous microvascular networks in the brain. *J Cereb Blood Flow Metab.* 2007;27:293–303.

29. Spillman WB, Robertson JL, Huckle WR, Govindan BS, Meissner KE. Complexity, fractals, disease time, and cancer. *Phys Rev E Stat Nonlin Soft Matter Phys.* 2004;70:061911.
30. Sporns O. Small-world connectivity, motif composition, and complexity of fractal neuronal connections. *Biosystems.* 2006;85:55–64.
31. Takahashi T. *Microcirculation in fractal branching networks.* Tokyo: Springer; 2014.
32. Vakoc BJ, Lanning RM, Tyrrell JA, Padera TP, Bartlett LA, Stylianopoulos T, et al. Three-dimensional microscopy of the tumor microenvironment in vivo using optical frequency domain imaging. *Nat Med.* 2009;15:1219–23.
33. Wang P, Li L, Zhang C, Lei Q, Fang W. Effects of fractal surface on C6 glioma cell morphogenesis and differentiation in vitro. *Biomaterials.* 2010;31:6201–6.
34. West GB, Brown JH, Enquist BJ. The fourth dimension of life: fractal geometry and allometric scaling of organisms. *Science.* 1999;284:1677–9.
35. Zamir M. Fractal dimensions and multifractality in vascular branching. *J Theor Biol.* 2001;212:183–90.
36. Zamir M. On fractal properties of arterial trees. *J Theor Biol.* 1999;197:517–26.
37. Zamir M, Phipps S. Network analysis of an arterial tree. *J Biomech.* 1988;21:25–34.
38. Di Ieva A. *Fractal Analysis of Microvascular Networks in Malignant Brain Tumors.* PhD Thesis. Medical University of Vienna, Vienna, Austria, 2011. Available from: [0](#)

Chapter 13

Fractal Analysis in Neurological Diseases

Francisco J. Esteban, Leticia Díaz-Beltrán, and Antonio Di Ieva

Abstract Over the last decades, fractal analysis has been applied to the study of the spatial and temporal complexity of a wide range of objects in biology and medicine, including the irregular and complex patterns of the nervous system. In clinical neurosciences, fractal geometry has emerged as a powerful tool to objectively analyze and quantify the intricate structures comprising the topological and functional complexity of the human brain, shedding light on the understanding of the brain function at a systems level. The fractal approach has the potential to allow physicians and scientists to predict clinical outcomes, classification between normal and pathological states, and, ultimately, the identification and diagnosis of certain neurological conditions. In this chapter, the main applications of fractal analysis into clinical neurosciences are reviewed, with special emphasis on the diagnostic precision of the fractal dimension value in different neurological diseases.

Keywords Brain • Clinical neurosciences • Fractal dimension • Fractal analysis • Magnetic resonance imaging • Neurology

In neurosciences, fractal analysis is used to measure the scaling inherent to neurological systems (from anatomic to histological structures), providing an index, the fractal dimension (FD), to estimate the topological complexity of the given object. Different types of neural structures, from neurons to complex networks, can be characterized as structural or dynamical fractals to quantify the intrinsic complexity. In this perspective, the spatial properties of the components of the nervous system, both at the macroscopic and microscopic levels, can be viewed as geometric

F.J. Esteban (✉) L. Díaz-Beltrán
Department of Experimental Biology, School of Sciences, University of Jaén, Jaén, Spain
e-mail: festeban@ujaen.es

A. Di Ieva, MD, PhD (✉)
Neurosurgery Unit, Faculty of Medicine and Health Sciences, Macquarie University,
Sydney, NSW, Australia

Garvan Institute of Medical Research, Sydney, NSW, Australia

Medical University of Vienna, Vienna, Austria

University of Toronto, Toronto, ON, Canada
e-mail: diieva@hotmail.com

fractals, while temporal properties of neurophysiological signals should be interpreted as dynamic fractals [15]. In this chapter, we review and describe different applications of “static” and “dynamic” fractal analysis in clinical neurology.

13.1 Geometric Fractal Analysis Applied to Neuroscience

Due to its sensitivity in identifying brain structural changes the FD, the index of complexity that assesses a fractal invariant detail within a pattern has been considered as a possible representative marker of the degree of brain damage in numerous neurological and neuropsychiatric conditions, even those detected in normal and pathological cerebral aging. Thus, the FD of white matter (WM) segmented from brain MRI scans, and calculated by means of the box-counting method, turned out to be significantly smaller in older subjects when compared to young adults, while conventional volumetric measurements for brain atrophy did not recognize WM changes with age [53]. Similarly, Mustafa et al. [40] pointed out individual differences in the FD of cerebral white matter that were significantly related with non-disease-state life course cognitive changes, gender- and WM volume independent (Figs. 13.1 and 13.2). King et al. [33] developed a novel approach to estimate the FD of the cortical ribbon and showed considerable differences between healthy controls and patients with mild Alzheimer’s disease (AD) in comparison with cortical thickness or gyrification index estimations (see below and Chap. 14). A different fractal dimension approach was also described in a following paper by King et al. [32], whereby the author proposed a new method, the custom-written cube-counting algorithm, to compute the local FD of the human cerebral cortex extracted from high-resolution MRI scans. In such a study, the ability of the local FD to identify regional variation in the brain structure when comparing a healthy subject with a patient diagnosed with Alzheimer’s disease was demonstrated.

Fractal analysis of brain MRI scans has also been used to identify morphological variations related to other cognitive and mental disorders. For example, Li et al. [35]

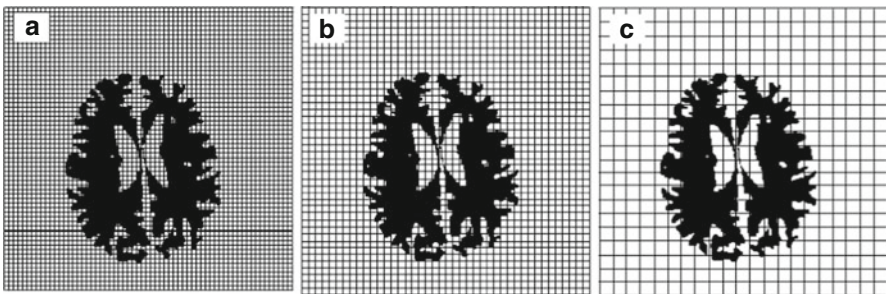


Fig. 13.1 (a–c) Example of the grid overlay in FD estimation for cerebral white matter using the box-counting method [40] (Reproduced under Creative Commons Attribution License (<http://creativecommons.org/licenses/by/2.0>))

used a robust geometric estimator, the fractal information dimension (FID), to detect changes of prefrontal cortical gyrification complexity in subjects diagnosed with attention deficit hyperactivity disorder (ADHD). Their study revealed that FID values increased when the degree of cortical convolution complexity was high, showing that this scale-free measure eluded the brain size effect commonly associated to conventional geometric parameters like cortical volume and thickness. Other volumetric structural alterations have been recognized in both brain white and gray matter (GM) in dyslexic individuals by Sandu et al. [46]. These authors proposed parameters such as the GM-WM ratio and the FD of the GM-WM border as dyslexia vulnerability markers, since they identified alterations in these measurements (notably in the left hemisphere). In a similar study with schizophrenia patients, some of these authors [45] also detected irregularities in the structural complexity of cortical folding, which were not found when applying conventional morphometric analysis techniques of MR images.

Additionally, fractal analysis has been extensively applied to study cerebral vascularization in its complete physiopathological range. Thus, different authors applied fractal-based approaches to characterize the complex spatiotemporal properties of cerebral blood circulation [7, 8, 23, 25, 34, 39, 42]. Likewise, Reishofer et al. [43] and Di Ieva et al. [16] estimated the morphological vascular complexity of brain arteriovenous malformations (AVMs) on MRI scans by means of the FD. In such studies, the FD of the nidus AVM has been proposed as a robust image angi-architectural parameter as well as potential prognostic surrogate biomarker in patients undergoing Gamma Knife radiosurgery (see Chap. 18). Fractal-based analysis and novel automated methods have also been applied for the characterization of retinal microvascular alterations of branching complexity and density as potential markers of stroke and in the wide spectrum of cerebrovascular diseases [10–12, 31, 41, 49] (see also Chap. 28).

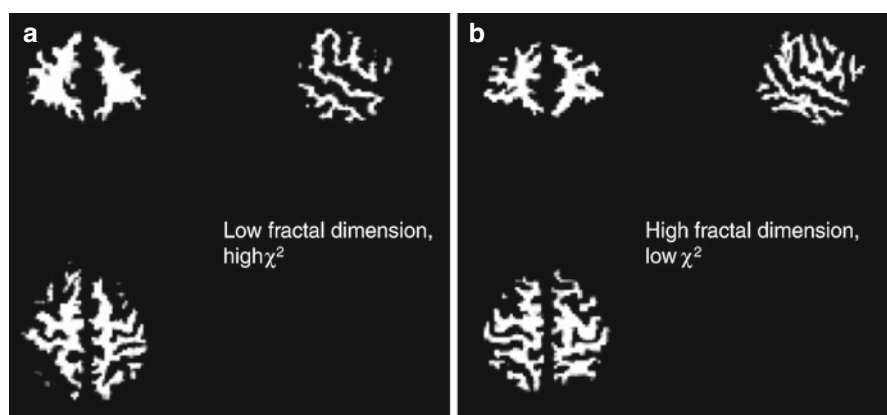


Fig. 13.2 (a, b) Examples of structural comparison between the low- and high fractal white matter in three different views; coronal, sagittal, and axial slices [40] (Reproduced under Creative Commons Attribution License (<http://creativecommons.org/licenses/by/2.0>))

In regard to other neurological diseases, fractal analysis of MRI scans has also offered promising parameters of potential clinical diagnostic relevance. Such is the case of multiple sclerosis (MS), where FD has been shown to be a potential early diagnostic estimator with a key role in clinical decision-making, since this parameter has been found to be able to detect and characterize changes in WM [20] and GM [19] in apparently normal MRI scans (those without visible MS cerebral lesions). Furthermore, Esteban et al. [18] applied fractal analysis to analyze the topological complexity of GM and WM and were able to quantify subtle alterations in the brain of premature infants with a prenatal diagnosis of severe intrauterine growth restriction, when comparing this parameter value with those of healthy premature children and full-term newborns. They concluded that FD could be considered a powerful tool for quantitative investigation of child brain structure and obtained significant results when they related the observed FD changes with neurodevelopmental functional disorders.

In regard to Parkinson's disease and spinocerebellar ataxia, Manabe et al. have used FD to quantify the patterns of postural instability, showing higher values in patients with a more advanced stage of disease [37].

Additionally, a recent study performed fractal analysis of human cerebellum regions in patients diagnosed with Chiari malformation type I syndrome (CM-I), a condition of the central nervous system (CNS) generally characterized by cerebellar tonsils herniation into the spinal canal [5]. This research showed that FD values of GM, WM, and cerebrospinal fluid (CSF) (calculated using the box-counting method) were significantly higher in CM-I subjects compared to those obtained from healthy controls. The authors suggested that FD measures of the human cerebellum might be considered a discriminative feature and a valuable image marker for the study of cerebellar anomalies of CM-I patients. Similarly, Wu et al. [50] also applied fractal analysis to investigate multiple system atrophy of the cerebellar type (MSA-C), a neurodegenerative disease of the CNS; they demonstrated that FD, also calculated using the box-counting method, was able to characterize the morphological changes of cerebellar structural complexity. Their results showed that MSA-C subjects have significantly smaller FD values in both cerebellar GM and WM when compared to normal individuals, revealing that this topological alteration in the WM controlled the structural degeneration of the cerebellum. Their research pointed out that the FD analysis strategy proves a more valuable method than traditional volumetric estimators when quantifying the morphological abnormalities of WM and GM, since it yields lower variances and less gender effect.

FD values of WM structure have also been quantified in MRI brain anatomical scans and correlated with motor function in the upper extremity (UE) in individuals who had suffered a stroke. In their work, Zhang et al. [52] set out two premises, the first one was that WM complexity would diminish after having a stroke, and the second one that WM complexity of unaffected areas of cortex would be associated to greater UE motor function. Their findings detected lower FD measures in the stroke-affected hemisphere, while higher WM complexity was related to greater motility of the affected limb; as for assessment of motor function in association with lesion volume, no correlation was found. These authors also suggested that FD may be considered a powerful clinical estimator for monitoring the degree of residual

WM structural, or neural, plastic alterations in patients recovering from stroke, with the final aim to guide forthcoming therapeutic strategies.

Finally, it is worth highlighting that the application of mono- and multi-fractal approaches to characterize neuronal, microglial, and immuno-inflammatory cells may provide a meaningful contribution to future researches and applications of tissue engineering and 3D modeling in neuroscience, as recently reviewed by Karperien and Jelinek [29].

13.2 Use of Dynamic Fractal Analysis in Neurology

The distinct strategies used in the characterization of temporal fractals have been proven as valuable tools in estimating the dynamic properties of nervous signals and monitoring time series in an effort to discriminate between health status and disease. In this regard, promising results were obtained when applying FD to evaluate brain complexity and dynamic changes in patients with autism [4] and AD [3]. High accuracy values have been achieved in patients affected by autism and AD using Katz's FD [30] of electroencephalogram (EEG) as a classifier for discriminating between disease and healthy states, as described in more detail in the section below.

Linear and fractal measures have also been applied for discriminating autism from other behavioral and developmental disorders. Thus, Cusenza et al. [13] explored EEG features in the awake and sleep state of autistic children in comparison with children suffering from mental retardation. In this study, quantitative EEG was revealed as a powerful tool for early autism diagnosis, since significant variations between autistic and mentally retarded EEG measures were found; specifically, autistic individuals showed higher complexity patterns while awake, whereas increased delta and gamma activity were also detected in their sleep state.

Furthermore, Michail et al. [38] estimated the FD of EEG to characterize the impact of lorazepam, a psychoactive drug with anxiolytic and sedative effects, on brain activity. The authors found a relationship between this drug and EEG FD that affects α and β bands complexity; concretely, this property increased in α bands while diminished in β bands after treatment. Additionally, nonlinear analyses performed on actigraphy data revealed that Katz's FD values were considerably smaller throughout the night in subjects with dementia (including AD patients) and aggressive behavior than those found in healthy controls, therefore, identifying alterations in the circadian rest-activity system motor in abnormal neurological conditions [6, 21].

On the other hand, a novel method for automatic seizure detection in epilepsy was proposed by Yuan et al. [51]. The authors applied a differential box-counting-based approach to characterize multichannel long-term EEG signals, achieving extremely accurate results that yielded higher significant sensitivity and specificity values and a smaller false detection rate than other conventional techniques for EEG epileptic seizure detection. A different method for the estimation of FD of multichannel EEG signals, based on the k -nearest neighbor algorithm [54, 55], has been also used to detect epileptic seizures (see below).

Finally, a recent study carried out by Lopez de Ipiña et al. [36] proposed Higuchi's, Katz's, and Castiglioni's [9] algorithms as the basis of new biomarkers derived from an automatic spontaneous speech analysis (ASSA). The authors quantified the FD and other parameters of speech waveforms time series to aid in Alzheimer's disease diagnosis [36].

13.3 Diagnostic Precision of Fractal Dimension

Several studies have been carried out using the FD as a parameter able to discriminate between healthy and disease states in clinical neurosciences, as described above and reviewed in [15, 17, 28]. In this scientific context, most of the obtained results have been described as significant by considering the conventional p-values. However, it is well known that the validity of a parameter as a good biomarker or as a surrogate endpoint depends on its diagnostic precision described mainly in terms of accuracy, sensibility, and specificity, among others, and independent of the level of significance related to conventional statistics. In this section, we focus our attention on those studies in which the discriminant capability of the FD between different neurological states was expressed in terms of diagnostic precision parameters (Table 13.1).

13.3.1 *Depression and Schizophrenia*

Depression, a mood disorder with prevalence in an 8–10% range of general population, has been detected through EEG signal analysis using 15 nonlinear features, including FD [2]. With the aim of real clinical application, Acharya et al. [2] developed a robust depression diagnostic system with a high classification accuracy (98%), sensitivity (97%), and specificity (98.5%). Interestingly, this noninvasive diagnostic procedure has been fully automatized in software with easy installation for computers in EEG facilities in hospitals. Moreover, the authors also proposed a unique value, the so-called depression diagnosis index (DDI), which can measure the severity of depression. However, the limited size of the dataset (15 healthy controls (HC) and 15 subjects with depression) requires further validation studies.

In a similar way, schizophrenia, a severe psychiatric disorder affecting around 0.4–0.6% of the world's population, has been analyzed using EEG signals through a channel selection and feature-based classification procedure, which also included FD parameterization [44]. In the best classifier scenario, the authors obtained high accuracy (92%), sensitivity (93%), and specificity (91%), thus being able to discriminate between normal participants and those with schizophrenia, and provided a useful complementary tool in the diagnosis of such psychiatric disease. This study was carried out on 20 patients and the same number of healthy controls, and it has not yet been validated with any other independent population.

Table 13.1 Summary of diagnostic precision parameters obtained through fractal analysis

Condition	Study	% accuracy	% sensitivity	% specificity	AROC value	TPV	FPV
Depression	Acharya et al. (2015) [2]	98	97	98.5	NP	NP	NP
Schizophrenia	Sabeti et al. (2011) [44]	92	93	91	NP	NP	NP
Alzheimer's disease	Ahmadlou et al. (2011) [3]	99.3	100	97.8	NP	NP	NP
	Henderson et al. (2006) [24]	NP	67	99.9	NP	NP	NP
	King et al. (2010) [33]	NP	NP	NP	0.84	NP	NP
	Gómez et al. (2009) [22]	87.8	80	95.2	0.9	NP	NP
Autism	Ahmadlou et al. (2010) [4]	90	NP	NP	NP	NP	NP
Epilepsy and seizure	Acharya et al. (2013) [1]	86–100	NP	NP	NP	NP	NP
Neural loss in retinal tissue	Zhang et al. (2015) [55]	NP	91/94.1 ^a	95.8	NP	NP	NP
	Somfai et al. (2014) [48]	NP	98	88	0.96	NP	NP
Brain tumor	Iftekharuddin et al. (2005) [27]	NP	NP	NP	NP	1.0	0.16
	Iftekharuddin et al. (2009) [26]	NP	NP	NP	NP	0.75–1.0	NP
	Smitha et al. (2015) [47]	NP	70.3	66.7	NP	NP	NP
	Di Ieva et al. (2016) [14]	NP	81	89	NP	NP	NP

TPV true positive value, FPV false positive value, NP not provided

^aWhen applied on seizure events

13.3.2 *Alzheimer's Disease and Autism*

Alzheimer's disease is a devastating neurodegenerative disorder with a continuous increasing incidence associated to aging. Its definitive diagnosis is only confirmed by histological postmortem analysis. Together with other attempts of noninvasive diagnosis based on cerebral resonance imaging or magnetoencephalography (see below), EEG nonlinear complexity characterization is becoming a promising field to obtain potential markers in AD. Ahmadlou et al. [3] have obtained a robust classification of AD patients and normal aging subjects using linear discriminant analysis on FD-related features. Interestingly, high accuracy (99.3%), sensitivity (100%), and specificity (97.8%) were obtained to classify the abovementioned groups, even though only 7 aged HC and 20 AD patients were included in this study. In addition, and in an effort to detect dementia as a risk factor for developing Alzheimer's disease, Henderson et al. [24] reported that FD analysis of EEG signals yield 67% sensitivity and 99.9% specificity. It is worth mentioning that the EEG signals analyzed by these authors were raw recordings without any preselection of components, making the procedure easy and quick to apply by a nonspecialist clinician within the growing population at risk.

On the other hand, FD computation has also been applied to the entire cerebral cortical ribbon obtained after the segmentation and processing of volumetric images from 35 HC and 35 subjects with mild Alzheimer's disease [33]. This procedure provided a receiver-operating characteristic (ROC) curve with an area-under-the-ROC curve (AROC) value of 0.84, which is an acceptable diagnostic predictive result.

When magnetoencephalograms (MEGs) are used to measure the cerebral background activity from AD patients [22], the FD characterization of these recordings showed high AROC values at each brain region analyzed (anterior 0.86, central 0.87, right lateral 0.89, posterior 0.89, left lateral 0.89). The highest AROC value (0.9) was obtained when the mean FD over all channels was calculated for the 20 AD patients and the 21 related elderly HC, with high-related accuracy (87.8%), sensitivity (80%), and specificity (95.2%).

Finally, Katz's FD of eyes-closed EEG data was proposed by Ahmadlou et al. [4] to characterize brain dynamical changes and complexity in nine autistic individuals in comparison with eight healthy subjects. The authors utilized a radial basis function classifier that yielded a 90% of accuracy for discriminating between the two groups, namely, the autistic and non-autistic children.

13.3.3 *Epilepsy*

Epilepsy is a chronic neurological disorder affecting around 1% of the world's population. Automatic detection of seizures becomes crucial for epilepsy diagnosis and long-term EEG monitoring of patients, and several procedures have been developed, most of them including the characterization of nonlinear features of EEG signals, and with an accuracy ranging from 86% to 100% (reviewed in [1]). Recently, Zhang et al. presented a seizure detection method also based on the

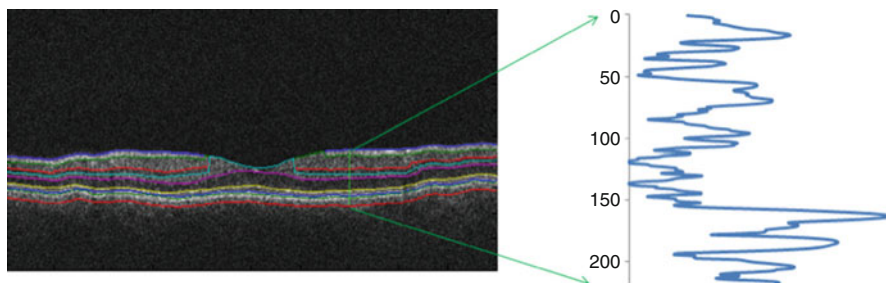


Fig. 13.3 Computation of the fractal dimension for the reflectivity profile of optical coherence tomography (OCT) images of the retinal layers [48] (Reproduced under Creative Commons Attribution License (<http://creativecommons.org/licenses/by/2.0>))

nonlinear FD analysis of EEG signals [54]. Their method, which includes deep methodological refinements when compared to the previous ones, was able to discriminate between seizure or non-seizure status with high sensitivity (91 %), specificity (95.8 %), and recognition rate (95.8 %) on the epoch-based assessments in 21 patients [55]. Moreover, when applied to seizure events (subsequent decisions of the same class, seizure or non-seizure, were grouped as an event) for clinical application, a sensitivity of 94.1 % and a false detection rate of 0.27/h were obtained [55].

13.3.4 Neural Loss in Retinal Tissue

Early neuronal loss in retinal tissue, which occurs in patients with diabetes or multiple sclerosis, can be characterized using structural information extracted from optical coherence tomography (OCT) images. From this point of view, Somfai et al. [48] computed the FD for the reflectivity profile of OCT images (Fig. 13.3) from 74 HC eyes and 43 patients affected by type-1 diabetes mellitus with mild diabetic retinopathy, after the automatic segmentation of the histological layers of the retina based on their optical densities. The highest FD discriminant (between healthy and disease groups) AROC value (0.96) obtained was related to the ganglion cell and inner plexiform layer (GCL + IPL) complex, with sensitivity of 98 % and specificity of 88 %. Interestingly, these authors also calculated the positive likelihood ratio thus detecting, with this value for the GCL + IPL complex, an increase about 70 % in the probability of early retinopathy development [48]. See also Chap. 28.

13.3.5 Brain Tumors

In a different context, fractal features have also been applied to automated brain tumor segmentation [26, 27]. The main procedure carried out by these authors was based on texture information, combining fractional Brownian motion (fBm)

and wavelet multiresolution analysis. ROC curves were obtained with the aim of evaluating tumor region performance, and the competence of the classifier was a true positive value of 1.0, with only 0.16 of false positive value, for a total number of 50 pediatric T1 magnetic resonance (MR) images analyzed [27]. When the abovementioned texture-informed procedure was applied together with intensity in multimodal MR images (T1-gadolinium enhanced, T2 and fluid attenuation inversion recovery [FLAIR] sequences), a true positive fraction value range between 0.75 and 1.0 (mean 0.9) was detected for the nine pediatric patients analyzed [26].

Brain tumor characterization and grading are fundamental features to know in clinical practice, above all in brain gliomas due to the well-known grade-aggressiveness relationship. When MR FLAIR images were characterized using FD, 70.3 % sensitivity and 66.7 % specificity diagnostic precision values were found related to the increase in the grade of glioma and discriminating most malignant ones [47]. FD has also been used to quantify the signal of MR susceptibility-weighted imaging (SWI) in patients affected by different types and grades of brain tumors, with a significant discrimination among low- and high-grade gliomas, lymphomas, metastasis, and meningiomas [14]. In the Di Ieva et al.'s study, a ROC analysis showed a cutoff FD value for differentiating low- from high-grade gliomas of 1.75, with a sensitivity 81 % and specificity 89 %. The fractal dimension of neuroradiological features has since been introduced as a novel image biomarker for glioma grading and tumor characterization, opening new perspectives in the computational modeling aimed to improve diagnosis of brain tumors and therefore patients' treatment and prognosis. For more details, see Chaps. 19, 20, 21, 22, 23, and 24.

13.4 Conclusion and Future Perspectives

The computation of the fractal dimension of neuroradiological and/or clinical features of neurological conditions (among others are cerebrovascular, oncological, and demyelinating pathologies) and the ability of FD to differentiate different states of disease further supports the transition of fractals from basic research to potential applications into neurology and clinical neurosciences. Fractal-based quantification of features can help reduce intra- and interobserver variability for classification and follow-up of neurological diseases, although it should be emphasized that the computational modeling has to be standardized in order to reduce methodological heterogeneity (see the "Black Box" concept in Chap. 12). Clinical neuroscientists (e.g., neurologists, neuropathologists, neuroradiologists, neurosurgeons) will eventually benefit from the use of fractal-based computational analyses for improving diagnosis and prognosis of patients, and eventually their therapeutical options as well as outcome.

References

1. Acharya UR, Sreec SV, Swapnad G, Martisa RJ, Surie JS. Automated EEG analysis of epilepsy: a review. *Knowl-Based Syst.* 2013;45:147–65.
2. Acharya UR, Sudarshan VK, Adeli H, Santhosh J, Koh JE, Puthankatti SD, et al. A novel depression diagnosis index using nonlinear features in EEG signals. *Eur Neurol.* 2015;74:79–83.
3. Ahmadlou M, Adeli H, Adeli A. Fractality and a wavelet-chaos methodology for EEG-based diagnosis of Alzheimer disease. *Alzheimer Dis Assoc Disord.* 2011;25:85–92.
4. Ahmadlou M, Adeli H, Adeli A. Fractality and a wavelet-chaos-neural network methodology for EEG-based diagnosis of autistic spectrum disorder. *J Clin Neurophysiol.* 2010;27:328–33.
5. Akar E, Kara S, Akdemir H, Kiris A. Fractal dimension analysis of cerebellum in chiari malformation type I. *Comput Biol Med.* 2015;64:179–86.
6. Besthorn C, Sattel H, Hentschel F, Daniel S, Zerfass R, Forstl H. Quantitative EEG in frontal lobe dementia. *J Neural Transm Suppl.* 1996;47:169–81.
7. Cassot F, Lauwers F, Lorthois S, Puwanarajah P, Duvernoy H. Scaling laws for branching vessels of human cerebral cortex. *Microcirculation.* 2009;16:331, 44, 2 p following 344.
8. Cassot F, Lauwers F, Fouard C, Prohaska S, Lauwers-Cances V. A novel three-dimensional computer-assisted method for a quantitative study of microvascular networks of the human cerebral cortex. *Microcirculation.* 2006;13:1–18.
9. Castiglioni P. What is wrong in katz’s method? comments on: “A note on fractal dimensions of biomedical waveforms”. *Comput Biol Med.* 2010;40:950–2.
10. Cavallari M, Stamile C, Umeton R, Calimeri F, Orzi F. Novel method for automated analysis of retinal images: results in subjects with hypertensive retinopathy and CADASIL. *Biomed Res Int.* 2015;2015:752957.
11. Cavallari M, Falco T, Frontali M, Romano S, Bagnato F, Orzi F. Fractal analysis reveals reduced complexity of retinal vessels in CADASIL. *PLoS One.* 2011;6:e19150.
12. Cheung CY, Tay WT, Ikram MK, Ong YT, De Silva DA, Chow KY, et al. Retinal microvascular changes and risk of stroke: the Singapore Malay eye study. *Stroke.* 2013;44:2402–8.
13. Cusenza M, Accardo A, Zanini S, Brambilla P. Analysis of awake and sleep EEG in autistic children. *Int J Bioelectromagnetism.* 2012;14:80–3.
14. Di Ieva A, Le Reste PJ, Carsin-Nicol B, Ferre JC, Cusimano MD. Diagnostic value of fractal analysis for the differentiation of brain tumors using 3-tesla MR susceptibility-weighted imaging. *Neurosurgery.* 2016.
15. Di Ieva A, Esteban FJ, Grizzi F, Klonowski W, Martin-Landrove M. Fractals in the neurosciences, part II: clinical applications and future perspectives. *Neuroscientist.* 2015;21:30–43.
16. Di Ieva A, Niamah M, Menezes RJ, Tsao M, Krings T, Cho YB, et al. Computational fractal-based analysis of brain arteriovenous malformation angioarchitecture. *Neurosurgery.* 2014;75:72–9.
17. Di Ieva A, Grizzi F, Jelinek H, Pellionisz AJ, Losa GA. Fractals in the neurosciences, part I: general principles and basic neurosciences. *Neuroscientist.* 2013;20:403–17.
18. Esteban FJ, Padilla N, Sanz-Cortes M, de Miras JR, Bargallo N, Villoslada P, et al. Fractal-dimension analysis detects cerebral changes in preterm infants with and without intrauterine growth restriction. *Neuroimage.* 2010;53:1225–32.
19. Esteban FJ, Sepulcre J, de Miras JR, Navas J, de Mendizabal NV, Goni J, et al. Fractal dimension analysis of grey matter in multiple sclerosis. *J Neurol Sci.* 2009;282:67–71.
20. Esteban FJ, Sepulcre J, de Mendizabal NV, Goni J, Navas J, de Miras JR, et al. Fractal dimension and white matter changes in multiple sclerosis. *Neuroimage.* 2007;36:543–9.
21. Etcher L, Whall A, Kumar R, Devanand D, Yeragani V. Nonlinear indices of circadian changes in individuals with dementia and aggression. *Psychiatry Res.* 2012;199:77–8.
22. Gomez C, Mediavilla A, Hornero R, Abasolo D, Fernandez A. Use of the Higuchi’s fractal dimension for the analysis of MEG recordings from Alzheimer’s disease patients. *Med Eng Phys.* 2009;31:306–13.

23. Heinzer S, Krucker T, Stampanoni M, Abela R, Meyer EP, Schuler A, et al. Hierarchical micro-imaging for multiscale analysis of large vascular networks. *Neuroimage*. 2006;32:626–36.
24. Henderson G, Ifeachor E, Hudson N, Goh C, Outram N, Wimalaratna S, et al. Development and assessment of methods for detecting dementia using the human electroencephalogram. *IEEE Trans Biomed Eng*. 2006;53:1557–68.
25. Herman P, Kocsis L, Eke A. Fractal branching pattern in the pial vasculature in the cat. *J Cereb Blood Flow Metab*. 2001;21:741–53.
26. Iftekharuddin KM, Zheng J, Islam MA, Ogg RJ. Fractal-based brain tumor detection in multi-modal MRI. *Appl Math Comput*. 2009;207:23–41.
27. Iftekharuddin KM, Islam MA, Shaik J, Parra C, Ogg R. Automatic brain-tumor detection in MRI: methodology and statistical validation. *SPIE Med Imag*. 2005;5747:2012–22.
28. John AM, Elfanagely O, Ayala CA, Cohen M, Prestigiacomo CJ. The utility of fractal analysis in clinical neuroscience. *Rev Neurosci*. 2015;26:633–45.
29. Karperien AL, Jelinek HF. Fractal, multifractal, and lacunarity analysis of microglia in tissue engineering. *Front Bioeng Biotechnol*. 2015;3:51.
30. Katz MJ. Fractals and the analysis of waveforms. *Comput Biol Med*. 1988;18:145–56.
31. Kawasaki R, Che Azemin MZ, Kumar DK, Tan AG, Liew G, Wong TY, et al. Fractal dimension of the retinal vasculature and risk of stroke: a nested case-control study. *Neurology*. 2011;76:1766–7.
32. King R. Computation of local fractal dimension values of the human cerebral cortex. *Appl Math*. 2014;5:1733–40.
33. King RD, Brown B, Hwang M, Jeon T, George AT. Alzheimer's disease neuroimaging initiative. Fractal dimension analysis of the cortical ribbon in mild Alzheimer's disease. *Neuroimage*. 2010;53:471–9.
34. Lauwers F, Cassot F, Lauwers-Cances V, Puwanarajah P, Duvernoy H. Morphometry of the human cerebral cortex microcirculation: general characteristics and space-related profiles. *Neuroimage*. 2008;39:936–48.
35. Li X, Jiang J, Zhu W, Yu C, Sui M, Wang Y, et al. Asymmetry of prefrontal cortical convolution complexity in males with attention-deficit/hyperactivity disorder using fractal information dimension. *Brain Dev*. 2007;29:649–55.
36. Lopez-de-Ipina K, Alonso-Hernández JB, Solé-Casals J, Travieso-González CM, Ezeiza A, Faúndez-Zanuy M, et al. Feature selection for spontaneous speech analysis to aid in Alzheimer's disease diagnosis: a fractal dimension approach. *Neurocomputing*. 2015;150:392–401.
37. Manabe Y, Honda E, Shiro Y, Sakai K, Kohira I, Kashihara K, et al. Fractal dimension analysis of static stabilometry in Parkinson's disease and spinocerebellar ataxia. *Neurol Res*. 2001;23:397–404.
38. Michail E, Chouvarda I, Maglaveras N. Benzodiazepine administration effect on EEG fractal dimension: results and causalities. *Conf Proc IEEE Eng Med Biol Soc*. 2010;2010:2350–3.
39. Minnich B, Bartel H, Lametschwandner A. Quantitative microvascular corrosion casting by 2D- and 3D-morphometry. *Ital J Anat Embryol*. 2001;106:213–20.
40. Mustafa N, Ahearn TS, Waiter GD, Murray AD, Whalley LJ, Staff RT. Brain structural complexity and life course cognitive change. *Neuroimage*. 2012;61:694–701.
41. Ong YT, De Silva DA, Cheung CY, Chang HM, Chen CP, Wong MC, et al. Microvascular structure and network in the retina of patients with ischemic stroke. *Stroke*. 2013;44:2121–7.
42. Panerai RB. Complexity of the human cerebral circulation. *Philos Trans A Math Phys Eng Sci*. 2009;367:1319–36.
43. Reishofer G, Koschutnig K, Enzinger C, Ebner F, Ahammer H. Fractal dimension and vessel complexity in patients with cerebral arteriovenous malformations. *PLoS One*. 2012;7:e41148.
44. Sabeti M, Katebi SD, Boostani R, Price GW. A new approach for EEG signal classification of schizophrenic and control participants. *Exp Syst Appl*. 2011;38:2063–71.
45. Sandu AL, Rasmussen Jr IA, Lundervold A, Kreuder F, Neckelmann G, Hugdahl K, et al. Fractal dimension analysis of MR images reveals grey matter structure irregularities in schizophrenia. *Comput Med Imaging Graph*. 2008;32:150–8.

46. Sandu AL, Specht K, Beneventi H, Lundervold A, Hugdahl K. Sex-differences in grey-white matter structure in normal-reading and dyslexic adolescents. *Neurosci Lett*. 2008;438:80–4.
47. Smitha KA, Gupta AK, Jayasree RS. Fractal analysis: fractal dimension and lacunarity from MR images for differentiating the grades of glioma. *Phys Med Biol*. 2015;60:6937–47.
48. Somfai GM, Tatrai E, Laurik L, Varga BE, Olvedy V, Smiddy WE, et al. Fractal-based analysis of optical coherence tomography data to quantify retinal tissue damage. *BMC Bioinform*. 2014;15:295, 2105-15-295.
49. Talu S. Multifractal characterisation of human retinal blood vessels. *Oftalmologia*. 2012;56:63–71.
50. Wu YT, Shyu KK, Jao CW, Wang ZY, Soong BW, Wu HM, et al. Fractal dimension analysis for quantifying cerebellar morphological change of multiple system atrophy of the cerebellar type (MSA-C). *Neuroimage*. 2010;49:539–51.
51. Yuan Q, Zhou W, Liu Y, Wang J. Epileptic seizure detection with linear and nonlinear features. *Epilepsy Behav*. 2012;24:415–21.
52. Zhang L, Butler AJ, Sun CK, Sahgal V, Wittenberg GF, Yue GH. Fractal dimension assessment of brain white matter structural complexity post stroke in relation to upper-extremity motor function. *Brain Res*. 2008;1228:229–40.
53. Zhang L, Dean D, Liu JZ, Sahgal V, Wang X, Yue GH. Quantifying degeneration of white matter in normal aging using fractal dimension. *Neurobiol Aging*. 2007;28:1543–55.
54. Zhang Y, Zhou W, Yuan S. Multifractal analysis and relevance vector machine-based automatic seizure detection in intracranial EEG. *Int J Neural Syst*. 2015;25:1550020.
55. Zhang Y, Zhou W, Yuan S, Yuan Q. Seizure detection method based on fractal dimension and gradient boosting. *Epilepsy Behav*. 2015;43:30–8.

Chapter 14

Fractal Dimension Studies of the Brain Shape in Aging and Neurodegenerative Diseases

Luduan Zhang and Guang H. Yue

Abstract The fractal dimension is a morphometric measure that has been used to investigate the changes of brain shape complexity in aging and neurodegenerative diseases. This chapter reviews fractal dimension studies in aging and neurodegenerative disorders in the literature. Research has shown that the fractal dimension of the left cerebral hemisphere increases until adolescence and then decreases with aging, while the fractal dimension of the right hemisphere continues to rise until adulthood. Studies in neurodegenerative diseases demonstrated a decline in the fractal dimension of the gray matter in Alzheimer's and multiple system atrophy of the cerebellar type, and in the fractal dimension of the white matter in amyotrophic lateral sclerosis, epilepsy, multiple sclerosis, multiple system atrophy of the cerebellar type, and stroke. Conversely, the fractal dimension of the gray matter increases in multiple sclerosis. Associations were found between the fractal dimension and clinical scores, showing the potential of the fractal dimension as a marker to monitor brain shape changes in normal or pathological processes and predict cognitive or motor function.

Keywords Alzheimer's • Amyotrophic lateral sclerosis • Aging • Epilepsy • Fractal dimension (FD) • Multiple sclerosis • Multiple system atrophy • Neurodegenerative disease • Shape complexity

L. Zhang, PhD (✉)

LZ Biomedical, LLC, 280 E 1st Ave, #513, Broomfield, CO 80038, USA
e-mail: LZhang@lzbiomed.com

G.H. Yue, PhD (✉)

Human Performance and Engineering Research, Kessler Foundation,
1199 Pleasant Valley way, West Orange, NJ 07052, USA

Department of Physical Medicine and Rehabilitation, Rutgers New Jersey Medical School,
Rutgers, The State University of New Jersey, Newark, NJ, USA
e-mail: GYue@kesslerfoundation.org

14.1 Introduction

Fractal analysis has been applied to the characterization of the nervous system, from simple cells to complex brain structures [7]. Studies have shown that fractal geometry can be used to quantify shape complexity changes of the brain with age [3, 10, 19, 23, 28, 36, 38, 42, 47, 50] and neurodegenerative diseases such as multiple sclerosis [8, 9], Alzheimer's [20, 21], amyotrophic lateral sclerosis [35], multiple system atrophy [48], stroke [49], and epilepsy [4, 12, 25]. The term "fractal" was introduced by Mandelbrot [27] to describe the irregular but self-similar shapes of natural objects. It summarizes the structural details of the object in a range of spatial scales into a numerical value (fractal dimension [FD]), which can serve as an index of morphometric variability and complexity of the object. The more complex the object (e.g., a more convoluted cortical surface, a white matter [WM] structure with a more complicated branched pattern), the higher its FD value (Fig. 14.1). The FD is based on a logarithmic scale, and small changes in the FD correspond to large changes in complexity [43]. The fractal geometry of the brain was presented by Hofman using gross specimen data [15] and confirmed by magnetic resonance imaging (MRI) studies [16, 22, 26, 51]. MRI has been frequently used to study brain shape. Besides a few specimen studies [15, 46], most fractal research has analyzed MRI data to evaluate brain shape complexity at macroscopic and microscopic scales using T1- [3, 4, 8–10, 12, 16, 19–26, 28, 35, 36, 38, 48–51] and T2-weighted magnetic resonance (MR) images [44], respectively.

This chapter reviews MRI-based fractal studies of the brain shape in aging and neurodegenerative diseases.

14.1.1 Anatomical Shape Features of Interest

Depending on the pathophysiological processes, FD values were computed on different shape features of the brain WM and gray matter (GM) to evaluate shape complexity changes with age or neurological diseases. Table 14.1 summarizes the shape features studied in the current literature. In general, three shape features were investigated in the WM fractal studies – interior (skeleton), surface (gray-white matter interface), and general structures (Fig. 14.1) [4, 8, 10, 12, 20, 26, 28, 35, 38, 48–51]. The skeleton describes a thin line of an object that summarizes its shape, size, orientation, and connectivity [5]. It represents the interior shape and is the essential structure of the WM. The surface is a set of boundary voxels in WM images. The general structure is the whole set of WM voxels. Besides the macroscopic structures described above, a study examined the microstructure of the WM using T2-weighted MR images [44].

In the GM fractal studies, the cortical surface was investigated because of the obvious fractal properties of the sulci-gyri convolution patterns. Specifically, pial surface (external cortical surface), gray-white matter interface (internal cortical

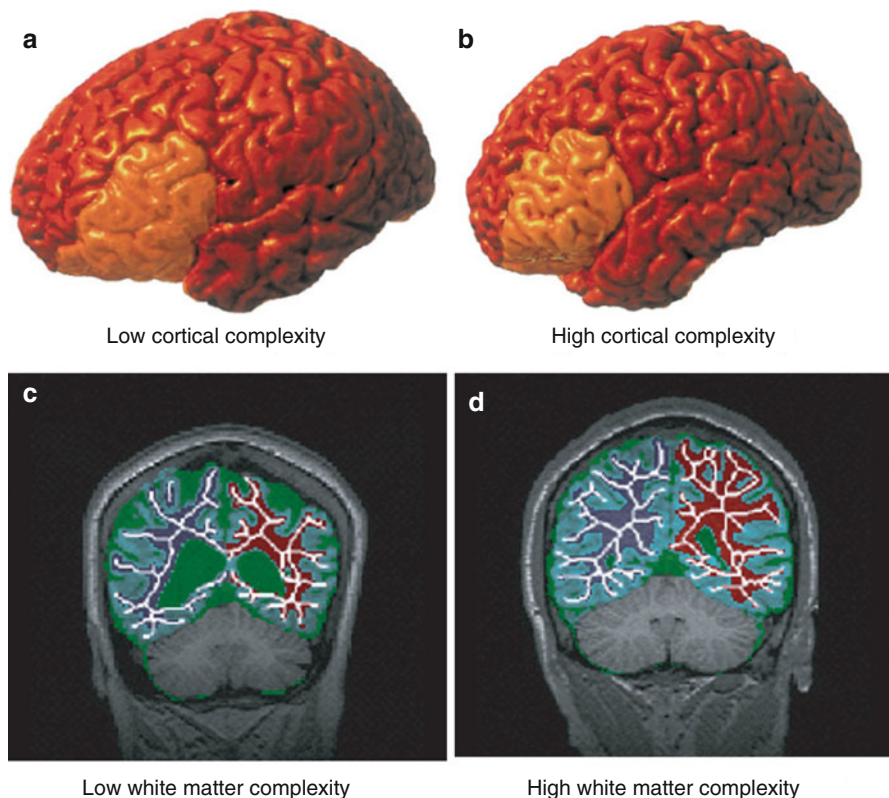


Fig. 14.1 Representative examples of brain shape complexity. Low and high cortical complexity in inferior frontal regions is shown in a 6-year-old female (**a**) and a 16-year-old female (**b**), separately. Low and high white matter complexity is demonstrated on a MR slice from an old subject (**c**) and a young subject (**d**). Low complexity values indicate a flat structure area with few secondary branches, while higher complexity values indicate a greater number of convolutions and more higher-order branches ((**a**, **b**) Reprinted from Blanton et al. [3], images courtesy of Arthur W. Toga, PhD, USC Laboratory of Neuro Imaging, and (**c**, **d**) reprinted from Zhang et al. [50], with permission from the publishers)

surface), and cortical ribbon (the cortical surfaces and the structure between them) structures were examined to assess cortical complexity changes (Fig. 14.2) [3, 9, 16, 19–25, 36, 42, 47, 48]. The gray-white matter interface may be considered as a shape feature of either the WM or the GM as it may reflect the changes of either or both of the structures.

Given that fractal properties arise secondary to gyrification [15], the FD of the cortical surface measures the folding pattern. Two studies reported a strong association between the FD of the pial surface and shape measures, such as folding area, sulcal depth, and curvature, and a weak association between the FD of the pial surface and cortical thickness [16, 18]. A recent study found strong positive correlations between the FD of the cortical ribbon and cortical thickness and between the FD of

Table 14.1 Anatomical shape features of interest and fractal dimension methods in brain shape studies in normal structure, aging, and neurodegenerative diseases

Pathology	Shape features of interest	MR	Fractal dimension methods
Normal structure	3D gray matter (cortical ribbon) [22]	T1	Fast Fourier transform-based method [22]
	2D skeleton of the cerebellar white matter [26]	T1	Box counting on 2D images [26]
	3D external cortical surface (pial surface) [16]	T1	Box counting on a 3D tessellated surface [16]
	3D white matter skeleton, surface and general structure [51]	T1	Box counting on 3D images [51]
Aging	<i>White matter</i>		
	3D skeleton, surface and general structure [10, 50]	T1	Box counting on 3D images [51]
	3D general structure [28, 38]	T1	Box counting on 3D images [28, 37, 38]
	Microstructure of deep white matter [44]	T2	Multifractal measure [44]
	<i>Gray matter</i>		
	3D external cortical surface [3]	T1	Surface-based [46]
	3D external cortical surface [42, 47]	T2	Box counting on 3D images [42, 47]
	Pseudo 3D-skeletonized cerebral surface [23]	T1	Box counting on 3D images [23]
	2D-skeletonized cerebral cortex [19]	T1	Box counting on 2D images [19]
	Surface of central sulcus [24]	T1	Surface-based [24, 46]
	3D cortical ribbon [36]	T1	Box counting on 3D images [37]
	2D coronal and axial profiles of the cerebral cortical ribbon [21]	T1	Box counting on 2D cortical ribbon images [21]
	3D cortical ribbon, 3D gray-white matter surface [20]	T1	Box counting on a 3D tessellated surface [16, 18, 20]
	3D white matter skeleton, surface and general structure [35]	T1	Box counting on 3D images [51]
Alzheimer's disease			
Amyotrophic lateral sclerosis			
Epilepsy	2D white matter contour (gray-white matter interface) [4]	T1, proton density	Box counting on 2D images [4]
	3D white matter surface [12]	T1	Surface based [12]
	3D external cortical surface [25]	T1	Surface based [45, 46]

Pathology	Shape features of interest	MR	Fractal dimension methods
Multiple sclerosis	2D white matter border, skeleton [8]	T1	Box counting on 2D images (HarFA software, http://www.fch.vutbr.cz/lectures/imagesci/ ; [51])
	3D gray matter (cortical ribbon) [9]	T1	Box counting on 3D images [9]
Multiple system atrophy of the cerebellar type	3D cerebellar white matter, cerebellar gray matter [48]	T1	Box counting on 3D images [48]; extended from HarFA 2D box counting; [51])
	2D white matter skeleton [49]	T1	Box counting on 2D images [49, 51]

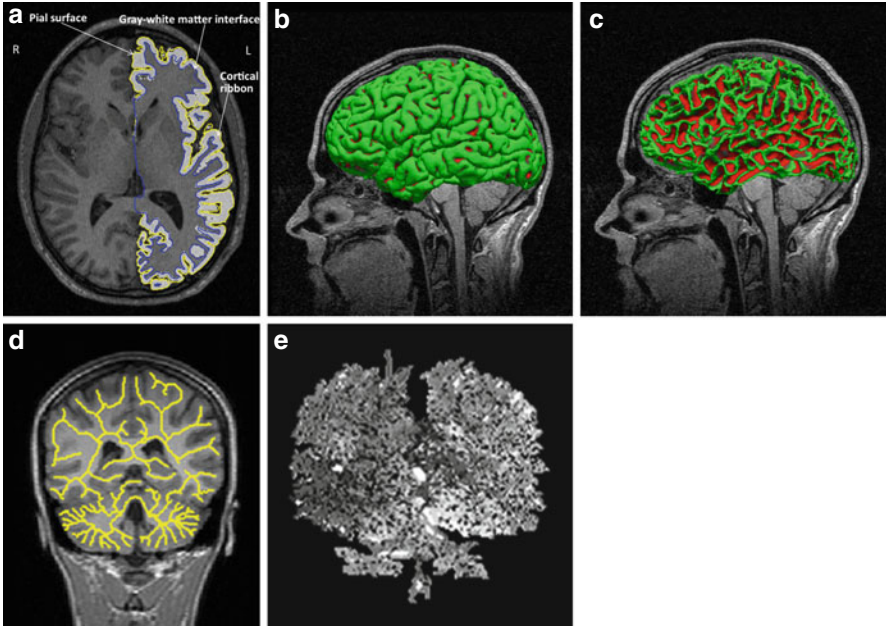


Fig. 14.2 Brain shape features on magnetic resonance imaging (MRI). (a) Illustration of the gray matter shape, including the pial surface, the gray-white matter interface, and the cortical ribbon. (b) Lateral visualization of the pial surface. (c) Lateral visualization of the gray-white matter interface (white matter surface) of the same subject demonstrated in (b). (d) 2D white matter skeleton of a MRI slice. (e) 3D white matter skeleton extracted from the same image shown in (d) ((a–c) Modified from Sandu et al. [36], images courtesy of Anca-Larisa Sandu, PhD, Aberdeen Biomedical Imaging Center, University of Aberdeen, UK, and (d, e) reprinted from Zhang et al. [51], with permission from the publishers)

the cortical ribbon and gyrification index [21]. Thus, in the neurodegenerative process, the effect of the decrease in the cortical thickness is complementary with the impact of the reduction in the gyrification index. Shape measurements such as thickness, sulcal depth, and curvature represent local features of the cortex. The gyrification index [52], a global descriptor of cortical complexity, is sensitive to the direction of the imaging slices [45]. These findings suggest the FD is a superior global measurement for the characterization of the folding pattern of the entire cortex. Figure 14.3 demonstrates the effects of the cortical thickness and gyrification index on the FD.

14.1.2 Fractal Dimension Methods

Several FD methods were used in the quantification of brain shape complexity (Table 14.1), including box-counting [4, 16, 18–21, 23, 26, 28, 37, 38, 42, 47–51], surface-based [3, 12, 24, 45, 46], and fast Fourier transform-based methods [22].

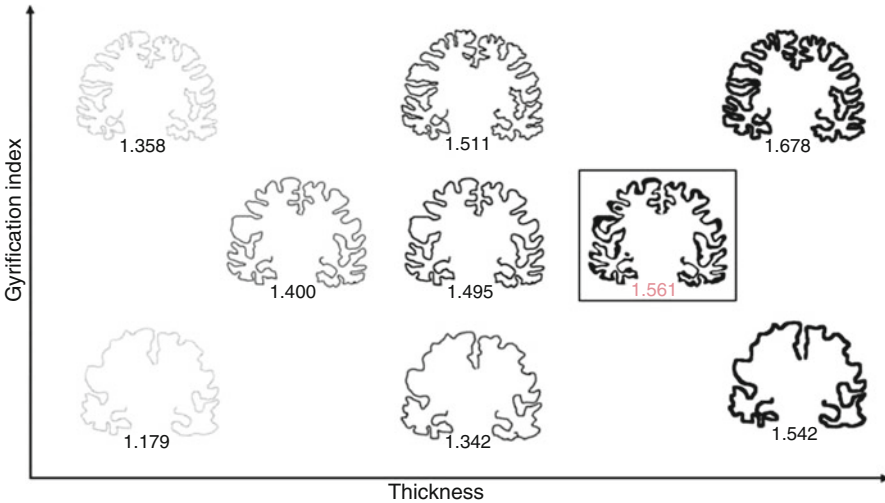


Fig. 14.3 The effects of cortical thickness and gyrification index on measured fractal dimensionality. A coronal slice from a control subject and its fractal dimension are seen in the box. The remaining cortical ribbons are artificial data demonstrating fractal dimension changes with variation in cortical thickness, gyrification index, and the combination of the two. The fractal dimension of each slice is indicated by the number below the slice. Changes in the cortical thickness are seen on the horizontal axis with increasing thickness toward the right. Changes in the gyrification index are seen on the vertical axis with values increasing upwards. Thinning of the cortical ribbon and lowering the gyrification index both decrease fractal dimensionality (Reprinted from King et al. [21], with permission from the publisher)

Among them, box counting is the most widely used technique because it can evaluate a fractal structure with or without strict self-similarity [51].

In general, the box-counting method works by repeatedly covering fractal images using meshes with different-sized boxes (r) and then counting the number of boxes (N) occupied by the studied structure [27]. The process results in a logarithmic function, $\ln(N) = D \cdot \ln(1/r) + \ln(k)$. The slope of the function (D) is referred to as the FD.

The surface-based algorithm was used to evaluate cortical surface complexity. It estimates the FD using the slope of a regression line between the logarithmic least squares of the surface area and the logarithmic spatial frequency of the surface mesh that models the cortex [3]. A box-counting algorithm has been used recently to compute the FD of tessellated cortical surfaces extracted from MR images to evaluate cortical complexity [16, 18, 20].

The Fourier-based method was proposed to examine cortical ribbon complexity, and the FD is dependent on the Fourier function of the cortical shape [22].

A multifractal analysis has been used to evaluate microstructural changes in the WM on T2-weighted MR images [44]. It divides an image into squares and the probability density of each square box is defined. The multifractal measure is computed from a series of equations derived from the slope of a log-log plot of the

probability and the size of the square [44]. Different from the conventional FD measure that evaluates macroscopic fractal structure, the multifractal index measures local microscopic shape changes by quantifying intensity fluctuation.

14.2 Fractal Dimension Studies of the Brain Shape

14.2.1 Aging

The changes of brain shape complexity occur throughout life span with age, involving both GM and WM [3, 10, 19, 23, 28, 36, 38, 42, 44, 47, 50].

The FD studies of GM structure have reported that cortical complexity increases in early fetal life [42, 47], from infancy (<1 year old) until puberty (15 years old) for the left hemisphere and until adulthood (>25 years old) for the right hemisphere [3, 19], and then decreases with aging [23, 36]. Specifically, the FD of the cortical surface was found to be relatively stable before 28 weeks of gestational age and increase rapidly afterwards [47]. Kalmanti and Maris measured the FD of the 2D-skeletonized cerebral cortex in 93 healthy individuals (3 months–78 years; mean \pm SD: 16.6 \pm 16.6 years old) that were divided into four groups: infants (<1 year old), children (1–10 years old), peripubertals (10–15 years old), and adults (>25 years old) [19]. They found that basal ganglia development, mainly in the left hemisphere, was heavily dependent upon age until adolescence (15 years old). Both left and right cortical complexity was equally developed between the ages of 1–15 years, while the right cortex continued to develop in adulthood. A smaller sample-size study ($n=24$) compared the FD scores of the external cortical surface between 24 normal children (6–11 years old [$n=13$]; mean \pm SD: 9.23 \pm 1.71 years old) and adolescents (12–16 years old [$n=11$]; mean \pm SD: 13.25 \pm 1.14 years old) and found that cortical complexity increased in the left and right inferior frontal and the left superior frontal regions [3]. Sandu et al. [36] investigated postadolescent developmental changes in cortical complexity by comparing the FD values of adolescents ($n=17$; 13.3–14.4 years old; mean \pm SD: 14.1 \pm 0.27 years old) with those of adults ($n=14$; 21–30.1 years old; mean \pm SD: 24.24 \pm 2.76 years old). They found significant reductions in the FD of the cortical ribbons for the whole brain, left and right hemispheres, and frontal and parietal lobes for both genders and only for males in the left temporal lobe. Lee et al. [23] compared the FD values of skeletonized cortical ribbons between healthy young ($n=31$; mean \pm SD: 24.48 \pm 5.02 years old) and old subjects ($n=31$; mean \pm SD: 63.23 \pm 9.42 years old) and found decreased FD scores in the old group. Besides the cortical studies, one group investigated age-related changing patterns in the shape complexity of the anterior and posterior walls of the central sulcus (CS) in 295 healthy subjects (18–94 years old) [24]. The authors found significant reductions in the FD of the posterior wall of the right CS and a trend of FD reduction in the anterior walls of the bilateral CS during normal aging. No age-related changes in the FD were observed for the posterior wall of the left CS. Research has shown that the complexity of the cortical surface has a

significant association with intelligence and education [16], which suggests that cortical complexity may serve as a biological marker of cognitive development.

Age-related WM FD changes throughout the adulthood (20–80 years old) demonstrated an inverse U-shape pattern, with a gradual increase from young to mid-age and a sharp decrease to the old ($n=209$) [10]. Specifically, the FD values of the WM general structure for the whole brain and each hemisphere increased until the late 40s and then decreased with age. The FD values of the WM skeletons for the whole brain and left hemisphere declined from the 20s to the age of 30, then rose until the age of 50, declined again to the age of 70, and then rose again. In contrast, the FD of the skeletons for the right hemisphere increased slightly until the 40s and reduced sharply afterwards. The FD reduction in aging was also observed in a smaller sample-size study (24 young subjects, 17–35 years old; mean \pm SD, 27.7 ± 4.4 years old; 12 old subjects, 72–80 years old; mean \pm SD, 74.8 ± 2.6 years old) that reported significant reductions in the FD of the WM skeleton of the whole brain and left hemisphere, and in that of the WM general structure of the whole brain [50]. This study also observed a nonuniform distributed pattern in the degeneration of WM complexity between the genders and across brain hemispheres, with a decreased WM interior shape complexity found in the left hemisphere in old men but in the right hemisphere in old women. Neither of the above two studies observed FD changes in the gray-white matter surface. A longitudinal study measured the FD of the WM general structure on 148 participants at ages 68 years and followed them until 73 years. The authors reported significant FD reductions in the WM over the 5-year period in late life [38]. These FD decreases were associated with cognitive function decline, specifically processing speed (Digital Symbol score), verbal memory (Auditory Verbal Learning Test), reasoning (Raven's Standard Progressive Matrices), and general cognitive ability after adjustment for childhood mental ability. This is consistent with a study that reported significant associations between the FD of brain WM structure and cognitive changes over the life course from age 11 to 68 years [28]. Specifically, the FD was correlated positively with lifelong fluid change, estimated by a standardized difference between Moray House Test (MHT) and Raven's Standard Progressive Matrices test (RPM), and negatively with a decline in cognition in late life, estimated by a standardized difference between the National Adult Reading Test (NART) and RPM. No significant correlations were found between fractal measures and the cognitive maturation from 11 years to adulthood, measured by the standardized difference between the MHT and NART. These results suggest that those with a greater brain WM structural FD had greater than expected fluid abilities at age 68 years than predicted by their childhood intelligence and less cognitive decline at age 68 years. Takahashi et al. [44] performed a multifractal study to examine age-related microstructural changes in the deep WM on T2-weighted MR images without visible abnormal intensities. They reported an increased multifractal measure in the frontal region, not in the parieto-occipital region, and a higher executive dysfunction score in healthy elderly subjects compared to young healthy controls. The executive dysfunction score was found to be positively associated with the multifractal measure in the frontal region, but not in the parieto-occipital region. These findings suggest that microstructural

changes in the WM preferentially occur in the frontal region during normal aging, and these changes are correlated with executive cognitive decline reflective of frontal-subcortical dysfunction [44]. The above studies suggest that WM complexity may predict retention of cognitive ability within late life.

14.2.2 Alzheimer's Disease

Alzheimer's disease (AD) is an irreversible, progressive brain disorder in which amyloid plaques and tau tangles present throughout the brain, and neurons degenerate and die, causing problems with memory, thinking, and behavior [33]. FD studies have demonstrated a decrease in the shape complexity of the cerebral cortex in AD on structural MR images [20, 21].

A decrease in the FD of the 2D cortical ribbon was found on the anterior tip of the temporal lobe, the mammillary bodies, the superior colliculus, the most posterior edge of the corpus callosum, the inferior colliculus, and the massa intermedia of the thalamus in patients with AD [21]. A further study by the same group demonstrated that the FD values of the 3D cortical ribbon and the gray-white matter surface were significantly lower in patients with mild AD than controls, with highly significant differences detected by the FD of the cortical ribbon [20]. Significant correlations were found between the cortical gyrification index and the FD scores of both the cortical ribbon and the gray-white matter surface. However, only the FD of the cortical ribbon had a significant association with cortical thickness and the most commonly used neuropsychiatric assessment battery in AD clinical trials, AD Assessment Scale cognitive (ADAS-cog) score. This study showed that the FD of the cortical ribbon had the highest discrimination power in separating controls and mild AD patients among the studied matrices, including cortical thickness, the gyrification index, and the FD measures of the gray-white matter surface and the pial surface. The FD of the pial surface was not recommended by the authors, since atrophic changes on the pial surface could either decrease or increase FD, depending on how the atrophy occurs. For example, two types of atrophic changes in the pial surface were observed in the brains used in the study: decreased folding area causing decreased complexity and increased sulcal depth leading to increased complexity. These studies demonstrate the potential clinical application of the FD as a quantitative marker of cortical structure in AD.

14.2.3 Amyotrophic Lateral Sclerosis

Amyotrophic lateral sclerosis (ALS) is a rapidly progressive neurodegenerative disease that attacks motor neurons responsible for controlling voluntary muscle activities [29]. ALS patients with frontotemporal dementia (ALS-FTD) were reported to have the greatest degeneration in WM shape complexity among ALS patients with

different clinical signs [35]. Four ALS patients subgroups were included in this study, including ALS-FTD, upper motor neuron (UMN)-predominant ALS patients with corticospinal tract (CST) hyperintensity on T2/PD-weighted images (ALS-CST+), UMN-predominant ALS patients without CST hyperintensity identified on T2/PD-weighted images (ALS-CST-), and ALS-classic patients (ALS-CI). Specifically, the FD values of the whole brain WM skeletons, right-hemisphere skeletons, and whole brain general structure were significantly reduced in the ALS-FTD patients when compared with the ALS-CST+ patients (Fig. 14.4). No significant voxel-based morphometry changes were found between the controls and the ALS patients and among the ALS subgroups. These findings may suggest that the FD is a more sensitive index of brain WM integrity than volumetric measurement in ALS population.

ALS functional rating scale (ALSFRS-R) is a measure of daily functional activity impairment (e.g., speech, swallowing, and walking) and used for evaluating the functional status of patients with ALS. The significant association between the FD and ALSFRS-R [35] indicates that WM shape complexity reflects the functional

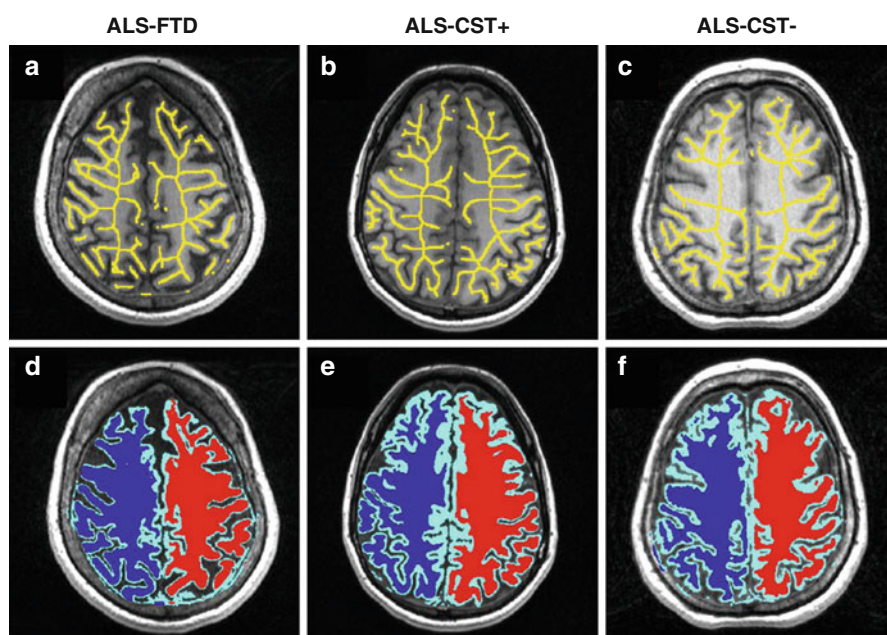


Fig. 14.4 2D illustration of reduced complexity in the white matter skeleton and general structure on anatomical MR images. The complexity levels of the WM skeleton and general structure were reduced in an ALS-CST- patient (c, f) and an ALS-FTD patient (a, d) compared to an ALS-CST+ patient (b, e). ALS-FTD: ALS patients with frontotemporal dementia. ALS-CST+: Upper motor neuron (UMN)-predominant ALS patients with corticospinal tract (CST) hyperintensity on T2-/PD-weighted images. ALS-CST-: UMN-predominant ALS patients without CST hyperintensity identified on T2-/PD-weighted images (Reprinted from Rajagopalan et al. [35], with permission from the publisher)

status of ALS patients, and the FD could potentially serve as a biomarker of ALS pathophysiology.

14.2.4 Epilepsy

Epilepsy is a neurological disorder in which nerve cell activity in the brain becomes disturbed, causing seizures and sometimes loss of consciousness [32]. Fractal studies have shown decreased cortical and WM complexity in epilepsy [4, 12, 25]. In the cortical complexity study, a decreased FD of the external cortical surface was found in all lobar regions except the right frontal region in patients with left mesial temporal lobe epilepsy [25]. In patients with right mesial temporal lobe epilepsy, decreased complexity was observed in the bilateral temporal, occipital, and left parietal regions. Cook, Free et al. investigated brain WM shape complexity in epilepsy by measuring the FD values of the 2D WM border and 3D WM surface on conventional MR images [4, 12]. FD reductions in the WM border (gray-white matter interface) were found in more than half of the patients with frontal lobe epilepsy without identifiable lesions on structural MR images [4]. In the 3D study, abnormal FD scores of the WM surface were found in 8 out of 16 patients with cryptogenic epilepsy and a gyral abnormality on MR images and in 9 out of 23 patients with epilepsy and normal MR images [12]. These findings suggest that the FD can be used to measure subtle cortical changes, and the disruption of the cortical ribbon appeared in many patients with epilepsy.

14.2.5 Multiple Sclerosis

Multiple sclerosis (MS) is a chronic inflammatory and neurodegenerative disease of the central nervous system in which axons have been denuded of the myelin sheaths that protect them and allow the conduction of nerve signals [17]. WM lesions are well recognized in MS [1], and extensive damage of GM has also been reported in recent studies [34, 53].

Esteban et al. reported decreased WM FD values and increased GM FD measures in patients with MS [8, 9]. Such different abnormality patterns of the GM and WM indicate that different pathological processes occurred in each structure. Specifically, the FD measurements of the gray-white matter interface (WM borders) and WM internal structures (WM skeletons) decreased significantly in patients with MS compared with healthy controls. The same FD decrease was found in all MS subtypes, including clinically isolated syndrome (CIS), relapsing-remitting MS (RRMS), secondary progressive MS (SPMS), and primary progressive MS (PPMS), for WM borders and in all subtypes except PPMS for WM skeletons. The decrease of the FD values in the WM borders was affected not only by the presence of MS plaques but also by changes in the non-visible WM abnormalities such as

normal-appearing WM. For the WM skeletons, the decrease was only observed in MR slices with MS lesions. The FD of the WM skeletons was found to be correlated with both T1 and T2 lesion load. No associations were found between the WM FD and MS-related clinical disability scales such as Expanded Disability Status Scale (EDSS) and the MS Functional Composite (MSFC) score [8].

The GM study focused on MS patients at the early to intermediate phases of the disease and found increased FD values in either first attacks of MS (FAMS) or relapsing-remitting MS (RRMS) compared with healthy subjects [9]. The FD of the RRMS was significantly higher than FAMS. These findings suggest that GM shape complexity is abnormal in patients with MS and the FD changes occur in the early stage of the disease and increase with disease progression. However, the authors stated that the FD of the GM in the progressive patients was difficult to estimate since GM atrophy was highly prominent in this subgroup. For the brain-lesion load, the FD of the GM was found to be correlated with T1 and T2 WM lesion load, but not with the GM atrophy or the disability scores such as EDSS and MSFC. Several explanations were provided in the study: (1) GM atrophy is less pronounced in the early stages of the disease, and there may be lack of statistical power to detect an association. (2) GM atrophy might preclude GM tissue damage that has been associated with the FD changes.

14.2.6 Multiple System Atrophy

Multiple system atrophy (MSA) is a progressive neurodegenerative disease in which different types of nerve cells in the brain and spinal cord lose function and die, affecting both autonomic nervous system and movement [30]. Research has shown that the FD of the cerebellar WM and GM decreased significantly in patients with MSA of the cerebellar type compared to controls. Such cerebellar degeneration was dominated by morphological changes in the cerebellar WM [48]. Although the FD was related to volumetric measurement in this study, it was suggested as a better index than the conventional volumetric measurement in assessing the shape changes of the WM and GM, since it generated smaller variances and less gender effects.

14.2.7 Stroke

A stroke occurs when the blood supply to an area of the brain is interrupted or when a blood vessel in the brain bursts, spilling blood into the spaces surrounding brain cells [31]. Brain cells die when the brain is deprived of oxygen and nutrients or there is bleeding into or around the brain.

One study has shown a decreased FD in brain WM following stroke (Fig. 14.5) [49]. The FD was lower in the stroke-affected hemisphere, and the greater FD of the residual WM was associated with less impaired upper extremity motor function in

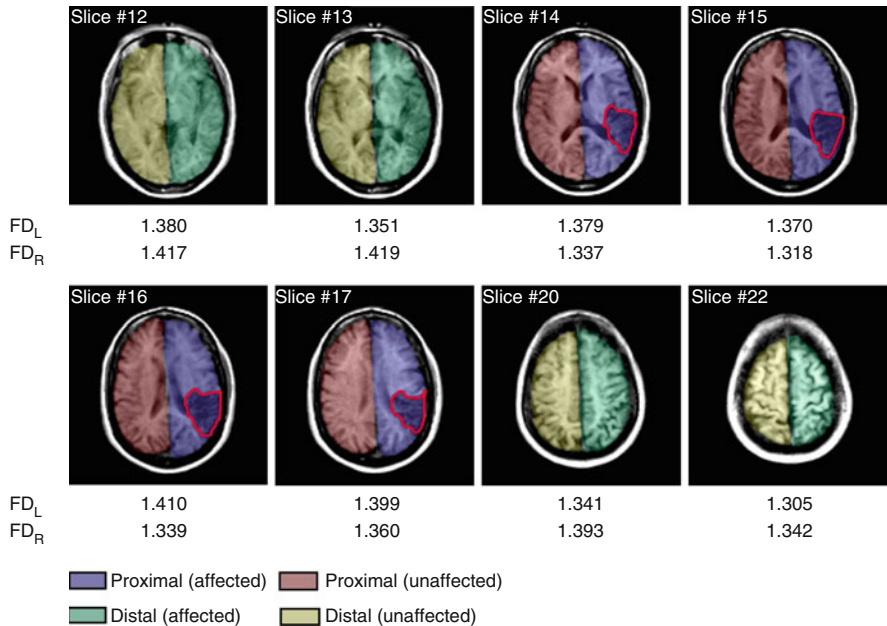


Fig. 14.5 Illustration of the fractal dimension (FD) values of the left and right white matter (WM) in eight horizontal slices from one subject with a right-hemisphere lesion (outlined in red). The FD values of the left hemisphere were smaller than those of the right hemisphere in slices without apparent lesions (slices #12, #13, #20, and #22). The FD values of the left hemisphere were greater than those of the right hemisphere in slices with a lesion (slices #14–#17). Images are displayed in neurological convention, with the left side corresponding to the left hemisphere. FD_L, the FD of the left WM skeleton; FD_R, the FD of the right WM skeleton. The colors were designated to illustrate regions of interest. Blue, proximal region on the affected side; red, proximal region on the unaffected side; green, distal region on the affected side; yellow, distal region on the unaffected side. Note that proximal region indicates slices with lesion and distal region specifies slices without lesion (Reprint from Zhang et al. [49], with permission from the publisher)

patients with left-subcortical or right-cortical lesions. This correlation was more robust in patients with right-hemisphere lesions. No significant associations were found between lesion volume and motor function, suggesting that, at least in this study, the FD was more sensitive in predicting upper extremity motor function than volumetric measurements post stroke. The FD may potentially serve as a useful clinical index to evaluate the level of residual WM structural changes following stroke or any accompanying brain plastic changes to guide future therapeutic interventions.

14.3 Discussion

FD studies have demonstrated that brain shape complexity changes with age throughout life and in neurodegenerative diseases (Table 14.2). In general, the FD of the GM increases in early fetal life [42, 47] and continues to develop equally in

Table 14.2 Fractal dimension changes of the brain shape with age and neurodegenerative diseases and their association with clinical scores and other morphometric measures

Pathology	Fractal dimension (FD)	Associations
Aging	↑FD of the external cortical surface in early fetal life [42, 47]; ↑FD of the left cerebral cortex from infancy till adolescence (1–15 years old) and then ↓ with aging; ↑FD of the right cortex till adulthood and then ↓ with aging [3, 19, 23, 36]	FD of the cortical surface ↔ cortical thickness, folding area in both hemispheres and several lobe regions, sulcal depth only in the left temporal region, IQ, and number of years of education [16]
	Inverse-U pattern on the FD of the white matter: ↑FD from young till mid-age then ↓ to the old [10, 38, 50]	FD of the white matter ↔ information processing speed (digital symbol score), verbal memory (auditory verbal learning test), reasoning (Raven's standard progressive matrices), general cognitive ability in specific models (with adjustment for childhood mental ability), lifelong fluid change (positive), and cognitive decline in late life (negative) [28, 38]
Alzheimer's disease (AD)	↓ FDs of the cortical ribbon and gray-white matter surface [20, 21]	FD of the cortical ribbon ↔ AD assessment scale cognitive (ADAS-cog) score [20]
		FDs of the cortical ribbon and gray-white matter surface ↔ cortical gyrification index, cortical thickness [20, 21]
Amyotrophic lateral sclerosis (ALS)	↓FD of the white matter in patients with different clinical signs; greatest reductions in ALS patients with frontotemporal dementia [35]	FD of the white matter ↔ ALS functional rating scale [35]
Epilepsy	↓FD of the external cortical surface in all lobar regions except the right frontal regions in patients with right mesial temporal lobe epilepsy; ↓FD of the external cortical surface in the bilateral temporal occipital, and left parietal regions in patients with right mesial temporal lobe epilepsy [25]	
	↓FD of the 2D WM contour in more than half of patients with frontal lobe epilepsy [4]	
	Abnormal FDs of WM surface in half of the patients with cryptogenic epilepsy and a gyral abnormality on MR images and 9/23 patients with epilepsy and normal MR images [12]	

(continued)

Table 14.2 (continued)

Pathology	Fractal dimension (FD)	Associations
Multiple sclerosis (MS)	↓ FD of the white matter border, skeleton in all MS and subtypes [8]	No associations between FDs of the white matter and gray matter and MS-related clinical disability scales (expanded disability status scale and MS functional composite score) [8, 9]
	↑ FD of the gray matter at the early to intermediate phases of disease [9]	FDs of the white matter skeletons and gray matter ↔ T1 and T2 WM lesion load [8, 9]
Multiple system atrophy of the cerebellar type	↓ FD of 3D cerebellar white matter, cerebellar gray matter [48]	FD ↔ volume [48]
Stroke	↓ FD of the white matter in the stroke-affected hemisphere [49]	FD of the residual white matter ↔ upper extremity motor function (Wolf motor function test, Fugl-Meyer motor assessment score) [49]

↓ decreased, ↑ increased, ↔ is associated with

the left and right hemispheres between 1 and 15 years old. After adolescence, the FD of the left cortex decreases, while the FD of the right cortex continues to increase until adulthood then decreases with aging [3, 19, 23, 36]. The inverse-U pattern of the FD changes of the left cortex agrees with the changing pattern of a metabolism measure, entropy production, over the same time frames [2]. The FD of the WM increases from young until mid-age and then decreases with aging [10, 38, 50]. The reduction in the FD of the WM and GM in late life with aging parallels with the decrease in glucose metabolism [41]. In the fractal studies of neurodegenerative diseases, the FD was found to decline in the GM in AD [20, 21] and MSA of the cerebellar type [48], and in the WM in ALS [35], epilepsy [4, 12, 25], MS [8], MSA of the cerebellar type [48], and stroke [49]. Such a decreased pattern is consistent with the metabolic studies demonstrating a decline in glucose metabolism with diseases [39]. An increased FD was found in the GM in MS [9] in which a rise in glucose metabolism was observed [39]. These findings may suggest a link between FD-measured shape complexity and metabolism, supporting the association between brain shape and function.

Besides the potential link between the FD and metabolism, the FD of brain shape has been found to be significantly associated with common clinical functional scores, such as AD Assessment Scale Cognitive Score [20], ALS Functional Rating Scale [35], and upper extremity motor function scores (Wolf Motor Function Test and Fugl-Meyer Motor Assessment Score) in stroke [49]. In addition, the changes of the WM FD with age match with the changing pattern of the cognitive abilities throughout the life [6, 28]. These studies suggest that the FD may be used as a quantitative index in the evaluation of the brain shape changes in aging, AD, ALS, or stroke. No associations were observed between the FD

and MS-related clinical disability scales (EDSS and MSFC) [8, 9]. This might be due to the interaction between the FD abnormality in the GM and WM. In the two MS fractal studies, the association of the FD with functional scores was investigated in the GM and WM separately. Further study may be needed to examine the relationship between the clinical scores and the combination of the FD measurements of the GM and WM to assess the usefulness of the FD in MS. The fractal studies in epilepsy [4, 12, 25] and MSA of the cerebellar type [48] did not address the associations between the FD and clinical scores, which are needed in the future to investigate the potential applications of FD analysis in these clinical settings.

To the best of our knowledge, no studies have systematically examined the pathophysiological mechanism of the FD changes with age and in neurodegenerative diseases. It is hypothesized that FD reductions in the brain WM could be due to axon loss, increased water content, decreased myelin content, and other inflammatory events that may lead to a more amorphous tissue. The decrease of the WM border can be due to both juxtacortical WM lesions and GM abnormalities [8]. The FD increase may be due to inflammatory component (i.e., microglial activation) and cellular changes (synapse pruning, demyelination, brain-blood barrier changes, etc.) [9].

Shape analysis has been suggested to provide new information that is not accessible by volumetric measurements [13]. Thus, the FD can be considered as an independent morphometric measure, although some studies showed that the FD was associated with volumetric measurements [8, 9, 48]. Moreover, research has shown that the FD is a more sensitive morphometric measure than volumetric measures to detect subtle structural changes in the brain WM [35, 48, 50]. Besides FD analysis, different approaches were used for quantifying brain topological changes in aging and neurodegenerative disorders, such as magnetization transfer ratio (MTR) [11, 40] or diffusion tensor imaging (DTI) [14]. These techniques may measure different morphological features due to different physical principles of each technique. No FD studies have addressed the relationship between the FD and MTR, DTI or magnetic resonance spectroscopy, which may be needed in the future to identify the biological usefulness of fractal analysis in aging and neurological disorders.

The FD measures of 2D and 3D shape features have been investigated in aging and diseases (Table 14.1). Although 3D measures are generally superior to 2D metrics, sometimes it is useful to evaluate local changes using 2D features [21, 49]. Studies may be needed in the future to extract local 3D shape features to assess local shape complexity changes.

In conclusion, a number of studies have shown the potential of the FD as a clinical measure in the evaluation of brain shape changes in aging and neurodegenerative diseases. In order for the FD technique to be more widely adopted in the clinical settings such as helping clinicians make more objective and accurate diagnosis of brain disease and injury, studies are needed in the future to investigate the associations between the FD measure and pathophysiological mechanism and to identify local shape features to assess changes in the region or regions to improve sensitivity and accuracy of the measurement.

References

1. Allen IV, McKeown SR. A histological, histochemical and biochemical study of the macroscopically normal white matter in multiple sclerosis. *J Neurol Sci.* 1979;41:81–91.
2. Aoki I. Entropy production in human life span: a thermodynamical measure for aging. *Age.* 1994;17:29–31.
3. Blanton RE, Levitt JG, Thompson PM, Narr KL, Capetillo-Cunliffe L, Nobel A, Singerman JD, McCracken JT, Toga AW. Mapping cortical asymmetry and complexity patterns in normal children. *Psychiatry Res.* 2001;107:29–43.
4. Cook MJ, Free SL, Manford MR, Fish DR, Shorvon SD, Stevens JM. Fractal description of cerebral cortical patterns in frontal lobe epilepsy. *Eur Neurol.* 1995;35:327–35.
5. Costa LDF, Cesar Jr RM. Shape analysis and classification: theory and practice. Boca Raton: CRC Press; 2001.
6. Crawford JR, Deary IJ, Starr J, Whalley LJ. The NART as an index of prior intellectual functioning: a retrospective validity study covering a 66-year interval. *Psychol Med.* 2001;31:451–8.
7. Di Ieva A, Esteban FJ, Grizzi F, Klonowski W, Martin-Landrove M. Fractals in the neurosciences, Part II: clinical applications and future perspective. *Neuroscientist.* 2015;21:30–43.
8. Esteban FJ, Sepulcre J, de Mendizábal NV, Goñi J, Navas J, de Miras JR, Bejarano B, Masdeu JC, Villoslada P. Fractal dimension and white matter changes in multiple sclerosis. *Neuroimage.* 2007;36:543–9.
9. Esteban FJ, Sepulcre J, de Miras JR, Navas J, de Mendizábal NV, Goñi J, Quesada JM, Bejarano B, Villoslada P. Fractal dimension analysis of grey matter in multiple sclerosis. *J Neurol Sci.* 2009;282:67–71.
10. Farahibozorg S, Hashemi-Golpayegani SM, Ashburner J. Age- and sex-related variations in the brain white matter fractal dimension throughout adulthood: an MRI study. *Clin Neuroradiol.* 2015;25:19–32.
11. Filippi M, Rocca MA, Martino G, Horsfield MA, Comi G. Magnetization transfer changes in the normal appearing white matter precede the appearance of enhancing lesions in patients with multiple sclerosis. *Ann Neurol.* 1998;43:809–14.
12. Free SL, Sisodiya SM, Cook MJ, Fish DR, Shorvon SD. Three-dimensional fractal analysis of the white matter surface from magnetic resonance images of the human brain. *Cereb Cortex.* 1996;6:830–6.
13. Gerig G, Styner M, Shenton ME, Lieberman JA. Shape versus size: improved understanding of the morphology of brain structures. In: *Proceedings of the MICCAI, LNCS 2208.* 2001. p. 24–32.
14. Goldberg-Zimring D, Mewes AU, Maddah M, Warfield SK. Diffusion tensor magnetic resonance imaging in multiple sclerosis. *J Neuroimaging.* 2005;15:68S–81.
15. Hofman MA. The fractal geometry of convoluted brains. *J Hirnforsch.* 1991;32:103–11.
16. Im K, Lee JM, Yoon U, Shin YW, Hong SB, Kim IY, Kwon S, Kim SI. Fractal dimension in human cortical surface: multiple regression analysis with cortical thickness, sulcal depth, and folding area. *Hum Brain Mapp.* 2006;27:994–1003.
17. Institute of Medicine (US) Committee on Multiple Sclerosis: Current Status and Strategies for the Future, Joy JE, Johnston Jr RB, editors. *Multiple sclerosis: current status and strategies for the future.* Washington, DC: National Academies Press (US); 2001.
18. Jiang J, Zhu W, Shi F, Zhang Y, Lin L, Jiang T. A robust and accurate algorithm for estimating the complexity of the cortical surface. *J Neurosci Methods.* 2008;172:122–30.
19. Kalmanti E, Maris TG. Fractal dimension as an index of brain cortical changes throughout life. *In Vivo.* 2007;21:641–6.
20. King RD, Brown B, Hwang M, Jeon T, George AT, Alzheimer's Disease Neuroimaging Initiative. Fractal dimension analysis of the cortical ribbon in mild Alzheimer's disease. *Neuroimage.* 2010;53:471–9.
21. King RD, George AT, Jeon T, Hynan LS, Youn TS, Kennedy DN, Dickerson B, Alzheimer's Disease Neuroimaging Initiative. Characterization of atrophic changes in the cerebral cortex using fractal dimensional analysis. *Brain Imaging Behav.* 2009;3:154–66.

22. Kiselev VG, Hahn KR, Auer DP. Is the brain cortex a fractal? *Neuroimage*. 2003;20:1765–74.
23. Lee JM, Yoon U, Kim JJ, Kim IY, Lee DS, Kwon JS, Kim SI. Analysis of the hemispheric asymmetry using fractal dimension of a skeletonized cerebral surface. *IEEE Trans Biomed Eng*. 2004;51:1494–8.
24. Li S, Xia M, Pu F, Li D, Fan Y, Niu H, Pei B, He Y. Age-related changes in the surface morphology of the central sulcus. *Neuroimage*. 2011;58:381–90.
25. Lin JJ, Salamon N, Lee AD, Dutton RA, Geaga JA, Hayashi KM, Luders E, Toga AW, Engel Jr J, Thompson PM. Reduced neocortical thickness and complexity mapped in mesial temporal lobe epilepsy with hippocampal sclerosis. *Cereb Cortex*. 2007;17:2007–18.
26. Liu JZ, Zhang LD, Yue GH. Fractal dimension in human cerebellum measured by magnetic resonance imaging. *Biophys J*. 2003;85:4041–6.
27. Mandelbrot BB. *The fractal geometry of nature*. New York: Freeman; 1982.
28. Mustafa N, Ahearn TS, Waiter GD, Murray AD, Whalley LJ, Staff RT. Brain structural complexity and life course cognitive change. *Neuroimage*. 2012;61:694–701.
29. National Institute of Neurological Disorders and Stroke. *Amyotrophic Lateral Sclerosis (ALS) Fact Sheet*. NIH Publication No. 13-916; 2013.
30. National Institute of Neurological Disorders and Stroke. *Multiple System Atrophy Fact Sheet*. NIH Publication No. 15-5597; 2014.
31. National Institute of Neurological Disorders and Stroke. *Stroke: Hope Through Research*. NIH Publication No. 9902222; 2004.
32. National Institute of Neurological Disorders and Stroke. *The Epilepsies and Seizures: Hope Through Research*. NIH Publication No. 15-156; 2015.
33. National Institute on Aging. *Alzheimer's Disease Fact Sheet*. NIH Publication No. 15-64243; 2015.
34. Pirko I, Lucchinetti CF, Sriram S, Bakshi R. Gray matter involvement in multiple sclerosis. *Neurology*. 2007;68:634–42.
35. Rajagopalan V, Liu Z, Allexandre D, Zhang L, Wang XF, Piro EP, Yue GH. Brain white matter shape changes in amyotrophic lateral sclerosis (ALS): a fractal dimension study. *PLoS One*. 2013;8(9):e73614.
36. Sandu AL, Izard E, Specht K, Beneventi H, Lundervold A, Ystad M. Post-adolescent developmental changes in cortical complexity. *Behav Brain Funct*. 2014;20:44.
37. Sandu AL, Rasmussen Jr IA, Lundervold A, Kreuder F, Neckelmann G, Hugdahl K, Specht K. Fractal dimension analysis of MR images reveals grey matter structure irregularities in schizophrenia. *Comput Med Imaging Graph*. 2008;32:150–8.
38. Sandu AL, Staff RT, McNeil CJ, Mustafa N, Ahearn T, Whalley LJ, Murray AD. Structural brain complexity and cognitive decline in late life – a longitudinal study in the Aberdeen 1936 Birth Cohort. *Neuroimage*. 2014;100:558–63.
39. Seely AJE, Newman KD, Herry CL. Fractal structure and entropy production within the central nervous system. *Entropy*. 2014;16:4497–520.
40. Seiler S, Pirpamer L, Hofer E, Duering M, Jouvent E, Fazekas F, Mangin JF, Chabriat H, Dichgans M, Ropele S, Schmidt R. Magnetization transfer ratio relates to cognitive impairment in normal elderly. *Front Aging Neurosci*. 2014;6:263.
41. Shen X, Liu H, Hu Z, Hu H, Shi P. The relationship between cerebral glucose metabolism and age: report of a large brain PET data set. *PLoS One*. 2012;7:e51517.
42. Shyu KK, Wu YT, Chen TR, Hen HY, Hu HH, Guo WY. Measuring complexity of fetal cortical surface from MR images using 3-D modified box-counting method. *IEEE Trans Instrum Meas*. 2011;60:522–31.
43. Smith Jr TG, Marks WB, Lange GD, Sheriff Jr WH, Neale EA. A fractal analysis of cell images. *J Neurosci Methods*. 1989;27:173–80.
44. Takahashi T, Murata T, Omori M, Kosaka H, Takahashi K, Yonekura Y, Wada Y. Quantitative evaluation of age-related white matter microstructural changes on MRI by multifractal analysis. *J Neurol Sci*. 2004;225:33–7.
45. Thompson PM, Lee AD, Dutton RA, Geaga JA, Hayashi KM, Eckert MA, Bellugi U, Galaburda AM, Korenberg JR, Mills DL, Toga AW, Reiss AL. Abnormal cortical complexity and thickness profiles mapped in Williams syndrome. *J Neurosci*. 2005;25:4146–58.

46. Thompson PM, Schwartz C, Lin RT, Khan AA, Toga AW. Three-dimensional statistical analysis of sulcal variability in the human brain. *J Neurosci.* 1996;16:4261–74.
47. Wu YT, Shyu KK, Chen TR, Guo WY. Using three-dimensional fractal dimension to analyze the complexity of fetal cortical surface from magnetic resonance images. *Nonlinear Dyn.* 2009;58:745–52.
48. Wu YT, Shyu KK, Jao CW, Wang ZY, Soong BW, Wu HM, Wang PS. Fractal dimension analysis for quantifying cerebellar morphological change of multiple system atrophy of the cerebellar type (MSA-C). *Neuroimage.* 2010;49:539–51.
49. Zhang L, Butler AJ, Sun CK, Sahgal V, Wittenberg GF, Yue GH. Fractal dimension assessment of brain white matter structural complexity post stroke in relation to upper-extremity motor function. *Brain Res.* 2008;1228:229–40.
50. Zhang L, Dean D, Liu JZ, Sahgal V, Wang X, Yue GH. Quantifying degeneration of white matter in normal aging using fractal dimension. *Neurobiol Aging.* 2007;28:1543–55.
51. Zhang L, Liu JZ, Dean D, Sahgal V, Yue GH. A three-dimensional fractal analysis method for quantifying white matter structure in human brain. *J Neurosci Methods.* 2006;150:242–53.
52. Zilles K, Armstrong E, Schleicher A, Kretschmann HJ. The human pattern of gyrification in the cerebral cortex. *Anat Embryol (Berl).* 1988;179:173–9.
53. Zivadinov R, Pirko I. Advances in understanding gray matter pathology in multiple sclerosis: are we ready to redefine disease pathogenesis? *BMC Neurol.* 2012;12:9.

Chapter 15

Fractal Analysis in Neurodegenerative Diseases

**Daniel Pirici, Laurentiu Mogoanta, Daniela Adriana Ion,
and Samir Kumar-Singh**

Abstract Neurodegenerative diseases are defined by progressive nervous system dysfunction and death of neurons. The abnormal conformation and assembly of proteins is suggested to be the most probable cause for many of these neurodegenerative disorders, leading to the accumulation of abnormally aggregated proteins like, for example, amyloid- β (A β) (Alzheimer's disease and vascular dementia), tau protein (Alzheimer's disease and frontotemporal lobar degeneration), α -synuclein (Parkinson's disease and Lewy body dementia), polyglutamine expansion (Huntington disease), or prion proteins (Creutzfeldt-Jakob's disease). An aberrant gain-of-function mechanism toward excessive intraparenchymal accumulation thus represents a common pathogenic denominator in all these proteinopathies. Moreover, depending upon the predominant brain area involvement, these different neurodegenerative diseases lead to either movement disorders or dementia syndromes, although the underlying mechanism(s) can sometimes be very similar, and at other occasions, clinically similar syndromes have quite distinct pathologies. Non-Euclidean image analysis approaches such as fractal dimension (FD) analysis have been applied extensively in quantifying highly variable morphopathological patterns, as well as many other connected biological processes; however, their application to understand and link abnormal proteinaceous depositions to other

D. Pirici, MD, PhD (✉)

Department of Research Methodology, University of Medicine and Pharmacy of Craiova,
Petru Rares Street 2, 200349 Craiova, Dolj, Romania
e-mail: danielpirici@yahoo.com

L. Mogoanta, MD, PhD

Department of Histology, University of Medicine and Pharmacy of Craiova,
Craiova, Romania

D.A. Ion, MD, PhD

Department of Physiopathology, University of Medicine and Pharmacy Carol Davila,
Bucharest, Romania

S. Kumar-Singh, MD, PhD

Molecular Pathology Group, Faculty of Medicine and Health Sciences, Cell Biology &
Histology and Translational Neuroscience Department, University of Antwerp,
Antwerpen, Belgium

clinical and pathological features composing these syndromes are yet to be clarified. Thus, this chapter aims to present the most important applications of FD in investigating the clinical-pathological spectrum of neurodegenerative diseases.

Keywords Fractal dimension • Amyloid plaques • Cortical atrophy • Cerebral blood flow • Electroencephalogram • Gait analysis • Demyelination

15.1 Alzheimer's Disease and Vascular Dementia

Alzheimer's disease (AD) is the most frequent form of neurodegenerative brain disease, and leads to a progressive loss of memory and cognitive abilities. It is responsible for the cognitive decline in up to three-quarters of all patients with dementia [43]. Deposition of amyloid- β ($A\beta$) plaques and tau neurofibrillary tangles (NFT) in affected brain regions are the two pathological hallmarks of AD [2, 81].

Amyloid plaques are extracellular insoluble protein aggregates composed of $A\beta$, a 40–43 amino acid peptide that results from abnormal processing of the amyloid precursor protein (APP) (Fig. 15.1). APP is a single transmembrane protein, and due to alternative splicing is expressed as 695, 751, and 770 amino acid long isoforms with APP695 being most abundantly expressed in neurons [42]. Constitutively, APP is processed by a series of proteases called α and γ secretases that cut the protein to generate extracellular soluble fragment (soluble-APP α) and an APP intracellular domain (AICD) fragment that bears multiple signaling roles, as well as N-truncated $A\beta$ fragment called p3 [16, 74]. In the $A\beta$ secretion pathway, however, APP is cleaved by β and γ secretases leading to secretion of the APP ectodomain (soluble-APP β), AICD, and $A\beta$ fragments of 40 ($A\beta$ 40) or 42 ($A\beta$ 42) amino acids [74]. It is speculated that any remaining uncleaved APP holoprotein at the cell surface can be re-internalized via clathrin-coated pits and subsequently recycled through the endosomal system [67]. Some of those proteins will be recycled to the cell surface, while others will enter the endosomes and lysosomes and will be degraded. $A\beta$ generated within the cells of the brain parenchyma (mostly but not exclusively neurons) is the probable source for the most $A\beta$ in extracellular amyloid plaques [11]. A complete image of the cellular $A\beta$ metabolism is still elusive; however, based on a number of in vitro experiments, it is believed that during the endosomal recycling, $A\beta$ 40 can be generated and released to the surface of the cells. Endoplasmic reticular (ER) vesicles show considerable amount of $A\beta$ 42, whereas Golgi vesicles contain both $A\beta$ 40 and $A\beta$ 42 [74]. Mutations in the genes encoding for APP and γ secretase-components called presenilins (*PSEN1* and 2) constitute an important cause of familial forms of AD, and the subsequent resulting phenotypes manifested as pure AD or associated with a predominant vascular pathology [31, 33, 83].

As already stated, amyloid depositions are basically extracellular aggregates, extremely complex in their composition, morphology, and localization. They can be present almost anywhere in the brain parenchyma, ranging from a diffuse to a more

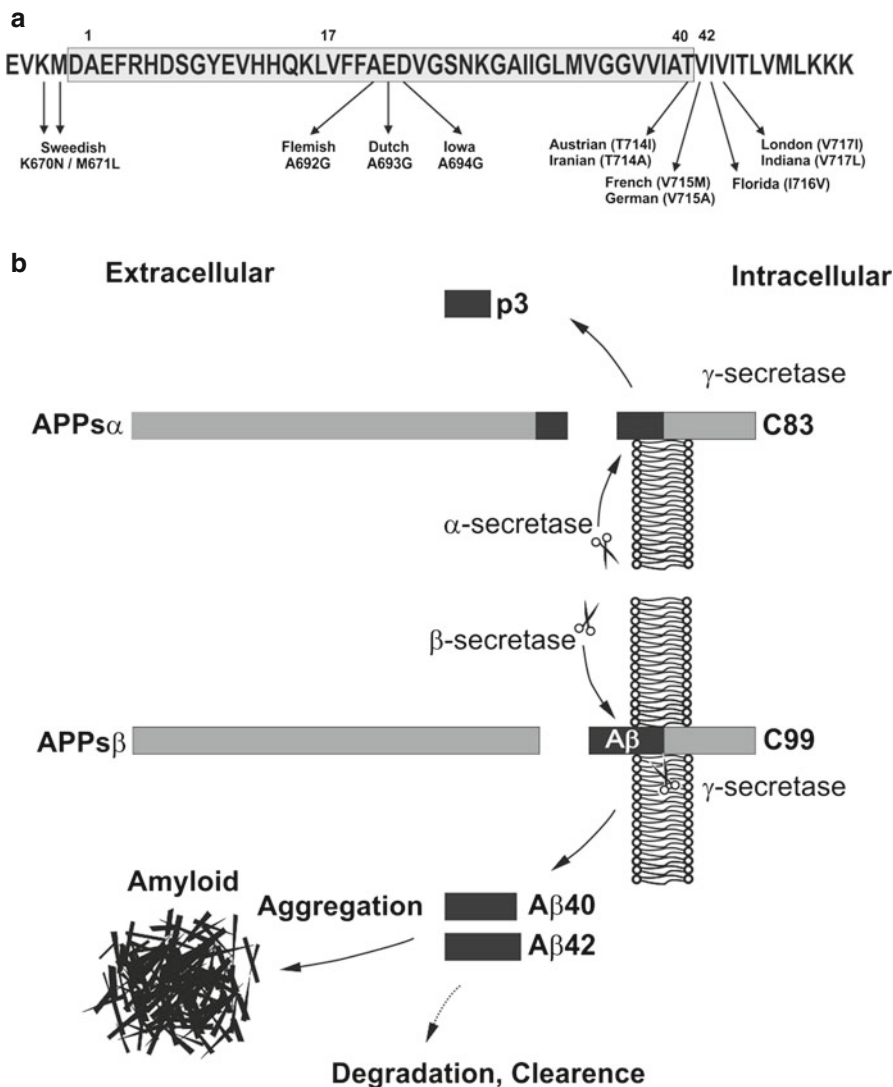


Fig. 15.1 Schematic diagram of the amyloid precursor protein (APP) with pathogenic mutations and metabolic processing. **(a)** The amino acid sequence of A β fragment exhibits common pathogenic amino acid substitutions. Sites of secretase cleavage points are indicated by *arrows* (position 1, 17, and 40–42 for β -, α -, and γ -secretases). **(b)** The constitutive proteolytic cleavage by α - and γ -secretases leads to the formation of the short p3 peptide, and the alternative pathway leads to the formation of A β peptide; in both cases, with a consecutive release of a C-terminal APP intracytoplasmic domain (C83 and C99) and APPs soluble fractions. A β 42 and A β 40 diffuse in the parenchyma and precipitate as fibrillar aggregates or “plaques”

dense texture, as well as in the walls of blood vessels, a feature known as cerebral amyloid angiopathy (CAA) [48, 80, 85]. Although numerous studies describe the overall diversity of all these depositions and their relation with the clinical evolution, there is also increasing evidence toward a close physiopathological connection between CAA, dense types of depositions, and the brain vasculature [50, 52]. Many lines of transgenic mice overexpressing mutant forms of APP and PSEN have been developed in an attempt to mimic the amyloid pathology observed in the brains of human AD patients [12, 28].

In both human pathology and mouse models, it has been showed that this diversity of plaques exhibits different affinities for fibril-binding dyes such as Congo red or Thioflavin S (ThS), the more positive deposits being thus considered more “compact” or “dense,” compared to the “diffuse” material negative for such fibril-binding dyes [48, 80, 85]. Moreover, relative proportions of A β 40 and A β 42 have also been found to differ between these types of plaques, for instance, diffuse deposits are shown to be composed predominantly of A β 42, while the compact plaques contain both A β 42 and A β 40 [21, 38]. Diffuse plaques are also considered to mature to compact plaques by co-depositing A β 40; however, recent data suggest that diffuse and dense plaques might in fact develop on distinct pathways [48, 80].

Subjective morphological classifiers such as “dense,” “diffuse,” or “reticular” as well as objective Euclidean morphometric features like areas, diameters, or densities have had limited utility in describing and classifying the highly variable amyloid patterns [48, 80, 85]. Complex and nonregular objects can be complementarily described utilizing more objective, scale-invariant parameters, which are generally studied under the concept of fractal dimension (FD). FD of an object is a measure of the morphological complexity of that object, the inner self-similarity as measured at different scales, or simply put, the efficiency with which the object is filling the space it occupies [54]. As already described before, this concept is now widely used in pathology to describe many highly irregular normal and pathologically occurring patterns and processes like changes in cerebral blood flow, tumor angiogenesis, and chromatin distribution in malignant cells [13, 53, 59]. Relatively recently, FD analysis has been introduced in studying AD for both pathology and brain-imaging studies.

15.1.1 Fractal Dimension: A Classifier for the AD Pathology

FD analysis has been utilized as a morphological classifier to study amyloid plaques in human, monkey, camel, dog, and felines, and although such an initial study has been based on a low number of analyzed amyloid deposits, it showed that diffuse plaques had significantly lower FD values compared to mature (dense or dense-core) plaques even when considering this across different species, a fact that showed support to the upcoming idea that these two types of deposits might form in different ways [57, 62]. Indeed, while diffuse plaques seem most probably to originate in the neuropil following an imbalance between the diffusion of A β oligomers and fibrils with different precipitation properties (mainly dictated by the A β 40/A β 42

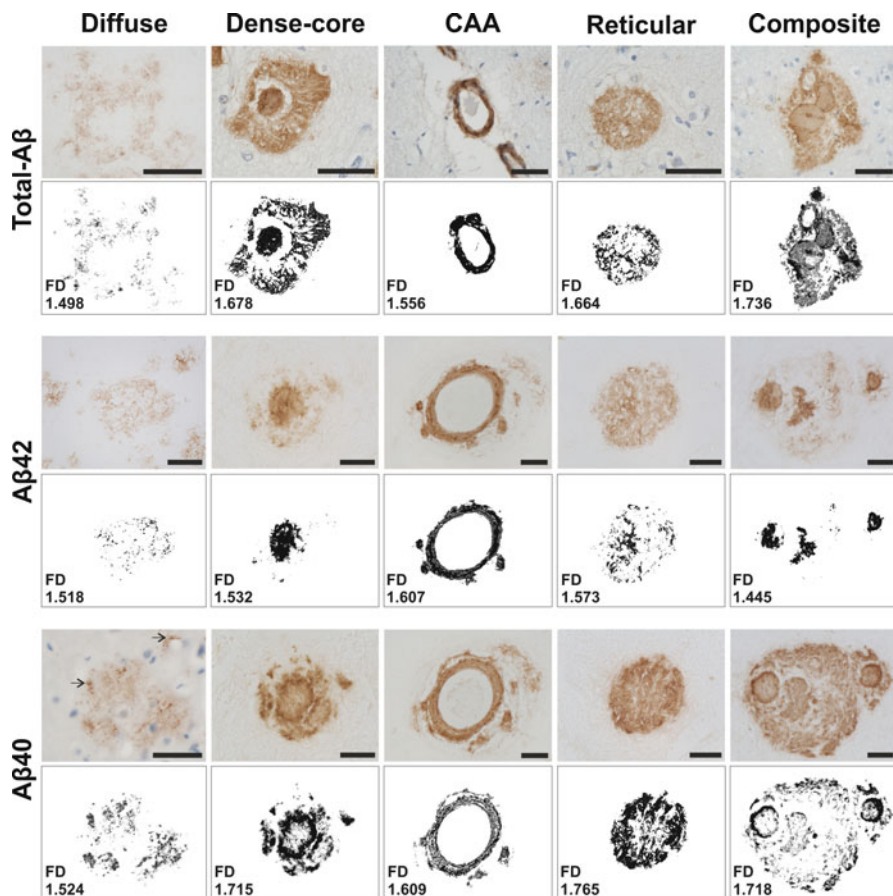


Fig. 15.2 Fractal analysis of the most prominent types of amyloid plaques in AD patients. Original immunohistochemistry images reflect exemplary types of plaques as detected by anti-total A β , A β 42, and A β 40 antibodies, and the binary images below represent correspondent segmented data for FD analysis. Respective FD values are illustrated in each binarized image; scale bar is 25 μ m (Reprinted from Pirici et al. [65], with permission of Elsevier)

ratios) (reviewed in [48, 49]) and the catabolic properties of a plethora of enzymes and cellular key players, for dense plaques there have been postulated theories that place them both as the developmental successors of diffuse deposits and as separate entities occurring at sites of perivascular amyloid drainage failure along the Virchow Robin spaces [18, 52, 80, 87].

A fractal analysis study assessing three most prominent types of plaques in human AD (diffuse, compact without a core, and dense core plaques), based on the box-counting algorithm applied on binarized images grabbed on slides after A β immunohistochemistry, showed important differences in the FD of these types of plaques [65]. This study involved studying more than 6,000 binarized images of amyloid plaques stained with A β 40, A β 42, and total A β immunohistochemistry

(IHC) (Fig. 15.2) [65]. Presuming that the complexity of plaques increases over time, the diffuse type of depositions seem to be the earliest plaques and parallel studies showing that diffuse type of depositions are the first type of plaques to appear in AD [80]. However, the different degrees of complexity also sustain an alternative hypothesis that the diffuse and compact plaques have different patterns of formation and evolution [62]. The evolutionary link between the coreless compact and dense core plaques is even more elusive. It is very much possible that the central halo observed in IHC for amyloid core is a method-dependent artifact, where anti-A β antibodies are unable to bind to the most compact amyloid, and remains an unstained central region. On the other hand, knowing the close pathological association of the dense core plaques with the vessels, it could also be that all three types of plaques follow a distinct pattern of evolution.

Assessing the FD of A β 40 component, the more soluble A β fraction responsible for the compactness of the plaques, could first of all differentiate between depositions from AD patients and sporadic plaques found in aged individuals (Fig. 15.3). Moreover, A β 40 FD values could also differentiate between the phenotypes induced by mutations that lead to different A β 40/A β 42 ratios and that for both human pathology and mouse models bearing these mutations [35, 51, 65]. In this line, a similar pattern of mostly dense-core plaques had been documented for patients bearing the APP Flemish (A692G) mutation and the APP Swedish mutation (APPK670N/M671)-bearing mouse model (or the Tg2576 line) [50, 52]. Although the sizes of plaques themselves differ grossly, they both showed a similar A β 40 FD profile, with data above the 95th percentile revealing almost identical values [65].

It has been suggested that increasing the relative levels of secreted A β 42 drives increasing burdens of parenchymal diffuse plaques [34, 52]. The A β 42 fraction is less soluble compared to A β 40, and this translates into less complex plaques' architecture (lower values for A β 42 FD) for PSEN1 mutation carriers and the corresponding mouse models [65], and other studies of amyloid deposition in human and animal aging conditions also revealed higher FD values for A β 40/dense plaques compared to A β 42/diffuse depositions [57, 62]. The higher diffusibility of A β 40 and thus its longer availability to form more complex patterns are again in perfect agreement with the observed FD differences.

Finally, compact plaques could be readily distinguished from diffuse plaques for all A β species and for both human patients and mouse models utilized [65]. Although it can be conceived that dense-core plaques represent advanced stages of development and compaction starting from diffuse plaques, or postproduction modulation, as microglia associate only with dense plaques and can phagocytize A β [17], it still remains to be shown that higher FD values truly reflect an increased histopathological modeling of the plaque.

Neurofibrillary tangles, the other pathological denominator of AD and other neurodegenerative diseases, have not been evaluated yet from a non-Euclidean morphological point of view, but since cognitive deficit is more strongly linked to NFT rather than amyloid plaques [9], this might be of interest in the future.

FD algorithms have also been used as a measure of complexity for dendritic neuronal arborization or glial cell meshwork [5, 56, 70, 72, 76]. The most abundant

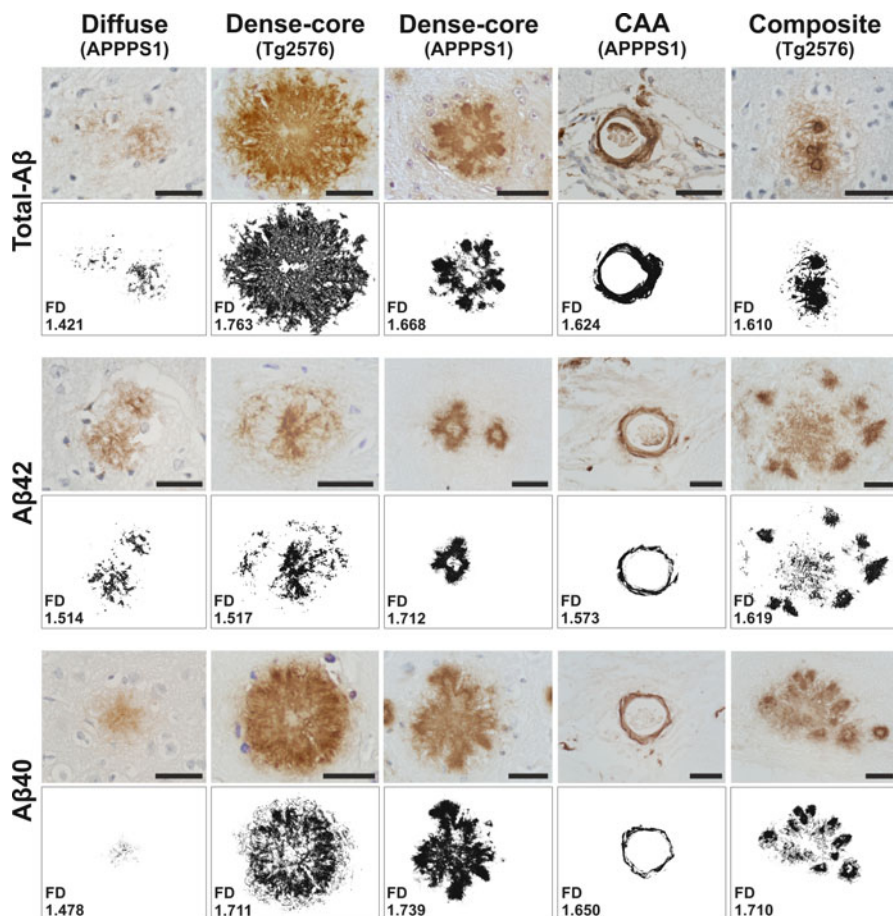


Fig. 15.3 Fractal analysis of the most prominent types of amyloid plaques in mouse models of amyloidosis. Original immunohistochemistry images reflect exemplary types of plaques as detected by anti-total A β , A β 42, and A β 40 antibodies, and the binary images below represent correspondent segmented data for FD analysis. Respective FD values are illustrated in each binarized image; scale bar is 25 μ m (Reprinted from Pirici et al. [65], with permission of Elsevier)

cellular component of the central nervous system (CNS), astrocytes, reacts to chronic/acute brain injury, became activated, and undergo a series of morphological and functional changes. Acutely reactive astrocytes become swollen, eosinophilic, with enlarged and eccentrically located nuclei, and with blunt processes, while in time, reactive astrocytes exhibit long cytoplasmic extensions that finally intercalate as a dense network of processes, a state called astrogliosis. The abundance of their specific cytoskeleton protein, glial fibrillary acidic protein (GFAP), makes them extremely visible by immunohistochemistry. Although their morphology is evidently depending on the subsequent pathology and evolutionary stages, a study analyzing fibrous, protoplasmatic, and activated astrocytes pooled together from mild dementia

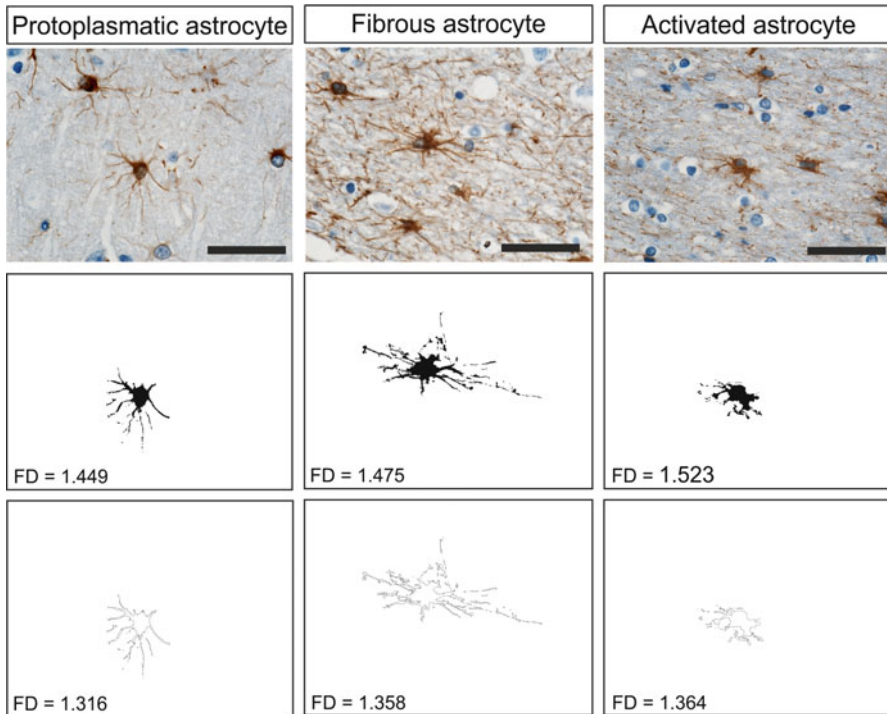


Fig. 15.4 Fractal analysis of three different types of astrocytes. The first row shows the original immunohistochemistry images, the second row shows the binary silhouette of the cells, and the last row shows the outline masks, each binarized image included the corresponding FD values (Reprinted from Pirici et al. [64], with permission of the Romanian Society of Morphology)

and recent as well as lacunar/chronic ischemic stroke patients revealed that these cell types share common features among these pathologies [64]. Thus, after calculating individual FD values for binarized silhouettes and outline masks, protoplasmic astrocytes had the smallest FD values (1.43 ± 0.04 for silhouettes/ 1.29 ± 0.03 for outlines), significantly different from fibrous ($1.46 \pm 0.06/1.34 \pm 0.02$) and activated astrocytes ($1.50 \pm 0.05/1.35 \pm 0.03$), for both stroke and dementia patients (Fig. 15.4) [64]. Although there was enough variability among astrocytes pooled from frontal, temporal, and striatal areas that did not allow any clear-cut differentiation between these areas for the same pathological subgroup, sporadic AD cases showed the smallest calculated FD values between all pathological instances only the temporal lobe areas [64]. Silhouette binarizations were, as expected, more informative than outlines, probably due to the loss of lacunarity data for the second type of image processing.

Astrocytic FD analysis could also combine functional data, as that it has been recently showed that, for example, water and glutamate buffering is done mostly by the same astrocytes showing a high degree of colocalization for aquaporin 4 (AQP4) and glutamate transporter 1 (GLT-1), the two main water and glutamate gates in the

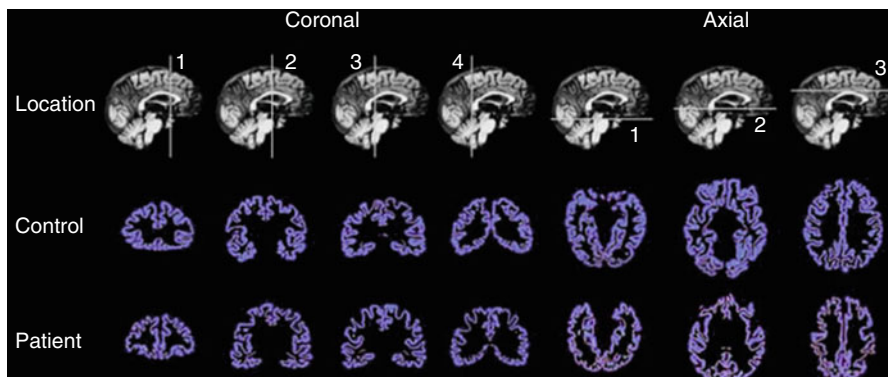


Fig. 15.5 Example of two-dimensional segmentation for fractal analysis of cortical ribbons from a control case and a patient with Alzheimer's disease. The *upper row* of images identifies the sectioning planes for seven different anatomical regions. The *middle* and *lower rows* display the cortical ribbons segmented from the brains of a control individual and from Alzheimer's disease patient brain, respectively, and extracted for analysis. Non-cortical areas (cerebellum, white matter, basal nuclei, and brain stem) were not considered for this analysis. The narrowing of the cortical ribbon and widened sulci are evidently leading to a less complex morphology and lower FD values for the FD patient (Reprinted from King et al. [45], with permission of Springer)

CNS [58]. Plausibly, FD analysis of astrocytes based on the immunohistochemistry expression patterns of these markers will shed more light into the behavior of different astrocyte classes and their interplay with the neuropil and the blood vessels.

15.1.2 *Imaging and Fractal Analysis in AD*

Quantitative brain MRI studies have greatly contributed to the knowledge of in vivo anatomical changes related to aging, and volumetric analysis can now reliably differentiate patients with AD from controls [15, 20, 22, 47, 63]. Moreover, the complexity and foldings of the cerebral cortex, as well as the complicated organization of the white matter fibers, have demonstrated that macroscopically the human brain exhibits fractal properties [23, 37, 46, 89]. In AD, loss of neurons and cerebral atrophy with widening of sulci and thinning and decreased folding of the cortical ribbon leads to a decreased complexity of the affected cortices [3].

Segmentation of two-dimensional cortical ribbons from control subjects and patients with mild to moderate Alzheimer's, followed by computation of the FD on the full thickness of the cortices using the box-counting algorithm revealed lower values for AD patients compared to age-matched controls (Fig. 15.5) [45]. This finding was evident especially in the medial temporal lobe, the superior and inferior colliculus, the mammillary bodies, the corpus callosum, and the thalamus [45]. Although assessing the complete thickness of the ribbons was superior as discriminating value to the analysis of only the outline of the pial surface or of the gray/

white matter junction, it was limited to the bidimensional sectioning of the cortices, not being able to take into account the entire cortical surface [37, 40, 45]. A more recent imaging study from the same group utilized a three-dimensional approach to analyze the ruggedness of the cortical ribbon layer based on the data of 70 patients (35 control patients and 35 patients with mild AD) imaged with a high-contrast magnetic resonance imaging technique (three-dimensional magnetization prepared rapid acquisition 3D inversion recovery or MP-RAGE) [44]. The pial surface, the gray/white matter boundary, and the total thickness of the cortex were segmented and analyzed based on a custom three-dimensional cube-counting fractal algorithm. The fractal dimensions of the total cortical ribbons was significantly higher for control compared to AD subjects; the gray/white matter boundary fractal dimension showed smaller but significant differences between the two pathologies, while the analysis of the pial surface revealed no significant difference between the two groups [44]. Only the total cortical thickness FD showed a significant correlation with cortical thickness itself and with the cognitive decline.

Single photon emission CT (SPECT) of the cerebral blood flow (CBF) has been used to evaluate and compare the dynamics of cerebral circulation and brain metabolism in dementia [26, 55]. In AD and vascular dementia (VaD), blood flow is reduced in temporoparietal areas even before cerebral atrophy is noticeable, and with the progress of dementia, the metabolic deficit extends toward the anterior areas of the brain [19, 25, 27, 39, 78]. Data suggest that reduced CBF in temporoparietal areas together with the atrophy of the medial temporal lobe are a feature of AD, and might be linked to the loss of entorhinal cortex neurons projecting toward the dentate gyrus of the hippocampus [41].

In order to objectivize the evaluation of tomograms, heterogeneity of CBF was assessed as the three-dimensional FD of SPECT images threshold using an intensity-cutoff algorithm, which proved that higher FD values indicate uneven CBF SPECT imaging [59, 61, 88]. Applied to the whole brain, this approach revealed significantly lower values for the control group compared to AD and VaD, and with no differences between AD and VaD [88]. When the authors looked individually at the anterior and posterior brain regions, for the AD patients, FD values were significantly higher for posterior areas, while VaD patients had higher FD values for anterior areas [88]. Moreover, posterior CBF heterogeneity was well correlated with the cognitive impairment in AD, being able to distinguish between mild stage AD and elderly controls [59, 61].

Aside functional MRI, the analysis of the *electroencephalogram (EEG)* is currently used as a diagnostic tool in patients with cognitive dysfunction involving either a general or a localized decline of the brain functions. In AD patients, this results in a shift of the EEG spectrum toward lower frequencies and decreased coherence between interhemispheric signal sources [79]. Given the nonlinear nature of the neuronal activity, EEG pattern analysis seemed a good candidate for FD analysis. For multiple recording locations, full spectrum EEG revealed significantly lower FD values for AD compared to age controls [6, 86]. In a more recent study, limited EEG in the β -band of the eyes-closed condition revealed an accuracy of 99.3%, with a sensitivity of 100% and a specificity of 97.8%, in discriminating AD

patients from age controls [1]. It has also been showed that magnetoencephalography recordings on 20 AD patients were significantly less complex and more regular in AD for 71 out of 148 recording channels compared to 21 age-control patients [30].

15.2 Other Neurodegenerative Diseases

Frontotemporal lobar degeneration (FTLD) consists of a spectrum of clinical syndromes exhibiting progressive degenerative changes in behavior, language, personality, cognitive skills, and motor function and is characterized by selective frontal and temporal lobe atrophy. FTD cases account for up to 20 % of all cases of dementia, having the same prevalence as AD in patients less than 65 years of age [69, 77]. Besides neuronal loss in the affected areas, there are five recognized FTLD pathological subtypes based on the immunoprofiles of a large spectrum of intraneuronal nuclear inclusions: (i) FTLD with tau-positive inclusions (tauopathies, or classically Pick's disease), (ii) FTLD with TDP-43-positive intraneuronal inclusions, (iii) FTLD with FUS pathology, (iv) FTLD with ubiquitin-only inclusions, and (v) FTLD with no inclusions. In approximately 50 % of the patients with FTLD, there is an autosomal dominant pattern of inheritance, and recent advances identified culprit mutations in the genes coding for *microtubule-associated protein tau (MAPT) gene on chromosome 17q21–22* [36], *progranulin gene on chromosome 17q21–22* [4, 14], *valosin-containing protein gene on chromosome 9p21–p12 (VCP)* [84], *TAR DNA-binding protein (TDP-43) on chromosome 1p36* [8], or *charged multivesicular body protein 2B gene (CHMP2B) on chromosome 3p13* [75].

SPECT imaging studies assessing the heterogeneity of CBF have also been done for FTLD patients compared to AD and control patients. In a study involving 21 FTLD patients and 21 AD patients in early stages of dementia, the authors utilized a derived FD function to assess technetium-99m hexamethylpropylene amine oxime SPECT scannings [60]. For heterogeneity analysis, SPECT imaging data were thresholded using a 35 % cutoff and a 50 % cutoff of the maximal voxel radioactivity, then FD values were calculated as the logarithms of the thresholds values and the remaining numbers of voxels for both anterior and posterior brain regions. While posterior FD values could not differentiate between FTLD and AD, anterior and anterior-to-posterior FD ratios showed significantly higher values for FTLD cases compared to AD patients [60]. Increased heterogeneity and reduced CBF in frontal, anterior cingulate, temporal, orbitofrontal, and ventrolateral prefrontal cortices had been already proved before in FTLD compared to AD, where this heterogeneity was more pronounced in parietal superior occipital and temporo-occipital cortices [82].

Parkinson's disease (PD) is another common type of dementia/dementia syndrome clinically presenting with a combination of clinical rigidity, bradykinesia, and resting tremor, and in later stages dementia. This neurodegenerative disease results from the death of dopamine-secreting cells in the substantia nigra, with dopamine synthesis balance being important, among others, for lowering the

inhibitory effect of basal ganglia over the motor system when voluntary movements are intended. This results in the overall reduction of the motor output, or bradykinesia [7]. As there are many causes and patterns of manifestation for movement disorders, these apparently chaotic changes have been ideally investigated through nonlinear algorithms like FD analysis. After recording in dynamics the position of the body during walking using a triaxial accelerometry technique, a study on 11 PD patients and 10 healthy elderly controls found out that fractal patterns of the movements were higher in PD patients for all three orthogonal axes compared to controls [73]. Moreover, it has been iterated that even normal gait has a stochastic fractal pattern which seems to be altered in PD to a point where it can be separated by machine learning and neural network classifiers, although long time recordings from gait signal are still necessary to warranty this hypothesis [32, 71]. This pattern seems to be present even at the level of individual human pallidal neurons modulated with dopamine; spike trains recorded from patients with PD during surgery for ablation of the globus pallidus lead to the conclusion that fractal dynamics may characterize the activity of single neurons in the CNS and act as an indicator of a dysfunctional CNS network [68].

Multiple sclerosis (MS) is the most common demyelinating disease of the human central nervous system leading initially to reversible neurological deficits and, in time, to permanent disability [10]. Although the etiology and pathogenesis of MS is poorly understood, with both genetic and environmental factors being incriminated, damage to the white matter is mediated by autoimmune mechanisms, including T cell-mediated and antibody-mediated injuries [29]. On gross examination of the brain sections, areas of demyelination can be observed as sharply demarcated zones, or “plaques,” distributed predominantly in the white matter but may involve gray matter as well. On microscopic examination, plaques are composed of perivascular mononuclear cell inflammatory infiltrates, moderate gliosis, activated microglia, myelin loss, and axonal swelling [66].

A study comparing control subjects with patients with MS on classical MR imaging revealed that skeletonized white matter had lower FD values for MS patients, for both visible and normal-appearing white matter, thus being able to detect changes even at an early phase of the disease [23]. Moreover, the same group showed that the FD of the segmented gray matter is increased in these patients compared to healthy controls, and this did not correlate with gray matter atrophy or neurological disability, suggesting that these changes might appear very early in the course of the disease [24].

15.3 Conclusion

The data presented in this chapter strongly suggest that FD analysis can be a valid tool not only for differentiating and grading pathological features in different types of neurodegenerative diseases based on histological texture analysis of specific proteinaceous depositions, but it can also lead to genotype-phenotype correlations, as

is the case with familial forms of AD, making this classifier both of a potential diagnostic aid and a tool for in depth investigation of the dynamic phenomena that lead to these distinct or overlapping syndromes.

Acknowledgments This work was supported by a grant of the Romanian National Authority for Scientific Research and Innovation, CNCS – UEFISCDI, project number PN-II-RU-TE-2014-4-0582, contract number 160/01.10.2015 and E05547 grant of the University of Antwerp. We thank Elsevier, Springer, and the Romanian Society of Morphology for permissions to partially reproduce previously published work.

References

1. Ahmadlou M, Adeli H, Adeli A. Fractality and a wavelet-chaos methodology for EEG-based diagnosis of Alzheimer disease. *Alzheimer Dis Assoc Disord*. 2011;25(1):85–92.
2. Alzheimer A. Über eine eigenartige erkrankung der Hirnrinde. *Zentralbl Nervenheilkunde Psychiatr*. 1907;18:177–9.
3. Arai H, Kobayashi K, Ikeda K, Nagao Y, Ogihara R, Kosaka K. A computed tomography study of Alzheimer's disease. *J Neurol*. 1983;229(2):69–77.
4. Baker M, Mackenzie IR, Pickering-Brown SM, Gass J, Rademakers R, Lindholm C, et al. Mutations in progranulin cause tau-negative frontotemporal dementia linked to chromosome 17. *Nature*. 2006;442(7105):916–9.
5. Behar TN. Analysis of fractal dimension of O2A glial cells differentiating in vitro. *Methods*. 2001;24(4):331–9.
6. Besthorn C, Sattel H, Geiger-Kabisch C, Zerfass R, Forstl H. Parameters of EEG dimensional complexity in Alzheimer's disease. *Electroencephalogr Clin Neurophysiol*. 1995;95(2):84–9.
7. Blandini F, Nappi G, Tassorelli C, Martignoni E. Functional changes of the basal ganglia circuitry in Parkinson's disease. *Prog Neurobiol*. 2000;62(1):63–88.
8. Borroni B, Bonvicini C, Alberici A, Buratti E, Agosti C, Archetti S, et al. Mutation within TARDBP leads to frontotemporal dementia without motor neuron disease. *Hum Mutat*. 2009;30(11):E974–83.
9. Braak H, Braak E. Neuropathological staging of Alzheimer-related changes. *Acta Neuropathol (Berl)*. 1991;82(4):239–59.
10. Calabresi PA. Diagnosis and management of multiple sclerosis. *Am Fam Physician*. 2004;70(10):1935–44.
11. Calhoun ME, Burgermeister P, Phinney AL, Stalder M, Tolnay M, Wiederhold KH, et al. Neuronal overexpression of mutant amyloid precursor protein results in prominent deposition of cerebrovascular amyloid. *Proc Natl Acad Sci USA*. 1999;96(24):14088–93.
12. Cavannah SE, Pippin JJ, Barnard ND. Animal models of Alzheimer disease: historical pitfalls and a path forward. *ALTEX*. 2014;31(3):279–302.
13. Cross SS. Fractals in pathology. *J Pathol*. 1997;182(1):1–8.
14. Cruts M, Gijsels I, van der Zee J, Engelborghs S, Wils H, Pirici D, et al. Null mutations in progranulin cause ubiquitin-positive frontotemporal dementia linked to chromosome 17q21. *Nature*. 2006;442(7105):920–4.
15. Csernansky JG, Wang L, Swank J, Miller JP, Gado M, McKeel D, et al. Preclinical detection of Alzheimer's disease: hippocampal shape and volume predict dementia onset in the elderly. *Neuroimage*. 2005;25(3):783–92.
16. Cupers P, Orlans I, Craessaerts K, Annaert W, De Strooper B. The amyloid precursor protein (APP)-cytoplasmic fragment generated by gamma-secretase is rapidly degraded but distributes partially in a nuclear fraction of neurones in culture. *J Neurochem*. 2001;78(5):1168–78.

17. D'Andrea MR, Cole GM, Ard MD. The microglial phagocytic role with specific plaque types in the Alzheimer disease brain. *Neurobiol Aging*. 2004;25(5):675–83.
18. D'Andrea MR, Nagele RG. Morphologically distinct types of amyloid plaques point the way to a better understanding of Alzheimer's disease pathogenesis. *Biotech Histochem*. 2010;85(2):133–47.
19. Deutsch G, Tweedy JR. Cerebral blood flow in severity-matched Alzheimer and multi-infarct patients. *Neurology*. 1987;37(3):431–8.
20. Dickerson BC, Sperling RA. Neuroimaging biomarkers for clinical trials of disease-modifying therapies in Alzheimer's disease. *NeuroRx*. 2005;2(2):348–60.
21. Dickson DW. The pathogenesis of senile plaques. *J Neuropathol Exp Neurol*. 1997;56(4):321–39.
22. Du AT, Schuff N, Kramer JH, Rosen HJ, Gorno-Tempini ML, Rankin K, et al. Different regional patterns of cortical thinning in Alzheimer's disease and frontotemporal dementia. *Brain*. 2007;130(Pt 4):1159–66.
23. Esteban FJ, Sepulcre J, de Mendizabal NV, Goni J, Navas J, de Miras JR, et al. Fractal dimension and white matter changes in multiple sclerosis. *Neuroimage*. 2007;36(3):543–9.
24. Esteban FJ, Sepulcre J, de Miras JR, Navas J, de Mendizabal NV, Goni J, et al. Fractal dimension analysis of grey matter in multiple sclerosis. *J Neurol Sci*. 2009;282(1–2):67–71.
25. Foster NL, Chase TN, Fedio P, Patronas NJ, Brooks RA, Di Chiro G. Alzheimer's disease: focal cortical changes shown by positron emission tomography. *Neurology*. 1983;33(8):961–5.
26. Frackowiak RS, Pozzilli C, Legg NJ, Du Boulay GH, Marshall J, Lenzi GL, et al. Regional cerebral oxygen supply and utilization in dementia. A clinical and physiological study with oxygen-15 and positron tomography. *Brain*. 1981;104(Pt 4):753–78.
27. Friedland RP, Budinger TF, Koss E, Ober BA. Alzheimer's disease: anterior-posterior and lateral hemispheric alterations in cortical glucose utilization. *Neurosci Lett*. 1985;53(3):235–40.
28. Games D, Adams D, Alessandrini R, Barbour R, Berthelette P, Blackwell C, et al. Alzheimer-type neuropathology in transgenic mice overexpressing V717F beta-amyloid precursor protein. *Nature*. 1995;373(6514):523–7.
29. Garg N, Smith TW. An update on immunopathogenesis, diagnosis, and treatment of multiple sclerosis. *Brain Behav*. 2015;5(9):e00362.
30. Gomez C, Mediavilla A, Hornero R, Abasolo D, Fernandez A. Use of the Higuchi's fractal dimension for the analysis of MEG recordings from Alzheimer's disease patients. *Med Eng Phys*. 2009;31(3):306–13.
31. Guerreiro R, Hardy J. Genetics of Alzheimer's disease. *Neurotherapeutics*. 2014;11(4):732–7.
32. Hausdorff JM. Gait dynamics, fractals and falls: finding meaning in the stride-to-stride fluctuations of human walking. *Hum Mov Sci*. 2007;26(4):555–89.
33. Hendriks L, van Duijn CM, Cras P, Cruts M, Van Hul W, van Harskamp F, et al. Presenile dementia and cerebral haemorrhage linked to a mutation at codon 692 of the b-amyloid precursor protein gene. *Nat Genet*. 1992;1:218–21.
34. Herzig MC, Winkler DT, Burgermeister P, Pfeifer M, Kohler E, Schmidt SD, et al. A beta is targeted to the vasculature in a mouse model of hereditary cerebral hemorrhage with amyloidosis. *Nat Neurosci*. 2004;7(9):954–60.
35. Hsiao K, Chapman P, Nilson S, Eckman C, Harigaya Y, Younkin S, et al. Correlative memory deficits, Abeta elevation, and amyloid plaques in transgenic mice. *Science*. 1996;274(5284):99–102.
36. Hutton M, Lendon CL, Rizzu P, Baker M, Froelich S, Houlden H, et al. Association of missense and 5'-splice-site mutations in tau with the inherited dementia FTDP-17. *Nature*. 1998;393(6686):702–5.
37. Im K, Lee JM, Yoon U, Shin YW, Hong SB, Kim IY, et al. Fractal dimension in human cortical surface: multiple regression analysis with cortical thickness, sulcal depth, and folding area. *Hum Brain Mapp*. 2006;27(12):994–1003.

38. Iwatsubo T, Saido TC, Mann DM, Lee VM, Trojanowski JQ. Full-length amyloid-beta (1-42(43)) and amino-terminally modified and truncated amyloid-beta 42(43) deposit in diffuse plaques. *Am J Pathol.* 1996;149(6):1823–30.
39. Jagust WJ, Friedland RP, Budinger TF, Koss E, Ober B. Longitudinal studies of regional cerebral metabolism in Alzheimer's disease. *Neurology.* 1988;38(6):909–12.
40. Jiang J, Zhu W, Shi F, Zhang Y, Lin L, Jiang T. A robust and accurate algorithm for estimating the complexity of the cortical surface. *J Neurosci Methods.* 2008;172(1):122–30.
41. Jobst KA, Smith AD, Barker CS, Wear A, King EM, Smith A, et al. Association of atrophy of the medial temporal lobe with reduced blood flow in the posterior parietotemporal cortex in patients with a clinical and pathological diagnosis of Alzheimer's disease. *J Neurol Neurosurg Psychiatry.* 1992;55(3):190–4.
42. Kang J, Muller-Hill B. Differential splicing of Alzheimer's disease amyloid A4 precursor RNA in rat tissues: PreA4(695) mRNA is predominantly produced in rat and human brain. *Biochem Biophys Res Commun.* 1990;166(3):1192–200.
43. Kawas CH. Clinical practice. Early Alzheimer's disease. *N Engl J Med.* 2003;349(11):1056–63.
44. King RD, Brown B, Hwang M, Jeon T, George AT, Alzheimer's Disease Neuroimaging I. Fractal dimension analysis of the cortical ribbon in mild Alzheimer's disease. *Neuroimage.* 2010;53(2):471–9.
45. King RD, George AT, Jeon T, Hynan LS, Youn TS, Kennedy DN, et al. Characterization of atrophic changes in the cerebral cortex using fractal dimensional analysis. *Brain Imaging Behav.* 2009;3(2):154–66.
46. Kiselev VG, Hahn KR, Auer DP. Is the brain cortex a fractal? *Neuroimage.* 2003;20(3):1765–74.
47. Korff ES, Wahlund LO, Visser PJ, Scheltens P. Medial temporal lobe atrophy on MRI predicts dementia in patients with mild cognitive impairment. *Neurology.* 2004;63(1):94–100.
48. Kumar-Singh S. Cerebral amyloid angiopathy: pathogenetic mechanisms and link to dense amyloid plaques. *Genes Brain Behav.* 2008;7 Suppl 1:67–82.
49. Kumar-Singh S. Hereditary and sporadic forms of abeta-cerebrovascular amyloidosis and relevant transgenic mouse models. *Int J Mol Sci.* 2009;10(4):1872–95.
50. Kumar-Singh S, Cras P, Wang R, Kros JM, van Swieten J, Lubke U, et al. Dense-core senile plaques in the Flemish variant of Alzheimer's disease are vasocentric. *Am J Pathol.* 2002;161(2):507–20.
51. Kumar-Singh S, Julliams A, Nuyens D, Labeur C, Vennekens K, Serneels S, et al. In vitro studies of Flemish, Dutch, and wild-type Amyloid β (A β) provide evidence for a two-stage A β neurotoxicity. *Neurobiol Dis.* 2002;11(2):300–10.
52. Kumar-Singh S, Pirici D, McGowan E, Serneels S, Ceuterick C, Hardy J, et al. Dense-core plaques in Tg2576 and PSAPP mouse models of Alzheimer's disease are centered on vessel walls. *Am J Pathol.* 2005;167(2):527–43.
53. Lennon FE, Cianci GC, Cipriani NA, Hensing TA, Zhang HJ, Chen CT, et al. Lung cancer—a fractal viewpoint. *Nat Rev Clin Oncol.* 2015;12:664–75.
54. Mandelbrot BB. Stochastic models for the Earth's relief, the shape and the fractal dimension of the coastlines, and the number-area rule for islands. *Proc Natl Acad Sci USA.* 1975;72(10):3825–8.
55. Mielke R, Pietrzyk U, Jacobs A, Fink GR, Ichimiya A, Kessler J, et al. HMPAO SPET and FDG PET in Alzheimer's disease and vascular dementia: comparison of perfusion and metabolic pattern. *Eur J Nucl Med.* 1994;21(10):1052–60.
56. Milosevic NT, Ristanovic D. Fractality of dendritic arborization of spinal cord neurons. *Neurosci Lett.* 2006;396(3):172–6.
57. Miyawaki K, Nakayama H, Matsuno S, Tamaoka A, Doi K. Three-dimensional and fractal analyses of assemblies of amyloid beta protein subtypes [A β 40 and A β 42(43)] in canine senile plaques. *Acta Neuropathol (Berl).* 2002;103(3):228–36.

58. Mogoanta L, Ciurea M, Pirici I, Margaritescu C, Simionescu C, Ion DA, et al. Different dynamics of aquaporin 4 and glutamate transporter-1 distribution in the perineuronal and perivascular compartments during ischemic stroke. *Brain Pathol.* 2014;24(5):475–93.
59. Nagao M, Murase K, Kikuchi T, Ikeda M, Nebu A, Fukuhara R, et al. Fractal analysis of cerebral blood flow distribution in Alzheimer's disease. *J Nucl Med.* 2001;42(10):1446–50.
60. Nagao M, Sugawara Y, Ikeda M, Fukuhara R, Hokoishi K, Murase K, et al. Heterogeneity of cerebral blood flow in frontotemporal lobar degeneration and Alzheimer's disease. *Eur J Nucl Med Mol Imaging.* 2004;31(2):162–8.
61. Nagao M, Sugawara Y, Ikeda M, Fukuhara R, Ishikawa T, Murase K, et al. Heterogeneity of posterior limbic perfusion in very early Alzheimer's disease. *Neurosci Res.* 2006;55(3):285–91.
62. Nakayama H, Kiatipattanasakul W, Nakamura S, Miyawaki K, Kikuta F, Uchida K, et al. Fractal analysis of senile plaque observed in various animal species. *Neurosci Lett.* 2001;297(3):195–8.
63. Nestor SM, Gibson E, Gao FQ, Kiss A, Black SE, Alzheimer's Disease Neuroimaging I. A direct morphometric comparison of five labeling protocols for multi-atlas driven automatic segmentation of the hippocampus in Alzheimer's disease. *Neuroimage.* 2013;66:50–70.
64. Pirici D, Mogoanta L, Margaritescu O, Pirici I, Tudorica V, Coconu M. Fractal analysis of astrocytes in stroke and dementia. *Rom J Morphol Embryol.* 2009;50(3):381–90.
65. Pirici D, Van Cauwenberghe C, Van Broeckhoven C, Kumar-Singh S. Fractal analysis of amyloid plaques in Alzheimer's disease patients and mouse models. *Neurobiol Aging.* 2011;32(9):1579–87.
66. Popescu BF, Lucchinetti CF. Pathology of demyelinating diseases. *Annu Rev Pathol.* 2012;7:185–217.
67. Rajendran L, Honsho M, Zahn TR, Keller P, Geiger KD, Verkade P, et al. Alzheimer's disease beta-amyloid peptides are released in association with exosomes. *Proc Natl Acad Sci USA.* 2006;103(30):11172–7.
68. Rasouli G, Rasouli M, Lenz FA, Verhagen L, Borrett DS, Kwan HC. Fractal characteristics of human Parkinsonian neuronal spike trains. *Neuroscience.* 2006;139(3):1153–8.
69. Ratnavalli E, Brayne C, Dawson K, Hodges JR. The prevalence of frontotemporal dementia. *Neurology.* 2002;58(11):1615–21.
70. Reichenbach A, Siegel A, Senitz D, Smith Jr TG. A comparative fractal analysis of various mammalian astroglial cell types. *Neuroimage.* 1992;1(1):69–77.
71. Sarbaz Y, Towhidkhal F, Jafari A, Gharibzadeh S. Do the chaotic features of gait change in Parkinson's disease? *J Theor Biol.* 2012;307:160–7.
72. Schaffner AE, Ghesquiere A. The effect of type 1 astrocytes on neuronal complexity: a fractal analysis. *Methods.* 2001;24(4):323–9.
73. Sekine M, Akay M, Tamura T, Higashi Y, Fujimoto T. Fractal dynamics of body motion in patients with Parkinson's disease. *J Neural Eng.* 2004;1(1):8–15.
74. Selkoe DJ. The cell biology of β -amyloid precursor protein and presenilin in Alzheimer's disease. *Trends Cell Biol.* 1998;8(11):447–53.
75. Skibinski G, Parkinson NJ, Brown JM, Chakrabarti L, Lloyd SL, Hummerich H, et al. Mutations in the endosomal ESCRTIII-complex subunit CHMP2B in frontotemporal dementia. *Nat Genet.* 2005;37(8):806–8.
76. Smith Jr TG, Behar TN, Lange GD, Marks WB, Sheriff Jr WH. A fractal analysis of cultured rat optic nerve glial growth and differentiation. *Neuroscience.* 1991;41(1):159–66.
77. Snowden JS, Neary D, Mann DM. Frontotemporal dementia. *Br J Psychiatry.* 2002;180:140–3.
78. Starkstein SE, Sabe L, Vazquez S, Teson A, Petracca G, Chemerinski E, et al. Neuropsychological, psychiatric, and cerebral blood flow findings in vascular dementia and Alzheimer's disease. *Stroke.* 1996;27(3):408–14.
79. Stevens A, Kircher T. Cognitive decline unlike normal aging is associated with alterations of EEG temporo-spatial characteristics. *Eur Arch Psychiatry Clin Neurosci.* 1998;248(5):259–66.

80. Thal DR, Capetillo-Zarate E, Del Tredici K, Braak H. The development of amyloid beta protein deposits in the aged brain. *Sci Aging Knowledge Environ.* 2006;2006(6):re1.
81. Trojanowski JQ, Shin RW, Schmidt ML, Lee VM. Relationship between plaques, tangles, and dystrophic processes in Alzheimer's disease. *Neurobiol Aging.* 1995;16(3):335–40.
82. Varrone A, Pappata S, Caraco C, Soricelli A, Milan G, Quarantelli M, et al. Voxel-based comparison of rCBF SPET images in frontotemporal dementia and Alzheimer's disease highlights the involvement of different cortical networks. *Eur J Nucl Med Mol Imaging.* 2002;29(11):1447–54.
83. Wattendorff AR, Bots GT, Went LN, Endtz LJ. Familial cerebral amyloid angiopathy presenting as recurrent cerebral haemorrhage. *J Neurol Sci.* 1982;55(2):121–35.
84. Watts GD, Wymer J, Kovach MJ, Mehta SG, Mumm S, Darvish D, et al. Inclusion body myopathy associated with Paget disease of bone and frontotemporal dementia is caused by mutant valosin-containing protein. *Nat Genet.* 2004;36(4):377–81.
85. Wisniewski HM, Bancher C, Barcikowska M, Wen GY, Currie J. Spectrum of morphological appearance of amyloid deposits in Alzheimer's disease. *Acta Neuropathol (Berl).* 1989;78(4):337–47.
86. Woyshville MJ, Calabrese JR. Quantification of occipital EEG changes in Alzheimer's disease utilizing a new metric: the fractal dimension. *Biol Psychiatry.* 1994;35(6):381–7.
87. Yamaguchi H, Nakazato Y, Shoji M, Takatama M, Hirai S. Ultrastructure of diffuse plaques in senile dementia of the Alzheimer type: comparison with primitive plaques. *Acta Neuropathol.* 1991;82(1):13–20.
88. Yoshikawa T, Murase K, Oku N, Imaizumi M, Takasawa M, Rishu P, et al. Heterogeneity of cerebral blood flow in Alzheimer disease and vascular dementia. *AJNR Am J Neuroradiol.* 2003;24(7):1341–7.
89. Zhang L, Liu JZ, Dean D, Sahgal V, Yue GH. A three-dimensional fractal analysis method for quantifying white matter structure in human brain. *J Neurosci Methods.* 2006;150(2):242–53.

Chapter 16

Fractal Analysis of the Cerebrovascular System Physiopathology

Martin Soehle

Abstract The cerebrovascular system is characterized by parameters such as arterial blood pressure (ABP), cerebral perfusion pressure (CPP), and cerebral blood flow velocity (CBFV). These are regulated by interconnected feedback loops resulting in a fluctuating and complex time course. Moreover, they exhibit fractal characteristics such as (statistical) self-similarity and scale invariance which could be quantified by fractal measures: These include the coefficient of variation, the Hurst coefficient H , or the spectral exponent α in the time domain, as well as the spectral index β in the frequency domain. Prior to quantification, the time series has to be classified as either stationary or nonstationary, which determines the appropriate fractal analysis and measure for a given signal class. CBFV was characterized as a nonstationary (fractal Brownian motion) signal with spectral index β between 2.0 and 2.3. In the high-frequency range (>0.15 Hz), CBFV variability is mainly determined by the periodic ABP variability induced by heartbeat and respiration. However, most of the spectral power of CBFV is contained in the low-frequency range (<0.15 Hz), where cerebral autoregulation acts as a low-pass filter and where the fractal properties are found. Cerebral vasospasm, which is a complication of subarachnoid hemorrhage (SAH), is associated with an increase in β denoting a less complex time course. According to the decomplexification theory of illness, such a diminished complexity could be explained by a restriction or even dropout of feedback loops caused by SAH.

Keywords Cerebral blood flow velocity • Hurst coefficient • Spectral exponent • Spectral index • Subarachnoid hemorrhage • Decomplexification • Fractal Brownian motion

M. Soehle, MD, PhD, MHBA
Department of Anesthesiology and Intensive Care Medicine, University of Bonn,
Bonn, Germany
e-mail: martin.soehle@ukb.uni-bonn.de

16.1 Introduction

Physiologic parameters such as arterial blood pressure (ABP) or cerebral blood flow (CBF) are not constant over time but fluctuate (Fig. 16.1). These fluctuations are either periodic, driven by an oscillatory process such as the heartbeat, or they are nonperiodic, for example, random or nonrandom. These nonperiodic fluctuations have been shown to contain valuable information recently [16]. A time series is regarded as fractal time series if it possesses the characteristics of self-similarity and scale invariance [12]. Fractal analysis allows to identify and quantify these characteristics.

16.2 Cerebral Autoregulation as a Feedback Loop

Cerebral perfusion pressure (CPP), which is calculated as the difference between mean arterial blood pressure (MAP) and intracranial pressure (ICP), is a major determinant of cerebral blood flow (CBF) [11]. CBF would decrease whenever CPP declines, which is prevented by the mechanism of cerebral pressure autoregulation [19]: As CPP drops cerebral arterioles dilate until CBF is restored. In reverse, cerebral arterioles constrict when CPP increases. In terms of control theory, cerebral pressure autoregulation is a feedback loop with CPP as input and CBF as output. In addition, CBF is determined by arterial carbon dioxide partial pressure ($p_a\text{CO}_2$) and cerebral metabolism as well [17, 23], which form two additional feedback loops that control CBF. In control theory, feedback loops are mathematically described by differential equations [9] which inherently exhibit a nonlinear behavior. This explains why the output parameter CBF shows nonlinear properties as will be discussed below. Many physiologic parameters, among others ABP, body temperature, arterial pH, and electrolyte concentrations, are controlled by feedback loops as well which keep them in a physiologic range. Thus the organism maintains its interior milieu by regulatory mechanisms, a concept known as homeostasis [7].

16.3 Variability and Complexity

Despite cerebral autoregulation, CBF varies notably: Oscillations induced by heartbeat are observed, which are seen in ABP likewise (Fig. 16.1). These periodic changes occur in a frequency range above 0.5 Hz = 30/min, which is too fast for autoregulation to react [10]. In the frequency range below, CBF variations of 5–10% (coefficient of variation = standard deviation/mean) are observed despite autoregulation [21, 29], which are highly irregular and complex. A loss of fluctuation might be of clinical relevance as it could be associated with increased morbidity and mortality. This has been extensively investigated for a different parameter, namely, heart rate variability (HRV), where a reduction of HRV is associated with

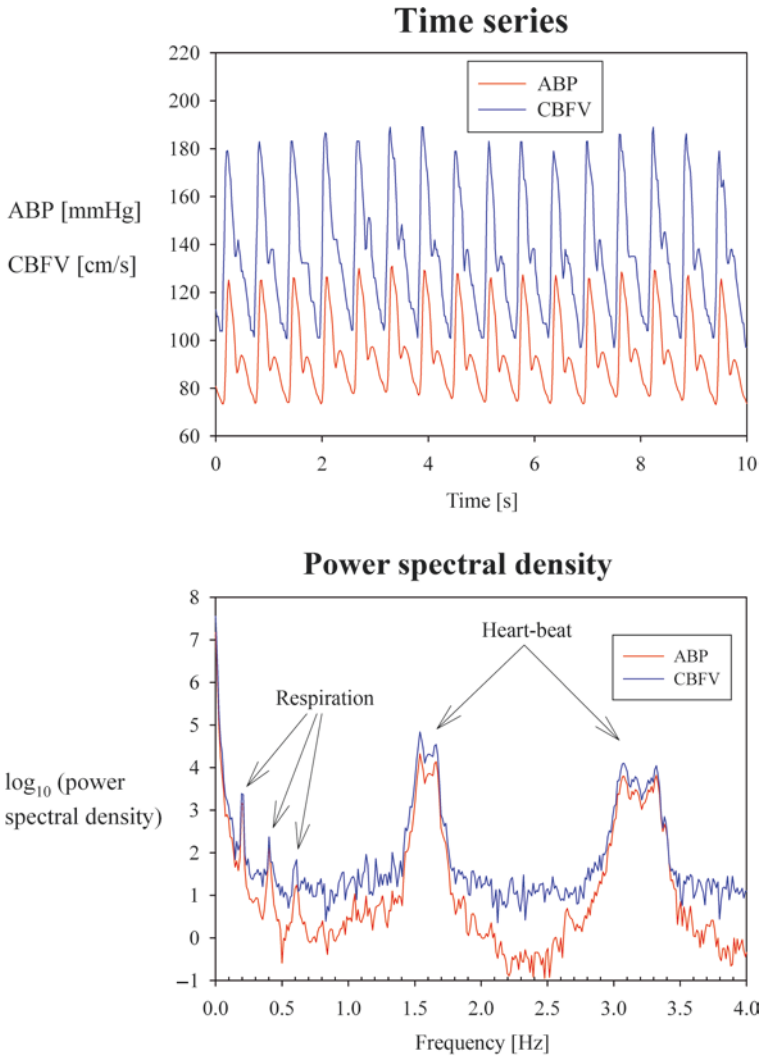


Fig. 16.1 Upper part: Time series of arterial blood pressure (ABP, shown in red) and cerebral blood flow velocity (CBFV, illustrated in blue) in a 48-year-old woman suffering from subarachnoid hemorrhage. The time course of CBFV follows that of its major determinant ABP. Lower part: The power spectral density of the ABP and CBFV time series shown above is presented at different frequencies. The peaks at 1.6 Hz ($\approx 96/\text{min}$) and 3.2 Hz are caused by the fundamental frequency related to heartbeat (96/min) and its second harmonic, respectively. Likewise peaks at 0.2 Hz ($\approx 12/\text{min}$), 0.4 Hz, and 0.6 Hz are related to respiration (respiratory rate = 12/min) and its higher harmonics. The highest power spectral density is obtained for frequencies between 0 and 0.15 Hz, a range where fractal characteristics were observed for both ABP and FV [29]

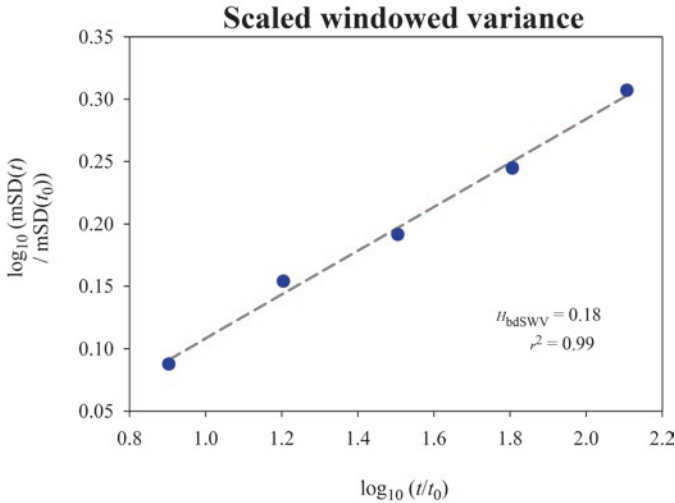


Fig. 16.2 Fractal analysis of cerebral blood flow velocity by means of bridge-detrended scaled windowed variance (bdSWV) [6]. The variance, or mean standard deviation (mSD) to be more precise, is calculated (and shown as *blue circles*) for five different signal lengths t , starting with reference length t_0 . Both the variance mSD (ordinate) and the signal length t (abscissa) are displayed on a logarithmic scale. The slope of the linear regression line (shown as *gray dashed line*) is denoted as the Hurst coefficient H_{bdSWV} . The correlation coefficient r^2 indicates the strength of the relationship between \log (variance) and \log (time scale)

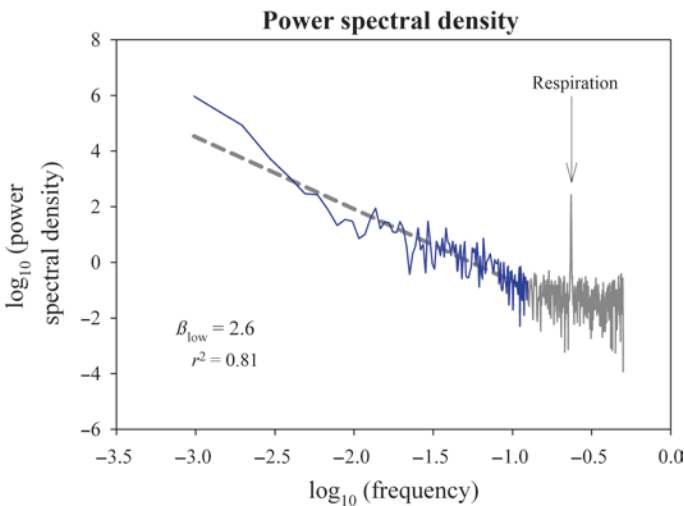


Fig. 16.3 Fractal analysis of cerebral blood flow velocity using the power spectral density method [13]. Both the power spectral density and the frequency are shown on a logarithmic scale. The peak at -0.63 ($=\log_{10}(0.23 \text{ Hz})$) is caused by respiration. Only frequencies below -0.9 ($=\log_{10}(0.125 \text{ Hz})$) are considered for further analysis (shown in *blue*): The negative slope of the linear regression line (shown as *gray dashed line*) of \log (power spectral density) on \log (frequency) is denoted as spectral index β_{low} . The strength of the relationship is displayed as correlation coefficient r^2

poorer prognosis and/or increased mortality in patients suffering from coronary artery disease [27], dilated cardiomyopathy [32], congestive heart failure [25], and postinfarction patients [18]. CBF variability has been investigated in patients suffering from subarachnoid hemorrhage (SAH), which is caused by a rupture of an aneurysm of a cerebral artery. SAH is associated with a high morbidity and mortality [8] not only due to the initial arterial hemorrhage but also due to the complication of cerebral vasospasm, which is characterized by a narrowing of cerebral arteries leading to cerebral ischemia [2].

16.4 Methodology of Variation and Fractal Analysis

Continuous CBF measurements are difficult in the clinical setting; therefore CBF velocity (CBFV) is assessed instead, which is a valid replacement as long as vessel diameter does not change during the measurement period [31]. To do so, transcranial Doppler sonography (TCD) is performed which enables to record time series of CBFV with high temporal resolution and long duration [1]. Variation of a time series can be quantified by calculating its standard deviation (SD):

$$SD = \sqrt{\frac{\sum (x - m)^2}{n - 1}}$$

where x denotes the data, m the mean, and n the number of samples. As the duration of a time series increases, its SD might either remain constant or vary which is denoted as *stationary* or *nonstationary*, respectively. The relative standard deviation or coefficient of variation CV is calculated as $CV = SD/m$.

For fractal analysis, the time series is investigated to possess fractal characteristics, one of which is *self-similarity*: Segments of a fractal are similar to larger segments or the whole [13]. This could refer to geometrical self-similarity as known from the Mandelbrot set or to statistical self-similarity as for the case of fractal time series. Here, the segments of the time series have similar statistic properties (e.g., SD) as the entire time series. This statistical similarity is independent of the time scale chosen, a property known as *scale invariance*. Different parameters exist to quantify a fractal time series, one of which is the Hurst coefficient H .

16.5 Hurst Coefficient H_{bdSWV}

H_{bdSWV} is calculated in the time domain using the bridge-detrended scaled windowed variance (bdSWV) method: First, a given fractal time series is bridge detrended to remove linear trends [6]. Then the time series is divided into (nonoverlapping) windows of length τ . The SD is calculated for each window and averaged yielding $mSD(\tau)$. This computation is repeated for a wide range of window sizes τ starting

with a reference window size τ_0 . Finally, $mSD(\tau)/mSD(\tau_0)$ is plotted versus τ/τ_0 on a double-logarithmic scale, and the Hurst coefficient H_{bdSWV} is estimated as the slope of the regression line [6, 20] (Fig. 16.2):

$$H_{\text{bdSWV}} = \frac{\log(mSD(\tau)/mSD(\tau_0))}{\log(\tau/\tau_0)}$$

H_{bdSWV} is applicable to nonstationary time series only [12]. Therefore the parameter spectral index β is calculated in the frequency domain, which differentiates between stationary and nonstationary time series.

16.6 Spectral Index β

As a general principle, a Fourier analysis is performed to obtain the power spectral amplitude $|A(f)|^2$ at frequency f [13]. According to the “1/f power law,” $|A(f)|^2$ decreases exponentially as frequency f increases in fractal time series [13] (Fig. 16.3):

$$|A(f)|^2 \propto cf^{-\beta}$$

where c is a constant and β is the spectral index, which is calculated as the negative slope of the linear regression line of $\log(|A(f)|^2)$ on $\log(f)$. Fractal time series with $1 < \beta < 3$ are characterized as nonstationary fractal Brownian motion (fBm) time series, whereas stationary fractal Gaussian noise (fGn) time series are having $-1 < \beta < 1$ [12].

16.7 Spectral Exponent α

The spectral exponent α can be calculated in the time domain by detrended fluctuation analysis (DFA) [24]: A given time series $y(k)$ of length N is detrended by subtracting the local trend $y_n(k)$ and its root mean square fluctuation $F(n)$ is determined as:

$$F(n) = \sqrt{\frac{1}{N} \sum_{k=1}^N [y(k) - y_n(k)]^2}$$

This computation is repeated for different time scales n , providing a relationship between $F(n)$ and n . The slope of the regression line of $\log[F(n)]$ and $\log(n)$ is denoted as the scaling exponent α , with higher α values indicating a smoother time series.

16.8 Fractal Analysis of Human CBFV

So far, fractal analysis of human CBFV has been performed in few patient studies only (see Table 16.1). These include studies in which the cerebrovascular system is either directly altered by an intracranial disease such as subarachnoid hemorrhage [29] or indirectly affected by causes such as cardiogenic shock [4] or autonomic failure [5]. In addition, fractal parameters of CBFV have been analyzed in healthy volunteers [28, 33, 34]. All studies identified fractal properties in their CBFV time series, such as scale invariance and self-similarity. They all classified CBFV as fractal Brownian motion (fBm), which is defined as having a spectral index $1 < \beta < 3$ [12]. Hence, CBFV is nonstationary which means that its observed variance increases with the length of the observation period [12]. Eke et al. [12] have stressed the importance of classifying fractal time series according to the dichotomous fGn/fBm model, as the signal class determines the appropriate method of quantifying its fractal properties. Values between 2.0 and 2.3 were observed for the fractal parameter β both in patients [5, 29] and healthy volunteers [34] using the power spectral density (PSD) method. This PSD technique has been described as being appropriate for both fGn and fBm signals. In contrast, Rossitti and Stephensen [28] as well as West et al. [33] observed higher β -values of 2.5 and 2.7, respectively, but they applied dispersional analysis, a method which should be used for fGn time series only [12]. Much lower β -values between 0.7 and 0.9 were described by Bellapart et al. [4] in healthy volunteers and cardiogenic shock patients. They applied DFA, a method that allows signal classification as fGn/fBm either, but leaves some uncertainty around α -values of 1.0. They reported an α between 0.86 and 0.97 which is in the area of uncertainty. Moreover, for DFA $2^{15} = 32,768$, samples are required to achieve a 95% precision [13]; however 6,000 samples were analyzed only. Zhang et al. [34] and Reynolds et al. [26] observed a kink in their PSD data and consequently calculated different β -values for different frequency ranges: They reported low β -values of 0.3 and 0.7 for the very low-frequency range 0.002–0.02 Hz [34] and 0.005–0.06 Hz [26], respectively. Many times higher β -values of 2.3 and 1.6 were calculated for the frequency range 0.02–0.5 Hz [34] and 0.06–0.5 Hz [26], respectively. Hence, CBFV might not only exhibit a monofractal, but probably a bifractal or even multifractal behavior.

Fractal parameters such as α , β , and H give more precise estimates, that is, less mean squared error ($MSE = \text{variance} + \text{bias}^2$), with increasing length of the time signal n . To obtain a detailed information in the low-frequency range (LF, < 0.15 Hz), low sampling frequencies (< 1 Hz) are desired which result in long recording times. However in clinical practice, long recording times (> 30 min) are hardly feasible in TCD, which is susceptible to probe dislocation, and will be tolerated neither by patients nor nursing staff for long periods. Therefore using the analysis techniques with the highest precision at a given signal length is preferred. The spectral index β obtained by power spectral density analysis reliably classifies a fractal time series as fGn or fBm, but gives imprecise estimates. Therefore, the Hurst exponent H is calculated as a fractal parameter, which gives two magnitude higher precision

Table 16.1 Fractal analysis studies of cerebral blood flow velocity (CBFV) obtained in healthy volunteers (upper part) or patients (lower part)

Reference	Subjects	Time series duration at $f_{(\text{samples}), \text{method}}$	Freq. range	Spectral index, β	Comments
Healthy volunteers					
Rossitzi and Stephensen [28]	$n=4$	512 s at 1 Hz ($n=512$), RD		(2.52±0.18)	$D=1.24\pm 0.09$
West et al. [33]	$n=6$	2 h, beat-to-beat, RD		(2.70±0.08)	$D=1.15\pm 0.04$
Zhang et al. [34]	$n=6$	512 s at 1 Hz, ($n=512$), PSD	0.002–0.02 Hz 0.02–0.5 Hz	0.34±0.09 2.31±0.08	
Patients					
Reynolds et al. [26]	$n=106$ Premature Neonates	3.4 min at 5 Hz ($n=1,024$), PSD	0.005–0.06 Hz 0.06–0.5 Hz	0.670 1.592	
Blaber et al. [5]	$n=2\times 8$ control vs. autonomic failure	$n=256$ beats, CGSA, PSD		2.0±0.15 2.2±0.2	60° tilt: $\beta=1.6\pm 0.25$ 60° tilt: $\beta=1.45\pm 0.2$ ($p<0.05$)
Bellapart et al. [4]	$n=3\times 5$ Healthy Card. shock without VAD Card. shock with VAD	5 min at 20 Hz ($n=6,000$), DFA	0.04–0.15 Hz	(0.72±0.32) (0.94±0.54) (0.90±0.40)	$\alpha=0.86\pm 0.16$ $\alpha=0.97\pm 0.27$ $\alpha=0.95\pm 0.20$
Soehle et al. [29]	$n=31$ SAH Before vasospasm Contralateral side of vasospasm	17 min at 1 Hz ($n=1,024$), PSD	0.001–0.125 Hz	1.97±0.35 2.09±0.56	During vasospasm: $\beta=2.23\pm 0.43$ ($p<0.05$) Side of vaso spasm: $\beta=2.29\pm 0.61$ ($p<0.05$)

$f_{(\text{samples}), \text{method}}$ sampling frequency, β spectral index as determined based on the power spectral density, n number of patients or number of samples, D fractal dimension as calculated by the relative dispersion (RD) method, PSD power spectral density, CGSA coarse-graining spectral analysis, α spectral exponent as determined by detrended fluctuation analysis (DFA), VAD ventricular assist device, SAH subarachnoid hemorrhage. Values of β shown in brackets are calculated as $\beta=5-2D$ or $\beta=2\alpha-1$. Values = mean ± standard deviation

estimates than PSD [12]. Depending on the fGn or fBm signal class, H is estimated using the dispersional or the bdSWV method, respectively [12]. Failure to match the fGn/fBm signal class with the appropriate method (dispersional/bdSWV method) results in serious error in estimating H [12]. A Hurst coefficient of 0.26 ± 0.13 was obtained for CBFV in SAH patients [29], which is similar to the value of 0.24 ± 0.02 obtained in the rat cerebral microcirculation [12]. In both studies, the Hurst coefficient was unequal to 0.5 which means that the variations in CBF are not random. Moreover, the H value < 0.5 indicates anticorrelation within the CBF time series, that is, increases of the signal in the past influence decreases at present. Hence a long-term memory [3, 13] was present in the CBF signal. In general, variability and fractal analysis provide complementary information: Whereas variation analysis investigates standard deviation on a single time scale only, bdSWV analyzes standard deviation over a wide range of time scales, and H quantifies the roughness of the time series on a time-invariant scale [3].

16.9 Decomplexification

Cerebral vasospasm, a complication of SAH which is characterized by a narrowing of cerebral arteries, is associated with a significant increase in the spectral index β (Table 16.1) [29]. Likewise, SAH patients exhibit a significant higher β on the side of vasospasm as compared to the contralateral non-vasospastic side [29]. Such an increase in β is equivalent to a less complex time course or decomplexification of CBFV, which could be explained by the decomplexification theory of illness [15]: Parameters such as CBF are regulated by multiple interconnected feedback loops resulting in a highly complex time course. In illness such as cerebral vasospasm, these feedback loops are either restricted in their range of action or even out of order which causes a less complex time course. Decomplexification has been shown in Cheyne-Stokes respiration, parkinsonian gait, neutrophil count in leukemia, and fever in Hodgkin's disease [15] as well as during intracranial hypertension following traumatic brain injury [30].

16.10 Frequency-Dependent CBF Variability

CBFV analysis in the frequency domain exhibits peaks in power spectral density which are related to heartbeat ($\sim 80\text{--}120 \text{ min}^{-1} = 1.3\text{--}2 \text{ Hz}$) and respiration ($\sim 8\text{--}20 \text{ min}^{-1} = 0.13\text{--}0.3 \text{ Hz}$) [29] (Fig. 16.1). Transfer function analysis reveals a high coherence between ABP and CFBV in the higher frequency range (HF, $> 0.15 \text{ Hz}$), which indicates that a high proportion of CBF variability is explained by likewise heartbeat and respiration induced fluctuations in ABP [22]. One might assume that the fractal behavior of CBFV might be simply explained by the fractal properties of ABP, a theory which is refuted by cerebral autoregulation (CA). CA behaves like a

high-pass filter, which freely passes fast ABP changes (>0.15 Hz) but effectively attenuates low-frequency (LF, <0.15 Hz) oscillations [5, 14]. In fact, it has been shown that changes in cerebrovascular resistance due to CA contribute significantly to CBF variability in the LF range [21]. Moreover, the LF range contains most of the spectral power (or variability) of CBF [21], and hence patient studies have focused on the LF range [4, 29]. The feedback loops of CA with its inherent nonlinear behavior are active in the LF range and could explain the fractal properties of CBF. However, the current available techniques of fractal analysis quantify fractal properties but cannot prove a causal relationship. Therefore, it has not been proven that the fractal behavior of CBF is due to the fractal behavior of CA.

16.11 Conclusions

Time series of CBF (and its surrogate CBFV) possess fractal properties such as scale invariance and self-similarity. Fractal analysis allows to quantify these properties and give insights into the system of cerebrovascular system pathophysiology in general and of cerebral autoregulation in particular. At a given signal length, the Hurst coefficient provides a more precise estimation than other fractal parameters; however different methods exist to calculate it based on the signal classification as fGn or fBm. Therefore, a correct signal classification is required which is based on the robust method of estimating the spectral index β by power spectral density analysis. Few studies have performed fractal analysis in patients with cerebrovascular system pathophysiology so far. Further studies are required to investigate the relationship between fractal analysis parameters and autoregulation impairment on the one side and patient outcome on the other side.

References

1. Aaslid R. Developments and principles of transcranial Doppler. In: Newell DW, Aaslid R, editors. *Transcranial Doppler*. New York: Raven Press Ltd.; 1992. p. 1–8.
2. Aaslid R. Hemodynamics of cerebrovascular spasm. *Acta Neurochir Suppl*. 1999;72:47–57.
3. Bassingthwaighe JB, Liebovitch LS, West BJ. Fractal measures of heterogeneity and correlation. In: Bassingthwaighe JB, Liebovitch LS, West BJ, editors. *Fractal physiology*. Oxford: Oxford University Press; 1994. p. 63–107.
4. Bellapart J, Chan GS, Tzeng YC, Ainslie PN, Dunster KR, Barnett AG, Boots R, Fraser JF. The effect of ventricular assist devices on cerebral blood flow and blood pressure fractality. *Physiol Meas*. 2011;32(9):1361–72.
5. Blaber AP, Bondar RL, Stein F, Dunphy PT, Moradshahi P, Kassam MS, Freeman R. Complexity of middle cerebral artery blood flow velocity: effects of tilt and autonomic failure. *Am J Physiol*. 1997;273(5 Pt 2):H2209–16.
6. Cannon MJ, Percival DB, Caccia DC, Raymond GM, Bassingthwaighe JB. Evaluating scaled windowed variance methods for estimating the Hurst coefficient of time series. *Physica A*. 1997;241(3–4):606–26.
7. Cannon WB. *The wisdom of the body*. New York: Norton W. W.; 1932.

8. Chiang VL, Claus EB, Awad IA. Toward more rational prediction of outcome in patients with high-grade subarachnoid hemorrhage. *Neurosurgery*. 2000;46(1):28–35, discussion 35–26.
9. Csete ME, Doyle JC. Reverse engineering of biological complexity. *Science*. 2002;295(5560):1664–9.
10. Czosnyka M, Brady K, Reinhard M, Smielewski P, Steiner LA. Monitoring of cerebrovascular autoregulation: facts, myths, and missing links. *Neurocrit Care*. 2009;10(3):373–86.
11. Czosnyka M, Piechnik S, Richards HK, Kirkpatrick P, Smielewski P, Pickard JD. Contribution of mathematical modelling to the interpretation of bedside tests of cerebrovascular autoregulation. *J Neurol Neurosurg Psychiatry*. 1997;63(6):721–31.
12. Eke A, Herman P, Bassingthwaite JB, Raymond GM, Percival DB, Cannon M, Balla I, Ikrenyi C. Physiological time series: distinguishing fractal noises from motions. *Eur J Physiol*. 2000;439:403–15.
13. Eke A, Herman P, Kocsis L, Kozak LR. Fractal characterization of complexity in temporal physiological signals. *Physiol Meas*. 2002;23:R1–38.
14. Giller CA. The frequency-dependent behavior of cerebral autoregulation. *Neurosurgery*. 1990;27(3):362–8.
15. Goldberger AL. Fractal variability versus pathologic periodicity: complexity loss and stereotypy in disease. *Perspect Biol Med*. 1997;40(4):543–61.
16. Goldberger AL, Amaral LA, Hausdorff JM, Ivanov P, Peng CK, Stanley HE. Fractal dynamics in physiology: alterations with disease and aging. *Proc Natl Acad Sci U S A*. 2002;99 Suppl 1:2466–72.
17. Harper AM, Glass HI. Effect of alterations in the arterial carbon dioxide tension on the blood flow through the cerebral cortex at normal and low arterial blood pressures. *J Neurol Neurosurg Psychiatry*. 1965;28(5):449–52.
18. Kleiger RE, Miller JP, Bigger Jr JT, Moss AJ. Decreased heart rate variability and its association with increased mortality after acute myocardial infarction. *Am J Cardiol*. 1987;59(4):256–62.
19. Lassen NA. Autoregulation of cerebral blood flow. *Circ Res*. 1964;15(Suppl):201–4.
20. Mandelbrot BB. Self-affine fractals and fractal dimension. *Phys Scr*. 1985;32:257–60.
21. Panerai RB. Complexity of the human cerebral circulation. *Philos Trans A Math Phys Eng Sci*. 2009;367(1892):1319–36.
22. Panerai RB, Eames PJ, Potter JF. Multiple coherence of cerebral blood flow velocity in humans. *Am J Physiol Heart Circ Physiol*. 2006;291(1):H251–9.
23. Paulson OB, Strandgaard S, Edvinsson L. Cerebral autoregulation. *Cerebrovasc Brain Metab Rev*. 1990;2(2):161–92.
24. Peng CK, Buldyrev SV, Havlin S, Simons M, Stanley HE, Goldberger AL. Mosaic organization of DNA nucleotides. *Phys Rev E Stat Phys Plasmas Fluids Relat Interdiscip Topics*. 1994;49(2):1685–9.
25. Ponikowski P, Anker SD, Chua TP, Szelemiej R, Piepoli M, Adamopoulos S, Webb-Peploe K, Harrington D, Banasiak W, Wrabec K, Coats AJ. Depressed heart rate variability as an independent predictor of death in chronic congestive heart failure secondary to ischemic or idiopathic dilated cardiomyopathy. *Am J Cardiol*. 1997;79(12):1645–50.
26. Reynolds KJ, Panerai RB, Kelsall AW, Rennie JM, Evans DH. Spectral pattern of neonatal cerebral blood flow velocity: comparison with spectra from blood pressure and heart rate. *Pediatr Res*. 1997;41(2):276–84.
27. Rich MW, Saini JS, Kleiger RE, Carney RM, teVelde A, Freedland KE. Correlation of heart rate variability with clinical and angiographic variables and late mortality after coronary angiography. *Am J Cardiol*. 1988;62(10 Pt 1):714–7.
28. Rossitti S, Stephensen H. Temporal heterogeneity of the blood flow velocity at the middle cerebral artery in the normal human characterized by fractal analysis. *Acta Physiol Scand*. 1994;151(2):191–8.
29. Soehle M, Czosnyka M, Chatfield DA, Hoeft A, Pena A. Variability and fractal analysis of middle cerebral artery blood flow velocity and arterial blood pressure in subarachnoid hemorrhage. *J Cereb Blood Flow Metab*. 2008;28(1):64–73.

30. Soehle M, Gies B, Smielewski P, Czosnyka M. Reduced complexity of intracranial pressure observed in short time series of intracranial hypertension following traumatic brain injury in adults. *J Clin Monit Comput.* 2013;27(4):395–403.
31. Sorteberg W. Cerebral artery blood velocity and cerebral blood flow. In: Newell DW, Aaslid R, editors. *Transcranial Doppler*. New York: Raven Press Ltd.; 1992. p. 57–66.
32. Tuininga YS, van Veldhuisen DJ, Brouwer J, Haaksma J, Crijns HJ, Man in't Veld AJ, Lie KI. Heart rate variability in left ventricular dysfunction and heart failure: effects and implications of drug treatment. *Br Heart J.* 1994;72(6):509–13.
33. West BJ, Zhang R, Sanders AW, Miniyar S, Zuckerman JH, Levine BD. Fractal fluctuations in transcranial Doppler signals. *Phys Rev E.* 1999;59(3):3492–8.
34. Zhang R, Zuckerman JH, Levine BD. Spontaneous fluctuations in cerebral blood flow: insights from extended-duration recordings in humans. *Am J Physiol Heart Circ Physiol.* 2000;278(6):H1848–55.

Chapter 17

Fractals and Chaos in the Hemodynamics of Intracranial Aneurysms

Gábor Závodszy, György Károlyi, István Szikora, and György Paál

Abstract Computing the emerging flow in blood vessel sections by means of computational fluid dynamics is an often applied practice in hemodynamics research. One particular area for such investigations is related to the cerebral aneurysms, since their formation, pathogenesis and the risk of a potential rupture may be flow-related. We present a study on the behavior of small advected particles in cerebral vessel sections in the presence of aneurysmal malformations. These malformations cause strong flow disturbances driving the system towards chaotic behavior. Within these flows the particle trajectories can form a fractal structure, the properties of which are measurable by quantitative techniques. The measurable quantities are well established chaotic properties, such as the Lyapunov exponent, escape rate and information dimension. Based on these findings, we propose that chaotic flow within blood vessels in the vicinity of the aneurysm might be relevant for the pathogenesis and development of this malformation.

Keywords Cerebral aneurysm • Computational fluid dynamics • Chaotic advection • Passive tracers • Fractals • Information dimension

G. Závodszy (✉) • G. Paál (✉)

Department of Hydrodynamic Systems, Budapest University of Technology and Economics, Műegyetem rakpart 3, Budapest 1111, Hungary
e-mail: gzavodszy@hds.bme.hu; gypaal@hds.bme.hu

G. Károlyi

Institute of Nuclear Techniques, Budapest University of Technology and Economics, Műegyetem rakpart 3, Budapest 1111, Hungary
e-mail: karolyi@reak.bme.hu

I. Szikora

Department of Neurointerventions, National Institute of Clinical Neurosciences, Amerikai str. 57, Budapest 1145, Hungary
e-mail: szikoraistvan@me.com

17.1 Introduction

Intracranial aneurysms are focal dilatations of branches of the circle of Willis, most frequently involving bifurcation points. Intracranial aneurysms are mostly of the *saccular* type (“berry” aneurysms) and affect about 2–5 % of the population. The aneurysm rupture incidence is 6–10 per 100,000 inhabitants per year. About 45 % of the ruptures may lead to death or permanent disability during the first year [12, 16, 32, 33]. Aneurysms are often incidentally found on imaging studies performed for different reasons. Neurosurgeons and neuro-interventionists often face the dilemma whether or not to treat unruptured aneurysms. Rupture can be catastrophic but the treatment risk itself is also non-negligible [12, 33].

The pathogenesis, growth and rupture of intracranial aneurysms is still not fully understood. It is likely a multifactorial disease, with genetic and hemodynamic factors, as well as life style and coexisting diseases playing a role. Recent research demonstrates a strong impact of hemodynamics on aneurysm initiation. Local changes of hemodynamics, particularly that of wall shear stress initiate focal vessel dilatation (vascular remodeling), that may result in unbalanced flow and further dilatation eventually resulting in aneurysm formation (see reviews and [13, 21]).

The treatment of intracranial aneurysms has undergone significant changes over the last few decades. Initially, open surgery was dominant during which a metallic clip was placed over the neck of the aneurysmal sac, thereby separating it from the blood flow in the parent artery. With the advent of less-invasive therapies, more and more aneurysms, particularly ruptured ones are treated by endovascular methods. In all these therapies the common goal is to reduce the blood flow in the aneurysmal sac and induce intrasaccular thrombosis leading to aneurysm occlusion. From a mechanical point of view, the aneurysm occlusion reduces the pressure and wall shear stress load on the aneurysm walls, slowing down or stopping the degeneration process. One of these methods, coil embolization, is based on filling the sac with microcoils, thereby increasing the flow resistance within the aneurysm sac [6]. Another attempt was to fill the sac with polymer foam, but it did not gain wide acceptance. Nowadays, by far the most popular method is to use flow diverter (FD) devices that are also called stents [22]. They are similar in appearance to the more well-known coronary stents, but their function is different. They are implanted within the parent artery in front of the neck of the aneurysm and the struts of the stents provide flow resistance. This flow resistance reduces the communication between the flow in the parent artery and the aneurysm and thus leads to the reduction of flow velocity in the sac.

As described above, the analysis of the flow parameters (e.g., wall shear stress, pressure, oscillatory shear index) may play a critical role in understanding the formation, growth and rupture of aneurysms. However, *in vivo* flow measurements using different imaging techniques do not provide the required spatial and temporal resolution. As a result, computational fluid dynamics (CFD) has been introduced into aneurysm research at an early stage. Using CFD, *ex vivo* numerical flow simulation is feasible. An overview of the generally applied experimental and computational methods is given in [24].

Initially, idealized models were used in simulations (such as a sphere attached to a cylindrical tube), later real geometries have been simulated [15]. The images are extracted from medical imaging studies such as 3D rotational subtraction angiography. Depending on the CFD method, the geometry is smoothed and remeshed or left in the original DICOM format.

Most of the commercial CFD codes use the so-called finite volume (FV) method, in which the investigated space domain is subdivided into small subvolumes and for each volume the discretized conservation equations are solved. This method needs smooth walls, and intermediate steps are required. An emerging other method to simulate flows is the so-called lattice Boltzmann method that uses simplified molecular level collision statistics, which, on the macroscopic level, leads to the same conservation laws. This method needs a voxel mesh. Medical imaging using the DICOM standard produces exactly that file format.

We note that since the image recording takes several seconds to complete, the geometry used in the simulations effectively represents a time-averaged surface during several cardiac cycles.

The flow simulation needs a lot of simplifying assumptions. First, that blood is assumed to be a Newtonian fluid. It is common consensus that the non-Newtonian properties of blood exert their effect only in small blood vessels, in the sub-millimeter range. As arteries of the circle of Willis are well above this size, the assumption is justified. Detailed discussion of the importance of non-Newtonian effects can be found in reviews [2, 3]. The second assumption is that the flow is laminar, incompressible. Considering the flow parameters, this is also reasonable. Third, the vessel walls are assumed to be rigid. Since the artery walls are flexible with a complicated material behavior, it is difficult to model them and compromises are necessary. In addition, little is known about the surrounding tissues that support the artery from outside. It seems that if we compare the elastic wall to the rigid wall case, in spite of some quantitative differences, the qualitative behavior of the flow is similar. Since brain arteries have little deformation during the cardiac cycle, for our purposes the rigid wall model is sufficient [14, 29].

A crucial point is the choice of the proper boundary conditions for the simulations. Very often CFD-based researchers do not reveal any details about this. Sticking with the assumption of rigid walls, the inlet and outlet boundary conditions have to be determined at the beginning and the end cross sections of the investigated artery segment. It has been shown that the inlet boundary condition has a much larger influence on the flow in the interesting region than the outlet one [29]. The inlet boundary condition is usually given by a time-dependent flow rate or velocity, the outlet one is by pressure. It would be desirable if the flow rate or velocity curve were patient-specific but it is rarely possible. Therefore, general flow rate curves are often used [5, 15]. If velocity is given at the inlet, a spatial distribution has to be given that can be uniform or parabolic, or even better, the spatio-temporal Womersley distribution [29]. The pressure at the outlet is usually assumed to be constant. This is justified by the fact that at the peripheries, on the level of capillaries, the cyclic variation of the flow is negligible.

Large amount of studies has been published in connection with flow simulation of intracranial aneurysms [3–5, 15]. Most of them aim at determining the temporal or spatial distribution of wall shear stress, or identify typical flow patterns [23]. It has become also possible to simulate treatments, in particular microcoils [30], or FD stents [31]. The development of CFD for intracranial aneurysms is progressing towards a semi-automatic easy-to-use CFD software with a few minutes of runtime for clinical applications.

For reasons provided later, the accuracy of the flow simulation is absolutely essential in this work. For this reason, we use an in-house lattice Boltzmann code. The detailed description of the code and the parameters can be found in [35]. In that work the code was validated against detailed velocity measurements in an aneurysm model.

In this chapter, the 2D geometries are idealized, artificial geometries, while the 3D geometry is extracted from CT-angiography images. The 3D geometry is the same one validated in [35]. The inlet boundary condition is a laminar paraboloid inflow profile whereby the peak of the profile changes temporally according to a synthetic volumetric flow rate curve which bears the main properties of a real heart-beat volume flow curve. This curve was used in several works, for example [15, 35]. The outlet boundary condition is constant pressure.

The accurate flow simulations provide a spatially and temporally well-resolved velocity field in and around the aneurysm. For the rest of this chapter, this velocity field will be considered as given and in this field a large number of individual particle paths are calculated. We describe how the time-varying flow field in and around an intracranial aneurysm results in the chaotic motion of particles transported by blood. We also show the fractal patterns traced out by these particles. For computational convenience, we use both a simple two-dimensional (2D) model for parametric studies, and also illustrate the generality of the phenomenon by using real, three-dimensional (3D) blood vessel geometries.

17.2 Fractal Patterns in Time-Dependent Flows

The motion of particles transported by moving fluid is known to be chaotic in many cases, a phenomenon called *chaotic advection* [1, 10]. Chaotic particle motion is associated with a sensitive dependence of particle paths on their initial position [27]. This means that particles that start near each other typically deviate rapidly from each other, the distance between the initially close particles typically diverges exponentially with time. This very strong separation of particles leads to the observation that a patch of particles, like a blob of dye, rapidly forms long and curving filaments. These filaments, formed by the stretching and folding action associated with chaos, form fractal structures that are hence traced out by ensembles of particles transported in the fluid.

In particular, motion of particles within blood vessels has been investigated from this point of view [17–19]. It has been found that a disruption of the flow, like a

branching, a narrowing or a bulge of the blood vessel can result in the chaotic motion of particles transported in the blood.

It has been speculated that the formation of fractal patterns by platelets has an important effect on platelet activation [17]. Similar effects were found previously in many situations ranging from microfluids through plankton blooms to environmental processes [26]. In cases when filamentary fractal patterns are generated in fluid flows, the underlying biological or chemical processes are enhanced by the large perimeter where the species can interact and by the strong chaotic mixing. This enhancement of processes manifests itself in a nontrivial, singular term in the chemical rate equations [9, 11, 28] or in the population dynamical equations [8, 20]. Hence the formation of fractal patterns in fluid flows is expected to have very important consequences on the underlying biochemical processes that take place in the blood as well [17, 34].

The simplest model to follow the motion of particles and to investigate their chaotic properties in a known flow field is to assume that the particles are very small and lack inertia. In this simplest approximation, the velocity of the particle coincides with the instantaneous velocity of the fluid at the location of the particle. For a steady (time-independent) flow, this would imply that the particle follows the streamlines of the flow. If, however, the flow is non-steady, like in case of blood pulsating periodically, the particle trajectories deviate from the streamlines, and can become very complex, chaotic, even if the flow itself is simple [1, 10].

When the size and inertia of particles is neglected, the equation of motion for a particle can be written as $d\mathbf{r}/dt = \mathbf{v}(\mathbf{r}, t)$, where $\mathbf{r}(t)$ is the position of the particle at time t , $\mathbf{v}(\mathbf{r}, t)$ is the speed of the fluid at position \mathbf{r} at time t . As discussed above, the right-hand side of this equation is known from numerical simulation. Hence this is a first-order, explicit differential equation for the particle position $\mathbf{r}(t)$. We solve this equation using the fourth order Runge-Kutta method [34]. Given an arbitrary initial position of a particle, we can follow its path along the blood vessel.

A few example particle paths are shown in Fig. 17.1 for a 3D aneurysm. Three particles were started from different but extremely close (within 1 μm) positions at the inlet of the shown segment, and their paths were traced numerically. For a while, the three particles moved along very similar paths, until they entered the aneurysm sac. There they spent very different times before leaving it, and both within the sac and after leaving it, they followed completely different paths. This picture illustrates the very sensitive dependence of the particle paths on their initial position, a unique sign of chaotic motion.

17.3 Basic Concepts Demonstrated on a Simplified 2D Case

The geometry of the surface of a real aneurysmal vessel section is rather intricate. Its shape is influenced by an immense number of factors. Thus, in order to be able to gain some general insight into the ongoing dynamics and the possible parameters driving it, a heavily simplified model was investigated first. This 2D model, shown



Fig. 17.1 Trajectories of three particles (*red, green, blue*) travelling through the transient flow field of a real aneurysm. Despite the small initial distance between the particles (within $1\ \mu\text{m}$) they travel along substantially different paths. The inlet is towards the bottom of the image, the three outlets are on the top and on the left side of the figure

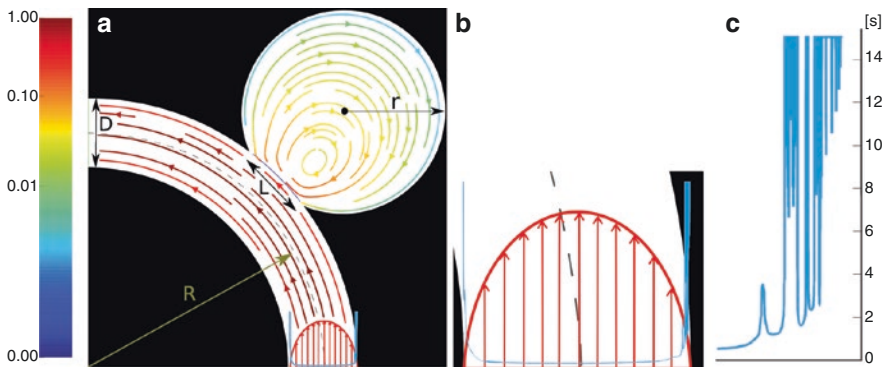


Fig. 17.2 (a) Synthetic aneurysm geometry automatically generated from the following parameters: aneurysmal sac radius (r), aneurysmal neck arc length (L), parent artery diameter (D), parent artery curvature defined by its radius (R). The typical velocity streamline arrangement is also shown in the figure colored by a normalized logarithmic scale. (b) The parabolic inlet velocity profile (*red*) is also shown together with the residence time (*light blue*) as a function of the initial position. (c) The enlarged residence time function

in Fig. 17.2a represents a synthetic cerebral aneurysmal case generated automatically from a few well selected parameters.

The reduced number of parameters and degrees of freedom leads to a higher computational efficiency and makes parametric studies more feasible. Hence a simple study which might indicate local tendencies around a physiologically correct general set of parameters becomes possible. Apart from the geometric

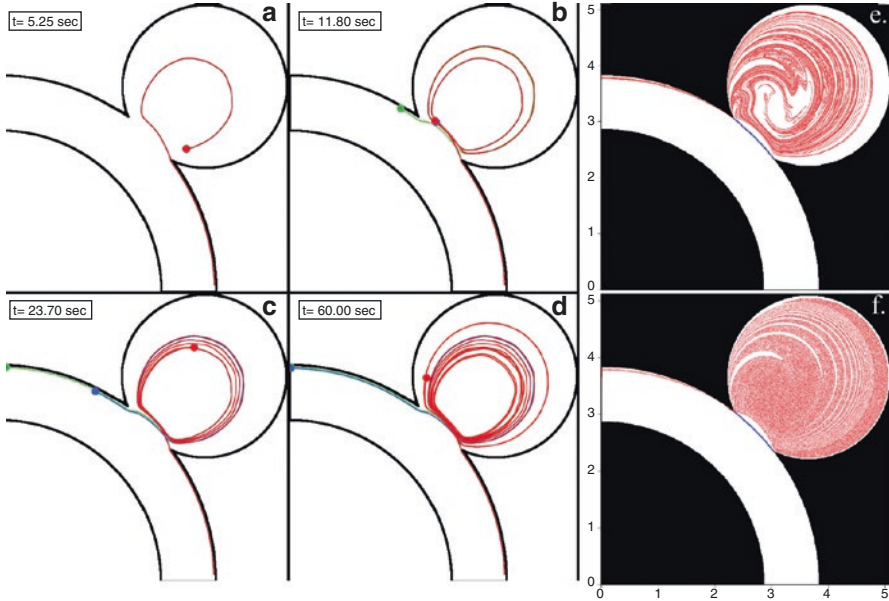


Fig. 17.3 (a–d) Sample of strongly deviating trajectories in the 2D flow. The three particles (*red, green, blue*) were started close to each other (a few μm), however, they spend significantly different amount of time in the central vortex. (e, f) Positions of one million tracer particles after 15 heart beat cycle (15 s) (e) initiated from a line segment across the inlet close to the wall and (f) initiated from within the aneurysmal sac using uniform spatial distribution

properties, this set includes several quantities associated with the flow condition such as the average flow velocity or the heart beat frequency. In our case the former is expressed as the non-dimensional Reynolds number (Re) using the inlet vessel diameter and the average inlet velocity at the systolic peak, the latter is defined through the Womersley number (Wo) with the same inlet diameter and the frequency of the heart beats. Applying the aforementioned numerical methods, this model yields a high resolution transient velocity field. The emergent flow field is smooth and laminar. Figure 17.2a displays a typical arrangement of streamlines within the computational domain. The qualitative picture of the flow remains the same under the effects of the different parameters. However, investigating the flow field from the viewpoint of tiny immersed particles, the picture varies substantially.

As we have seen in the previous section in the 3D case, the time it takes the particles to enter and leave the aneurysm sac may vary greatly as we change slightly their initial positions. The same behavior can be observed in the case of our simplified 2D model, as shown in Fig. 17.3a–d. Here, three particle paths are shown with a very small difference in their initial position (approximately $6 \mu\text{m}$). The particles follow the same path until they reach the aneurysm, they penetrate it, and start to whirl around inside the sack. It is the particle with the green path

that leaves the sac first, after about 11 s, that is, 11 heartbeat periods. Later, after about 22 s, the particle with blue path exits. However, the particle with the red path is still within the aneurysm after 60 s (that is, roughly after 60 heartbeats). This indicates that the residence time can be a quite irregular function of the initial conditions, as also shown in Fig. 17.2b, c. Here, as a function of the initial position, we can see in light blue the time it takes the particle to pass along the vessel segment. For particles in the center of the blood vessel, the residence time is short and is a regular function of the initial position: these particles do not enter the aneurysm, they just follow the undisturbed part of the flow. However, particles at the edge have a chance to enter the sac and to get trapped there for a long time. We see here that the residence time depends sensitively on the initial position of these particles. Particles initially close to each other can have very different residence times. The sensitive dependence on the initial position is, again, a unique sign of chaotic particle motion.

Residence times shown in Fig. 17.2b, c feature a large number of peaks, that is, many particles have anomalously long residence times (up to 15 heart beats in this case). In fact, in such flows it is known that there is an infinity of initial positions with infinitely long residence times [10]. These initial positions form a fractal set, and they all belong to particle paths that are trapped forever in the vessel segment shown in the figure.

To better understand what happens to those particles that are trapped within the aneurysm, we follow many particles from the vicinity of the wall initiated from a straight line. Figure 17.3e shows where these particles are to be found after 15 s. We see that the particles, originally along a straight line, either leave the vicinity of the aneurysm or spread along an intricate curve within the aneurysm. The particles that have not left the sack trace out a filamentary fractal pattern.

This intricate pattern is caused by the existence of a mathematical object called *chaotic set* within the aneurysm. The chaotic set is a union of all particle paths that eternally stay within the aneurysm. Neither in the future nor in the past they are to be found outside the aneurysm. Examples for such particles can be periodic particle paths that, after one or more periods of the flow, return to their previous position then follow the same path again and again. In typical chaotic systems, the number of such periodic particle paths increases *exponentially* with the length of the time period [10, 27]. That is, the number of periodic particle paths increases very strongly with the length of the period, the longer we wait the more periodic paths reveal themselves to an observer.

It is important to note that the chaotic set consists of infinitely many particle paths, but it is still exceptional that a particle path belongs to the chaotic set. In mathematical term, the chaotic set is a set of measure zero among all possible particle paths, typically all particles leave the aneurysm sooner or later. Also, the particle paths that belong to the chaotic set are unstable in the sense that any small deviation from the particle path will result in a completely different path, leaving the aneurysm after some time.

Nevertheless, these trapped paths have a great effect on other particle paths. Whenever a particle gets close to a particle path that belongs to the chaotic set, like

those in Fig. 17.3e with long residence time, for a while it follows segments of particle paths belonging to the set: the closer it gets to the chaotic set the longer it takes to leave its vicinity. This effect generates the peaks on the residence time plot shown in Fig. 17.2b, c: the high peaks correspond to particles that spend a long time wandering chaotically in the vicinity of the chaotic set. This implies that the particles trapped for a long time close to the chaotic set will eventually form the image shown in Fig. 17.3f.

The property that an unstable chaotic set governs the other particle paths forming a fractal pattern as shown in Fig. 17.3e is quite robust. For example, changing fine details of the shape of the aneurysm does not result in a qualitative change in the fractal pattern of particles.

17.4 Measuring Chaotic Quantities from Residence Times

A relatively simple technique to measure important quantities that characterize chaotic motion is the free energy formalism [25]. We initiate a large number of particles along a line segment of length L so that this segment contains at least some high peaks of the residence time, that is, it contains particle initial positions that approach the chaotic set. Then we measure the residence time for each particle, see Fig. 17.4a for an example, and count the number $N(t)$ of intervals along L with residence time longer than t .

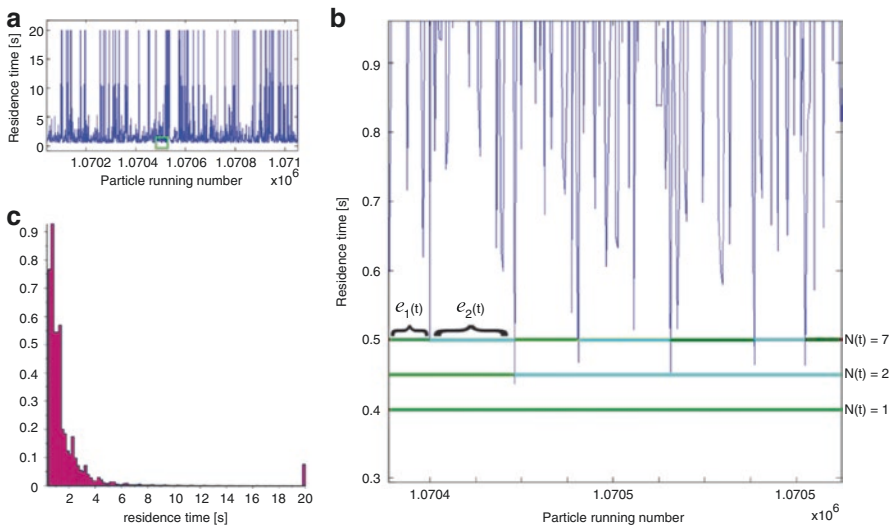


Figure 17.4 (a) A typical residence time plot. (b) Enlarged region from the residence time plot from the green rectangle with the explanation of quantities for the computation of the $bF(b)$ function. (c) Histogram of residence times, note the final peak which represents the particles still trapped after 20 s

Let $l_i(t)$, $i=1 \dots N(t)$ denote the length of these intervals along L , see Fig. 17.4b. For a large enough t the free energy function $F(b)$ can be defined as in [25]:

$$e^{-bF(b)} \sim \sum_i l_i(t)^b.$$

The important quantities describing chaotic advection can be derived from this function [25]. For instance, the fractal dimension D_0 of the set of infinitely high peaks in Fig. 17.4a can be found as the b value at which $bF(b)$ equals zero. In this case, it is more robust [34] to obtain the information dimension D_1 of the same set, which usually is not far from D_0 .

Another important quantity is the average Lyapunov exponent, which is the average rate of exponential separation of initially close particles. This can also be obtained from $F(b)$ as the slope of the $bF(b)$ function at $b=1$.

Also, the escape rate can be obtained from $F(b)$. The escape rate is the exponential rate of decay of the number of particles still staying within the investigated segment of the blood vessel. It can be considered as the reciprocal of the average lifetime of chaotic motion within the vessel segment [27]. It is computed simply as the value of $F(b)$ at $b=1$ [25].

The study used a default parameter set (see Table 17.1 for details) as a basis for comparison. These parameters reflect a general realistic physiological case. In every additional sample, one parameter was either increased or decreased significantly relative to these values. This change results in a modified flow field and consequently in modified paths for the tracer particles. The major question here is, how the changes in the parameters affect the chaotic behavior of the particles.

The answer can be extracted from the results of the numerical simulations. We compute the flow field, then follow many particle trajectories to generate the residence times in each parameter set-up. Using the residence times, we derive chaotic quantities. The change in the obtained chaotic characteristic numbers, listed in Table 17.2, indicates the effects of local deviations from the default parameter set, and might give additional insight on what to expect in the 3D realistic cases.

Table 17.2 shows the change in the major measurable chaotic properties as a function of the change in the default parameter set. The table contains several intuitive and a few counter-intuitive results. Regarding the first group: one major separation point for the advected particles is the distal part of the neck of the aneurysm. In a

Table 17.1 The default set of parameter values containing both the geometric and the flow parameters

Parameter	Value
r	1.5 [mm]
R	3.5 [mm]
L	1 [mm]
D	1 [mm]
Re	100 [-]
Wo	1.36 [-]

Table 17.2 Results of the parametric study of the most important quantities characterizing the chaotic particle motion

Changed parameter and the amount of change	D_1 (information dimension)	κ (escape rate)	λ (Lyapunov exponent)
Default set of parameters	0,922	0,019	0,243
Parent artery radius (R) +2,5 [mm]	0,927	0,024	0,330 ↑
Parent artery radius (R) -2,5 [mm]	0,937 ↑	0,016	0,257
Parent artery diameter (D) +0,5 [mm]	0,919	0,024	0,301
Parent artery diameter (D) -0,5 [mm]	0,911	0,009 ↓	0,100 ↓
Sac neck width (L) +1,0 [mm]	0,853 ↓↓	0,056 ↑	0,383 ↑
Sac neck width (L) -0,5 [mm]	0,923	0,017	0,219
Sac radius (r) +2,5 [mm]	0,902	0,005 ↓↓	0,046 ↓↓
Sac radius (r) -0,7 [mm]	0,923	0,064 ↑↑	0,826 ↑↑
Flow velocity (Re) +50	0,926	0,053 ↑	0,712 ↑↑
Flow velocity (Re) -90	0,916	0,018	0,208 ↓
Heart beat freq. (Wo) +0,56 (0,5 s cycle)	0,879 ↓	0,040 ↑	0,332 ↑
Heart beat freq. (Wo) -0,4 (2 s cycle)	0,935 ↑	0,003 ↓↓	0,049 ↓↓

The significant deviations from the default values are denoted by colored arrows

geometry with decreased bulge radius and maintained velocity the overturn time of the particles trapped in the vortex inside the aneurysm is shorter, thus the particles revisit this region of separation more often. This should result in an increased Lyapunov exponent, as well as an increased escape rate. Since the overturn frequency strongly influences the stretching effect of the flow as well, the increase in the Lyapunov exponent is expected to be more dominant. Increasing the radius should produce the opposite results. This is well reflected in Table 17.2. The change in the flow velocity has a similar effect. Its increase will yield higher escape rates, since the average velocity increases throughout the domain, and also causes a higher vortex velocity, thus shorter overturn-times and an increased Lyapunov exponent. For the second group, where Table 17.2 gives less plausible results, an interesting example is the outcome of changing the heart beat frequency. The shorter cycle time increased and the longer cycle time strongly decreased the escape rate. This might not be directly obvious, since the average flow velocity remained the same. However, the increased frequency provides an increased excitation for the flow possibly driving it towards stronger chaotic behavior. Another example is the change in the width of the neck of the aneurysm. On the one hand, changing it modifies the escape rate significantly. The wider the neck is, the lower the escape rate becomes. On the other hand, it has only a moderate effect on the Lyapunov exponent. As a result, in accordance with the Kantz-Grassberger relation [7], it modifies the fractal dimension of the particle trajectories. Increasing the neck width decreases the fractal dimension. Fractal dimension can be thought of as a measure of how densely the chaotic trajectories are packed in space. Therefore, a higher D_1 implies a stronger overall effect of the chaotic behavior on the flow.

17.5 Appearance of Chaotic Flow Inside Intracranial Aneurysms

The previous part of this chapter introduced some concepts on what might be expected in simplified cases based on some basic geometric and fluid flow properties. Comparing cases of real geometries, however, seems to be a more challenging task. Since every geometry is unique, the combined effects of the different parameters (which are naturally immensely more numerous than in our simplified case) yield a single result. This renders carrying out a parametric study nearly impossible. Nevertheless, we might showcase the effects of changing the Reynolds number with relative ease by changing the inlet flow velocity. Figure 17.5a, b shows the inlet cross section of the vessel geometry shown in Fig. 17.1, it is the same geometry used in [35] for code validation and in [34] for the exploration of fractal properties. The color of every point on the surface represents the residence time of a particle initiated from that particular point. Similarly to the simplified case, there are initial locations from where the particles take much more time to leave the investigated domain than one would expect based on the average flow velocity, for some examples see Fig. 17.1. Particles travelling these paths are usually trapped in some vortex residing mainly inside the aneurysmal sac or in some cases near vessel bifurcation points. On several occasions, the aneurysm displays a very intricate flow profile possibly incorporating multiple vortices enabling for even more intertwined particle paths. In the current case, the aneurysm has a single vortex core under the investigated boundary conditions. In Fig. 17.5a we present the residence times on the inlet cross section at a Reynolds number of 50. In Fig. 17.5b we present the same cross section with a different boundary condition: the Reynolds number was increased to 450. The difference is clearly visible. Increasing the flow velocity resulted in a richer, more complex pattern that displays the signs of the well-known ‘stretching and folding’ actions related to chaos. In our experience, based on ten different geometries, this phenomenon seems to be general, though different models are affected to a different extent.

17.6 Concluding Remarks

Some researchers believe that the rupture risk is associated with the irregularity of the flow pattern around the region of the aneurysm [5]. According to our findings, the emergent flow properties are in strong connection with the chaotic behavior of the advection in it. Thus, the measured quantities might be used as an indicator on the flow pattern complexity. Quantitative measures of the chaotic and fractal behavior for the same geometry, similarly to those for the 2D simplified geometry here, were computed in [34]. It was also discussed in [17] that chaotic advection is capable of influencing the ongoing biochemical reactions significantly. It can be speculated that this might induce a cascade of far ranging changes in the ongoing processes from endothelial functions to nutrition mechanisms leading to altered behavior in the wall

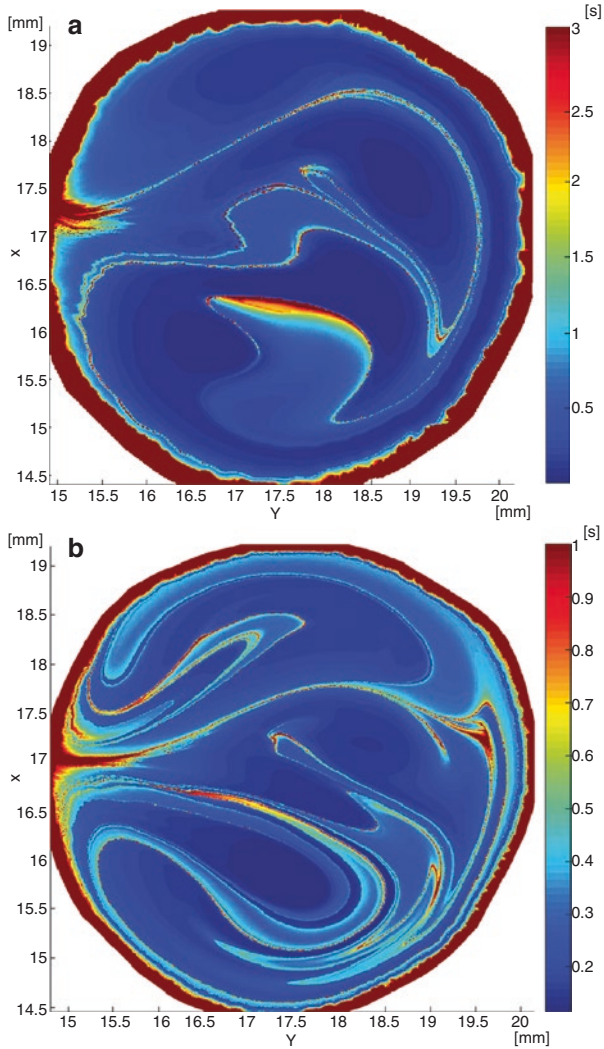


Fig. 17.5 Residence times of the particles initiated from the inlet cross section of the parent artery in case of (a) $Re = 50$ and (b) $Re = 450$. Note that the color scales are different due to the different average velocity

tissues. For example, the wall of these arteries are dependent on oxygenated blood for their metabolic needs. The presence of chaotic structures might alter the residence time and thus the level of deoxyhemoglobin present inside the aneurysm.

Therefore, using this study about the very fabric of the emergent flow structures, the chaotic quantities might turn out to be useful for characterizing cerebral aneurysms as they might predict the biochemical behavior of the concerned vessel section.

Acknowledgements Financial support from OTKA no. K 100894 and NK 100296, as well as from the KTIA_NAP_13-1-2013-0001 Hungarian Brain Research Program is gratefully acknowledged.

References

1. Aref H. Stirring by chaotic advection. *J Fluid Mech.* 1984;143:1–21.
2. Campo-Deaño L, Oliveira MS, Pinho FT. A review of computational hemodynamics in middle cerebral aneurysms and rheological models for blood flow. *Appl Mech Rev.* 2015;67(3):030801.
3. Castro MA, Olivares MCA, Putman CM, Cebral JR. Unsteady wall shear stress analysis from image-based computational fluid dynamic aneurysm models under Newtonian and Casson rheological models. *Med Biol Eng Comput.* 2014;52(10):827–39.
4. Cebral JR, Castro M, Appanaboyina S, Putman CM, Millan D, Frangi AF, et al. Efficient pipeline for image-based patient-specific analysis of cerebral aneurysm hemodynamics: technique and sensitivity. *Med Imag IEEE Trans.* 2005;24(4):457–67.
5. Cebral JR, Castro MA, Burgess JE, Pergolizzi RS, Sheridan MJ, Putman CM. Characterization of cerebral aneurysms for assessing risk of rupture by using patient-specific computational hemodynamics models. *Am J Neuroradiol.* 2005;26(10):2550–9.
6. Guglielmi G, Viñuela F, Dion J, Duckwiler G. Electrothrombosis of saccular aneurysms via endovascular approach: part 2: preliminary clinical experience. *J Neurosurg.* 1991;75(1):8–14.
7. Kantz H, Grassberger P. Repellers, semi-attractors, and long-lived chaotic transients. *Physica D Nonlinear Phenom.* 1985;17(1):75–86.
8. Károlyi G, Péntek Á, Scheuring I, Tél T, Toroczkai Z. Chaotic flow: the physics of species coexistence. *Proc Natl Acad Sci.* 2000;97(25):13661–5.
9. Károlyi G, Péntek Á, Toroczkai Z, Tél T, Grebogi C. Chemical or biological activity in open chaotic flows. *Phys Rev E.* 1999;59(5):5468.
10. Károlyi G, Tél T. Chaotic tracer scattering and fractal basin boundaries in a blinking vortex-sink system. *Phys Rep.* 1997;290(1):125–47.
11. Károlyi G, Tél T. Chemical transients in closed chaotic flows: the role of effective dimensions. *Phys Rev Lett.* 2005;95(26):264501.
12. Kelly P, Stein J, Shafqat S, Eskey C, Doherty D, Chang Y, et al. Functional recovery after rehabilitation for cerebellar stroke. *Stroke.* 2001;32(2):530–4.
13. Lasheras JC. The biomechanics of arterial aneurysms. *Annu Rev Fluid Mech.* 2007;39:293–319.
14. Oubel E, De Craene M, Putman CM, Cebral JR, Frangi AF. Analysis of intracranial aneurysm wall motion and its effects on hemodynamic patterns. In: *Medical imaging. San Diego: International Society for Optics and Photonics; 2007.* p. 65112A.
15. Paál G, Ugron A, Szikora I, Bojtár I. Flow in simplified and real models of intracranial aneurysms. *Int J Heat Fluid Flow.* 2007;28(4):653–64.
16. Ropper AH, Zervas NT. Outcome 1 year after SAH from cerebral aneurysm: management morbidity, mortality, and functional status in 112 consecutive good-risk patients. *J Neurosurg.* 1984;60(5):909–15.
17. Schelin AB, Károlyi G, De Moura A, Booth N, Grebogi C. Chaotic advection in blood flow. *Phys Rev E.* 2009;80(1):016213.
18. Schelin AB, Károlyi G, De Moura AP, Booth NA, Grebogi C. Fractal structures in stenoses and aneurysms in blood vessels. *Philos Trans R Soc Lond A: Math Phys Eng Sci.* 2010;368(1933):5605–17.
19. Schelin AB, Károlyi G, De Moura AP, Booth N, Grebogi C. Are the fractal skeletons the explanation for the narrowing of arteries due to cell trapping in a disturbed blood flow? *Comput Biol Med.* 2012;42(3):276–81.

20. Scheuring I, Károlyi G, Toroczkai Z, Tél T, Péntek Á. Competing populations in flows with chaotic mixing. *Theor Popul Biol.* 2003;63(2):77–90.
21. Sforza DM, Putman CM, Cebal JR. Hemodynamics of cerebral aneurysms. *Annu Rev Fluid Mech.* 2009;41:91.
22. Szikora I, Berentei Z, Kulcsar Z, Marosfoi M, Vajda Z, Lee W, et al. Treatment of intracranial aneurysms by functional reconstruction of the parent artery: the Budapest experience with the pipeline embolization device. *Am J Neuroradiol.* 2010;31(6):1139–47.
23. Szikora I, Paál G, Ugron A, Nasztanovics F, Marosfoi M, Berentei Z, et al. Impact of aneurysmal geometry on intraaneurysmal flow: a computerized flow simulation study. *Neuroradiology.* 2008;50(5):411–21.
24. Taylor CA, Draney MT. Experimental and computational methods in cardiovascular fluid mechanics. *Annu Rev Fluid Mech.* 2004;36:197–231.
25. Tél T. Fractals, multifractals, and thermodynamics. *Z Naturforsch A.* 1988;43(12):1154–74.
26. Tél T, de Moura A, Grebogi C, Károlyi G. Chemical and biological activity in open flows: a dynamical system approach. *Phys Rep.* 2005;413(2):91–196.
27. Tél T, Gruiz M. *Chaotic dynamics: an introduction based on classical mechanics.* Cambridge, UK: Cambridge University Press; 2006.
28. Toroczkai Z, Károlyi G, Péntek Á, Tél T, Grebogi C. Advection of active particles in open chaotic flows. *Phys Rev Lett.* 1998;80(3):500.
29. Ugron Á, Paál G. On the boundary conditions of cerebral aneurysm simulations. *Mech Eng.* 2014;58(1):37–45.
30. Ugron Á, Szikora I, Paál G. Haemodynamic changes induced by intrasaccular packing on intracranial aneurysms: a computational fluid dynamic study. *Interv Med Appl Sci.* 2012;4(2):78–84.
31. Ugron Á, Szikora I, Paál G. Measurement of flow diverter hydraulic resistance to model flow modification in and around intracranial aneurysms. *Interv Med Appl Sci.* 2014;6(2):61–8.
32. Vlák MH, Algra A, Brandenburg R, Rinkel GJ. Prevalence of unruptured intracranial aneurysms, with emphasis on sex, age, comorbidity, country, and time period: a systematic review and meta-analysis. *Lancet Neurol.* 2011;10(7):626–36.
33. Wiebers DO, Torner JC, Meissner I. Impact of unruptured intracranial aneurysms on public health in the United States. *Stroke.* 1992;23(10):1416–9.
34. Závodszy G, Károlyi G, Paál G. Emerging fractal patterns in a real 3D cerebral aneurysm. *J Theor Biol.* 2015;368:95–101.
35. Závodszy G, Paál G. Validation of a lattice Boltzmann method implementation for a 3D transient fluid flow in an intracranial aneurysm geometry. *Int J Heat Fluid Flow.* 2013;44:276–83.

Chapter 18

Fractal-Based Analysis of Arteriovenous Malformations (AVMs)

Antonio Di Ieva and Gernot Reishofer

Abstract Arteriovenous malformations (AVMs) are cerebrovascular lesions consisting of a pathologic tangle of the vessels characterized by a core termed the nidus, which is the “nest” where the fistulous connections occur. AVMs can cause headache, stroke, and/or seizures. Their treatment can be challenging requiring surgery, endovascular embolization, and/or radiosurgery as well. AVMs’ morphology varies greatly among patients, and there is still a lack of standardization of angioarchitectural parameters, which can be used as morphometric parameters as well as potential clinical biomarkers (e.g., related to prognosis).

In search of new diagnostic and prognostic neuroimaging biomarkers of AVMs, computational fractal-based models have been proposed for describing and quantifying the angioarchitecture of the nidus. In fact, the fractal dimension (FD) can be used to quantify AVMs’ branching pattern. Higher FD values are related to AVMs characterized by an increased number and tortuosity of the intranidal vessels or to an increasing angioarchitectural complexity as a whole. Moreover, FD has been investigated in relation to the outcome after Gamma Knife radiosurgery, and an inverse relationship between FD and AVM obliteration was found.

Taken altogether, FD is able to quantify in a single and objective value what neuro-radiologists describe in qualitative and/or semiquantitative way, thus confirming FD as a reliable morphometric neuroimaging biomarker of AVMs and as a potential surrogate imaging biomarker. Moreover, computational fractal-based techniques are under investigation for the automatic segmentation and extraction of the edges of the nidus in neuroimaging, which can be relevant for surgery and/or radiosurgery planning.

A. Di Ieva, MD, PhD (✉)

Neurosurgery Unit, Faculty of Medicine and Health Sciences, Macquarie University, Sydney, Australia

Garvan Institute of Medical Research, Sydney, NSW, Australia

Medical University of Vienna, Vienna, Austria

University of Toronto, Toronto, ON, Canada

e-mail: diieva@hotmail.com

G. Reishofer (✉)

Department of Radiology, MR-Physics, Medical University of Graz, Graz, Austria

e-mail: gernot.reishofer@medunigraz.at

Keywords Angioarchitecture • Arteriovenous malformation • AVM • Box counting • Fractal dimension • Gamma Knife radiosurgery • Minkowski dimension • Outcome

18.1 Introduction

Arteriovenous malformations (AVMs) are vascular lesions of the brain and, more rarely, of the spinal cord, occurring with an incidence of 1/100,000/year and prevalence of 18/100,000/year [1]. In about 70% of cases, AVMs present with hemorrhage, accounting for 2% of all strokes, while in 20% of patients, seizures are the first presentation. In some cases, AVMs can be asymptomatic or can cause headache, focal neurological deficits, cognitive dysfunction, and pulsatile tinnitus. The combined rate of mortality and major morbidity related to untreated AVMs is of 2.7% per year [22].

Morphologically, AVMs consist of a pathologic tangle of vessels, i.e., fistulous connections of afferent arteries draining blood directly into dilated efferent draining veins without the interposition of the brain parenchyma (Fig. 18.1). The core of the AVMs is defined as the nidus, which is the nest where the pathologic connections occur. Their treatment can be challenging requiring surgery (by means of microneurosurgery techniques), endovascular embolization or radiosurgery (e.g., Gamma Knife), or a combination of such modalities. The aim of the treatment is the removal and/or obliteration of the nidus in order to lower the risk of bleeding and/or seizures.

Several systems have been proposed to classify AVMs, with the most used and clinically relevant being the Spetzler-Martin classification system [28] and its subsequent modification, the Spetzler-Ponce classification system [27]. Both systems quantify specific features in a final score, i.e., (a) the size of the nidus, (b) the functional eloquence of the brain region where the AVM is located, and (c) the type of venous drainage. On one hand these systems are very relevant because they are related to outcome (prognostication) and therapy modality, but on the other hand no information is added in regard to the angioarchitecture. AVMs with the same score can show completely different shapes, different number of vessels forming the nidus, peculiar branching patterns, and distinct geometrical complexity. To overcome this limitation, several methods have been proposed for the morphometric analysis of AVMs, including a computational fractal-based approach, as discussed in this chapter.

18.2 Neuroimaging of AVMs

The diagnosis of AVMs is based on multimodal imaging techniques, which encompass various magnetic resonance imaging (MRI) techniques, computed tomography (CT), and catheter biplane digital subtraction angiography (DSA), which is still

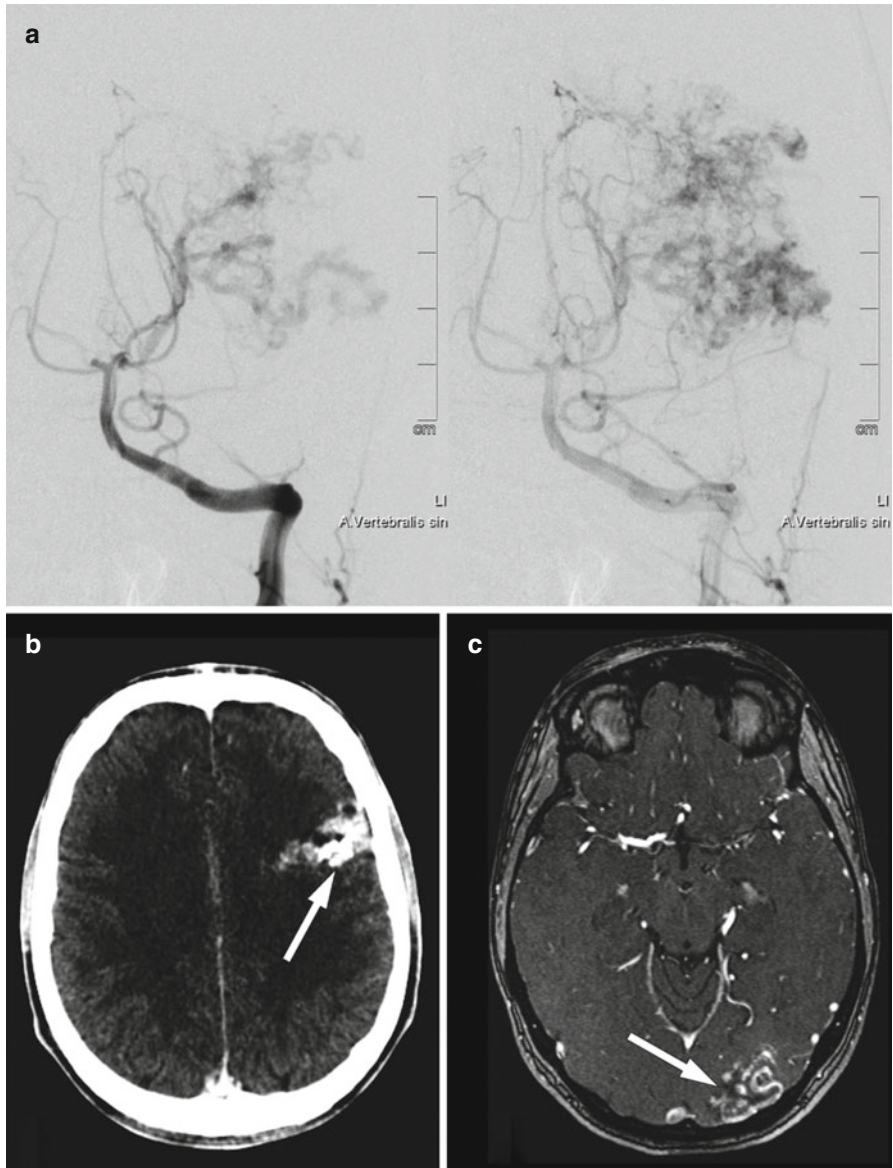


Fig. 18.1 CTA and MRA for different patients with AVM. (a) DSA of the vertebral artery imaged in an earlier phase (*left*) giving more weight to the feeding arteries and imaged in a later phase (*right*) giving a better contrast to the nidus. (b) CTA and (c) MRA of a unilateral AVM of two different patients marked with a *white arrow*

considered as the gold-standard technique [21] (Fig. 18.1). The high temporal resolution of DSA allows the subsequent subtraction of a baseline image from contrast-enhanced images. Different states of contrast media uptake provide an excellent differentiation between the arteries, the veins, and the nidus. However, since this technique only generates 2D information from two orthogonal directions, the entire geometrical complexity of the nidus and the vascular system is not fully represented. Magnetic resonance angiography (MRA) and computed tomography angiography (CTA) overcome this limitation and provide a 3D representation of the vasculature. In MRA, techniques with contrast media (CE-MRA) or without contrast media (TOF-MRA) can be used to visualize the vascular tree. A disadvantage of all standard 3D techniques utilizing contrast media (MRA and CTA) is given by the fact that generated images are snapshots of the contrast media flowing through the vascular system. This means that imaging an early phase put stronger weights on the arterial system while imaging a later phase puts more weights on the venous system. The time between bolus injection and data acquisition is therefore crucial for the image quality and a challenging task. 4D techniques that are available for both MR and CT are able to measure sequential angiograms and allow analyzing the dynamics of the flow within the AVM. Dynamic CT angiography (dCTA) provides good spatial and temporal resolution but expose the patient to a high dose of ionizing radiation [20]. In MRI, dynamic contrast-enhanced sequences (DCE-MRI) based on T1-weighted MR scans are used to provide an overview about the AVM flow dynamics (Fig. 18.2), but this technique is limited in spatial and temporal resolution. Recent developments in MR imaging utilize advanced imaging reconstruction techniques such as highly constrained back projection with phase contrast as a constrained (HYPR flow) to improve spatial and temporal resolution [29].

For the optimal representation of the acquired data, several techniques exist for image fusion in multimodal imaging and 3D rendering of the AVM [29].

18.3 AVMs' Angioarchitecture Morphometrics

AVMs vary greatly among patients, and experts have attempted to classify them based on several angioarchitectural parameters, by looking for similar clinical presentation and posttreatment outcome. However, these parameters have not been standardized.

An objective morphostructural analysis of AVMs should provide useful information for classification, prognostication, therapeutic decisions and follow-up.

Several grading systems have been proposed, which generally take into account the number of feeding arteries from the different vascular territories, the size and location of the AVM, and other features, with the Spetzler-Martin (5-tiered score) and Spetzler-Ponce (3-tiered score) as the most clinically relevant and used ones, as previously quoted. By the way, such classification systems do not take into account the morphological complexity of the nidus, referring to its geometry only in terms of the size. Of course, AVMs having the same Euclidean parameters (i.e., maximal

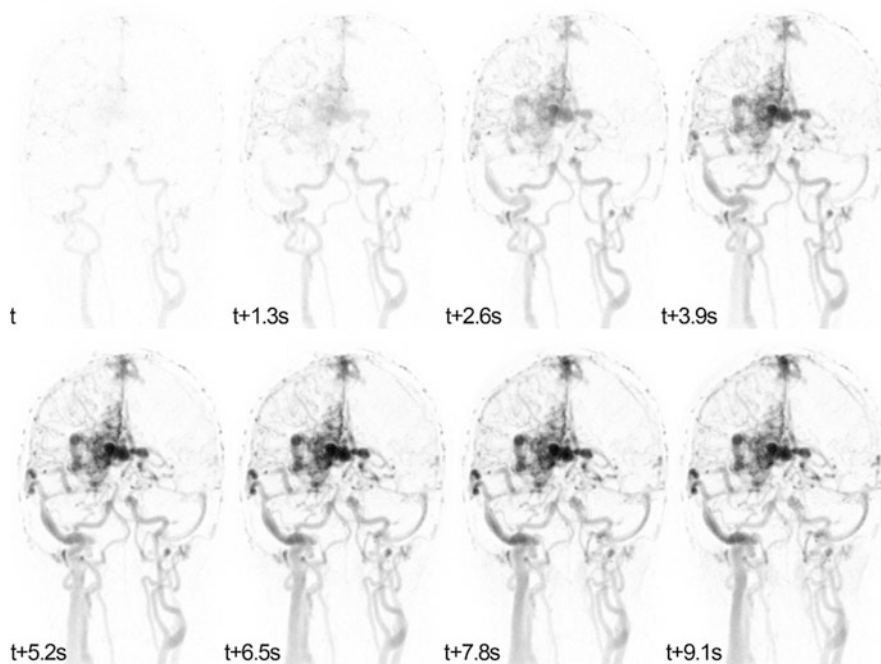


Fig. 18.2 Maximum intensity projection of a 4D dynamic MRA with a temporal resolution of 1.3 s (Images are displayed in inverted view)

diameter and volume) may have a very different pattern of distribution of the vessels forming the nidus (e.g., different density, compactness, tortuosity of the vessels, in one word, different angioarchitecture). Moreover, the distribution of the vessels within the nidus can leave different grades of “gaps” among the vessels themselves. According to the nonlinearity of the AVM’s shape, “compactness” and “diffuseness” of the nidus have been investigated as a better mean of quantification; these parameters have been shown to be important factors in predicting the difficulty to resect an AVM [11].

Fractal analysis is a novel computer-aided mathematical model, which has also been shown to have several applications in clinical neurosciences, including neuroimaging [7]. Fractal dimension and lacunarity seem to offer valid tools to quantify AVM’s geometrical complexity, as presented hereinafter.

18.4 Computational Fractal-Based Analyses of AVMs

Fractal analysis is a mathematical model that, among other parameters, offers the fractal dimension (FD) and lacunarity as measures of the roughness and/or geometrical complexity of natural objects, including physiological and pathological brain

structures in neuroimaging. As several natural objects characterized by a branching pattern, AVMs are suitable to fractal analysis as well. Computing FD of the nidus by means of the box-counting method, for example, adds an objective morphometric parameter to quantify the space-filling properties of the tangle itself, thus offering a potential morphometric biomarker, which could be added into the existing classification systems.

18.4.1 AVMs' Fractal Dimension

The first study that investigated AVMs by means of FD was published by Reishofer et al. in 2012 [25]. Given the fact that the direct observation of the nidus' vasculature using MRI angiography is not an easy task due to limited spatial resolution, the architecture of surrounding arteries was analyzed by means of different measures of FD. The nidus can be supplied by one or more feeding arteries that are directly connected to draining veins leading to a vascular system with a higher geometrical complexity compared to a normal vascular system. The aim of this study was to investigate whether FD, obtained from 3D-time-of-flight (TOF) MR images, is a suitable biomarker to represent changes in the vascular geometry and furthermore whether FD is related to pathologic and physiological parameters such as the nidus size and vascular flow.

Ten patients with a unilateral supratentorial AVM and ten healthy controls participated in this study. The patients and controls underwent a standard MR imaging protocol including T_1 - and T_2 -weighted sequences, 3D-TOF, and dynamic contrast-enhanced (DCE) MR imaging. 3D-TOF MR angiography is an imaging technique that allows the visualization of the cerebral arterial system with high accuracy up to small vessel diameters. The following parameters were used to visualize cerebral arteries covering the circle of Willis and vertebral-basilar arteries: TR = 22 ms, TE = 3.68 ms, flip angle = 18° , FOV = 200 mm, phase FOV = 75%, image matrix = 384×288 , number of slabs = 3, slices/slab = 52, and slice thickness = 0.65 mm. DCE-MRI data were acquired to image the vascular flow using a 3D-FLASH sequence with the following parameters: TR = 2.67 ms, TE = 1.05 ms, flip angle = 16° , FOV = 230 mm, image matrix = 320×320 , number of slabs = 1, slices/slab = 12, and slice thickness = 6 mm. A dose of 0.2 ml/kg body weight contrast agent (ProHance®, Bracco Diagnostics, Inc., Princeton, NJ, USA) was injected intravenously via a power injector (Spectris; Medrad Inc., Indianola, PA, USA) at a flow rate of 3 ml/s. All measurements were carried out on a 3 T Tim Trio system (Siemens Medical Systems, Erlangen, Germany) using a 12-channel head coil. The following image processing steps have been applied in order to prepare 3D-TOF data for fractal analysis (Fig. 18.3):

- Normalization to the standard MNI space (Montreal Neurological Institute) by means of linear co-registration using FLIRT [16] from the FMRIB Software Library (FMRIB Centre, University of Oxford, UK; <http://www.fmrib.ox.ac.uk/>)

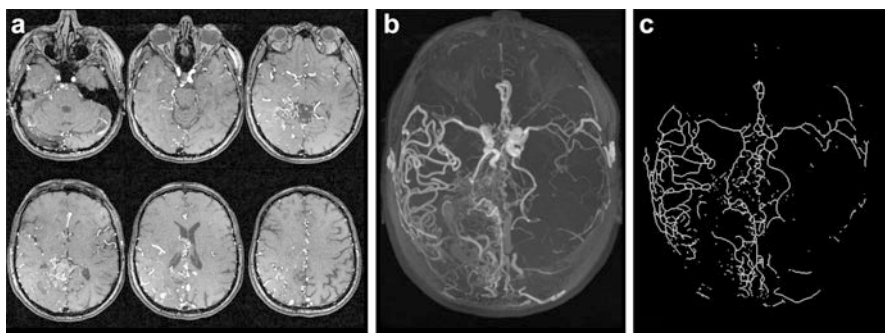


Fig. 18.3 Normalized 3D-TOF images (a) provide the basis for MIP images (b). FD evaluated from MIP images after the image processing step segmentation, binarization, and skeletonization (c) (From Reishofer et al. [25])

fsl/fsl/downloading.html) to account for intersubject variability regarding head size and FOV positioning.

- Maximum intensity projection (MIP) was performed to generate a two-dimensional representation of the 3D-TOF data using MRICro software (Chris Rorden, University of Nottingham, UK; <http://www.nitrc.org/frs/download.php/414/mrzip.zip>).
- The background was separated from the vascular tree using a k-means clustering algorithm.
- Images were converted into binary images and skeletonized using the ImageJ software v.1.45 (Wayne Rasband, National Institutes of Health, USA; <http://rsbweb.nih.gov/ij/download.html>).
- To enable a statistical comparison between the hemisphere with AVM and the hemisphere without AVM for both, patients and controls, the images (364× pixel) were split into two halves (182×436 pixel) and analyzed separately.

The fractal dimension was approximated using the box-counting dimension (D_b) and the Minkowski dimension (D_m) [17]. All of the fractal measurements were evaluated for the whole brain in patients (P_{total}) and healthy controls (HC_{total}) and also for both hemispheres separately in patients (P_{AVM} , $P_{no\ AVM}$) and controls (HC_{left} , HC_{right}). A 2×2 mixed-design ANOVA test with a within-subject factor of hemisphere (for patients, AVM, no AVM; for healthy controls, left, right) and a between-subject factor of group (P, HC) was applied to test for significant differences.

Patients showed significantly higher FD values for both methods in hemispheres with AVM compared with the hemispheres without AVM (D_b , $p=0.002$; D_m , $p=0.002$). Controls had similar values for FD in both hemispheres with no significant differences in FD (D_b , $p=0.982$; D_m , $p=0.892$). No significant differences were observed comparing the non-affected hemisphere of patients with healthy controls (HC_{left} , D_b , $p=0.574$; D_m , $p=0.918$; HC_{right} , D_b , $p=0.691$; D_m , $p=0.872$) but significant differences when comparing the patient's hemisphere with AVM with the hemispheres of healthy controls (HC_{left} , D_b , $p=0.015$; D_m , $p=0.020$; HC_{right} , D_b , $p=0.010$; D_m , $p=0.024$) (Fig. 18.4).

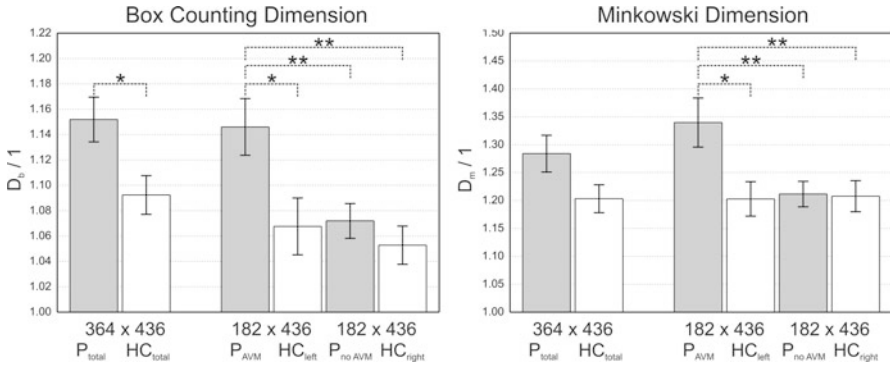


Fig. 18.4 Mean values of D_b (left side) and D_m (right side) comparing patients (P_{total}) with healthy controls (HC_{total}) for the whole image, hemispheres of patients with AVM (P_{AVM}) compared to the hemisphere without AVM ($P_{no AVM}$), and comparison of the left and right hemispheres of healthy controls (HC_{left} , HC_{right}). Asterisks indicate significant differences in group comparisons: * $p < 0.05$, ** $p < 0.01$

These results suggest that FD is a sensitive parameter able to detect changes in the geometrical complexity of the cerebral arterial system with high accuracy.

Values of FD are strongly correlated to physiological and pathologic parameters. This has been demonstrated by correlating FD with the maximum slope of contrast media transit obtained from dynamic contrast-enhanced (DCE) MRI data. A linear regression analysis showed a strong and positive linear correlation between FD of the affected hemisphere and the maximum slope of contrast media transit for D_b and D_m (D_b , $r = 0.913$; $p < 0.0001$; D_m , $r = 0.926$; $p < 0.0001$) (Fig. 18.5). Given the fact that the amount of arterial inflow is related to the number of vessels feeding the nidus, this result was not unexpected. A strong correlation was also found between FD and the nidus size (D_b , $r = 0.944$; $p < 0.0001$; D_m , $r = 0.963$; $p < 0.0001$). The nidus size was estimated from DSA data. This strong correlation is not that obvious but suggests that there is a relation between vascular complexity and nidus size.

It has to be noted that absolute values obtained from the box-counting method are dependent from the image matrix size [24]. Giving the fact that the box size is doubled at each iteration step starting with the size of 1 pixel, a complete covering of the image is only possible if the dimensions of the image to be analyzed are given as a power of two. If this is not the case, FD is dependent from the initial location of the grid. To overcome these limitations in the box-counting method, extensions of this technique have been proposed [19] such as the sliding box-counting dimension. When using this technique, each box is slid over the image overlapping the previous box making this method independent from the initial state but at the cost of computational time. The assessment of FD by evaluating the Minkowski dimension uses a different concept in which the structure itself is covered through geometrical objects such as circles, triangles, or squares making this method independent from different image matrix sizes. Another limitation is given by the fact that an MIP of 3D-TOF MR images is only an approximate representation of the vascular system. Superimposed

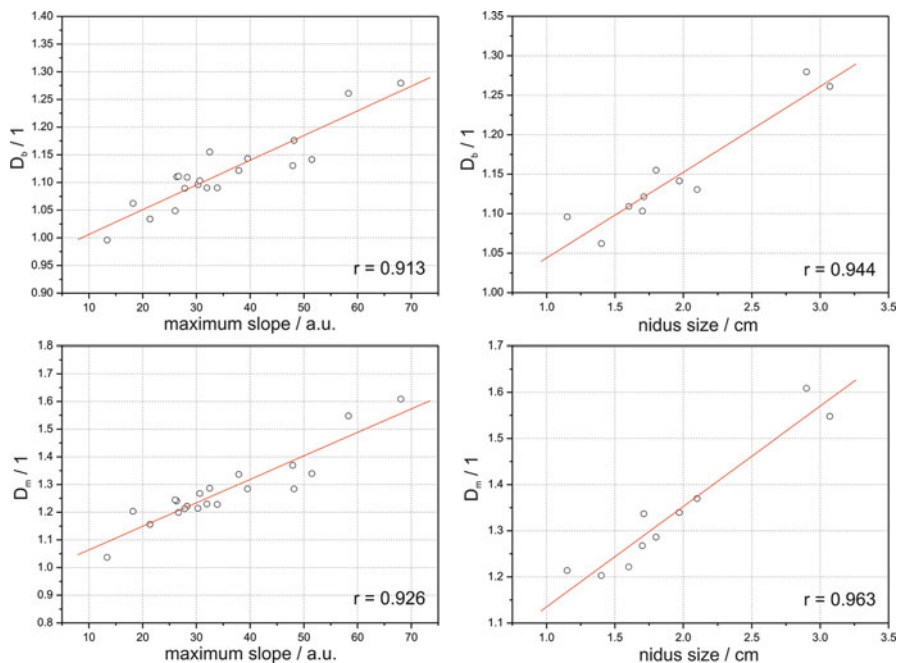


Fig. 18.5 Correlation between FD values (D_b , D_m) and the maximum slope of contrast media transit obtained from DCE-MRI data (*first column*) and correlation between FD values (D_b , D_m) and the nidus size evaluated from X-ray angiography data (*second column*)

vessels cannot be discriminated for a fixed projection plane, but since the projection of a fractal from an m -dimensional space into a $(m-1)$ dimensional subspace is well defined [12], FD from MIP images is an acceptable approximation. However, FD analysis of the vascular cerebral system is a simple and robust technique that yields an objective measure and may assist neuroradiologists in the diagnosis of complex cerebrovascular diseases.

18.4.2 Fractal Dimension of the Nidus and Its Relevance in Radiosurgery

Di Ieva et al. investigated the applicability of FD as a potential neuroimaging biomarker of the AVMs' angioarchitecture, especially in relation to the patients' outcome and follow-up in radiosurgery [9]. The Gamma Knife (GK) radiosurgery treatment, as well as other radiosurgical modalities, is aimed to obliterate the fistulous connections within the nidus, lowering the risk of bleeding. By means of specialized equipment, the stereotactic GK focuses multiple beams of radiation on the target (e.g., a brain tumor or AVM). The radiosurgical effect of obliteration of the vessels occurs over time, in general in 2–3 years; the 3-year obliteration rates following stereotactic

radiosurgery range from 60 to 86.6% [3, 13, 23]. The box-counting method was used for the FD computation in a retrospective case series of 54 patients affected by brain AVMs who underwent GK radiosurgery at the University of Toronto (Ontario, Canada) [9]. In this study, almost 54% of patients presented with hemorrhage, 13% only with headache, 9% with seizures, while other patients were incidentally diagnosed or reported minor focal neurological deficits. All of the patients underwent multimodal imaging, including CTA, MRA, and angiogram as well, but in order to standardize the image and the following fractal analysis, only MRA images performed on the same scanner with the same parameters were considered in the analysis. By means of such selection in the inputs (see the “black box” concept in Chap. 12), it was possible to obtain a homogeneous dataset for analysis. 3T GE Medical System Signa HDxt with an eight-channel head coil was used for all patients, with the following MRI parameters: axial 2D FRSE sequence with a rectangular matrix of 320, echo train length of 15, TR of 5,500 ms and TE of 91 ms, slice thickness of 2 mm without interslice gap, and with a rectangular field of view of 20 cm resulting in plane resolution of 0.625 mm square. Images were transferred to the radiosurgery software, which is a modification of CMI software (Montreal Stereotactic Planning System; CMI Services, Montreal, QC, Canada) [2] (see methods in [9]). A 4C GK radiosurgery system (Leksell Gamma Knife® Perfexion™, Sweden) was used for the stereotactic radiosurgery treatment. A standard dose of 25 Gray (Gy) for AVM volumes <4 cm³ and 20 Gy for volumes >4 cm³ was administered (limiting to 15 Gy the dose to the nidus whether near to eloquent brain areas). Checking the imaging 3 years after the treatment, the outcome of radiosurgery was dichotomized as complete obliteration, defined as the total disappearance of the nidus on the MRA, no abnormal flow voids on MRI and no early draining vein on the angiogram.

The image analysis was based on the following steps (Fig. 18.6):

- Selection of the MR sequences (FRFSE T2 post-gadolinium) and images containing the nidus.
- Selection of the nidus itself (the “region of interest” (ROI)), according to the outline of the target zone for the radiosurgical procedure, as chosen by consensus of six experts (including neurosurgeons, neuroradiologist, radiation oncologist, and physicist).
- Normalization of the intensity of the pixels within the ROI, according to the Brightness Progressive Normalization (BPN) algorithm, introduced by C. Russo [26], which allows to use a single gray-scale threshold for the automatic segmentation of the nidal vessels [10].
- Segmentation of the nidal vessels.
- Application of the box-counting method. A fractal window in a two-order scale was chosen, starting at the highest resolution of the MR images ($\epsilon_{\min} = 0.86 \text{ mm}$ – $\epsilon_{\max} = 86 \text{ mm}$). Monofractal behavior was found in such range.

The obtained FD values were statistically compared to (a) several angioarchitectural parameters, commonly used by the neuroradiologist for the qualitative description of the nidus (e.g., arterial enlargement, flow-related or intranidal aneurysms, flow pattern, neoangiogenesis, venous ectasia, nidus size, number of draining veins,

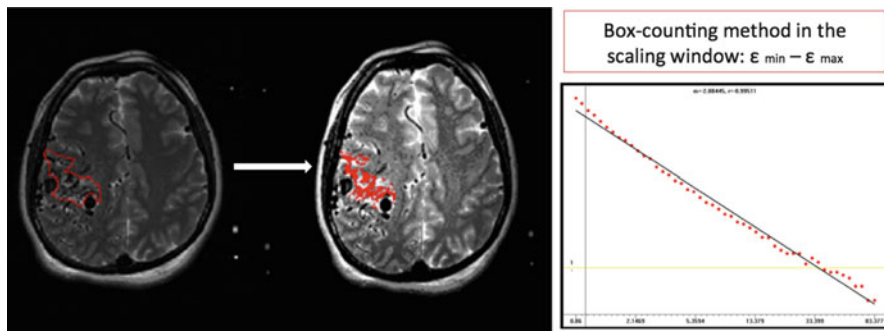


Fig. 18.6 Computation of FD on MR images of AVMs. The region of interest of the AVM is manually segmented on each slice, and an RGB threshold is used for the computer-aided segmentation of the vessels forming the nidus. The box-counting method is then applied in the fractal window, and the results are plotted on a graph, the slope of which represents FD (From Di Ieva et al. [8], reprinted with Permission of the Publisher)

Table

18.1 Angioarchitectural parameters associated with fractal dimension in brain AVMs

Angioarchitectural parameter
Arterial enlargement presence
Presence of non-sprouting angiogenesis
Presence of sprouting angiogenesis
Flow pattern
Venous ectasia
Presence of venous rerouting
Presence of pseudo-phlebitic pattern
Size

venous drainage type, presence of pseudo-phlebitic pattern, etc.) and (b) the radio-surgical outcome, in terms of obliteration, 3 years after the treatment.

In regard to the angioarchitectural parameters, FD was strongly associated with volume and size of the nidus, and significant associations were also found with several other indices (Table 18.1). These results suggested that FD is able to quantify in a single and objective value what neuroradiologists otherwise describe in qualitative and/or semiquantitative way, confirming FD as a reliable morphometric neuroimaging biomarker of AVMs. Higher FD values may signify that the AVM has more tortuous and compact vessels within the nidus, for example, with a higher grade of roughness.

Regarding the outcome, only few morphometric parameters were significantly associated with it, including the presence of sprouting angiogenesis, moderate-to-high flow pattern, and the presence of a venous pouch. Size and venous drainage were both strongly related to outcome, signifying that bigger AVMs (>3 cm of diameter) and/or with deep venous drainage are more related to incomplete obliteration, with a lower chance to be completely cured by means of GK radiosurgery alone. Although no statistical significance was found, interestingly enough the

AVMs with higher FD values had a lower chance of complete obliteration at the follow-up (i.e., lower response to GK) (Fig. 18.7). Every increase in FD value by 0.1 was associated to a 1.21 increase of odds to get an incomplete obliteration. This inverse relationship between FD and AVM obliteration should be further investigated, but at least it would suggest that the fractal analysis may add some parameters to the morphometric of AVMs to predict whether a patient will respond or not to radiosurgery alone and whether he/she will require alternative treatment or a combination of therapeutic modalities (e.g., embolization and/or surgery for “pruning” the nidus, followed by radiosurgery to obliterate the remaining fistulous vessels). The potential of FD as clinical surrogate biomarker for prognosis should be further investigated in larger prospective studies.

Moreover the technique could be extended to other neuroimaging modalities (e.g., DSAs), as well as to the same sequence imaged over time, in order to make a longitudinal analysis of FD during the patients’ follow-up. The longitudinal analysis could offer some indices for prognostication too. For example, in a case in which an AVM is radiologically followed over time (e.g., every 6 months), if the FD values remain constant, it may signify that the patient most likely is a nonresponder to

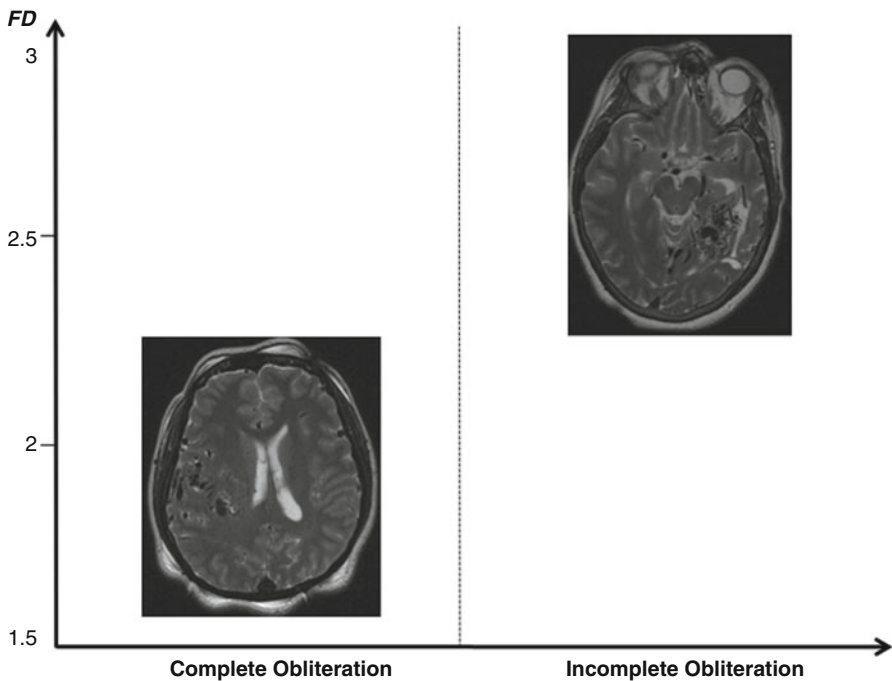


Fig. 18.7 Relating between AVMs’ angioarchitecture (quantified by means of FD) and radiosurgical outcome: the nidus with lower geometrical complexity (lower computed fractal dimension, on the *left*) might have higher chance to be completely obliterated after Gamma Knife radiosurgery treatment, while an incomplete obliteration could occur in a more geometrical complex nidus (higher FD, on the *right*) (From Di Ieva et al. [8], reprinted with Permission of the Publisher)

radiosurgery and may require further treatment (e.g., multimodal treatment with endovascular embolization and/or microneurosurgery). More studies are warranted to validate such computational methods for the assessment of the AVM angioarchitecture in relation to the outcome.

18.5 Limitations

As it may occur in several other neuroimaging analyses, the major limitation of the application of fractal analysis to AVMs' morphometrics is related to the image analysis itself, i.e., to the choice of the ROI (the edges of the nidus). This procedure is in fact generally performed on a consensus of experts, who may introduce some intra- and interobserver variability; moreover, it is time-consuming too. The imaging parameters, as well as the fractal analysis ones, have to be standardized in order to obtain a homogeneous dataset to be analyzed and a homogeneous series of output data, which can correctly be related to some clinical information.

Several techniques are under investigation for the automatic extraction of the ROI as well as for the standardization of the methods of segmentation of the intracranial vessels, as summarized in the following paragraph.

18.6 Computational Techniques for the Automatic Nidus Identification

Several computational techniques are under investigation for the automatic extraction of the nidus' edge from the neuroradiological images. The pixel profiling technique is one of the most promising methods to classify and automatically extract the nidus' edges, by means of a computerized analysis of the pixel intensity distribution inhomogeneity [5]. Threshold-based segmentation of the AVM's vascular tree or voxel-wise support vector machine (SVM) and fuzzy logic have been proposed also as a novel and promising means for fast image extraction of the nidus and therapy planning [4, 14, 15].

Computational fractal-based methods have been investigated as well for the computer-aided identification of the nidus [8]. Lahmiri et al. recently computed FD of cerebral hemispheres via the scaling exponent of detrended fluctuation analysis (DFA), using it in an SVM to differentiate the nonpathologic cerebral hemisphere from the one affected by an AVM, obtaining a perfect classification accuracy [18] (see also Chap. 19). A further method for the automatic detection of AVMs in MR images was developed by computing several fractal-based parameters (including the Hurst exponent) into a supervised machine-learning algorithm, resulting in a computational method for the ROI detection as well as a further conformation of the fractal properties and scale-invariant structure of the AVMs (see methods in [18]). Moreover, assuming that the different pixel distribution within the nidus in MR

imaging may affect the variance (or clustering volatility) of the general pixel distribution in images of normal brains, the generalized autoregressive conditional heteroskedasticity (GARCH) technique, initially proposed for clustering financial time series data [6], was applied for quantifying such differences [8]. The GARCH technique was demonstrated to be potentially helpful in automatically detecting or characterizing the AVMs' nidus.

These computational methods seem to be promising for the automatic segmentation and features extraction of the AVMs, but should be tested on different images (different MRI sequences as well other modalities, including CTAs and DSAs) and on larger patients' series.

18.7 Conclusion

Fractal analysis is a novel approach to quantify the vascular complexity of the arteriovenous malformations. Higher FD values are related to AVMs characterized by an increased number and tortuosity of the intranidal vessels, or to an increasing angioarchitectural complexity as a whole, confirming FD as a reliable computational morphometric neuroimaging biomarker. Moreover FD might be a potential surrogate biomarker for treatment response as well, relevant for prognostication. Fractal analysis can add some parameters, which could be added into a multiparametric morphometric analysis of the angioarchitecture of the nidus itself in relation to some relevant clinical information. The use of lacunarity should be also investigated as angiostructural morphometric parameter. Further studies are required to extend the application of fractal analysis for the study of AVMs.

References

1. Al-Shahi R, Warlow C. A systematic review of the frequency and prognosis of arteriovenous malformations of the brain in adults. *Brain*. 2001;124:1900–26.
2. Andrade-Souza YM, Zadeh G, Ramani M, Scora D, Tsao MN, Schwartz ML. Testing the radiosurgery-based arteriovenous malformation score and the modified spetzler-martin grading system to predict radiosurgical outcome. *J Neurosurg*. 2005;103:642–8.
3. Aoki Y, Nakagawa K, Tago M, Terahara A, Kurita H, Sasaki Y. Clinical evaluation of gamma knife radiosurgery for intracranial arteriovenous malformation. *Radiat Med*. 1996;14:265–8.
4. Babin D, Spyranis M, Pizurica A, Philips W. Pixel profiling for extraction of arteriovenous malformation in 3-D CTA images. *Conf Proc IEEE Eng Med Biol Soc*. 2013;2013:5449–52.
5. Babin D, Pizurica A, Bellens R, De Bock J, Shang Y, Goossens B, et al. Generalized pixel profiling and comparative segmentation with application to arteriovenous malformation segmentation. *Med Image Anal*. 2012;16:991–1002.
6. Bollerslev T. Generalized autoregressive conditional heteroskedasticity. *J Econ*. 1986;31:307–27.
7. Di Ieva A, Esteban FJ, Grizzi F, Klonowski W, Martin-Landrove M. Fractals in the neurosciences, part II: clinical applications and future perspectives. *Neuroscientist*. 2015;21:30–43.
8. Di Ieva A, Boukadoum M, Lahmiri S, Cusimano MD. Computational analyses of arteriovenous malformations in neuroimaging. *J Neuroimaging*. 2014;25:354–60.

9. Di Ieva A, Niamah M, Menezes RJ, Tsao M, Krings T, Cho YB, et al. Computational fractal-based analysis of brain arteriovenous malformation angioarchitecture. *Neurosurgery*. 2014;75:72–9.
10. Di Ieva A, Matula C, Grizzi F, Grabner G, Trattnig S, Tschabitscher M. Fractal analysis of the susceptibility weighted imaging patterns in malignant brain tumors during antiangiogenic treatment: technical report on four cases serially imaged by 7 T magnetic resonance during a period of four weeks. *World Neurosurg*. 2012;77:785.e11–e21.
11. Du R, Keyoung HM, Dowd CF, Young WL, Lawton MT. The effects of diffuseness and deep perforating artery supply on outcomes after microsurgical resection of brain arteriovenous malformations. *Neurosurgery*. 2007;60:638,46; discussion 646–8.
12. Falconer K. *Fractal geometry: mathematical foundations and applications*. New Jersey: Wiley; 2003.
13. Flickinger JC, Pollock BE, Kondziolka D, Lunsford LD. A dose-response analysis of arteriovenous malformation obliteration after radiosurgery. *Int J Radiat Oncol Biol Phys*. 1996;36:873–9.
14. Forkert ND, Illies T, Goebell E, Fiehler J, Saring D, Handels H. Computer-aided nidus segmentation and angiographic characterization of arteriovenous malformations. *Int J Comput Assist Radiol Surg*. 2013;8:775–86.
15. Forkert ND, Schmidt-Richberg A, Fiehler J, Illies T, Moller D, Saring D, et al. 3D cerebrovascular segmentation combining fuzzy vessel enhancement and level-sets with anisotropic energy weights. *Magn Reson Imaging*. 2013;31:262–71.
16. Jenkinson M, Smith S. A global optimisation method for robust affine registration of brain images. *Med Image Anal*. 2001;5:143–56.
17. Kanmani S, Rao CB, Raj B. On the computation of the minkowski dimension using morphological operations. *J Microsc*. 1993;170:81–5.
18. Lahmiri S, Boukadoum M, Di Ieva A. Detrended fluctuation analysis of brain hemisphere magnetic resonance imaging to detect cerebral arteriovenous malformations. *Circuits and Systems (ISCAS), IEEE International Symposium*. 2014;2409–12.
19. Lopes R, Betrouni N. Fractal and multifractal analysis: a review. *Med Image Anal*. 2009;13:634–49.
20. Matsumoto M, Kodama N, Endo Y, Sakuma J, Suzuki K, Sasaki T, et al. Dynamic 3D-CT angiography. *AJNR Am J Neuroradiol*. 2007;28:299–304.
21. McGee KP, Ivanovic V, Felmlee JP, Meyer FB, Pollock BE, Huston 3rd J. MR angiography fusion technique for treatment planning of intracranial arteriovenous malformations. *J Magn Reson Imaging*. 2006;23:361–9.
22. Ondra SL, Troupp H, George ED, Schwab K. The natural history of symptomatic arteriovenous malformations of the brain: a 24-year follow-up assessment. *J Neurosurg*. 1990;73:387–91.
23. Pollock BE, Lunsford LD, Kondziolka D, Maitz A, Flickinger JC. Patient outcomes after stereotactic radiosurgery for “operable” arteriovenous malformations. *Neurosurgery*. 1994;35:1,7; discussion 7–8.
24. Pruess SA. Some remarks on the numerical estimation of fractal dimension. In: Barton CC, La Pointe PR, editors. *Fractals in the earth sciences*. New York: Plenum Press; 1995. p. 10.
25. Reishofer G, Koschutnig K, Enzinger C, Ebner F, Ahammer H. Fractal dimension and vessel complexity in patients with cerebral arteriovenous malformations. *PLoS One*. 2012;7:e41148.
26. Russo C. Brightness progressive normalization. 2012. Webpage: http://www.fractal-lab.org/Downloads/bpn_algorithm.html. Accessed on Feb 2016.
27. Spetzler RF, Ponce FA. A 3-tier classification of cerebral arteriovenous malformations. *Clinical article*. *J Neurosurg*. 2011;114:842–9.
28. Spetzler RF, Martin NA. A proposed grading system for arteriovenous malformations. *J Neurosurg*. 1986;65:476–83.
29. Wu Y, Chang W, Johnson KM, Velikina J, Rowley H, Mistretta C, et al. Fast whole-brain 4D contrast-enhanced MR angiography with velocity encoding using undersampled radial acquisition and highly constrained projection reconstruction: image-quality assessment in volunteer subjects. *AJNR Am J Neuroradiol*. 2011;32:E47–50.

Chapter 19

Fractals in Neuroimaging

Salim Lahmiri, Mounir Boukadoum, and Antonio Di Ieva

Abstract Several natural phenomena can be described by studying their statistical scaling patterns, hence leading to simple geometrical interpretation. In this regard, fractal geometry is a powerful tool to describe the irregular or fragmented shape of natural features, using spatial or time-domain statistical scaling laws (power-law behavior) to characterize real-world physical systems. This chapter presents some recent works on the usefulness of fractal features, mainly the fractal dimension and the related Hurst exponent, in the characterization and identification of pathologies and radiological features in neuroimaging.

Keywords Computed tomography • Detrended fluctuation analysis • Fractal dimension • Hurst exponent • Magnetic resonance imaging • Neuroimaging • Classification • Statistical tests

S. Lahmiri, PhD (✉)

Faculty of Engineering, Centre for Pattern Recognition and Machine Intelligence,
Concordia University, Montreal, QC, Canada
e-mail: salim.lahmiri.1@ens.etsmtl.ca

M. Boukadoum, PhD

Department of Computer Science, University of Quebec at Montreal, Montreal, QC, Canada
e-mail: boukadoum.mounir@uqam.ca

A. Di Ieva, MD, PhD (✉)

Neurosurgery Unit, Faculty of Medicine and Health Sciences, Macquarie University,
Sydney, NSW, Australia

Garvan Institute of Medical Research, Sydney, NSW, Australia

Medical University of Vienna, Vienna, Austria

University of Toronto, Toronto, ON, Canada

e-mail: diieva@hotmail.com

19.1 Introduction

Fractal analysis is becoming an attractive method in biomedical engineering to describe and quantify the morphological complexity in computed tomography (CT) and magnetic resonance imaging (MRI). In recent years, it has been applied in neuroimaging for automatic classification purposes, in the context of medical diagnosis and prognostication [21, 23–26]. Indeed, fractal features such as the fractal dimension have been found to be effective in describing the complex morphology of the cortex and hence suitable to distinguish between different physiopathological states in brain MR imaging [4].

Fractal analysis has been adopted in several studies on brain magnetic resonance image classification, thanks to the ability it provides to evaluate the self-affinity at different scales and the long-range correlations of an image [11, 34] and to use the results for discrimination. Recent works in the field have assumed high self-affinity and long-range correlation in normal brain MRI in comparison to those of some neurological diseases, based on the hypotheses that brain morphology is more regular in healthy subjects and that differences can be detected and quantified by means of fractal analysis [4, 21, 23–26].

This chapter reviews recent works related to the usefulness of fractal analysis to characterize MRI features, especially by means of the fractal dimension (FD) and Hurst exponent (HE) and therefore help detect neurological pathologies through the morphological changes they bring to a normal brain image. The chapter is organized as follows: Sect. 19.2 presents recent works on the classification of brain magnetic resonance images by using fractal metrics as the main features; Sect. 19.3 reviews other works with different application of fractals in neuroimaging. In Sect. 19.4 some conclusions and future perspectives are summarized. A technical description of fractal analyses techniques used in brain magnetic resonance image classification is given in the appendix, including classic range-scale analysis, detrended fluctuation analysis (DFA), and generalized Hurst exponent.

19.2 Fractals in Brain Magnetic Resonance Image Classification

A new MRI classification approach based on fractal geometry and the spectral energy distribution of edges in brain magnetic resonance images was proposed by Lahmiri and Boukadoum [26] to identify patients affected by Alzheimer's disease (AD), brain tumors (e.g., gliomas), brain infections, as well as demyelinating diseases such as multiple sclerosis (MS). Edges represent abrupt changes in image intensity, their distributions in normal and abnormal brain MR images can be different, and thus the authors used morphological properties for distinguishing normal anatomical silhouettes from abnormal ones. The considered features were the fractal dimension of edges after expressing the initial image as an analytic object and

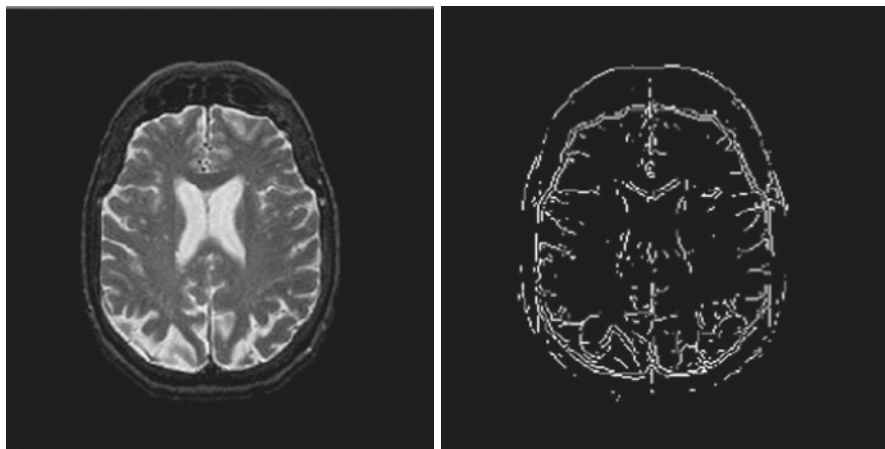


Fig. 19.1 Normal MRI (*left*) and its Sobel-filtered image in Hilbert domain (*right*)

the skewness (used to measure symmetry/asymmetry in the data distribution) and kurtosis (used to measure the degree of tailedness in the data distribution) of its energy distribution at different frequencies. More specifically, the Hilbert transform [14] was applied to the brain MR images in the first step, and the Sobel filter [33] was applied to the Hilbert-transformed image to detect strong edge strength at the brain boundaries affected by pathologies. Figure 19.1 shows an example of a normal MRI and its Sobel-filtered image in Hilbert domain. The extracted edges are analyzed for feature extraction by the box-counting method-based fractal [11, 15] and the Fourier power spectrum [12]. A feature vector was built with the obtained image fractal dimension and the skewness and kurtosis of the spectral energy distribution of the Sobel-processed image. Figure 19.2 provides an example of spectral energy distribution from which skewness and kurtosis were computed. Finally, the feature vector was fed to a backpropagation neural network [13] trained by the scaled conjugate numerical algorithm [13, 29] to perform classification. The proposed fractal dimension and spectral energy (FDSE) distribution system outperformed the popular discrete wavelet transform (DWT) and principal component analysis (PCA)-based means of analysis [19]. Indeed, the approach based on the FD, skewness, and kurtosis of the edge spectrum energy distribution achieved $91.78 \pm 0.0148\%$ correct classification rate of the normal against images in different pathological conditions (e.g., Alzheimer's disease, gliomas and metastases, herpetic infections, and MS as well), while the conventional DWT-PCA-based approach achieved $82.69 \pm 0.0796\%$ correct classification rate.

In a subsequent study, Lahmiri and Boukadoum [25] described a modification of the work in [26] that is suitable for pathologies such as gliomas and brain metastases. The brain MR images were converted to a one-dimensional signal by row concatenation to speed up feature extraction, and the skewness and kurtosis were replaced by additional geometrical features of the image. Detrended fluctuation analysis was adopted as an alternative method to determine the local trends in a

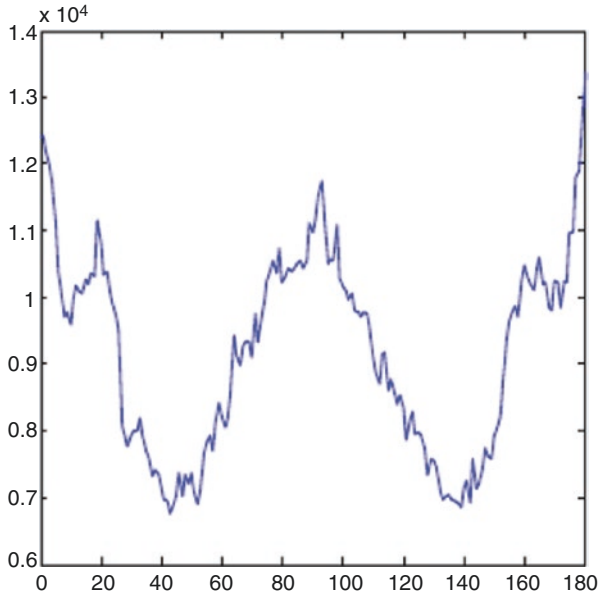


Fig. 19.2 Spectral energy distribution of the normal Sobel-filtered image in Hilbert domain

biological signal and measure its level of persistence. It differs from the box-counting method to evaluate the fractal nature of an image by evaluating its stability in regard to trend removal. This in turn leads to a more robust estimate of the scaling properties in a nonstationary environment. In both cases, the fractal aspect of the processed image is evaluated with the Hurst exponent (see [Appendix](#)). In the new work, the feature vectors were composed of the box counting-based Hurst exponent, the DFA-based Hurst exponent, and the energy of the detrended fluctuations of the derived bio-signal. Figure 19.3 plots in log-log coordinates the relationship between the detrended fluctuation function and the granularity of analysis (number of bins per signal; see Eq. 19.7 in [Appendix](#)) for signals of healthy patients vs. AD ones, where the red curve is the empirical DFA and the blue line is the theoretical DFA for a random walk signal, for which the DFA is a straight line with a 45° slope. The support vector machine (SVM) with quadratic kernel was chosen as the main classifier, and it achieved 100% detection accuracy of normal brain image against glioma and metastatic bronchogenic carcinoma, regardless of whether the processed 1D signal was obtained by concatenating the rows or columns of the MR image.

A potential improvement upon the basic Hurst exponent analysis to characterize the fractal feature of brain magnetic resonance images is multiscale analysis (MSA) [8]. Multiscale analysis uses the generalized Hurst exponent method, which determines the scaling properties of a signal by computing the q th-order moments of the distribution of the signal's increments [8]. MSA can detect many types of signal dependencies with a high computational efficiency. Since each order q allows the estimation of a different Hurst exponent, varying this value allows obtaining the multifractal spectrum of the signal in a straightforward way. Furthermore, by using

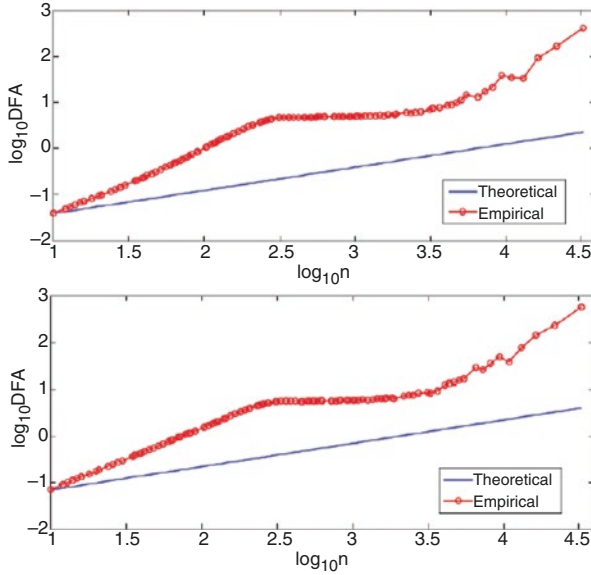


Fig. 19.3 DFA ($F(n,N)$) plot of a normal (*top*) and AD signal (*bottom*) as a function of binning

MSA as an alternative for the box counting-based Hurst exponent and DFA-based exponent estimation, the feature extraction time is reduced considerably. In [25], MSA was investigated for the classification of normal against AD images. Figures 19.4 and 19.5 plots in log-log coordinates the obtained relationship between the generalized Hurst exponent $H(q)$ and the time scale of analysis for different orders q (see Eq. 19.9 in Appendix) of normal brain images versus patients affected by Alzheimer's disease. The extracted fractals were used as features to differentiate healthy brain MRI from those of AD by SVM classifier. The results indicated a $99.18 \pm 0.01\%$ classification accuracy, 100% sensitivity, and $98.20 \pm 0.02\%$ specificity. These results showed the potential of using multiscale fractal analysis to differentiate healthy brain images from ones affected by Alzheimer's disease in near real time as the MSA algorithm took only 5.64 s to analyze a brain MRI.

In a further work, Lahmiri and Boukadoum [22] extended the work in [25] to a multi-classification problem. They explored the effectiveness of classifying brain images of healthy subjects against those with AD or mild cognitive impairment (MCI) by using support vector machines. Three experiments were conducted: in the first one, the SVM was trained to classify AD against normal images. In the second experiment, the SVM was trained to classify AD against MCI, and, in the third experiment, a multiclass SVM was trained to simultaneously classify all three types of images. In order to statistically evaluate the discriminative power of the Hurst exponent, two statistical tests were performed. The first one tested the null hypothesis of equal means for the HE values of healthy MCI and AD data based on the F-statistic of an analysis of variance (ANOVA) test. The second test checked the null hypothesis of equal distribution variances based on the Brown-Forsythe statistic. The results from these statistical tests indicated rejection of the two hypotheses

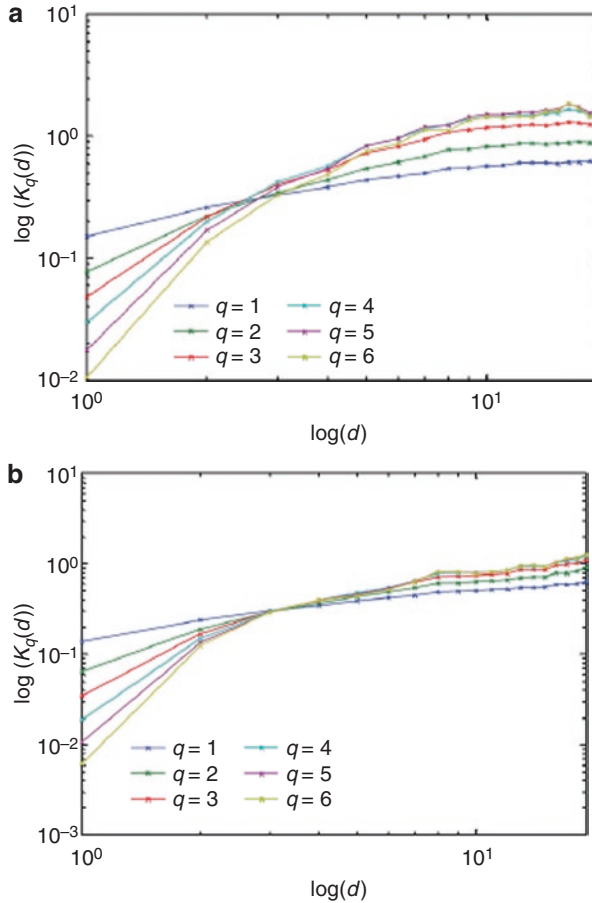


Fig. 19.4 Multiscale analysis results on log-log scale of healthy image (a) and AD (b)

at the 5 % level of significance for all scales of analysis (the obtained p-values were all <0.05). Therefore, it was concluded that the distributions of HEs between images of normal brain and images of patients affected by MCI and AD are statistically different. Thus, these fractal measures are potentially discriminative to distinguish normal MCI and AD images. Indeed, the classification results indicated that the SVM achieved $97.08 \pm 0.05\%$ correct classification rate, $98.09 \pm 0.04\%$ sensitivity, and $96.07 \pm 0.07\%$ specificity for the classification of healthy against MCI images, thus outperforming recent works found in the literature. For the classification of MCI against AD, the SVM achieved $97.5 \pm 0.04\%$ correct classification rate, 100% sensitivity, and $94.93 \pm 0.08\%$ specificity. The third experiment also showed that the multiclass SVM provided highly accurate classification results. The processing time for a given image was 25 s. From these findings, the authors concluded that this approach is efficient and may be promising for clinical applications.

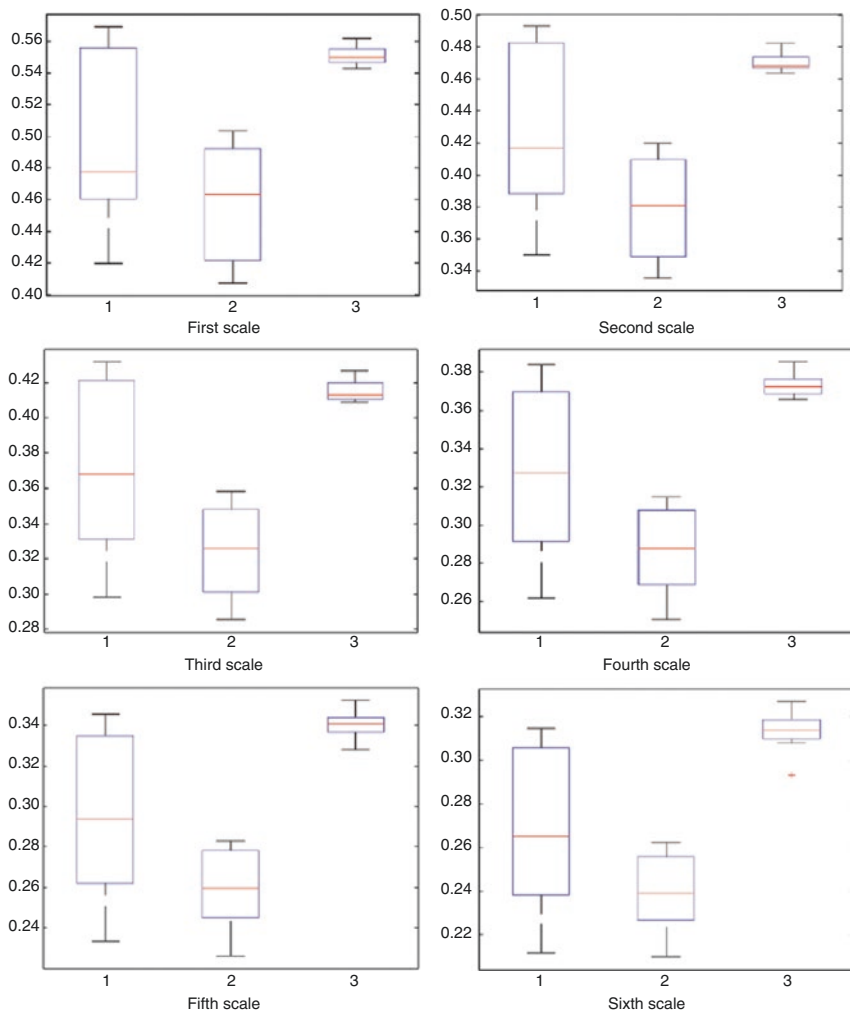


Fig. 19.5 Multiscale analysis-based boxplots in brain imaging of patients affected by MCI (1), AD (2), vs. images of disease-free brains (3)

19.3 Other Applications of Fractal Analysis in Neuroimaging

In the context of brain tumor detection, the fractal dimension was found to be effective in distinguishing between tumor and nontumor regions in various imaging modalities. For instance, Zook and Iftekharuddin [36] used the analysis of variance (ANOVA) to test whether fractal dimension statistics in healthy subjects are significantly different from those affected by brain tumors. They found that FD might be exploited successfully to determine the possible presence and location of brain

tumors in MR and CT images. Wardlaw et al. [35] quantified the blood oxygen level-dependent (BOLD) signals' temporal complexity using the fractal dimension with the purpose to allow maps to be generated that are physiologically distinctive in nature and allow potential insight into tumor microvasculature. In other words, they used fractal dimension mapping to identify physiological regions that are dominated by low-frequency vascular components or by high-frequency components. They concluded that low fractal dimension regions are significant as they highlight probable regions of regularized tumor metabolism and microvascular patterns. Iftekharuddin et al. [16] investigated the effectiveness of fusing two texture features along with intensity in multimodal magnetic resonance images for pediatric brain tumor segmentation and classification. The two texture features were obtained with the piecewise-triangular-prism-surface-area (PTPSA) algorithm for fractal feature extraction and the fractional Brownian motion (fBm) framework, which combines both fractal and wavelet analyses, for fractal wavelet feature extraction. The ensuing tests were applied to MRI T1, T2, and fluid-attenuated inversion recovery (FLAIR) sequences, and the obtained experimental results showed that the fusion of fractal, fractal wavelet, and intensity features in multimodality MR images offers better tumor segmentation results when compared to that of just fractal and intensity features in single modality MR images. Indeed, the segmentation accuracy was 100%. In addition, the classification results obtained with a multilayer feedforward neural network with automated Bayesian regularization to classify the tumor regions from nontumor regions indicated that the true-positive fraction (TPF) values range from 75 to 100% for different patients, with the average value of 90%. Di Ieva et al. used fractal analysis to characterize MR susceptibility-weighted images and to differentiate types and grades of brain tumors [3, 6] (see Chap. 20).

Other studies [6, 7] have also focused on the role of fractal dimension in the characterization of brain images. In a recent work, Akar et al. [1] estimated the fractal dimension of the cerebellum in order to characterize Chiari malformation type I (CM-I). They calculated the areas of white matter (WM) and gray matter (GM) and computed the corresponding fractal dimension values by using the 2D box-counting method in healthy and CM-I patients' magnetic resonance images. The obtained results indicated that CM-I patients had significantly higher fractal dimension values of GM and WM tissues compared to healthy patients. In addition, they found that the fractal dimension and area values of GM tissues in the patients group were correlated. They concluded that the fractal dimension values of the cerebellum may be a useful marker for investigation of CM-I patients. Sandu et al. [32] used fractal dimension values to reveal brain structure irregularities in patients with schizophrenia as they allow quantifying the shape complexity of cortical folding of the human brain. They segmented magnetic resonance images and the calculated fractal dimension values for the gray/white matter boundary for the whole brain and the hemispheres separately by using the box-counting and Minkowski-Bouligand methods. The authors found that the patients affected by schizophrenia showed higher FD values than the healthy group, for the whole brain volume and right hemi-

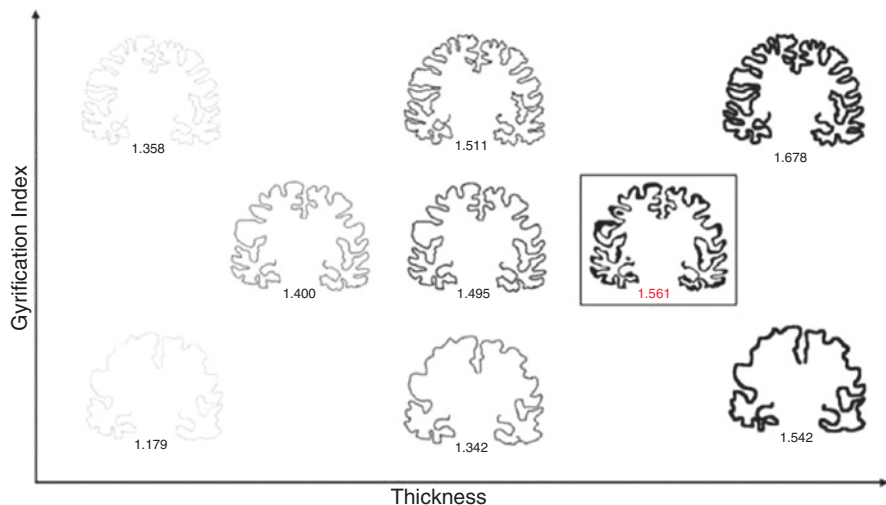


Fig. 19.6 Changes in cortical thickness (*horizontal axis*) and gyrification index (*vertical axis*) of the brain (coronal slice from a control healthy subject seen in the box) affect the fractal dimension (indicated by the number below the slice) of the cortical ribbons (Reprinted from King et al. [37], with permission from Springer)

sphere. King et al. [20] computed the fractal dimension of the cortical ribbon to distinguish between normal controls and mild Alzheimer's disease patients using a custom cube-counting triangle-intersection algorithm (Fig. 19.6). They found that the fractal dimension of the cortical ribbon showed statistically high differences between the control and Alzheimer's disease subjects. It was concluded that the fractal dimension of the cerebral cortical ribbon is a useful quantitative marker of cerebral cortex structure in mild Alzheimer's disease.

The fractal analysis has been shown also to be more accurate than other methods for the detection of changes in the brain white matter in diseases such as multiple sclerosis and amyotrophic lateral sclerosis (ALS) [9, 10, 31]. Esteban et al. [9, 10] investigated whether fractal dimension estimates of gray matter in T1 magnetic resonance imaging sequences can identify gray matter abnormalities in patients with multiple sclerosis in the early phase of the disease. First, the image was segmented by a voxel-based morphometric approach optimized for multiple sclerosis. Then, they estimated the three-dimensional FD of the gray matter in multiple sclerosis patients and healthy controls. They found that patients with multiple sclerosis had a significant increase in the fractal dimension of the gray matter in comparison to the images of the healthy group. Figure 19.7 shows examples of white matter skeleton images in healthy subjects vs. some pathological conditions.

The FD measures were also used in various other neuroimaging applications. Jayasuriya et al. [17] used FD estimates of the textures present on MR images to

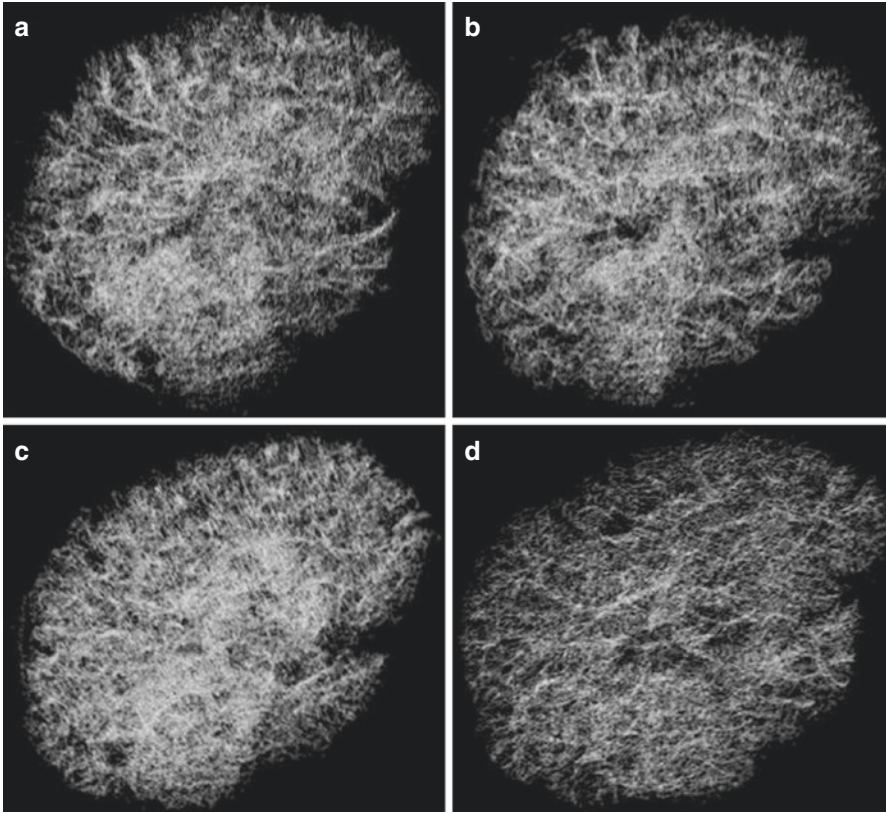


Fig. 19.7 3D rendering of white matter skeleton image in a typical (a) control subject, (b) amyotrophic lateral sclerosis (ALS) patient with dementia, (c) ALS patient with corticospinal tract hyperintensity, and (d) ALS patient without corticospinal tract hyperintensity. The FD has been shown to be more sensitive than volumetric voxel-based morphometry in detecting changes of white matter (Reprinted from Rajagopalan et al. [31], with permission from the Publisher)

detect the midsagittal plane (MSP) of the brain. They found that fractal dimension measures are robust in identifying this symmetry plane in three-dimensional brain magnetic resonance images. In addition, they were found to be robust with respect to strong noise and low resolution. An optimized vascular fractal tree models using the level set distance function was developed in [2] to construct a region of human cerebral vasculature, which is enclosed in a realistic brain envelope. The optimized vascular fractal tree model was found to be successful in producing a geometrically optimized model of the cerebral vasculature with the preferential distribution of large arteries on the brain cortex. Computational fractal-based models have also been applied for the characterization of water molecule diffusion in vivo on diffusion tensor MR imaging [18].

A comprehensive survey on fractals in neuroimaging can be found in [4], as well as in Chaps. 13, 14, 18, 20, and 21.

19.4 Conclusion and Future Perspective

The efficacy of fractal-based features for the classification of brain magnetic resonance images is demonstrated through many recent studies in this area of biomedical engineering. Range-scale analysis, detrended fluctuation analysis, and multiscale analysis based on the generalized Hurst exponent were adopted to estimate fractal features; artificial neural networks and support vector machines were employed to perform classification. The performance of fractal-based features was compared to conventional methods. The results so far show the effectiveness of fractal features in classification of healthy against unhealthy images both in binary and multi-classification schemes.

For future works, several directions have been proposed in the literature. For instance, previous works [21, 23, 24] can be extended by focusing on the appropriate selection of scale-based features and applying the fractal-based features to other brain imaging modalities such as functional magnetic resonance imaging, CT, and positron-emission tomography (PET). Zook and Iftekharuddin [36] suggested including examining the effects of tumor type and size as well as the effect of noise in fractal dimension analysis. Wardlaw et al. [35] recommended to effectively filter the cardiac and respiratory frequencies from the BOLD signal prior to generating fractal dimension maps so as to improve identification of regions of active metabolism. Iftekharuddin et al. [16] suggested to direct future works to discriminate multiple types of brain tissues such as the white matter, gray matter, cerebrospinal fluid, and skull from solid tumor and edema. Akar et al. [1] recommended comparing the effectiveness of fractal dimension measures in detecting Chiari malformation type I anomaly with other disorders such as MS, fibromyalgia, migraine, spinal cord tumors, and Chiari Malformation type II. Jayasuriya et al. [17] suggested using the location of midsagittal plane for asymmetry analysis of pathological brains. The use of fractal analysis in aneurysms and arteriovenous malformations, aimed at identifying new diagnostic and prognostic neuroimaging biomarkers of cerebrovascular diseases [5], are discussed in Chaps. 17 and 18, respectively.

In the connectomic era, new insights will be offered by the application of computational fractal-based analyses into the studies of diffusion tensor imaging. Moreover, the application of fractal analysis to nuclear medicine tools (single-photon emission computed tomography (SPECT) and positron-emission tomography (PET)) may offer new biomarkers useful in the clinical setting [28].

As can be seen from these potential perspectives, the field is still open for discovery and improvement.

Appendix: Fractal Analysis Techniques

In this appendix, we summarize fractal analyses techniques used in recent studies related to brain magnetic resonance image classification, including classic range-scale analysis, detrended fluctuation analysis, and generalized Hurst exponent.

Range-Scale-Based Hurst Exponent

The Hurst exponent H [15] characterizes the scaling behavior of the range of cumulative deviations of a given signal y from its mean. The evaluation of Hurst exponent H following methodology of Mandelbrot and Wallis [27] and called range-scale (R/S) analysis uses the range of the partial sums of deviations of the signal y from its mean, rescaled by its standard deviation. The R/S statistic is given by:

$$(R/S)_n = \frac{1}{\sigma_n} \left[\max_{1 \leq k \leq n} \sum_{j=1}^k (y_j - \bar{y}_n) - \min_{1 \leq k \leq n} \sum_{j=1}^k (y_k - \bar{y}_n) \right] \quad (19.1)$$

Where n is the length of the signal, \bar{y} is its mean and σ is its standard deviation given by:

$$\sigma_n = \left[\frac{1}{n} \sum_{j=1}^n (y_j - \bar{y}_n)^2 \right]^{1/2} \quad (19.2)$$

Hurst [15] found that many natural signals can be empirically described by the following relation:

$$(R/S)_n = (n/2)^H \quad (19.3)$$

The exponent H is estimated for the whole signal length n . Mandelbrot and Wallis [27] incorporated the ordinary least square regression to estimate it:

$$\log[(R/S)_n] = \alpha + H \log(n) + \varepsilon \quad (19.4)$$

where $\log(\cdot)$ is the logarithmic operator, α is the constant term of the regression, and ε is the error term.

There exists a simple relationship between Hurst exponent and the fractal dimension D of the original signal. For instance, if the signal is self-similar and self-affine, the relationship is $D=2-H$ [11] Thus, Hurst exponent also measures the global fractal dimension or roughness of a one-dimensional signal.

Detrended Fluctuation Analysis

Peng et al. [30] developed the detrended fluctuation analysis (DFA) to appropriately handle nonstationary data. Its main advantage is avoiding the spurious detection of long-range dependence due to nonstationary data. For a given signal y , the algorithm is described as follows:

- (a) Define the suite x_n of the cumulative series of original signal y_i fluctuations about its mean:

$$x_n = \sum_{i=1}^n (y_i - \bar{y}) \quad (19.5)$$

- (b) Divide x_n divided into boxes of equal length τ .
 (c) In each box, fit the local trend of x_n by a polynomial $P(\tau, n)$ that represents the local trend of the box.
 (d) For the given τ box size, compute the root-mean-squared detrended fluctuation of the signal x_n as:

$$F(\tau, n) = \sqrt{\frac{1}{n} \sum_{i=1}^n (x_i - P(\tau, n))^2} \quad (19.6)$$

The last step is repeated for each of the available τ scales (box size) to obtain the empirical relationship between the overall fluctuation $F(\tau, n)$ and the box size τ :

$$F(\tau, n) \propto \tau^\alpha \quad (19.7)$$

The scaling exponent α quantifies the empirical strength of the long-range power-law correlations of the signal. If the signal is not random, it is characterized by long-range correlation features.

Generalized Hurst Exponent

Consider a signal $s(t)$ defined at discrete time intervals $t = \nu, 2\nu - T$ over a period T that is an integer multiple of ν . Then, the q th-order moments of the distribution that characterize the statistical evolution of $s(t)$ is defined as follows [8]:

$$K_q(d) = \frac{\langle \|s(t+d) - s(t)\|^q \rangle}{\langle |s(t)|^q \rangle} \quad (19.8)$$

where $d \in [\nu, d_{max}]$ is a time interval and d_{max} is its predetermined upper limit. The generalized Hurst exponent $H(q)$ is defined from the scaling behavior of $K_q(d)$ according to the following empirical relation [8]:

$$K_q(d) \propto \left(\frac{d}{\nu} \right)^{qH(q)} \quad (19.9)$$

If $Kq(d)$ and d satisfy a linear relationship in log-log scale for a given order q , the Hurst exponent $H(q)$ can be estimated by running a linear regression of $\log(Kq(d))$ versus $\log(d)$. The generalized Hurst exponent $H(q)$ describes the long-memory dependence or persistence in the signal $s(t)$. The multiscaling structure of signal $s(t)$ is related to the different orders q of $H(q)$.

In general, when $H(q) > 0.5$, the signal fluctuations related to order q are persistent. When $H(q) < 0.5$, the signal fluctuations related to order q are anti-persistent. Finally, the signal fluctuations are those of a random walk if $H(q) = 0.5$ [8]. Notice that $H(q=2)$ corresponds to the classic Hurst exponent.

In order to determine Hurst exponent, the original MRI is transformed first into a one-dimensional signal by row concatenation [21, 22, 25, 26]. Then, classic range-scale analysis, detrended fluctuation analysis, and generalized Hurst exponent are applied to the obtained one-dimensional signal.

References

1. Akar E, Kara S, Akdemir H, Kiris A. Fractal dimension analysis of cerebellum in chiari malformation type I. *Comput Biol Med.* 2015;64:179–86.
2. Bui AV, Manasseh R, Liffman K, Sitalo ID. Development of optimized vascular fractal tree models using level set distance function. *Med Eng Phys.* 2010;32:790–4.
3. Di Ieva A, Le Reste PJ, Carsin-Nicol B, Ferre JC, Cusimano MD. Diagnostic value of fractal analysis for the differentiation of brain tumors using 3-tesla MR susceptibility-weighted imaging. *Neurosurgery.* 2016.
4. Di Ieva A, Esteban FJ, Grizzi F, Klonowski W, Martin-Landrove M. Fractals in the neurosciences, part II: clinical applications and future perspectives. *Neuroscientist.* 2015;21:30–43.
5. Di Ieva A, Boukadoum M, Lahmiri S, Cusimano MD. Computational analyses of arteriovenous malformations in neuroimaging. *J Neuroimaging.* 2014;25:354–60.
6. Di Ieva A, God S, Grabner G, Grizzi F, Sherif C, Matula C, et al. Three-dimensional susceptibility-weighted imaging at 7 T using fractal-based quantitative analysis to grade gliomas. *Neuroradiology.* 2013;55:35–40.
7. Di Ieva A, Matula C, Grizzi F, Grabner G, Trattnig S, Tschabitscher M. Fractal analysis of the susceptibility weighted imaging patterns in malignant brain tumors during antiangiogenic treatment: technical report on four cases serially imaged by 7 T magnetic resonance during a period of four weeks. *World Neurosurg.* 2012;77:785.e11–21.
8. Di Matteo T. Multi-scaling in finance. *Quant Finan.* 2007;7:36.
9. Esteban FJ, Sepulcre J, de Miras JR, Navas J, de Mendizabal NV, Goni J, et al. Fractal dimension analysis of grey matter in multiple sclerosis. *J Neurol Sci.* 2009;282:67–71.
10. Esteban FJ, Sepulcre J, de Mendizabal NV, Goni J, Navas J, de Miras JR, et al. Fractal dimension and white matter changes in multiple sclerosis. *Neuroimage.* 2007;36:543–9.
11. Feder J. *Fractals.* plenum press. New York: Plenum Press; 1988.
12. Gonzalez RC, Woods RE. *Digital image processing.* 3rd ed. Pearson, Prentice Hall, New Jersey, USA; 2009.
13. Haykin S. *Neural networks and learning machines.* 3rd ed. Pearson, Prentice Hall, New Jersey, USA; 2008.
14. Huang NE, Shen Z, Long SR. A new view of water waves – the Hilbert spectrum. *Annu Rev Fluid Mech.* 1999;31:417–57.
15. Hurst HE. Long-term storage capacity of reservoirs. *Trans Am Soc Civ Eng.* 1951;116:770–808.

16. Iftekharruddin KM, Zheng J, Islam MA, Ogg RJ. Fractal-based brain tumor detection in multi-modal MRI. *Appl Math Comput.* 2009;207:23–41.
17. Jayasuriya SA, Liew AW, Law NF. Brain symmetry plane detection based on fractal analysis. *Comput Med Imaging Graph.* 2013;37:568–80.
18. Jian B, Vemuri BC, Ozarslan E, Carney PR, Mareci TH. A novel tensor distribution model for the diffusion-weighted MR signal. *Neuroimage.* 2007;37:164–76.
19. Jolliffe IT. *Principal component analysis.* 2nd ed. New York: Springer-Verlag, New York; 2002.
20. King RD, Brown B, Hwang M, Jeon T, George AT. Alzheimer's disease neuroimaging initiative. Fractal dimension analysis of the cortical ribbon in mild alzheimer's disease. *Neuroimage.* 2010;53:471–9.
21. Lahmiri S, Boukadoum M. Automatic brain MR images diagnosis based on edge fractal dimension and spectral signature. *IEEE EMBC.* 2012;2012:6243–6.
22. Lahmiri S, Boukadoum M. New approach for automatic classification of alzheimer's disease, mild cognitive impairment and healthy brain magnetic resonance images. *IET Healthc Technol Lett.* 2014;1:32–6.
23. Lahmiri S, Boukadoum M, Di Ieva A. Detrended fluctuation analysis of brain hemisphere magnetic resonance imaging to detect cerebral arteriovenous malformations. *Circuits and Systems (ISCAS), IEEE International Symposium 2014.* pp. 2409–12.
24. Lahmiri S, Boukadoum M. Automatic detection of alzheimer disease in brain magnetic resonance images using fractal features. *IEEE EMBC Neural Eng.* 2013;1508:1508.
25. Lahmiri S, Boukadoum M. Alzheimer's disease detection in brain magnetic resonance images using multiscale fractal analysis. *ISRN Radiol.* 2013;2013:627303.
26. Lahmiri S, Boukadoum M. Automatic brain MR images diagnosis based on edge fractal dimension and spectral energy signature. *Conf Proc IEEE Eng Med Biol Soc.* 2012;2012:6243–6.
27. Mandelbrot BB, Wallis JR. Noah, Joseph, and operational hydrology. *Water Resour Res.* 1968;4:909–18.
28. Michalleg F, Dewey M. Fractal analysis in radiological and nuclear medicine perfusion imaging: a systematic review. *Eur Radiol.* 2014;24:60–9.
29. Möller MF. A scaled conjugate gradient algorithm for fast supervised learning. *Neural Netw.* 1993;6:525–33.
30. Peng CK, Buldyrev SV, Havlin S, Simons M, Stanley HE, Goldberger AL. Mosaic organization of DNA nucleotides. *Phys Rev E Stat Phys Plasmas Fluids Relat Interdiscip Topics.* 1994;49:1685–9.
31. Rajagopalan V, Liu Z, Allexandre D, Zhang L, Wang XF, Pioro EP, et al. Brain white matter shape changes in amyotrophic lateral sclerosis (ALS): a fractal dimension study. *PLoS One.* 2013;8:e73614.
32. Sandu AL, Rasmussen Jr IA, Lundervold A, Kreuder F, Neckelmann G, Hugdahl K, et al. Fractal dimension analysis of MR images reveals grey matter structure irregularities in schizophrenia. *Comput Med Imaging Graph.* 2008;32:150–8.
33. Sonka M. *Image processing analysis and computing vision.* London: Brooks/Cole; 2001.
34. Stanley HE, Amaral LAN, Goldberger AL, Havlin S, Ivanov PC, Peng CK. Statistical physics and physiology: monofractal and multifractal approaches. *Physica A.* 1999;270:309–24.
35. Wardlaw G, Wong R, Noseworthy MD. Identification of intratumour low frequency microvascular components via BOLD signal fractal dimension mapping. *Phys Med.* 2008;24:87–91.
36. Zook JM, Iftekharruddin KM. Statistical analysis of fractal-based brain tumor detection algorithms. *Magn Reson Imaging.* 2005;23:671–8.
37. King et al. Characterization of atrophic changes in the cerebral cortex using fractal dimensional analysis. *Brain Imaging Behav.* 2009;3(2):154–66.

Chapter 20

Computational Fractal-Based Analysis of MR Susceptibility-Weighted Imaging (SWI) in Neuro-oncology and Neurotraumatology

Antonio Di Ieva

Abstract Susceptibility-weighted imaging (SWI) is a magnetic resonance imaging (MRI) technique able to depict the magnetic susceptibility produced by different substances, such as deoxyhemoglobin, calcium, and iron. The main application of SWI in clinical neuroimaging is detecting microbleedings and venous vasculature. Quantitative analyses of SWI have been developed over the last few years, aimed to offer new parameters, which could be used as neuroimaging biomarkers. Each technique has shown pros and cons, but no gold standard exists yet. The fractal dimension (FD) has been investigated as a novel potential objective parameter for monitoring intratumoral space-filling properties of SWI patterns. We showed that SWI patterns found in different tumors or different glioma grades can be represented by a gradient in the fractal dimension, thereby enabling each tumor to be assigned a specific SWI fingerprint. Such results were especially relevant in the differentiation of low-grade versus high-grade gliomas, as well as from malignant gliomas versus lymphomas.

Therefore FD has been suggested as a potential image biomarker to analyze intrinsic neoplastic architecture in order to improve the differential diagnosis within clinical neuroimaging, determine appropriate therapy, and improve outcome in patients.

These promising preliminary findings could be extended into the field of neurotraumatology, by means of the application of computational fractal-based analyses for the qualitative and quantitative imaging of microbleedings in traumatic brain injury patients. In consideration of some evidences showing that SWI signals are correlated with trauma clinical severity, FD might offer some objective prognostic biomarkers.

A. Di Ieva, MD, PhD
Neurosurgery Unit, Faculty of Medicine and Health Sciences, Macquarie University,
Sydney, NSW, Australia

Garvan Institute of Medical Research, Sydney, NSW, Australia

Medical University of Vienna, Vienna, Austria

University of Toronto, Toronto, ON, Canada

e-mail: diieva@hotmail.com

In conclusion, fractal-based morphometrics of SWI could be further investigated to be used in a complementary way with other techniques, in order to form a holistic understanding of the temporal evolution of brain tumors and follow-up response to treatment, with several further applications in other fields, such as neurotraumatology and cerebrovascular neurosurgery as well.

Keywords Brain tumors • Fractal dimension • SWI • Susceptibility-weighted imaging • Traumatic brain injury

20.1 Introduction

Susceptibility-weighted imaging (SWI) is a magnetic resonance imaging (MRI) technique, introduced in the mid-1990s [31, 33]. SWI is able to depict the magnetic susceptibility produced by different substances, such as deoxyhemoglobin, calcium, and iron, with a high sensitivity, relative to other MRI sequences. SWI is mainly used to show vasculature (e.g., intratumoral microvasculature in brain tumors) and microhemorrhages, offering a valid tool to investigate several neurological diseases (e.g., multiple sclerosis) along with neurotrauma in traumatic brain injury (TBI) patients and grade tumors, and assist in determining treatment or prognosis. Several applications have been reviewed in the different fields of clinical neurosciences, namely, neurology, neuro-oncology, cerebrovascular diseases, neurotraumatology, and functional neurosurgery (see [17]), summarized in Table 20.1.

Table 20.1 Synopsis of the applications of SWI in different fields of clinical neurosciences [17]

Applications of SWI in the clinical neurosciences	
Neurology	Multiple sclerosis, amyotrophic lateral sclerosis
	Iron deposits
	Brain calcifications
	Stroke
Neuro-oncology	Brain tumor architecture, vasculature, bleedings, necrosis
	Brain tumor differential diagnosis (grading and histotypes)
	Differential diagnosis between brain abscess and tumor
	Brain tumor follow-up and/or response to treatment
Cerebrovascular	Thrombosis detection
	Stroke
	Vascular malformations
Neurotraumatology	Hemorrhage/microhemorrhage detection in TBI
	Dichotomize hemorrhagic from nonhemorrhagic diffuse axonal injury (DAI)
Functional neurosurgery	Anatomical localization of veins and deep gray nuclei for targeting in deep brain stimulation and Gamma Knife Radiosurgery

20.2 Technical Aspects of SW Imaging

The signal intensity on the MR image is determined by three basic parameters: (1) proton density (PD), (2) T1 relaxation time, and (3) T2 relaxation time. The T1 (longitudinal) and T2 (transverse) relaxation times define the way protons revert back to their resting states after the initial radio-frequency (RF) pulse. The transverse magnetization starts decreasing in magnitude immediately as protons start going out of phase. This process of dephasing and reduction in the amount of transverse magnetization is called transverse relaxation. Spin-spin relaxation (T2) and local field inhomogeneities (T2*) are the two mechanisms leading to dephasing and form the basis of transverse relaxation in gradient recalled echo (GRE) sequences [13]. Substances causing local field inhomogeneities, and therefore T2* shortening, include deoxyhemoglobin, iron, calcium, metallic implants, paramagnetic contrast, and blood products (iron). As a result of T2* shortening, these substances cause signal loss on T2*-GRE images and produce areas of hypointensity, which can be detected.

A major limitation with GRE is the fact that T2* is a 2D sequence that produces thicker image slices if a long echo time (TE) is used [33], which causes smaller hemorrhages to not be depicted in T2* images [53]. The ability to employ a long TE while still preserving image quality can only be accomplished with 3D GRE [33]. This idea, initially developed by Reichenbach et al. [75], nonetheless exploits the blood-oxygen level-dependent (BOLD) effect and uses refined phase data for contrast enhancement in MR images [33].

The SW sequence is a high-spatial resolution T2*-weighted sequence with additional post-processing using both the magnitude and phase information. To create SW images, a high-pass filter is used to develop a phase mask from MR phase images [33]. The filtered phase images are then multiplied with the magnitude images to enhance the conspicuity of smaller veins and other substances causing susceptibility effects [13]. By performing the aforementioned steps, SW phase images can be used for the differentiation between diamagnetic (i.e., calcium) and paramagnetic (i.e., deoxyhemoglobin, hemosiderin, and ferritin) substances [91].

SW images can be further analyzed by determining the maximum intensity projection (MIP) and minimum intensity projection (mIP), which provide information on the voxels presenting with the maximum and minimum intensities, respectively. This information on MIP and mIP found via SW images is especially useful to visualize the geometry of cerebral veins and deep gray matter structures, among other components in the brain.

SWI has been used in MR machines at different magnetic fields, including 1.5 Tesla (T), 3 T (high magnetic field), and 7 T (ultrahigh magnetic field). The higher the magnetic field, the higher signal-to-noise (SNR) ratio, thereby offering higher resolution of fine details in the brain structures, such as submillimeter-sized veins which are not possible to see by means of other neuroimaging techniques [23]. Very high field strengths may cause distortion of some structures characterized by high iron or calcium concentration [59] and create susceptibility artifacts, especially in proximity of the bone.

20.3 SWI in Neuro-oncology

Several studies have shown the higher sensitivity of SWI in relation to other MRI techniques (such as T1, T2, contrast-enhanced T1, and FLAIR) to detect microvasculature and intratumoral microhemorrhages in brain tumors. Table 20.2 offers a synopsis of the current literature on SWI in neuro-oncology. As illustrated in Chap. 24, microvasculature might be used to differentiate brain tumors of different histological grades, such as low-grade gliomas (grades I and II according to the World Health Organization, WHO 2007, classification system¹) from high-grade gliomas (grades III and IV). Glioblastoma multiforme (grade IV) is among the most vascularized human cancer [56] also showing a very high microvascular heterogeneity [22]. Moreover, its architectural heterogeneity (*multiforme*, from Latin, means “multishapes”) is also shown by the presence of necrotic and/or hemorrhagic areas. Importantly, these differences can be clearly depicted in SW images (Fig. 20.1).

20.3.1 Morphometrics and Fractal-Based Analysis of SWI in Brain Tumors

Several morphometric techniques have been suggested to quantify the different patterns shown in SW images in order to differentiate between tumor subtypes (Table 20.3). These techniques demonstrate the potential validity of SWI as an image biomarker useful in the differential diagnosis in neuroimaging. For example, hypointense spots on SWI images have been quantified by the frequency and maximum diameter [93]. Furthermore, the hypointense dot-like or linear structures shown in SW imaging of brain tumors have been quantified in terms of intratumoral susceptibility signals (ITSSs), by means of a semiquantitative method, which has been shown to be useful in differentiating cerebral lymphomas from high-grade gliomas. By means of this technique, GBM has been shown to have higher ITSSs scores compared to lymphomas. More specifically, GBMs typically elicit a much higher intratumoral SWI signal relative to lymphomas, which show very little, if any, intratumoral SWI signal [70, 72]. However, a major limitation of this technique pertains to the subjectivity of the measure since the computation of ITSSs is mainly operator-dependent. Hori et al. introduced a grading system based on the ratio of SWI hypointensity relative to the size of the tumor, which led to a more accurate correlation between score and tumoral grade being found, when compared to grading [37]. The susceptibility grading system ranges from 0 (no SWI hypointensity detectable) to 3 (presence of vascular structures alone), with grade I signifying hypointensity in less than half of the tumor (and, according to the authors, related to bleeding), while the minimum requirement for grade II is characterized by

¹At the time of the chapter writing, the WHO classification system for brain tumors published in 2016 was not available yet.

Table 20.2 Literature synopsis of applications on SWI in neuro-oncology

Author, year of publication, Ref	Main findings
<i>Studies supporting SWI usage</i>	
Baldawa et al., 2012 [5]	Blooming effects shown in SWI indicating intratumoral hemorrhage
Bian et al., 2014 [10]	7 T SWI is more effective in detecting number of CMBs from radiation injury involving the frontal lobe, parietal lobe, cerebellum, or brainstem; 7 T and 3 T SWI are equally sensitive in detecting amount of CMBs if radiotherapy applied to temporal lobe or basal ganglia
Ding et al., 2014 [24]	PCNSL has fewer intralesional vessels found on SWI relative to high-grade gliomas and brain metastases
Deistung et al., 2013 [16]	QSM, which uses SWI data, can differentiate intratumoral hemorrhagic components from calcification in glioblastoma
Di Ieva et al., 2012 [21]	Fractal analysis applied in SW images effectively monitored changes in intratumoral microvasculature in patients undergoing antiangiogenic therapy
Di Ieva et al., 2013, 2016 [18, 19]	Fractal analysis applied in SW images objectively determined tumor grades in gliomas and differentiated different brain tumor histotypes
Fellah et al., 2011 [25]	SWI can monitor changes in intratumoral microvasculature over time in patients undergoing antiangiogenic medication
Furtner et al., 2014 [27]	PCNSL can be differentiated from GBM based on ITSSs. A threshold of 1.5 ITSSs or higher is indicative of GBM, while an ITSS value less than 1.5 is suggestive of PCNSL
Grabner et al., 2012 [29]	SWI at 7 T depicts intratumoral microvasculature and microhemorrhages in patients taking antiangiogenic medication; SWI findings correlate with histopathology
Hori et al., 2010 [37]	Ratio of hypointensity from SW images within tumor boundaries is the most objective measure in grading
Jurkiewicz et al., 2010 [45]	SWI detected hemosiderosis after tumor resection
Kim et al., 2009 [47]	ITSSs observed in SWI can differentiate high- and low-grade tumors
Li et al., 2010 [49]	SWI can clearly depict intratumoral hemorrhage and microvasculature; image findings correlated with pathology
Li et al., 2015 [50]	Low-grade gliomas have less ITSSs compared to high-grade gliomas
Löbel et al., 2010 [53]	SWI detected more hemorrhages over time than T2*
Lou et al., 2009 [55]	SWI can clearly detect early BGG, tumor visibility on SWI poorer in late BGG
Lou et al., 2012 [54]	SWI can differentiate between intracranial ectopic germinoma from subacute lacunar infarct using hypointensity differences
Lupo et al., 2012 [58]	More CMBs discovered in the previous tumor region after radiation therapy using 7 T SWI
Lupo et al., 2013 [57]	Higher percent volume of hypointensity on SW image of a T1-weighted contrast-enhancing lesion best predicted patient response to concomitant therapy

(continued)

Table 20.2 (continued)

Author, year of publication, Ref	Main findings
Menon et al., 2009 [61]	SWI could detect calcification in subfrontal gangliocytoma
Moeninghoff et al., 2010 [63]	7 T SWI allowed intratumoral vessel branches 250 μ m in size to be depicted
Nishiguchi et al., 2013 [65]	SW-PRESTO can assess ischemia before and after tumor embolization surgery
Nossek et al., 2009 [68]	SWI helped to determine tumor malignancy based on microvascular assessment
Park et al., 2009 [69]	Use ITSSs in SW images to objectively grade tumors; ITSS correlate with rCBVmax
Park et al., 2010 [70]	GBM distinguished from metastatic tumors using ITSSs in SW images
Peters et al., 2012 [72]	Glioblastoma correctly differentiated from lymphomas using ITSSs in SWI
Peters et al., 2013 [71]	SWI can detect lesions in medulloblastoma patients who underwent radiation therapy
Radbruch et al., 2012 [74]	PQ of ITSSs can distinguish between cerebral metastases originating from different sources (e.g., breast carcinoma and malignant melanoma); however, PQ could not differentiate between all metastases types (e.g., breast carcinoma and bronchial carcinoma)
Sehgal et al., 2006 [78]	SWI more sensitive than contrast-enhanced T1 and T2 in depicting tumor boundaries, intratumoral microvasculature, and internal architecture; vessel findings in SWI correlate with histopathology
Toh et al., 2012 [82]	SWI can distinguish glioblastoma from brain abscess, unlike in T2
Vossough et al., 2012 [86]	Red nucleus degeneration seen in SWI after tumor resection in the posterior fossa
Wieczorek-Pastusiak et al., 2013 [88]	“Vessel view” computer counting program found more vessels in SWI than contrast-enhanced T1
Wu et al., 2009 [90]	SWI found more (smaller) calcified lesions than CT
Zeng et al., 2011 [92]	SWI can assess the extent of radiation injury based on the number of hemorrhagic lesions; findings matched histopathology
Zhang, 2009 [30]	Small brain metastases less than 1 cm and CMBs found in SWI, but not seen in contrast-enhanced T1 and T2*
Zulfiqar et al., 2012 [96]	Greater number of calcium deposits found intratumorally when using SWI and conventional MRI together, compared to conventional MRI alone
<i>Studies not supporting SWI usage</i>	
Gramsch et al., 2013 [30]	SWI lesions did not correlate with metastases transformation; abnormalities on contrast-enhanced T1 can detect metastases

Courtesy of Timothy Lam

CMBs cerebral microbleeds, *PCNSL* primary central nervous system lymphomas, *QSM* quantitative susceptibility mapping, *ITSSs* intratumoral susceptibility signals, *BGG* basal ganglia germinoma, *SW-PRESTO* SW principles of echo shifting with a train of observations, *rCBVmax* maximum relative cerebral blood volume, *GBM* glioblastoma multiforme, *PQ* percentagewise quantification

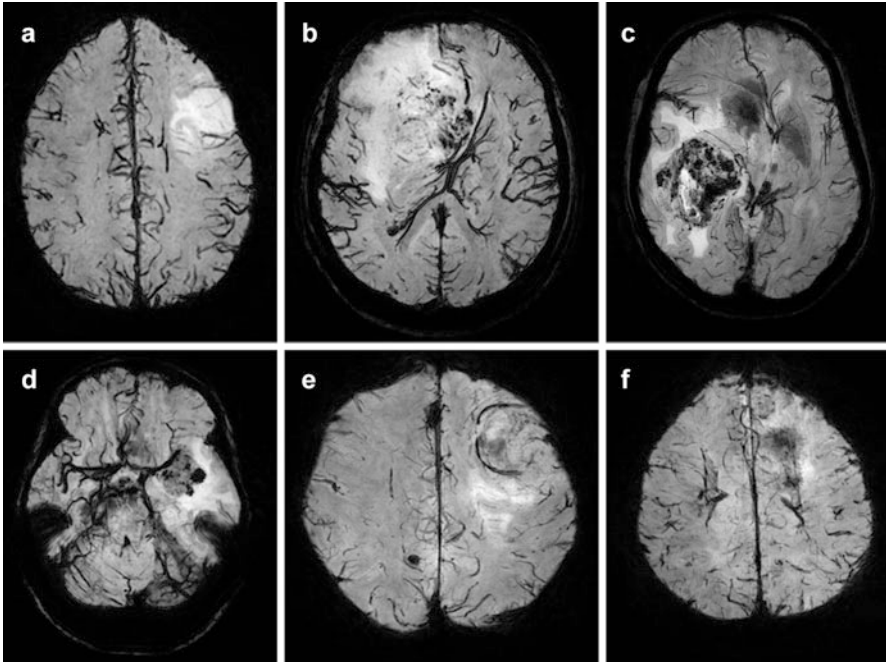


Fig. 20.1 Examples of different tumors showing distinct SWI signal patterns, shown in minimal intensity projection. (a) Left frontal grade II glioma ($FD_{SWI} = 1.25$). (b) Right fronto-callosal grade III glioma ($FD = 2.02$). (c) Right temporal grade IV glioma ($FD_{SWI} = 2.40$). (d) Left temporal metastasis ($FD_{SWI} = 2.10$). (e) Left frontal meningioma ($FD_{SWI} = 1.88$). (f) Left frontal lymphoma ($FD_{SWI} = 1.87$) (Reproduced from Di Ieva, Le Reste et al. [18] with permission of the Publisher)

hypointensity found in more than half of the tumor in one or more SW images depicting linear and/or tortuous shapes (which is associated with bleeding and/or vascular structures). This technique offered advancement in the quantification of the intratumoral SWI patterns, although still limited by some intra- and interobserver variability [19]. In order to overcome the subjectivity of the scoring systems, percentage-wise quantification (PQ) of the ITSSs has been suggested to be useful in characterizing brain metastases, although the technique focuses on quantitative aspects while neglecting the distribution and morphology of ITSS [74].

Quantitative susceptibility mapping (QSM) offers a very promising mean for susceptibility quantification of different brain structures [16, 32]. Specifically, QSM has the potential to produce lesion-specific susceptibility maps (derived from GRE phase data), which can provide more information on blood products and calcification [15, 77]. The ability to detect calcification in tumors can be useful for tumor grading and in deciding patient prognosis as calcification in tumors have been found to be associated with longer patient survival compared to tumors without calcification [44, 78].

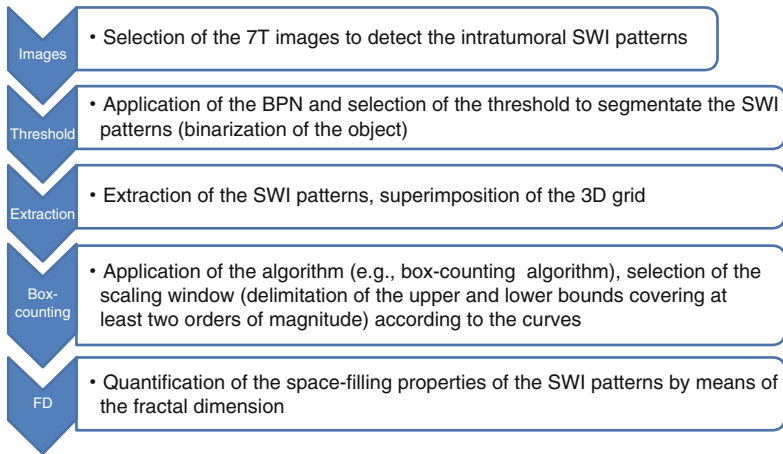
Finally, a computational fractal-based method to quantify the intratumoral SWI patterns was introduced by Di Ieva et al. in 2012 [19, 21]. The geometrical complex-

Table 20.3 Morphometric analyses used to quantify SWI in brain tumors

Technique	Description	Pros	Cons
Frequency and maximum diameter	Computer aided or manual count and measure of the hypointensity spots	Easy to be performed	It does not consider the morphology and distribution of the spots
ITSSs	Semiquantitative method to assess the morphology of the SWI signals	Useful for comparison among different tumors	Biased by operator-dependent variability
SWI/volume	Grading system based on the ratio of SWI hypointensity relative to the size of the tumor	Useful for comparison among different tumors	Limited by some intra- and interobserver variability
PQ	Quantification of the percentage of ITSSs	Very useful for comparison and follow-up	Strictly quantitative with no consideration on the shape and distribution of ITSSs
QSM	Quantification in ppm of the susceptibility of distinct anatomical and pathological regions of the brain	Very promising for precise susceptibility quantification of different structures	Requires optimal post-processing
FD _{SWI}	Fractal dimension computed by means of the box-counting method expressing the space-filling properties of the SWI pattern within the tumor	Single value able to give in a snapshot information on density, roughness, and geometrical complexity of the SWI pattern	Requires optimal computational processing. Not able to give information on the density alone, for example, but all the morphometric findings as a whole

FD_{SWI} SWI fractal dimension, *ITSSs* intratumoral susceptibility signals, *ppm* part per million, *PQ* percentage-wise quantification, *QSM* quantitative susceptibility mapping

ity of the intratumoral SWI-related architecture, resulting from microbleedings, necrotic areas, and/or neoplastic microvasculature, was quantified by means of the fractal dimension (FD). Most importantly, a relationship between FD of the SWI patterns (FD_{SWI}) and glioma grades was found [19]. FD was computed by means of the box-counting method. According to the principles of fractal geometry, higher values of FD signify higher space-filling properties of the intratumoral SWI patterns, meaning a higher density and geometrical complexity of the microvasculature and/or microbleedings within the tumor. It should be emphasized that apparently small changes of FD correspond to a high increase of the space-filling properties of the SWI patterns, when considering a linear approximation in a small interval of the nonlinear FD parameter. For example, an increase of the FD value from 2.07 to 2.23 corresponds to an increase of about 20% of the geometrical complexity of the object. Computing the FD on the stacks of MR images (i.e., on the 3D reconstructions of the tumor) gives rise to fractal values, whose non-integer and nonlinear values are included in a 3D space, between 0 and 3. Figures 20.2 and 20.3 show the algorithm and technique for the computation of FD of SWI patterns.



Pseudocode of the box-counting algorithm

For $Z=1$ to (number of images of the 7T-MR stack)

$Array[Z]=Binarize(image[Z])$

$L=\epsilon_{min}$

while $L<\epsilon_{max}$

$n[L]=count\ boxes\ on\ 3D\ grid\ of\ size\ L\ on\ Array$

$L=L*1.1$

$FD=-[Slope\ of\ log(L)\ vs\ -log(n)\ graph]$

Fig. 20.2 Algorithm and pseudo-code used to measure the 3D fractal dimension of the SWI patterns on 7 T MR images (BPN brightness progressive normalization [76]) (Reproduced from Di Ieva et al. [21] with permission of the Publisher. The same algorithm has been used also on 3 T MR images [18])

When analyzing the SWI 7 T MR images of 36 patients affected by grades II–IV gliomas, we found a trend of higher FD values in higher-grade gliomas [19]. The mean FD value was 2.086 ± 0.413 , with the FD values ranging from a mean value of 1.682 ± 0.278 in grade II to 2.247 ± 0.358 in grade IV gliomas ($p < 0.05$) (Fig. 20.4). Figure 20.5 illustrates some examples of different intratumoral SWI patterns, which were found in the study.

To this first demonstration that fractal analysis in SW imaging can offer reliable and useful morphometric image biomarkers to distinguish between low- and high-grade gliomas, the application of the methods was extended further to other kinds of brain tumors, such as brain metastases, meningiomas, and lymphomas as well [18]. Moreover, considering that 7 T MR scanners are very expensive, not easily available, and are mostly used for research purposes, the study was performed at 3 T, to show the feasibility of this computational neuroimaging technique on more commonly available scanners. In this study, we considered 78 patients affected by brain

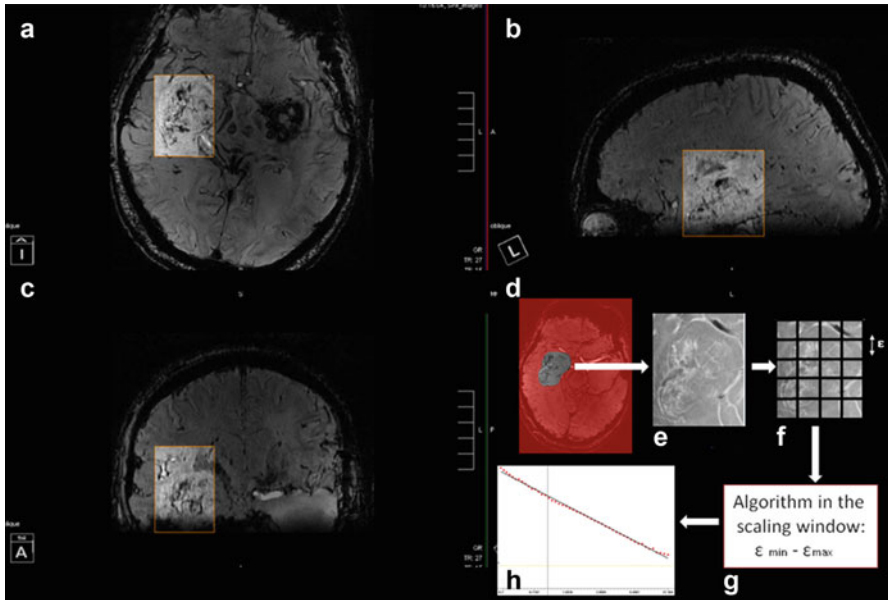


Fig. 20.3 Method used for fractal analysis of 3 and 7 T MR-SWI images. In the example, (a) axial, (b) sagittal, and (c) coronal sections of 7 T MR images (Magnetom 7 T, Siemens Healthcare, Erlangen, Germany, performed at the Medical University of Vienna, Austria) centered on a recurrence of GBM (in the insets). In (d), the region of interest was extracted (i.e., the tumor), and (e) there were segmentation and subsequent binarization of the SWI patterns (in the figure, the signal has been inverted, i.e., the SWI black hypointensities appear here as white). (f) Superimposition of the grid of boxes of ϵ size. The Z-axis sequential sections for the 3D reconstruction are shown according to the algorithm in Fig. 20.2. (g) Repetition of the algorithm with ϵ of different sizes in the scaling window ranging from $\epsilon_{\min} = 0.23$ to $\epsilon_{\max} = 23$ mm (10% increment of the box size at each step until to reach ϵ_{\max}). (h) Results plotted on a log-log graph (x-axis, ϵ , the side length of the box; y-axis, $N(\epsilon)$, on the grid, the number of boxes of ϵ side which cover completely the SWI patterns). The slope of the graph of $\log [N(\epsilon)]$ against $\log (1/\epsilon)$ represents the fractal dimension. The software for the analysis was developed in visual C++ language by Carlo Russo (Reproduced from Di Ieva et al. [21] with permission of the Publisher)

tumors of different histopathology (13 grade II gliomas, 11 grade III, and 25 grade IV gliomas; 15 metastases from different sources; 8 grade I meningiomas; and 6 primary B-cell lymphomas), computing the FD_{SWI} as well as the volume fraction of the SWI signal within the tumors. Both values were able to differentiate low grade from grades III and IV gliomas, as well as metastases and meningiomas, although FD alone was statistically more significant, even to differentiate lymphomas (mean $FD_{SWI} = 1.69 \pm 0.59$) from GBM (mean $FD_{SWI} = 2.03 \pm 0.45$, $p < 0.05$) (Fig. 20.1) [18]. These results confirmed the findings of the previous study performed at 7 T. More importantly, these findings demonstrate that the computational fractal-based analysis of the SWI patterns can help differentiate contrast-enhancing lesions, which often poses problems in the differential diagnosis for neuroimaging, such as between lymphomas and malignant gliomas.

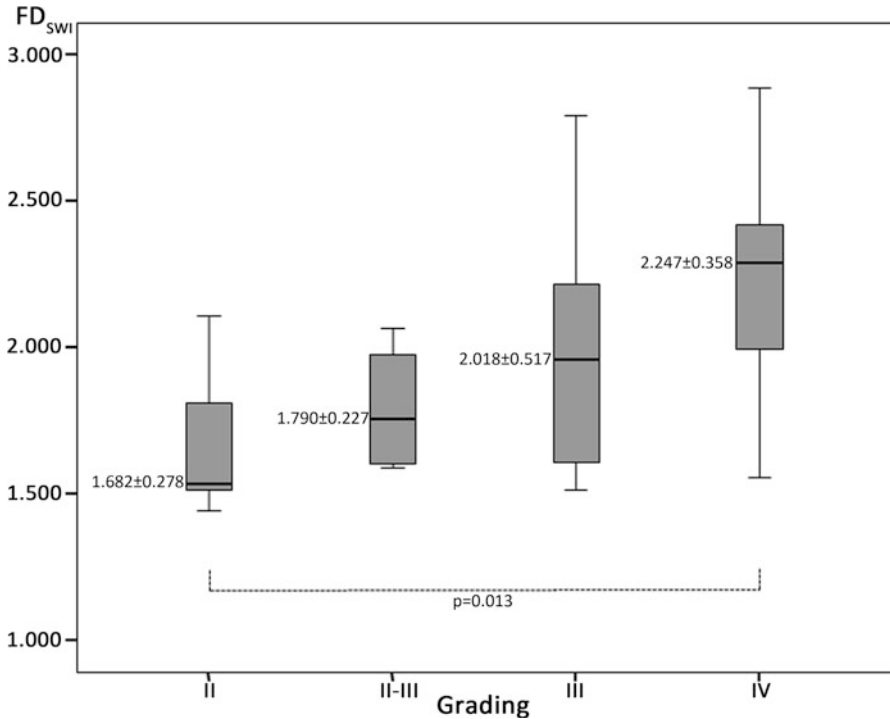


Fig. 20.4 Box plots showing the FD_{SWI} values for each histopathological group of gliomas. Four cases were histopathologically considered “ambiguous” and were put in the group “II–III” grades. The overall significance was statistically significant, $p < 0.05$, with the strongest significance in the grade II versus grade IV gliomas ($p = 0.013$) (Reproduced from Di Ieva et al. [19] with permission of the Publisher)

Taken together, our findings showed that lower FD_{SWI} values are associated with tumoral vasculature, while higher values (signifying more space-filling objects) associated with intratumoral bleedings and/or necrotic areas, as previously indicated in qualitative, semiquantitative, and quantitative studies [20, 29, 37]. FD_{SWI} appears to be a reliable morphometric parameter of the tumoral architecture, showing a gradient of complexity among tumors of different histotype and demonstrating the ability to quantify the “architectural fingerprinting,” which has also been shown in the histological features and microvasculature of brain tumors as seen in histopathology [20] (see Chaps. 23 and 24).

Besides the grading and differentiation of brain tumors (*diagnostic aim*), SWI has also been applied longitudinally in follow-up analyses of patients, in order to track tumor evolution and/or treatment response (*follow-up aim*). Different percentages of SWI hypointensity in brain tumors have in fact been correlated to different response to therapy in newly diagnosed GBM [57]. Antiangiogenic drugs (e.g., bevacizumab, an antibody targeted against the vascular endothelial growth factor (VEGF)) can be used in recurrences of malignant gliomas, having three

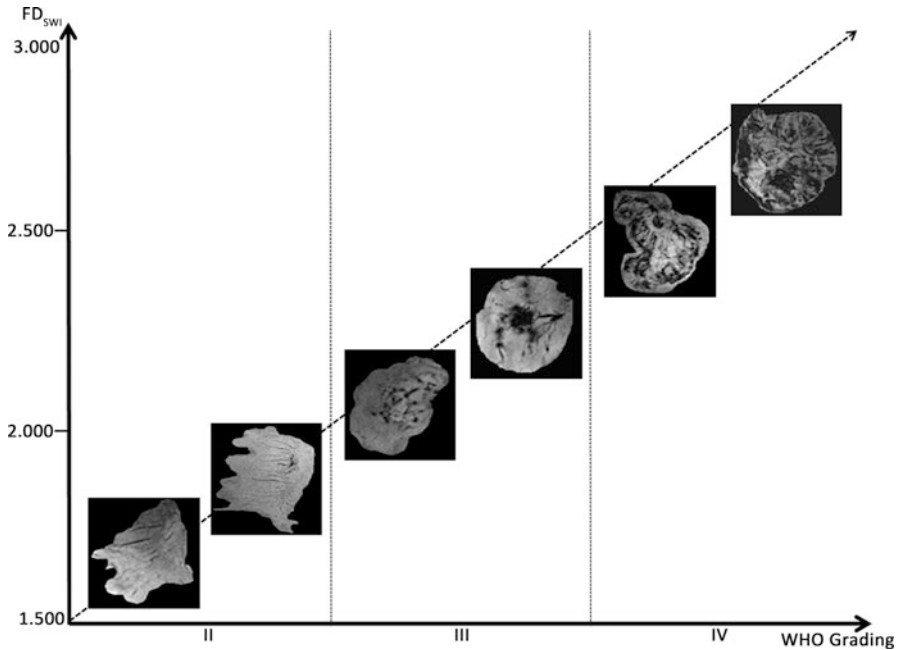


Fig. 20.5 Schema showing the correlation between the histological glioma grade and the FD_{SWI} values. The intratumoral SWI patterns consist of vascular structures (linear structures in grade II tumors, increasing in tortuosity and density in higher-grade gliomas) and conglomerated dot shapes, which most likely indicate intralesional bleeding and/or necrotic areas (as evident in grades III and IV gliomas). It should be noted that the image and fractal analysis were performed on the 3D volume of the reconstruction of the entire tumor in MRI, while the images showed here are selections of the axial sections taken from the whole stack (Reproduced from Di Ieva et al. [19] with permission of the Publisher)

fundamental effects: (1) inhibition of the neoplastic angiogenesis, (2) normalization of the angioarchitecture (resulting in a more efficient delivery of drugs and oxygen to the cancer cells) [43], and (3) reduction of the peritumoral edema [2, 26, 67]. Intratumoral and/or brain bleedings are rare but known side effects of the treatment. SWI can be potentially used to assess whether antiangiogenic therapy is producing favorable effects (like decreased intratumoral microvasculature) or unfavorable results (increased intratumoral microvasculature in nonresponder patients and/or microbleedings).

We conducted a pilot study on the application of computational fractal-based analysis to quantify the changes of the intratumoral SWI patterns, visualized by means of ultrahigh field (7 T) MRI, in four patients affected by malignant glioma recurrences undergoing second-line treatment with bevacizumab, and followed longitudinally [21]. The imaging was in fact performed at time T_0 (before beginning the antiangiogenic treatment) and repeated 2 weeks (T_1) and 4 weeks (T_2) after therapy was initiated. In two patients (like in the case illustrated in Fig. 20.6), it was shown that the microvascular proliferation and eventually the intratumoral bleedings were

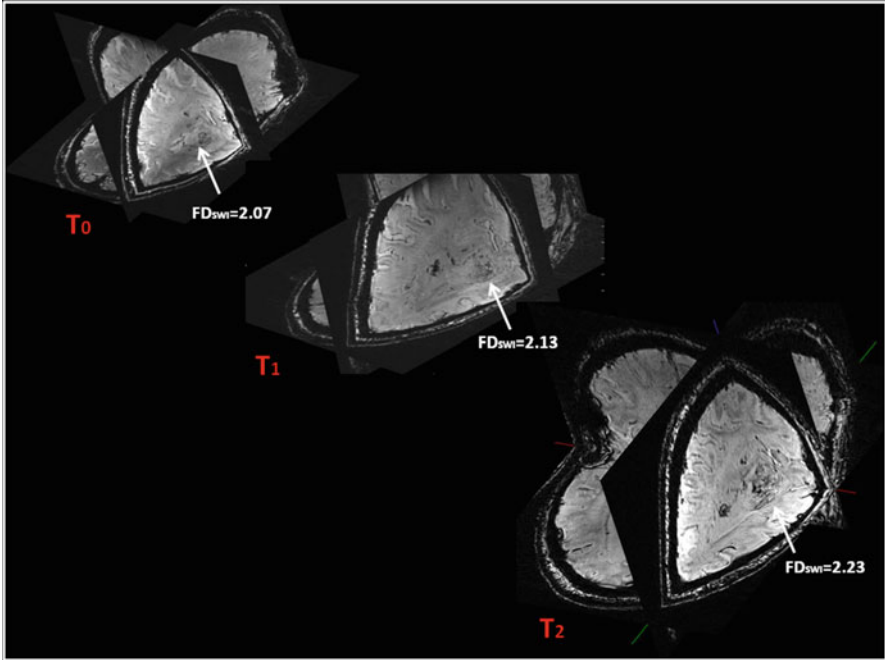


Fig. 20.6 Multiplanar reconstructions of the 7 T SWI MR images in time T_0 , which were repeated serially after 2 (T_1) and 4 weeks (T_2) since the beginning of antiangiogenic treatment. The *white arrows* show the recurrence of the GBM, and from T_0 to T_2 , it is evident that there is an increase in the signal of the SWI patterns. The value of the fractal dimension of the intratumoral SWI patterns (FD_{SWI}), reported for each temporal sequence, increased over time (see text) (Reproduced from Di Ieva et al. [21] with permission of the Publisher)

increasing over time, as confirmed by the increase of the value of FD from T_0 to T_1 . This means that, despite the antiangiogenic treatment, over a 1-month longitudinal follow-up, there was an increase in the intratumoral microvasculature and/or intratumoral bleedings, thereby suggesting that the patient is nonresponsive and/or experiencing side effects of the antiangiogenic treatment itself (like intratumoral bleeding). These morphological changes, qualitatively described by the neuroradiologists and quantitatively shown by the morphometric fractal analysis, were associated with a progressive neurological decline of the patients, who died within 10 weeks. A third patient was shown to improve neurologically after the antiangiogenic treatment. Although in this patient the neuroradiologist reported only a reduction of the peritumoral edema and no differences regarding the tumor itself, the computational analysis revealed a minimal decrease of FD over time ($FD_{SWI} = 2.34$ in T_0 , decreasing to 2.26 at T_1 and T_2). The fourth patient showed an improvement in the peritumoral edema along with improvement in clinical and neurological status (albeit temporarily), without any differences in FD_{SWI} values (however, this is because the tumor mainly presented a large necrotic area, visualized in forms of a huge black spot in SWI).

Although this was a limited study performed on a very small cohort of cases, it was the first to introduce fractal analysis as a quantitative method for objectively comparing sequential images taken during the neuroradiological follow-up of patients affected by brain cancer. Moreover, although such computational analysis can be performed on lower magnetic fields, it has been shown that 7 T MRI is also the best means to visualize the presumed intratumoral vascularity in gliomas [64].

Nonetheless, it has to be emphasized that it is anatomically incorrect to speak about “microvasculature.” In fact the mean radius of capillaries is 5–10 μm , while even by means of 7 T MRI, the smallest detectable vessel diameter is about 0.3 mm. Therefore by means of neuroradiological imaging, it is not possible to visualize tiny angiogenic sprouts, for example, as it happens in histology. This is precisely the reason why we introduced the “microvascular fractal dimension” in histopathology, but in neuroradiology such term was replaced with “FD of the SWI pattern” [19, 20].

20.4 Future Perspective of SWI in Neurotraumatology

Traumatic brain injury is a leading cause of death and disability worldwide. Efforts to develop better biomarkers of brain injury are important to improve diagnosis, treatment, and prognosis of these patients. Newer MRI techniques hold promise in providing such a biomarker. SWI is an effective imaging technique to detect microbleedings in the white matter of patients after TBI [33]. Specifically, SWI is more sensitive in comparison to other techniques to detect very small cerebral microbleedings in the brainstem and corpus callosum. This neuroradiological technique has been shown to be useful in dichotomizing diffuse axonal injury (DAI) patients as hemorrhagic and nonhemorrhagic, which is very useful in terms of a clinical perspective since treatment, outcome, and prognosis between these two groups of patients are quite different [85]. Table 20.4 summarizes selected literature on the application of SWI to TBI patients.

Besides from differentiating between the subtypes of DAI, SWI can provide details on the clinical status of TBI patients. For example, the number and volume of SWI hypointensities in TBI patients have been correlated to the scores of the most used scale in neurotraumatology, the Glasgow Coma Scale (GCS) [3, 15, 28, 69, 79, 81]. This means that SWI hypointensities are correlated with trauma clinical severity, and its quantification can offer some prognostic indicators (*prognostic surrogate biomarkers*). Furthermore, microbleeds can be quantified with the use of susceptibility maps [32]. Finally, the computational fractal-based analysis of SWI patterns holds promise in the quantification and description of brain lesions in TBI patients, with higher FD_{SWI} associated with worse prognosis, especially with higher FD_{SWI} values in the brainstem [Di Ieva, unpublished data].

Table 20.4 Literature synopsis of applications of SWI in neurotraumatology

Author, year of publication, Ref	Main findings
<i>Studies supporting SWI usage</i>	
Akiyama et al., 2009 [1]	SWI detected three times more lesions than T2*
Babikian et al., 2005 [4]	Lesions detected on the brainstem, thalamus, and basal ganglia offered the best prediction of neuropsychological outcome
Beauchamp et al., 2011 [8]	SWI found more lesions than CT and T2 MRI, even if MRI not performed until 2–8 weeks after TBI onset
Beauchamp et al., 2013 [7]	More lesions seen on SWI correlated with lower intellectual ability
Benson et al., 2012 [9]	Lesion volume in SWI could determine the severity of clinical outcome
Choi et al., 2014 [14]	Additional lesions found with SWI, but not FLAIR, were a good predictor of poor clinical outcome
Colbert et al., 2010 [15]	Presence of microhemorrhage was the best predictor of outcome in children with nonaccidental trauma
Geurts et al., 2012 [28]	SWI detected most lesions, especially in the brainstem and corpus callosum, compared with T2, T2*, and FLAIR
Hasiloglu et al., 2011 [34]	SWI found more lesions than T2 and T2* in amateur boxers
Helmer et al., 2014 [35]	SWI can detect changes in hypointensity of smaller (<5 mm) cerebral microbleeds over different time points in patients who had concussions
Henry et al., 2015 [36]	SWI could detect shearing of axons in the corpus callosum and prefrontal cortex
Huang et al., 2013 [38]	SWI lesions in the brainstem could differentiate DAI from cerebral fat embolism
Huang et al., 2015 [39]	The presence of cerebral microbleeds detected in SW images of mTBI patients was related to deficits in short-term memory, as assessed by the digit span test
Iwamura et al., 2011 [41]	The number of lobes with grade III (supratentorial) hemorrhage seen in SW image correlated well with poor outcome and consciousness disturbance
Liu et al., 2015 [51]	Greater number of cerebral microbleeds was detected on SWI relative to T2* imaging in patients with mTBI. The number of microbleeds found on SW images could predict the incidence of post-concussive syndrome, whereby an increase in every microbleed would increase the risk of post-concussive syndrome by 1.5 times
Liu et al., 2016 [52]	Based on quantitative susceptibility mapping (QSM), the susceptibility-weighted imaging and mapping (SWIM) technique represents a novel method that could detect and differentiate between hemorrhage and deep veins in TBI patients with high sensitivity and specificity
Moeninghoff et al., 2015 [62]	7 T SWI can detect greater numbers of cerebral microbleeds at a similar and higher spatial resolution compared to 3 T SWI

(continued)

Table 20.4 (continued)

Author, year of publication, Ref	Main findings
Niwa et al., 2011 [66]	Hypointensity changes in SW images indicate hemorrhage progression over long term
Park et al., 2009 [69]	CMBs in the frontal, occipital lobes, and brainstem seen only for TBI patients
Sigmund et al., 2007 [79]	SWI detects more lesions than T2 and FLAIR
Spitz et al., 2013 [81]	SWI is more sensitive than FLAIR to detect lesions from TBI, more lesions indicative of poorer neuropsychological outcome
Tong et al., 2003 [84]	SWI detected more lesions than T2-GRE, especially in the brainstem, corpus callosum, and cerebellum
Tong et al., 2004 [83]	Lesions found on SW images in 7 of 9 brain regions indicate higher likelihood of poor outcome
Toth et al., 2013 [85]	SWI can distinguish between mTBI with and without hemorrhage
Wang et al., 2011 [87]	SWI can detect hemorrhage in patients with acute cervical spinal cord injury
Wu et al., 2010 [89]	SWI effective in detecting intraventricular hemorrhage
<i>Studies not supporting SWI usage</i>	
Chastain et al., 2009 [12]	Median lesion number or volume on SW image could not predict good and poor outcome
Keightley et al., 2012 [46]	SWI could not detect structural abnormalities after child concussion or mTBI
Maugans et al., 2012 [60]	Structural damage not observed in children with sports-related concussion

Courtesy of Timothy Lam

TBI traumatic brain injury, *mTBI* mild traumatic brain injury

20.5 Limitations

The methodological limitations pertaining to the application of fractal analysis to MR-SWI imaging are related to the image resolution and intensity of the SWI signal, as already discussed above. Moreover, SWI requires post-processing computation, while the parameters as well as the number of multiplied phase masks should be standardized, in order to make the input data homogeneous (see Chap. 12). The choice of the threshold to segment and automatically extract the SWI hypointensities can be affected by an operator-dependent variability, and this can affect the fractal dimension computation as well. In order to solve the problem of different luminosities being found in different MR images, we introduced an algorithm for the progressive normalization of brightness, which normalizes the luminosity intensity, thereby making it possible to use the same threshold to extract the SWI hypointensities from each image [21, 76].

As summarized in [21], further studies should be focused on the following objectives:

1. Decrease the operator-dependent variability in selecting the edges of the tumor by moving toward automatic detection of the tumor outline using fractal-based algorithms [40, 48, 95] (see also Chap. 19) or neural networks [6, 42, 94].
2. Improve the imaging and post-processing parameters to standardize the methods and to reduce technical variability.
3. Compare 3 and 7 T MR images to the histological findings from brain tumors to definitively assess the significance of SWI patterns, similar to studies that were performed with 3 T MRI [73].
4. Combine the fractal analysis of SWI patterns at 7 T with some quantitative measurements of vessel morphology, as defined by magnetic resonance angiography [11] or perfusion parameters [80] to find valid and objective indexes for monitoring patients affected by brain tumors.
5. Associate the fractal quantification of the SWI patterns with other neuroradiological parameters, including (but not limited to) the volume of the tumor, peritumoral edema, or the histogram analysis of diffusion tensor imaging-derived maps.
6. Look for any robust correlation of the neuroradiological morphometric findings with clinical parameters, and subsequently test them as reliable predictive or prognostic biomarkers.

Due to high translationality of this field of research, the solution of these problems requires a multidisciplinary collaboration of distinct specialists working together in different fields: points 1 and 2 should be investigated by computer scientists, technicians, and engineers, for example, point 3, by neuroradiologists and neuropathologists and points 4–6, by a large group of different biomedical specialists, including neurosurgeons, biologists, epidemiologists, oncologists, and radiotherapists.

20.6 Conclusion

SWI has been shown to offer some diagnostic and prognostic indexes, but it is of paramount importance to underline that it should be used in a complementary way with other techniques, such as perfusion and diffusion imaging, in order to get a holistic knowledge of the temporal evolution of brain tumors as well as to follow up response to treatment. SWI can still be developed, and several issues on processing procedures or correlation with neuroradiological results, for example, have yet to be explored and addressed, but here we focus on the fact that SWI research should also be aimed to decrease the reliance on intra- and interobserver variability in order to enhance the quantification and objectivity of SWI. Fractal analysis can help in such aim, offering computational fractal-based parameters (e.g., FD of the SWI pattern) as potential neuroimaging biomarkers, in neuro-oncology as well as in neurotraumatology, although the field could be expanded into other applications as well (e.g., follow-up of arteriovenous malformations or cavernomas).

References

1. Akiyama Y, Miyata K, Harada K, Minamida Y, Nonaka T, Koyanagi I, et al. Susceptibility-weighted magnetic resonance imaging for the detection of cerebral microhemorrhage in patients with traumatic brain injury. *Neurol Med Chir (Tokyo)*. 2009;49:97, 9; discussion 99.
2. Arrillaga-Romany I, Norden AD. Antiangiogenic therapies for glioblastoma. *CNS Oncol*. 2014;3:349–58.
3. Ashwal S, Tong KA, Ghosh N, Bartnik-Olson B, Holshouser BA. Application of advanced neuroimaging modalities in pediatric traumatic brain injury. *J Child Neurol*. 2014;29:1704–17.
4. Babikian T, Freier MC, Tong KA, Nickerson JP, Wall CJ, Holshouser BA, et al. Susceptibility weighted imaging: neuropsychologic outcome and pediatric head injury. *Pediatr Neurol*. 2005;33:184–94.
5. Baldawa SS, Bele K, Menon G, George CV, Abraham M, Nair S. Susceptibility-weighted imaging: a new tool for detection of intratumoral bleeding and subarachnoid hemorrhage – report of two cases. *Clin Neuroradiol*. 2012;22:257–61.
6. Bay OF, Usakli AB. Survey of fuzzy logic applications in brain-related researches. *J Med Syst*. 2003;27:215–23.
7. Beauchamp MH, Beare R, Ditchfield M, Coleman L, Babl FE, Kean M, et al. Susceptibility weighted imaging and its relationship to outcome after pediatric traumatic brain injury. *Cortex*. 2013;49:591–8.
8. Beauchamp MH, Ditchfield M, Babl FE, Kean M, Catroppa C, Yeates KO, et al. Detecting traumatic brain lesions in children: CT versus MRI versus susceptibility weighted imaging (SWI). *J Neurotrauma*. 2011;28:915–27.
9. Benson RR, Gattu R, Sewick B, Kou Z, Zakariah N, Cavanaugh JM, et al. Detection of hemorrhagic and axonal pathology in mild traumatic brain injury using advanced MRI: implications for neurorehabilitation. *NeuroRehabilitation*. 2012;31:261–79.
10. Bian W, Hess CP, Chang SM, Nelson SJ, Lupo JM. Susceptibility-weighted MR imaging of radiation therapy-induced cerebral microbleeds in patients with glioma: a comparison between 3T and 7T. *Neuroradiology*. 2014;56:91–6.
11. Bullitt E, Ewend M, Vredenburg J, Friedman A, Lin W, Wilber K, et al. Computerized assessment of vessel morphological changes during treatment of glioblastoma multiforme: report of a case imaged serially by MRA over four years. *Neuroimage*. 2009;47 Suppl 2:T143–51.
12. Chastain CA, Oyoyo UE, Zipperman M, Joo E, Ashwal S, Shutter LA, et al. Predicting outcomes of traumatic brain injury by imaging modality and injury distribution. *J Neurotrauma*. 2009;26:1183–96.
13. Chavhan GB, Babyn PS, Thomas B, Shroff MM, Haacke EM. Principles, techniques, and applications of T2*-based MR imaging and its special applications. *Radiographics*. 2009;29:1433–49.
14. Choi JI, Kim BJ, Ha SK, Kim SH, Lim DJ, Kim SD. Comparison of subgroups based on hemorrhagic lesions between SWI and FLAIR in pediatric traumatic brain injury. *Childs Nerv Syst*. 2014;30:1011–9.
15. Colbert CA, Holshouser BA, Aen GS, Sheridan C, Oyoyo U, Kido D, et al. Value of cerebral microhemorrhages detected with susceptibility-weighted MR imaging for prediction of long-term outcome in children with nonaccidental trauma. *Radiology*. 2010;256:898–905.
16. Deistung A, Schweser F, Wiestler B, Abello M, Roethke M, Sahn F, et al. Quantitative susceptibility mapping differentiates between blood depositions and calcifications in patients with glioblastoma. *PLoS One*. 2013;8, e57924.
17. Di Ieva A, Lam T, Alcaide Leon P, Bharatha A, Montanera W, Cusimano MD. Magnetic resonance susceptibility weighted imaging (SWI) in neurosurgery: current applications and future perspectives. *J Neurosurg*. 2015;123(6):1463–75.
18. Di Ieva A, Le Reste PJ, Carsin-Nicol B, Ferre JC, Cusimano MD. Diagnostic value of fractal analysis for the differentiation of brain tumors using 3-tesla MR susceptibility-weighted imaging. *Neurosurgery*. 2016.

19. Di Ieva A, Göd S, Grabner G, Grizzi F, Sherif C, Matula C, et al. Three-dimensional susceptibility-weighted imaging at 7 T using fractal-based quantitative analysis to grade gliomas. *Neuroradiology*. 2013;55:35–40.
20. Di Ieva A. Fractal analysis of microvascular networks in malignant brain tumors. *Clin Neuropathol*. 2012;31:342–51.
21. Di Ieva A, Matula C, Grizzi F, Grabner G, Trattnig S, Tschabitscher M. Fractal analysis of the susceptibility weighted imaging patterns in malignant brain tumors during antiangiogenic treatment: technical report on four cases serially imaged by 7 T magnetic resonance during a period of four weeks. *World Neurosurg*. 2012;77:785.e11–21.
22. Di Ieva A, Grizzi F, Sherif C, Matula C, Tschabitscher M. Angioarchitectural heterogeneity in human glioblastoma multiforme: a fractal-based histopathological assessment. *Microvasc Res*. 2011;81:222–30.
23. Di Ieva A, Tschabitscher M, Galzio RJ, Grabner G, Kronnerwetter C, et al. The veins of the nucleus dentatus: anatomical and radiological findings. *Neuroimage*. 2011;54:74–9.
24. Ding Y, Xing Z, Liu B, Lin X, Cao D. Differentiation of primary central nervous system lymphoma from high-grade glioma and brain metastases using susceptibility-weighted imaging. *Brain Behav*. 2014;4:841–9.
25. Fellah S, Girard N, Chinot O, Cozzone PJ, Callot V. Early evaluation of tumoral response to antiangiogenic therapy by arterial spin labeling perfusion magnetic resonance imaging and susceptibility weighted imaging in a patient with recurrent glioblastoma receiving bevacizumab. *J Clin Oncol*. 2011;29:e308–11.
26. Friedman HS, Prados MD, Wen PY, Mikkelsen T, Schiff D, Abrey LE, et al. Bevacizumab alone and in combination with irinotecan in recurrent glioblastoma. *J Clin Oncol*. 2009;27:4733–40.
27. Furtner J, Schopf V, Preusser M, Asenbaum U, Woitek R, Wohrer A, et al. Non-invasive assessment of intratumoral vascularity using arterial spin labeling: a comparison to susceptibility-weighted imaging for the differentiation of primary cerebral lymphoma and glioblastoma. *Eur J Radiol*. 2014;83:806–10.
28. Geurts BH, Andriessen TM, Goraj BM, Vos PE. The reliability of magnetic resonance imaging in traumatic brain injury lesion detection. *Brain Inj*. 2012;26:1439–50.
29. Grabner G, Nobauer I, Elandt K, Kronnerwetter C, Woehrer A, Marosi C, et al. Longitudinal brain imaging of five malignant glioma patients treated with bevacizumab using susceptibility-weighted magnetic resonance imaging at 7 T. *Magn Reson Imaging*. 2012;30:139–47.
30. Gramsch C, Gorické SL, Behrens F, Zimmer L, Schadendorf D, Krasny A, et al. Isolated cerebral susceptibility artefacts in patients with malignant melanoma: metastasis or not? *Eur Radiol*. 2013;23:2622–7.
31. Haacke EM, Lai S, Yablonskiy DA, Lin W. In vivo validation of the bold mechanism: a review of signal changes in gradient echo functional MRI in the presence of flow. *Int J Imaging Syst Technol*. 1995;6(2–3):153–63.
32. Haacke EM, Liu S, Buch S, Zheng W, Wu D, Ye Y. Quantitative susceptibility mapping: current status and future directions. *Magn Reson Imaging*. 2015;33:1–25.
33. Haacke EM, Xu Y, Cheng YC, Reichenbach JR. Susceptibility weighted imaging (SWI). *Magn Reson Med*. 2004;52:612–8.
34. Hasiloglu ZI, Albayram S, Selcuk H, Ceyhan E, Delil S, Arkan B, et al. Cerebral microhemorrhages detected by susceptibility-weighted imaging in amateur boxers. *AJNR Am J Neuroradiol*. 2011;32:99–102.
35. Helmer KG, Pasternak O, Fredman E, Preciado RI, Koerte IK, Sasaki T, et al. Hockey concussion education project, part 1. susceptibility-weighted imaging study in male and female ice hockey players over a single season. *J Neurosurg*. 2014;120:864–72.
36. Henry LC, Burkhart SO, Elbin RJ, Agarwal V, Kontos AP. Traumatic axonal injury and persistent emotional lability in an adolescent following moderate traumatic brain injury: a case study. *J Clin Exp Neuropsychol*. 2015;37:439–54.
37. Hori M, Mori H, Aoki S, Abe O, Masumoto T, Kunimatsu S, et al. Three-dimensional susceptibility-weighted imaging at 3 T using various image analysis methods in the estimation of grading intracranial gliomas. *Magn Reson Imaging*. 2010;28:594–8.

38. Huang LC, Wu MN, Chen CH, Huang P. Susceptibility-weighted imaging in patient with consciousness disturbance after traffic accident. *Am J Emerg Med.* 2013;31:261.e1–3.
39. Huang YL, Kuo YS, Tseng YC, Chen DY, Chiu WT, Chen CJ. Susceptibility-weighted MRI in mild traumatic brain injury. *Neurology.* 2015;84:580–5.
40. Islam A, Reza SM, Iftekharuddin KM. Multifractal texture estimation for detection and segmentation of brain tumors. *IEEE Trans Biomed Eng.* 2013;60:3204–15.
41. Iwamura A, Taoka T, Fukusumi A, Sakamoto M, Miyasaka T, Ochi T, et al. Diffuse vascular injury: convergent-type hemorrhage in the supratentorial white matter on susceptibility-weighted image in cases of severe traumatic brain damage. *Neuroradiology.* 2012;54:335–43.
42. Jaffar MA, Ain Q, Choi TS. Tumor detection from enhanced magnetic resonance imaging using fuzzy curvelet. *Microsc Res Tech.* 2012;75:499–504.
43. Jain RK. Normalization of tumor vasculature: an emerging concept in antiangiogenic therapy. *Science.* 2005;307:58–62.
44. Jenkinson MD, du Plessis DG, Smith TS, Joyce KA, Warnke PC, Walker C. Histological growth patterns and genotype in oligodendroglial tumours: correlation with MRI features. *Brain.* 2006;129:1884–91.
45. Jurkiewicz E, Pakula-Kosciesza I, Barszcz S, Nowak K, Swieszkowska E, Roszkowski M. Usefulness of magnetic resonance imaging with SWI sequence (susceptibility-weighted imaging) in diagnosing cerebral hemosiderosis – case report. *Pol J Radiol.* 2010;75:47–50.
46. Keightley ML, Chen JK, Pito A. Examining the neural impact of pediatric concussion: a scoping review of multimodal and integrative approaches using functional and structural MRI techniques. *Curr Opin Pediatr.* 2012;24:709–16.
47. Kim HS, Jahng GH, Ryu CW, Kim SY. Added value and diagnostic performance of intratumoral susceptibility signals in the differential diagnosis of solitary enhancing brain lesions: preliminary study. *AJNR Am J Neuroradiol.* 2009;30:1574–9.
48. Lahmiri S, Boukadoum M. Automatic brain MR images diagnosis based on edge fractal dimension and spectral energy signature. *Conf Proc IEEE Eng Med Biol Soc.* 2012;2012:6243–6.
49. Li C, Ai B, Li Y, Qi H, Wu L. Susceptibility-weighted imaging in grading brain astrocytomas. *Eur J Radiol.* 2010;75:e81–5.
50. Li X, Zhu Y, Kang H, Zhang Y, Liang H, Wang S, et al. Glioma grading by microvascular permeability parameters derived from dynamic contrast-enhanced MRI and intratumoral susceptibility signal on susceptibility weighted imaging. *Cancer Imaging.* 2015;15:4, 015-0039-z.
51. Liu G, Ghimire P, Pang H, Wu G, Shi H. Improved sensitivity of 3.0 tesla susceptibility-weighted imaging in detecting traumatic bleeds and its use in predicting outcomes in patients with mild traumatic brain injury. *Acta Radiol.* 2015;56:1256–63.
52. Liu J, Xia S, Hanks RA, Wiseman NM, Peng C, Zhou S, et al. Susceptibility weighted imaging and mapping of micro-hemorrhages and major deep veins after traumatic brain injury. *J Neurotrauma.* 2016;33:10–21.
53. Lobel U, Sedlacik J, Sabin ND, Kocak M, Broniscer A, Hillenbrand CM, et al. Three-dimensional susceptibility-weighted imaging and two-dimensional T2*-weighted gradient-echo imaging of intratumoral hemorrhages in pediatric diffuse intrinsic pontine glioma. *Neuroradiology.* 2010;52:1167–77.
54. Lou X, Tian C, Chen Z, Ma L. Differential diagnosis of infarct-like intracranial ectopic germinomas and subacute lacunar infarct on susceptibility-weighted imaging. *J Magn Reson Imaging.* 2012;36:92–8.
55. Lou X, Ma L, Wang FL, Tang ZP, Huang H, Cai YQ, et al. Susceptibility-weighted imaging in the diagnosis of early basal ganglia germinoma. *AJNR Am J Neuroradiol.* 2009;30:1694–9.
56. Louis DN, Ohgaki H, Wiestler OD, Cavenee WK. WHO classification of tumours of the central nervous system. 4th ed. Lyon: International Agency for Research on Cancer (IARC); 2007.
57. Lupo JM, Essock-Burns E, Molinaro AM, Cha S, Chang SM, Butowski N, et al. Using susceptibility-weighted imaging to determine response to combined anti-angiogenic, cytotoxic, and radiation therapy in patients with glioblastoma multiforme. *Neuro Oncol.* 2013;15:480–9.

58. Lupo JM, Chuang CF, Chang SM, Barani IJ, Jimenez B, Hess CP, et al. 7-tesla susceptibility-weighted imaging to assess the effects of radiotherapy on normal-appearing brain in patients with glioma. *Int J Radiat Oncol Biol Phys*. 2012;82:e493–500.
59. Maderwald S, Thurling M, Kuper M, Theysohn N, Muller O, Beck A, et al. Direct visualization of cerebellar nuclei in patients with focal cerebellar lesions and its application for lesion-symptom mapping. *Neuroimage*. 2012;63:1421–31.
60. Maugans TA, Farley C, Altaye M, Leach J, Cecil KM. Pediatric sports-related concussion produces cerebral blood flow alterations. *Pediatrics*. 2012;129:28–37.
61. Menon G, Patro SN, Krishnakumar K, Kesavadas C, Nair S, Radhakrishnan VV. Subfrontal gangliocytoma masquerading as olfactory groove meningioma. *Br J Neurosurg*. 2009;23:79–82.
62. Moenninghoff C, Kraff O, Maderwald S, Umutlu L, Theysohn JM, Ringelstein A, et al. Diffuse axonal injury at ultra-high field MRI. *PLoS One*. 2015;10, e0122329.
63. Moenninghoff C, Kraff O, Schlamann M, Ladd ME, Katsarava Z, Gizewski ER. Assessing a dysplastic cerebellar gangliocytoma (Lhermitte-Duclos disease) with 7T MR imaging. *Korean J Radiol*. 2010;11:244–8.
64. Moenninghoff C, Maderwald S, Theysohn JM, Kraff O, Ladd ME, El Hindy N, et al. Imaging of adult astrocytic brain tumours with 7 T MRI: preliminary results. *Eur Radiol*. 2010;20:704–13.
65. Nishiguchi T, Iwakiri T, Hayasaki K, Ohsawa M, Yoneda T, Mitsuhashi Y, et al. Post-embolisation susceptibility changes in giant meningiomas: multiparametric histogram analysis using non-contrast-enhanced susceptibility-weighted PRESTO, diffusion-weighted and perfusion-weighted imaging. *Eur Radiol*. 2013;23:551–61.
66. Niwa T, de Vries LS, Benders MJ, Takahara T, Nikkels PG, Groenendaal F. Punctate white matter lesions in infants: new insights using susceptibility-weighted imaging. *Neuroradiology*. 2011;53:669–79.
67. Norden AD, Young GS, Setayesh K, Muzikansky A, Klufas R, Ross GL, et al. Bevacizumab for recurrent malignant gliomas: efficacy, toxicity, and patterns of recurrence. *Neurology*. 2008;70:779–87.
68. Nossek E, Bashat DB, Artzi M, Rosenberg K, Lichter I, Shtern O, et al. The role of advanced MR methods in the diagnosis of cerebral amyloidoma. *Amyloid*. 2009;16:94–8.
69. Park JH, Park SW, Kang SH, Nam TK, Min BK, Hwang SN. Detection of traumatic cerebral microbleeds by susceptibility-weighted image of MRI. *J Korean Neurosurg Soc*. 2009;46:365–9.
70. Park SM, Kim HS, Jahng GH, Ryu CW, Kim SY. Combination of high-resolution susceptibility-weighted imaging and the apparent diffusion coefficient: added value to brain tumour imaging and clinical feasibility of non-contrast MRI at 3 T. *Br J Radiol*. 2010;83:466–75.
71. Peters S, Pahl R, Claviez A, Jansen O. Detection of irreversible changes in susceptibility-weighted images after whole-brain irradiation of children. *Neuroradiology*. 2013;55:853–9.
72. Peters S, Knoss N, Wodarg F, Cnyrim C, Jansen O. Glioblastomas vs. lymphomas: more diagnostic certainty by using susceptibility-weighted imaging (SWI). *Röfo*. 2012;184:713–8.
73. Pinker K, Noebauer-Huhmann IM, Stavrou I, Hoeffberger R, Szomolanyi P, Karanikas G, et al. High-resolution contrast-enhanced, susceptibility-weighted MR imaging at 3T in patients with brain tumors: correlation with positron-emission tomography and histopathologic findings. *AJNR Am J Neuroradiol*. 2007;28:1280–6.
74. Radbruch A, Graf M, Kramp L, Wiestler B, Floca R, Baumer P, et al. Differentiation of brain metastases by percentage-wise quantification of intratumoral-susceptibility-signals at 3Tesla. *Eur J Radiol*. 2012;81:4064–8.
75. Reichenbach JR, Venkatesan R, Schillinger DJ, Kido DK, Haacke EM. Small vessels in the human brain: MR venography with deoxyhemoglobin as an intrinsic contrast agent. *Radiology*. 1997;204:272–7.
76. Russo C. Brightness progressive normalization. 2012. Webpage: http://www.fractal-lab.org/Downloads/bpn_algorithm.html. Accessed on Feb 2016.

77. Schweser F, Deistung A, Lehr BW, Reichenbach JR. Differentiation between diamagnetic and paramagnetic cerebral lesions based on magnetic susceptibility mapping. *Med Phys.* 2010;37:5165–78.
78. Sehgal V, Delproposto Z, Haddar D, Haacke EM, Sloan AE, Zamorano LJ, et al. Susceptibility-weighted imaging to visualize blood products and improve tumor contrast in the study of brain masses. *J Magn Reson Imaging.* 2006;24:41–51.
79. Sigmund GA, Tong KA, Nickerson JP, Wall CJ, Oyoyo U, Ashwal S. Multimodality comparison of neuroimaging in pediatric traumatic brain injury. *Pediatr Neurol.* 2007;36:217–26.
80. Sorensen AG, Batchelor TT, Zhang WT, Chen PJ, Yeo P, Wang M, et al. A “vascular normalization index” as potential mechanistic biomarker to predict survival after a single dose of cediranib in recurrent glioblastoma patients. *Cancer Res.* 2009;69:5296–300.
81. Spitz G, Maller JJ, Ng A, O’Sullivan R, Ferris NJ, Ponsford JL. Detecting lesions after traumatic brain injury using susceptibility weighted imaging: a comparison with fluid-attenuated inversion recovery and correlation with clinical outcome. *J Neurotrauma.* 2013;30:2038–50.
82. Toh CH, Wei KC, Chang CN, Hsu PW, Wong HF, Ng SH, et al. Differentiation of pyogenic brain abscesses from necrotic glioblastomas with use of susceptibility-weighted imaging. *AJNR Am J Neuroradiol.* 2012;33:1534–8.
83. Tong KA, Ashwal S, Holshouser BA, Nickerson JP, Wall CJ, Shutter LA, et al. Diffuse axonal injury in children: clinical correlation with hemorrhagic lesions. *Ann Neurol.* 2004;56:36–50.
84. Tong KA, Ashwal S, Holshouser BA, Shutter LA, Herigault G, Haacke EM, et al. Hemorrhagic shearing lesions in children and adolescents with posttraumatic diffuse axonal injury: improved detection and initial results. *Radiology.* 2003;227:332–9.
85. Toth A, Kovacs N, Perlaki G, Orsi G, Aradi M, Komaromy H, et al. Multi-modal magnetic resonance imaging in the acute and sub-acute phase of mild traumatic brain injury: can we see the difference? *J Neurotrauma.* 2013;30:2–10.
86. Vossough A, Ziai P, Chatzkel JA. Red nucleus degeneration in hypertrophic olivary degeneration after pediatric posterior fossa tumor resection: use of susceptibility-weighted imaging (SWI). *Pediatr Radiol.* 2012;42:481–5.
87. Wang M, Dai Y, Han Y, Haacke EM, Dai J, Shi D. Susceptibility weighted imaging in detecting hemorrhage in acute cervical spinal cord injury. *Magn Reson Imaging.* 2011;29:365–73.
88. Wiczorek-Pastusiak J, Kocinski M, Razniewski M, Strzelecki M, Stefanczyk L, Majos A. An attempt toward objective assessment of brain tumor vascularization using susceptibility weighted imaging and dedicated computer program – a preliminary study. *Pol J Radiol.* 2013;78:50–6.
89. Wu Z, Li S, Lei J, An D, Haacke EM. Evaluation of traumatic subarachnoid hemorrhage using susceptibility-weighted imaging. *AJNR Am J Neuroradiol.* 2010;31:1302–10.
90. Wu Z, Mittal S, Kish K, Yu Y, Hu J, Haacke EM. Identification of calcification with MRI using susceptibility-weighted imaging: a case study. *J Magn Reson Imaging.* 2009;29:177–82.
91. Yamada N, Imakita S, Sakuma T, Takamiya M. Intracranial calcification on gradient-echo phase image: depiction of diamagnetic susceptibility. *Radiology.* 1996;198:171–8.
92. Zeng QS, Kang XS, Li CF, Zhou GY. Detection of hemorrhagic hypointense foci in radiation injury region using susceptibility-weighted imaging. *Acta Radiol.* 2011;52:115–9.
93. Zhang W, Zhao J, Guo D, Zhong W, Shu J, Luo Y. Application of susceptibility weighted imaging in revealing intratumoral blood products and grading gliomas. *J Radiol.* 2010;91:485–90.
94. Zhu Y, Yan H. Computerized tumor boundary detection using a hopfield neural network. *IEEE Trans Med Imaging.* 1997;16:55–67.
95. Zook JM, Iftekharruddin KM. Statistical analysis of fractal-based brain tumor detection algorithms. *Magn Reson Imaging.* 2005;23:671–8.
96. Zulfiqar M, Dumrongpisutikul N, Intrapromkul J, Yousem DM. Detection of intratumoral calcification in oligodendrogliomas by susceptibility-weighted MR imaging. *AJNR Am J Neuroradiol.* 2012;33:858–64.

Chapter 21

Texture Estimation for Abnormal Tissue Segmentation in Brain MRI

Syed M.S. Reza, Atiq Islam, and Khan M. Iftekharuddin

Abstract This chapter discusses multi-fractal texture estimation and characterization of brain lesions (necrosis, edema, enhanced tumor, non-enhanced tumor, etc.) in magnetic resonance (MR) images. This work formulates the complex texture of tumor in MR images using a stochastic model known as multi-fractional Brownian motion (mBm). Mathematical derivations of the mBm model and corresponding algorithm to extract the spatially varying multi-fractal texture feature are discussed. Extracted multi-fractal texture feature is fused with other effective features to enhance the tissue characteristics. Segmentation of the tissues is performed by using a feature-based classification method. The efficacy of the mBm texture feature in segmenting different abnormal tissues is demonstrated using a large-scale publicly available clinical dataset. Experimental results and performance of the methods confirm the efficacy of the proposed technique in an automatic segmentation of abnormal tissues in multimodal (T_1 , T_2 , Flair, and $T_{1\text{contrast}}$) brain MRIs.

Keywords Brain tumor • Segmentation • Texture feature • Lesion • Classification • Multi-modal MR.

21.1 Introduction

Brain tumor segmentation in MR image is clinically significant for tumor diagnosis and grading, therapy, medication dose selection, surgery, and patient follow-up. Manual delineation of lesions by radiologists for large volumes is tedious, error-prone, and often suffers from variability. Therefore, robust tumor volume segmentation as

S.M.S. Reza (✉) • K.M. Iftekharuddin
Vision Lab, Department of Electrical and Computer Engineering,
Old Dominion University, Norfolk, VA 23529, USA
e-mail: sreza002@odu.edu; kiftekha@odu.edu

A. Islam
Applied Research, Ebay Inc, San Jose, CA 95125, USA
e-mail: atislam@ebay.com

well as classification of different tumor tissues such as active tumor (enhanced and non-enhanced), necrosis, and edema are required. However, automatic segmentation of brain tumor and other abnormal tissues is a challenging task in medical image analysis due to the unpredictable appearance of these different tissues and their abnormal infiltrations among healthy tissues, variations in intensity, shape, size, and location in the MRI. The problem is further complicated by the MR artifacts, for example, intensity inhomogeneity, bias in the magnetic field, and noise in the signals.

Many different automatic brain tumor segmentation techniques proposed in the literature are based on either features or atlas-dependent registration or a combination of both. Since our developed texture-based tumor segmentation method is a feature-based method [24], we briefly provide a literature review on recent feature-based techniques. Among the recent feature-based techniques, Lee et al. [11] propose support vector machine (SVM)-based discriminative random fields (DRFs) with a set of multi-scale image and spatial alignment-driven features, spatial probabilities of normal tissues (white matter, gray matter, cerebrospinal fluid), spatial expected intensity maps, and left-to-right symmetry characteristics. However, the method does not allow training and inter-patient testing across the different patients. Corso et al. [5] use the conditional random field (CRF) to model cascade of boosted discriminative classifier. Popuri et al. [22] study Dirichlet-priors, Gabor-like texton [12], and the level set features to build statistical models for brain tissues. However, level sets techniques are very sensitive to initialization and tend to suffer from boundary leaking problems. Zikic et al. [27] use spatial nonlocal features and initial probabilities with the classification forest (CF) to segment the brain tumor. Bauer et al. [3] integrate random forest (RF) classification with hierarchical CRF regularization in an energy minimization scheme. In [7], Geremia et al. introduce a symmetry feature and use discriminative random decision forest for voxel-wise classification of tumor voxels. Tustison et al. [26] use Gaussian mixture model (GMM) and maximum a priori estimation with Markov random fields (MAP-MRF) to generate connected component-based geometric features for brain tumor classification. Meier et al. in [17] extend the discriminative model [3] to a generative-discriminative hybrid model which generates initial tissue probabilities for enhancing the classification and spatial regularization. The authors extract 44 features including first-order texture, gradient information, symmetry features, and seven voxel-wise tissue probabilities for brain tumor segmentation. Other important texture-based techniques are also found in the literature. Ghoneim et al. [15] have proposed a 3D co-occurrence matrix-based texture analysis to classify gliomas. However, they use a manually segmented volume of the region of interest. Pachai et al. [19] have shown a multi-resolution pyramid algorithm to segment multiple sclerosis lesions in brain MR image. Pitiot et al. [21] have presented a texture-based MR image segmentation approach with a novel combination of two-stage hybrid neural classifier.

However, none of the features used in the above techniques capture the multi-resolution spatially varying properties of the brain tissues. We argue that the complex structure of brain tumor in MRI may be more amenable to multi-scale spatially variable texture analysis such as piecewise triangular prism surface area (PTPSA) [24] and mBm [24]. The detailed multi-resolution analysis of fractal feature such as

mBm [9] enables capturing the randomly varying spatial tumor texture at different scales. In our prior works [2, 9, 24], we study the effectiveness of these features and feature selection methods for segmenting posterior-fossa tumor. In [9], we show that fractal feature-based technique is also efficient in segmenting different types of tumor such as medulloblastoma, astrocytoma, and low-grade gliomas. In [23, 24], we use these sophisticated texture features, fractal PTPSA and mBm along with intensity and intensity differences among the modalities to analyze multimodal MRI for characterizing the different abnormal and normal brain tissues.

21.2 Background Review

Different techniques mentioned in the previous section clearly indicate that extracting effective feature is one of the key factors for successful segmentation. Fractal-based spatially varying texture can be one of the effective features for the segmentation of abnormal brain tissues in MRI. This section briefly reviews relevant background about our proposed fractal-based texture fractal-PTPSA [8] and multi-resolution mBm texture modeling [9] and feature extraction. The detailed mathematical derivations of mBm can be found in [8, 9].

21.2.1 Fractal (PTPSA) Texture Feature Extraction

A fractal is an irregular geometric object with infinite nesting of a self-similar structure at multiple scales. The concept of the fractal is first proposed by Mandelbrot [16] to describe the geometry of the natural objects. The fractal dimension (FD) feature is a non-integer real number that characterizes the texture of objects. In a prior work [8], we investigate statistically the effectiveness of PTPSA feature for brain tumor detection. In PTPSA, the image is divided into several equal sub-images. For each sub-images (Fig. 21.1), the intensities of the four corners (I_1, I_2, I_3, I_4) and their average (I_c) at the center pixel form four triangles (ABE, ADE, DCE, BCE).

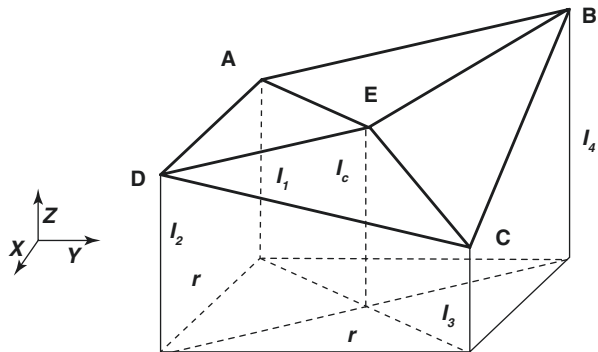


Fig. 21.1 Illustration of fractal PTPSA feature extraction for a sub-image [1]

The FD is calculated by the slope of the log-log plot of the total surface areas of the four triangles vs. sub-image size.

21.2.2 Multi-fractal Brownian Motion (mBm) Process and Feature Extraction

The mBm is a nonstationary zero-mean Gaussian random process that corresponds to the generalization of fractional Brownian motion (fBm). The fBm is a part of the set $1/f$ process and considered to be homogeneous or mono-fractal. The Hurst index (Holder exponent), H in fBm process, is same at all-time instances. The value of $H(0 < H < 1)$ determines the randomness of the fBm process, for example, if $H=0.01$, the signal is very rough, while for $H=0.99$, the signal is very smooth. Figure 21.2 shows an example of a simulated 1-D fBm process vs. time plots for different H values. The figure confirms variation of signal roughness with the variation of H values. However, like many other natural signals, the roughness of the tumor texture varies in space; therefore tumor texture is more amenable to multi-fractal structure. Consequently this work attempts to estimate tumor texture using the *mBm* process. In mBm process the Hurst index, H , is a time-varying parameter, which effectively captures the spatially varying heterogeneous texture of brain tissues.

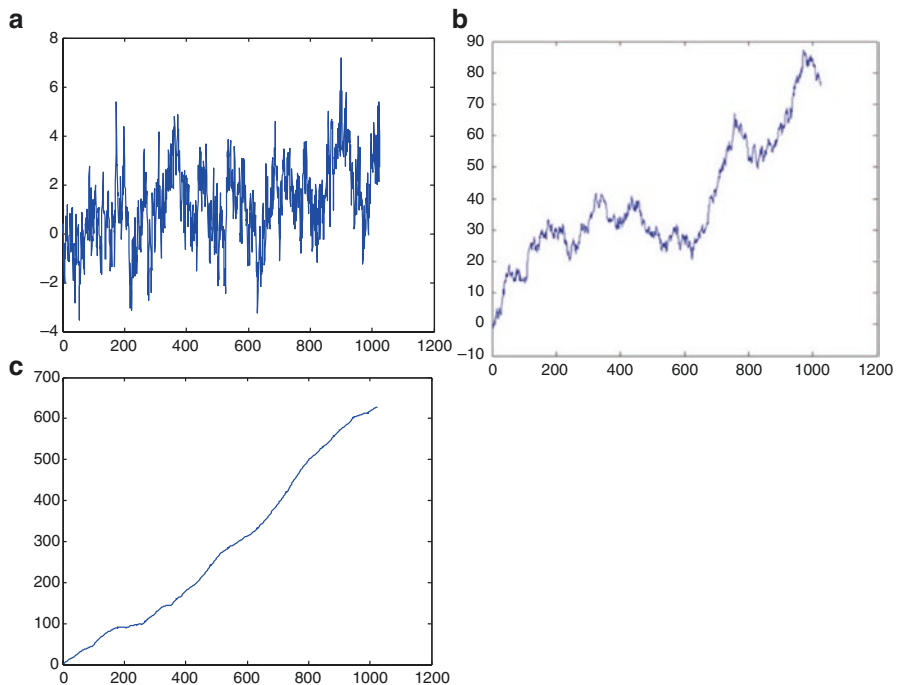


Fig. 21.2 Simulated 1-D fBm process with different H values: (a) $H=0.01$; (b) $H=0.5$; (c) $H=0.99$ [9]

The mBm process is defined as $x(at) = a^{H(t)}x(t)$, where $x(t)$ is the mBm process with a scaling factor, a , and the time-varying Hurst index, $H(t)$. The covariance function for a 2-D mBm process is given as

$$\gamma_z(\vec{u}, \vec{v}) = E(z(\vec{u})z(\vec{v})) = \frac{\sigma_u^2}{2} \left[|\vec{u}|^{2H(\vec{u})} + |\vec{v}|^{2H(\vec{v})} - |\vec{u} - \vec{v}|^{2H(\vec{u})} \right] \quad (21.1)$$

where $z(\vec{u})$ is the mBm process, \vec{u} denotes the vector position (u_x, u_y) of a point in the process, σ_u^2 is the variance, and $H(\vec{u})$ is the Hurst index for a 2-D signal. In order to estimate H from multi-scales, multi-resolution wavelet decomposition is used. After series of mathematical derivations, the expectation of the squared magnitude of wavelet coefficients $E\left\{|W_z(\vec{b}, a)|^2\right\}$ is given by

$$E\left\{|W_z(\vec{b}, a)|^2\right\} = \frac{1}{M+N} \sum_{x=0}^{N-1} \sum_{y=0}^{M-1} |W_z(\vec{b}, a)|^2 \quad (21.2)$$

where a and b is the scaling factor and 2D translation vector of the wavelet basis. Here, N and M are the dimensions of the image. The Hurst index for 2D image is calculated as follows:

$$2H(\vec{u}) = \lim_{a \rightarrow 0^+} \frac{\log\left(\left(\frac{1}{M+N}\right) \sum_{x=0}^{N-1} \sum_{y=0}^{M-1} |W_x(b, a)|^2\right)}{\log a} \quad (21.3)$$

Finally FD is obtained as

$$\text{FD} = E + 1 - H(u), \quad (21.4)$$

where E is the Euclidean dimension ($E=2$ for 2-D images).

For a given image we first divide the image into nonoverlapping blocks or sub-images and calculate the FD for that corresponding sub-image. The process is repeated for all the sub-images. The simplified algorithm for mBm texture feature extraction is shown in Fig. 21.3.

The detailed mathematical derivations of mBm and the description of the above algorithm shown in Fig. 21.3 for mBm texture feature can be found in [9].

21.3 Methodology

In this section, we describe our developed pipeline for abnormal brain tissue segmentation from the 3D MRI volume images (T1, T2, T1c, and Flair). Figure 21.4 shows the steps in the pipeline, which is the proposed method in our previous work

Algorithm 1: The mBm process computation for tissue texture extraction

MultiFD(*image*, *block_size*, *wavelet*, *level*)

image: $N \times M$ brain MRI

wavelet: Wavelet filter that verifies the usual admissibility criterion

level: The number of wavelet levels used to compute FD ($level > 1$)

1. For each block of size *block_size* from image do
 - a. For *a* in 1 to *level*
 - i. Compute the wavelet coefficients at scale *a*.
 - ii. Compute $E\{|W_z(\vec{b}, a)|^2\}$ as shown in (21.2)
 - b. Compute $H(\vec{u})$ from the linear regression of $\log(E\{|W_z(\vec{b}, a)|^2\})$ versus $\log(a)$ as shown in (21.3).
 - c. Compute FD in each image block as shown in (21.4):

$$FD = 2 + 1 - H(\vec{u})$$
2. end

Fig. 21.3 Algorithm for mBm texture feature extraction [9]

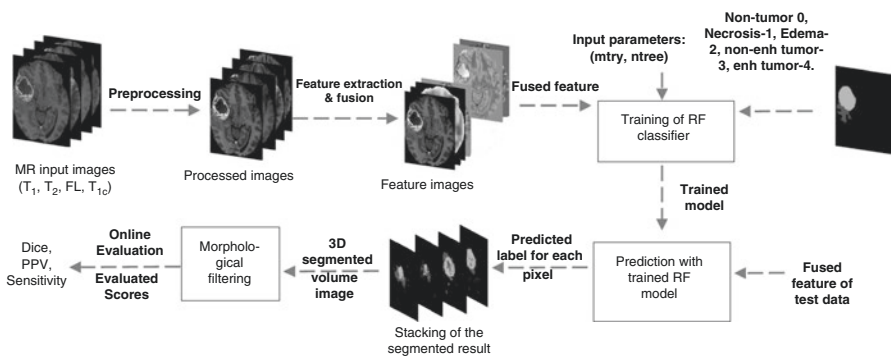


Fig. 21.4 Generic flow diagram of the proposed method [24]

[24]. The process starts with linear co-registration among the modalities, which reduces the alignment, rotation, and scaling mismatches. Then 2D MRI slices are obtained from 3D volume for subsequent processing. We briefly discuss each of the steps in Fig. 21.4 below.

21.3.1 Preprocessing

The preprocessing step involves aligning and co-registration among the channels, resampling, skull stripping, MR bias field, and intensity inhomogeneity correction. Co-registration is performed to correct the misalignment among the modalities and can be done with several tools such as SPM, ITK, and Slicer3D. MR bias field signal is a low-frequency and very smooth signal that blurs the image and reduces the high-frequency components from the images. Therefore, it is very important to reduce the bias field corrected and several techniques are found in literature. In this work, we perform MRI bias correction with N4ITK [25] MRI bias correction tool of Slicer3D. In order to minimize the intensity inhomogeneity of the MR image, intensity normalization is performed. The intensity normalization for MR images is very important because the intensity of the same tissue type can vary from patient to patient and even slice to slice of the same patient. Several MR intensity inhomogeneity correction techniques [10, 18] are available in literature. The intensity

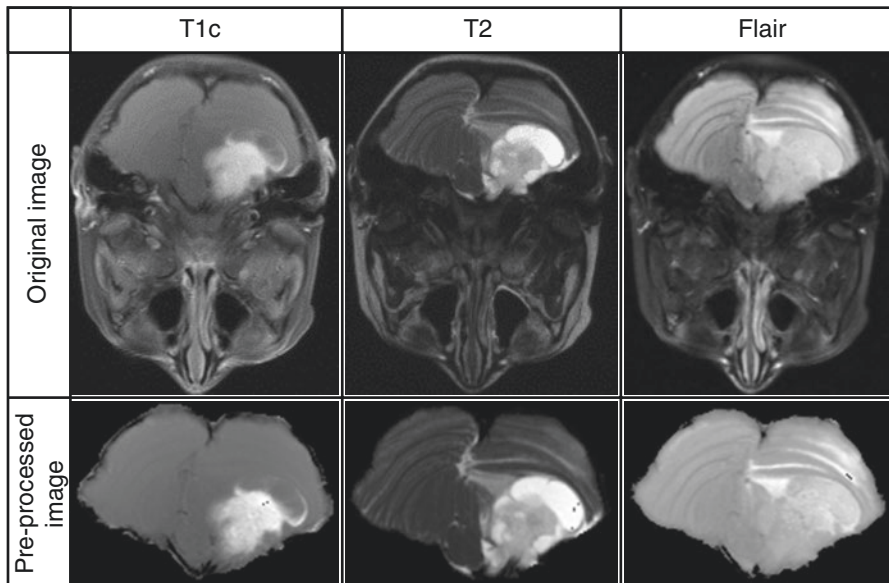


Fig. 21.5 Example images of original (*top row*) and preprocessed images (*bottom row*)

inhomogeneity correction method in [18] is a two-step normalization method [18], where the image histograms are modified such that the histograms match a mean histogram obtained using the training data. After inhomogeneity correction, the intensity values for the same tissue in different MR images fall into a single range of the scale. The method in [10] also comprises two steps. In the first step, 10-point histogram matching is performed, where the reference images of four modalities are an arbitrary set from a single patient data. Intensity values below the mean of the input volume are considered as the background pixel and excluded from the histogram matching process. Next step is normalizing all the intensity values around the mean intensity value of cerebrospinal fluid (CSF). In [10], two class classification (CSF vs. rest) is performed using the random forest to separate the CSF from the other tissues. We notice that simply threshold the intensity differences among the modalities gives a fair output to get the CSF mask. We take the histogram matched images, inhomogeneity corrected images, and this CSF mask as features. Figure 21.5 shows example images of original and preprocessed images.

21.3.2 Feature Extraction, Fusion, Ranking, and Selection

For each slice of the input images, we extract two primary sets of features such as nonlocal and spatial/texture:

- *Feature type 1 (nonlocal feature)*: The nonlocal features are the pixel intensities of four MRI modalities and corresponding differences of pixel intensities among the modalities. These features do not depend on the local texture patterns, and, thus, we named it as nonlocal features. We use the intensities (I_{T1} , I_{T2} , I_{F1} , I_{T1c}) and the intensity differences ($d_1 = I_{T1} - I_{T2}$, $d_2 = I_{T2} - I_{F1}$, $d_3 = I_{F1} - I_{T1c}$) to capture the global characteristics of different tissues. These different features (d_1 , d_2 , d_3) describe the amount of intensity variation at each pixel among the MR modalities. It is instinctive that different tissues (WM, GM, CSF, tumor-core, necrosis, and edema) may display a different amount of intensity variation among the modalities. A similar type of difference features is also used in [27].
- *Feature type 2 (spatial/texture feature)*: The spatial or texture features are those features that depend on the local texture pattern of an area. As the tumor is the uncontrolled growth of the tissues, it infiltrates into the surroundings and takes a different texture pattern which is expected to be different from the non-tumor region. In order to characterize the tumor surface variation, we employ our novel fractal texture features such as fractal PTPSA, mBm [1, 2, 9]. More details on our fractal texture features can be found in [2, 9]. We also use regular Gabor-like texton [12] since these features have an important association for image segmentation. Texton features are useful to decompose an image into its constituent components and reduce the redundant information. In general total 48 filters including 3-scales, 6-orientations, 2-phases, and 8-center-surround derivatives are used in texton feature extraction process. Instead of using all 48 texton filter's

outputs, we manually selected few filters which show visually significant differences among the abnormal and normal tissue regions.

- *Feature fusion:* After feature extraction from each corresponding slices, we perform feature domain fusion. Each row of resulting fused feature matrix represents all the feature values for a corresponding pixel location of the brain. To illustrate this fusion, let us consider each of the input image volumes are of size $V(= X \times Y \times Z)$, where X , Y , and Z indicate the number of row, column, and slices of an input image, respectively. For N_f number of features extracted, the 3D fused feature matrix will be of size $(N_r \times N_f \times Z)$, where $N_r(= X \times Y)$ is the number of rows in the feature matrix, N_f is the number of columns, and Z is the number of slices as usual.
- *Feature ranking and selection:* We know that all the features are not equally important and redundancy among the features degrades the classifier's performance. To identify the most useful features from the whole feature set, different feature ranking and selection methods are used. From the recent techniques, we use mutual information-based implementation of minimum redundancy maximum relevance (mRMR) [20] feature ranking technique. The method works in two steps. In the first step, it uses mutual information to search the maximum relevance between the individual feature and the class label. However, the features selected with the maximum relevance could have high redundancy among them, and it is intuitive that combination of these redundant features may have poor class-discriminating power. Therefore, in the second step, the method uses the minimal redundancy to select the mutually exclusive features. In this work, we perform the feature ranking on the whole feature set and then heuristically select 19 top-ranked features out of 38 features. Among all the features we noticed that the intensity, intensity differences, and the mBm features are in the top ranking list. This confirms the effectiveness of our novel texture features (mBm and PTPSA) in segmenting posterior-fossa brain tumor in our previous work [2, 9].

21.3.3 Classification with Random Forest

Random forest for classification which is also known as classification forest (CF) has a very fast and efficient multiclass handling capability. In this work, we use CF [4] for the tissue classification. The classification forests are ensembles of binary classification trees which are formed using randomly drawn data samples and features/predictors. This random selection of data samples and also the subset of feature/predictors help CF to perform robust classification compared to other classifiers such as support vector machines and neural networks. In CF classification method, each tree offers a classification/vote and for prediction the class with the maximum votes is assigned as the final label. Instead of voting, class probability may also be used. In that case, at each node n , classification tree randomly takes a subset of training samples X_n and predicts a class probability, $p_i^n(\Omega_i|x)$, where p_i is the probability of the sample x in class Ω_i . Depending on the feature dimension, CF randomly

resamples the training dataset at every node and assigns the partitions X_L and X_R to the left/right nodes. Tree growing continues up to a certain tree depth (D_T). In the testing phase, the overall probability is calculated as the average of all tree probabilities. Finally, the class with the highest probability is assigned as the actual class. More details about CFs can be found in [6].

In general, the classical random forests algorithm for both classification and regression starts with drawing the N_{tree} bootstrap samples from the training dataset which is the number of trees necessary for good predictions. Next step is to grow the classification trees for each bootstrap data sample where at each node, randomly sampled m_{try} predictors are chosen and the best split searched from the chosen predictors. Finally, for a new data sample, the predictions of all N_{tree} classification trees are collected and averaged for final output. Usually the parameters N_{tree} and m_{try} are fixed heuristically for the best performance. In our case, we gradually increase N_{tree} and m_{try} each at a time and observed the overall classification performance. After extensive investigation, we set $N_{\text{tree}}=100$ and $m_{\text{try}}=4$ in this work. The detailed description of the RF classifier's training and testing used in this work can be found in [13].

21.4 Results and Discussion

This section reports the segmentation results obtained from the predicted pixel labels of the RF classifier. These 2D abnormal tissue segments are then stacked to generate volume image. Figures 21.6 and 21.7 show example tissue segments using three slices taken from randomly chosen patients of training and test cases, respectively.

Evaluation: The following similarity coefficients are exploited to evaluate any of our segmentation performance:

1. Dice Coefficient = $2TP/(2TP+(FP+FN))$
2. Sensitivity = $\frac{TP}{TP + FN}$

where TP = true positive, FP = false positive, and FN = false negative. Three different categories such as complete tumor, tumor core, and other tissues are considered for the evaluation. The details on these three categories are as follows: complete tumor (1-necrosis, 2-edema, 3-non-enhancing tumor, 4-enhanced tumor), tumor core (3-non-enhanced tumor, 4-enhanced tumor), and individual tissues.

Quantitative Evaluation: We evaluate our preliminary abnormal tissue segmentation results using the BRATS-2013 [13] and BRATS-2014 [14] clinical dataset. BRATS-2013 dataset consists of multi-contrast MR scans from 65 glioma patients with low-grade (astrocytoma or oligoastrocytomas) and high-grade (anaplastic astrocytoma and glioblastoma multiforme) tumors. Similarly, BRATS-2014 dataset

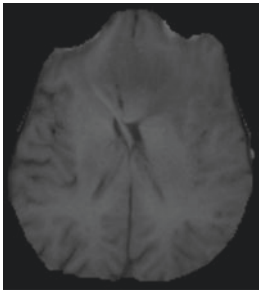
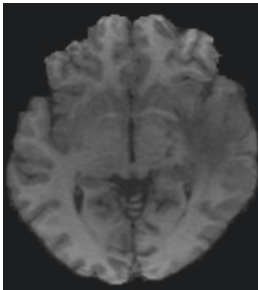
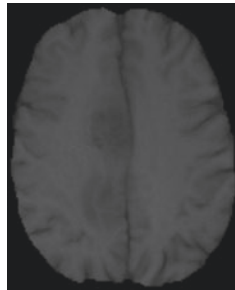
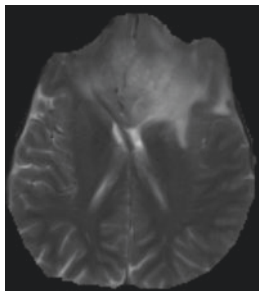
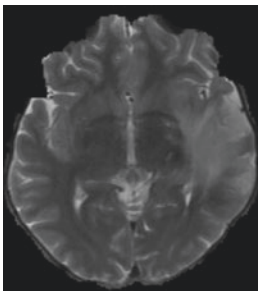
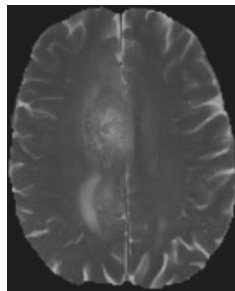
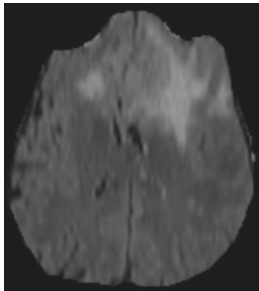
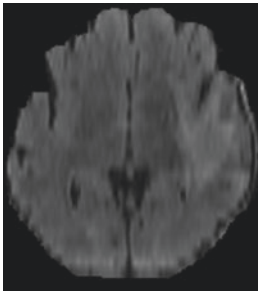
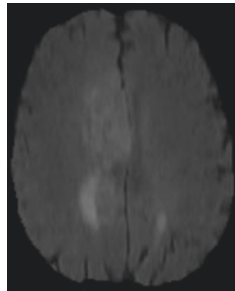
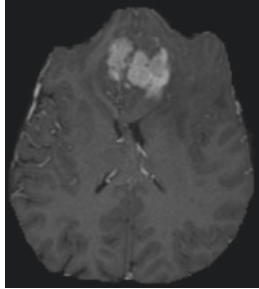
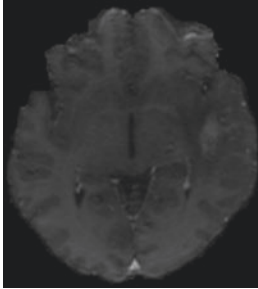
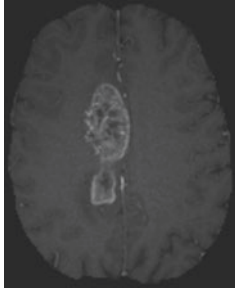
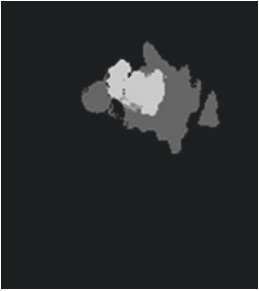
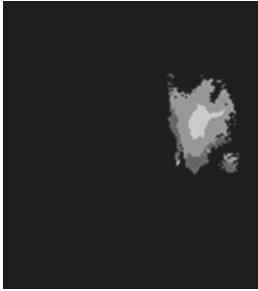




	Example image 1	Example image 2	Example image 3
T1			
T2			
Flair			
T1c			

Fig. 21.6 Segmented tissues with corresponding input and ground-truth images of three training patients. Each column represents an example set of multimodality MRI slices. Input: T1, T2, Flair, T1contrast. Output: segmented image and ground-truth. Labels in the ground-truth: 1-necrosis, 2-edema, 3-non-enhancing tumor, 4-enhancing tumor, 0-everything else

Fig. 21.6 (continued)

	Example image 1	Example image 2	Example image 3
Segmented image			
Ground Truth			

consists of 400 patients' images. We perform threefold within patient cross-validation on 213 training patients of BRATS-2014 dataset; the average scores using the proposed method are shown in Table 21.1. Our segmentation rate using threefold cross-validation varies: 73–87% using Dice overlap metric for tumor core and complete tumor, respectively. In low standard deviation, 8–24% indicates that the proposed method offers consistent results for different abnormal tissue segmentation.

The patient-wise cross-validation results using our algorithm in Table 21.1 suggest that one may obtain reasonably good results for any representative patient dataset. In order to measure the robustness of the method, we use the trained RF classifier with BRATS-2013 data and test on BRATS-2014 dataset. Quantitative scores of 213 training patients of BRATS-2014 with the proposed method (Fig. 21.4) are shown in Table 21.2.

Results in Table 21.2 shows that the Dice score varies from 63 to 76% using the proposed method, which is very promising. From the tissue-wise results, we notice that our texture-based method performs comparatively better for larger lesion size (edema and enhanced tumor), while for smaller lesions the performance is compromised. We realize that the interpolation method in the texture feature extraction process penalizes the detail of the smaller lesions, and thus the classification performance is less than satisfactory. Again from the patient-wise results, we notice that the proposed algorithm usually performs better for high-grade (HG) tumors than

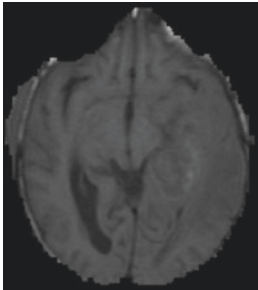
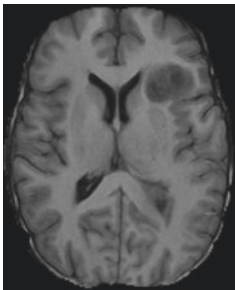
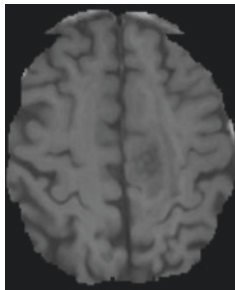
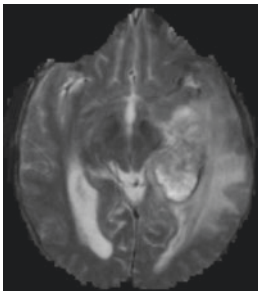
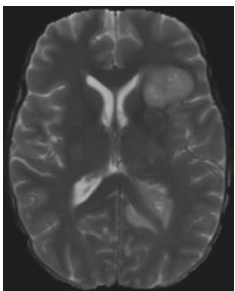
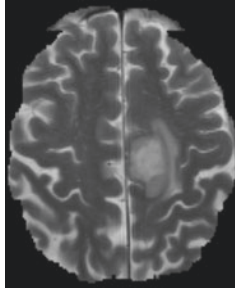
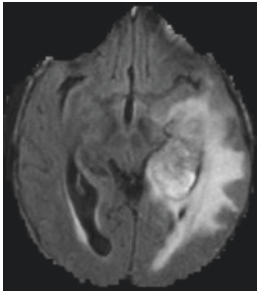
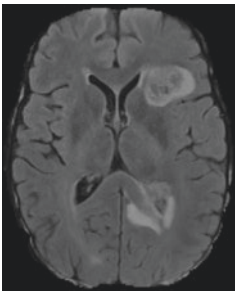
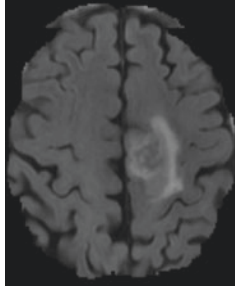
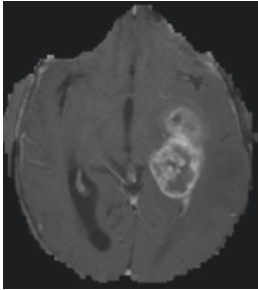
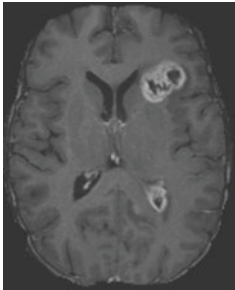
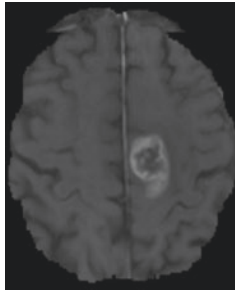
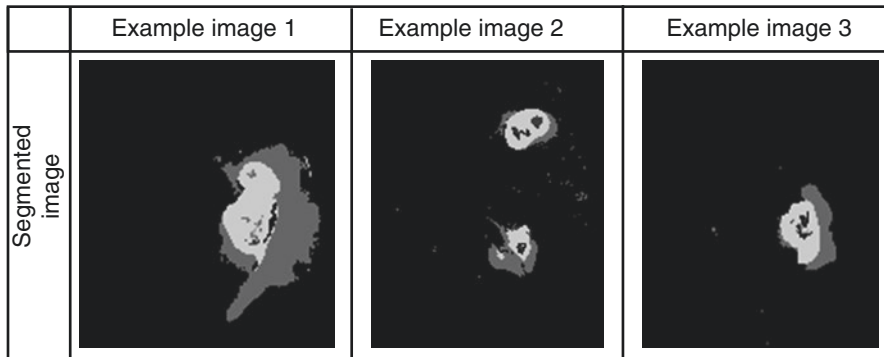
	Example image 1	Example image 2	Example image 3
T1			
T2			
Flair			
T1c			

Fig. 21.7 Segmented tissues with corresponding input and output images of three test patients. Each column represents an example set of multimodality MRI slices. Input: T1, T2, flair, T1contrast. Output: segmented image. Labels in the ground-truth: 1-necrosis, 2-edema, 3-non-enhancing tumor, 4-enhancing tumor, 0-everything else

Fig. 21.7 (continued)

low-grade (LG) tumors. Therefore, we observe that the MRI containing HG tumor surface may contain higher randomness in texture. In summary, the results in these tables show that our proposed method is effective in segmenting different grades of glioma tumors.

21.5 Conclusion and Future Work

In this chapter, we propose novel texture feature estimation technique using the fractal nature of the brain tissues. The extracted texture features in the MRIs are shown to be effective in discriminating the abnormal and normal brain tissues. The developed feature-based segmentation method is evaluated using a large-scale publicly available clinical dataset known as BRATS. Experimental results obtained with LG and HG patient data confirm the efficacy of our method for multiclass abnormal brain tissue segmentation. Our results also offer comparable brain tumor segmentation performance when compared to the other state-of-the-art works posted on the BRATS website [13]. The method offers comparatively higher Dice overlap score for larger size tumors in comparison with smaller ones. Further, substantial false positives in our detections and presence of anomaly in the segmented tumor core area compromise the overall performance. More investigation for the lesions with smaller size is required. Our future works include study of more effective features and sophisticated feature selection technique for improved brain tumor segmentation.

Table 21.1 Average tumor segmentation (threefold within patient cross-validation) results of 213 patients (BRATS-2014) using the proposed method

	Dice											
	Sensitivity					Sensitivity						
	Necrosis	Edema	Non-enh	Enhance	Core	Complete	Necrosis	Edema	Non-enh	Enhance	Core	Complete
Mean	0.42	0.76	0.13	0.74	0.73	0.87	0.72	0.80	0.09	0.84	0.72	0.89
Std.	0.30	0.13	0.13	0.23	0.24	0.08	0.34	0.15	0.11	0.21	0.26	0.09

Table 21.2 Average tumor segmentation results of 213 patients of BRATS-2014 using the proposed method. RF classifier is trained with 20 HG patients of BRATS-2013

	Dice											
	Sensitivity					Sensitivity						
	Necrosis	Edema	Non-enh	Enhance	Core	Complete	Necrosis	Edema	Non-enh	Enhance	Core	Complete
Mean	0.31	0.62	0.03	0.63	0.63	0.76	0.49	0.59	0.02	0.85	0.62	0.71
Std.	0.27	0.17	0.05	0.28	0.22	0.15	0.31	0.18	0.03	0.18	0.23	0.18

Acknowledgments This work is partially supported through a grant from NCI/NIH (R15CA115464). Brain tumor image data used in this work were obtained from the NCI-MICCAI BRATS 2012, 2013, and 2014 Challenge on Multimodal Brain Tumor Segmentation.

References

1. Ahmed S, Iftexharuddin KM, Ogg RJ, Laningham FH. Efficacy of texture, shape and intensity features for robust posterior-fossa tumor segmentation in MRI. *Proc SPIE Vol 2009* (vol. 7260. pp. 726020–1).
2. Ahmed S, Iftexharuddin KM, Vossough A. Efficacy of texture, shape, and intensity feature fusion for posterior-fossa tumor segmentation in MRI. *Inf Technol Biomed IEEE Trans on*. 2011;15(2):206–13.
3. Bauer S, Fejes T, Slotboom J, Wiest R, Nolte LP, Reyes M. Segmentation of brain tumor images based on integrated hierarchical classification and regularization. In *MICCAI BraTS Workshop*. Nice, France: Miccai Society 2012.
4. Breiman L. Random forests. *Mach Learn*. 2001;45(1):5–32.
5. Corso JJ, Yuille A, Sicotte NL, Toga AW. Detection and segmentation of pathological structures by the extended graph-shifts algorithm. In: *Medical image computing and computer-assisted intervention—MICCAI 2007*. Berlin: Springer; 2007. pp. 985–93.
6. Criminisi A, Shotton J. *Decision forests for computer vision and medical image analysis*. London: Springer Science & Business Media; 2013.
7. Geremia E, Menze BH, Ayache N. Spatial decision forest for glioma segmentation in multi-channel MRI. In *MICCAI BraTS Workshop*. Nice, France: Miccai Society 2012.
8. Iftexharuddin KM, Jia W, Marsh R. Fractal analysis of tumor in brain MR images. *Mach Vis Appl*. 2003;13(5–6):352–62.
9. Islam A, Reza S, Iftexharuddin KM. Multifractal texture estimation for detection and segmentation of brain tumors. *Biomed Eng IEEE Trans on*. 2013;60(11):3204–15.
10. Kleesiek J, Biller A, Urban G, Kothe U, Bendszus M, Hamprecht F. Ilastik for multi-modal brain tumor segmentation. *Proceedings of MICCAI 2013 Challenge on Multimodal Brain Tumor Segmentation (BRATS 2013)*, (2014). Boston, MA, USA.
11. Lee CH, Schmidt M, Murtha A, Bistriz A, Sander J, Greiner R. Segmenting brain tumors with conditional random fields and support vector machines. In: *Computer vision for biomedical image applications*. Berlin: Springer; 2005. p. 469–78.
12. Leung T, Malik J. Representing and recognizing the visual appearance of materials using three-dimensional textons. *Int J Comput Vis*. 2001;43(1):29–44.
13. Multimodal Brain Tumor Segmentation challenge 2013 (MICCAI-BRATS-2013). Available from <http://martinos.org/qtm/miccai2013/results.html>.
14. Multimodal Brain Tumor Segmentation challenge 2014 (MICCAI-BRATS-2014). Available from <https://sites.google.com/site/miccaibrats2014/>.
15. Mahmoud-Ghoneim D, Toussaint G, Constans JM, Jacques D. Three dimensional texture analysis in MRI: a preliminary evaluation in gliomas. *Magn Reson Imaging*. 2003;21(9):983–7.
16. Mandelbrot BB. *The fractal geometry of nature*. W.H. Freeman, New York, 1983.
17. Meier R, Bauer S, Slotboom J, Wiest R, Reyes M. A hybrid model for multimodal brain tumor segmentation. *Multimodal Brain Tumor Segmentation*. 2013;31, Nagoya, Japan.
18. Nyúl LG, Udupa JK, Zhang X. New variants of a method of MRI scale standardization. *Med Imaging IEEE Trans on*. 2000;19(2):143–50.
19. Pachai C, Zhu YM, Grimaud J, Hermier M, Dromigny-Badin A, Boudraa A, Gimenez G, Confavreux C, Froment JC. A pyramidal approach for automatic segmentation of multiple sclerosis lesions in brain MRI. *Comput Med Imaging Graph*. 1998;22(5):399–408.

20. Peng H, Long F, Ding C. Feature selection based on mutual information criteria of max-dependency, max-relevance, and min-redundancy. *Patterns Anal Mach Intell IEEE Trans on*. 2005;27(8):1226–38.
21. Pitiot A, Toga AW, Ayache N, Thompson P. Texture based MRI segmentation with a two-stage hybrid neural classifier. In *Neural Networks, 2002. IJCNN'02. Proceedings of the 2002 International Joint Conference on Neural Networks*. Honolulu, Hawaii. 2002 (Vol. 3, pp. 2053–2058). IEEE.
22. Popuri K, Cobzas D, Murtha A, Jägersand M. 3D variational brain tumor segmentation using Dirichlet priors on a clustered feature set. *Int J Comput Assist Radiol Surg*. 2012;7(4):493–506.
23. Reza S, Iftekharuddin KM. Multi-class abnormal brain tissue segmentation using texture features. *Proc NCI-MICCAI BRATS*. 2013;1:38–42.
24. Reza S, Iftekharuddin KM. Multi-fractal texture features for brain tumor and edema segmentation. In: *SPIE medical imaging. International Society for Optics and Photonics*; 2014. pp. 903503–903503.
25. Tustison N, Gee J. N4ITK: Nick's N3 ITK implementation for MRI bias field correction. *Insight Journal*. 2009:30.
26. Tustison, N., Wintermark, M., Durst, C., Avants, B.: ANTs and Arboles. In: *Proceedings of MICCAI-BRATS*, pp. 47–50 (2013), Nagoya, Japan.
27. Zikic D, Glocker B, Konukoglu E, Shotton J, Criminisi A, Ye D, Demiralp C, Thomas OM, Das T, Jena R, Price SJ. Context-sensitive classification forests for segmentation of brain tumor tissues. In *Proc MICCAI-BRATS*. 2012, Nice, France.

Chapter 22

Tumor Growth in the Brain: Complexity and Fractality

Miguel Martín-Landrove, Antonio Brú, Antonio Rueda-Toicen, and Francisco Torres-Hoyos

Abstract Tumor growth is a complex process characterized by uncontrolled cell proliferation and invasion of neighboring tissues. The understanding of these phenomena is of vital importance to establish appropriate diagnosis and therapy strategies and starts with the evaluation of their complexity with suitable descriptors produced by scaling analysis. There has been considerable effort in the evaluation of fractal dimension as a suitable parameter to describe differences between normal and pathological tissues, and it has been used for brain tumor grading with great success. In the present work, several contributions, which exploit scaling analysis in the context of brain tumors, are reviewed. These include very promising results in tumor segmentation, grading, and therapy monitoring. Emphasis is done on scaling analysis techniques applicable to multifractal systems, proposing new descriptors to advance the understanding of tumor growth dynamics in brain. These techniques serve as a starting point to develop innovative practical growth models for therapy simulation and optimization, drug delivery, and the evaluation of related neurological disorders.

Miguel Martín-Landrove, Antonio Rueda-Toicen, and Francisco Torres-Hoyos, Members of the Physics and Mathematics in Biomedicine Consortium

M. Martín-Landrove (✉)

Centre for Molecular and Medical Physics, Faculty of Science,
Universidad Central de Venezuela, Caracas, Venezuela

Centre for Medical Visualization, National Institute for Bioengineering,
Universidad Central de Venezuela, Caracas, Venezuela
e-mail: mglmrtn@gmail.com

A. Brú

Department of Applied Mathematics, Universidad Complutense de Madrid, Madrid, Spain

A. Rueda-Toicen

Centre for Medical Visualization, National Institute for Bioengineering, Universidad Central de Venezuela, Caracas, Venezuela

Algorithmic Nature Group, LABORES for the Natural and Digital Sciences, Paris, France

F. Torres-Hoyos

Physics Department, Universidad de Córdoba, Córdoba, Colombia

Keywords Brain tumor • Fractals in biomedicine • Cancer • Fractal analysis • Tumor growth • Prognosis • Complex networks • Multifractal systems

22.1 Introduction

Tumors exhibit a complex and irregular geometry due to the uneven spatial distribution of their cells. This irregular geometry appears during their growth processes, and it is apparent in a tumor interface with its host, on a tumor vascular network, and even on a tumor's spatial diffusion through time. Fractal geometry provides a notion of dimension that characterizes these complex and irregular objects. In the case of brain tumors, medical imaging technology has been fundamental for the geometrical analysis and quantification of tumor lesions. Magnetic resonance imaging techniques with standard contrast enhancement, dynamic contrast enhancement, and susceptibility weighting give detailed geometrical information with excellent spatial resolution and quality. When applied to the central nervous system, the precise characterization of tumor geometry, in all of its complexity, makes an important contribution to the understanding of brain tumor pathology. This precise geometric characterization leads to new methods for tumor segmentation and tissue classification in enhanced contrast MRI [22–24], tumor grading [17, 23], and therapy monitoring [15, 23]. Parameters extracted from the complex tumor growth dynamics [1–6, 38, 55] can be used to validate tumor growth models [9, 27, 39, 52] for therapy simulation and prognosis [53]. Also, brain tumor complexity and neural brain complexities can be taken into account to produce models that estimate neurological implications of tumor resection [60] and neurological disorders [18, 21] due to the presence of brain tumors.

The sections in this document are organized as follows: first, we present a survey on the use of fractal capacity dimension, as estimated by the box-counting algorithm, to characterize tissue properties and assess tumor grading, perform therapy monitoring, and segment MR images of pathological brain tissue using texture analysis. Next, we present the use of a scaling analysis approach to estimate growth parameters extracted from tumor interface dynamics and their relation to fractal dimensions. Finally, some multifractal analysis techniques are discussed, e.g., a time-like series derived from a tumor interface's rugosity and its associated complex network analysis, which we present as a natural way to describe a tumor's complexity.

22.2 Fractal Dimension and Brain Tumors

Fractal dimension has been used to characterize morphological irregularities in cancer pathologies and to assess their grade and malignancy [50, 59]. In particular, it has been used to establish clear geometrical differences between normal, dysplastic,

and neoplastic tissues [32, 33]. In the case of brain tumors, fractal dimension, as box-counting or capacity dimension, has been used for tumor segmentation in brain images [22–24, 61], tumor grading [17, 23], and assessment of the effects of therapy [15, 23]. In these applications, magnetic resonance images with contrast enhancement [23], susceptibility-weighted MRI (which are known as SWI [15, 17]), and histological brain tumor specimens [11–14, 16] have been evaluated. The magnetic resonance imaging modalities used in these studies have high spatial resolution and provide a proper rendering of tumor lesion features.

Di Ieva et al. [17] estimated fractal capacity dimension on 7 Tesla susceptibility-weighted magnetic resonance images, SWI-MRI, for glioma tumor grading. Their results show a significant increasing trend ($p < 0.05$) of intratumoral SWI-MRI fractal dimension with tumor grade, i.e., 1.682 ± 0.278 for grade II, 2.018 ± 0.517 for grade III, and 2.247 ± 0.358 for grade IV gliomas with a statistical significance difference of $p = 0.013$ between grade II and grade IV gliomas (see Chap. 20). In a previous work [15], fractal capacity dimension was used to monitor the effects of antiangiogenic treatments. This was done on 7 T susceptibility-weighted magnetic resonance images, to evaluate in vivo the response to therapy. In this work, patients received antiangiogenic treatment with bevacizumab and recurrent lesions were tracked down during a 4-week period by estimating the fractal capacity dimension. The cases that were analyzed in [15] include three glioblastomas multiforme and one anaplastic astrocytoma. In the cases where the antiangiogenic treatment was effective, the fractal dimension remains a constant 2.40 or went down slightly (2.34–2.26). On the other hand, the failure of treatment could be identified by a small increase in fractal dimension (2.23–2.26) in the case of an anaplastic astrocytoma, or a very large increase (2.06–2.23) for a glioblastoma multiforme. Fractal dimension variations indicate the partial success of antiangiogenic therapy toward a normalization of tumor vasculature [26], i.e., a more ordered vascular state, or a failure, detected as an increment of the vascular disorder, expressed through this parameter. These results together [15, 17] suggest that fractal dimension estimation of 7 T SWI-MRI patterns can be used to qualitatively and quantitatively describe malignant brain tumors and their evolution during antiangiogenic therapy.

Fractal dimension was proposed by Gazit et al. [19] to account for a geometrical description of tumor vascular architecture [57] during tumor growth and regression. In a recent review, Di Ieva [11] proposed the use of different morphometric parameters to characterize brain tumor vascularity, categorizing them as Euclidean or fractal, being fractal dimension a more objective parameter than Euclidean morphometric parameters to assess tumor microvasculature. Applied to histological specimens of pituitary adenomas [12, 13], the microvascular fractal dimension was estimated as 1.42 ± 0.14 , compared to the estimated value for pituitary gland of 1.58 ± 0.10 . Furthermore, Di Ieva et al. [15] applied a fractal-based image analysis technique to quantify the microvasculature in histological specimens, which were classified according the World Health Organization, WHO [36], as grade II and III gliomas. The statistical analysis [16] showed the fractal-based indexes as the most discriminant parameters to describe the geometry of the microvessels. Box-counting

dimension was calculated locally, $lbcD$, for a scale range from 1 to 1,000 μm . Additionally, the microvascular fractal dimension, mvF_D , which is the fractal capacity dimension of the microvascular pattern for the whole specimen, in a scale range from 50 to 2,000 μm , was used to characterize the fractal geometry of the vascular network. Particularly in [16], the authors established a correlation between the angi-score assigned by a neuropathologist and the fractal-based variables, $lbcD$ and mvF_D , as a computer-assisted and fractal-based morphometric assessment of tumor microvasculature. The correlation was established as follows: 0, no clusters, 1.28 ± 0.11 ; 1, presence of clusters, 1.43 ± 0.09 ; and 2, very prominent clusters, 1.60 ± 0.07 (see also Chap. 24). Furthermore, the microvascular network complexity, expressed as the fractal dimension parameter, is correlated to the uptake of (11) C-methionine (MET) assessed by PET in glioblastoma multiforme [14]. In this work, patients with a previous MET PET study underwent a total resection of the brain tumor, yielding histological specimens that were stained with hematoxylin/eosin and analyzed by two neuropathologists to assess a diagnosis of grade IV glioblastoma multiforme. Histological specimens were used to evaluate fractal dimension according to the methods proposed [11–13, 16]. Results indicate that fractal dimension ranged between 1.19 and 1.77, with a mean value of 1.415 ± 0.225 , and the standardized uptake value for (11) C-methionine ranged between 1.30 and 5.30, with a statistically significant direct correlation ($p=0.02$) between these parameters.

Risser et al. [47] studied normal and tumorous three-dimensional (3D) microvascular networks in primate and rat brains and performed fractal and power spectrum analysis on high-resolution synchrotron tomography images. Scale invariant fractal properties appear in a range from 1.4 μm up to 40–65 μm for normal vascular networks. A wider range is expected for tumor vascular networks. Fractal dimension was estimated by two methods, box-counting and sandbox [54, 56]. In the sandbox method, N points are selected randomly over the structure, and for each point i the number of points inside a box of size r , $M_i(r)$ is calculated. Afterwards, the relationship between the average value of $M(r)$ and r is used to estimate the fractal capacity dimension. Box-counting fractal dimension for normal vascular networks range from 1.55 to 1.7, while sandbox fractal dimension ranges from 1.55 to 1.9. In the case of tumor vascular networks, the ranges are 1.9 to 2.2 (box-counting method) and 1.9 to 2.4 (sandbox method), showing a clear difference between normal and tumor vascular networks.

Iftekharuddin et al. [22–24] and Zook et al. [61] proposed three modified box-counting algorithms for fractal geometry analysis on contrast-enhanced MRI images which have been widely used for brain tumor detection and fractal dimension estimation. The most commonly used method, piecewise-threshold-box-counting (PTBC) [23], uses a threshold in the pixel intensity values. Other proposed methods are the improved piecewise-modified-box-counting (PMBC) and the piecewise-triangular-prism-surface-area (PTPSA) [23, 61]. In the proposed methods, pixel intensity is considered as a third dimension, making them very suitable for the fractal analysis of texture. In [22, 24] the authors proposed the modeling of the irregularities in the image texture through fractional Brownian motion, fBm, which was introduced by Mandelbrot et al. [37] and depends on a single parameter, the Hurst

exponent, H [37]. Once H is determined, fractal dimension can be easily estimated through the simple relationship $D_f = D_E + 1 - H$, where D_E is the Euclidean dimension of the space where the fractal structure is contained. The fBm has proven to be successful in modeling a variety of physical phenomena and non-stationary processes that share essential properties such as self-similarity, scale invariance, and fractal dimension. The authors [22, 24] developed a theoretical framework that combines wavelet analysis with multiresolution fBm to estimate fractal dimension. In [24] the authors proposed a feature extraction methodology based on the fusion, with a self-organizing map, of multiple fractal measures computed in the contrast-enhanced T₁, T₂, and FLAIR magnetic resonance imaging modalities. After this feature extraction, the authors use this information for the training of a supervised neural network that classifies image regions as tumorous or non-tumorous [24] (see also Chap. 21).

Fractal dimension can also be extracted from the tumor interface after performing an image segmentation process. Martín-Landrove et al. [38, 40], Pereira et al. [42], Quintana et al. [43], and Torres-Hoyos et al. [55] analyzed tumor interfaces extracted from contrast-enhanced magnetic resonance images and determined the fractal capacity dimension of the tumor interface. The analysis of a 3D tumor interface in brain tumor data is shown in Table 22.1, which includes data from The Cancer Imaging Archive [8] for high-grade gliomas and image databases for meningiomas. The analysis shown in Table 22.1 yields the result that fractal capacity dimension for glioblastoma multiforme is 2.11 ± 0.08 and for meningioma, 1.91 ± 0.06 . Recently, Smitha et al. [51] analyzed fluid attenuation inversion recovery (FLAIR) MR images and obtained variations in the fractal dimension of the tumor contours of low-grade gliomas, 1.243 ± 0.127 , and of high-grade gliomas, 1.338 ± 0.248 , with a statistical significance level of $p=0.04$.

Summarizing, the set of fractal dimensions, each one associated to a particular feature of the tumor lesion, e.g., contrast agent intensity, image texture, vascularity, and tumor interface, supply an adequate description to characterize the transitions from normal to dysplastic to neoplastic tissue [32, 33]. This description is of great help in diagnosis and therapy monitoring. Fractal capacity dimension is in general very easy to calculate by box-counting or sandbox algorithms, which makes it useful for its extended use in clinical applications and computer-aided diagnosis. However, fractal capacity dimension alone does not adequately describe multifractal systems [20, 34, 40, 54], so a more general approach to assess the complex behavior of cancer has to be addressed.

22.3 The Scaling Analysis Approach

Besides fractal dimension, there are other ways to describe the fractal geometry of a system. Many other exponents can be derived from the observed power-law behavior through scale transformations. Tumors are complex adaptive systems that can be characterized by dynamics similar to power-law behavior. The growth of

Table 22.1 In vivo results for the local roughness exponent, α_{loc}

Type	# Cases	α_{loc}
Glioblastoma ^b	107	0.89 ± 0.08
Grade I glioma ^b	19	0.81 ± 0.08
Grade II glioma ^b	11	0.86 ± 0.07
Grade III glioma ^b	7	0.86 ± 0.10
Metastasis ^a	47	0.81 ± 0.11
Vestibular schwannoma ^a	64	0.74 ± 0.10
Meningioma ^a	118	0.76 ± 0.08
Craniopharyngioma ^a	1	0.71
Pituitary adenoma ^a	9	0.76 ± 0.08
Space-occupying lesion ^a	42	0.80 ± 0.09

^aBenign tumor information was obtained by analyzing local image databases

^bGlioma and glioblastoma information was obtained through the image analysis of The Cancer Imaging Archive, National Cancer Institute [7, 8]

tumors, in both resected and in vitro samples, has been characterized using a combination of fractal and scaling analysis techniques [2–5, 26]. These studies have shown that tumor contours exhibit super-rough scaling dynamics described by the Family-Vicsek *ansatz* [29] at the local as well as the global level. As a consequence, the tumor interface can be parameterized by a local roughness exponent, α_{loc} , and also by a global roughness exponent, $\alpha > 1$ [2–5]. The local roughness exponent relates the scale-averaged width of the interface between tumor and host to the scale of growth given by the arc length l , exhibiting power-law behavior [2–5] for small l :

$$W(l, t) \sim l^{\alpha_{loc}} \tag{22.1}$$

with W given by [9]:

$$W(l, t) = \left\{ \frac{1}{l} \sum_{r_i \in l} [r_i(t) - r_{il}]^2 \right\}_L^{1/2} \tag{22.2}$$

where $\langle r_i \rangle_l$ represents the average radius, measured from the tumor center, over an interface segment of arc length l , and $\{*\}_L$ represents the average over all realizations (all possible arcs of length l) in the interface perimeter L , as shown in Fig. 22.1.

In relation to brain tumors, Brú et al. [2] report in vitro results on cellular line C6 of rat astrocyte glioma that yield the following set of exponents: $\alpha_{loc} = 0.87 \pm 0.05$, $\alpha = 1.5 \pm 0.1$, $z = 4.0 \pm 0.2$, $\beta = 0.375 \pm 0.03$, and $\beta^* = 0.15 \pm 0.05$. These results are consistent with a molecular beam epitaxy (MBE) growth model. The same fractal and scaling analysis has been applied to brain tumors in MRI with contrast enhancement [38, 55], both with 2D slice images [38] and 3D volumetric [55] images. For each case, the distribution of contrast within the tumors exhibit a clearly different

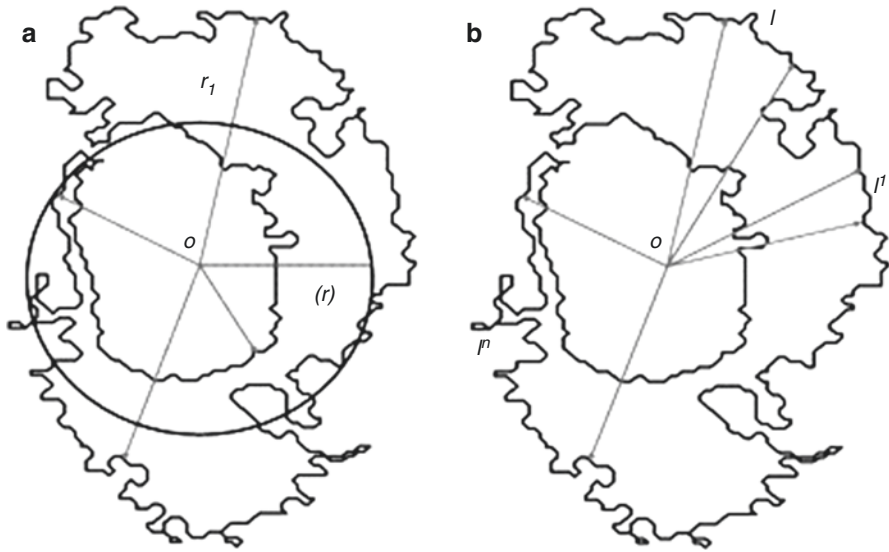


Fig. 22.1 (a) Average radii obtained over a tumor interface's contour. (b) Arc length for different scales

pattern for high-grade gliomas, such as glioblastomas, compared to benign tumors, e.g., acoustic neuroma (i.e., vestibular schwannomas), as depicted in Fig. 22.2.

Contrary to *in vitro* experiments, measurements *in vivo* for clinical applications can only yield a reduced set of exponents, due to missing information about the initial conditions of the tumor growth process. In this case, only α_{loc} and possibly α can be determined. Scaling analysis can be performed either on tumor contours in 2D slice images or tumor surfaces in 3D volumetric images. Scaling analysis of *in vivo* cases yields power-law behavior for small scale lengths (Fig. 22.3) similar to *in vitro* cases.

Moreover, if the growth process follows a dynamic scaling as described by the Family-Vicsek *ansatz* [29], fractal dimension and local roughness exponent are related in a general way [1, 29], i.e., their sum is equal to the embedding dimension of the shape, or Euclidean dimension:

$$\alpha_{\text{loc}} + d_f = d_E \quad (22.3)$$

This property provides a way of estimating the fractal dimension that doesn't depend on box-counting algorithms. It can also be used to double check measurements or even to discern the nature of the growth process, i.e., whether it follows the Family-Vicsek *ansatz* or not, suggesting a different kind of *ansatz*. Results from contrast-enhanced MRI obtained from multicenter databases are summarized in Table 22.1. In particular, big databases [41], such as The Cancer Imaging Archive [7, 8], allow for extensive statistical analysis. It is important to point out that the values of the local roughness exponent for Grade I through Grade III gliomas and

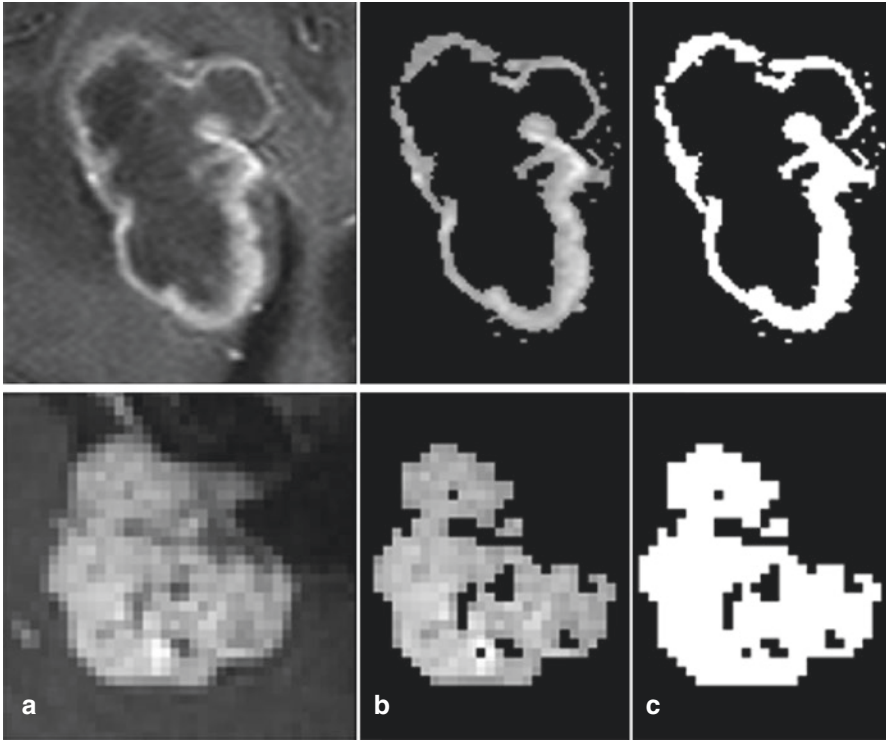


Fig. 22.2 Contrast distribution patterns: *top*, glioblastoma multiforme; *bottom*, vestibular schwannoma. (a) Contrast-enhanced MRI, (b) segmented image using the k-means clustering algorithm, showing original voxel intensity, and (c) binary image (mask) used for tumor interface delineation

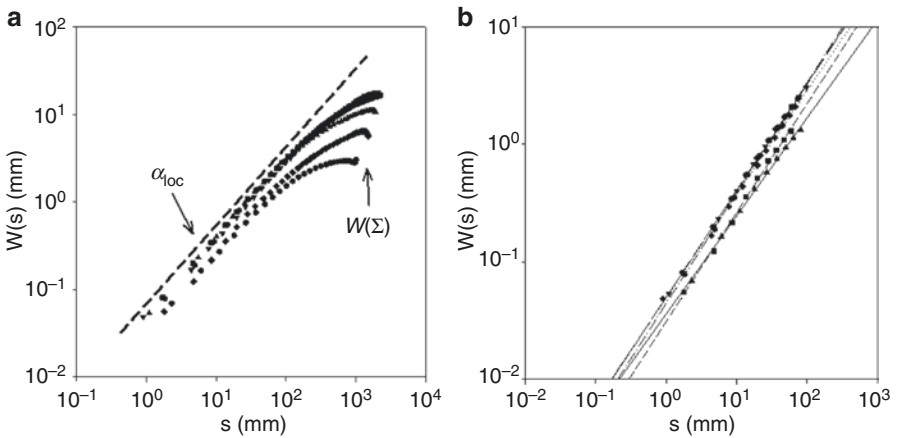


Fig. 22.3 (a) Typical log-log plot with power-law behavior at small scale length s , indicating exponent α_{loc} as the slope of the regression line, and the saturation values for large scale length, $W(\Sigma)$ where Σ denotes the size of the tumor. (b) Power-law behavior for high-grade glioma data, in this case a glioblastoma multiforme

glioblastoma are in correspondence to those obtained by Brú et al. [2] for the cellular line C6 of rat astrocyte glioma; also there seems to be a slight dependence of the local roughness exponent on tumor grade, and a significant difference with benign tumors, such as meningiomas and schwannomas. Metastases, which exhibit a great variability, possibly dependent on histological properties of primary tumors, have a mean α_{loc} similar to low-grade gliomas. Data in Table 22.1 are particularly abundant for glioblastoma and meningioma, so it is possible to obtain distributions of α_{loc} for these extreme types of brain tumors, as shown in Fig. 22.4. Also, the capacity or box-counting fractal dimension can be calculated to check if Eq. (22.3) holds. For the glioblastoma case, $\alpha_{loc} = 0.89 \pm 0.08$, $d_f = 2.11 \pm 0.08$, and $\alpha_{loc} + d_f = 3.00 \pm 0.13$, while the result for meningiomas is $\alpha_{loc} = 0.76 \pm 0.08$, $d_f = 1.91 \pm 0.06$, and $\alpha_{loc} + d_f = 2.67 \pm 0.11$. These results suggest that at least for these benign brain tumors, meningiomas, the dynamic scaling associated to the tumor growth process does not scale according to the Family-Vicsek *ansatz*, while definitively, glioblastomas do, a result consistent with what is qualitatively observed in the contrast distribution patterns shown in Fig. 22.2.

Also, from the analysis of Table 22.1, there is a correlation between tumor grade and local roughness exponent, α_{loc} , which can be used as a measure to estimate degree of malignity. In the case of metastases, even though they are not primary brain tumors, the analysis of their growth parameters could help advance the understanding of primary tumor growth behavior.

It is possible to obtain the roughness exponent α , which is related to the interface width, W , through the power-law behavior [1, 5, 29]:

$$W_{sat}(R) \sim R^\alpha \tag{22.4}$$

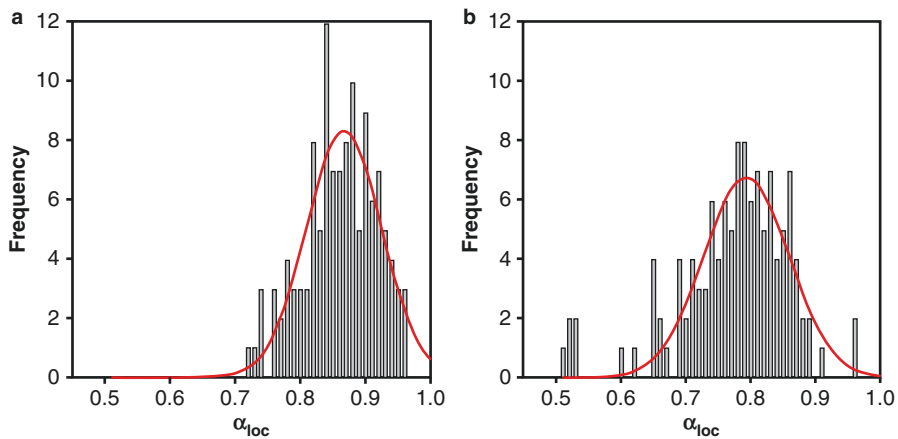


Fig. 22.4 Distributions of the local roughness exponent, α_{loc} for (a) glioblastoma multiforme and (b) meningioma. Red lines indicate a gaussian fit

where R is the mean radius of the tumor as a measure of its size, and it is assumed that for *in vivo* tumors, the saturation condition is attained, i.e., that the lateral correlation length for the interface fluctuations is comparable or larger than the size of the system [1, 29]. Results are shown in Fig. 22.5.

Summarizing, according to the results shown in Fig. 22.5, glioblastomas and metastases exhibit an exponent $\alpha > 1$, which corresponds to a super-rough dynamics for the tumor growth process, denoting the highly invasive character that's typical of malignant neoplastic tissue, which is characterized by high proliferation and diffusion to the tumor interface. On the other hand, for benign tumors such as meningiomas and acoustic schwannomas, the fact that the condition stated in Eq. (22.3) is not fulfilled, i.e., the dynamic scaling for the growth process is not of the Family-Vicsek type, and that $\alpha < 1$ indicates that the growth dynamics can be explained as a

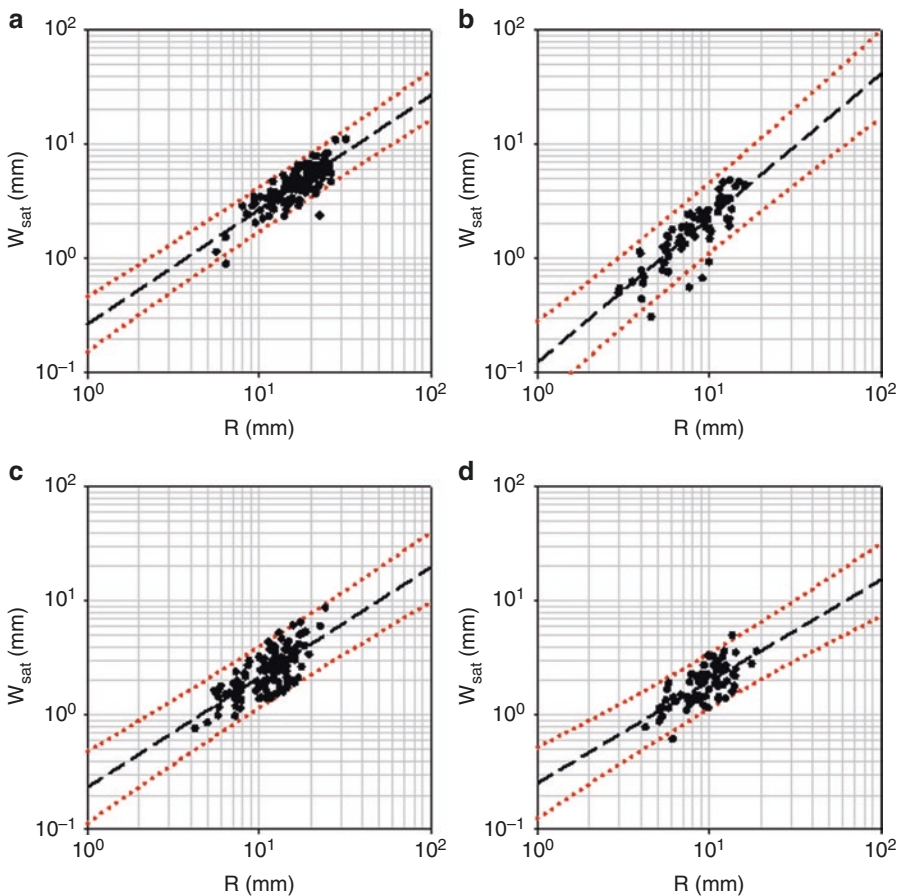


Fig. 22.5 Power-law behavior given by Eq. (22.4); (a) glioblastoma multiforme, $\alpha=1.002$, (b) metastasis, $\alpha=1.262$, (c) meningioma, $\alpha=0.963$, and (d) vestibular schwannoma, $\alpha=0.889$. Red lines represent prediction intervals

bulk proliferative process, with no diffusion to the tumor interface. As a conclusion, the analysis of different geometrical and growth parameters and their relationships brings forth a clearer picture of the tumor growth model, even for single event data, which is the common clinical situation. The availability of imaging data at different times, which is present in common clinical therapy follow up protocols, allows for the quantification of changes based in this new set of parameters, changing the overall growth model for the untreated tumor. For example, Brú et al. [4] demonstrated how tumor growth exponents and growth models are modified, when an immune response is considered. The changes in growth exponents could be suitable descriptors for therapy monitoring in radiotherapy, chemotherapy, or immunotherapy.

22.4 Data Time-Like Series, Visibility Graphs, and Complex Networks

Tumor classification has also been performed using more general definitions of the fractal dimension (such as the fractal correlation dimension) that are pertinent for multifractal systems [20, 34, 35, 54]. Multifractal analysis has established quantitative differences between malignant and benign brain tumors [40, 42, 43]. In most of these studies, the tumor interface is extracted from image data, and synthetic “time” series are created; multifractal analysis is then applied on these series. Martín-Landrove et al. [40] estimated fractal correlation dimension assuming a time-like series codified by Freeman’s chain code, obtaining a significant difference between malignant (1.05 ± 0.02) and benign tumors (1.12 ± 0.04). Quintana et al. [43] extracted the tumor interface by methods of adaptive deformable models, or snakes, and used the energy density functional to codify the synthetic time series. The authors obtained a significant difference in fractal correlation dimension between malignant (1.22 ± 0.10) and benign (1.10 ± 0.07) tumors.

Multifractal analysis has been recently used to generate texture descriptors and perform image segmentation [25, 45, 46]. Reza et al. [45, 46] used multi-fractional Brownian motion, mBm [25], and multifractal detrended fluctuation analysis, MF DFA [28], to classify brain tumors either as high-grade or low-grade gliomas [45] and for brain tumor and edema segmentation.

Brú et al. [6] have established a link between the evolution of complex networks and the dynamical processes that produce rough and fractal-like interfaces. The degree of the nodes in these networks change through time as the interface evolves. The application of this network methodology enables the uncovering of so-called “scale-free” temporal and geometric features that remain invariant as the interface grows. This invariance is detected in the degree distribution of a visibility graph derived from the contour.

This approach could possibly be used to understand tumor interface dynamics. The data set, formed by the distance from the center of mass of the tumor interface points at a given time, can be transformed into a graph by applying the visibility algorithm as defined by Lacasa et al. [30, 31]. The visibility graph seeks to capture the

geometrical correlations that exist among the discrete points that constitute the tumor interface. The general procedure is illustrated in Fig. 22.6. Initially, the cloud of points that belong to the tumor interface is determined by a segmentation algorithm. Afterwards, the radius for each interface point, as measured from the center of mass of the tumor lesion, is mapped on a two-dimensional array that registers the corresponding slice and angular position. Synthetic one-dimensional “time series” are constructed from this dataset; each of the pixels in the tumor’s contour becomes a node on the associated visibility graph, where the properties of the contour are encoded.

Among these properties is the connectivity of the visibility graph. This connectivity can be described by the simple counting of edges for each node in the network, this count is defined as the degree of a node. The result of this computation for all the nodes in the network is a distribution of degrees. If one considers this distribution as a probability distribution, $P(k)$, it represents how a particular node, i , selected randomly, is connected to exactly k nodes. Figure 22.7 shows preliminary results for $P(k)$ obtained from visibility networks extracted from tumor interface of malignant and benign brain tumors.

Brú et al. [6] established $P(k)$ for six different interface growth models, Edwards-Wilkinson (EW), Kardar-Parisi-Zhang (KPZ), random deposition (RD), random deposition with surface relaxation (RDSR), Eden, and molecular beam epitaxy (MBE), showing that the visibility network analysis leads to a fine discrimination of

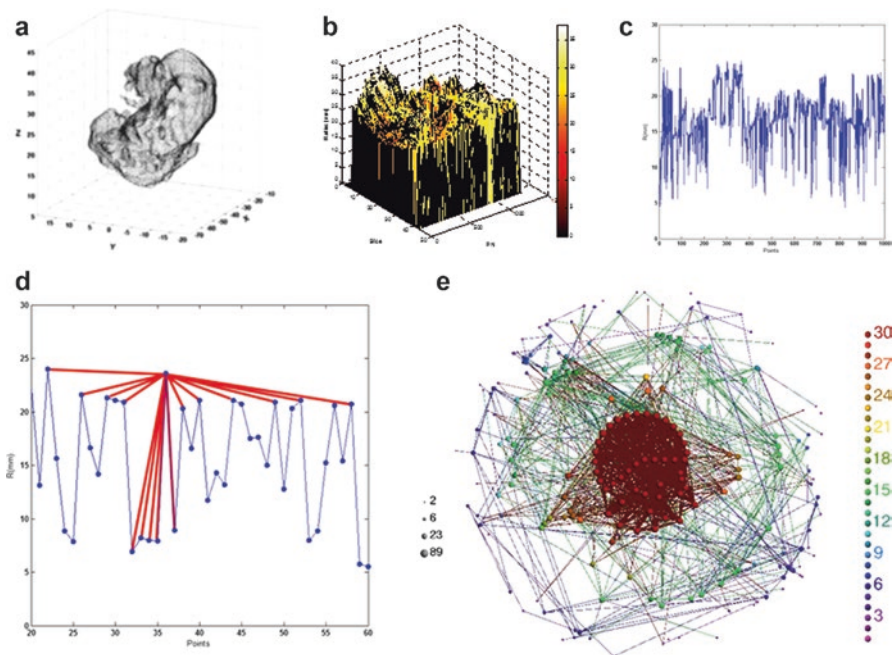


Fig. 22.6 (a) Cloud of points in the tumor interface. (b) Two-dimensional radii dataset. (c) One-dimensional “time series”. (d) Visibility graph. (e) Complex network analysis

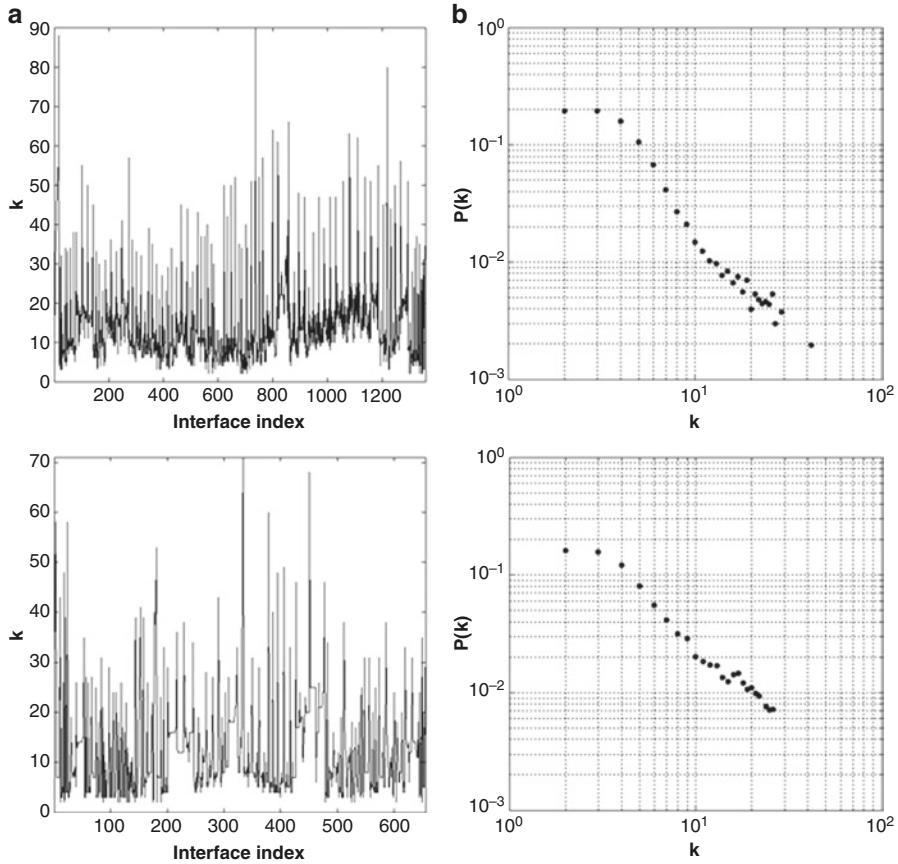


Fig. 22.7 Visibility graph analysis for 2D tumor interface. (a) Number of connections, k , between network points along a maximum interface contour, (b) degree probability distribution, $P(k)$. *Top* results are for glioblastoma multiforme, *bottom* for meningioma

growth dynamics and allows to discern the most convenient model to describe them. Consequently, in the application of this formalism [6], the differences observed in Fig. 22.7 between meningioma and glioblastoma multiforme can be used not only to estimate a parameter difference between the two conditions, e.g., an exponent in a power-law behavior of $P(k)$ but also to discriminate between different models that can be proposed for the tumor interface growth. Indeed, there are notorious differences for the exponent, i.e., -1.73 for benign brain tumors and -2.51 for glioblastoma multiforme, as can be seen by the average behavior in $P(k)$, shown in Fig. 22.8.

Moreover, the study of the morphology of the visibility network [30, 31] can be used to establish further differences and correlations between different growth models of the tumor interface. Rueda-Toicen et al. [49] proposed a method based on the traveling salesman problem to obtain the visibility network and corresponding graph. An example of this approach is shown in Fig. 22.9, where the visibility

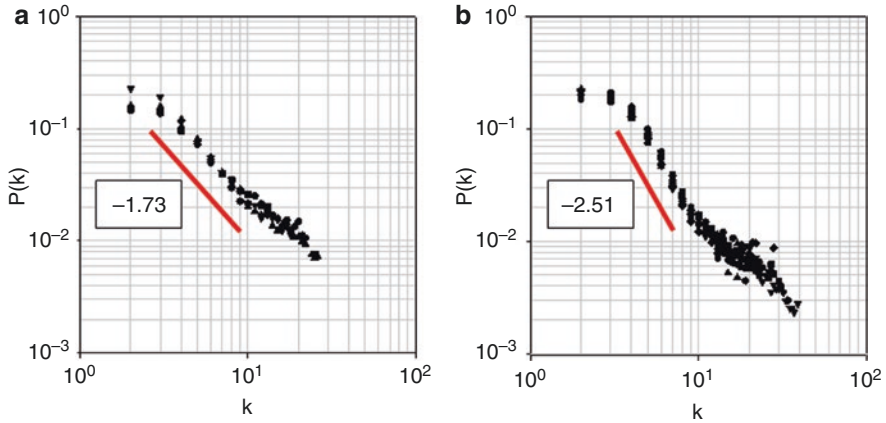


Fig. 22.8 Comparison of the degree probability distribution, $P(k)$, in different brain tumor groups, (a) benign tumors such as acoustic schwannomas and meningiomas, with a connectivity exponent of -1.73 , and (b) glioblastomas, with exponent -2.51

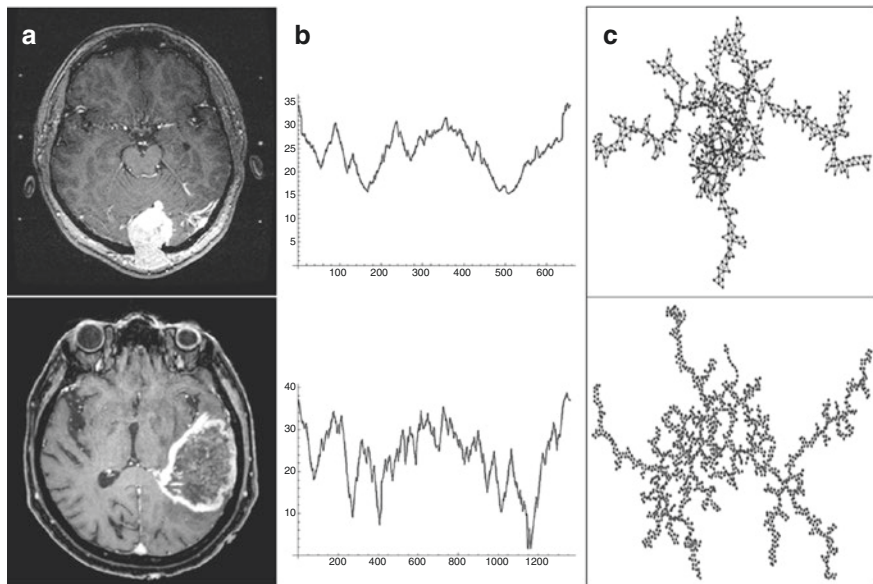


Fig. 22.9 Comparison of complex network analysis between meningioma, *top*, and glioblastoma multiforme, *bottom*. (a) Magnetic resonance images with contrast enhancement, (b) time-like series obtained using a solution of the travelling salesman problem for the points on the biggest contour in the tumor interface, and (c) the corresponding visibility graphs. Hurst exponents were estimated for the synthetic time series: glioblastoma multiforme, $H=0.92$, and meningioma, $H=0.90$. The datasets and *Mathematica* code used to generate the synthetic time series and their associated visibility graphs (shown here using a spring embedding) and estimate the Hurst exponent are available at [49]

network of the contour of a glioblastoma multiforme, a tumor with a characteristically high rugosity (Fig. 22.9c bottom), is shown next to the appreciably less complex visibility network of a meningioma (Fig. 22.9c top), a tumor with a smoother contour. The analysis of the generated time-like series can also be used to estimate generalized fractal dimensions and singularity exponents [20, 44, 48, 56].

22.5 Conclusions and Future Prospects

Fractal analysis applied to brain tumor lesions has permitted quantitative tissue characterization, tumor grading, and the quantification of changes in vascularity associated to cancer pathologies. Nevertheless, in most of the known applications, fractal capacity dimension is the sole descriptor used to account for the complexity associated to the tumor lesion and is estimated by the box-counting algorithm or through a limited use of the sandbox algorithm. This analysis is usually performed in a scale range for which auto similar and auto affine scaling properties of the system are evident [35]. Moreover, estimation of fractal dimensions depends strongly on the size and resolution of the data, restricting its application to particular image acquisition protocols of difficult implementation in clinical routine. In order to further advance in the understanding of tumor complexity, it is necessary to study other possible descriptors, such as generalized fractal dimensions [44, 56] and singularity exponents [20, 48], and the corresponding relationships among them. To fulfill this task, cancer detection methods must use higher resolution medical images, to extend somewhat the scale range and size of the data. The definition of physical parameters, obtained through the integration of information of different imaging modalities, which could act as suitable biomarkers for fractal analysis, is also highly relevant. Even though the complex dynamics of tumor growth requires a profound and extensive analysis to describe them appropriately, fractal capacity dimension has proven to be a fine and effective descriptor to establish differences between tissue properties through the transition from normal to neoplastic tissue, making it suitable to be incorporated in clinical protocols and medical decisions.

Cancer therapy often damages healthy cells and tissues and then side effects are common. The successful planning of treatments, like radiosurgery or chemotherapy with high precision and high sensitivity, has the benefit of reducing negative side effects on the patient, while producing the desirable outcome of eliminating as much of the neoplasm as possible. A correct characterization of tumors is essential to achieve optimal treatment planning. A pervasive problem in oncology is that traditional treatment planning disregards the individual evolution of a patient's tumor, applying the maximum tolerable dose of radiation or chemotherapy on a fixed regular schedule. It has been shown that individualized treatment plans that consider the evolution of a patient's tumor can help in the reduction of the dosage of radiation or chemicals and the application of "correct" models [9, 27, 39, 52, 53] (correct in the sense that these models have appropriate dynamical parameters and scaling behavior) is of major importance. Thus, the accurate modeling of tumor

growth can help in the production of clearer prognoses and better informed treatment choices.

Finally, the proposal of new descriptive methods based on scaling and multifractal analysis, time-like series, and complex networks opens a vast set of future possibilities. As an example of this, the analysis of results in Table 22.1 suggests that a relationship between tumor grade and the local roughness exponent, α_{loc} , can be established with potential applications in methods for tumor diagnosis and classification. Also, the analysis of complex networks associated to time-like series derived from tumor features and shown in Figs. 22.7, 22.8, and 22.9 is very promising. As frequently occurs in natural phenomena, the geometrical nature of tumors is multifractal. The scaling analysis performed on them must account for this fact and be done in a rigorous manner, to determine relevant fractal dimensions and power-law behaviors. Recently, the goodness of fit of power-law distributions to empirical data has been called into question [10, 58], and the use of modern statistical techniques has shown that many datasets commonly described as power laws are best fitted by log-normal or exponential distributions. Even though the scaling analysis techniques mentioned in this survey have shown descriptive and discriminative power, the use of other probability distributions to describe and predict the growth of tumors in the brain must also be considered. Such an approach will benefit the understanding of tumor growth and, as a consequence, improve diagnosis and therapy.

References

1. Barabasi AL, Stanley HE. Fractal concepts in surface growth. Cambridge, UK: Cambridge University Press; 1995.
2. Brú A, Pastor JM, Fernaud I, Bru I, Melle S, Berenguer C. Super-rough dynamics on tumor growth. *Phys Rev Lett*. 1998;81:4008–11.
3. Brú A, Albertos S, López JA, Brú I. The universal dynamics of tumor growth. *Biophys J*. 2003;85:2948–61.
4. Brú A, Albertos S, López García-Asenjo JA, Brú I. Pinning of tumoral growth by enhancement of the immune response. *Phys Rev Lett*. 2004;92(23):238101-1, 238101-4.
5. Brú A, Casero D, de Franciscis S, Herrero MA. Fractal analysis and tumor growth. *Math Comput Model*. 2008;47:546–59.
6. Brú A, Alós E, Nuño JC, Fernández de Dios M. Scaling in complex systems: a link between the dynamics of networks and growing interfaces. *Sci Rep*. 2014;4:7550. 1–7.
7. Chang H, Fontenay GV, Han J, Cong G, Baehner FL, Gray JW, Spellman PT, Parvin B. Morphometric analysis of TCGA glioblastoma multiforme. *BMC Bioinforma*. 2011;12:484–95.
8. Clark K, Vendt B, Smith K, Freymann J, Kirby J, Koppel P, Moore S, Phillips S, Maffitt D, Pringle M, Tarbox L, Prior F. The Cancer Imaging Archive (TCIA): maintaining and operating a public information repository. *J Digit Imaging*. 2013;26(6):1045–57.
9. Clatz O, Sermesant M, Bondiau P-Y, Delingette H, Warfield SK, Malandain G, Ayache N. Realistic simulation of the 3-D growth of brain tumors in MR Images coupling diffusion with biomechanical deformation. *IEEE Trans Med Imaging*. 2005;24(10):1334–46.
10. Clauset A, Shalizi CM, Newman MEJ. Power-law distributions in empirical data. *SIAM Rev*. 2009;51(4):661–703.

11. Di Ieva A. Angioarchitectural morphometrics of brain tumors: are there any potential histopathological biomarkers? *Microvasc Res.* 2010;80:522–33.
12. Di Ieva A, Grizzi F, Ceva-Grimaldi G, Russo C, Gaetani P, Aimar E, Levi D, Pisano P, Tancioni F, Nicola G, Tschabitscher M, Dioguardi N, Rodriguez y Baena R. Fractal dimension as a quantifier of the microvasculature of normal and adenomatous pituitary tissue. *J Anat.* 2007; 211:673–80.
13. Di Ieva A, Grizzi F, Gaetani P, Goglia U, Tschabitscher M, Mortini P, Rodriguez y Baena R. Euclidean and fractal geometry of microvascular networks in normal and neoplastic pituitary tissue. *Neurosurg Rev.* 2008;31:271–81.
14. Di Ieva A, Grizzi F, Tschabitscher M, Colombo P, Casali M, Simonelli M, Widhalm G, Muzzio PC, Matula C, Chiti A, Rodriguez y Baena R. Correlation of microvascular fractal dimension with positron emission tomography [¹¹C]-methionine uptake in glioblastoma multiforme: preliminary findings. *Microvasc Res.* 2010;80:267–73.
15. Di Ieva A, Matula C, Grizzi F, Grabner G, Trattnig S, Tschabitscher M. Fractal analysis of the susceptibility weighted imaging patterns in malignant brain tumors during antiangiogenic treatment: technical report on four cases serially imaged by 7 T magnetic resonance during a period of four weeks. *World Neurosurg.* 2012;77:785.e11–21.
16. Di Ieva A, Bruner E, Widhalm G, Minchev G, Tschabitscher M, Grizzi F. Computer-assisted and fractal-based morphometric assessment of microvasculature in histological specimens of gliomas. *Sci Rep.* 2012;2:429–38.
17. Di Ieva A, Göd S, Grabner G, Grizzi F, Sherif C, Matula C, Tschabitscher M, Trattnig S. Three-dimensional susceptibility-weighted imaging at 7 T using fractal-based quantitative analysis to grade gliomas. *Neuroradiology.* 2013;55:35–40.
18. Douw L, van Dellen E, de Groot M, Heimans JJ, Klein M, Stam CJ, Reijneveld JC. Epilepsy is related to theta band brain connectivity and network topology in brain tumor patients. *BMC Neurosci.* 2010;11:103–12.
19. Gazit Y, Baish JW, Safabakhsh N, Leunig M, Baxter LT, Jain RK. Fractal characteristics of tumor vascular architecture during tumor growth and regression. *Microcirculation.* 1997;4(4):395–402.
20. Halsey TC, Jensen MH, Kadanoff LP, Procaccia I, Shraiman BI. Fractal measures and their singularities: the characterization of strange sets. *Phys Rev A.* 1986;33(2):1141–51.
21. Heimans JJ, Reijneveld JC. Factors affecting the cerebral network in brain tumor patients. *J Neurooncol.* 2012;108:231–7.
22. Iftekharuddin KM, Parra C. Multiresolution-fractal feature extraction and tumor detection: analytical model and implementation. *Proc SPIE Wavelets: Appl Sig Image Process X.* 2003;5207:801–12.
23. Iftekharuddin KM, Jia W, Marsh R. Fractal analysis of tumor in brain MR images. *Mach Vis Appl.* 2003;13:352–62.
24. Iftekharuddin KM, Zheng J, Islam MA, Ogg RJ. Fractal-based brain tumor detection in multimodal MRI. *Appl Math Comput.* 2009;207:23–41.
25. Islam A, Reza S, Iftekharuddin KM. Multi-fractal texture estimation for detection and segmentation of brain tumors. *IEEE Trans Biom Eng.* 2013;60(11):3204–15.
26. Jain RK. Normalization of tumor vasculature: an emerging concept in antiangiogenic therapy. *Science.* 2005;307:58–62.
27. Jbabdi S, Mandonnet E, Duffau H, Capelle L, Swanson KR, Péligrini-Issac M, Guillemin R, Benali H. Simulation of anisotropic growth of low-grade gliomas using diffusion tensor imaging. *Magn Reson Med.* 2005;54:616–24.
28. Kantelhardt JW, Zschiegner SA, Koscielny-Bunde E, Havlin S, Bunde A, Stanley HE. Multifractal detrended fluctuation analysis of nonstationary time series. *Physica A.* 2002;316:87–114.
29. Family F, Vicsek T. Dynamics of fractal surfaces. Singapore: World Scientific; 1991.
30. Lacasa L, Luque B, Ballesteros F, Luque J, Nuño JC. From time series to complex networks: the visibility graph. *Proc Natl Acad Sci U S A.* 2008;105:4972–5.

31. Lacasa L, Luque B, Luque J, Nuño JC. The visibility graph: a new method for estimating the Hurst exponent of fractional Brownian motion. *EPL*. 2009;86:30001. 1–5.
32. Landini G, Rippin JW. Fractal dimensions of the epithelial-connective tissue interfaces in pre-malignant and malignant epithelial lesions of the floor of the mouth. *Anal Quant Cytol Histol*. 1993;15(2):144–9.
33. Landini G, Rippin JW. How important is tumour shape? Quantification of the epithelial-connective tissue interface in oral lesions using local connected fractal dimension analysis. *J Pathol*. 1996;179:210–7.
34. Lopes R, Betrouni N. Fractal and multifractal analysis: a review. *Med Image Anal*. 2009;13:634–49.
35. Losa GA. The fractal geometry of life. *Riv Biol*. 2009;102:29–60.
36. Louis DN, Ohgaki H, Wiestler OD, Cavenee WK, Burger PC, Jouvet A, Scheithauer BW, Kleihues P. The 2007 WHO classification of tumours of the central nervous system. *Acta Neuropathol*. 2007;114:97–109.
37. Mandelbrot BB, Van Ness JW. Fractional Brownian motions, fractional noises and applications. *SIAM Rev*. 1968;10(4):422–37.
38. Martín-Landrove M, Pereira D. Fractal properties and critical exponents in tumor. *Ciencia*. 2008;16:205–9.
39. Martín-Landrove M, Torres-Hoyos F. Geometry of tumor growth in brain. *Revista de la Facultad de Ingeniería. Univ Cent de Venezuela*. 2013;28(4):79–88.
40. Martín-Landrove M, Pereira D, Caldeira ME, Itriago S, Juliac M. Fractal analysis of tumoral lesions in brain. *Conf Proc IEEE Eng Med Biol Soc*. 2007;2007:1306–9.
41. Megalooikonomou V, Ford J, Shen L, Makedon F, Saykin A. Data mining in brain imaging. *Stat Methods Med Res*. 2000;9:359–94.
42. Pereira D, Zambrano C, Martín-Landrove M. Evaluation of malignancy in tumors of the central nervous system using fractal dimension. *Conf Proc IEEE Eng Med Biol Soc*. 2000;3:1775–8.
43. Quintana A, Martín-Landrove M, Pereira D. Fractal properties and critical exponents for tumor staging and classification. *Proceedings of III international congress on computational bioengineering*. 2007. p. 385–90.
44. Rényi A. On measures of information and entropy. *Proceedings of the fourth Berkeley symposium on mathematics, statistics and probability*. Vol. 1 University of California Press, 1961, p. 547–561.
45. Reza S, Iftekharuddin KM. Multi-fractal texture features for brain tumor and edema segmentation. *Proc SPIE Med Imaging Conf. San Diego, California, USA, 2014*;9035:903503-1-10.
46. Reza S, Mays R, Iftekharuddin KM. Multi-fractal detrended texture feature for brain tumor classification. *Proc SPIE Med Imaging Conf. 2015*;9414:941410-1-6.
47. Risser L, Plouraboué F, Steyer A, Cloetens P, Le Duc G, Fonta C. From homogeneous to fractal normal and tumorous microvascular networks in the brain. *J Cereb Blood Flow Metab*. 2007;27:293–303.
48. Roberts AJ, Cronin A. Unbiased estimation of multi-fractal dimensions of finite data sets. *Physica A*. 1996;233:867–78.
49. Rueda-Toicen A, Martín-Landrove M. Visibility graphs of brain tumor interfaces, code repository. https://bitbucket.org/antonio_rt/visibility-graphs-of-brain-tumor-interfaces.
50. Sedivy R. Fractal tumors: their real and virtual images. *Wien Klin Wochenschr*. 1996; 108:547–51.
51. Smitha KA, Gupta AK, Jayasree RS. Fractal analysis: fractal dimension and lacunarity from MR images for differentiating the grades of glioma. *Phys Med Biol*. 2015;60:6937–47.
52. Swanson KR, Bridge C, Murray JD, Alvord Jr EC. Virtual and real brain tumors: using mathematical modeling to quantify glioma growth and invasion. *J Neurol Sci*. 2003;216:1–10.
53. Swanson KR, Alvord Jr EC, Murray JD. Dynamics of a model for brain tumors reveals a small window for therapeutic intervention. *Discret Contin Dyn Syst Ser B*. 2004;4(1):289–95.

54. Tél T, Fülöp Á, Vicsek T. Determination of fractal dimensions for geometrical multifractals. *Physica A*. 1989;159:155–66.
55. Torres Hoyos F, Martín-Landrove M. 3-D *in vivo* brain tumor geometry study by scaling analysis. *Physica A*. 2012;391:1195–206.
56. Vicsek T. Mass multifractals. *Physica A*. 1990;168:490–7.
57. Vicsek T. *Fractal growth phenomena*. Singapore: World Scientific; 1992.
58. Virkar Y, Clauset A. Power-law distributions in binned empirical data. *Ann Appl Stat*. 2014;8(1):89–119.
59. Waliszewski P. Complexity, dynamic cellular network, and tumorigenesis. *Pol J Pathol*. 1997;46:235–41.
60. Wang H, Douw L, Hernández JM, Reijneveld JC, Stam CJ, Van Mieghem P. Effect of tumor resection on the characteristics of functional brain networks. *Phys Rev E*. 2010;82:021924-1-13.
61. Zook JM, Iftekharuddin KM. Statistical analysis of fractal-based brain tumor detection algorithms. *Magn Reson Imaging*. 2005;23:671–8.

Chapter 23

Histological Fractal-Based Classification of Brain Tumors

Omar S. Al-Kadi and Antonio Di Ieva

Abstract The structural complexity of brain tumor tissue represents a major challenge for effective histopathological diagnosis. Tumor vasculature is known to be heterogeneous and mixtures of patterns are usually present. Therefore, extracting key descriptive features for accurate quantification is not a straightforward task. Several steps are involved in the texture analysis process where tissue heterogeneity contributes to the variability of the results. One of the interesting aspects of the brain lies in its fractal nature. Many regions within the brain tissue yield similar statistical properties at different scales of magnification. Fractal-based analysis of the histological features of brain tumors can reveal the underlying complexity of tissue structure and angiostructure, also providing an indication of tissue abnormality development. It can further be used to quantify the chaotic signature of disease in order to distinguish between different temporal tumor stages and histopathological grades.

Brain meningioma subtype classifications improvement from histopathological images is the main focus of this chapter. Meningioma tissue texture exhibits a wide range of histological patterns whereby a single slide may show a combination of multiple patterns. Distinctive fractal patterns quantified in a multiresolution manner would be for better spatial relationship representation. Fractal features extracted from textural tissue patterns can be useful in characterizing meningioma tumors in terms of subtype classification, a challenging problem compared to histological

O.S. Al-Kadi (✉)

Institute of Bioengineering, Ecole Polytechnique Fédérale de Lausanne (EPFL),
Lausanne, Switzerland

King Abdullah II School for IT, University of Jordan, Amman, Jordan

e-mail: omar.alkadi@epfl.ch; o.alkadi@ju.edu.jo

A. Di Ieva, MD, PhD

Neurosurgery Unit, Faculty of Medicine and Health Sciences, Macquarie University,
Sydney, NSW, Australia

Garvan Institute of Medical Research, Sydney, NSW, Australia

Medical University of Vienna, Vienna, Austria

University of Toronto, Toronto, ON, Canada

grading, and furthermore can provide an objective measure for quantifying subtle features within subtypes that are hard to discriminate.

Keywords Fractal dimension • Texture analysis • Brain histopathology • Meningioma • Tissue characterization • Pattern classification

23.1 Introduction

Diagnosis of brain tumors is mainly based on visual examination of cell morphology and tissue distribution. The accurate diagnosis of histopathological brain tissue is essential for selecting the appropriate treatment procedure. However, the various cellular arrangements and complex tissue vasculature renders the brain one of the most challenging and complex organs in the human body. Additionally, tumor angiogenesis further increases the heterogeneity of the complex cellular- and tissue-level spatial relationships.

The unique folding of brain tissue in a *fractal-like* geometry is an interesting characteristic that is worthy of attention. The development of consistent fractal patterns in normal brain tissue acts as a sign of order and represents how well structured the patterns can be. The fractal characteristics of the brain reflect its complexity.

Fractal analysis in tissue characterization has been deployed in many useful applications in histopathological imaging [24]. The development of a computer-aided diagnostic system based on fractal-model design to assist in histological diagnosis of brain tumors is significant for effective management of disease. This could improve a pathologist's ability to accurately detect and characterize subtle tissue abnormalities and hence lead toward a more reliable diagnosis and promoting better patient outcome.

Quantifying the fractal properties of pathological tissue and cellular properties by means of its textural patterns resembles how pathologists perceive and identify distinctive features of disease. A computer-aided diagnostic system can play the role of a visual perception function through mimicking the behavior of pathologists: firstly by perceiving the different unique patterns in an image (e.g., extracting fractal features) and then by using past experience and experimental knowledge to link the perceived patterns and appropriate diagnosis (e.g., decision making-algorithms). This has an advantage over the classical visual diagnosis approach. Limitations due to subjective factors in the classical visual diagnosis approach like preconception, expectations, relying on diligence, and fatigue contribute to differences in image perception, which leads to inter- and intra-observer variability assessments. In contrast, an automated decision system can overcome such bias in diagnosis by maintaining consistent perceived patterns. It would also enhance the ability to discriminate complex texture patterns that would otherwise be difficult via ordinary human vision. Computer-assisted tools can therefore help in offering objective diagnostic and prognostic image biomarkers to improve patients' management.

23.2 Fractal Morphometry of Tissue Complexity

The concept of *fractality* is used to: (a) analyze complex patterns that look the same across different scales of magnification, (b) describe the self-similarity of irregular and self-similar objects in nature, and (c) quantify the surface roughness and geometrical complexity of objects [34]. Various researchers have been investigating the application of fractal analysis to imagery in a number of diverse fields including, but not limited to, physics [9], acoustics, geology [1], ecology [21], radiology [2], and fluid mechanics [36]. In histopathology, the fractal geometry has been used as a measure of morphological complexity of cells and tissues providing compact description of the textural characteristics for both normal and pathological cases [24].

Histopathological assessment is mainly based on the study of underlying biological features of disease for clinical diagnosis. Certain descriptive features can reveal more details when examined at increasing resolution. Many tissue patterns tend to exhibit statistically self-similar features at different levels and in different sizes. The assessment of the pattern irregularity at different scales could assist in better understanding tissue pathology and thus assist pathologists in identifying type and grade of disease. However, fractality in textural patterns of histopathological tissue is considered *quasi-fractal*, as they scale in a statistical fashion. Biological tissues, like several natural objects, are fractals in a limited range of magnification (in the so-called “fractal window”). The resemblance between shapes seen at different scales is usually approximate and is considered to be random rather than strictly self-similar. The exhibited geometrical variability mainly refers to deviations in cell structures and distributions over the tissue sample.

The application of the fractal approach in histopathology also has a potential role in characterizing the morphological information for deeper insight and understanding the biology of tumor tissues. Tumor vasculature is spatially heterogeneous and does not have a clear hierarchical organization consisting of irregularly formed vessels that are both leaky and often permeable. This heterogeneity in tissue texture calls for a method that can improve the capability of discriminating higher order statistical textural information, which would otherwise be difficult using classical examination approaches. The size and geometrical parameters of irregular and complex structures in tumor tissue differ when examined at increasing resolution. Hence fractal geometry, which best characterizes non-Euclidean structures, can be used to measure topological and geometrical properties of irregular and complex structures in tumor tissue.

23.2.1 Fractal Dimension Estimation

Fractal pattern analysis has been applied to many of the physiological processes in biomedical research. Unlike Euclidean geometry that is best developed to measure regular structures, complex biological structures, which are known to be

irregular, could be best quantified based on the principles of fractal geometry. The fractal dimension (FD) and other related dimensional parameters provide a compact representation of the complexity of the biological patterns. Nevertheless, the accuracy of FD estimation depends on the precision of the input shape description, and therefore several estimation methods have been developed for this purpose.

FD is widely used as a tool to quantify the geometrical complexity of a structure by means of its space filling properties. There are several methods used to inspect self-similarity and dedicated to providing a reliable estimate of the FD. The most well-known methods are briefly discussed below:

- *Fractional Brownian motion (fBm)*: The fBm is a non-stationary model known for its capability to describe random phenomena [37]. It is a generalization of the Brownian motion where the increments of the process are normally distributed but not independent [34]. The correlation of a random process $B(t)$ can be represented as the expected value $E(B)$ of the product of non-overlapping increments of the fBm process:

$$E\left((B(t) - B(0)) \cdot (B(t+h) - B(t))\right) = \left((t+h)^{2H} - t^{2H} - h^{2H}\right) / 2 \quad (23.1)$$

where the Hurst index, H , is a real number in the range $(0, 1)$ and describes the roughness of the motion, with a higher value leading to a smoother motion [33]. The value of H determines the process of the fBm, such that when $H > 1/2$ indicates a positive correlation between the increments. A Brownian motion is achieved for the special case $H = 1/2$, and the increments are negatively correlated when $H < 1/2$. For an image, H is practically estimated by plotting the mean absolute difference of pixel pairs as a function of scale on a log-log scale (see Fig. 23.1), where H will represent the slope of the curve that is used to estimate the FD as: $FD = 2 - H$.

- *Box-counting*: Is a recursive method that involves covering the contour lines with a grid of n -dimensional boxes having a side-length δ and counting the number of non-empty boxes $N(\delta)$. An overlaying grid approximates each contour line and then the number of boxes or cells intersections is counted. The smaller the size of the boxes becomes, the larger the length estimate as finer details are captured. The technique is performed recursively with different box sizes covering the contour lines.

For a one-dimensional curve having a length L , the relation can be expressed as [34, 50]: $N(\delta) \approx \frac{L}{\delta}$. Then the generalized form of the slope of the logarithmic plot of the number of boxes against their size would represent the FD (see Fig. 23.2):

$$N(\delta) \propto \frac{1}{\delta^{FD}} \quad (23.2)$$

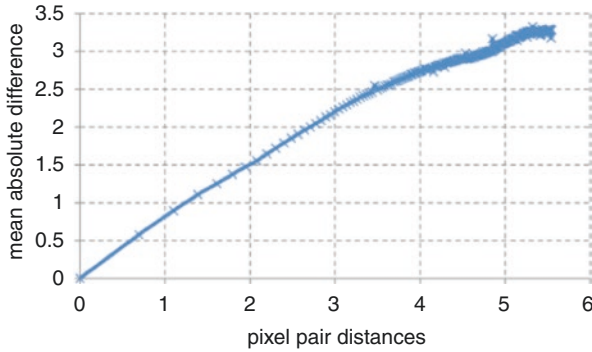


Fig. 23.1 Mean absolute difference versus pixel pair distances in log-log coordinates for a transitional meningioma histopathological image in Fig. 23.4 (Image reproduced from [6])

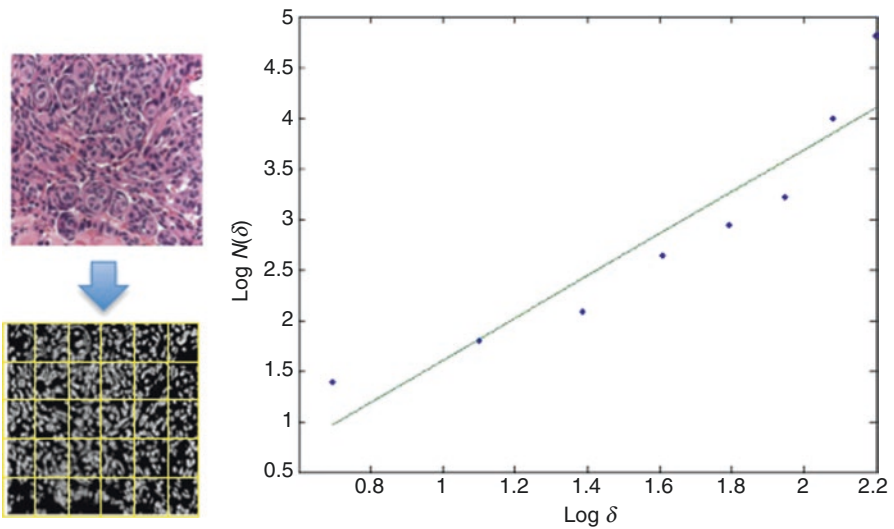


Fig. 23.2 Application of the box-counting method to a transitional meningioma subtype image (FD=1.81). [left] Histopathological image and corresponding segmented cell nuclei image covered with a set of squares, where the squares covering the cell nuclei are iteratively counted; [right] estimating the FD from the slope of the linear regression line of the log-log plot between number of squares $N(\delta)$ and square size δ

$$FD = \lim_{\delta \rightarrow 0} \frac{\log N(\delta)}{\log(\delta)} \tag{23.3}$$

Also based on the same principle but with a different shape, *prism-counting* was introduced [12], where the combined area of four-sided triangular prisms defined by the corner points is computed and summed over the surface. Similarly, the iterative *Epsilon-Blanket* method computes the FD of a scale-varying curve (or

surface) based on the corresponding area (or volume) [39]. The set of points that lie at a certain distance ε from the curve are used in forming a blanket having a strip of width of 2ε covering the curve, and for different values of ε . The FD for a curve can be calculated using the relation $L(\varepsilon) \propto \varepsilon^{1-\text{FD}}$, where $L(\varepsilon)$ is the curve length defined from the blanket area $A(\varepsilon)$ as $L(\varepsilon) = A(\varepsilon)/2\varepsilon$. For the case of a surface, the blanket is formed from a set of points in the three-dimensional space, which are also ε far from the surface and having a width of 2ε . The surface area is defined as $A(\varepsilon) = V(\varepsilon)/2\varepsilon$, and the FD is estimated from the relation $A(\varepsilon) = \varepsilon^{2-\text{FD}}$.

- *Walking divider*: This method uses a ruler or a chord length acting as a *step size* and then measures the number of steps or *length* required to cover the fractal curve, which can be represented as [34] $L(\delta) = K\delta^{1-\text{FD}}$, where $L(\delta)$ is length of trail, δ is the step size, and K is a constant. The method operates by iteratively walking the divider along the curve and then counting the number of steps required to cover the curve for each case. This process is repeated at different resolutions, and the FD, which is the relation between the step size and chord length, can be estimated.
- *Power spectrum*: Given a signal $f_i = 1, 2, \dots, N$ (where N has the power of 2), the Fourier power spectrum can be used to estimate the FD as $\hat{P}_i = c|k_i|^{-\beta}$, where c is a constant and the spectral exponent β , which relates to the FD, can be estimated by fitting the least squares error line to the data. Also, since the Fourier transform of the *autocorrelation function* is the power spectrum of the function [40], the autocorrelation function ρ as a function of the shifting distance a expressed as $\rho(a) \propto a^{-2\text{FD}}$ can also be used to estimate the FD.
- *Area/perimeter relationship*: In this approach, the FD is estimated based on the power law relationship, where the areas and the respective perimeters of the different curves of a group are measured [51]. The boundary perimeter P is related to the enclosed area (A) by $A = kP^{\text{FD}/2}$ for $1 < \text{FD} < 2$, where k is a constant for a given shape (e.g., 4 for square and $2\sqrt{\pi}$ for a circle, etc.).
- *Pixel dilation*: This method relates the FD to the curve border length. The dilation operation is performed by convolving various filters having different diameters with the curve border. The computed area would be divided by the size of the kernel, and a log-log plot would be used to determine the slope of the linear regression line S ; and hence the $\text{FD} = 1 - S$.

23.2.2 Related Work

Significant progress has been made to understand how irregular shapes and structures relate to the analysis of morphological complexity of tumor cells and tissues. A number of research studies have been applied to histopathological images for different tumors in an attempt to automate the diagnosis procedure. Some relied on a single texture measure for feature extraction, such as extraction of wavelet-based

features [28, 41, 46], or employing other measures like the gray-level co-occurrence matrix or color space features for classification [8, 45]. Multiple measures for classification have been applied as well, such as using spatial and frequency texture features for classification by regression trees analysis [52]. Topological properties of the brain histopathological tissue were also extracted by a graph-based representation through probabilistically assigning a link between a pair of cells [14]. Morphological characteristics for feature extraction was applied in [48, 54], while others focused more on classifier improvement [19, 44]. However, the complexity and hierarchical structures of the vascular histopathological patterns in the brain are technically challenging to characterize [31]. The spatial resolution is also not sufficient to resolve the complex structure of capillary vessels [22] and to reliably collect morphometric data from histopathological tissue at high resolutions [11, 25]. Therefore, the fractal characteristics of the pathologic vascular networks was exploited to resolve structure complexity and to derive meaningful features that could assist in the diagnosis and/or staging of tumors. Fractal geometry was introduced as a better mean of quantifying the microvasculature of normal pituitary glands and pituitary adenomas, and it was found that the use of the surface FD is more appropriate than microvessel density estimates [15]. Also in another work, statistical analysis was performed to study the fractal microvasculature and provide a quantitative assessment of grade complexity for WHO grade II and III gliomas [18]. The angioarchitecture heterogeneity of gliomas was shown to be able to distinguish the tissue variability between the different grades and can be used to differentiate low-grade from malignant tumors in histological specimens [16, 17].

In regard to brain meningiomas, Table 23.1 lists work recently performed for the purpose of automated histopathological subtype classification. All approaches developed in Table 23.1 were applied to the same meningioma dataset, which facilitates the comparison between the different classification results. This thereby avoided possible deformation in tissue appearance due to variation in tissue sample preparation/protocol or inconsistency attributed to stain reactivity from different manufacturers or using different microscopic scanners. This would be useful in preventing such variation effects on subsequent quantitative analysis. Moreover, Table 23.1 shows that the highest classification accuracy was achieved once the fractal analysis was performed in a multiresolution manner. The FD measure can breakdown the complexity of tumor heterogeneity and hence better discern the pathological patterns between the different subtypes.

The way the FD meaningfully relates to underlying physiology, in terms of quantifying tumor texture heterogeneity – as the rougher the surface the more chaotic the tissue structure [4–6] – explains the better performance of the fractal-based method compared to other texture analysis methods, hence providing a reliable characterization for diagnostic interpretation of histopathological images. The general design of a computer-aided diagnosis system and the effectiveness of histological fractal-based analysis in quantifying spatial heterogeneity in meningioma brain tumor subtypes are discussed next.

Table 23.1 Different texture analysis methods for histopathological brain meningioma classification

Reference	Features	Classification	Cross-validation	Accuracy (%)
Lessmann et al. [28]	Color transforms and wavelet transform	Self-organizing map	Unsupervised (clustering)	79.00
Wirjadi et al. [53]	Gray-level and color features	Classification and regression trees	Hold-out	83.40
Qureshi et al. [43]	Wavelet packet and Local binary patterns	Support vector machine	5-fold	80.00
Qureshi et al. [42]	Wavelet packet and gray-level co-occurrence	Support vector machine	5-fold	82.10
Fatima et al. [20]	Morphological and gray-level co-occurrence features	Multilayer perceptron neural network	Leave-one-patient-out	92.50
Zeng et al. [55]	Morphological and color features	<i>K</i> -Nearest neighbor	Leave-one-out	85.00
Strange and Zwigelaar [47]	Morphological features	Random forest	10-fold	91.25
Al-Kadi [4, 5]	Fractal dimension and wavelet packets	Bayesian	Hold-out	92.50
Al-Kadi [6]	Fractal dimension, lacunarity, and wavelet packets	Support vector machine	Leave-one-patient-out	94.12

23.3 Automated Histopathological Image Analysis

General model design for automated histopathological tissue characterization and classification, which is also applicable to brain tumor subtype classification, is briefly discussed below:

23.3.1 Image Preparation

A tissue specimen runs through several basic preparation steps before it is ready for image texture analysis. This includes chemical fixation for cell/tissue preserving, tissue dehydration processing for replacing with an embedding medium, wax embedding, sectioning of samples so the microstructure can be clearly observed, and hematoxylin and eosin (H&E) staining – or using any other suitable stains – to increase tissue contrast and highlight cell nuclei features. Once the tissue samples are treated with the appropriate histology stain, images are acquired at a certain magnification level via microscopic imaging and made ready for histopathological analysis. Figure 23.3 illustrates a typical computer-aided diagnosis system, which can be used to implement histopathological diagnosis.

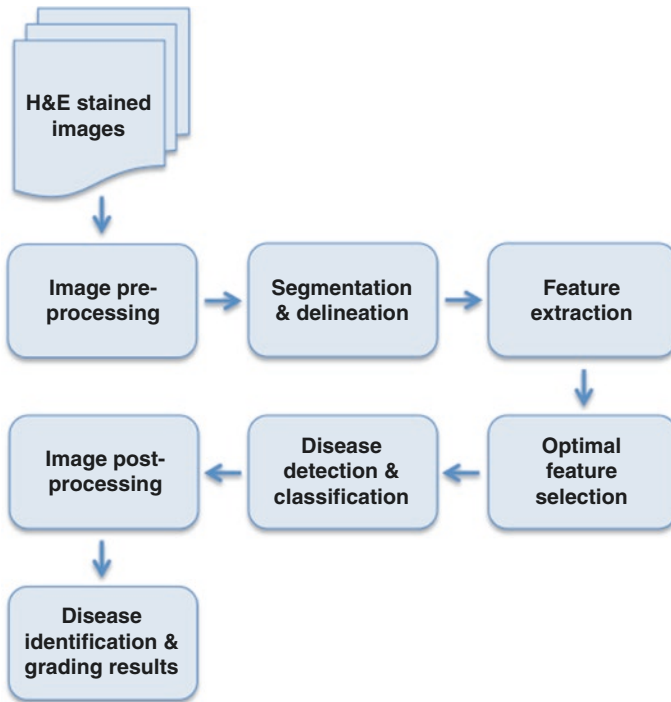


Fig. 23.3 A typical computer-aided diagnosis system for classification and grading of histopathological images

23.3.2 *Pre-processing and Focal Regions Segmentation*

Pre-processing is associated with improving the features of interest that assist in determining the pathology. Particular image structures are enhanced for simultaneous visualization of the feature and image space, providing a method for exploration of correlations of texture patterns in the feature space to histological image characteristics.

Image regions having certain textural properties considered essential in the diagnosis process can be highlighted by different pre-processing approaches such as color normalization and separation to overcome stain artifacts; subsampling while preserving the minimum sampling rate (i.e., Nyquist rate); smoothing and denoising by simple Gaussian/median filtering or by employing adaptive filtering techniques that could reduce local tissue deformation while preserving edges and fine structures; contrast stretching and histogram equalization; or by other image enhancement techniques (e.g., dynamic range compression operations). Segmentation and delineation techniques such as nonlinear thresholding, edge detection, active contours, labeling, or clustering can follow the pre-processing stage for separating the foreground focal regions from the image background.

23.3.3 *Feature Extraction and Classification*

This stage is considered the heart of the computer-aided diagnosis system. Tissue patterns' characteristics are quantitatively captured for classification based on textural, spectral, morphometric, or color space features and could be performed at different resolution levels. This is followed by feature reduction, providing an effective way to select the most relevant features for alleviating the *curse of dimensionality* and achieving more accurate classification. The features can be refined using linear methods such as principle component analysis and linear discriminant analysis or by nonlinear methods via mapping to higher dimensional feature space. The cost of prediction errors can be considered in the following stage of disease detection and classification by means of machine learning (i.e., supervised classification, similarity function) or statistical tests. Then efficiency is assessed by the accuracy of the quantitative representation to classify patterns. Gaining significant acceptance by pathologists usually relies on achieving effective diagnostic performance while maintaining a certain degree of simplicity, i.e., avoiding behaving like a black-box. Accuracy can be improved either by developing an effective feature extraction algorithm, which can provide high quality features, or by designing a sophisticated classifier that can deal with nonlinear and high dimensional features; the main focus of this chapter will be on the former problem.

23.3.4 *Qualitative Enhancement and Grading Results*

Pathologist may choose to add complementary pathological guided post-processing operations (e.g., morphological operations, shape extraction, annotation, etc.) to further “qualitatively” refine the results to be optimized for visual appearance. The system terminates with the disease identification and grading results stage, providing a complementary “second opinion” to pathologists in the diagnosis process.

23.4 Characterizing Tissue via Fractal Properties

Large numbers of cell nuclei are expected to set the structure of the tissue patterns at low magnification levels and few cell nuclei at medium and high magnifications. However, images of tissue texture usually tend to have a composite of multi-patterns. The different patches encountered within these patterns can be exploited to analyze the fractality or statistical scale invariance of tissue and hence the possibility of characterizing tumor features, e.g., its microvascularization [26]. The appearance of tissue patterns can reflect its abnormality in a sense that more chaotic vasculature means a “rougher” texture surface and hence a higher FD [3]. The development of a tumor alters the structure of the tissue in a disorganized fashion, thus tissue

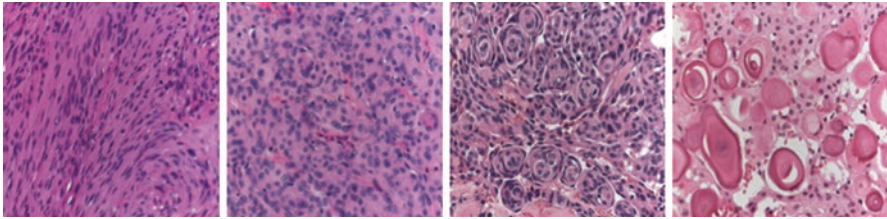


Fig. 23.4 Four types of grade I meningioma, from *left to right* (fibroblastic, meningothelial, transitional, and psammomatous)

patterns are not identical in all image samples and a certain degree of variation exists within and between image samples. Tissue heterogeneity places tissue patterns commonly in the category of stochastic textures that can exhibit quasi of *fractal-like* characteristics over several scales of magnification.

Pathologists usually look for several discriminative features that are indicative of tumor cells, e.g., abnormal size, shape, color, and arrangement. As an example of histological brain tumors, Fig. 23.4 shows four subtypes of grade I meningioma tissue biopsies distinguished according to the World Health Organization grading system [32]. Meningiomas exhibit a wide range of histological patterns and a single meningioma may show a combination of patterns. Patterns of tissue textures ranging from fine (micro-scale) to coarse (macro-scale) are encountered therein. An example of the former is the arrangement of fibroblastic and transitional cells in a concentric circle or whirlpool shape, while the large round nuclei in the meningothelial and the many cystic spaces in the psammomatous bodies contribute to the coarseness of the latter texture pattern. The histopathological features as an indication of tumor subtype are summarized in Table 23.2.

From a texture analysis perspective, the descriptive fractal features should characterize the qualitative characteristics used in clinical practice. This would assist in discarding irrelevant details and improve tissue classification of the different subtypes. More precisely, the subtle tissue distribution and the prominent cell nuclei arrangements in the coarse texture can be simultaneously localized and hence used for tumor subtypes differentiation. As for the tissue stochastic texture where it does not usually have a repetitive pattern but homogeneous statistical properties, the

Table 23.2 Main histological textural features for the four grade I meningioma subtype images shown in Fig. 23.4

Subtype	Characteristics
Fibroblastic	Spindle-shaped cells resembling fibroblasts in appearance, with abundant amounts of pericellular collagen
Meningothelial	Broad sheets or lobules of fairly uniform cells with round or oval nuclei
Psammomatous	A variant of transitional meningiomas with abundant psammoma bodies and many cystic spaces
Transitional	Contains whorls, few psammoma bodies, and cells having some fibroblastic features (i.e., spindle-shaped cells)

directionality and density of the discontinuities in the texture's surface help locate changes in the pathological state of tissue. Moreover, tissue with a large amount of edges is considered rich with features, which will make the feature extraction algorithm more capable of delivering a better characterization.

23.5 Quasi-fractal Texture Representation

Tumors tend to introduce irregularity into tissue pattern structure and cause deviations in cell nuclei distribution. This disorder increases the surface roughness of the examined texture pattern and affects pattern fractality. Regarding histopathological patterns, not all parts show self-similarity at different scales due to the inherent variability and effect of disease. A FD estimation method that can give an accurate estimation of the quasi-fractal texture patterns would be required. The box-counting and fBm algorithms are widely used for FD estimation as they can be applied to patterns that are not self-similar (nonlinear fractal images) and are relatively easy for empirical estimation [38]. Therefore a comparison is made between the two methods when applied to histopathological images of brain meningioma (see Fig. 23.5). Examining the output FD texture images, the fBm generates more visible discontinuities compared to the box-counting method. More discontinuities in the absence of significant tissue deformation would mean a texture with richer information and hence a more reliable estimation of the roughness of the image surface. Thus, we can say that the fBm is better suited to represent textures with textures having fine structures, as the case with histopathological images.

23.6 Multi-fractality Analysis

Histopathological tissue properties of brain tumors can be investigated at different levels of resolution. This is essential to determine the grading of tumor progression, as fine fractal structures within the tumor tissue could be subtle or not easy to discern. The cell nuclei texture, shape, orientation, intensity, and denseness are different from one subtype to another and sometimes within the same subtype. The fine fractal structures having low contrast would be best characterized at higher resolution levels, and vice versa. Therefore an integrated approach that incorporates both low and high levels of resolution can better account for morphological variability.

Advanced fractal analysis of tissue texture could be performed by estimating the FD and corresponding lacunarity measures at different levels of resolutions. The employment of fractal analysis in a multiresolution approach facilitates revealing many of the fine cellular and tissue details and in a sense assessing tissue irregularities at multiple scales of different resolutions. A wavelet packet – which is a generalized multiresolution approach – can decompose the complexity of the texture pattern into different frequency subbands, giving the opportunity to characterize the texture structure at the appropriate frequency channel. A Daubechies wavelet, which

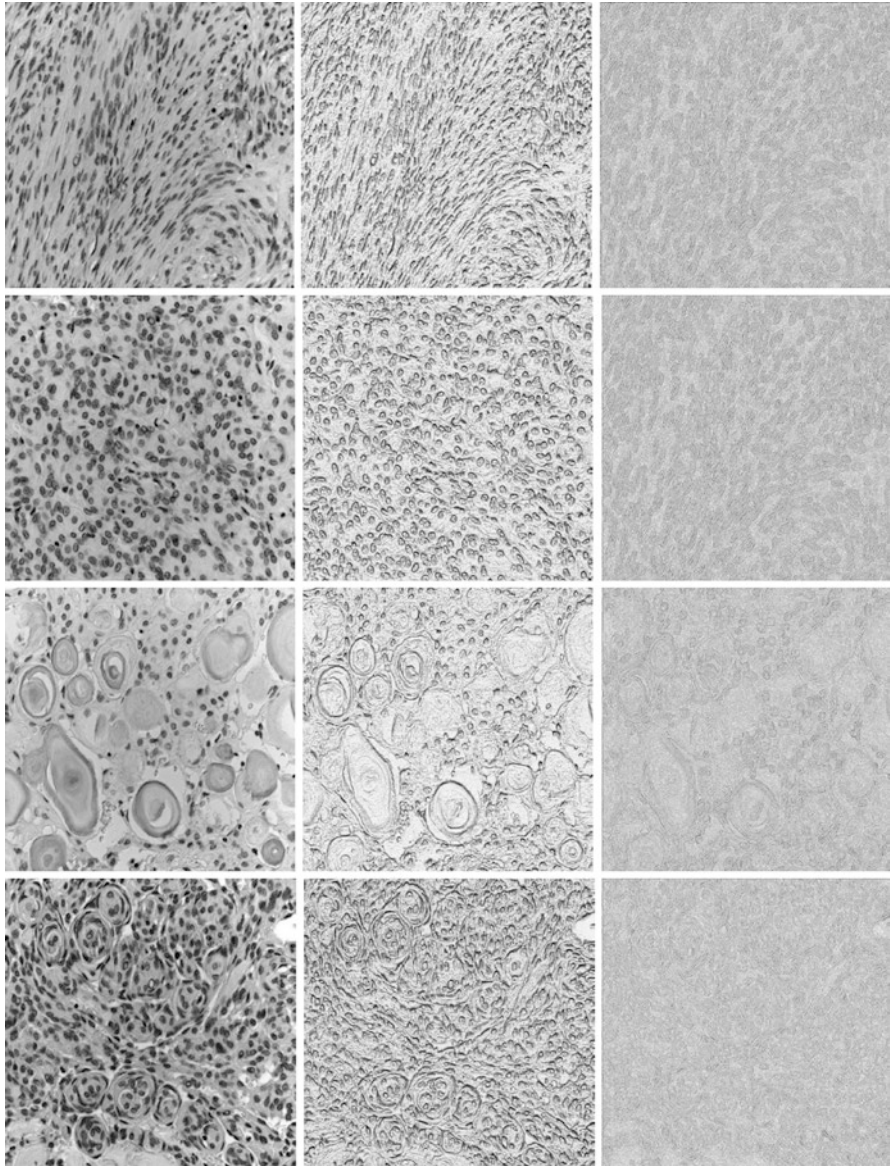


Fig. 23.5 First column represents the blue channel image for meningioma fibroblastic, meningothelial, psammomatous, and transitional subtypes, whereas the second and third columns are their corresponding fractal dimension images computed using the fractional Brownian motion and the differential box-counting algorithm, respectively

is widely used in characterizing signals exhibiting fractal patterns [13], can be used to obtain the wavelet packet subbands. Each subband is analyzed using its associated FD instead of energy, which has the advantage of being less sensitive to linear transformations of image intensity and abrupt changes in tissue texture [6, 7]. Then

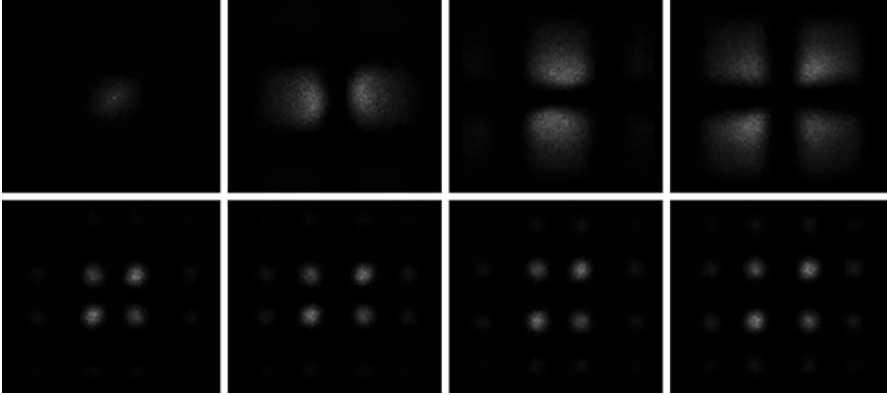


Fig. 23.6 Example of fibroblastic meningioma power spectrum of low-low, low-high, high-low, and high-high wavelet packet subbands for the first (*upper row*) and third (*lower row*) levels of resolution (Image reproduced from Al-Kadi [6])

the subband with the highest FD would be chosen for further decomposition in a tree-structured approach [4]. This facilitates the investigation of the possibility of higher frequency channels to provide significant information on tumor vascularization. Figure 23.6 supports this trend where the middle and high wavelet packet subbands for the first level of decomposition had a stronger power spectrum – the distribution of image power at a certain spatial frequency – as compared to the low frequency channels. This indicates that the multiresolution fractal analysis can better detect the fractal characteristics inherent in meningioma tissue texture.

23.6.1 Assessing Fractal Texture Heterogeneity

In order to differentiate between two textures if they have identical FD values, even though the two textures might not look similar, the lacunarity – which is a measure of deviation from scale translation invariance of the FD texture – can assist in quantifying aspects of patterns that exhibit scale-dependent changes in structure [23, 30, 34]. Namely, lacunarity measures the “lumpiness” of the fractal data, providing meta-information about the dimension of the fractal texture. The lower the lacunarity value, the more heterogeneous the examined fractal area, and vice versa. Given a fractal image I_{FD} , the lacunarity (L) can be defined in terms of the ratio of the variance over the mean value as in (4), where M and N represent the size of I_{FD} [40]:

$$L = \frac{\frac{1}{MN} \sum_{x=0}^{M-1} \sum_{y=0}^{N-1} I_{FD}(x, y)^2}{\left(\frac{1}{MN} \sum_{x=0}^{M-1} \sum_{y=0}^{N-1} I_{FD}(x, y) \right)^2} - 1 \quad (23.4)$$

Table 23.3 Fractal dimension (FD) and its corresponding lacunarity (L) for each of the histopathological patterns I shown in Fig. 23.3

Fibroblastic			Meningothelial			Transitional			Psammomatous		
I	FD	L	I	FD	L	I	FD	L	I	FD	L
1	1.73	0.034	1	1.75	0.036	1	1.80	0.025	1	1.70	0.042
2	1.77	0.029	2	1.76	0.033	2	1.81	0.025	2	1.67	0.046
3	1.79	0.031	3	1.76	0.032	3	1.80	0.024	3	1.68	0.041
4	1.74	0.033	4	1.77	0.034	4	1.75	0.031	4	1.69	0.042

To practically represent how lacunarity can further differentiate between two or more texture patterns that may exhibit similar dimensions, different texture images representing meningioma grade I patterns were used. After generating pixel-by-pixel FD images from each of the meningioma patterns, some of the textural patterns, although different, had their FD values similar as shown in Table 23.3. Therefore computing corresponding lacunarity can add another dimension for discrimination between *FD-alike* textures. The spatial scale invariance that the FD exhibits can be complemented with the property of translation invariance of the *lacunarity* measure, hence providing a rich description of pattern texture. For example, in Table 23.3, FD values of 1.77 and 1.75 were recorded for image textures 2 and 4 and 1 and 4 corresponding to the fibroblastic and meningothelial and meningothelial and transitional tumor subtypes of grade I meningiomas, respectively. This also reflects on the complementary relation between FD and lacunarity, where the many cystic spaces represented as large gaps between the psammoma bodies in the psammomatous subtype contribute to a higher lacunarity value. At the same time, this means less tissue heterogeneity, i.e., low FD value, as the associated structure sparsity can cause fewer occurrences of sudden perturbations within the fractal texture. Thus the size distribution of the gaps within the fractal texture can act as another dimension to quantify the spatial heterogeneity and further differentiate between fractal textures having similar dimensions, but with different appearance.

23.6.2 Performance Under Tissue Distribution Variation

Varying amounts and types of noise are inevitable during histological processing that affect the accuracy of the estimated texture measures. Natural variation in cell structures and distribution of cells in histological tissue contributes to texture complexity, while induced noise (i.e., color variations in tissue appearance) would increase disorder and reduce the quality of the extracted features. An intuitive approach would be to mitigate the impact of noise before reaching the feature extraction stage and then leaving the task of quantifying texture complexity to the feature extraction methods to deal with.

Variations in the staining conditions of histopathological samples may arise due to different factors. Examples of major sources of noise that can affect tissue biopsies,

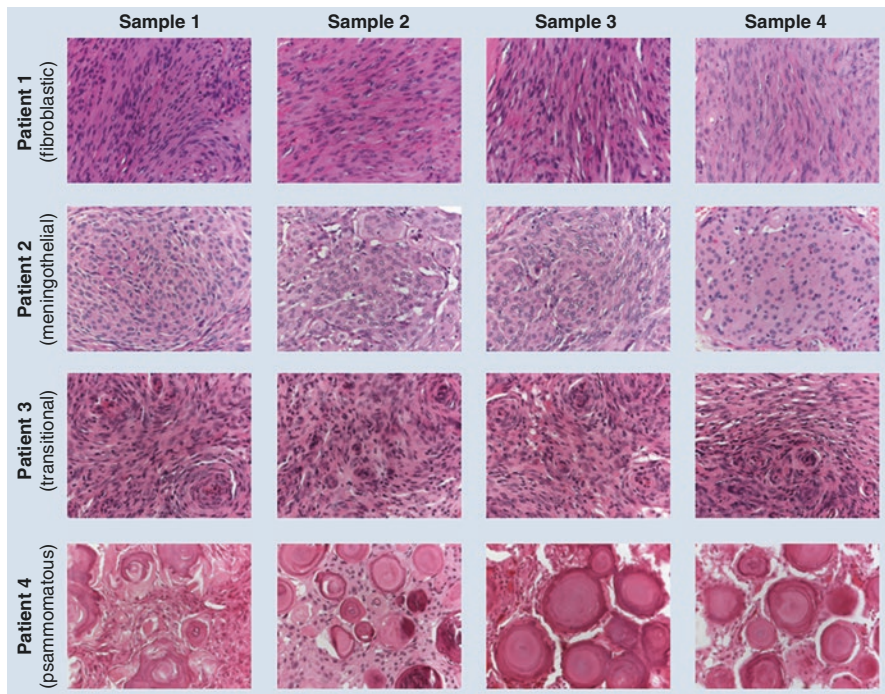


Fig. 23.7 Four different histopathological samples from four different patients showing the meningeoma image texture behavior heterogeneity within the same tissue case (patient)

but not limited to, include uneven distribution of staining, poor contrast between H&E stains, nuclear staining errors, appearance of reddish-brown nuclei, dark precipitate on slides, and white patches on slides after deparaffinization step. A number of color normalization methods have been developed to deal with the issue of color variation in histopathology images caused by inconsistent biopsy staining [10, 27, 29, 35, 56]. However, the capability of the texture analysis method to accurately characterize tumor heterogeneity relies on how well it will perform under inter- and intra-subtype variability. Distinctive textural characteristics related to each subtype could be obscured and would vary from one sample to another when extracted from a single patient (see Fig. 23.7); also samples extracted from different patients within a subtype would vary as well (see Fig. 23.8). This renders the characterization of the different discriminating textural histological features even more challenging, given that this inherent variation would reduce the separability between the subtype classes as illustrated in Fig. 23.8. For instance, the fibroblastic subtype is harder to differentiate, as it can be easily misclassified to transitional or meningothelial subtypes due to the heterogeneity of the tissue cell nuclei [49].

Practically, different images for certain meningeoma subtypes do not necessarily have an identical structure or the same number of cells. The diverse texture measures attempt to effectively quantify the structural complexity despite the uncertainty associated with the image texture surface. Therefore the performance of

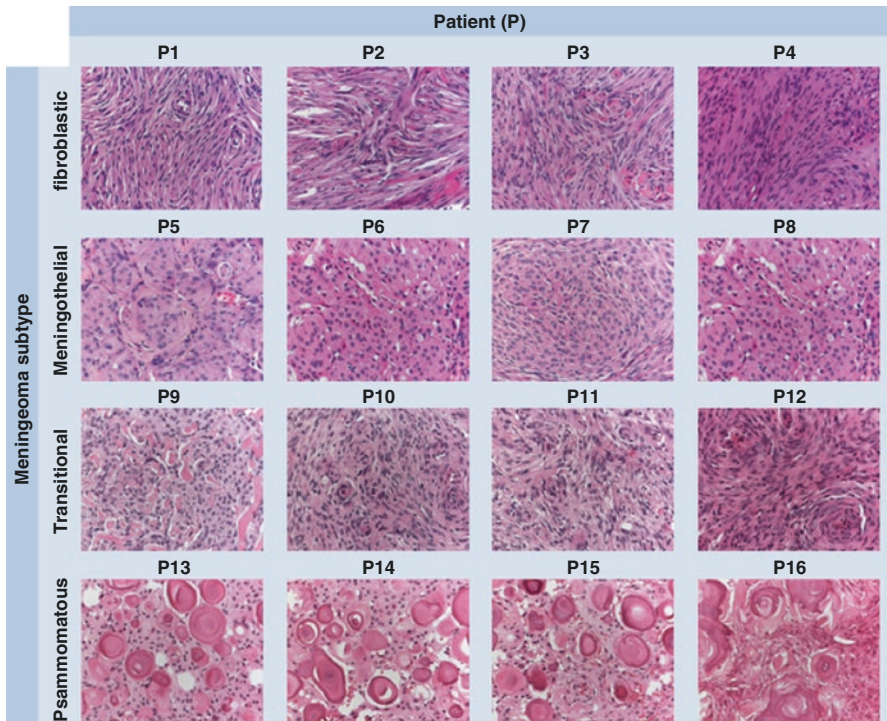


Fig. 23.8 Histopathological image samples extracted from 16 different patients referring to 4 different subtypes. The *first row* shows four different samples from four patients having a meningioma fibroblastic subtype; similarly for the rest of the cases. The different samples show that the simple observation of separation between the different subtypes is generally difficult to capture in an analytic solution

statistical and model-based texture analysis methods was investigated under different cell tissue density conditions in [5]. It was found that texture analysis performance based on FD method was more stable in medium cell density and was less susceptible to tissue heterogeneity in sparse image structures (i.e., tissue with low cell nuclei density). Overall, the histological fractal-based features showed significantly improved classification performance as compared to other well-known statistical and model-based texture analysis methods [6].

23.7 Diagnostic Challenges and Future Perspectives

Thus far, histological fractal-based analyses of brain tumors have shown that they can effectively describe tissue complexity and irregularity. Nevertheless, time has come to assess how reliable the developed algorithms and techniques are under different variability conditions. An extensive application of these fractal analysis techniques to a wider patient population will assist in gaining wider acceptance in the clinical

practice as an essential tool for diagnosis that complements the pathologists' perceptive abilities. This includes having a large unified and publicly available dataset of brain histopathological images for various grades and subtypes. The database should simulate the diverse tissue variation and artifacts encountered in pathological diagnosis; whether it was due to human interaction (i.e., user or protocol variation), stain reactivity from different providers, or use of microscopic scanners from different manufacturers with different parameters of digitalization. Moreover, to assure clinical significance, other implementation issues related to how the developed methods are relatively easy for empirical estimation and how computationally complex in respect to running time and memory usage should be evaluated as well. Hence the robustness of the methods developed by investigators can be justifiably compared.

23.8 Conclusion

The aim of this chapter was to provide insight on the usefulness of the FD for classifying brain histopathology images. In particular, the employment of fractal analysis in a multiresolution approach for an improved tissue texture characterization. Combining the FD with the lacunarity measure can provide a good synergy for enhancing the capability for recognizing textural patterns exhibiting scale- and translation-invariant properties (i.e., characterizing the complexity and homogeneity, respectively).

Computer-aided diagnosis for histopathological image analysis has become essential in tumor grading and classification. This is attributed to the advances of algorithms and methodologies in tumor tissue characterization that allows for faster and more accurate clinical decision-making. However, due to the large variations and complexity in tumor tissue, differences among subtypes could be subtle, as brain meningiomas exhibit a wide range of histological patterns and a single meningioma may show a composite of multi-patterns. A wise approach is to relate the extracted features with the geometrical properties of irregular and complex structures in tumor tissue, hence exploiting the fractality characteristics of brain tissue can better represent tissue complexity and heterogeneity of textural patterns. Currently, histological fractal-based methods are expected to play a promising role as tumor-grading tools that are minimally operator dependent to reduce variability associated with the manual grading system and thereby reducing uncertainty that may impact patient outcome.

References

1. Agterberg FP. Fractals and spatial statistics of point patterns. *J Earth Sci.* 2013;24(1):1–11.
2. Al-Kadi OS, Watson D. Texture analysis of aggressive and non-aggressive lung tumor CE CT images. *IEEE Trans Biomed Eng.* 2008;55(7):1822–30.

3. Al-Kadi OS. Tumour grading and discrimination based on class assignment and quantitative texture analysis techniques. PhD Thesis. Brighton: University of Sussex; 2009.
4. Al-Kadi OS. A fractal dimension based optimal wavelet packet analysis technique for classification of meningioma brain tumours. IEEE International Conference on Image Processing; 2009. p. 4125–8.
5. Al-Kadi OS. Texture measures combination for improved meningioma classification of histopathological images. *Pattern Recog.* 2010;43(6):2043–53.
6. Al-Kadi OS. A multiresolution clinical decision support system based on fractal model design for classification of histological brain tumours. *Comput Med Imaging Graph.* 2015;41:67–79.
7. Al-Kadi OS, Chung DYF, Carlisle RC, Coussios CC, Noble JA. Quantification of ultrasonic texture intra-heterogeneity via volumetric stochastic modeling for tissue characterization. *Med Image Anal.* 2015;21(1):59–71.
8. Alexandratou E, Yova D, Gorpas D, Maragos P, Agrogiannis G, Kavantzias N. Texture analysis of tissues in Gleason grading of prostate cancer. In: Farkas DL, Nicolau DV, Leif RC, editors. *Imaging, manipulation, and analysis of biomolecules, cells, and tissues VI.* San Jose, CA: Proceedings of the Society of Photo-Optical Instrumentation Engineers; 2008. p. 685904–8.
9. Aushev AA, Barinov SP, Vasin MG, Drozdov YM, Ignatev YV, Izgorodin VM, et al. Alpha-spectrometry and fractal analysis of surface micro-images for characterisation of porous materials used in manufacture of targets for laser plasma experiments. *Quant Electron.* 2015;45(6):533–9.
10. Bautista PA, Yagi Y. Staining correction in digital pathology by utilizing a dye amount table. *J Digit Imaging.* 2015;28(3):283–94.
11. Cassot F, Lauwers F, Fouard C, Prohaska S, Lauwers-Cances V. A novel three-dimensional computer-assisted method for a quantitative study of microvascular networks of the human cerebral cortex. *Microcirculation.* 2006;13(1):1–18.
12. Clarke KC. Computation of the fractal dimension of topographic surfaces using the triangular prism surface area method. *Comput Geosci.* 1986;12(5):713–22.
13. Daubechies I. The wavelet transform, time-frequency localization and signal analysis. *IEEE Trans Inf Theory.* 1990;36(5):961–1005.
14. Demir C, Gultekin SH, Yener B. Learning the topological properties of brain tumors. *IEEE/ACM Trans Comput Biol Bioinform.* 2005;2(3):262–70.
15. Di Ieva A, Grizzi F, Ceva-Grimaldi G, Aimar E, Serra S, Pisano P, et al. The microvascular network of the pituitary gland: a model for the application of fractal geometry to the analysis of angioarchitecture and angiogenesis of brain tumors. *J Neurosurg Sci.* 2010;54(2):49–54.
16. Di Ieva A, Grizzi F, Sherif C, Matula C, Tschabitscher M. Angioarchitectural heterogeneity in human glioblastoma multiforme: a fractal-based histopathological assessment. *Microvasc Res.* 2011;81(2):222–30.
17. Di Ieva A. Fractal analysis of microvascular networks in malignant brain tumors. *Clin Neuropathol.* 2012;31(5):342–51.
18. Di Ieva A, Bruner E, Widhalm G, Minchev G, Tschabitscher M, Grizzi F. Computer-assisted and fractal-based morphometric assessment of microvasculature in histological specimens of gliomas. *Sci Rep.* 2012;2:429–38.
19. Estevez J, Alayon S, Moreno L, Sigut J, Aguilar R. Cytological image analysis with a genetic fuzzy finite state machine. *Comput Methods Programs Biomed.* 2005;80:S3–15.
20. Fatima K, Arooj A, Majeed H. A new texture and shape based technique for improving meningioma classification. *Microsc Res Tech.* 2014;77(11):862–73.
21. Feng YJ, Liu Y. Fractal dimension as an indicator for quantifying the effects of changing spatial scales on landscape metrics. *Ecol Indic.* 2015;53:18–27.
22. Gazit Y, Berk DA, Leunig M, Baxter LT, Jain RK. Scale-invariant behavior and vascular network formation in normal and tumor-tissue. *Phys Rev Lett.* 1995;75(12):2428–31.
23. Gefen Y, Meir Y, Mandelbrot BB, Aharony A. Geometric implementation of hypercubic lattices with noninteger dimensionality by use of low lacunarity fractal lattices. *Phys Rev Lett.* 1983;50(3):145–8.

24. Gurcan MN, Boucheron LE, Can A, Madabhushi A, Rajpoot NM, Yener B. Histopathological image analysis: a review. *Biom Eng IEEE Rev.* 2009;2:147–71.
25. Heinzer S, Krucker T, Stampanoni M, Abela R, Meyer EP, Schuler A, et al. Hierarchical micro-imaging for multiscale analysis of large vascular networks. *Neuroimage.* 2006;32(2): 626–36.
26. Jackson T. Modeling tumor vasculature: molecular, cellular, and tissue level aspects and implications. New York: Springer; 2012.
27. Khan AM, Rajpoot N, Treanor D, Magee D. A nonlinear mapping approach to stain normalization in digital histopathology images using image-specific color deconvolution. *IEEE Trans Biomed Eng.* 2014;61(6):1729–38.
28. Lessmann B, Nattkemper TW, Hans VH, Degenhard A. A method for linking computed image features to histological semantics in neuropathology. *J Biomed Inform.* 2007;40:631–41.
29. Li X, Plataniotis KN. A complete color normalization approach to histopathology images using color cues computed from saturation-weighted statistics. *IEEE Trans Biomed Eng.* 2015;62(7):1862–73.
30. Lin B, Yang ZR. A suggested lacunarity expression for sierpinski carpets. *J Phys A Math Gen.* 1986;19(2):L49–52.
31. Lorthois S, Cassot F. Fractal analysis of vascular networks: insights from morphogenesis. *J Theor Biol.* 2010;262(4):614–33.
32. Louis DN, Ohgaki H, Wiestler OD, Cavenee WK, Burger PC, Jouvet A, et al. The 2007 WHO classification of tumours of the central nervous system. *Acta Neuropathol.* 2007;114(2): 97–109.
33. Mandelbrot BB, van Ness JW. Fractional Brownian motions, fractional noises and applications. *SIAM Rev.* 1968;10(4):422–37.
34. Mandelbrot BB. Fractal geometry of nature. San Francisco: Freeman; 1982.
35. Onder D, Zengin S, Sarioglu S. A review on color normalization and color deconvolution methods in histopathology. *Appl Immunohistochem Mol Morphol.* 2014;22(10):713–9.
36. Paggi M, He QC. Evolution of the free volume between rough surfaces in contact. *Wear.* 2015;336:86–95.
37. Pantic I, Dacic S, Brkic P, Lavrnja I, Jovanovic T, Pantic S, et al. Discriminatory ability of fractal and grey level co-occurrence matrix methods in structural analysis of hippocampus layers. *J Theor Biol.* 2015;370:151–6.
38. Peitgen HO, Jürgens H, Saupe D. Chaos and fractals: new frontiers of science. 2nd ed. New York: Springer; 2004.
39. Peleg S, Naor J, Hartley R, Avnir D. Multiple resolution texture analysis and classification. *Pattern Anal Mach Intel IEEE Trans.* 1984;6(4):518–23.
40. Petrou M, Gacia Sevilla P. Image processing: dealing with texture. Chichester, England: Wiley; 2006.
41. Qian W, Zhukov T, Song DS, Tockman MS. Computerized analysis of cellular features and biomarkers for cytologic diagnosis of early lung cancer. *Anal Quant Cytol Histol.* 2007; 29(2):103–11.
42. Qureshi H, Rajpoot N, Wilson R, Nattkemper T, Hans VH, editors. Comparative analysis of discriminant wavelet packet features and raw image features for classification of meningioma subtypes. Medical image understanding and analysis. Aberystwyth: BMVA; 2007.
43. Qureshi H, Sertel O, Rajpoot N, Wilson R, Gurcan M. Adaptive discriminant wavelet packet transform and local binary patterns for meningioma subtype classification. *Med Image Comput Comput-Assist Interv Proc.* 2008;5242:196–204.
44. Seker H, Odetayo MO, Petrovic D, Naguib RNG. A fuzzy logic based-method for prognostic decision making in breast and prostate cancers. *IEEE Trans Inf Technol Biomed.* 2003;7(2): 114–22.
45. Sertel O, Kong J, Catalyurek UV, Lozanski G, Saltz JH, Gurcan MN. Histopathological image analysis using model-based intermediate representations and color texture: follicular lymphoma grading. *J Signal Proc Syst Signal Image Video Technol.* 2009;55(1–3):169–83.

46. Sertel O, Kong J, Shimada H, Catalyurek UV, Saltz JH, Gurcan MN. Computer-aided prognosis of neuroblastoma on whole-slide images: classification of stromal development. *Pattern Recog.* 2009;42(6):1093–103.
47. Strange H, Zwiggelaar R. Meningioma subtype classification using morphology features and random forests. In: Gurcan MN, Madabhushi A, editors. *Medical imaging 2013: digital pathology*. Lake Buena Vista, FL: Proceedings of SPIE; 2013. p. 8676.
48. Thiran JP, Macq B. Morphological feature extraction for the classification of digital images of cancerous tissues. *IEEE Trans Biom Eng.* 1996;43(10):1011–20.
49. Tropine A, Dellani PD, Glaser M, Bohl J, Ploner T, Vucurevic G, et al. Differentiation of fibroblastic meningiomas from other benign subtypes using diffusion tensor imaging. *J Magn Reson Imaging.* 2007;25(4):703–8.
50. Turner MJ, Andrews PR, Blackledge JM. *Fractal geometry in digital imaging*. San Diego: Academic; 1998.
51. Turner MR. Texture-discrimination by Gabor functions. *Biol Cybern.* 1986;55(2–3):71–82.
52. Wiltgen M, Gerger A, Wagner C, Bergthaler P, Smolle J. Evaluation of texture features in spatial and frequency domain for automatic discrimination of histologic tissue. *Anal Quant Cytol Histol.* 2007;29(4):251–63.
53. Wirjadi O, Breuel T, Feiden W, Kim YJ, editors. *Automated feature selection for the classification of meningioma cell nuclei*. *Bildverarbeitung für die Medizin*; 2006.
54. Wittke C, Mayer J, Schweiggert F. On the classification of prostate carcinoma with methods from spatial statistics. *IEEE Trans Inf Technol Biomed.* 2007;11(4):406–14.
55. Zeng Z, Tong Z, Han Z, Zhang Y, Zwiggelaar R. The classification of meningioma subtypes based on the color segmentation and shape features. In: Li S, Jin Q, Jiang X, Park JJ, editors. *Frontier and future development of information technology in medicine and education*. *Lecture Notes in Electrical Engineering*. New York: Springer; 2014. p. 2669–74.
56. Zengin S, Sakar M, Onder D, Sarioglu S. Color correction of stained tissue section images by histogram transfer according to control images. *Anal Quant Cytol Histol.* 2015;37(3):177–86.

Chapter 24

Computational Fractal-Based Analysis of Brain Tumor Microvascular Networks

Antonio Di Ieva and Omar S. Al-Kadi

Abstract Brain parenchyma microvasculature is set in disarray in the presence of tumors, and malignant brain tumors are among the most vascularized neoplasms in humans. As microvessels can be easily identified in histologic specimens, quantification of microvasculature can be used alone or in combination with other histological features to increase the understanding of the dynamic behavior, diagnosis, and prognosis of brain tumors. Different brain tumors, and even subtypes of the same tumor, show specific microvascular patterns, as a kind of “microvascular fingerprint,” which is particular to each histotype. Reliable morphometric parameters are required for the qualitative and quantitative characterization of the neoplastic angio-architecture, although the lack of standardization of a technique able to quantify the microvascular patterns in an objective way has limited the “morphometric approach” in neuro-oncology.

In this chapter we focus on the importance of the computational-based morphometrics, for the objective description of the tumoral microvascular fingerprinting. By also introducing the concept of “angio-space,” which is the tumoral space occupied by the microvessels, we here present fractal analysis as the most reliable computational tool able to offer objective parameters for the description of the microvascular networks.

A. Di Ieva, MD, PhD (✉)

Neurosurgery Unit, Faculty of Medicine and Health Sciences, Macquarie University, Sydney, NSW, Australia

Garvan Institute of Medical Research, Sydney, NSW, Australia

Medical University of Vienna, Vienna, Austria

University of Toronto, Toronto, ON, Canada

e-mail: diieva@hotmail.com

O.S. Al-Kadi

Institute of Bioengineering, Ecole Polytechnique Fédérale de Lausanne (EPFL), Lausanne, Switzerland

King Abdullah II School for IT, University of Jordan, Amman, Jordan

The spectrum of different angioarchitectural configurations can be quantified by means of Euclidean and fractal-based parameters in a multiparametric analysis, aimed to offer surrogate biomarkers of cancer. Such parameters are here described from the methodological point of view (i.e., feature extraction) as well as from the clinical perspective (i.e., relation to underlying physiology), in order to offer new computational parameters to the clinicians with the final goal of improving diagnostic and prognostic power of patients affected by brain tumors.

Keywords Angioarchitecture • Brain tumor • Fractal dimension • Fractal analysis • Glioblastoma multiforme • Microvasculature

24.1 Introduction

The brain is among the most perfused organs of the human body, and in order to meet its high metabolic demand, it has one of the most complex vascular and microvascular systems. Different regions of the brain are characterized by specific microvascular networks [8, 22–24, 38] whose level of complexity most likely reflects the function related to that specific area [11]. Since tumors are supported by different patterns of vascularization [34], it is possible to speculate that tumorigenesis (i.e., the sequential accumulation of mutations within tissue cells) is related to the disarray of the physiological microvascular bed or even related to a programmed rearrangement of a new and specific microvascular network. The study of the neoplastic angioarchitecture seems to be of paramount importance not only for research purposes but for clinical applications as well since it has been shown that the “normalization” of the abnormal microvascular architecture of tumors by means of anti-angiogenic agents, for example, can reduce regional hypoxia and eventually increase the efficacy of therapies [32, 33]. According to this model, the imbalance between pro- and anti-angiogenic factors in a tumor disorganizes the angioarchitecture, which might be brought back from its irregular pathological state to a physiologic state and then “normalized.” Fractal analysis offers several tools for the quantification and temporal follow-up of such angiostructural changes [25, 44].

24.2 Brain Tumors and Vascularization

The latest available World Health Organization (WHO 2007¹) grading system classifies brain tumors according to histological features in a sort of benign-to-malignant gradient (from grade I to grade IV, with grade IV being the most malignant) [41].

¹At the time of the chapter writing, the WHO classification system for brain tumors published in 2016 was not available yet.

The grading has diagnostic, prognostic, and therapeutic value, considering that grade I lesions have low proliferative and infiltrative potential, and can be virtually cured by means of surgery and/or radiosurgery alone, while grade IV cancer requires multimodal approaches (i.e., surgery followed by radio-chemotherapy) and has fatal prognosis.

Malignant brain tumors are among the most vascularized tumors in humans [41]. As microvessels can be easily identified in biopsy specimens, it has been suggested that quantification of microvasculature might be used alone or in combination with other histological features to increase the understanding of the dynamic behavior and prognosis of brain tumors, as well as for diagnostic purposes. However, microvasculature is not always considered a feature related to brain tumor grading. Microvascular proliferation is considered a histopathological hallmark of glioblastoma multiforme (GBM) [41], which is the most frequent and malignant glioma (WHO grade IV), but the differences in microvasculature between grade II and III gliomas, for example, are less clear and not used for grading. Also, meningiomas of different grades, as well as meningiomas in comparison to hemangiopericytomas, clearly display different vascular patterns (see Table 24.1), but other features are still used to differentiate the different grades and/or tumors [2]. This is also related to the lack of standardization of a technique able to quantify the microvascular patterns in an objective way.

The vascularization of malignant brain tumors is the target for anti-angiogenic treatment (such as bevacizumab), providing reasoning on the importance of the different methods in quantifying and assessing the changes in tumor microvasculature. On one hand, it is true that different brain tumors show different angiogenic patterns, but on the other it seems that single histotypes, such as GBM, show a very highly heterogeneous microangioarchitecture [5, 17, 18, 45]. We here summarize the concepts and methods related to microvascular detection and image analysis for the following morphometric analyses.

24.2.1 Immunohistochemistry (IHC)

In histological specimens, microvessels can be detected by means of IHC. Several antibodies have been described for the immunodetection of the endothelium, each one with its own pros and cons, summarized in Table 24.2. The most commonly

Table 24.1 Examples of brain tumors showing peculiar microvasculatures

Different brain tumors	Same brain tumors of different grades
Gliomas, gliosarcomas, metastases, lymphomas	Gliomas: grades I to IV
Meningiomas vs. hemangiopericytomas	Meningiomas: grades I to III
Pituitary adenomas vs. normal pituitary gland	

Table 24.2 Vascular markers commonly used in immunohistochemistry

Antibody	Description	Pros	Cons
CD31	Also known as platelet-endothelial cell adhesion molecule (PECAM-1); membrane-bound glycoprotein and member of the immunoglobulin family	Stains vessels in both neoplastic and healthy tissue; sufficient sensitivity for blood vessels of all sizes	Frequent antigen loss during retrieval
CD34	Endothelial membrane-bound glycoprotein	Stains blood vessels of all sizes	Pan-endothelial: stains newly formed as well as preexisting vessels, making it ineffective for visualizing only angiogenesis. May lack sensitivity in some tissues
CD105	Endothelial membrane-bound glycoprotein; essential for angiogenesis. Also called endoglin	Stains only newly-formed blood vessels during tumorigenesis; good for visualizing angiogenesis	Ineffective as pan-endothelial marker; weak or no staining in normal tissue
Factor VIII	Glycoprotein polymer involved in platelet aggregation; comprised of von Willebrand factor and smaller antihemophilic factor	Effective for larger vessels staining	Lacks sensitivity for smaller vessels in comparison of other antibodies
Endocan	Cell-specific-molecule-1, proteoglycan secreted by endothelial cells; regulated by vascular endothelial growth factor and related to angiogenesis	Marker of small and large neoangiogenic vessels	Scattered immunostaining of vessels; generally not expressed in non-tumoral tissues

See review in Di Ieva et al. [21]

used are CD34 and CD31 (CD refers to “cluster of differentiation”), which are considered pan-endothelial markers, while CD105 and Endocan are more commonly used for newly formed vessels (i.e., in the process of angiogenesis). Factor VIII and Ulex europeus agglutinin I (UEAI) have almost fallen into disuse due to their multiple limitations. The ratios of CD34:CD105, CD34:Endocan, or CD31:Endocan immunoreactive vessels can provide the “angiogenic fraction” of the tumor [Di Ieva, unpublished results].

24.3 Morphometrics of Microvasculature

Qualitative rather than quantitative analyses have generally been used to describe the differences in the vascularization of the normal brain vs. brain tumors.

It has been suggested that vessel quantification can be added into the tumor classification system for grading as well as for prognostication. If the aim is to provide a morphometric biomarker (i.e., predicting patient prognosis, treatment response, etc.), the limitations are due to the lack of standardization of the proposed parameters. Morphometrics aims to reduce shapes to numbers, offering a reductionist approach to describe the geometrical complexity of natural objects. In pathology, morphometric analyses add a quantitative element to the qualitative description of the tissue [11], generating continuous variables, which can be used for statistical comparison.

Defining the “tumor-space” as the neoplastic volume, the “angio-space” refers to the proportion of microvessels filling such volume, not just in terms of quantity but also in terms of size, shape, and pattern of distribution [11].

Pathologists recognize distinct vascular angiogenic subtypes, described as palisades, glomeruloid vascular proliferation, vascular garlands, vascular clusters, and microvascular sprouting, and may also use semiquantitative scores to quantify the level of “clusterization” of the microvessels [20] (see Table 24.3). This seems to be relevant, especially when considering the relationship between vascular patterns and clinical outcomes, as different angiogenic protein expression associated with different angioarchitecture can respond in different ways to chemotherapy [5]. These descriptions lack standardization and some intra- and interobserver variability may be present.

Since the introduction of the use of the vessel density in 1972 [6], several other parameters have been proposed as potential “quantitators” of the microvascular system, used to quantify the angio-space (Tables 24.3 and 24.4).

We here classify these morphometric parameters in “Euclidean-based” and “fractal-based” parameters.

Table 24.3 Morphometric parameters used to quantify the angio-space

Euclidean-based parameters	Fractal-based parameters
Microvessel density (MVD)	Fractal dimension (FD), microvascular fractal dimension (mvFD)
Density/number of vessels	Local box-counting dimension
Total vascular area (TVA)	Tortuosity
Local vascular area (in the hot spot)	Lacunarity
Perimeter	Representative elementary volume (REV) length scale
Mean diameter of the microvessels	Hurst exponent
Branching count	
Major and minor axis length	
Pathologist-based analysis	Other non-Euclidean parameters
Semiquantitative scoring systems, that is, 0 (no clusters), 1 (clusters), 2 (very prominent clusters)	Compactness
	Shape factor
	Distance maps
	Microvascular structural entropy

Table 24.4 Morphometric parameters used to quantify the microvascular pattern identified in histological specimens of grade II and III gliomas

Angioarchitectural morphometric parameters	
A_{rum}	Area covered by the specimen of brain tumor on the histological section
TVA	Total vascular area, the area of the microvessels of the whole specimen
A%	Ratio between TVA and A_{rum}
MVs/mm ²	Microvascular density expressed as the mean number of microvessels per mm ²
Hot spot	1 mm ² area of the specimen having the highest local A(%)
Local A(%)	The % vascular area in the hot spot
mvFD	Microvascular fractal dimension: monofractal dimension of the microvascular pattern of the whole specimen (in a pre-determined scaling window)
loc mvFD	Local mvFD: monofractal dimension of the microvascular pattern expressed in the hot spot area (scaling window, $\epsilon_{min} = 1 \mu\text{m}$; $\epsilon_{max} = 100 \mu\text{m}$)
loc bcD	Local box-counting dimension: value of fractal dimension estimated by the box-counting method in a non-monofractal range (scaling window, $\epsilon_{min} = 1 \mu\text{m}$; $\epsilon_{max} = 1,000 \mu\text{m}$)

From Di Ieva et al. [20]

24.3.1 Euclidean-Based Parameters

One of the most used parameters is the microvessel density (MVD), based on the measure of the number of immunostained microvessels per square millimeter in the most densely vascularized area of the histological specimen (termed “hot spot”). Different techniques have been proposed for the MVD calculation, and several seminal papers have investigated its role in every human tumor (see review in [14]), including the brain and pituitary tumors (reviews in [13, 14]), but in conclusion it has been shown that it is not a valid measure for guiding and/or evaluating anti-angiogenic treatment [31], nor for distinguishing different grades of brain tumors. All the histological analyses are limited by the sampling, especially in GBMs, which show a very high histologic heterogeneity. The greatest limitation of the use of the MVD is the choice of the hot spot, due to (a) high inter- and intra-observer variability in its selection, (b) potential lack of representativity of the whole specimen, and (c) potential lack of representation of a complex 3D structure, such as the microvascular tree, in a 2D histological area [15, 18, 43].

Other Euclidean parameters can be computed on the histological specimens of brain tumors (see Table 24.3). Multiparametric analyses of combinations of such indices have shown microvascular morphometrics as a valid tool to differentiate different grades of brain tumors [18, 37, 45].

The greatest limitation of the described parameters is that Euclidean geometry can only quantify regular and smooth objects, and therefore can only offer approximations of the roughness expressed by natural objects, such as the microvascular trees. The complexity of vascular systems depends on (a) the number of vessels, (b) their size and shape, and (c) the pattern of the vessel distribution and the nonlinear, temporal, and spatial advance of the promotion, progress, mediation, and inhibition

of angiogenesis generating the complex ramified network irregularly filling the environment surrounding the tumor, which can be described by Euclidean geometry only with great approximation [28].

Fractal geometry overcomes the limits of Euclidean parameters. The fractal-based parameters are described next.

24.3.2 Image Analysis

The first step to apply any morphometric analyses on the neoplastic angio-space is the choice of the technique to visualize the microvessels and the following image analysis, which should be standardized (see Chap. 12) (Fig. 24.1).

When the target of analysis is the microvascular network, several issues have to be considered, for example, whether the analysis is performed on the basis of the space-filling area of the vessels or on skeletonized representations of the microvessels.

In the image analysis, eventual artifacts related to the segmentation of immunoreactive vessels have to be considered. For example, nonspecific immunoreactivity can limit the automatic detection of the vessels, as in the case when antigens diffuse to other compartments (e.g., CD34 antigens which immunostain cell nuclei or necrotic areas rather than endothelial cells). In such cases, a pathologist is still required to identify any artifacts, which should be eliminated from the analysis.

Other digital image acquisition calibration parameters should be standardized as well, in terms of regulating the light intensity of the microscope, maintaining the same resolution over the whole series, and using an identical threshold to extract the

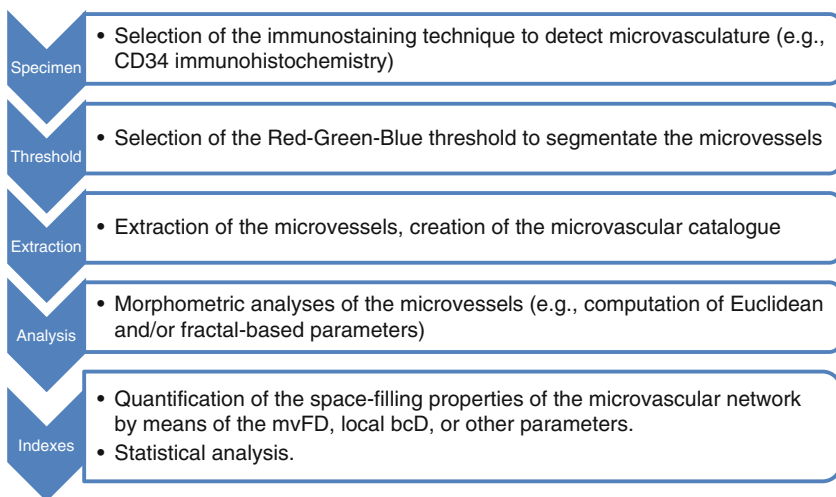


Fig. 24.1 Flowchart used for image and morphometric analyses of microvasculature in histological specimens

immunoreactive vessels. A virtual microscope can be used to digitize the entire specimen rather than few areas selected manually. The vessels can be extracted as a whole from the specimen and organized in a vascular catalog, giving a snapshot on the number and shape of the microvessels within the specimen (Fig. 24.2).

24.4 Fractal-Based Morphometric Analyses of Microvessels

Fractal geometry provides a computer-aided method to describe and quantify the roughness and geometrical complexity of the microvessels distributed within the tumor, as it has been shown in a vast variety of neoplasia, including prostate, kidney, lung, colon, skin, and brain tumors as well. By concentrating on the irregularity of tumor growth rather than individual measure of size (such as diameter and volume or other Euclidean parameters), fractal geometry is well suited to quantify the morphological features that pathologists have long used to describe malignancies in a qualitative way (i.e., wrinkled borders within the host tissue, random microvascular patterns, etc.) [4]. Several researchers have demonstrated the fractality (or “semi-fractality”) and multifractality of the vascular and microvascular trees of many tissues and organs, in physiologic as well as pathologic states, including the human brain [1, 2, 4, 8–10, 26, 27, 29, 35, 40, 44, 47].

The main aim of computational fractal-based analysis of the microvascular patterns is the quantification of parameters, which can be used as surrogate biomarkers.

24.4.1 Microvascular Fractal Dimension (*mvFD*)

The most widely used parameter in fractal geometry is the fractal dimension (FD or D_F), which describes the space-filling properties of irregularly shaped objects [3, 9, 10, 26]. FD has been shown to be the most robust estimator of vascular networks [36, 49]. Extending the use of FD to the quantification of microvessels, the microvascular fractal dimension (*mvFD*) quantifies the space-filling properties of the microvessels within a tissue; in the case of a tumor, *mvFD* quantifies the level of geometrical complexity of the microvessels embedded within the tumor. The *mvFD* adds a qualitative component to the parameterization of the angio-space, trying to answer the following question: assuming an equal number of vessels, what can be said about their shape, size, and pattern of distribution? This means that histological specimens of similar or different tissues can show the same value of MVD or total vascular area, for example, but a very different pattern of distribution, with different values of *mvFD*. Of course, it can also happen that histological tissues with same *mvFD* values differ for the Euclidean parameters, making the approaches complementary methods of quantification. Therefore,

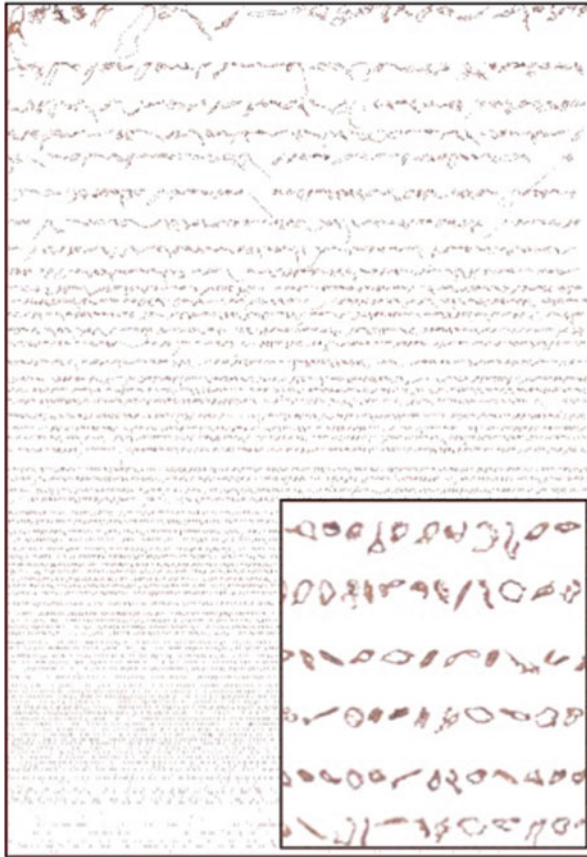


Fig. 24.2 Example of a vascular catalog (in this case, of a glioblastoma multiforme, GBM, with magnification of the vessels in the *inset*). The catalogs give information at a glance on number and shapes of all the microvessels extracted from the entire specimen

mvFD offers useful information about the tumoral space filled by microvessels. The parameter is computer aided, and its objective measure makes it a comparable parameter among different operators. If it is important to analyze the distribution of the vessels within the tissue, by means of FD, for example, it is equally important to analyze complementary parameters, the “vascular gappiness,” that is, the avascular spaces, by means of the lacunarity or other methods, like the distance maps [44].

In a 2D histological specimen, mvFD ranges from 0 to 2. For example, a tumor with a hypothetical mvFD value of 1.95 owns a microvascular network almost filling its area, like the Peano’s curve, with a very complex geometric and highly space-filling microvascular pattern (Fig. 24.3). This microvascular pattern virtually fills the whole tissue in which it is embedded, reducing the avascular spaces to the minimum (therefore increasing the lacunarity) [3] (Fig. 24.4). In the 3D space, such

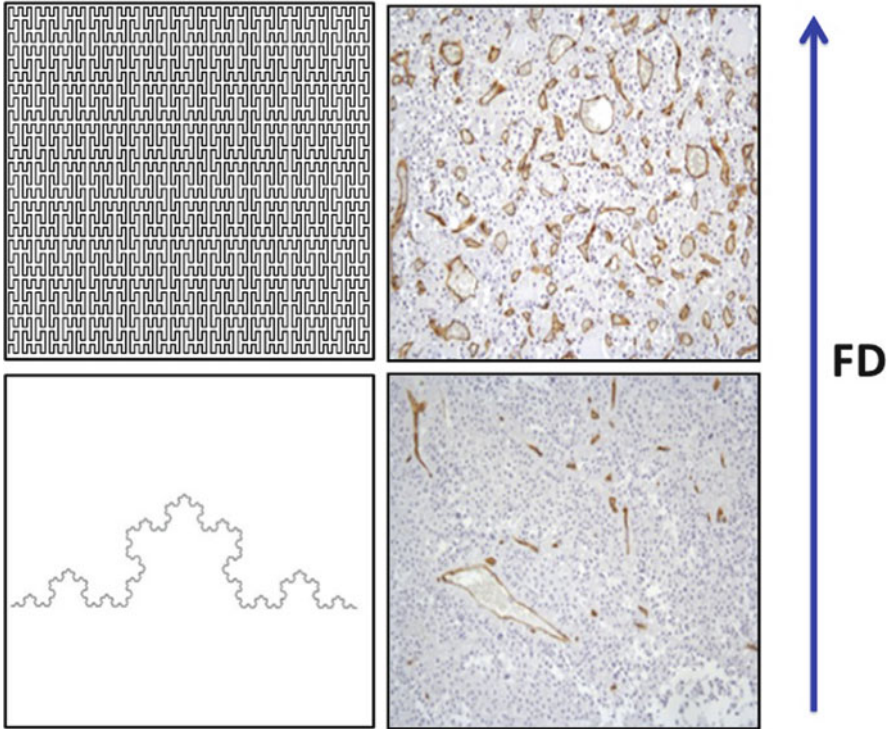


Fig. 24.3 Values of the fractal dimension (FD) on a 2D plane, comparing two fractal objects with the microvasculature (endothelial CD34 immunostaining) of a pituitary adenoma (*lower image*) with the specimen of a normal pituitary gland. The *lower image on the left* shows the Koch's curve ("snowflake"), with $FD = 1.26$. FD increases in more space-filling objects, namely, in the Peano's curve (*higher image on the left*, with $FD \approx 2$) and in the microvasculature of the normal pituitary gland, which is more homogeneously distributed within the parenchyma of the gland

as in electron microscopy reconstructions of the microvascular trees in the 3D volume, FD trends toward a maximal value of 3 [44, 47].

In several kinds of tissues, it has been shown that FD and lacunarity values differ in the physiological and pathological vascular networks [3, 19, 25]. This means that the disarray of the microvascular network, which extends from the normal tissue (e.g., the brain) to the tumor, can be quantified by means of fractal analysis, in a kind of gradient of morphometric differences between tissues. Based on the evidence that the neoplastic microvascular network is abnormal, it has been experimentally shown that the "normalization" of such disarray can be used for therapeutic purposes, as previously quoted, and the FD can be used as a surrogate biomarker for diagnosis and/or treatment follow-up [3, 25]. By means of 2D and 3D analyses, FD values of normal brain microvasculature have been found to be higher than that of neoplastic regions, meaning that the normal brain is better suited to more space-occupying microvasculature [3, 25, 47]. However, due to the

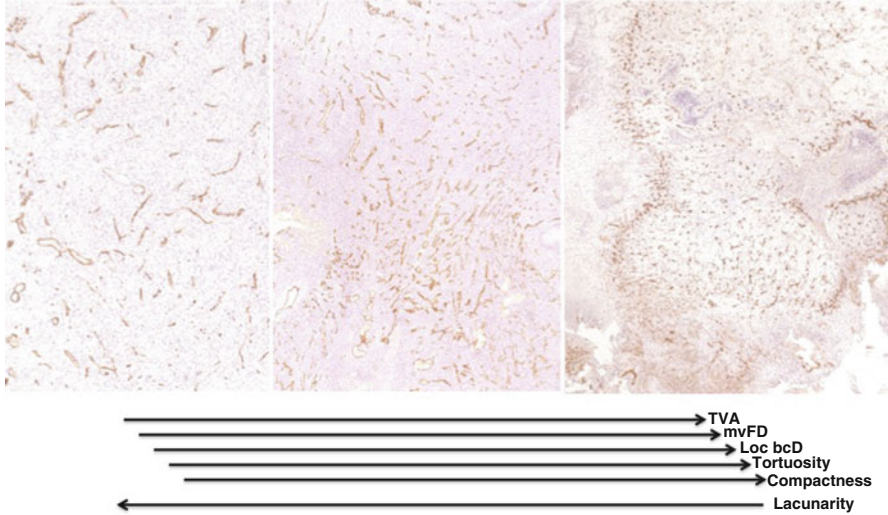


Fig. 24.4 Specimens of three cases of GBM, showing different microvasculature (microvessels detected by using antibodies raised against CD34 with brown coloration). The angio-space of each tumor can be described by means of several parameters (*TVA* total vascular area, *mvFD* microvascular fractal dimension, *loc bcD* local box-counting dimension. See Table 24.4)

use of different methods and techniques, these results are controversial. For example, in one experimental study, the vascular FD values of primate and rat brain tumors have been found to be higher than those of normal brain parenchyma, thus indicating a greater metabolic supply and bigger surface area for gas exchange within the tumors [44]. In numerical terms, fractal-based demonstration that tumoral and normal vascular networks are intrinsically different; Baish et al. introduced a complementary metric to the FD, the tortuosity, defined as the ratio between the minimum vascular path joining two points and their geometric distance from each other [3]. A greater tortuosity has been correlated with a worse response to drugs, confirming again the importance of the analysis of the angio-structure from the therapeutic perspective.

Among several reasons, including their relative simplicity and the speed to be computed, the most used methods to compute mvFD are the box-counting and the sandbox methods (see Chap. 2). These methods have been applied to whole histological specimens of brain tumors as well as on selected spots. The choice of the “hot spot” can be performed manually (i.e., the pathologist chooses the area subjectively considered to be the most vascularized and representative of the microvascular network of the tumor) or by computer-aided methods (e.g., the spot with the highest vascular area, as calculated by the computer). The first method is biased by the introduction of the operator-dependent choice of the hot spot, while the second method can be biased by the operator-dependent choice of the threshold to automatically extract the immunoreactive vessels from the specimen or from manually

erasing artifacts outside the region of interest. An ideal method should be objective and reproducible, without any operator-dependent biases. Moreover, as it often happens in pathology, the analysis can be biased by the choice of the specimen itself (the problem of sampling, which could not be representative of the whole tumor, like a sample resembling a WHO grade II glioma within a grade III tumor). To limit this problem, other parameters have been introduced.

24.4.2 Local Fractal Dimension and Local Box-Counting Dimension

In order to avoid the sampling of nonrepresentative areas of the tumors such as necrotic areas, the local fractal dimension considers FD in the hot spot. The subjective selection of the hot spot would limit the objective reproducibility of such parameters in the same way as with the MVD. In order to avoid such limitations, the hot spot can be automatically chosen, for example, by computing the vascular area for each 1 mm² area on a grid drawn on the specimen (Fig. 24.5) and extracting the spot with the highest ratio (immunoreactive surface of vessels/tumoral area). Once selected, the 1 mm² spot with the highest vascular area becomes the hot spot for the following analysis (Figs. 24.5 and 24.6). On such a spot, the local mvFD can be computed. A previous analysis showed that a monofractal behavior was found considering a two orders of magnitude window, that is, between 1 and 100 μm [20]. Assuming an average microvessel diameter between 5 and 10 μm , such a fractal window considers the smallest features of the microvessels (i.e., the roughness of the outline), as well as the agglomerate of micro-clusters of vessels (at the magnitude of 100 μm). As shown, this was considered insufficient to cover the entirety of the histopathological features of the microvessels, such as the macro-agglomerates in large clusters (like the garland-like vascular structures). A fractal window ranging between 1 μm and 1 mm, that is, covering three orders of magnitude, was considered significant to cover all of the mean histopathological characteristics of the microvessels, including the intrinsic morphologic features and their clustering properties. Applying the box-counting method in such a range, a monofractal behavior was not confirmed (see Fig. 24.6), although a similar slope of the curve was found across all the analyzed specimens. The several power laws showed that glioma microvasculature clearly demonstrates a multifractal distribution of geometrical complexity of the glioma's microvessels when observed at various scales of magnification. The slope of a straight line interpolating the points on the log-log graphs was considered as the mean value expressing the space-filling properties of the microvessels in the hot spot, and the value was indicated as the local box-counting dimension (local bcD) [20]. Both mvFD and local bcD express, in a single variable, the ability of the microvessels to fill the space in which they are embedded (i.e., the tumor), which is a characteristic intrinsically correlated to their number, size, shape, and distribution pattern.

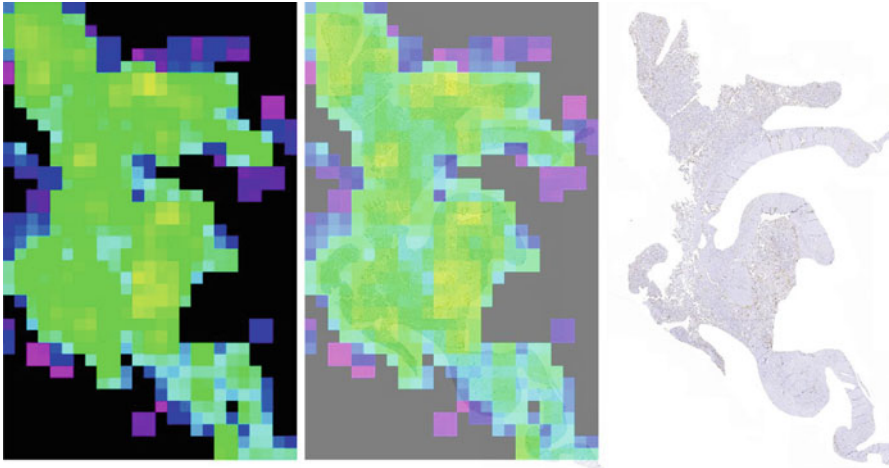


Fig. 24.5 Microvascular map for the automatic selection of the hot spot. Over-imposing a grid of 1 mm^2 boxes on the entire specimen, the vascular area can be computed on each box and a color map can be associated to the different ratios. In this example, the yellow boxes represent the regions of the specimen with the highest vascular area. Raw data show also the value of the vascular area for each box, and the one with the highest value is automatically chosen as hot spot for the following computational analyses (software by Carlo Russo)

24.5 Fractal-Based Analysis of the Angio-Space in Brain Pathology

We define the concept of “angio-space” as the set of parameters quantifying the microvasculature within a tumor or the tumoral space occupied by its own angioarchitecture (Di Ieva [19] and unpublished data). According to the speculation that different tumors, or even different subtypes of the same tumor have a specific “microvascular fingerprint” [19], it has been speculated that a gradient of geometrical representation (and then of fractal angioarchitectural parameters, including FD) exists between physiological and pathological tissues, as well as different states of the same tissues. The pituitary gland is an exemplary model: Euclidean-based approaches (i.e., vascular area and MVD) and fractal-based analyses have clearly shown that it is not only more vascularized but also exhibits a higher microvascular heterogeneity and geometrical complexity in the comparison of the pituitary adenomas [13, 16, 21]. Regarding the different subtypes of pituitary adenomas, analyses of the MVD have shown very discordant results [13], with some preliminary fractal-based analyses not showing any statistically significant differences in the angioarchitecture of micro- vs. macro-adenomas, for example [Di Ieva, unpublished results]. The pituitary gland is a simple model from which to extend the fractal analysis of the microvasculature to the study of brain tumors, by analyzing histological specimens treated with antibodies raised against the endothelium (in the whole specimen and/or hot spots), or volumetric reconstructions of histological

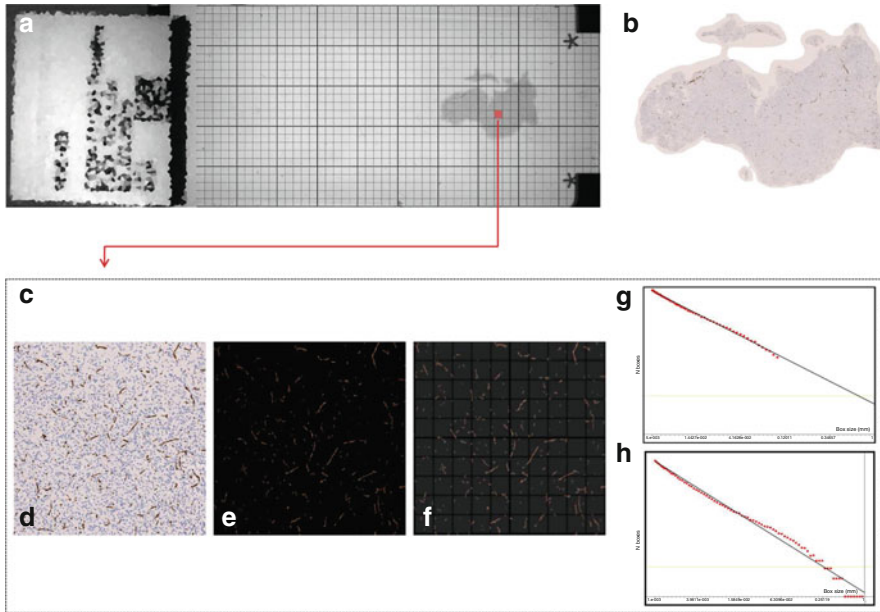


Fig. 24.6 Computer-aided technique for fractal analysis of the microvasculature in histological specimens. Estimation of the morphometric fractal parameter in the whole section and in the hot spot region of specimens of brain gliomas; detection of microvessels using antibodies raised against CD34. The extraction of the whole specimen and the segmentation of the immunoreactive vessels (**a**, **b**) allow the automatic measurement of the morphometric parameters listed in Table 24.4. Moreover, a grid of boxes measuring 1 mm to a side length is superimposed on the whole histological section. For each box, the ratio between the local vascular area and the local neoplastic area is calculated [*local A*(%)] ; the box with the highest *local A*(%) is automatically selected and extracted to be used as the “hot spot” representative of the whole specimen (**c**). (**d**) Hot spot of the specimen, automatically extracted. (**e**) Selection of the RGB threshold to automatically extract the CD34+ vessels. (**f**) Box-counting method: superimposition on the image of grids with boxes of different lengths, from a minimum size (ϵ_{min}) to a maximum size (ϵ_{max}), in the pre-selected scaling window. (**g**) A monofractal behavior was found by limiting the scaling window to a range of two orders of magnitude ($\epsilon_{min} = 1 \mu\text{m} - \epsilon_{max} = 100 \mu\text{m}$). The slope of the obtained curve is the microvascular fractal dimension (mvFD) [Axes of the log-log graph (box-counting method): X-axis=Box size (mm); Y-axis=N Boxes]. (**h**) Considering that a maximum size of the box of $100 \mu\text{m}$ does not cover the complete hot spot, a wider scaling window was also applied (Reproduced from Di Ieva et al. [20])

tissues and/or radiological images (see Chaps. 19, 20, 21, 22, and 23). If the pituitary gland shows a relatively low variability of the microvascular patterns (meaning that the vascular network is quite homogeneous) [12], malignant brain tumors show very high microvascular heterogeneity. By analyzing 114 GBM specimens, a mean mvFD value of about 1.44 (ranging 1.06–1.87) was found, with a coefficient of variation (CV, standard deviation divided by the mean) of 44% [18]. For comparison, the CV of pituitary adenomas was found less than 10% [12]. This very high

variability in the space-filling properties of microvasculature of GBM reflects the very high angioarchitectural heterogeneity shown by this malignant tumor. The microvascular networks of GBM can be represented in a very broad and continuous spectrum of possible geometric configurations; this was the first mathematical demonstration that GBM is *multiforme* (from the Latin meaning “multi-shapes”) also in relation to its microvasculature [18].

Morphometric and computational fractal-based analyses also showed that grade II gliomas have different angio-spaces in comparison to grade III gliomas (Fig. 24.7). Among several morphometric parameters, the local mvFD and especially the local bcD were shown to be the most reliable quantitative indicators of the neoplastic microvasculature, making them potential surrogate biomarkers [20]. The histopathological grading of gliomas can be challenging in some cases, especially in grade II vs. grade III gliomas, and the erroneous diagnosis can result in patients’ over- or undertreatment [48]. For this reason, computational methods, which can help in differential diagnosis, are more than welcome to be added in the pathologists’ and clinicians’ armamentarium.

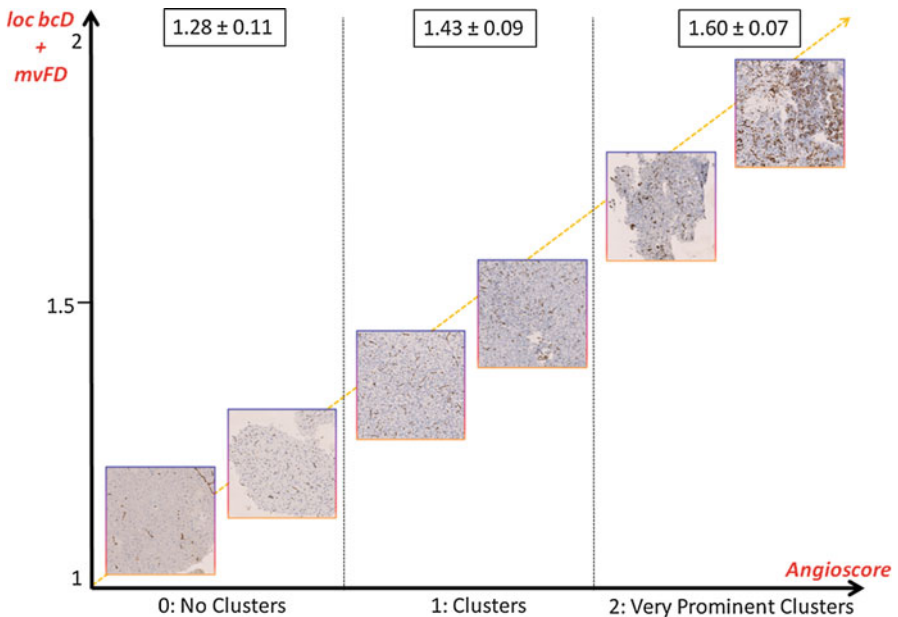


Fig. 24.7 Correlation between the fractal angiormorphometric parameters and the level of clustering of the microvessels. Schema showing the correlation between the angioscore assigned by the neuropathologist to each specimen and the fractal-based variables [local box-counting dimension (loc bcD) and microvascular fractal dimension (mvFD)]. The value reported for each angioarchitectural group is the mean value of loc bcD \pm standard deviation. The yellow line indicates the increasing grade of malignancy of the tumor. The fractal parameters assigned nearly 75% of the gliomas to the correct histological grade and angioscore (Reproduced from Di Ieva et al. [20])

24.6 Limitations

If fractal-based angioarchitectural classification of brain tumors can be useful for diagnostic and prognostic purposes, there are still some limitations to acknowledge. For a description of the limitation of image and fractal analysis, see Chaps. 1 and 12. Below, we summarize some main points. First of all, according to the basic principles of fractal geometry, it does not mean that objects owning the same mvFD, for example, show the same microvascular pattern. As previously stated, this means that fractal indexes should be analyzed as complementary to other morphometric parameters in a multiparametric analysis.

When the analysis is performed on histological specimens, the sampling problem can limit its benefit. The analysis of the whole specimen or of the computationally chosen most representative spot of the specimen tends to decrease the limitations of other analyses, like the MVD-based ones, but a histological sample still often does not represent anything more than a very small fraction of the whole tumor, and this should be taken into consideration. The estimation of a 2D representation of the microvascular tree could not reflect the real 3D complexity of the microvascular network, because 2D methods performed on histological specimens are length related rather than mass related, and this can underestimate the true 3D complexity of the tree in the space [7, 42]. This issue can be limited by using volumetric analyses and 3D reconstructions of tissues. The effect of geometrical deformation (e.g., cracks) during the process of sample preparations, and other artifacts such as nonhomogeneity of staining, may also have some impact on the accuracy of the fractal analysis. For this reason, also the sampling, immunostaining and preparation of the histological specimen should be standardized.

Moreover, the histological section represents a “snapshot” in time, a “frozen photo” of the tumor at the moment of the surgical operation, and each quantification refers to that specific moment, not taking in account the dynamic process on the temporal trend of the tumor. For this reason, the temporal changes of tumors should also be considered by means of neuroradiological and/or nuclear medicine findings over time (such as perfusion parameters or methionine uptake in PET, positron emission tomography) [17].

As previously stated, the value of FD and other fractal-based parameters is highly dependent on the image analysis parameters (and “pixel related”, according to the resolution). Several research inquiries have considered different tissues (brain cortex, tumors) in different models (humans, rats), visualized in different ways after undergoing different treatments. When comparing the several values found in the published research, a plethora of results show contrasting findings, and this could be avoided only by a standardization of techniques, materials, and methods.

The standardization ought to be done also in the analytical analysis of the fractal parameters. It is in fact known that biological fractals, such as microvascular networks, are statistically self-similar only within a specific scaling window (i.e., covering at least two orders of magnitude) [40]. The choice of different windows may give different results, and such choice should be standardized as well or at least

justified: if a window ranging 1–100 μm , for example, considers a FD that reflects the organization of the vessels in micro-clusters and their roughness, on the other hand, a range of 100–10,000 μm does not take into account the roughness of the single vessels but rather the distribution of vascular clusters on a larger scale [14]. The lack of standardization of all these elements could produce results no more comparable between different laboratories. Last but not least, microvessels cannot be real fractals, as pointed out, and the “fractalization” of such natural objects can be a mathematical idealization limited by computational manipulation. In order to avoid the several definitions expressed in the very thick related literature on fractality, quasi-fractality, pseudo-fractality, or multifractality of microvessels [27, 39, 46, 50, 51], it is here enough to say that fractal analysis, far from being an infallible and universal method, is still able to offer several reliable parameters for an objective, reproducible, and realistic description and quantification of the microvasculature in normal as well as pathological tissues.

24.7 Future Perspectives and Conclusion

As the architectural pattern of each tumor seems to be its specific microvascular fingerprinting, objective and reproducible morphometric biomarkers are required to describe and quantify the so-called angio-space. Such indexes should be (a) able to quantify what pathologists describe in a qualitative way on the histological specimens of tumors, (b) objective, that is, not affected by intra- and interobserver variability, and (c) clinically meaningful, having prognostic and/or predictive value [20]. Fractal analysis offers several parameters that are promising candidates for such purposes.

In addition, the methodological phase of testing morphometric parameters should be followed by clinically oriented research; to be tested as a potential biomarker, in fact, the morphometric fractal-based parameters should be analyzed in the same way that new oncologic therapies are introduced into clinical practice, in step-by-step successive phases of study [30]. Although the translation of the concept of “fractal microvasculature” into clinical practice (i.e., from “bench to bedside”) is still difficult to be realized [11], it should be emphasized that the research in the field of microvessel morphometrics should run alongside research focused on tumoral angiogenesis (research on molecular biomarkers, such as vascular endothelial growth factor, hypoxia-induced factor, etc.), in order to offer a holistic view on the effects of structure and function on the environment and viability of brain tumors. This means that the morphometric analyses should run alongside the biological approach. Moreover, morphometric analyses should be integrated into *in vivo* techniques (neuroimaging and nuclear medicine methods) to follow-up brain tumors and response to treatment.

In light of the speculations and findings that have been illustrated in this chapter, computational fractal-based and multiparameter morphometric analyses will ultimately find its place in the oncologist’s toolbox as a conventional diagnostic procedure.

References

1. Al-Kadi OS. Texture measures combination for improved meningioma classification of histopathological images. *Pattern Recog.* 2010;43:2043–53.
2. Al-Kadi OS. A multiresolution clinical decision support system based on fractal model design for classification of histological brain tumours. *Comput Med Imaging Graph.* 2015;41:67–79.
3. Baish JW, Gazit Y, Berk DA, et al. Role of tumor vascular architecture in nutrient and drug delivery: an invasion percolation-based network model. *Microvasc Res.* 1996;51:327–46.
4. Baish JW, Jain RK. Fractals and cancer. *Cancer Res.* 2000;60:3683–8.
5. Birner P, Piribauer M, Fischer I, et al. Vascular patterns in glioblastoma influence clinical outcome and associate with variable expression of angiogenic proteins: Evidence for distinct angiogenic subtypes. *Brain Pathol.* 2003;13:133–43.
6. Brem S, Cotran R, Folkman J. Tumor angiogenesis: a quantitative method for histologic grading. *J Natl Cancer Inst.* 1972;48:347–56.
7. Caserta F, Eldred WD, Fernandez E, et al. Determination of fractal dimension of physiologically characterized neurons in two and three dimensions. *J Neurosci Methods.* 1995;56:133–44.
8. Cassot F, Lauwers F, Fouard C, et al. A novel three-dimensional computer-assisted method for a quantitative study of microvascular networks of the human cerebral cortex. *Microcirculation.* 2006;13:1–18.
9. Cross SS, Start RD, Silcocks PB, et al. Quantitation of the renal arterial tree by fractal analysis. *J Pathol.* 1993;170:479–84.
10. Cross SS. The application of fractal geometric analysis to microscopic images. *Micron.* 1994;25:101–13.
11. Di Ieva A, Tschabitscher M. Fractal-based classification of brain tumors angioarchitecture. In: Murray SR, Mitchell EW, editors. *Classification and applications of fractals: new research.* New York: Nova Science Publishers; 2012. p. 205–16.
12. Di Ieva A, Grizzi F, Ceva-Grimaldi G, et al. Fractal dimension as a quantifier of the microvasculature of normal and adenomatous pituitary tissue. *J Anat.* 2007;211:673–80.
13. Di Ieva A, Grizzi F, Gaetani P, et al. Euclidean and fractal geometry of microvascular networks in normal and neoplastic pituitary tissue. *Neurosurg Rev.* 2008;31:271–81.
14. Di Ieva A. Angioarchitectural morphometrics of brain tumors: are there any potential histopathological biomarkers? *Microvasc Res.* 2010;80:522–33.
15. Di Ieva A, Grizzi F. Microvessel density. *J Neurosurg Pediatr.* 2010;6:304–6; author reply 306.
16. Di Ieva A, Grizzi F, Ceva-Grimaldi G, et al. The microvascular network of the pituitary gland: a model for the application of fractal geometry to the analysis of angioarchitecture and angiogenesis of brain tumors. *J Neurosurg Sci.* 2010;54:49–54.
17. Di Ieva A, Grizzi F, Tschabitscher M, et al. Correlation of microvascular fractal dimension with positron emission tomography [(11)C]-methionine uptake in glioblastoma multiforme: preliminary findings. *Microvasc Res.* 2010;80:267–73.
18. Di Ieva A, Grizzi F, Sherif C, et al. Angioarchitectural heterogeneity in human glioblastoma multiforme: a fractal-based histopathological assessment. *Microvasc Res.* 2011;81:222–30.
19. Di Ieva A. Fractal analysis of microvascular networks in malignant brain tumors. *Clin Neuropathol.* 2012;31:342–51.
20. Di Ieva A, Bruner E, Widhalm G, et al. Computer-assisted and fractal-based morphometric assessment of microvasculature in histological specimens of gliomas. *Sci Rep.* 2012;2:429.
21. Di Ieva A, Weckman A, Di Michele J, et al. Microvascular morphometrics of the hypophysis and pituitary tumors: from bench to operating theatre. *Microvasc Res.* 2013;89:7–14.
22. Duvernoy HM, Delon S, Vannson JL. Cortical blood vessels of the human brain. *Brain Res Bull.* 1981;7:519–79.
23. Duvernoy HM. Vascularization of the cerebral cortex. *Rev Neurol (Paris).* 1999;155:684–7.
24. Duvernoy HM. Comments on the microvascularization of the brain. *Cerebrovasc Dis.* 2006;21:423–4.

25. Gazit Y, Baish JW, Safabakhsh N, et al. Fractal characteristics of tumor vascular architecture during tumor growth and regression. *Microcirculation*. 1997;4:395–402.
26. Goldberger AL, West BJ. Fractals in physiology and medicine. *Yale J Biol Med*. 1987;60:421–35.
27. Grasman J, Brascamp JW, Van Leeuwen JL, et al. The multifractal structure of arterial trees. *J Theor Biol*. 2003;220:75–82.
28. Grizzi F, Russo C, Colombo P, et al. Quantitative evaluation and modeling of two-dimensional neovascular network complexity: the surface fractal dimension. *BMC Cancer*. 2005;5:14.
29. Grizzi F, Colombo P, Taverna G, et al. Geometry of human vascular system: is it an obstacle for quantifying antiangiogenic therapies? *Appl Immunohistochem Mol Morphol*. 2007;15:134–9.
30. Hainfellner JA, Heinzl H. Neuropathological biomarker candidates in brain tumors: key issues for translational efficiency. *Clin Neuropathol*. 2010;29:41–54.
31. Hlatky L, Hahnfeldt P, Folkman J. Clinical application of antiangiogenic therapy: microvessel density, what it does and doesn't tell us. *J Natl Cancer Inst*. 2002;94:883–93.
32. Jain RK. Normalizing tumor vasculature with anti-angiogenic therapy: a new paradigm for combination therapy. *Nat Med*. 2001;7:987–9.
33. Jain RK. Normalization of tumor vasculature: an emerging concept in antiangiogenic therapy. *Science*. 2005;307:58–62.
34. Jain RK, di Tomaso E, Duda DG, et al. Angiogenesis in brain tumours. *Nat Rev Neurosci*. 2007;8:610–22.
35. Kedzia A, Rybaczuk M, Andrzejak R. Fractal dimensions of human brain cortex vessels during the fetal period. *Med Sci Monit*. 2002;8:MT46–51.
36. Kirchner LM, Schmidt SP, Gruber BS. Quantitation of angiogenesis in the chick chorioallantoic membrane model using fractal analysis. *Microvasc Res*. 1996;51:2–14.
37. Korkolopoulou P, Patsouris E, Kavantzias N, et al. Prognostic implications of microvessel morphometry in diffuse astrocytic neoplasms. *Neuropathol Appl Neurobiol*. 2002;28:57–66.
38. Lauwers F, Cassot F, Lauwers-Cances V, et al. Morphometry of the human cerebral cortex microcirculation: general characteristics and space-related profiles. *Neuroimage*. 2008;39:936–48.
39. Lorthois S, Cassot F. Fractal analysis of vascular networks: insights from morphogenesis. *J Theor Biol*. 2010;262:614–33.
40. Losa GA. The fractal geometry of life. *Riv Biol*. 2009;102:29–59.
41. Louis DN, Ohgaki H, Wiestler OD, et al. WHO classification of tumours of the central nervous system. Lyon: International Agency for Research on Cancer (IARC); 2007.
42. Mandelbrot BB. *The fractal geometry of nature*. New York: W.H. Freeman; 1982.
43. Preusser M, Heinzl H, Gelpi E, et al. Histopathologic assessment of hot-spot microvessel density and vascular patterns in glioblastoma: poor observer agreement limits clinical utility as prognostic factors: a translational research project of the European organization for research and treatment of cancer brain tumor group. *Cancer*. 2006;107:162–70.
44. Risser L, Plouraboue F, Steyer A, et al. From homogeneous to fractal normal and tumorous microvascular networks in the brain. *J Cereb Blood Flow Metab*. 2007;27:293–303.
45. Sharma S, Sharma MC, Gupta DK, et al. Angiogenic patterns and their quantitation in high grade astrocytic tumors. *J Neurooncol*. 2006;79:19–30.
46. Takahashi T. *Microcirculation in fractal branching networks*. Tokyo: Springer; 2014.
47. Vakoc BJ, Lanning RM, Tyrrell JA, et al. Three-dimensional microscopy of the tumor microenvironment in vivo using optical frequency domain imaging. *Nat Med*. 2009;15:1219–23.
48. van den Bent MJ. Interobserver variation of the histopathological diagnosis in clinical trials on glioma: a clinician's perspective. *Acta Neuropathol*. 2010;120:297–304.
49. Vico PG, Kyriacos S, Heymans O, et al. Dynamic study of the extraembryonic vascular network of the chick embryo by fractal analysis. *J Theor Biol*. 1998;195:525–32.
50. Zamir M. On fractal properties of arterial trees. *J Theor Biol*. 1999;197:517–26.
51. Zamir M. Fractal dimensions and multifractality in vascular branching. *J Theor Biol*. 2001;212:183–90.

Chapter 25

Fractal Analysis of Electroencephalographic Time Series (EEG Signals)

Włodzimierz Klonowski

Abstract Nonlinear methods are better suited for analysis of EEG signals than so-called linear methods like fast Fourier transform (FFT). In this chapter, we illustrate the use of the Higuchi's fractal dimension method. We present several examples of the usefulness of this method in application to sleep-EEG analysis, revealing influence of electromagnetic fields, monitoring anesthesia, and assessing bright light therapy (BLT) and electroconvulsive therapy (ECT). We conclude that Higuchi's fractal dimension method is very useful in the analysis of EEG signals.

Keywords Fractal dimension • Time series • Biosignal • EEG • Electroencephalogram

25.1 Introduction

In 1875 Richard Caton (1842–1926), a medical doctor from Liverpool, published in British Medical Journal his research that demonstrated electrical activity of the brains of the rabbit and the monkey [5]. He is cited in multiple scientific papers, but not many researchers have really read it (Fig. 25.1). It looks like a contemporary brief abstract: length of 10 sentences, 239 words.

It is often said that the first human EEG signals were registered by German psychiatrist Hans Berger (1873–1941) from Jena [4] who first succeeded in recording brain electrical activity through the scalp, using a vacuum tube as an amplifier and a double-coil galvanometer. By the way, EEG was registered already in 1890 by Polish scientists from Jagiellonian University in Cracow – Adolph Beck (1863–1942) and Napoleon Nikodem Cybulski (1854–1919) [3, 7].

Electromagnetic activity of the brain fascinated not only medical doctors. One can find EEG shown even on postal stamps, like that Italian stamp of 1988 showing

W. Klonowski, PhD, DSc
Nalecz Institute of Biocybernetics and Biomedical Engineering,
Polish Academy of Sciences, Warsaw, Poland
e-mail: wklonowski@gmail.com

Fig. 25.2 Italian postal stamp (1988) depicting epileptic EEG and St. Valentine – patron of epileptics. The text reads: “Di epilessia si può guarire” (*You can be cured of epilepsy*) (cf. [10])



a representation of an epileptic EEG and St. Valentine who is patron saint of both lovers and epileptics (Fig. 25.2).

Application of EEG in clinical medicine increased tremendously in the second half of the twentieth century. The EEG “bible” *Electroencephalography* appeared in 1981; its 5th edition has already more than 1,300 double-column pages and it weighs more than 3 kg [29]. What a difference when compared with that first paper by Caton!

Despite a century of clinical use, the underlying origins of EEG rhythms have remained a mystery. Hameroff and Penrose [11] suggested that EEG rhythms as well as consciousness derive from “quantum vibrations in microtubules, protein polymers inside brain neurons, which both govern neuronal and synaptic function, and connect brain processes to self-organizing processes in the fine scale” and that from a practical standpoint, treating brain microtubule vibrations could benefit a host of mental, neurological, and cognitive conditions.

Until the 1990s EEG signals were registered with analog recorders – ink pens writing on a paper tape – and were considered to be continuous. The development of personal computers made possible digitalization of recording process [34] – signals are probed with some frequency and subsequent probes are saved in computer memory as series of discrete numbers and not as continuous functions of time. And for the analysis of these signals computerized methods of time series analysis are used, leading to semiautomatic EEG interpretation.

However, when using the analog EEG equipment, doctors get accustomed to interpret EEG signals in terms of superposition of continuous waves of some characteristic frequencies. Most often paper tape was moving 3 cm per second and on the tape there were vertical lines each 3 cm. If the doctor counted 12 maxima between such two vertical lines, it was interpreted as presence of waves of frequency 12 Hz, which was called alpha rhythm. Since the introduction of digital EEG recorders, the most often applied algorithm for EEG signal analysis has been the fast Fourier transform (FFT) (more precisely – its discrete version) that is supposed to enable to decompose the signal into a linear combination of simple sinusoidal waves of different frequencies, so it is called spectral analysis.

25.2 Nonlinearity and Nonstationarity

It is often forgotten that analysis of signals produced by a system is done not for characterizing just these signals but for characterizing the system itself – its states and dynamics [27, 28] what in engineering is called *system identification*. It is often quite a complicated task because biological systems are *nonlinear* and *nonstationary*. And so are *biosignals*, i.e. signals generated by biological systems and *time series* representing biosignals.

A vast majority of analytical methods that were developed before the introduction of computers was applicable in principle only to so-called linear systems. An ideal linear system is one whose reaction is simply proportional to the applied input signal (stimulus); more precisely, when the input is a linear combination (i.e. a sum with constant coefficients) of some component signals, the output is the same linear combination of individual outputs that would be produced by each input component separately (the so-called superposition principle). When observing outputs of a linear system for different inputs, one may deduce a lot about the system itself. In a case of nonlinear system, it is much more complicated. “(Non)linearity of signals” most often means (non)linearity of the systems that produce these signals. Moreover, signals produced by nonlinear systems are often highly nonstationary. A stationary time series is one whose statistical description is invariant with respect to time origin or time shifts; nonstationary time series is one whose average value is not constant but exhibits abrupt discontinuities of trends either one whose correlation or covariance structure changes with time.

For nonlinear and nonstationary systems, results of FFT analysis of output signals are not related in a simple way to the input signals and to the state of the system itself. The same concerns WT (wavelet transform), MP (matching pursuit), and other *linear methods* that in theory fulfill superposition principle. Linear methods decompose analyzed signal into a linear combination of components from a given “vocabulary set.” In fact, there always exists infinite number of such “good” linear combinations, and additional discretionary assumptions are needed to choose one that is “just right.”

Even in simple cases, linear methods may give misleading results (Fig. 25.3) and also may fail to provide the exact location of “events” along time axis. One often forgets that linear methods are in principle applicable only to stationary signals (Fig. 25.4). Routine artifacts’ correction in EEG signals may lead to nonstationarities and so to unreliable results of Fourier analysis.

25.3 Fractal Analysis of EEG

The human brain is a nonlinear system; it is probably the most complex system ever known. So, application of linear methods to EEG signals generated under different input conditions – with eyes open and closed as well as using photostimulation or

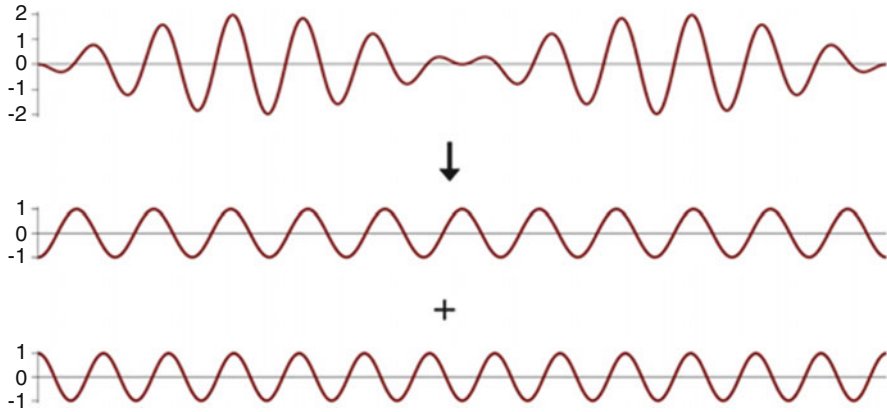


Fig. 25.3 Fourier decomposition of a signal of frequency 12 Hz with the amplitude modulated with frequency 1 Hz (*upper*) results in two harmonic signals – one with frequency 11 Hz and another with frequency 13 Hz; the basic frequency 12 Hz completely disappears [23]

hyperventilation (these conditions are usually used in all routine EEG registrations), during sleep, under anesthesia, under pulsed electromagnetic field, etc. – may lead to unreliable results. Multichannel EEG contains information about changes in activity of different parts of the brain due to physiological and pathological processes, but using linear methods of EEG analysis it is often not easy to draw conclusions about brain states and dynamics.

Nonlinear methods, like fractal analysis [1, 26], are better suited for this purpose, but they still bring a lot of confusion. Fractal methods characterize signals by the quantity called *fractal dimension*, FD . Unfortunately, what in scientific literature is called *fractal dimension* has many different meanings. FD of a time series may be calculated directly in time domain. It is a measure of *complexity* of the signal represented by analyzed time series.

Despite of the fact that frequency and phase-space methods are often used in biomedical research [32, 35, 37], it seems that time domain-based FD algorithms are more effective than the frequency domain-based algorithms [31]. There exist several algorithms of calculating FD of a time series in time domain. We have chosen Higuchi's method [12, 13, 15] because of its simplicity. Below, when we use the term fractal dimension, we will mean *Higuchi's fractal dimension*, denoted as D_f . D_f has obvious lower and upper limits, equal, respectively, 1 and 2, since $(D_f - 1) * 100$ shows what is the percentage of 2D plane that is "occupied" by the curve representing the given time series as the function of time; simple curves have Euclidean dimension equal 1 and so $D_f = 1$, while a curve representing pure noise "fills up" practically 100% of the plane and so its $D_f = 2$.

Any time series may be characterized by its D_f , $1 < D_f < 2$. It is not necessary to make surrogate data test before applying Higuchi's fractal dimension algorithm because *it does not matter if the analyzed signal is really chaotic* – it may be deterministic, stochastic, nonstationary, and noisy. Moreover, generation of sur-

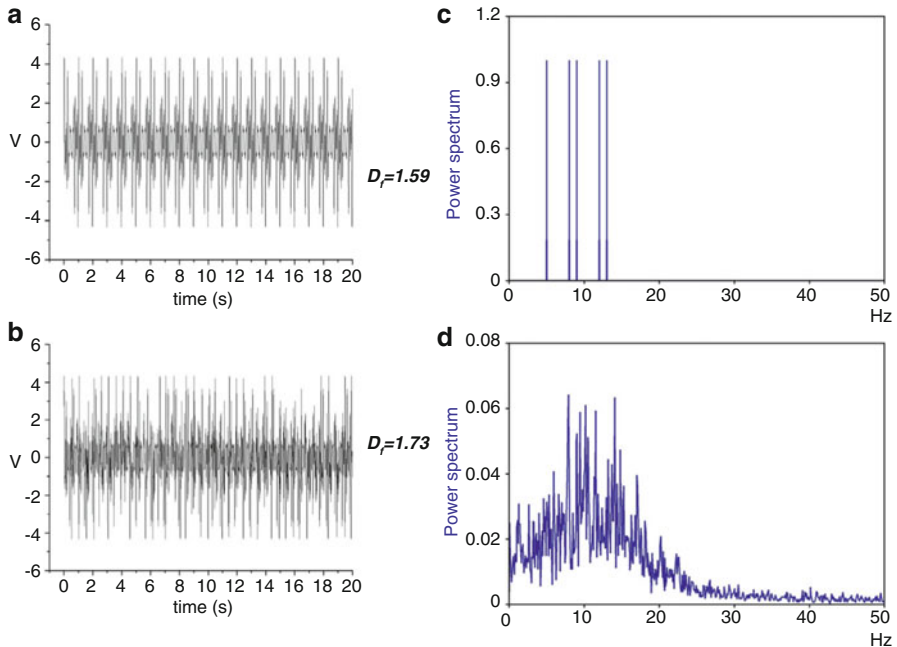


Fig. 25.4 FFT applied to two similar signals – stationary (*upper left, a*) and nonstationary (*lower left, b*) give dramatically different results (*right, c, d*). The stationary signal (**a**) was generated by adding five harmonic waves of different frequencies that are well seen in its Fourier spectrum (**c**); then randomly chosen small segments were removed from this stationary signal, so forming a nonstationary signal (**b**). Decomposition of this nonstationary signal using FFT leads to a very “rich” spectrum of frequencies (**d**), so that it is impossible to recognize five original frequencies. On the other hand, application of Higuchi’s algorithm gives similar values of average fractal dimension, D_f , for both signals [23]

rogate data often applies linear transformations like FFT and reverse FFT that may show serious shortcomings (Fig. 25.4).

Running Higuchi’s fractal dimension, $D_f(t)$, may be calculated using a moving window as short as 70–100 data points. Using artificially generated signals consisting of stitched fragments of different so-called Weierstrass functions, we have demonstrated that running fractal dimension well detects changes of signal’s stationarity [22]. That is exactly why it can be applied to nonstationary signals.

One may find opinions that nonlinear methods are very sensitive to noise and also that to use these methods, one needs very long epochs of analyzed signals. The truth is often exactly opposite [23]. For example, the method of the so-called correlation dimension (of an attractor eventually observed when EEG time series are embedded in a phase space) needs signals of thousand points to be applied [17, 32]; Higuchi’s fractal dimension may be calculated for a short signal containing as few as 100 points. Fractal dimension $D_f(t)$ is quite insensitive to noise – adding artificial

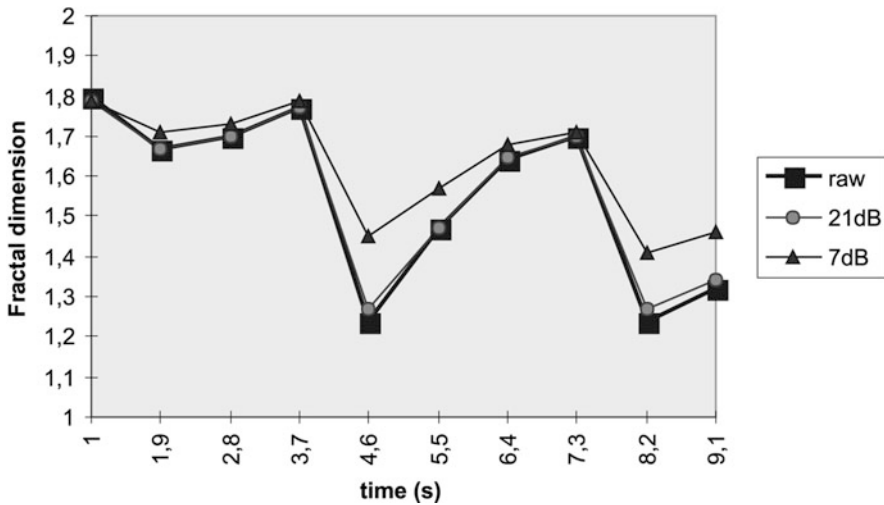


Fig. 25.5 Fractal dimension a short epoch of EEG data compared with fractal dimension calculated for the same data with artificially added noise. When signal-to-noise ratio is 21 dB, there is practically no difference with the fractal dimension for raw data; when signal-to-noise ratio is 7 dB, the differences are still small and the “tooth” is still preserved [17]

noise to the signal does not change characteristic qualitative features of the transformed signal, $D_f(t)$, and changes fractal dimension values only slightly (Fig. 25.5).

Calculation of $D_f(t)$ may be considered as a transformation of the analyzed signal in time domain, transformation that compresses the data. So, it is much easier to observe qualitative changes of the analyzed signal while just looking at the graph of its $D_f(t)$ than while looking at graph of the time series itself. While changes in the analyzed EEG signal may be barely noticed, just a visual inspection of its $D_f(t)$ may clearly demonstrate changes evoked by the external stimulus. For example, changes of $D_f(t)$ due to photostimulation that is routinely used in EEG registration procedures show that the brain reaction is the most intensive when a healthy person is stimulated with light flashing with frequency of 18 Hz (Fig. 25.6). In some neurological diseases, sensitivity to light may be changed.

It is important that there do not exist “normal values” of D_f . One should compare D_f for the given subject in different moments (“before” and “after,” [9]) rather than compare D_f of different subjects at the given moment. Averaging individual D_f values over a group of subject may lead to unreliable results. Therapy of some pathological states is based on controlling chaos in the brain by chemical drugs or by physical fields. So, changes in EEG signal complexity measured by Higuchi’s fractal dimension may be used for the assessment of the applied therapy.

For those who become attached to Fourier analysis, it is of importance that there exist simple relation between $D_f(t)$ and results of spectral analysis. Namely, when during some time interval $D_f(t)$ increases, then in the spectrum of the analyzed signal power of higher frequencies also increases (Fig. 25.7).

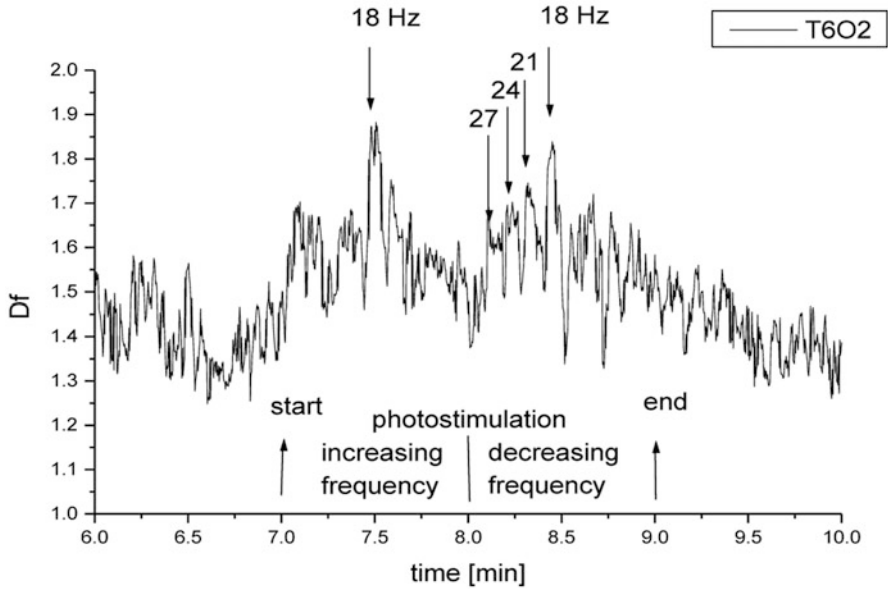


Fig. 25.6 Changes in fractal dimension of EEG signal (T6-O2) of a healthy person evoked by photostimulation during routine EEG examination [20]

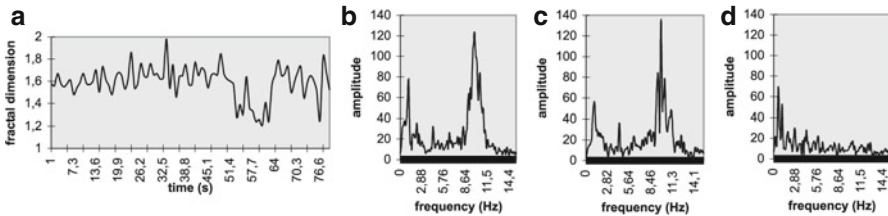


Fig. 25.7 Fractal dimension of EEG signal correlates with the spectrum of the signal. (a) Fractal dimension for 80 s. EEG epoch; (b–d) FFT analysis for 10 s intervals of the same EEG-epoch: (b) for the interval 1–10 s, for which fractal dimension is around average; (c) for the interval 40–50 s, for which fractal dimension is above average; (d) for the interval 54–64 s, for which fractal dimension is below average [15]

25.4 Examples of Application of Fractal Analysis to EEG Signals

We have applied fractal analysis of EEG signals to several biomedical issues [20, 25] such as monitoring the depth of anesthesia, sleep staging, seasonal affective disorder (SAD), and influence of electromagnetic fields generated by cellular phones.

25.4.1 Seasonal Affective Disorder: Artifacts in EEG May Be Important for Diagnosis

Routinely the changes in EEG signals due to eye blinking are considered to be artifacts and are eliminated from the signal before its spectral analysis. By applying fractal analysis, we have found that analysis of short time EEG signal intervals around the moments of eyes-opening/eyes-closing may serve as an important tool in assessing influence of bright light therapy (BLT) in patients with seasonal affective disorder (SAD) [6]. Fractal analysis shows that when an eyes-opening event occurs, fractal dimension grows from 1.1–1.3 to 1.5–1.6 in the occipital channels and even to 1.8 in the frontal channels; when the eyes remain open fractal dimension diminishes, to rise again when an eyes-closing event occurs (Fig. 25.8).

We found that in patients suffering from SAD the “relaxation” of D_f after eyes-opening/eyes-closing is slower than in healthy subjects [6], but after BLT speed of relaxation becomes much closer to that of healthy persons. It suggests that adaptation to the environment is much slower in persons with SAD and that BLT causes the adaptation to be quicker. We also introduced a parameter characterizing changes of the fractal dimension of EEG signal during eyes-opening and subsequent eyes-closing – *open/closed-eyes ratio (FD-ratio)*. We observed that in healthy subjects, this ratio is close to 1.0. For SAD patients the *FD-ratio* highly correlates with patients’ assessment based on psychological Hamilton Depression Rating Scale (HDRS). In patients high on HDRS, *FD-ratio* differs from 1.0, but after phototherapy the *FD-ratio* “normalizes” – it becomes closer to 1.0. Fractal analysis of epochs in EEG signal containing eye blinking “artifacts” may help doctors in diagnosis of SAD and in assessing BLT therapy impact on the patient.

We have also demonstrated that in patients suffering from SAD the mean D_f of EEG signal is smaller than in healthy subjects and that BLT makes the mean value of D_f in those suffering with SAD to increase. But application of $D_f(t)$ for assessing therapy of persons with SAD is interesting also because it illustrates the fact that the speed of changing of D_f may be of greater importance than the specific values of D_f . Any short-lasting disturbance of a sensory stimuli causes changes in EEG signal, but shortly after it “relaxation” occurs and the state that was before the disturbance is regained more or less rapidly.

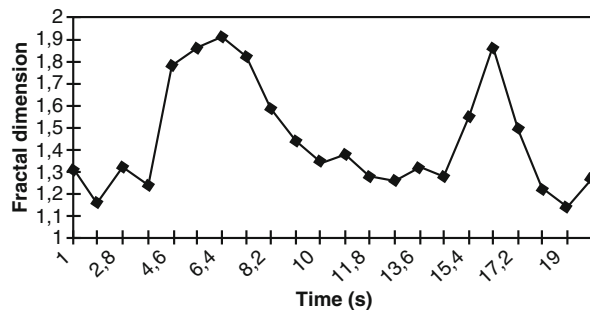


Fig. 25.8 Higuchi’s fractal dimension of 20 s EEG epoch (P4-O2) with eyes-opening (in the 4. s) and eyes-closing (in the 15. s) [6]

25.4.2 Sleep Staging: One May Analyze Raw EEG Data Without Artifact Elimination

Unlike in the case of BLT, sleep staging requires very long, whole night acquisition of EEG signals. So it is important to propose quick semiautomatic method for analysis of these records for sleep diagnostics. And our method is also based on fractal analysis [18].

It is possible to determine ranges of D_f corresponding to wakefulness and different sleep stages. Clinicians have suggested using for this purpose current source density (CSD) signals, i.e. from EEG signal at given electrode, the mean of the signals on four neighbor electrodes is subtracted; for example, C3_CSD signal is calculated as

$$C3_CSD = [(F3 - C3) + (T3 - C3) + (P3 - C3) + (Cz - C3)] / 4.$$

CSD signal is the first approximation of the surface Laplacian.

For C3_CSD signals using clinician-made hypnograms of 15 healthy subjects, we have found the following ranges of D_f [16] (Fig. 25.9):

- Awake: $1.6 \leq D_f$
- Stage 1: $1.525 \leq D_f < 1.6$
- REM: $1.475 \leq D_f < 1.525$
- Stage 2: $1.385 \leq D_f < 1.475$
- Stage 3: $1.305 \leq D_f < 1.385$
- Stage 4: $D_f < 1.305$

If the intervals are chosen, then a very quick sleep stager based on $D_f(t)$ may easily be constructed. And the agreement of hypnograms obtained by this computerized method with the hypnograms obtained by the human scorer is about 70%. Computerized methods that are based on comparison of automatic classification of sleep stages (in our case based

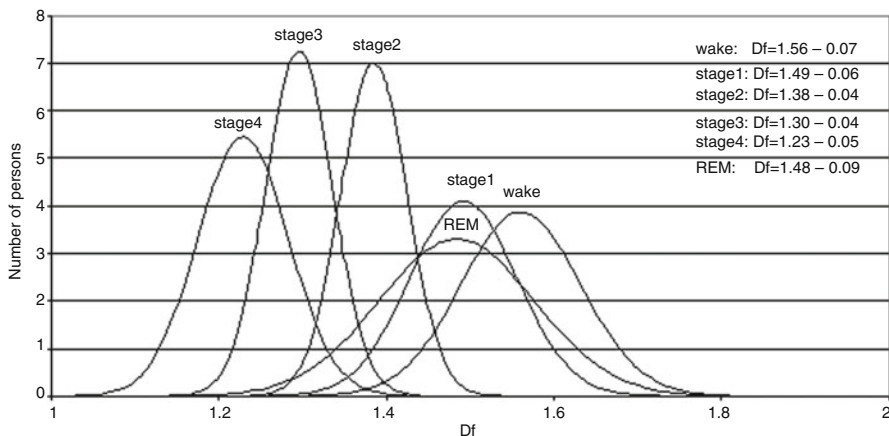


Fig. 25.9 Distribution of D_f of C3_CSD in various sleep stages for a group of 15 healthy persons

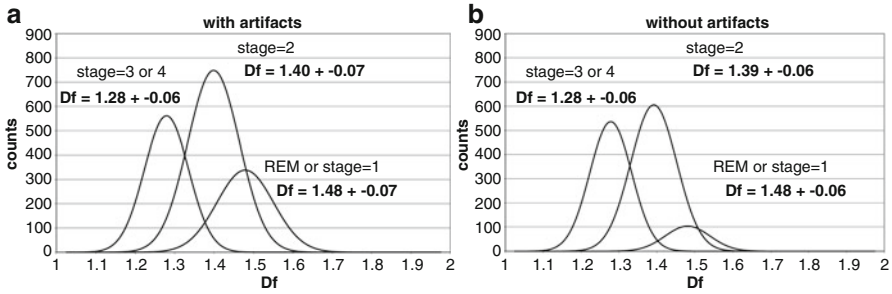


Fig. 25.10 Comparison of D_f distributions during stage 3/4, stage 2, and stage 1/REM, calculated from the same EEG signal of a healthy person C3_CSD, sampling frequency 128 Hz, 4 s window = 1 “count”): raw signal (with artifacts, **a**) and after removing of artifacts by a specialists (without artifacts, **b**). Mean fractal dimension is insensitive to artifacts – numbers of counts are smaller in the second case, but D_f remains the same in both cases [14]

on fractal dimension of EEG signal) and automatic classification will not be better than classifications made by human scorers that had been used “to instruct” the algorithm. By the way, human scorers can have an inter-scorer (human-human) agreement of much less than 70%. Visual evaluation of sleep stages according to Rechtschaffen and Kales [33] has rather limited inter-rater reliability as demonstrated in the experiment made by physicists on physicians [30] – hypnograms constructed by several sleep specialists based on the same EEG record turned out to be extremely different. Our sleep stager may be individualized by the user – clinician can introduce ranges of D_f for different sleep stages based on his/her own data and even correct them for individual patients if necessary.

It is important that if one combine stage 1 and REM as well as stage 3 and stage 4, one gets practically the same results in staging while analyzing raw EEG signal as while analyzing the same signal without artifacts [14] (Fig. 25.10). Such a quick analysis of raw data may be useful in health screening.

25.4.3 Influence of Electromagnetic Fields: Comparing Qualitative Features of $D_f(t)$

The influence of external electromagnetic fields (EMF) on the human brain is not fully understood, because it depends on so many individual characteristics of the brain at the given moment as well as on several characteristics of applied field and its changes in time. Comparing fractal dimension of EEG signal registered under the influence of EMF, e.g. when the patient is lying down on a so-called magnetic mattress when the intensity of the applied field has different values, we may point at persons who are hypersensitive to applied EMF [15, 21] (Fig. 25.11).

We have compared results of linear Fourier analysis of EEG signals with those obtained by fractal analysis using Higuchi’s method while analyzing the influence of cellular phones [8]. Why spectral analysis seemed to demonstrate usefulness of so-called neutralizing protective devices (NPDs) for all users, fractal analysis shown that such devices may probably be useful only for about 15% of population – those who may really belong to a *high-risk (hypersensitive)* group of cellular phone users.

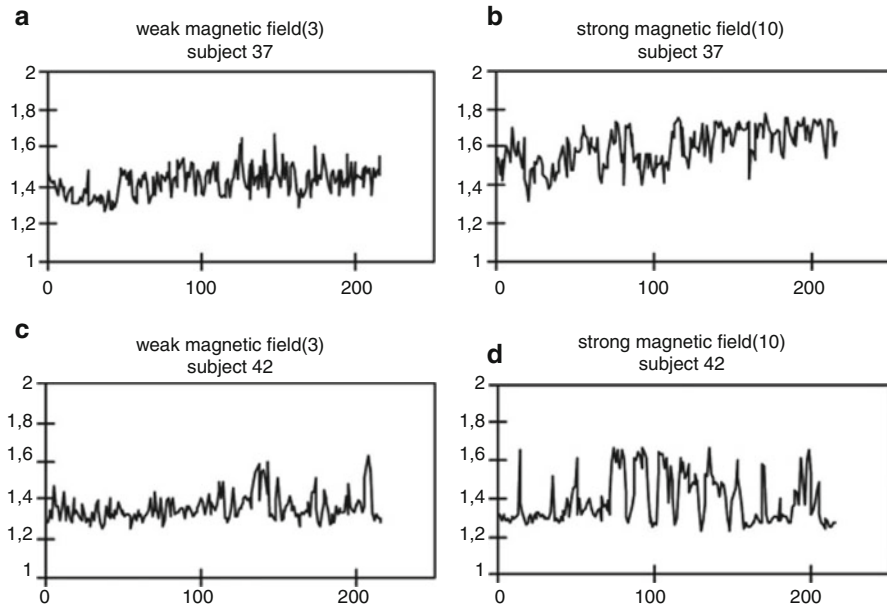


Fig. 25.11 $D_f(t)$ of EEG signal calculated for two healthy persons lying down on a “magnetic mattress.” One unit on horizontal axes denotes 5 s. For the first 7 min (84 units) magnetostimulation is “off”; for the next 7 min (75–168 units) magnetostimulation is “on”; then magnetostimulation is “off” again. In “weak” (according to the scale on the mattress’ pilot) magnetic field (a, c), none of the subjects shows noticeable reaction; in “strong” magnetic field, reaction of subject 42 is much more profound (d) than that of subject 37 (b)

Our fractal method may serve for quick and easy assessment of *individual susceptibility* to EMF used in mobile communication as well as for testing of different cellular phone models for their certification by the appropriate institutions. So-called norms of exposure to EMF mislead even medical doctors. They are based only on *thermal interactions* as characterized by the so-called specific absorption rate (SAR) while they completely neglect *informational interactions* [24] that show much more complicated dependence on interpersonal differences.

25.4.4 Epileptic Seizures and Epileptic-Like Seizures in Economic Organisms

During epileptic seizure chaos in the brain diminishes, neurons start firing in coordinated manner, and fractal dimension of EEG signal suddenly drops down (Fig. 25.12a). *Yes, it is healthy to be chaotic!* It is very interesting that in an “economic organism” (and economists do like such personifications) one may observe very similar phenomena, usually named “financial crisis” [10]. The possibility of prediction of epileptic seizures based on $D_f(t)$ of EEG signal as well as the possibility of predicting economic failure based on fractal analysis of economic indices like Dow Jones needs further intensive investigations.

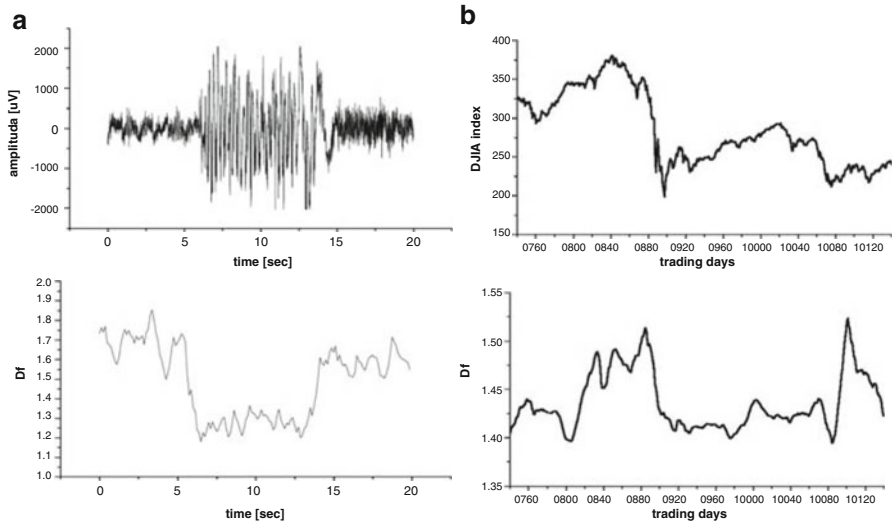


Fig. 25.12 Diminishing of D_f calculated from EEG registered during epileptic seizure (*upper left*), means diminishing of chaos in the human brain. During epileptic seizure (**a**), diminishing of D_f calculated from Dow Jones index from the period of “Big Crash” of the 1920s (*upper right*) shows striking similarity with epileptic seizure, despite of the huge difference in time scales. It does justify the concept of “epileptic seizures in economic organisms” (**b**) [20]

25.4.5 Psychiatry: Assessing Effects of Electroconvulsive Therapy

Electroconvulsive therapy (ECT) (also known as *electroshocks*) is a successful treatment for depression and other mental disorders. We have analyzed nonstationary EEG signals measured on frontal electrodes of patients who have received ECT. The effects of ECT on the patients are monitored with EEG. EEG evoked by ECT (ECT-EEG) exhibits specific patterns with four phases, but there are differences between individuals. $D_f(t)$ may be a help for clinicians to simplify analysis of ECT-EEG (Fig. 25.13) and to find new properties not identified by other methods. For example, it was found that psychotic depressed patients show higher increase of $D_f(t)$ in phase 4. in comparison with bipolar depressed patients, so indicating a difference in neurodynamics between two groups.

25.4.6 Anesthesiology: Monitoring the Depth of Anesthesia

The so-called bispectral index (BIS) used in the BIS Monitors (Aspect Medical Systems, Newton, MA, USA) is commonly accepted as a measure of the depth of anesthesia, but the algorithms used in BIS Monitors are not in public domain. We have proposed a new method of monitoring the depth of anesthesia by assessing complexity of EEG signal based on Higuchi’s fractal dimension [2, 19].

In addition to registration of EEG signal and BIS, the depth of anesthesia was continuously tested and classified by a specialist-anesthesiologist to six OAA/S levels (*Observer's Assessment of Alertness and Sedation*); patients were judged to be conscious if the OAA/S score was between 3 and 5 and unconscious if the OAA/S score was less than 3. Example of our results is shown on Fig. 25.14. It seems that $D_f(t)$ of EEG signal despite of its simplicity is even better suited for monitoring of the depth of anesthesia and sedation than BIS index.

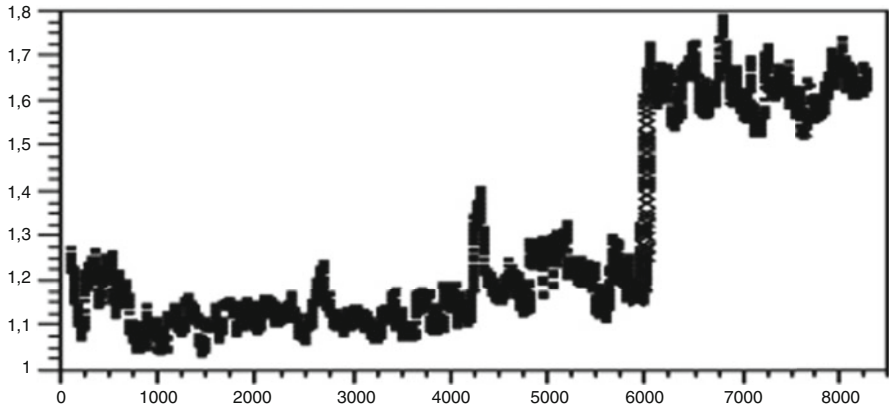


Fig. 25.13 $D_f(t)$ of ECT-EEG on Fp1 clearly indicates transition from phase 3. to phase 4. not easily identified in the signal itself nor by other methods of analysis [36]

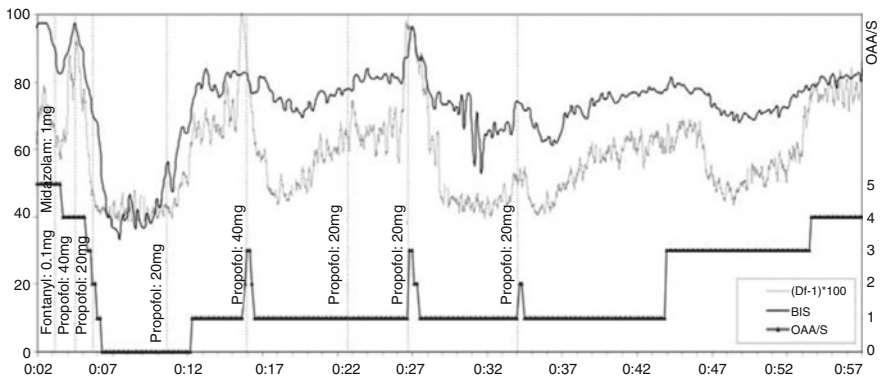


Fig. 25.14 Anesthesia was controlled according to BIS (target BIS value between 60 and 80) with intermittent boluses of propofol. At 16. and 27. min, sedation was lightened to level 3 in OAA/S score (black step curve, right-side scale). At those moments fractal dimension of EEG (lower light-gray curve) drawn here as $(D_f - 1) * 100$ to be easily compared with BIS index (upper dark-gray curve) (cf. left-side scale), rose rapidly to reach the highest value. BIS increased only once (at 27. min), while at 16 min it remained practically unchanged. Awakening during surgical procedure and at the end of it can be predicted by rise of $(D_f - 1) * 100$ toward its highest value

25.5 Conclusions

Any biosignal used in clinical setting has to be appropriately processed and visualized. EEG signal is used for monitoring the state of the brain. We have performed translational researches regarding the representation and analysis of the EEG signal complexity based on Higuchi's algorithm, and we have drawn multidisciplinary applications.

Our methods of EEG signal analysis are based on Higuchi's algorithm [8]. Higuchi's fractal dimension is a quantifier that can be evaluated directly in time domain without reconstruction of a strange attractor in a multidimensional phase space. The algorithm is easy and fast in comparison with other methods and gives compression of information. The algorithm is also very quick and maybe implemented in real time even on a PC. Contrary to other methods (such as the correlation dimension), it requires only short time intervals – a window containing 100 data point is enough to calculate one value of Higuchi's fractal dimension.

The algorithm is also highly insensitive to noise. These properties are very important since EEG signal is very noisy and remains stationary only during short intervals. One often forgets that linear methods like FFT or wavelet transform work properly only for stationary signals.

Nonlinearity in the brain is observed even at the neuronal level since the dynamical behavior of individual neurons is governed by threshold and saturation phenomena. It is obvious for any physicist that human organism is a highly complex nonlinear system. Development of personal computers enables wider and wider application of nonlinear methods, but linear methods are still in use because of the long-time tradition since they could have been applied using just pen and paper. Fractal dimension method may be very useful for medical assessment and diagnosis, in particular when combined with new nanosensors used for biosignal registration.

Acknowledgments W. Klonowski acknowledges the support of Nalecz Institute of Biocybernetics and Biomedical Engineering of the Polish Academy of Sciences, Warsaw, through statutory activities.

References

1. Acardo A, et al. Use of the fractal dimension for the analysis of electroencephalographic time series. *Biol Cybern.* 1997;77:339–50.
2. Ahmadi B, Amirfattahi R. Comparison of correlation dimension and fractal dimension in estimating BIS index. *Wirel Sens Netw.* 2010;2:67–73.
3. Beck A. Die Bestimmung der Localisation des Gehirn- und Rückenmarks-functionen Vermittelst der Electricischen Erscheinungen [The determination of the localisation of the brain and spinal cord functions by way of electrical appearances]. *Zentralblatt Physiol.* 1890;4:473–6.
4. Berger H. Ueber das Elektroenkephalogramm des Menschen. *Arch Psychiatr Nervenkr.* 1929;87:527–70.

5. Caton R. The electric currents of the brain. *Br Med J.* 1875;2:278.
6. Ciszewski J, et al. Application of chaos theory for EEG-signal analysis in patients with seasonal affective disorder. *Med Biol Eng Comput.* 1999;37:359–60.
7. Coenen A, Zayachkivska O. Adolf Beck: a pioneer in electroencephalography in between Richard Caton and Hans Berger. *Adv Cogn Psychol.* 2013;9:216–21.
8. Di Ieva A, et al. Fractals in the neurosciences, part II: clinical applications and future perspectives. *Neuroscientist.* 2015;21:30–43.
9. Georgiev S, et al. EEG fractal dimension measurement before and after human auditory stimulation. *Biogeosciences.* 2009;12:70–81.
10. Haas LF. Neurological stamp. Hans Berger (1873–1941), Richard Caton (1842–1926), and electroencephalography. *J Neurol Neurosurg Psychiatry.* 2003;74:9.
11. Hameroff S, Penrose R. Consciousness in the universe: a review of the ‘Orch OR’ theory. *Phys Life Rev.* 2013.
12. Higuchi T. Approach to an irregular time series on the basis of the fractal theory. *Phys D.* 1988;31:277–83.
13. Higuchi T. Relationship between the fractal dimension and the power law index for a time series: a numerical investigation. *Phys D.* 1990;46:254–64.
14. Klonowski W, et al. Nonlinear dynamics from conformons to human brain. *Technol Health Care.* 2001;9:88–9.
15. Klonowski W, et al. Nonlinear dynamics algorithms for time series analysis: implementation in EEG-data acquisition/analysis system. In: Klonowski W, editor. *Attractor, signals, and syn-ergetics*, pp. 553–560, proceedings of the 1st European Interdisciplinary School on Nonlinear Dynamics for System and Signal Analysis EUROATTRACTOR2000. Lengerich: Pabst Science Publishers; 2002.
16. Klonowski W, et al. Complexity of EEG-signal in time domain: possible biomedical application. In: Boccaletti S et al., editors. *Experimental Chaos*, AIP conference proceedings, vol. 622. New York: Melville; 2002. p. 155–60.
17. Klonowski W. Chaotic dynamics applied to signal complexity in phase space and in time domain. *Chaos Solitons Fractals.* 2002;14:1379–87.
18. Klonowski W et al. Sleep-EEG analysis using Higuchi’s fractal dimension. Proceedings of the International Symposium on Nonlinear Theory and its Applications NOLTA 2005, Bruges, Belgium, 18–21 Oct, pp. 222–225. <http://www.ieice.org/proceedings/NOLTA2005/HTMLS/paper/5025.pdf>.
19. Klonowski W, et al. Monitoring the depth of anaesthesia using fractal complexity method. In: Novak MN, editor. *Complexus mundi. Emergent patterns in nature*. New Jersey: World Scientific; 2006. p. 333–42.
20. Klonowski W. From conformons to human brains: an informal overview of nonlinear dynamics and its applications in biomedicine. *Nonlinear Biomed Phys.* 2007;1:5. <http://www.nonlinearbiomedphys.com/content/pdf/1753-4631-1-5.pdf>.
21. Klonowski W. Nonlinear EEG-signal analysis reveals hypersensitivity to electromagnetic fields generated by cellular phones. *IFMBE Proc.* 2007;14:1056–8.
22. Klonowski W. Neuroscience and nonlinear dynamics. *IFMBE Proc.* 2009;22:1236–40.
23. Klonowski W. Everything you wanted to ask about EEG but were afraid to get the right answer. *Nonlinear Biomed Phys.* 2009;3:2. <http://www.nonlinearbiomedphys.com/content/pdf/1753-4631-3-2.pdf>.
24. Klonowski W. Informational interactions and the brain: nonlinear dynamics reveals individual (hyper)sensitivity to EMF. *Far East J Dyn Sys.* 2010;13:129–37.
25. Klonowski W, et al. Complexity measures of brain electrophysiological activity: in consciousness, under anaesthesia, during epileptic seizure, and in physiological sleep. *J Psychophysiol.* 2010;24:131–5.
26. Losa GA. The fractal geometry of life. *Riv Biol.* 2009;102:29–59.
27. Lutzenberger W, et al. Dimensional analysis of the human EEG and intelligence. *Neurosci Lett.* 1992;143(1–2):10–4.

28. Lutzenberger W, et al. Fractal dimension of electroencephalographic time series and underlying brain processes. *Biol Cybern.* 1995;73:477–82.
29. Niedermeyer E, Da Silva FL, Editors. *Electroencephalography. Basic principles, clinical application, and related fields.* 5th ed. Philadelphia: Lippincott, Williams & Wilkins (Wolter Kluwer Co); 2005.
30. Penzel T, et al. Reliability of visual evaluation of sleep stages according to Rechtschaffen and Kales from eight polysomnographs by nine sleep centres [in German]. *Somnology.* 2003;7:49–58.
31. Phothisonothai M, et al. A comparison of actual and artifactual features based on fractal analyses: resting-state MEG data. *Adv Intell Sys Comput.* 2013;212:1257–65.
32. Pritchard WS, Duke DW. Dimensional analysis of no-task human EEG using the Grassberger-Procaccia method. *Psychophysiology.* 1992;29:182–92.
33. Rechtschaffen A, Kales A. *A manual of standardized terminology, techniques, and scoring for sleep stages in human subjects.* Washington, DC: GPO; 1968.
34. Schwartz BE. The advantages of digital over analog recording techniques. *Electroencephalogr Clin Neurophysiol.* 1998;106:1113–7.
35. Stam CJ. Nonlinear dynamical analysis of EEG and MEG: review of an emerging field. *Clin Neurophysiol.* 2005;116:2266–301.
36. Wahlund B, et al. EEG data, fractal dimension and multivariate statistics. *J Comput Sci Eng.* 2010;3:10–6.
37. Watt RC, Hameroff SR. Phase space electroencephalography (EEG): a new mode of intraoperative EEG analysis. *Int J Clin Monit Comput.* 1988;5:3–13.

Chapter 26

On Multiscaling of Parkinsonian Rest Tremor Signals and Their Classification

Lorenzo Livi

Abstract Self-similar stochastic processes and broad probability distributions are ubiquitous in Nature and in many man-made systems. The brain is a particularly interesting example of (natural) complex system where those features play a pivotal role. In fact, the controversial yet experimentally validated “criticality hypothesis” explaining the functioning of the brain implies the presence of scaling laws for correlations. Recently, we have analyzed a collection of rest tremor velocity signals recorded from patients affected by Parkinson’s disease, with the aim of determining and hence exploiting the presence of scaling laws. Our results show that multiple scaling laws are required in order to describe the dynamics of such signals, stressing the complexity of the underlying generating mechanism. We successively extracted numeric features by using the multifractal detrended fluctuation analysis procedure. We found that such features can be effective for discriminating classes of signals recorded in different experimental conditions. Notably, we show that the use of medication (L-DOPA) can be recognized with high accuracy.

Keywords Scaling • Fluctuation analysis • Parkinsonian rest tremors • Deep brain stimulation • Classification

26.1 Introduction

Memory is one of the most interesting aspects characterizing many natural, social, and financial processes [6, 17, 23]. Memory can be quantified in different ways, depending on the particular features and effects that one wants to highlight. One of the most common approaches in the study of real-valued time series is the analysis of the autocorrelation function. However, autocorrelation captures only linear contributions of the

L. Livi
Department of Computer Science, Ryerson University,
350 Victoria Street, Toronto, ON M5B 2K3, Canada
e-mail: llivi@scs.ryerson.ca

past on future events. A more general setting is offered by measures based on mutual information, such as excess entropy and related quantities [9, 13, 56]. In the linear setting provided by the study of the autocorrelation function, the memory extent can be quantified as the characteristic time scales defining the decay of the autocorrelation. A time series possesses short memory when such decay is consistent with an exponential functional form, meaning that the influence of the past to the current state is limited in time. On the other hand, when the decay follows a power law, the time series is said to manifest *long-term correlations* (LTC), and the strength of such correlations is referred to as the degree of *persistence* of the generating stochastic process. Persistence of a (stationary) stochastic process [46] is quantified by the self-similarity coefficient, called Hurst exponent $H \in [0, 1]$. In practice, when the process corresponds to uncorrelated noise, we obtain $H = 0.5$; if the process is persistent (correlated) or anti-persistent (anti-correlated), H will be greater than and less than 0.5, respectively.

Several methods have been proposed to extract and analyze the fluctuations of the stationary component of a time series [2, 22, 45, 54], including the well-known detrended fluctuation analysis (DFA). DFA has been shown to be successful in a broad range of applications [30, 34, 49]. The DFA procedure has been generalized [5, 12, 31, 41] in order to account for multiscaling, implying the use of several scaling exponents each one tailored for a different magnification level of the fluctuations. A time series is called fractal or multifractal whether a single or multiple scaling exponents are necessary in order to characterize the fluctuations. Multifractal time series are also characterized by a nontrivial *multifractal spectrum*, also called singularity spectrum, which provides a synthetic description of the process complexity. Multifractality could emerge also as a by-product of an underlying heavy-tailed distribution of the data [18]. Two prototypical examples of self-similar processes are fractional Brownian motion and fractional Lévy stable motion [23]. Both families of processes are characterized by stationary increments. In the first case, the increments follow a Gaussian distribution, while in the latter increments are distributed according to an α -stable distribution, accounting thus also for heavy tails – the latter is in fact a generalization of the former since a Gaussian distribution is a particular example of α -stable distribution.

Fractal and multifractal analysis of time series plays a pivotal role in many scientific contexts, including neuroscience and medicine in general [15, 16, 44, 55]. Typical examples of applications are human gait analysis [19], background neuronal noise-like activity in the human and mouse hippocampus [48], analysis of cervical tissue samples [21], MRIs for tumor characterization [29], EEG signals [33], protein contact networks [37], and electromyograms for the diagnosis of neuromuscular diseases [52].

Parkinson's disease (PD) is a neurodegenerative disorder that targets the central nervous system. Such a disease is characterized by the progressive loss of dopaminergic neurons in the substantia nigra of the midbrain. The most evident symptoms associated with PD are tremors, bradykinesia, rigidity, and postural instability, while in more advanced stages of the disease, other factors might be present, such as different types of cognitive impairments (e.g., dementia) and changes in behavior and/or emotional states [8, 25]. The causes of PD are, however, still largely unknown. This has led to multidisciplinary research involving, for instance, the use of artificial neural networks for the purpose of prediction of related signals [20, 57] and mutual information-based methods for detecting upper limb motor dysfunction [14]. Deep

brain stimulation [38, 39, 42, 51] is a neurosurgical procedure that involves a surgical intervention to implant electrodes in brain areas suitable for receiving electrical impulses [3]. DBS proved to be effective in the treatment of PD and other diseases, such as obsessive-compulsive disorders [10].

In our recent study [35], we have analyzed 48 signals recorded from 12 distinct subjects affected by PD [8, 24, 53]. Tremor signals were recorded by means of a velocity laser pointed to the patients' index finger. For each subject, signal recording was performed in four different settings, given by the combination of the use of DBS and L-DOPA medication. Using the same data, Yulmetyev et al. [58] performed a comprehensive analysis by using the statistical theory of non-Markov processes and flicker-noise spectroscopy. In addition, the attenuation effects of DBS on locomotion and tremor over different time scales were further investigated by Beuter and Modolo [7], who developed a computational model of biological neural networks.

In our work [35], we have analyzed such data by focusing on LTC and multifractal signatures, both used for the purpose of representation (e.g., feature extraction) and further discriminative analyses. In order to obtain a baseline for comparison, the developed feature-based representation (FBR) was compared with the one offered by the power spectra. Our results showed that such rest tremor signals present a clear multifractal signature and different forms of LTC. Notably, the effect of medication was clearly recognizable in the signals, suggesting also a qualitative change of LTC from anti-persistent to persistent. We successively tested several instances of the two FBRs of the signals in the setting of supervised classification and (nonlinear) feature transformation. We considered three different classification problems involving the recognition of (i) the presence of medication, (ii) the use of DBS, and (iii) the high- and low-amplitude tremor groups. Classification results showed that the use of medication can be discriminated with higher accuracy. In particular, results with the highest accuracy were obtained with a parsimonious, two-dimensional representation encoding only the magnitude of the LTC and multifractality present in the signals.

Experimental evidence suggests that such a two-dimensional time series representation could play an important role in clinical applications involving the study of Parkinsonian rest tremors. In addition, our results reconfirmed the (already well-known) usefulness of fractal analysis in the analysis biomedical signals.

The structure of this chapter is as follows. In Sect. 26.2 we provide the details of multifractal detrended fluctuation analysis (MFDFA), the procedure used to calculate LTC and MFS. In Sect. 26.3 we describe the results presented in Livi et al. (2016). Finally, in Sect. 26.4 we offer concluding remarks and discuss future directions.

26.2 Multifractal Detrended Fluctuation Analysis for Nonstationary Time Series

Conventional methods employed to analyze the LTC properties of a time series (e.g., fluctuation, spectra, and R/S analysis [4, 47, 49]) could be misleading when such time series are affected by non-stationarities [11, 30]. In many cases a process is driven by an underlying trend [27], which operates at specific time scales, like

seasons in the analysis of data related to a natural phenomenon and days in financial market analysis. Usually, when investigating memory properties of a process, one is interested in the fractal properties pertaining the intrinsic fluctuations of the process. Several methods have been proposed to extract and analyze the fluctuations of the stationary component of a time series, such as DFA, detrended moving average [2], wavelet leaders [1, 54], adaptive fractal analysis [45], and the so-called geometric-based approaches [22]. The DFA procedure has been generalized in the so-called multifractal detrended fluctuation analysis (MFDFA) [5, 12, 31, 41], which accounts also for multiscaling thus implying the possibility to characterize a time series from a multilevel perspective.

In the following, we provide the essential technical details regarding MFDFA [31]. A very useful and hands-on guide discussing the details of MFDFA has been recently published by Ihlen [28], which includes also a link to a ready-to-use MATLAB® toolbox.

Given a time series x of length N , the following steps are performed in order to estimate the LTC and multifractal properties of x . MFDFA operates by analyzing the profile $Y(i)$, which is obtained by integrating $x(j)$, with $j=1,2,\dots,i$. Y is then divided in nonoverlapping segments of equal length s . Since N might not be a multiple of s , the operation is repeated by starting from the opposite end, obtaining thus a total of segments. Successively, a local detrending operation is executed by calculating a polynomial function on each of the segments. Computing a local fit helps removing non-stationarities compatible with trends that are well modeled by polynomial functions. The degree of the fitting polynomial has to be tuned according to the expected trending order of the time series. For instance, by choosing a quadratic function, it would be possible to remove quadratic trends in Y and, accordingly, linear trends in the original time series, x . However, periodic or fast-changing trends require different and more advanced methods of detrending [36].

The procedure then computes the local variance, denoted as $F^2(v,s)$, for each segment $v=1, \dots, 2N_s$. The q th-order moment of the local variance over all segments is evaluated as

$$F_q(s) = \left\{ \frac{1}{2N_s} \sum_{v=1}^{2N_s} [F^2(v,s)]^{q/2} \right\}^{1/q}, \quad (26.1)$$

with $q \in \mathbb{R}$. The q -dependence of the fluctuation function (26.1) allows to highlight the contributions of both high and low fluctuation magnitudes. Hence, the q parameter serves as a sort of lens in order to inspect the time series at different resolutions. Notably, for $q > 0$ large fluctuations have higher impact in Eq. 26.1; conversely, for $q < 0$ the impact of the smaller fluctuations is enhanced. The case $q=0$ cannot be computed by means of Eq. 26.1 and so a logarithmic form has to be used [31]. In order to check if the scaling of the variance is self-similar, the last steps are repeated for different scales s of increasing size.

The self-similarity exponent characterizing the scaling of the fluctuations can be determined by computing the slope of the doubly logarithmic plot of $F_q(s)$ versus s ,

computed for each value of q . If the series x is long-term correlated, then $F_q(s)$ is well approximated – for large values of s – by the power law form:

$$F_q(s) \sim s^{H(q)}. \quad (26.2)$$

The $H(q)$ exponent is the generalization of the Hurst exponent; the original DFA formulation is obtained setting $q=2$. When $H(2) > 1/2$ the time series possesses long-term, positive correlations; for $H(2) < 1/2$ the series is anti-correlated; and $H(2) = 1/2$ indicates that the series is compatible with uncorrelated noise – e.g., white Gaussian noise. A homogeneous scaling over all fluctuation magnitudes indicates that $H(q)$ is independent from q , suggesting that the series is monofractal. For instance, monofractal time series can be obtained by exploiting the fractional Brownian motion model. On the other hand, when the small fluctuations scale differently from the large ones, then the series could be considered as multifractal. Many real-world time series possess multifractal properties. Synthetic examples can be easily obtained as well by exploiting the α -stable distributions proper of the Lévy motion.

The self-similarity exponent, $H(q)$, can be used to bridge time series with the conventional fractal and multifractal analysis of measures [26]. This is performed by exploiting the concept of generalized partition function, $Z_q(s)$. Starting from Eq. 26.1 and using Eq. 26.2, it is possible to define

$$Z_q(s) = \sum_{v=1}^{N/s} [F(v, s)]^q \sim s^{\tau(q)}, \quad (26.3)$$

where $\tau(q) = qH(q) - 1$ is the q -order mass exponent (also called Rényi scaling exponent) of the generalized partition function. The multifractal spectrum, denoted as $f(\alpha)$, provides a compact description of the multifractal character of the time series. It can be obtained via the Legendre transform of $\tau(q)$:

$$f(\alpha) = q\alpha - \tau(q), \quad (26.4)$$

where α is equal to the derivative of $\tau(q)$ with respect to q . It is worth noting that $f(\alpha)$ corresponds to the Hausdorff dimension of a subset of the input data where the Hölder exponent is equal to α . Using $\tau(q)$ it is possible to express the generalized Hurst exponent, $H(q)$, directly in terms of α and $f(\alpha)$, and vice versa:

$$\alpha = H(q) + q \frac{\partial H(q)}{\partial q}; f(\alpha) = q[\alpha - H(q)] - 1. \quad (26.5)$$

The multifractal spectrum (26.5) encodes important information regarding the degree of multifractality and the peculiar sensitivity of the time series to fluctuations with high/low magnitudes. The width of the support of $f(\alpha)$, shortened in the following as MFSW, is defined as

$$\Delta\alpha = \alpha(q_{\min}) - \alpha(q_{\max}). \tag{26.6}$$

MFSW offers an important quantitative indicator of the multifractal signature that is present in the data. The higher the width, the higher the complexity of the time series. In Eq. 26.6, q_{\min} and q_{\max} represent the lower and upper values adopted for the q range, respectively.

26.3 Evidence of Multiscaling in Parkinsonian Rest Tremor Velocity Signals

In the following, we use the quantities introduced above in order to characterize time series representing rest tremor velocity signals recorded from patients affected by Parkinson’s disease.

Figure 26.1 offers a visual representation of the statistics for H and MFSW for the three different categorizations of the data. LTC properties of the signals yield statistically significant differences only when considering the impact of medications. It can be observed that the use of L-DOPA changes the signal LTC properties toward the positively correlated pole, while in the absence of medication, the signals are clearly anti-correlated (upper panels). In our opinion, this is an interesting aspect that stresses the need for further developments in future research studies. All signals are multifractal with a relevant multifractal signature quantified by the MFSW (middle panels). It is worth noting that the multifractal signature is sufficiently

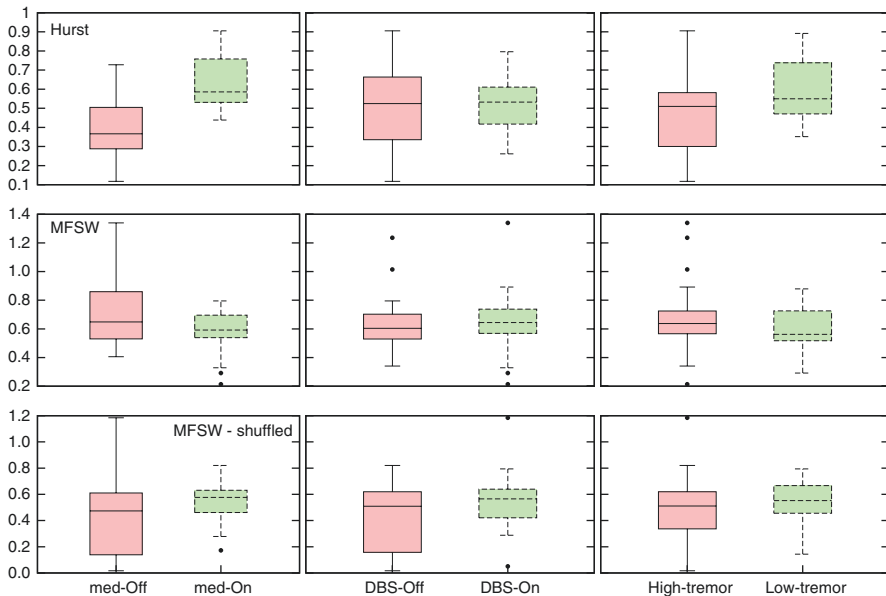


Fig. 26.1 Statistics of all Parkinsonian rest tremor signals (Taken from Livi et al. [34])

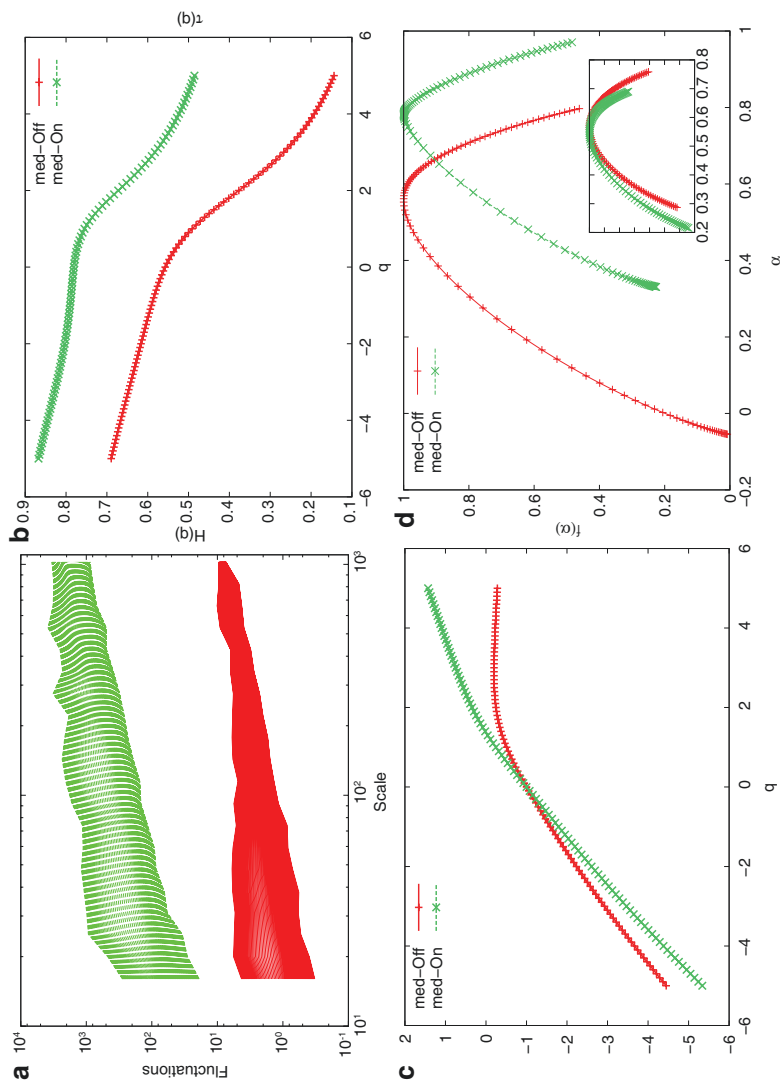


Fig. 26.2 Details of MFDFA calculations for patient “Hg2.” Scaling of fluctuations in (a) has been vertically displaced in order to improve visualization. The effect of medication produces signals with higher persistence, as shown by the generalized Hurst exponents in (b). The multifractality is evident from the non-linear nature of the q -order mass exponent in (c) and the considerable width of the MFS in (d). *Inset* in (d) shows spectra calculated after shuffling the time series

preserved after shuffling the time series (lower panels), suggesting that LTC are not the only source for the observed multifractality. In fact, shuffling the time series destroys LTC and any deterministic trend that might influence the actual degree of multifractality present in the data. As discussed in Ref. [31], multifractality could be observed as consequence of LTC, a broad probability density function of the data, or as a combination of both cases.

Let us focus now on a specific patient. We take into account the effect of using the medication on the resulting LTC and multifractal properties. Figure 26.2 shows four plots depicting the scaling of the fluctuations (Fig. 26.2a), the generalized Hurst exponents (Fig. 26.2b) while varying q , the q -order mass exponents (Fig. 26.2c), and finally the MFS (Fig. 26.2d). As it is possible to observe, the use of medication (indicated as med-On) yields a persistent signal ($H(2)=0.67$), while without medication we obtain anti-persistence ($H(2)=0.38$). This is an important qualitative difference noted in the data. In addition, we notice that the use of medication produces a signal with a narrower MFS than considering the signal recorded without the medication effect ($\Delta\alpha=0.64$ vs. $\Delta\alpha=0.85$). This suggests that the absence of medication produces a tremor velocity signal with a richer and hence more complex structure, i.e., more heterogeneous in terms of scaling. The negative correlation dimension ($\tau(2)=-0.26$) for the med-Off case is a direct consequence of the anti-persistence. Finally, as previously mentioned, shuffling the time series does not entirely destroy the multifractality of the signals. Table 26.1 summarizes all relevant quantities.

Let us now turn our attention to the problem of classifying such signals. Automatic classification of rest tremor signals is an important and useful research objective.

A first step in this direction when processing time series consists in reducing the dimensionality of the extracted features. To this end, we have used principal component analysis (PCA) and its nonlinear version called kernel-PCA (kPCA) [50]. In order to provide evidence for the effectiveness of the developed FBR using LTC and MFSW, in the following we report the results obtained on three different classification problems conceived on the same dataset. Notably, we face the problem of discriminating between the two groups (high- and low-amplitude tremors) and recognizing the use of both medications and DBS.

We have selected the well-known support vector machine (SVM) as supervised classification system [50], which is configured with a Gaussian kernel. Notably, we used a version known as C-SVM, where C is a hyper-parameter controlling the complexity of the resulting model; in SVM the structural complexity of the model is measured by considering the number of SVs computed during the training stage. SVM offers an efficient and fast solution for classification problems, even when dealing with a dataset of limited size (as in our case). Both hyper-parameters, i.e., C and the width of the Gaussian kernel, are determined by preliminary tests using a grid search scheme. Since our dataset, regardless of the adopted FBR, is limited to 48 patterns, we tested the recognition capability of C-SVM according to the leave-one-out setting: each pattern is tested on one pattern at a time by learning a C-SVM model on the remaining 47 patterns. We report the number of errors (for each class), AUC, and the average number of SVs as an indicator of C-SVM model structural complexity.

Table 26.2 summarizes the results for the three classification problems presented in [35]. For each classification problem, we report the results obtained on the five

Table 26.1 Summary of results shown in Fig. 26.2

	med-Off	med-On
$H(2)$	0.38	0.67
$\tau(2)$	-0.26	0.35
$\Delta\alpha$	0.85	0.64
$\Delta\alpha$ (shuffled)	0.47	0.49

Table 26.2 Classification results

Representation	Dimension	Errors	AUC	SVs
<i>med-Off/med-On</i>				
H-MFSW	2	7 (5/24, 2/24)	0.85	35.2
MFS-PCA	4	16 (8/24, 8/24)	0.67	44.2
MFS-kPCA	4	16 (10/24, 6/24)	0.67	31.6
POWER-PCA	2	22 (22/24, 0/24)	0.54	46.0
POWER-PCA	3	22 (22/24, 0/24)	0.54	46.5
POWER-PCA	4	23 (23/24, 0/24)	0.52	46.5
POWER-kPCA	2	13 (13/24, 0/24)	0.73	31.5
POWER-kPCA	3	9 (9/24, 0/24)	0.81	31.1
POWER-kPCA	4	8 (8/24, 0/24)	0.83	31.1
<i>DBS-Off/DBS-On</i>				
H-MFSW	2	48 (24/24, 24/24)	0.00	47.0
MFS-PCA	4	29 (14/24, 15/24)	0.40	47.0
MFS-kPCA	4	26 (8/24, 18/24)	0.46	44.6
POWER-PCA	2	48 (24/24, 24/24)	0.00	46.9
POWER-PCA	3	48 (24/24, 24/24)	0.00	46.9
POWER-PCA	4	48 (24/24, 24/24)	0.00	46.9
POWER-kPCA	2	23 (3/24, 21/24)	0.52	45.2
POWER-kPCA	3	23 (3/24, 21/24)	0.52	45.3
POWER-kPCA	4	23 (3/24, 21/24)	0.52	45.9
<i>High-tremor/low-tremor</i>				
H-MFSW	2	16 (16/16, 0/32)	0.50	32.7
MFS-PCA	4	21 (14/16, 7/32)	0.45	39.2
MFS-kPCA	4	15 (12/16, 3/32)	0.58	32.2
POWER-PCA	2	16 (16/16, 0/32)	0.50	31.3
POWER-PCA	3	16 (16/16, 0/32)	0.50	31.5
POWER-PCA	4	16 (16/16, 0/32)	0.50	32.2
POWER-kPCA	2	13 (12/16, 1/32)	0.61	29.2
POWER-kPCA	3	14 (13/16, 1/32)	0.58	30.2
POWER-kPCA	4	14 (13/16, 1/32)	0.58	28.9

Taken from Livi et al. [35]

Three different classification problems are faced by considering several feature-based, low-dimensional representations: recognition of (i) medication Off-On, (ii) DBS Off-On, and (iii) high-low amplitude tremor

FBRs under consideration. For POWER-PCA and POWER-kPCA we use, in both cases, the first two, three, and four principal components in order to evaluate the performances by varying the dimensionality of the representation space given by the Fourier power spectrum. Results show that the effect of medication allows for a more accurate classification. We note that the best result (achieving AUC equal to 0.85) is obtained with the parsimonious, two-dimensional representation denoted as H-MFSW. The per-class errors are also more balanced with respect to the results obtained with the two-dimensional version of POWER-kPCA. In general, results for the last two problems, namely, “DBS-Off/DBS-On” and “high-tremor/low-tremor,” are not convincing – we obtain results compatible with a random classifier. This fact suggests that the effect of medication on the 48 subjects seems to be more characterizing, allowing for an effective classification regardless of the use of DBS or the membership to the high- or low-amplitude rest tremor groups.

26.4 Concluding Remarks and Future Research Perspectives

Methods for analyzing the (multi)fractal properties of time series are instrumental for investigating the nonlinearity of biomedical signals recorded from the brain. Here we discussed recent results [35] obtained on a collection of signals recorded from patients affected by Parkinson’s disease. We have shown that the analysis on long-term correlations and multifractal properties allows to deduce important insights on such signals. Our results show that use of medication (L-DOPA) can be recognized with high accuracy. A result of notable interest is the fact that the use of medication implies a qualitative change in long-term correlation features with statistically significant differences. In fact, experimental conditions involving the use of medication produce signals with positive correlations; the absence of medication produces signals having negative self-similar correlations. Successively, we have exploited features of correlations and multifractality for the purpose of developing feature-based representations of the original time series. Classification results show that the use of medication can be recognized with higher accuracy. Notably, best results have been obtained by means of a parsimonious, two-dimensional representation of the original time series. Such representation encodes only the Hurst exponent and a signature of complexity as expressed by the width of the multifractal spectrum.

Future research directions include the possibility to exploit the so-called local Hurst exponent [40] and a direct estimation of the multifractal spectrum [12], which proved to be effective also with time series of limited length. Another future direction could be the analysis of the (multi)scaling of the cross-correlation [32, 43]. In such a scenario, the idea is to perform a multilevel analysis of pairs of signals in order to characterize the complexity of their coupling over time.

We believe that the presented results could be potentially useful to neuroscientists, suggesting the relevance of using long-term correlations and multifractal signatures for the analysis Parkinsonian rest tremor velocity signals. The developed two-dimensional representation provides a parsimonious and cost-effective

description for rest tremor signals. We suggest that it could be adopted in different real-world clinical settings, even by considering resource-constrained scenarios (e.g., on hardware having a limited computational capability).

References

1. Abry P, Wendt H, Jaffard S. When Van Gogh meets Mandelbrot: multifractal classification of painting's texture. *Sig Process.* 2013;93(3):554–72.
2. Arianos S, Carbone A. Detrending moving average algorithm: a closed-form approximation of the scaling law. *Phys A Stat Mech Appl.* 2007;382(1):9–15.
3. Balachandran R, Welch EB, Dawant BM, Fitzpatrick JM. Effect of MR distortion on targeting for deep-brain stimulation. *IEEE Trans Biomed Eng.* 2010;57(7):1729–35.
4. Barunik J, Kristoufek L. On Hurst exponent estimation under heavy-tailed distributions. *Phys A Stat Mech Appl.* 2010;389(18):3844–55.
5. Bashan A, Bartsch R, Kantelhardt JW, Havlin S. Comparison of detrending methods for fluctuation analysis. *Phys A Stat Mech Appl.* 2008;387(21):5080–90.
6. Beran J, Feng Y, Ghosh S, Kulik R. Long-memory processes. Heidelberg: Springer; 2013.
7. Beuter A, Modolo J. Delayed and lasting effects of deep brain stimulation on locomotion in Parkinson's disease. *Chaos Interdiscip J Nonlinear Sci.* 2009;19(2):026114.
8. Beuter A, Titcombe MS, Richer F, Gross C, Guehl D. Effect of deep brain stimulation on amplitude and frequency characteristics of rest tremor in Parkinson's disease. *Thalamus Relat Syst.* 2001;1(3):203–11.
9. Bialek W, Nemenman I, Tishby N. Predictability, complexity, and learning. *Neural Comput.* 2001;13(11):2409–63.
10. Bronstein JM, Tagliati M, Alterman RL, Lozano AM, Volkmann J, Stefani A, Horak FB, Okun MS, Foote KD, Krack P, et al. Deep brain stimulation for Parkinson disease: an expert consensus and review of key issues. *Arch Neurol.* 2011;68(2):165.
11. Chen Z, Ivanov PC, Hu K, Stanley HE. Effect of nonstationarities on detrended fluctuation analysis. *Phys Rev E.* 2002;65:041107.
12. Chhabra A, Jensen RV. Direct determination of the $f(\alpha)$ singularity spectrum. *Phys Rev Lett.* 1989;62:1327–30.
13. Crutchfield JP, Feldman DP. Regularities unseen, randomness observed: levels of entropy convergence. *Chaos Interdiscip J Nonlinear Sci.* 2003;13(1):25–54.
14. de Oliveira ME, Menegaldo LL, Lucarelli P, Andrade BLB, Büchler P. On the use of information theory for detecting upper limb motor dysfunction: an application to Parkinson's disease. *Phys A Stat Mech Appl.* 2011;390(23):4451–8.
15. Di Ieva A, Grizzi F, Jelinek H, Pellionisz AJ, Losa GA. Fractals in the neurosciences, part I general principles and basic neurosciences. *Neuroscientist.* 2014;20(4):403–17.
16. Di Ieva A, Esteban FJ, Grizzi F, Klonowski W, Marín-Landrove M. Fractals in the neurosciences, part II clinical applications and future perspectives. *Neuroscientist.* 2015;21(1):30–43.
17. Donner RV, Potirakis SM, Barbosa SM, Matos JAO, Pereira AJSC, Neves LJPF. Intrinsic vs. spurious long-range memory in high-frequency records of environmental radioactivity. *Eur Phys J Spec Top.* 2015;224(4):741–62.
18. Drożdż S, Kwapien J, Oświęcimka P, Rak R. Quantitative features of multifractal subtleties in time series. *EPL (Europhys Lett).* 2009;88(6):60003.
19. Dutta S, Ghosh D, Chatterjee S. Multifractal detrended fluctuation analysis of human gait diseases. *Front Physiol.* 2013;4:274.
20. Engin M, Demirağ S, Engin EZ, Çelebi G, Ersan F, Asena E, Çolakoğlu Z. The classification of human tremor signals using artificial neural network. *Expert Syst Appl.* 2007;33(3):754–61.

21. Fabrizio M, Moinfar F, Jelinek HF, Karperien A, Ahammer H. Fractal analysis of cervical intraepithelial neoplasia. *PLoS One*. 2014;9(10):e108457.
22. Fernández-Martínez M, Sánchez-Granero MA, Segovia JET. Measuring the self-similarity exponent in Lévy stable processes of financial time series. *Phys A Stat Mech Appl*. 2013;392(21):5330–45.
23. Gao J, Cao Y, Tung W-W, Hu J. Multiscale analysis of complex time series: integration of chaos and random fractal theory, and beyond. New York: Wiley; 2007.
24. Goldberger AL, Amaral LAN, Glass L, Hausdorff JM, Ivanov PC, Mark RG, Mietus JE, Moody GB, Peng C-K, Stanley HE. Physiobank, physiotookit, and physionet components of a new research resource for complex physiologic signals. *Circulation*. 2000;101(23):215–20.
25. Haeri M, Sarbaz Y, Gharibzadeh S. Modeling the Parkinson's tremor and its treatments. *J Theor Biol*. 2005;236(3):311–22.
26. Harte D. *Multifractals: theory and applications*. Boca Raton: CRC Press; 2010.
27. Hu K, Ivanov PC, Chen Z, Carpena P, Stanley HE. Effect of trends on detrended fluctuation analysis. *Phys Rev E*. 2001;64:011114.
28. Ihlen EAF. Multifractal analyses of human response time: potential pitfalls in the interpretation of results. *Front Hum Neurosci*. 2014;8:523.
29. Islam A, Reza SMS, Iftekharuddin KM. Multifractal texture estimation for detection and segmentation of brain tumors. *IEEE Trans Biomed Eng*. 2013;60(11):3204–15.
30. Kantelhardt JW. Fractal and multifractal time series. In: Meyers RA, editor. *Mathematics of complexity and dynamical systems*. New York: Springer; 2011. p. 463–87.
31. Kantelhardt JW, Zschiegny SA, Koscielny-Bunde E, Havlin S, Bunde A, Stanley HE. Multifractal detrended fluctuation analysis of non-stationary time series. *Phys A Stat Mech Appl*. 2002;316(1):87–114.
32. Kwapien J, Oświęcimka P, Drożdż S. Detrended fluctuation analysis made flexible to detect range of cross-correlated fluctuations. *Phys Rev E*. 2015;92:052815.
33. Li J, Cichocki A. Deep learning of multifractal attributes from motor imagery induced EEG. In: Loo C, Yap K, Wong K, Teoh A, Huang K, editors. *Neural information processing*, volume 8834 of *Lecture Notes in Computer Science*. Switzerland: Springer International Publishing; 2014. pp. 503–510.
34. Livi L, Maiorino E, Rizzi A, Sadeghian A. On the long-term correlations and multifractal properties of electric arc furnace time series. *Int J Bifurcation Chaos*. 2016;26(1):1650007.
35. Livi L, Sadeghian A, Sadeghian H. Discrimination and characterization of Parkinsonian rest tremors by analyzing long-term correlations and multifractal signatures. *IEEE Trans Biomed Eng*. 2016.
36. Maiorino E, Bianchi F, Livi L, Rizzi A, Sadeghian A. Data-driven detrending of nonstationary fractal time series with echo state networks. *ArXiv preprint arXiv:1510.07146*, Oct. 2015.
37. Maiorino E, Livi L, Giuliani A, Sadeghian A, Rizzi A. Multifractal characterization of protein contact networks. *Phys A Stat Mech Appl*. 2015;428:302–13.
38. Mayberg HS, Lozano AM, Voon V, McNeely HE, Seminowicz D, Hamani C, Schwab JM, Kennedy SH. Deep brain stimulation for treatment-resistant depression. *Neuron*. 2005; 45(5):651–60.
39. McIntyre CC, Hahn PJ. Network perspectives on the mechanisms of deep brain stimulation. *Neurobiol Dis*. 2010;38(3):329–37.
40. Molino-Minero-Re E, García-Nocetti F, Benítez-Pérez H. Application of a time-scale local Hurst exponent analysis to time series. *Digit Sig Process*. 2015;37:92–9.
41. Oświęcimka P, Kwapien J, Drożdż S. Wavelet versus detrended fluctuation analysis of multifractal structures. *Phys Rev E*. 2006;74:016103.
42. Oluigbo CO, Salma A, Rezaei AR. Deep brain stimulation for neurological disorders. *IEEE Rev Biomed Eng*. 2012;5:88–99.
43. Oświęcimka P, Drożdż S, Forczek M, Jadach S, Kwapien J. Detrended cross-correlation analysis consistently extended to multifractality. *Phys Rev E*. 2014;89(2):023305.
44. Rasouli G, Rasouli M, Lenz FA, Verhagen L, Borrett DS, Kwan HC. Fractal characteristics of human Parkinsonian neuronal spike trains. *Neuroscience*. 2006;139(3):1153–8.

45. Riley MA, Bonnette S, Kuznetsov N, Wallot S, Gao J. A tutorial introduction to adaptive fractal analysis. *Front Physiol.* 2012;3:371.
46. Sánchez M, Trinidad JE, García J, Fernández M. The effect of the underlying distribution in Hurst exponent estimation. *PloS ONE.* 2014;10(5):e0127824.
47. Serinaldi F. Use and misuse of some Hurst parameter estimators applied to stationary and non-stationary financial time series. *Phys A Stat Mech Appl.* 2010;389(14):2770–81.
48. Serletis D, Bardakjian BL, Valiante TA, Carlen PL. Complexity and multifractality of neuronal noise in mouse and human hippocampal epileptiform dynamics. *J Neural Eng.* 2012;9(5):056008.
49. Shao Y-H, Gu G-F, Jiang Z-Q, Zhou W-X, Sornette D. Comparing the performance of FA, DFA and DMA using different synthetic long-range correlated time series. *Sci Rep.* 2012;2:835.
50. Shawe-Taylor J, Cristianini N. Kernel methods for pattern analysis. Cambridge, UK: Cambridge University Press; 2004.
51. Slow EJ, Hamani C, Lozano AM, Poon YY, Moro E. Deep brain stimulation for treatment of dystonia secondary to stroke or trauma. *J Neurol Neurosurg Psychiatry.* 2015;86(9):1046–8.
52. Talebinejad M, Chan ADC, Miri A. Multiplicative multi-fractal modeling of electromyography signals for discerning neuropathic conditions. *J Electromyogr Kinesiol.* 2010;20(6):1244–8.
53. Titcombe MS, Glass L, Guehl D, Beuter A. Dynamics of parkinsonian tremor during deep brain stimulation. *Chaos Interdiscip J Nonlinear Sci.* 2001;11(4):766–73.
54. Wendt H, Abry P. Multifractality tests using bootstrapped wavelet leaders. *IEEE Trans Signal Process.* 2007;55(10):4811–20.
55. West BJ. Fractal physiology, vol. 2. Oxford: Oxford University Press; 1994.
56. Wibral M, Lizier JT, Priesemann V. Bits from brains for biologically inspired computing. *Front Robot AI.* 2015;2:5.
57. Wu D, Warwick K, Ma Z, Burgess JG, Pan S, Aziz TZ. Prediction of Parkinson's disease tremor onset using radial basis function neural networks. *Expert Syst Appl.* 2010;37(4):2923–8.
58. Yulmetyev RM, Demin SA, Panishev OY, Hänggi P, Timashev SF, Vstovsky GV. Regular and stochastic behavior of Parkinsonian pathological tremor signals. *Phys A Stat Mech Appl.* 2006;369(2):655–78.

Chapter 27

Fractals and Electromyograms

Sridhar Poosapadi Arjunan and Dinesh Kant Kumar

Abstract The complexity nature of the physiological time series can be analysed using fractal theory. The nonlinearity of physiological systems have important relevance in modelling complicated surface electromyogram (sEMG) where the interactions and crosstalk occur over a wide range of temporal and spatial scales. Fractal theory-based analysis is one of the most promising new approaches for extracting such hidden interactions from physiological time series signal like sEMG, which can provide information regarding the characteristic temporal scales and the adaptability of muscle activity response. This chapter investigates the use of fractal theory for analysis of sEMG signal for applications in rehabilitation and age-related changes in the muscle properties and contraction.

Keywords Fractal • Surface electromyogram • Fractal dimension • Complexity

27.1 Introduction

Fractals refer to objects or signal patterns that have fractional dimension. These objects exhibit self-similarity. This defines that the objects or patterns on any level of magnification will yield a structure that resembles the larger structure in complexity [32]. The measured property of the fractal objects is scale dependant and has self-similar variations in different time scales. Fractal dimension of a process measures its complexity, its spatial extent or its space filling capacity and is related to shape and dimensionality of the process [17]. The concept of fractal can be applied to physiological process that is self-similar over multiple scales in time and has broadband frequency spectrum. Fractals manifest a high degree of visual complexity [20].

Biosignals such as sEMG are a result of the summation of identical motor units that travel through tissues and undergo spectral and magnitude compression. SEMG signal in time has the property that patterns (Motor unit action potentials) observed

S.P. Arjunan (✉) • D.K. Kumar
School of Engineering, RMIT University, Melbourne, VIC, Australia
e-mail: sridhar.poosapadiarjunan@rmit.edu.au

at one sampling rate are statistically similar to the patterns observed at lower sampling rates. These statistically similar patterns suggest that sEMG has self-similarity property [2]. Researchers have studied fractal properties of physiological signals to characterize normal and pathological signals [1]. To better represent the properties of sEMG signal, fractal dimension (FD) of sEMG has been investigated in various studies [2, 22, 37].

Several studies [2–4, 8, 17, 20, 22] have reported the use of fractal theory to analyse sEMG. These studies determined that fractal dimension can be used to quantify the complexity of motor unit recruitment patterns. They also demonstrated that the fractal dimension of sEMG signal is correlated with force of contraction.

Fractal dimension represents the scale invariant nonlinear property of the source of the signal and is an index for describing the irregularity of a time series. FD describes the space filling properties of the object or the curve [7], and in the case of sEMG signal, it shows the property of the muscle based on the motor unit recruitment and synchronization. It should be a measure of the muscle complexity to perform a particular movement or contraction and not a measure of the level of muscle activity.

Study by Basmajian and De Luca [6] has indicated that for low level of isometric muscle contraction, there is no change in the size of the muscle while there is measurable change in the muscle dimension during higher levels of muscle contractions and during non-isometric contraction.

27.2 Surface Electromyogram (sEMG)

Surface electromyography (sEMG) is the recording of the muscle's electrical activity from the surface of the skin. In clinical application, sEMG is used for the diagnosis of neuromuscular disorder and for rehabilitation. It is also used for device control applications where the signal is used for controlling devices such as prosthetic devices, robots and human-machine interface.

The advantage of sEMG is due to its non-invasive recording technique, and it provides a safe and easy recording method. The underlying mechanism of sEMG is very complex [18] because there are number of factors such as neuron discharge rates, motor unit recruitment and the anatomy of the muscles and surrounding tissues that contribute to the signal and its recording. In this chapter, basic concepts of generation of sEMG signals and its application will be described.

27.2.1 Generation of sEMG

SEMG signal is generated by the electrical activity of the muscle fibres active during a contraction. The signal sources located at the depolarized zones of the muscle fibres are separated from the recording electrodes by muscle tissues, which act as

spatial low-pass filters on the (spatial) potential distribution. It is closely related to the muscle activity, muscle size and a measure of the functional state of muscle fibres [6].

27.2.2 Factors That Influence sEMG

The action potentials recorded in sEMG signals are generated by the electrical activities in the muscle (Fig. 27.1). The signal contains information related to muscle contraction and condition. Therefore, it is useful to analyse the signal to reveal the information without the need to intervene the muscle. The information in sEMG signal is related to the following factors that influence the signal.

- Level of contraction
- Localized muscle fatigue
- The thickness of body tissue
- The interelectrode distance
- The artefacts and noises
- Crosstalk muscle signals

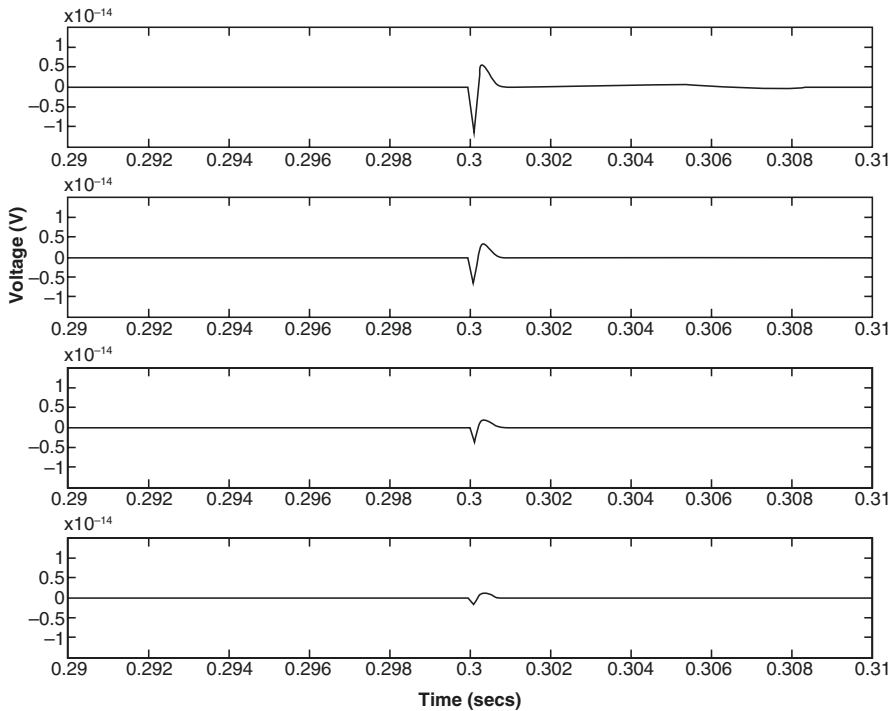


Fig. 27.1 Simulated motor unit action potential (Source: Arjunan and Kumar [3])

27.3 Fractal Analysis of sEMG

Rehabilitation process, clinical diagnosis and basic investigations are critically dependent on the ability to record and analyse physiological signals like ECG, EEG and EMG. However, the traditional analyses of these signals have not kept pace with major advances in technology that allow for recording and storage of massive datasets of continuously fluctuating signals. Although these complex signals have recently been shown to represent processes that are nonlinear and nonstationary in nature, the methods used to analyse these data often assume to be linear and stationary. Such conventional techniques include analysis of means, standard deviations and other features of histograms, along with classical power spectrum analysis [12, 18, 23].

Studies have shown that sEMG signals may contain hidden information that is not extractable with conventional methods of analysis [12, 19, 23, 28]. Such hidden information promises to be of clinical value as well as to relate to basic mechanisms of muscle property and activity function. Fractal-based analysis is one of the most promising new approaches for extracting such hidden information from physiological time series signal like sEMG, which can provide information regarding the characteristic temporal scales and the adaptability of muscle activity response [7–9, 31].

27.3.1 Self-Similarity of sEMG

In complex biosignals like sEMG, there exists self-similarity phenomenon, in which there is a small structure (motor unit) that statistically resembles the larger structure. The source of sEMG is a set of similar action potentials originating from different locations in the muscles. Because of the self-similarity of the action potentials that are the source of the sEMG recordings over a range of scales, sEMG has fractal properties.

The self-similarity property of sEMG was tested using the following procedure mentioned in the study by Kalden and Ibrahim [24].

- If $y(k)$ be a time series signal, then $y^m(k)$ is the *aggregated process* with nonoverlapping blocks of size ‘ m ’ such that

$$y^{(m)}(k) = \frac{1}{m} \sum_{l=0}^{m-1} y(km-l) \quad (27.1)$$

- For the signal or process, $y(k)$ to be self-similar, the variance of the aggregated process decays slowly with m , and this self-similarity is measurable by H , that is,

$$\text{Var}\left(y^{(m)}\right) \approx m^{-\beta} \quad (27.2)$$

- with $0 < \beta < 1$ and

$$H = 1 - \beta / 2 \quad (27.3)$$

where H expresses the degree of self-similarity; large values indicate stronger self-similarity.

27.4 Method to Determine Fractal Dimension

Fractal dimension (FD) analysis is frequently used in physiological signal processing like sEMG, EEG and ECG [14, 20, 34]. Applications of FD in these physiological signals include two types of approaches [15]:

1. *Signals in the time domain*

This approach estimates the FD directly in the time domain or original waveform domain, where the waveform or original signal is considered a geometric figure.

2. *Signals in the phase space domain*

Phase space approaches estimate the FD of an attractor in state space domain. Calculating the FD of waveforms is useful for transient detection, with the additional advantage of fast computation. It consists of estimating the dimension of a time-varying signal directly in the time domain, which allows significant reduction in program runtime [15]. Fractal dimension of sEMG is calculated to determine the transients in sEMG that is related to the overall complexity of the muscle properties.

Three of the most following prominent methods for computing the FD of a waveform [21, 25, 35] have been applied to the analysis of signals and a variety of engineering systems:

- Higuchi's algorithm [21]
- Katz's algorithm [25]
- Petrosian's algorithm [35]

Studies by Esteller et al. [15] have shown that Higuchi's algorithm provides the most accurate estimates of the FD. Katz's method was found to be less linear and its calculated FD was exponentially related to the known FD, whereas Petrosian's algorithm was found to be relatively linear and demonstrated the least dynamic range for the estimated FD. Based on this, Higuchi's algorithm was considered for the computation of FD of sEMG in this study.

27.5 Computation of Fractal Dimension Using Higuchi's Algorithm

FD was calculated using Higuchi's algorithm [15, 21], for non-periodic and irregular time series. This algorithm yields a more accurate and consistent estimation of FD for physiological signals than other algorithms [15].

The first step for computing the FD requires the computation of the length of the curve, X_k^m , for a time signal sampled at a fixed sampling rate, $x(n) = X(1), X(2), X(3), \dots, X(N)$ as follows:

$$L_m(k) = \frac{\left\{ \left[\sum_{i=1}^{\left[\frac{N-m}{k} \right]} |X(m+ik) - X(m+(i-1).k)| \right] \right\} \frac{N-1}{\left[\frac{N-m}{k} \right].k}}{k}$$

The term $\frac{N-1}{\left[\frac{N-m}{k} \right].k}$ represents the normalization factor for the curve length of subset time series. The length of the curve for the time interval $k, \langle L(k) \rangle$ is defined as the average value over k sets of $L_m(k)$. If $L(k) \propto k^{-D}$, then the curve is fractal with the dimension D .

27.6 Relation of FD to sEMG

Fractal dimension of sEMG has been found sensitive to magnitude and rate of muscle force generated. The fractal dimension is introduced as the index for describing the irregularity of a time series in place of the power law index. Studies [2–4, 20, 22] have demonstrated that fractal information of sEMG is useful for characterizing the signal and identifying the complexity in the patterns of the signal.

Anmuth et al. [2] determined that there was a small change of the fractal dimension of the EMG signal and this was linearly related to the activation of the muscle measured as a fraction of maximum voluntary contraction. They also observed a linear relationship between the fractal dimension and the flexion-extension speeds and load. FD of a structure measures its complexity, spatial extent or its space filling capacity and is related to shape and dimensionality of the process [7]. Complexity here refers to the change in detail with respect to change in scale.

The most important inherent properties of muscle include muscle dimensions and its capacity to produce and maintain force. These properties may change with the change in shape and contraction of the muscle and presence of other simultaneously active muscles. In order to test the complexity of the muscle activation, the authors reported a study [3, 29] on determining the fractal features from sEMG signal during four different wrist and finger flexion.

SEMG signals were recorded from four recording locations in the surface of the forearm as shown in Fig. 27.2. The fractal features were computed to observe the change in the complexity and strength in muscle activation during different finger and wrist flexions. Figure 27.3 shows the plot of the fractal features: maximum fractal length and fractal dimension for four different flexions. Maximum fractal length is denoted as the length of the fractal object at the lowest scale [3]. Based on

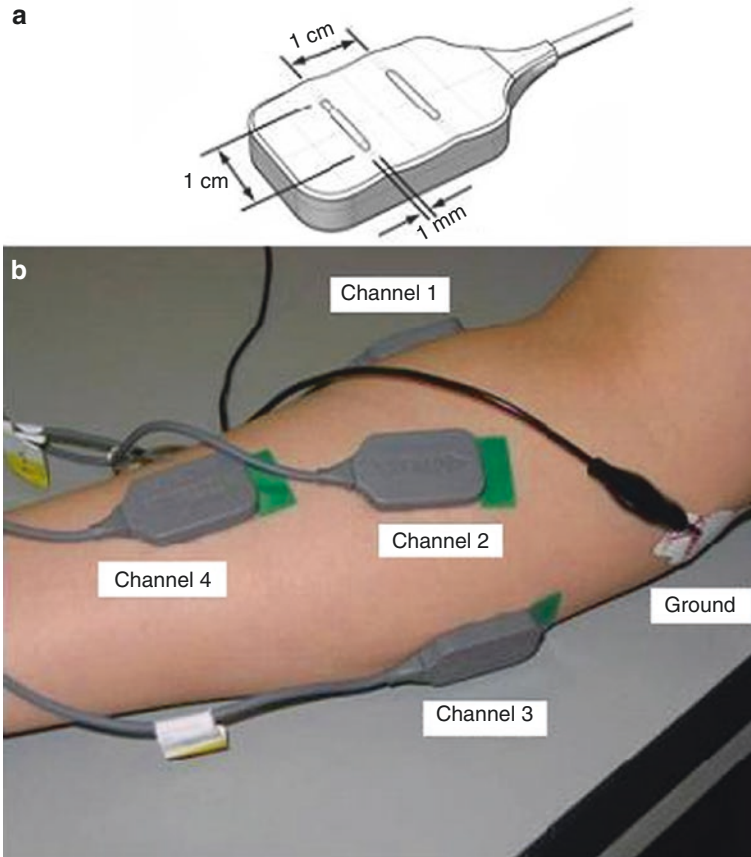


Fig. 27.2 Four recording locations in the surface of the forearm (Source: Arjunan[29] and Arjunan and Kumar [3])

the complexity and strength of muscle contraction, the four different finger movements can be differentiated using these features. It is observed that the fractal dimension reflects the change in the complexity in muscle activity pattern recorded from different muscles while performing particular movement.

27.7 Age-Related Decrease in Fractal Dimension of Surface Electromyogram

One of the changes that have been observed and widely accepted is that with ageing, there is a reduction in muscle control and increase in variation in force of muscle contraction [5, 16, 33, 37] and is one of the causes of injuries and falls among the elderly [27]. The study by Lipsitz and Goldberger [30] has observed a reduction in

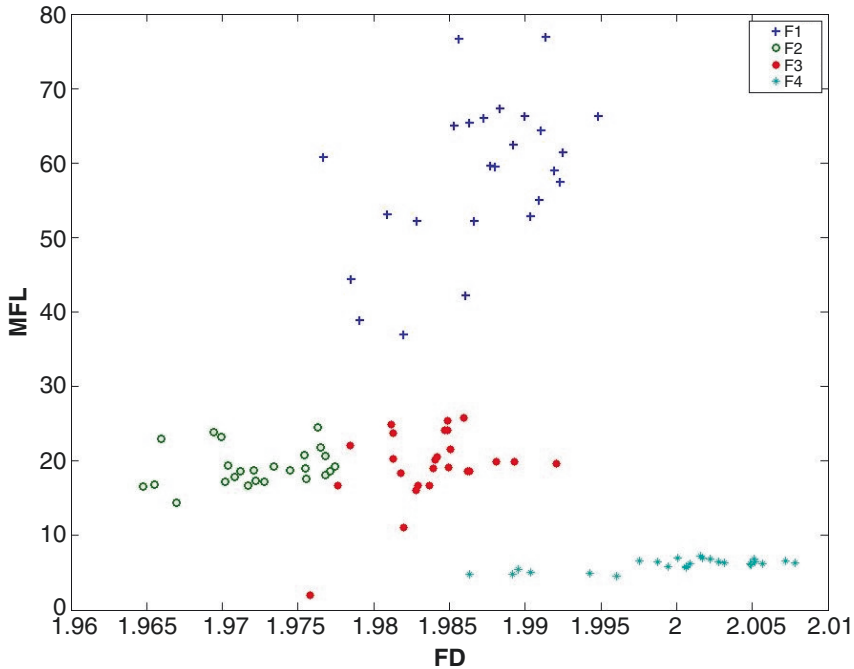


Fig. 27.3 Scatter plot of fractal features (maximum fractal length (MFL) and fractal dimension (FD)) for four different flexions: *F1*, all fingers and wrist flexion; *F2*, index and middle finger flexion; *F3*, wrist flexion towards little finger; and *F4*, little and ring finger flexion (Source: Arjunan and Kumar [3])

the complexity of a physiological or behavioural control system with age and disease. Their research reported that the reduced complexity reflects the underlying structural and functional changes in the organization of the system. A loss in system complexity is reflected by the loss or impairment of functional components and/or due to altered nonlinear coupling between the components. This loss in turn is observed as the reduction in the complexities at the structural and functional levels in the brain, skin, eye and cardiac cycle [4, 10, 11, 26, 36].

The study by Arjunan and Kumar [36] has established the association of ageing with the reduction in the fractal dimension of surface electromyogram. Figure 27.4 shows the change in the complexity (fractal dimension) of sEMG signal recorded from biceps muscle of the people aged 20–69 years while performing a certain isometric muscle contraction. The results show that the FD reduces with the progress of age. The reduction in FD could indicate a reduction in the number of motor unit and may indicate the increase in the motor unit density. This is consistent with the findings by other researchers who have studied the change in FD due to the changes in different organs and tissues with age. Studies have reported the reduction in FD with age for the skin texture, pigmentation and vascularity [30], the retina vessels [11, 26] and the loss of neuron ramification [7]. Fractal dimension of sEMG has also been used for analysis of muscle fatigue and to investigate the changes in the muscle properties due to this condition [8].

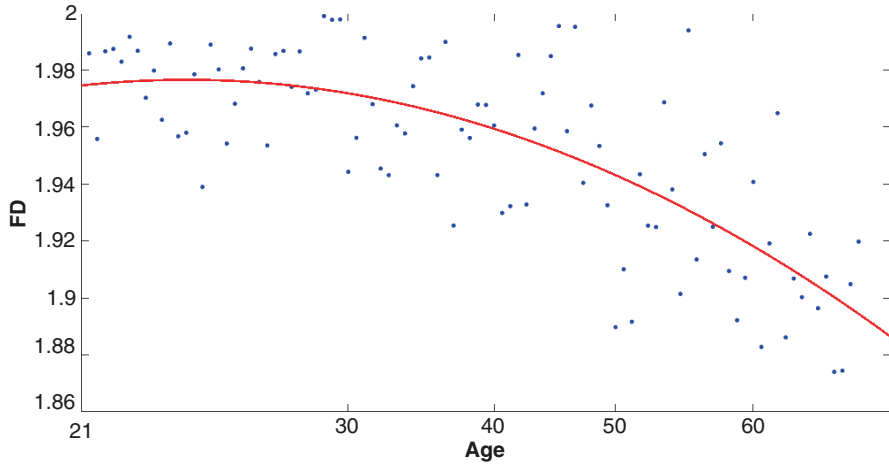


Fig. 27.4 Fractal dimension (FD) of sEMG recorded from biceps muscle of the people ageing from 20 to 69 years

27.8 Summary

Clinical diagnosis and medical investigations are critically dependent on the ability to record and analyse physiological signals like ECG, EEG and EMG. However, the traditional analyses of these signals are currently not suitable with major advances in technology that allow for recording and storage of massive datasets of continuously fluctuating signals. Although these typically complex signals have recently been shown to represent processes that are nonlinear, nonstationary and non-equilibrium in nature, the methods used to analyse these data often assume linearity, stationarity and equilibrium-like conditions. In particular, studies have shown that sEMG signals may contain hidden information that is not extractable with conventional methods of analysis [4, 11, 13, 15]. Such hidden information will provide important and critical information to be of clinical value as well as to relate to basic mechanisms of muscle property and activity function.

References

1. Acharya, Bhat SP, Kannathal N, Rao A, Lim CM. Analysis of cardiac health using fractal dimension and wavelet transformation. *ITBM-RBM*. 2005;26(2):133–9.
2. Anmuth CJ, Goldberg G, Mayer NH. Fractal dimension of electromyographic signals recorded with surface electrodes during isometric contractions is linearly correlated with muscle activation. *Muscle Nerve*. 1994;17(8):953–4.
3. Arjunan SP, Kumar DK. Decoding subtle forearm flexions using fractal features of surface electromyogram from single and multiple sensors. *J Neuroeng Rehabil*. 2010;7:53.
4. Arjunan SP, Kumar DK. Age-associated changes in muscle activity during isometric contraction. *Muscle Nerve*. 2013;47:545–9.

5. Barry BK, Carson RG. The consequences of resistance training for movement control in older adults. *J Gerontol A Biol Sci Med Sci*. 2004;59(7):730–54.
6. Basmajian J, De Luca CJ. *Muscles alive: their functions revealed by electromyography*. 5th ed. Baltimore: Williams & Wilkins; 1985.
7. Bassingthwaite J, Liebovitch L, West B. *Fractal physiology*. New York: Oxford University Press; 1994. p. 29–30.
8. Beretta-Piccoli M, D'Antona G, Barbero M, Fisher B, Dieli-Conwright CM, et al. Evaluation of central and peripheral fatigue in the quadriceps using fractal dimension and conduction velocity in young females. *PLoS One*. 2015;10(4):e0123921.
9. Bourke P. 'Self similarity', fractals, chaos; 2007. URL: <http://local.wasp.uwa.edu.au/pbourke/fractals/selfsimilar/>.
10. Brown M, Hasser EM. Complexity of Age-related change in skeletal muscle. *J Gerontol J Gerontol A Biol Sci Med Sci*. 1996;51(2):B117–23.
11. Che Azemin MZ, Kumar DK, et al. Age-related rarefaction in the fractal dimension of retinal vessel. *Neurobiol Aging*. 2012;33(1):194.e1–4.
12. Chen W-T, Wang Z-Z, Ren X-M. Characterization of surface EMG signals using improved approximate entropy'. *J Zhejiang Univ Sci B*. 2006;7(10):844–8.
13. Doherty TJ, Vandervoort AA, Taylor AW, Brown WF. Effects of motor unit losses on strength in older men and women'. *J Appl Physiol*. 1993;74:868–74.
14. Durgam V, Fernandes G, Preiszl H, Lutzenberger W, Pulvermuller F, Birbaumer N. Fractal dimensions of short eeg time series in humans. *Neurosci Lett*. 1997;225(2):77–80.
15. Esteller R, Vachtsevanos G, Echaz J, Litt B. 'A comparison of waveform fractal dimension algorithms', circuits and systems I: fundamental theory and applications. *IEEE Transactions on [see also Circuits and systems I: regular papers, IEEE Transactions on]*. 2001;48(2): 177–83.
16. Galganski ME, Fuglevand AJ, Enoka RM. Reduced control of motor output in a human hand muscle of elderly subjects during submaximal contractions. *J Neurophysiol*. 1993;69: 2108–15.
17. Gitter JA, Czerniecki MJ. Fractal analysis of the electromyographic interference pattern. *J Neurosci Methods*. 1995;58(1–2):103–8.
18. Graupe D, Cline WK. Functional separation of SEMG signals via arma identification methods for prosthesis control purposes. *IEEE Trans Syst Man Cybern*. 1975;5(2):252–9.
19. Goldberger AL, Amaral LAN, Glass L, Hausdorff JM, Ivanov PC, Mark RG, Mietus JE, Moody GB, Peng C-K, Stanley HE. PhysioBank, PhysioToolkit, and PhysioNet: components of a new research resource for complex physiologic signals. *Circulation*. 2000;101(23): e215–20.
20. Gupta V, Suryanarayanan S, Reddy NP. Fractal analysis of surface EMG signals from the biceps. *Int J Med Inform*. 1997;45(3):185–92.
21. Higuchi T. Approach to an irregular time series on the basis of the fractal theory. *Phys D*. 1988;31(2):277–83.
22. Hu X, Wang ZZ, Ren XM. Classification of surface EMG signal with fractal dimension. *J Zhejiang Univ Sci B*. 2005;6(8):844–8.
23. Huang H-P, Chen C-Y. Development of myoelectric discrimination system for a multi-degree prosthetic hand. *IEEE Int Conf Robot Autom*. 1999;3:2392–7.
24. Kalden R, Ibrahim S. Searching for self-similarity in GPRS. In *PAM 2004: passive and active network measurement*. Springer-Verlag, Berlin Heidelberg 2004. p. 83–92.
25. Katz MJ. Fractals and the analysis of waveforms. *Comput Biol Med*. 1988;18(3):145–56.
26. Kaplan DT, Furman MI, Pincus SM, Ryan SM, Lipsitz LA, Goldberger AL. Aging and the complexity of cardiovascular dynamics. *Biophys J*. 1991;59:945–9.
27. Kinoshita H, Francis PR. A comparison of prehension force control in young and elderly individuals. *Eur J Appl Physiol*. 1996;74:450–60.
28. Kleine BU, van Dijk JP, Lapatki BG, Zwarts MJ, Stegeman DF. Using two-dimensional spatial information in decomposition of surface EMG signals. *J Electromyogr Kinesiol Off J Int Soc Electrophysiological Kinesiol*. 2007;17(5):535–48.

29. Arjunan SP. Fractal features of surface electromyogram: A new measure for low level muscle activation. Diss. RMIT University, 2008.
30. Lipsitz LA, Goldberger AL. Loss of 'complexity' and aging: potential applications of fractals and chaos theory to senescence. *JAMA*. 1992;267:1806–9.
31. Lowery MM, O'Malley MJ. Analysis and simulation of changes in EMG amplitude during high-level fatiguing contractions. *IEEE Trans Biomed Eng*. 2003;50(9):1052–62.
32. Mandelbrot BB. *Fractals: form, chance, and dimension*. 1st ed. San Francisco: Freeman; 1977.
33. Merletti R, Farina D, Gazzoni M, Schieroni MP. Effect of age on muscle functions investigated with surface electromyography. *Muscle Nerve*. 2002;25(1):65.
34. Peng C-K, Hausdorff JM, Goldberger AL. Fractal mechanisms in neural control: Human heartbeat and gait dynamics in health and disease. In: Walleczek J, ed. *Nonlinear Dynamics, Self-Organization, and Biomedicine*. Cambridge: Cambridge University Press, 1999. pp. 66–96.
35. Petrosian A. Kolmogorov complexity of finite sequences and recognition of different preictal EEG patterns. In *Proceedings of the Eighth IEEE Symposium on Computer-Based Medical Systems IEEE, Lubbock, USA; 1995*. p. 212–17.
36. Wong KCL, Wang L, Zhang H, Liu H, Shi P. Computational complexity reduction for volumetric cardiac deformation recovery. *J Signal Process Syst*. 2009;55:281–96.
37. Xu Z, Xiao S. Fractal dimension of surface EMG and its determinants. In *Engineering in Medicine and Biology Society, 1997. Proceedings of the 19th annual international conference of the IEEE'*, Vol. 4. p. 1570–73.

Chapter 28

Fractal Analysis in Neuro-ophthalmology

Giorgio Bianciardi, Maria Eugenia Latronico, and Claudio Traversi

Abstract Fractal analysis has been proven useful in diagnosis and prognosis of the patient in several neuro-ophthalmological disorders. In our experience, entropy was able to differentiate optic neuritis and nonarteritic anterior ischemic optic neuropathy and geometric complexity to objectively quantize the alteration of corneal innervation in Sjogren's syndrome patients.

Keywords Entropy • Geometrical complexity • Sjogren's syndrome • Optic neuritis • Nonarteritic anterior ischemic optic neuropathy • Differential diagnosis

28.1 Eye and Nervous System

The eye gives organism the ability to process visual detail, detecting visible light in order to build a representation of the surrounding environment at the cerebral cortex level as well as enabling several nonimage functions.

The eye is one of the most complex and important sensory organs in the human body. It provides the ability to see in both bright and dim light as well as to focus on near and far objects and to distinguish millions of colors.

A complex innervation is present: the retina, the first neural structure of the eye, from which the optic nerve departs electric signals toward the cerebral cortex; the infraorbital, lacrimal, lingual, nasociliary, and supraorbital nerves; as well as the corneal nerve plexus. Nerves and plexi need microvascular support. The complex appearance of microvascular networks and nervous plexi are microscopic features where fractal analysis reveals its powerful ability to discriminate among health and pathology.

G. Bianciardi, MS, MD, PhD (✉)
Department of Medical Biotechnologies, University of Siena, Siena, Italy
e-mail: giorgio.bianciardi@unisi.it

M.E. Latronico, MD • C. Traversi, MD
Department of Medical Sciences, Surgery and Neurosciences, University of Siena,
Siena, Italy

28.2 Retinal Microvascular Networks and Ophthalmopathies

Several works have used fractal geometry to study the retinal microvascular network [4, 23, 31, 32, 38]. In these works, the fractal dimension of the retinal microvasculature has been used as a statistical descriptor able to support the diagnosis of several diseases, also revealing the status of other vascular districts [29].

It has been shown that the retinal vascular network in health condition has a fractal dimension, D_0 (geometric complexity) close to the value of a diffusion-limited aggregation (DLA) process ($D \approx 1.70$) [23, 32], while in pathologic condition that value may change. Doubal et al. [21] have found a low value of fractal dimension of retinal vessels, associated to the lacunar stroke. Cavallari et al. [15] found a low value in fractal dimension related to the reduction in complexity of retinal vessels, reflecting the alteration of the brain microvessels in patients with CADASIL (cerebral autosomal dominant arteriopathy with subcortical infarcts and leukoencephalopathy). In these works, fractal analysis has been demonstrated as a sensitive tool to assess changes of retinal vessel branching, able to reflect the early brain microvessel alterations.

Another fractal parameter, lacunarity, has been applied to characterize diseases, helping in differential diagnosis. Lacunarity may be considered a measure of heterogeneity, as well as the degree of invariance to change of the fractal object. Whereas the fractal dimension (geometric complexity) indicates how much space is filled by the object, lacunarity describes the distribution of the sizes of gaps or lacunae surrounding the object within the image, describing the empty space around the object [25]. This parameter, which has the capacity to recognize different fractal structures owning the same fractal dimension, was employed to discover alterations in the arteries and retinal veins [26], as well as to diagnose retinas with amblyopia [44].

The retina vessel network, described by generalized dimensions and singularity spectrum, has a multifractal structure (an object having different fractal properties in its different region) [41]. These multifractal approaches were able to characterize the retinal vascular architecture disorder in several diseases [43–45].

Particularly, in diabetes mellitus, fractal analysis has been applied in several works to describe its secondary microvascular complications. The diabetic retinopathy is a severe condition, one of the causes of vision impairment and blindness, where the secondary microvascular complication occurs [1]. It is caused by hyperglycemia that promotes structural/functional alterations of retinal capillaries [19]. The early stage of retinopathy is termed as non-proliferative diabetic retinopathy (NPDR), a disease characterized by microaneurysms, hemorrhages, and capillary closures [4, 16, 19]. The subsequent stage, or proliferative phase, is characterized by neovascularization with an increase of the ischemic regions, hemorrhages in the vitreous cavity, and tractional retinal detachment [19, 47]. Vision impairment, at first, and, thereafter, blindness are the final consequence.

At the beginning, fractal analysis gave rise to contradictory results, at least apparently [24]. Avakian et al. [3] observed a reduction of the density of vessel complexity in

the retinal macular region in patients with NPDR, in comparison to the normal retina macular region. On the other side, Cheung et al. [17] reported increase of the retinal vasculature fractal dimension associated with early NPDR signs in young individuals with type 1 diabetes, consequential to the development of the diabetic retinopathy [28]. In a more recent clinic-based prospective study of 172 participants, the fractal dimension of the retinal microvasculature in healthy subjects resulted slightly lower than the corresponding value of mild NPDR patients, but higher than the corresponding value of moderate NPDR subjects. Severe NPDR presented the lowest value of fractal dimension. In this work, the fractal parameter permitted a more complete understanding of the early pathophysiological mechanism of diabetes [45].

28.3 Our Experience: Neuro-ophthalmological Disorders

In our experience, fractal approaches clearly distinguished among diagnostic classes, revealing its ability to help clinicians to identify neuro-ophthalmopathies and to improve treatments [11, 12]. Below, we show that fractal analysis of the retinal microvasculature is able to differentiate optic neuritis and nonarteritic anterior ischemic optic neuropathy: the two most prevalent non-glaucomatous optic neuropathies [18]. Furthermore, fractal analysis of corneal nerve plexus was able to objectively characterize aspects of the Sjogren's syndrome.

28.3.1 *Optic Neuritis Versus Nonarteritic Anterior Ischemic Optic Neuropathy: Retinal Microvasculature*

Recovery of visual function, visual-field testing abnormalities, pain induced by ocular movements, cup-to-disk ratio, presence and/or distribution of optic disk edema, and fluorescein angiography together with age at diagnosis may help to differentiate optic neuritis (ON) and nonarteritic anterior ischemic optic neuropathy (NAION) [2, 18]. However, even by using several different approaches, ON and NAION frequently present overlapping clinical profiles and sometimes appear difficult to distinguish on clinical grounds at initial presentation [51]. It is fundamental to establish an early differential diagnosis, having the ON patient a clear tendency to develop multiple sclerosis [5, 7, 8].

To facilitate early diagnosis, researchers have focused on objective morphological analysis of the retrobulbar tract and the head of the optic nerve, in order to reduce the bias caused by subjective medical interpretations [14]. Optic nerve analyses by means of magnetic resonance imaging, digital stereoscopy, and Heidelberg retina tomography are some examples of how new technologies can quantitatively document peculiar clinical findings in ON, NAION, and other optic nerve diseases [20, 35, 40]. Furthermore, the study of optic nerve head circulation by means of

laser-based blood flow measuring techniques has quantitatively demonstrated optic nerve head circulatory abnormalities in patients with ON and NAION [27]. In effect, in the multifactorial etiology of NAION and ON, optic nerve inflammation and optic nerve head ischemia, respectively, play important roles [50].

In order to verify whether the fractal analysis of the optic nerve head vascularity could help in the differential diagnosis between NAION and ON, we have evaluated the information dimension (entropy) of the optic nerve head vascular patterns, as observed by fluorescein angiography.

28.3.1.1 Patients

The criteria for patients' admittance with NAION to the study were unilateral disk swelling with clinical features consistent with NAION, no recovery of visual function in the first month of follow-up, exclusion of arteritic anterior ischemic optic neuropathy either on clinical grounds or following a negative temporal artery biopsy, negative magnetic resonance imaging of the brain and orbits, no other ocular pathology, and no neurological diseases that might influence or explain the patient's visual symptoms. The patient admittance criteria with ON were unilateral visual impairment associated with impaired color vision and visual-field loss, presence of disk edema or absence of disk edema, young age (≤ 35 years), ocular pain associated with eye movements, recovery of visual function in the first month of follow-up, no other ocular pathology, and no neurological diseases that might influence or explain the patient's visual symptoms; history or detection of multiple sclerosis confirmed the diagnosis [8].

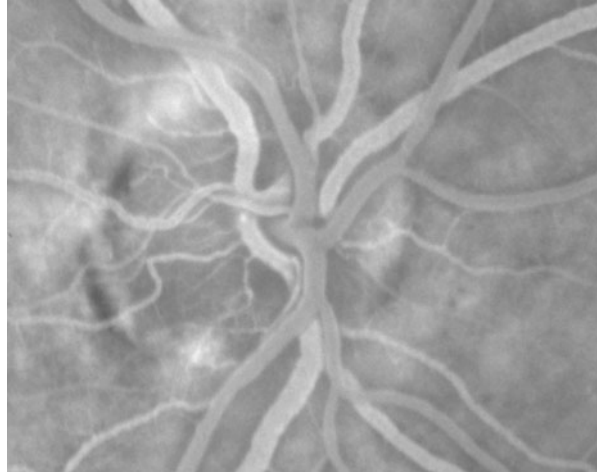
Ten cases of NAION and ten cases of ON with presence of disk edema were studied. The unaffected eye of the patient was used as control. All patients were examined using a fluorescein angiogram within the first 2 weeks after they reported the first symptoms and before treatments; all patients gave informed consent. The protocol for this research project was approved by the Ethics Committee of the University of Siena, and it conforms to the provisions of the Declaration of Helsinki, 1955 (as revised, Edinburgh, 2000).

28.3.1.2 Image Analysis

Static fluorescein angiogram was performed (IMAGENet 2000, v.2.0, Topcon). The early, intermediate, and late phases of the angiogram were studied. Images of the early venous phase of the angiogram (around 20 s) gave the best visualization of the optic disk vessels and were saved. The same magnification was used for every patient (Fig. 28.1).

A manual outline of the trajectories of the two-dimensional microvascular network was performed down to microvessels of 20 μ of diameter, processed to threshold the vessel network without background interference and converted into an outline of 1 pixel by means of Jmicrovision, <http://www.jmicrovision.com>, and Image Analyzer, <http://www.fosshub.com/Image-Analyzer.html>, softwares (Fig. 28.2).

Fig. 28.1 Fluorescein angiogram. Unaffected eye (control)



Entropy, D1

The images were represented on a graphic window of 501×429 pixels (1 pixel = $4 \mu\text{m}$). To evaluate the information present in the pattern, information dimension (entropy, D1), a robust estimate from a finite amount of data that gives the probability of finding a point in the image [34, 39], was calculated. Briefly, the set was covered with boxes of linear size, d , keeping track of the mass, m_i (the amount of pixels), in each box (from 10 to 100 pixels), and the local information entropy, $I(d)$, was calculated (summation of the number of points in the i -th box divided by the total number of points in the set, multiplied for its logarithm) [22]. A log-log plot was performed ($I(d)$ against d). The plot of the logarithm of $I(d)$ against the logarithm of d was a straight line with a negative slope equal to $-D1$ (Fig. 28.3).

The method was implemented using Benoit 1.3 software (TruSoft Int'l Inc, <http://trusoft-international.com/benoit.html>) and validated by computer-generated Euclidean and fractal shapes of known information dimensions. Inter- and intra-observers errors were $<3\%$.

28.3.1.3 Statistical Analysis

Mann-Whitney test was used to ascertain the significance among the groups; regression analysis was used to ascertain the log-log plot linearity.

28.3.1.4 Results

Fractal analysis showed that the optic nerve head microvasculature was fractal (log-log plot, $r > 0.99$, Fig. 28.3).

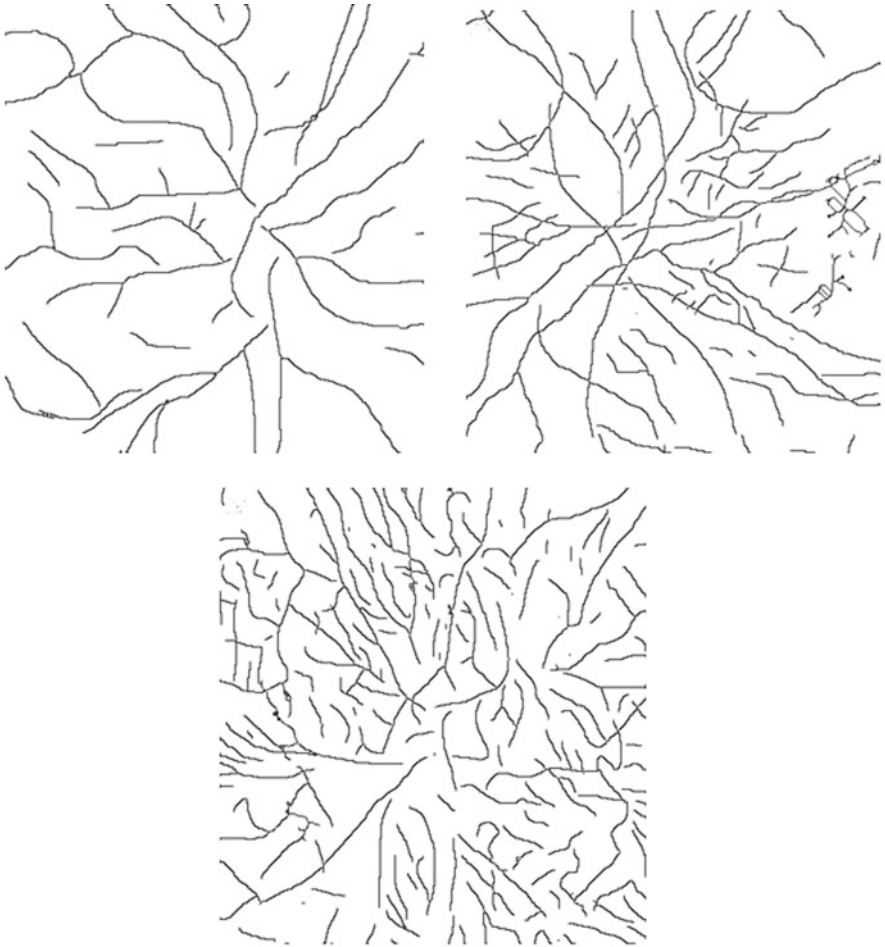


Fig. 28.2 Trajectories of the optic nerve head microvasculature. Control eye (*top, left*); nonarteritic anterior ischemic optic neuropathy (NAION, *top, right*), optic neuritis with optic disk edema (ON, *bottom*)

ON and NAION cases presented higher entropy values of the optic nerve head vascular pattern than controls. Entropy statistically distinguished among the three classes (healthy subjects vs. NAION vs. ON patients) ($p < 0.01$; $p < 0.01$) (Table 28.1).

28.3.2 Sjogren's Syndrome: Corneal Nerve Plexus

Among the many causes of dry eye diseases, Sjogren's syndrome (SS) is a multifactorial disorder mainly affecting the salivary and lacrimal glands with an autoimmune basis [13]. The peak incidence is in the fourth and fifth decades of life, with a female to male ratio of 9:1. The incidence of primary SS reported in literature varies between

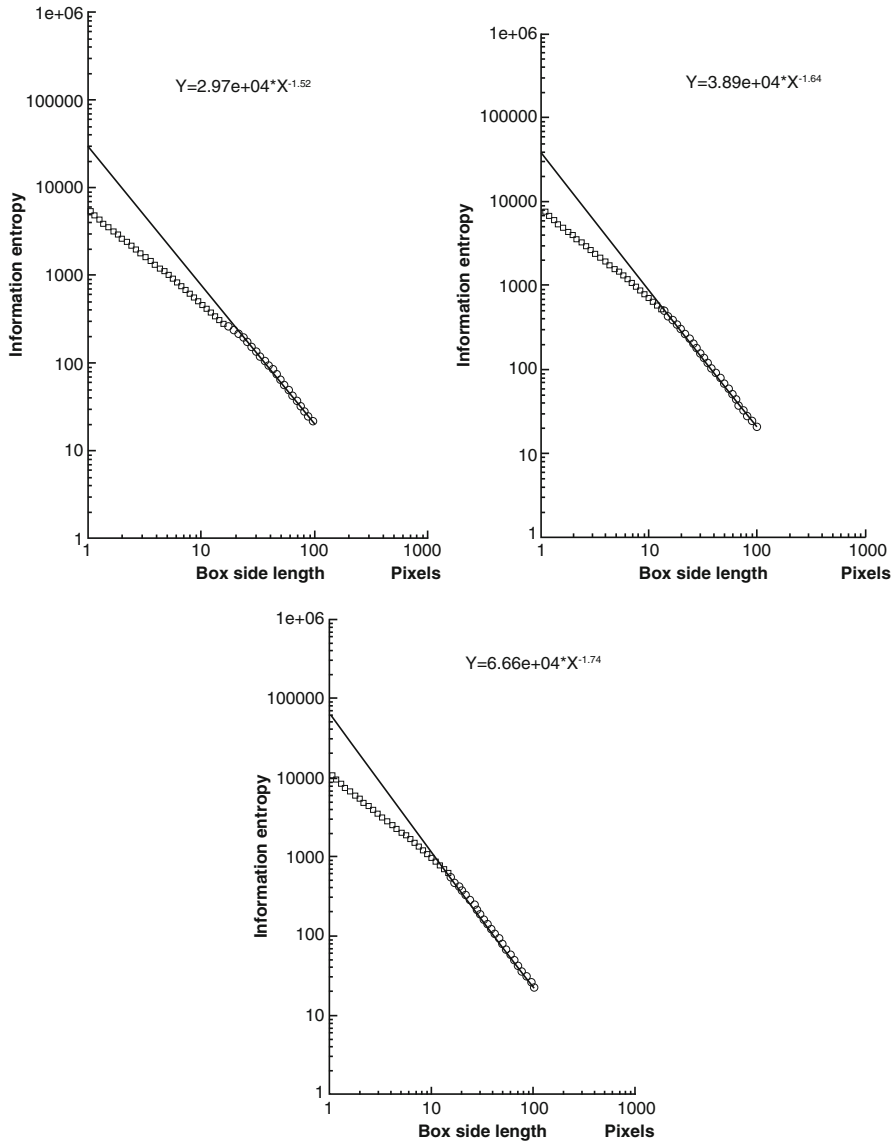


Fig. 28.3 Log-log plots. The exponent is the local information dimension, or entropy of the image (the same of Fig. 28.2). Control eye (*top, left*), NAION (*top, right*), ON (*bottom*)

3/100,000 and 5/100,000 [36]. One of its main clinical manifestations is the keratoconjunctivitis sicca (KCS) [33]. In primary SS (SSI), the presence of specific antibodies (SSA, SSB, ANA, ENA), signs of mononuclear cells infiltration in the exocrine glands, and reduced tear and saliva secretions are described. In secondary SS (SSII), the typical symptoms of the primary form are coupled by other well-defined autoimmune disorders (rheumatoid arthritis, systemic lupus erythematosus, scleroderma) [6, 9].

Table 28.1 Entropy, D1, of the optic nerve head vascularization, cases vs. control (mean \pm standard deviation)

Subjects	D1 (SD)
ON ^a with optic disk edema	1.74 (0.025)*, **
NAION ^b	1.63 (0.02)*
Controls	1.53 (0.02)

Entropy of the optic nerve head vascularization distinguishes among ON, NAION and healthy subjects: **ON with optic disk edema vs. control, $p < 0.001$; *ON with optic disk edema vs. NAION, $p < 0.01$; *NAION vs. control, $p < 0.01$

^aOptic neuritis

^bNonarteritic anterior ischemic optic neuropathy

The ocular surface is considered a morphofunctional unit comprising lachrymal film, cornea, limbus, conjunctiva, mucoepidermal junction, accessory lachrymal glands, meibomian gland, and innervation. The alteration of only one of those components is followed by pathologic events that extend to the other structures. In SS, KCS is the primitive disease of the ocular structure, presumably [33]. Surface morphologic changes, including the presence of inflammatory cells and the expression of histocompatibility antigens (HLA-DR), suggest the participation of the epithelium and subepithelium innervation, with a consequent reduction of corneal sensitivity [36]. Thus, it is necessary to study the modification of the corneal surface and of its innervation for better understanding the physiopathology of SS and also in order to choose the right therapeutic treatments [9, 37].

The use of the in vivo confocal microscopy permits the study of the microscopic morphology of the cornea with a resolution comparable to the histologic examination and without invasivity [48, 49, 54]. In order to obtain diagnostic data related to the corneal microstructure in Sjogren's syndrome, we have evaluated the geometric complexity of the corneal nerve fiber distribution observed by confocal microscopy.

28.3.2.1 Patients

Diagnosis of SSI or SSII was made according to the Japanese consensus criteria (biopsy of salivary glands and blood tests). Informed consent was obtained from all the subjects. Examination procedures were board reviewed, and the study was conducted in accordance with the tenets of the Declaration of Helsinki, 1955 (as revised, Edinburgh, 2000).

Twenty patients (4 men and 16 women) with SSI and 10 sex- and age-matched controls were studied. None of the patients had a history of Steven Johnson syndrome, lymphoma, AIDS, corneal dystrophy, inflammation, therapies with anti-glaucoma drugs or steroids, and use of contact lenses. The results were compared with the ones of healthy control subjects.

28.3.2.2 Image Analysis

In vivo laser confocal microscopy (670 nm red wavelength, helium neon diode laser source) was performed on the subjects by a HRT II Rostock Corneal Module (Heidelberg Engineering GmbH, Dossenheim, Germany). A drop of anesthetic (oxybuprocaine chloride 0.4%) was instilled in the lower conjunctival fornix before examination. During the test, the microscope object lens was covered with a gel (hydroxypropyl methylcellulose) and placed in direct contact with the corneal surface. Proper alignment and position of the head was maintained with the help of a dedicated target mobile red fixation light for the contralateral eye. A digital camera mounted on a side arm provided to monitor the position of the objective lens on the eye surface. A scan of the full thickness of the cornea was automatically performed for each participant, in order to identify the corneal nerve plexus (Fig. 28.4).

Single-pixel contours of the images were automatically extracted by a Canny edge filter (Digital Image Magnifier software by Strikos Nikolaos, <http://www.soft-oxi.com/digital-image-magnifier.html>) (Fig. 28.5).

Geometric Complexity, D_0

The images were represented on a graphic window of 500×500 pixels (1 pixel = $1 \mu\text{m}$). The box-counting local fractal dimension of the image was measured [22, 52]. Briefly, the image was covered with boxes of linear size, d (from 10 to 100 pixels), and the amount of boxes containing any part of the outline, $N(d)$, was counted.

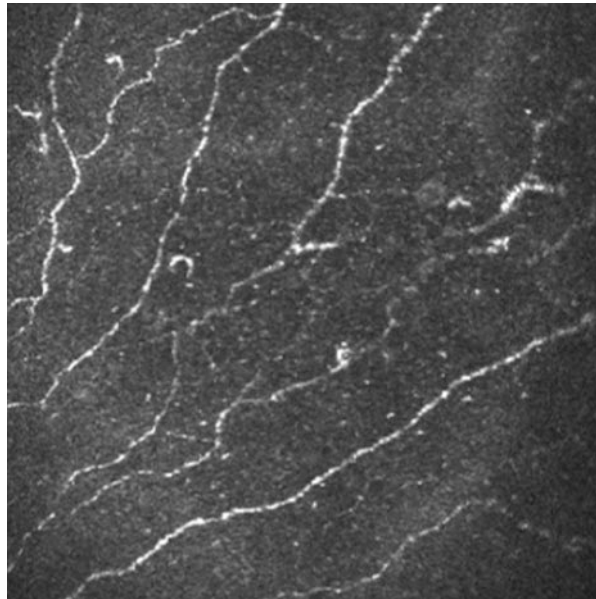


Fig. 28.4 Image of the corneal nerve fibers after in vivo laser confocal microscopy in a healthy subject

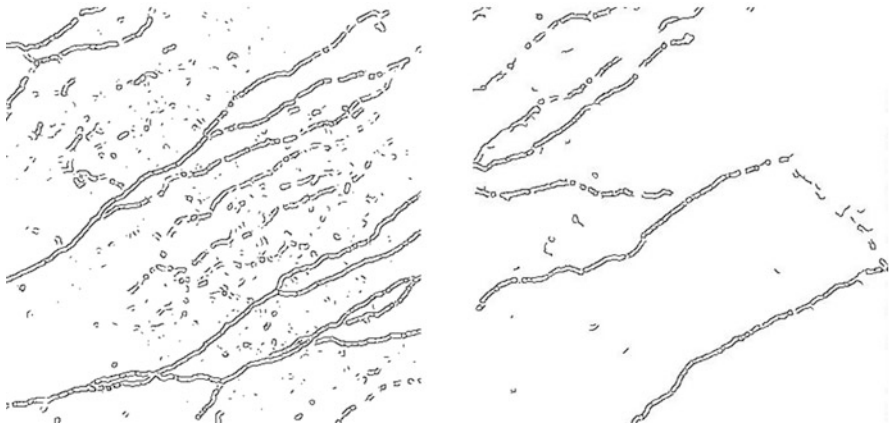


Fig. 28.5 Single-pixel contours of the corneal nerve fibers images extracted by a Canny edge filter. Healthy subject (*left*), Sjogren's syndrome patient (*right*). The skeletonized images were submitted to the fractal analysis in order to evaluate the geometric complexity of the nerve fibers distribution

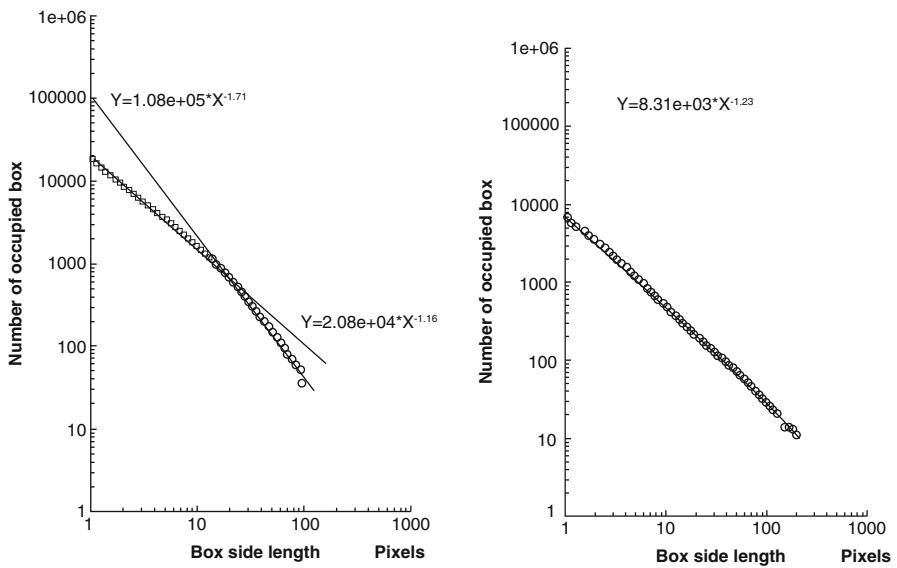


Fig. 28.6 Log-log plots. The exponent is the geometric complexity of the image (the same of Fig. 28.5). The healthy subject shows a multifractal aspect (*left*), while in the Sjogren's syndrome patient, one line only is detected (*right*) (note also that the geometric complexity is decreased in the patient)

The plot of the logarithm of $N(d)$ against the logarithm of d was a straight line with a negative slope equal to $-D_0$ (Fig. 28.6).

The method was implemented using Benoit 1.3 software (TruSoft Int'l Inc, <http://trusoft-international.com/benoit.html>) and validated by computer-generated

Euclidean and fractal shapes of known fractal dimensions. Inter- and intra-observer errors were <3 %.

28.3.2.3 Statistical Tests

Mann-Whitney test was used to ascertain the significance between the groups; regression analysis was used to ascertain the log-log plot linearity.

28.3.2.4 Results

Fractal analysis showed that the corneal nerve distribution was fractal (log-log plot, $r > 0.99$, Fig. 28.6).

In healthy subjects, the local fractal dimension was close to the value of the diffusion-limited aggregation process, a typical value of geometric complexity in normal individuals (Table 28.2) [10, 53], with a multifractal aspect (Fig. 28.6, left) [30]. In SS patients, D0 values decreased and the multifractal aspect was lost (Fig. 28.6, right).

28.4 Discussion

We have reviewed papers where fractal analysis has proven to be a useful tool in diagnosis and prognosis of the patient in several neuro-ophthalmological disorders, and we have presented our experience in the field. We have presented the entropy evaluation of the retinal microvasculature in optic neuritis vs. nonarteritic anterior ischemic optic neuropathy and healthy condition and the geometric complexity evaluation of the corneal nerve plexus in Sjogren’s syndrome patients vs. healthy subjects. In both, fractal parameters were able to distinguish among diagnostic classes and to objectively quantify the optic nerve head microvasculature or the corneal nerve plexus distribution. These results add new information to previous data obtained by us [11, 12, 46].

Subjects	D0 (SD)
Sjogren’s syndrome	1.17 (0.03) ***
Healthy controls	1.64 (0.05)

Table 28.2 Geometric complexity, D0, of the corneal nerve plexus, case vs. control (mean ± standard deviation)

Geometric complexity of the corneal nerve fiber distribution in Sjogren’s syndrome patients is lower than in healthy subjects. Healthy individuals show geometric complexity values close to the diffusion-limited aggregation process

*** $p < 0.001$

References

1. Antonetti DA, Barber AJ, Bronson SK, Freeman WM, et al. Diabetic retinopathy seeing beyond glucose-induced microvascular disease. *Diabetes*. 2006;55:2401–11.
2. Arnold AC, Badr MA, Hepler RS. Fluorescein angiography in nonischemic optic disc oedema. *Arch Ophthalmol*. 1996;114:293–8.
3. Avakian A, Kalina RE, Sage EH, Rambhia AH, et al. Fractal analysis of region-based vascular change in the normal and non-proliferative diabetic retina. *Curr Eye Res*. 2002;24:274–80.
4. Azemin MZ, Kumar DK, Wong TY, Kawasaki R, Mitchell P, Wang JJ. Robust methodology for fractal analysis of the retinal vasculature. *IEEE Trans Med Imaging*. 2011;30:243–50.
5. Balcer LJ. Clinical practice. Optic neuritis. *N Engl J Med*. 2006;354:1273–80.
6. Barabino S, Montaldo E, Solignani F, et al. Immune response in the conjunctival epithelium of patients with dry eye. *Exp Eye Res*. 2010;91:524–9.
7. Beck RW, Arrington J, Murtagh FR, Cleary PA, Kaufman DI. Brain magnetic resonance imaging in acute optic neuritis: experience of the optic neuritis study group. *Arch Neurol*. 1993;50:841–6.
8. Beck RW, Cleary PA, Trobe JD, et al. The effect of corticosteroids for acute optic neuritis on the subsequent development of multiple sclerosis. *N Engl J Med*. 1993;329:1764–9.
9. Bherens A, Doyle JJ, Stern L, et al. Dysfunctional tear syndrome: a Delphi approach to treatment recommendation. *Cornea*. 2006;25:900–7.
10. Bianciardi G. Differential diagnosis: shape and function, fractal tools in the pathology lab. *Nonlinear Dyn Psychol Life Sci*. 2015;19(4):437–64.
11. Bianciardi G, Latronico ME, Traversi C. Decreased geometric complexity of corneal nerve fibers distribution in Sjogren's syndrome patients. *Int J Ophthalmic Pathol Res*. 2015;4:2.
12. Bianciardi G, Latronico ME, Traversi C. Entropy of corneal nerve fibers distribution observed by laser scanning confocal microscopy: A noninvasive quantitative method to characterize the corneal innervation in Sjogren's syndrome patients. *Microsc Res Tech*. 2015;78(12):1069–74.
13. Buchholz P, Steeds CS, Ster LS, et al. Utility assessment to measure the impact of dry eye disease. *Ocul Surf*. 2006;4:155–61.
14. Burgoyne CF. Image analysis of optic nerve disease. *Eye*. 2004;18:1207–13.
15. Cavallari M, Falco T, Frontali M, Romano S, Bagnato F, Orzi F. Fractal analysis reveals reduced complexity of retinal vessels in CADASIL. *PLoS ONE*. 2011;6:1–4.
16. Chen C, Shah CP. Review of therapeutic advances in diabetic retinopathy. *Adv Endocrinol Metab*. 2011;2:39–53.
17. Cheung N, Donaghue KC, Liew G, Rogers S, Wang J, Lim SW, Jenkins AJ, Hsu W, Lee M, Wong TY. Quantitative assessment of early diabetic retinopathy using fractal analysis. *Diabetes Care*. 2009;32:106–10.
18. Collington-Robe NJ, Feke GT, Rizzo III JF. Optic nerve head circulation in nonarteritic anterior ischemic optic neuropathy and optic neuritis. *Ophthalmology*. 2004;111:1663–72.
19. Crawford TN, Alfaro DV, Kerrison JB, Jablon EP. Diabetic retinopathy and angiogenesis. *Curr Diabetes Rev*. 2009;5:8–13.
20. Danesh-Meyer H, Savino PJ, Spaeth GL, Gamble GD. Comparison of arteritis and nonarteritic anterior ischemic optic neuropathies with the Heidelberg retina tomograph. *Ophthalmology*. 2005;112:1104–12.
21. Doubal FN, MacGillivray TJ, Patton N, Dhillon B, Dennis MS, Wardlaw JM. Fractal analysis of retinal vessels suggests that a distinct vasculopathy causes lacunar stroke. *Neurology*. 2010;74:1102–7.
22. Falconer K. *Fractal geometry: mathematical foundations and applications*. Chichester: Wiley; 1990.
23. Family F, Masters BR, Platt DE. Fractal pattern formation in human retinal vessels. *Phys D*. 1989;38:98–103.

24. Kunicki ACB, Oliveira AJ, Mendonça MBM, Barbosa CTF, Nogueira RA. Can the fractal dimension be applied for the early diagnosis of non-proliferative diabetic retinopathy? *Braz J Med Biol Res.* 2009;42:930–4.
25. Gould DJ, Vadakkan TJ, Poché RA, Dickinson ME. Multifractal and lacunarity analysis of microvascular morphology and remodeling. *Microcirculation.* 2011;18:136–51.
26. Landini G, Murray PI, Misson GP. Local connected fractal dimensions and lacunarity analyses of 60° fluorescein angiograms. *Invest Ophthalmol Vis Sci.* 1995;13:2749–55.
27. Leiba H, Rachmiel R, Harris A, Kagemann L, Pollack A, Zalish M. Optic nerve head blood flow measurements in nonarteritic anterior ischemic optic neuropathy. *Eye.* 2000;14:828–33.
28. Lim SW, Cheung N, Wang J, Donaghue KC, et al. Retinal vascular fractal dimension and risk of early diabetic retinopathy. *Diabetes Care.* 2009;32:2081–3.
29. Lin F, Zhu P, Huang F, Li Q, Yuan Y, Gao Z, et al. Aortic stiffness is associated with the central retinal arteriolar equivalent and retinal vascular fractal dimension in a population along the southeastern coast of China. *Hypertens Res.* 2015;38:342–8.
30. Lopes R, Betrouni N. Fractal and multifractal analysis: a review. *Med Image Anal.* 2009;13:634–49.
31. Mancardi D, Varetto G, Bucci E, Maniero F, Guiot C. Fractal parameters and vascular networks: facts & artifacts. *Theor Biol Med Model.* 2008;5:1–8.
32. Masters BR. Fractal analysis of the vascular tree in the human retina. *Annu Rev Biomed Eng.* 2004;6:427–52.
33. McGinnigles S, Naroo SA, Eperjesi F, et al. Evaluation of dry eye. *Surv Ophthalmol.* 2012;57(4):293–316.
34. Mendonça MBM, Garcia CAA, Nogueira RA, Gomes MAF, Valença MM, Oréface F. Fractal analysis of retinal vascular tree: segmentation and estimation methods. *Arq Bras Oftalmol.* 2007;70:413–22.
35. Morgan JE, Sheen NJL, North RV, Choong Y, Ansari E. Digital imaging of the optic nerve head: monoscopic and stereoscopic analysis. *Br J Ophthalmol.* 2005;89:879–84.
36. Moss SE, Klein R, Klein BE, et al. Incidence of dry eye in a older population. *Arch Ophthalmol.* 2004;122:221–32.
37. Nichols KK, Nickols JJ, Zadnick K. Frequency of dry eye diagnostic test procedures used in various modes of ophthalmic practise. *Cornea.* 2000;19:477–82.
38. Parsons-Wingenter P, Elliott KE, Clark JI, Farr AG. Fibroblast growth factor-2 selectively stimulates angiogenesis of small vessels in arterial tree. *Arterioscler Thromb Vasc Biol.* 2000;20:1250–6.
39. Pitsianis N, Bleris G, Argyrakis P. Information dimension in fractal structures. *Phys Rev B.* 1989;39(10):7097–100.
40. Rizzo III JF, Andreoli CM, Rabinov JD. Use of magnetic resonance imaging to differentiate optic neuritis and nonarteritic anterior ischemic optic neuropathy. *Ophthalmology.* 2002;109:1679–84.
41. Stanley HE, Meakin P. Multifractal phenomena in physics and chemistry. *Nature.* 1988;335:405–9.
42. Stern ME, Gao J, Schwalb TA, et al. Conjunctival T-cell subpopulations in Sjogren's and non Sjogren's patients with dry-eye. *Invest Ophthalmol Vis Sci.* 2002;43:2609–14.
43. Stošić T, Stošić BD. Multifractal analysis of human retinal vessels. *IEEE Trans Med Imaging.* 2006;25:1101–7.
44. Țălu Ș, Vlăduțiu C, Popescu LA, Lupașcu CA, Vesa ȘC, Țălu SD. Fractal and lacunarity analysis of human retinal vessel arborisation in normal and amblyopic eyes. *HVM Bioflux.* 2012;5:45–51.
45. Țălu Ș, Mihai Călugăru D, Lupașcu CA. Characterisation of human non-proliferative diabetic retinopathy using the fractal analysis. *Int J Ophthalmol.* 2015;8(4):770–6.
46. Traversi C, Bianciardi G, Tasciotti A, et al. Fractal analysis of fluoroangiographic patterns in anterior ischaemic optic neuropathy and optic neuritis: a pilot study. *Clin Exp Ophthalmol.* 2008;36:323–8.

47. Tremolada G, Del Turco C, Lattanzio R, Maestroni S, Maestroni A, Bandello F, Zerbini G. The role of angiogenesis in the development of proliferative diabetic retinopathy: impact of intravitreal anti-vegf treatment. *Exp Diabetes Res.* 2012;2012:728325.
48. Villani E, Gilamberti D, Viola F, et al. The cornea in Sjogren syndrome: an in vivo confocal study. *IOVS.* 2007;48(5):2017–22.
49. Wakamatsu TH, Sato EA, Matsumoto Y, et al. Conjunctival in vivo scanning laser microscopy in patients with Sjogren syndrome. *IOVS.* 2015;1(1):144–50.
50. Wang L, Cull G, Cioffi GA. Depth of penetration of scanning laser Doppler flowmetry in the primate optic nerve. *Arch Ophthalmol.* 2001;119:1810–4.
51. Warner JE, Lessell S, Rizzo III JF, Newman NJ. Does optic disc appearance distinguish ischemic optic neuropathy from optic neuritis. *Arch Ophthalmol.* 1997;115:1408–10.
52. Weibel ER. Fractal geometry: a design principle for living organisms. *Am J Physiol.* 1991;261:361–9.
53. Witten TA, Sander LM. Diffusion limited aggregation, a kinetic critical phenomenon. *Phys Rev Lett.* 1981;47:1400–3.
54. Zhang X, Chen Q, Cui L, et al. Tear dynamic and corneal confocal microscopy of subjects with mild self reported office dry eye. *Ophthalmology.* 2011;118(5):902–7.

Chapter 29

Fractals in Affective and Anxiety Disorders

Sergio Iglesias-Parro, Maria Felipa Soriano, and Antonio José Ibáñez-Molina

Abstract In this chapter, we review the research that has applied fractal measures to the study of the most common psychological disorders, that is, affective and anxiety disorders. Early studies focused on heart rate, but diverse measures have also been examined, from variations in subjective mood, or hand movements, to electroencephalogram or magnetoencephalogram data. In general, abnormal fractal dynamics in different physiological and behavioural outcomes have been observed in mental disorders. Despite the disparity of variables measured, fractal analysis has shown high sensitivity discriminating patients from healthy controls. However, and because of this heterogeneity in measures, the results are not straightforward, and more studies are needed in this promising line.

Keywords Fractal • Affective disorder • Anxiety • Complexity

29.1 Introduction

It has recently been stated that chaos is inherent to natural systems [34]. For example, a healthy heart shows some form of chaotic rate, whereas low variability in the heart rate is a pathological sign [16]. Chaos has the characteristic of appearing random and unpredictable at certain scales but retains a highly defined and overall predictable form. Chaos and fractals are two central concepts within nonlinear dynamics. Nonlinear approaches can provide valuable insights into complex human behaviours and, subsequently, into dysfunctions of human behaviours such as mental disorders.

S. Iglesias-Parro, PhD (✉) • A.J. Ibáñez-Molina, PhD
Department of Psychology, University of Jaén,
Paraje las Lagunillas s/n, Jaén 23071, Andalucía, Spain
e-mail: siglesia@ujaen.es; aibanez@ujaen.es

M.F. Soriano
Department of Mental Health Service, Hospital San Agustín de Linares,
Avda. S. Cristóbal, s/n, Linares (Jaén) 23700, Spain
e-mail: mfsoria@ugr.es

In this chapter, we will review the research that has applied fractal measures to the study of the most common mental disorders, that is, affective and anxiety disorders. Early studies focused on heart rate, but diverse variables have also been examined, from subjective mood, to hand movements. Recent studies have mostly implemented fractal measures to neurophysiological data, such as electroencephalogram (EEG) or magnetoencephalogram (MEG). In general, there is growing evidence about abnormal fractal dynamics in different physiological and behavioural measures in mental disorders [41].

29.2 Fractals and Affective Disorders

Affective disorders include mainly depressive (unipolar) disorders and bipolar disorders. Depression is one of the most prevalent mental diseases, and the first cause of major disability in the world, according to the World Health Organisation. People suffering depression experience low mood but also loss of interest and pleasure, poor concentration, feeling of worthlessness and, occasionally, self-harm ideation that can lead to suicide. Patients with bipolar disorders shift between depressive episodes and manic episodes, when they feel unusually euphoric, full of energy, and show an inflated self-esteem.

Some authors have proposed that patients with affective disorders suffer an alteration of the fractal organisation of their biological rhythms [3]. Among these biological rhythms, heart rate, gait temporal patterns, or even mood temporal fluctuations, have been studied. For example, Kojima et al. [24] have shown that patients with depression have reduced heart rate variability and low fractal dynamics of heart rate. Decreased heart rate variability may be one of the causes of increased cardiovascular mortality in depressed patients. Comparable results have been obtained for patients with bipolar disorder [29]. These authors found that the heart rate's regularity (reflected in a decrease in entropy) correlated with the severity of depressive and anxiety symptoms.

Fractal analyses have also been applied to movement patterns in depression. Aybek et al. [3] evaluated the stride interval in human gait in ten depressed patients and ten healthy controls. The temporal organisation of the stride interval is thought to be neither random nor regular but to have a complex fractal-like structure characterised by self-similarity over multiple time scales. The authors compared stride patterns in patients with major depression and healthy participants through a system of sensors attached to each wrist. They found that fluctuations of activity in both hands displayed a fractal pattern in healthy controls. Importantly, the stride pattern of depressed participants showed higher fractal values than controls. These results point to an alteration of the fractal organisation of motor activity in depression. Moreover, the nonlinear measures of movement patterns were similar in both groups; therefore, fractal analysis discriminates better between depressive and control groups. As we mentioned previously, the fractal organisation of biological rhythms is thought to correspond to an ideal homeostatic regulation and more prone

to respond to sudden changes than a regular organisation. Altered fractal pattern of activity in depressed patients might render movements less able to adapt to change; and this could lead to an increased risk of fall [3].

Another interesting line of research has applied nonlinear analyses to the study of variations of mood. In a pioneering work [17], Gottschalk et al. employed daily mood records from patients with bipolar disorder and healthy participants over a time course of 1–2.5 years in order to examine temporal fluctuations of mood in bipolar disorders. They evaluated the obtained time series to identify whether the temporal pattern of mood originated from a periodic, a random, or a deterministic source. Results indicated that the correlation dimension, a nonlinear measure, could account for self-rated mood in patients. Mood in patients was significantly more organised than mood in normal participants, and it could be characterised as a low-dimensional chaotic process rather than as a random process. Following this line, Woyshtville et al. [40] analysed the time course of self-rated mood from 36 patients with affective instability and 27 controls. They asked participants to rate their daily mood in a visual analogue scale for 90 days. Time series were analysed with the mean squared successive difference (MSSD), power spectral density (PSD), and fractal dimension (FD). The authors found that patients demonstrated substantially more variability than controls on the MSSD, but less complexity as measured by the FD. In sum, despite the chaotic and irregular mood variability of patients, affective variations were less complex, in patients than in controls.

These results were replicated in some subsequent studies [19]; however, they have been recently questioned [31]. Specifically Moore et al. [3] examined mood time series from eight patients with bipolar disorder, over a time period of 5 years. They concluded that nonlinear methods have no advantage over linear methods in accounting for variations of mood in bipolar disorders. Clearly more studies, ideally with larger samples, are necessary to elucidate whether mood variations in bipolar patients are better described by linear or nonlinear analyses.

Previously described studies are based on the observation that some clinical features of affective disorders repeat over a range of time scales. Nonlinear approaches to sequential observational data (in this case, self-rated mood) can provide new insights about the underlying processes that generate the observable patterns.

Finally, most studies involving fractal analyses in affective disorders have focused on electroencephalographic signals (EEG). As brain behaves as a complex nonlinear system, it has been proposed that nonlinear methods for analyses of the EEG signal provide more reliable information about brain functioning, compared to linear methods. In this line, Klonowsky et al. [23] analysed the FD of EEGs from patients with affective disorders, with the Higuchi's algorithm (HFD). They calculated FD-ratio, based on differences of FD between eyes-open EEGs and eyes-closed EEGs; and they found that FD-ratio was highly correlated with depressive symptoms. The following study [6] examined the FD of the EEG in bipolar patients with a manic episode and found that EEG FD was significantly increased in these patients relative to healthy controls. As we mentioned previously, Higuchi's FD is a measure of complexity of a time series. As applied to EEGs, HFD seems to indicate

the level of complexity on which brain regions function or interact, on a scale ranging from fully deterministic to fully random.

In another study, Ahmadlou et al. [2] evaluated the complexity of EEGs from patients with major depressive disorders, with Katz's FD (KFD) and HFD. Results showed higher HFD in frontal lobes of the brain of patients compared to controls, in beta and gamma sub-bands. Additionally, the authors found an accuracy of 91.3% in the classification of patients and controls based on HFD of frontal beta sub-band, whereas KFD revealed no differences between frontal EEGs from depressive and control participants.

Since then, some efforts have been made to improve detection of people with depression on the basis of nonlinear features from the EEG. Thus, Hosseinfard et al. [21] analysed EEGs from 45 depressed patients and 45 normal participants, with different nonlinear measures (detrended fluctuation analysis, HFD, correlation dimension and Lyapunov exponents). They found that the highest classification accuracy (83.3%) was obtained with the correlation dimension. However, when all nonlinear features were combined, a classification accuracy of 90% was reached. Similarly, Bachamn et al. [4] compared spectral asymmetry index and HFD for discrimination between depressive and control participants. They analysed eyes closed EEGs data and found an increase of HFD in depressed participants in all EEG channels. HFD provided the true detection rate of 94% in the depressive group and 76% in the control group.

The finding of a greater complexity in the EEG from depressed patients has been replicated with other nonlinear non-fractal measures. For example, Li et al. [26] registered EEG from 62 schizophrenic patients, 48 depressed patients, and 26 controls, at rest and while performing mental arithmetic tasks. They analysed the complexity of the EEG signal with the Lempel-Ziv complexity (LZC) algorithm. LZC is a nonparametric metric that assesses the number of distinct substrings and their rate of recurrence along the time series, assigning higher values to more complex data. Obtained results showed that both groups of patients had a higher LZC than the control group. Surprisingly, depressed patients showed a higher LZC than patients with schizophrenia, both at rest and during the mental arithmetic task. A later study by Mendez et al. [27] provided further evidence. They applied LZC analysis to magnetoencephalography (MEG) data from 20 patients with a major depressive disorder and 19 healthy controls. They detected that LZC was higher in patients than in controls. More interestingly, complexity values in patients decreased after 6 months of pharmacological treatment; and this reduction in complexity with treatment correlated with the degree of clinical symptom remission.

In sum, evidence points to a greater complexity in the EEG of patients with depression. This is congruent with findings with other mental disorders, such as schizophrenia [10]. Although the interpretation of these findings should be cautious, one possible meaning of brain complexity is that it reflects the system's ability to adapt quickly and efficiently in a changing environment. According to this idea, affective disorders might be characterised by a poorer capacity (at different biological levels) to respond to environmental changes.

29.3 Fractals and Anxiety Disorders

Anxiety is a feeling that usually arises when a person feels threatened. It is characterised by feelings of worry, ruminations, and unpleasant physical sensations. Anxiety can be, at certain levels, useful in some situations. However, when this emotion is extremely intense, whereby it becomes the usual response in most inoffensive situations or it affects most domains in a person's daily life, it is then considered a disorder. The distinction between normal anxiety and a clinical disorder is not always clear. There are a wide variety of anxiety disorders, including generalised anxiety disorder, panic disorder, obsessive-compulsive disorder (OCD), post-traumatic stress disorder (PTSD), or phobic disorders, among others.

Although anxiety disorders are the most common mental disorders, literature on the fractal properties of its structural or functional states is scarce. Still, some evidence has found that estimators as the fractal dimension can contribute to the understanding of neural basis of anxiety disorders.

One clear relationship between anxiety and fractality in the signals from the brain was provided by [15]. They explored the HFD in neurotic EEG participants while they were undertaking a simple auditory oddball task. In this task, participants are presented with sequences of two types of tones that they need to detect or just listen to passively. The authors registered the EEG of a large group of participants that were divided into two groups, neurotic and stable participants, according to the Eysenck Personality Questionnaire (EPQ). When the authors compared the HFD of the neurotic group with the HFD of the stable group, they did not find significant differences in the HFD of the basal EEG (before stimulation); however, and more interestingly, the HFD was higher for the neurotic group 0–100 ms after stimuli presentation. This result indicated that the structural properties of the EEGs in the case of neurotics were more complex only when they were processing the tones. In order to understand why complexity is higher for neurotics only during stimuli processing, we need to consider that, for all participants, the HFD after stimuli presentation is widely reduced in the time range of 0–400 ms. From a physiological point of view, it corresponds to a synchronic cortical response directed to process and become aware of the externally presented stimulus. Then, it can be inferred that neurotics, when compared with stable participants, tend to reduce the processing of external and salient events. Hence, it is reasonable to think that the characteristics of neuroticism as negative thoughts, anxiety, and anger tend to maintain a high level of EEG complexity due to a reduced external focus of attention.

Although Georgiev et al. [15] did not find fractal changes in the resting condition for participants with neurotic traits of personality, there is some evidence indicating that, indeed, the resting brain of patients with anxious symptoms exhibits distinct fractal properties. One example is provided by Chae et al. [7] in a study designed to measure the correlation dimension (D_2) of patients with PTSD. In their study, Chae et al. recorded the EEGs with 82 s length from 16 electrodes during a resting state period and found that D_2 was significantly lower in the PTSD group than in the healthy group. Because this difference was consistent all across the scalp, it can be

concluded that PTSD deviates the by-default processing of the waking brain toward a less complex functional regime. This decrement in complexity might reflect that cortical activation becomes simpler with recurrent evocation of traumatic stimuli. In other words, it might be possible that PTSD patients show a reduced by-default functional repertoire of the resting brain that mostly represents rehearsals of the same traumatic events.

In a recent study [14], Gentili et al. also tested the hypothesis that anxiety modulates the resting brain. In an fMRI study, they measured the Hurst exponent to healthy participants. Although there was no anxious stimulation during the experimental session, participants showed a positive correlation between the Hurst exponent and the low fluctuation of the BOLD (blood oxygen level dependent) activity in posterior cingulate/precuneus, inferior parietal sulci, and the parahippocampus areas of the brain. As these regions are mostly related with the by-default function of the brain, it can be suggested that social anxiety traits shapes the global brain activity and might trigger nonadaptive reactions in social situations.

From the already explained results, it might be concluded that anxiety has an influence in the complexity of the brain signals, as the EEGs, both during reactions to stimuli and the resting state. However, it is well known that conventional fractal analyses are not sensitive to time fluctuations in the complexity of the signal [43]. In many cases, different scaling exponents are required for different parts of the time series (e.g. [22]); that is, non-stationary signals, as, for example, EEGs, may have a non-single scaling in different segments of the series. Hence, non-stationary EEG series can be characterised as multifractals with a variety of scaling behaviours. As a consequence, it would be possible that the multifractality of brain signals from anxiety patients or participants with anxiety traits differ from those of the reference groups. In this line, Dik et al. [9] investigated the multifractality of the EEGs from patients with anxious phobic disorders. They explored changes in the EEG responses during psychogenic pain before and after a psychorelaxation treatment. Multifractal characteristics can be detected in time series by estimating local changes of the scaling properties in short segments of the signal. Hence, it is sensitive to structural changes in time that corresponds to different fractal properties. In this study, the degree of multifractality was estimated to EEG recordings during perception of psychogenic pain in the case of patients, and tactile evoked pain in the case of healthy participants. Multifractality of the EEG during pain perception was different in both groups, suggesting that the cortical generation of pain in patients was different in space and time than the cortical pattern that gives rise to pain in healthy participants. Interestingly, when a psychorelaxation technique was applied to the clinical group, the width of the scaling behaviour was reduced to approach the values of the healthy group. In other words, after psychorelaxation, the range of exponents that characterise the multifractal structure of the EEG in the clinical group was similar to the one in the healthy group. This result suggests that anxiety enhances pain perception by increasing the rate of change in the cortical patterns of activation. This dynamical process is reflected in the EEGs as a multifractal with a wide range of scaling exponents.

Finally, it is noteworthy that anxiety symptoms are related not only with the characteristics of brain function; structural properties of the brain in patients with anxiety symptoms might present a reduced FD. In this line, Ha et al. [18] calculated the three-dimensional FD of cerebral cortical surface measured with MRI to patients with OCD and schizophrenia. Their results indicated that schizophrenic patients exhibited lower FD than OCD patients and controls. Interestingly, OCD patients showed lower FD than controls indicating that their cortical surface was less folded than the healthy group. This is a very relevant finding, and we believe that its clinical implications should be explored in further experiments.

29.4 Fractals in Affective and Anxiety Disorders Treatments

Treatment of mental disorders has taken many forms, from the use of electroconvulsive therapy to hypnosis or meditation through the use of psychotropic drugs. In this section, we will briefly review the studies that have addressed the study of mental disorders treatment from a nonlinear perspective.

The analysis of FD concerning the treatment of mental disorders dates back the beginning of the nineties. In 1996, [35] already pointed out the importance of analysing the EEG characteristics associated with the electroconvulsive therapy (ECT) in order to predict its efficacy in the treatment of severe depression. Specifically, they found a significant positive relationship between degree of postictal suppression and the remission depressive symptoms. Following that work, Gangadhar et al. [13], using the Katz algorithm, computed the FD for early-, mid-, and post-seizure phases of ictal EEG after 4 weeks of either once per week or three times per week of ECT treatment. Depression severity was measured by the 21 items of Hamilton Rating Scale for Depression. They found that, apart from the number of ECT sessions per week (one or three), the only significant predictor of clinical remission was the post-seizure FD of EEG. Specifically, Gangadhar et al. found lower values of FD during the period immediately following electrically induced seizure only in the participants who showed later a remission. According to the authors, reduced post-seizure FD could reflect postictal suppression, which in turn could indicate a greater brain response.

In the study of nonlinear systems, transitions between chaotic dynamics to periodic ones (or vice versa) are called bifurcations. These bifurcations have been proposed as useful tools in modelling the transitions that occur from healthy to pathological states [26]. However, because the empirical study of transitions from a healthy brain to a pathological one is not always possible, some authors have considered the reverse transition, namely, the clinical improvement due to treatment [37], as a valid strategy to understand mental illness. In this vein, Thomasson et al. [37] recorded the electrical brain activity on 31 scalp regions in 3 clinically depressed participants and 1 healthy control. At each of the 31 EEG channels, local measures of entropy were estimated as well as a measure of global entropy for the global EEG averaged over the 31 channels. The participants' EEG was recorded every 2 days for

2 or 3 weeks. Additionally, in order to study fluctuations of mood, rating scales of depression were collected during treatment. Measures of global entropy decreased along treatment and showed a significant correlation with the score on global rating scales of depression. Regarding the healthy control participant, entropy increased along recording sessions and did not covary with self-assessments of depression.

Treatment of mental disorders often involves the use of psychotropic drugs. These substances seem to have a specific effect in brain functioning, their own 'EEG portraits', according to Fingelkurts et al. [12]. Thus, classical spectral analysis shows that barbiturates induce bursts in EEG signal [32], whereas benzodiazepines seem to produce an increase in slow (delta and theta) and fast (beta) rhythms (although see [12]) while reducing power in the alpha range [11]. FD has also been studied in relation with psychotropic drugs. In this regard, Chouvarda et al. [8] analysed the FD dynamics after benzodiazepines (lorazepam) intake. Lorazepam is a benzodiazepine drug with short to medium duration of action. It has anxiolytic, sedative/hypnotic, anticonvulsant and muscle relaxant effects by slowing down the central nervous system. Fourteen participants took 2.5 mg of verum/placebo, and their EEG was recorded at resting state, for 3 min each hour during 24 h. FD was significantly higher in almost all channels in the verum than in the placebo condition, although these differences diminished with time. Participants that received placebo did not exhibit any significant variation in FD values with time. A follow-up study with the same dataset [28] compared the effect of lorazepam across frequency bands on Higuchi FD [20] 1 h before and 2 h after drug intake. Results showed that FD significantly increased 2 h after drug intake compared to baseline. Moreover, alpha band after drug intake was significantly lower than at baseline, but beta band was significantly higher after drug intake than at baseline. The authors proposed that, since beta band contains high-frequency components, its increase contributes to the complexity of the EEG signal, which in turns leads to a subsequent increase of FD.

In a study conducted by Mendez et al. [29], the complex brain pattern associated to antidepressant intake was analysed. Twenty participants, moderately to severely depressed, completed a minimum 3-week medication washout before the first baseline pretreatment MEG scan. After the first scan, participants began antidepressant intake (mirtazapine, 30 mg once per day). After 6 months of treatment, participants received a second resting-state 5 min MEG scan. Depression improvement was evaluated with the Hamilton Rating Scale for Depression. After treatment, a significant reduction in the depression questionnaire scores was observed. When baseline MEG was compared with posttreatment MEG scan, a significant reduction in Lempel-Ziv complexity in anterior regions was observed, but only for young patients (<47 years). These results indicating a reduction in brain complexity following treatment of depression are in accordance with the aforementioned results obtained by [37].

Hypnosis and meditation procedures are often successfully used to facilitate treatments in stress-dependent disorders, such as anxiety, depression or dependencies, or pain relief in patients with hypertensive disorders, burn injury, arthritis, cancer or chronic back problems [30, 39]. Hypnosis is an altered state of consciousness that is considered to involve high attentional resources. Various

attempts have been made in order to characterise the therapeutic effect of hypnosis. In this vein Solhjoo et al. [33] analysed the EEG recordings of five highly hypnotisable participants, according to the Stanford Hypnotic Clinical Scale. Participants were asked to engage in two experimental tasks (relaxation and imagination) during normal and hypnotic states. In each condition, 1 m length EEG segments were obtained. Each segment was then divided in 12 segments of 5 s length each. Frequency (power spectral density components) and chaotic (Petrosian and Higuchi FD) features were extracted from segments and submitted to a Hidden Markov Model classifier. All measures discriminated between mental states, but the nonlinear ones (specifically, the Higuchi FD) showed a better behaviour of classifying mental states than frequency-based features.

Yargholi and Nasrabadi [42] conducted a study in order to find out the impact of the depth of hypnosis on EEG signals recorded, while the individuals were performing mental tasks. EEG signals from 33 participants were recorded in an eyes-closed relaxation state and under hypnosis, and Higuchi FD was obtained for each recording channel. During hypnosis, participants had to perform different tasks, and this performance was used as an index of the depth of hypnosis. According with their performance, participants were classified in three groups: low, medium and highly hypnotisable. The results of the study showed that chaotic characteristics of some channels could serve to discriminate among participants depending on their hypnotisability.

Meditation has been proposed as a technique to increase focused internalised attention. Empirical evidence has supported the efficacy of meditation in the treatment of mental disorders [5]. Research has tried to characterise the brain signature of meditation from a nonlinear point of view. Thus, Aftanas and Golocheikine [1] studied how the dynamically changing inner experience during meditation could be indexed by the nonlinear dimensional complexity of EEG, compared with a more traditional frequency-based analysis. EEG was recorded at rest with eyes closed and during meditation in 20 experienced meditators. The EEG was segmented in 8.192 s. length epochs, and frequency band power analysis and nonlinear analysis (point correlation dimension) were conducted. Obtained results revealed a significant decrease of point correlation dimension over anterior-frontal and centro-frontal regions, suggesting that controlled allocation of attention resources was required for the maintenance of the meditative state. On the other hand, linear measures analysis revealed theta power increase over anterior electrodes and alpha power decrease in meditation state when compared with baseline.

Another study compared complexity measures of the EEG signal in experienced meditators before and during meditation [38]. Each 1 of the 22 participants underwent 5 meditation phases that were monitored using an EEG scanner. Among the five experimental phases, participants underwent a 10 m baseline without meditation, a 30 m of calming meditation and a 30 m phase of insight meditation. FD as well as permutation entropy were obtained from EEG. For both types of meditation, global permutation entropy decreased, although not significantly. In contrast, the FD for both types of meditation increased. This increase was significant only in calming meditation.

29.5 Conclusions

Fractal analysis can be a valuable tool in the evaluation of mental diseases or treatment outcomes. As we have reviewed, mental complexity reflects a system's ability to adapt to a constantly changing environment. Such adaptation capacity is often impaired in patients with mental illnesses.

The studies that we have reviewed suggest that fractal dimension is increased in brain signals of patients with an affective disorder. Moreover, successful antidepressant treatments (such as ECT or antidepressant drugs) usually diminish fractal dimension restoring it to healthy levels. Studies have also shown an altered fractal dynamic in the heart rate, subjective mood variability, or even the temporal pattern of movements, in affective patients. Fewer studies have focused on patients with anxiety disorders, and evidence is not so clear. It seems that the fractal dimension of the EEG is decreased in patients with anxiety disorders and that anxiolytic drugs increase EEG complexity.

Therefore, complexity (and fractal dimension) is up or down in affective and anxiety disorders. This divergence of results can be observed in other mental disorders; for example, both increased and decreased complexities in the EEGs from schizophrenic patients have been reported. The inconsistency can result from different sources. First, the biological signal evaluated (ECG, EEG, daily self-rated mood) and complexity measures vary considerably across studies. Second, mental disorders are heterogeneous in their clinical presentation and in the pathological mechanisms responsible of their apparition. Finally, as Takahashi highlighted [36], age-related complexity changes must be considered when investigating pathological brain, because typical brain complexity is not constant across the vital cycle. Evidence points clearly that, in different mental disorders, the normal organisation that characterises a healthy functioning deteriorates, and it is replaced by abnormal dynamics.

On the other hand, the interpretation of the scarce results we have summed is not straightforward. We believe that an interesting interpretation about complexity and mental illness is the one put forward by Yan and Tsai [41]. According to these authors (see Fig. 29.1), healthy mental function is complex in an optimal degree, and it can deteriorate into two distinct pathological paths: order and randomness. For example, patients with mania exhibit behaviours that seem to have an extreme randomness (word salad, loosening of associations, impulsive behaviour), while patients with an obsessive-compulsive disorder perform actions that seem extremely rigid and repetitive. These macroscopic observations of psychopathology should be linked to microscopic phenomenon, such as heart or brain activity. The brain's ability to adapt to the environment depends on the underlying neuronal functioning, which can be measured by complexity analysis at the microscopic level. The authors propose that mental illness is characterised by a loss of brain complexity. This brain dysfunction gives rise to altered dynamics in cognition, emotion, and behaviour, where we can observe either extremely ordered or extremely random patterns.

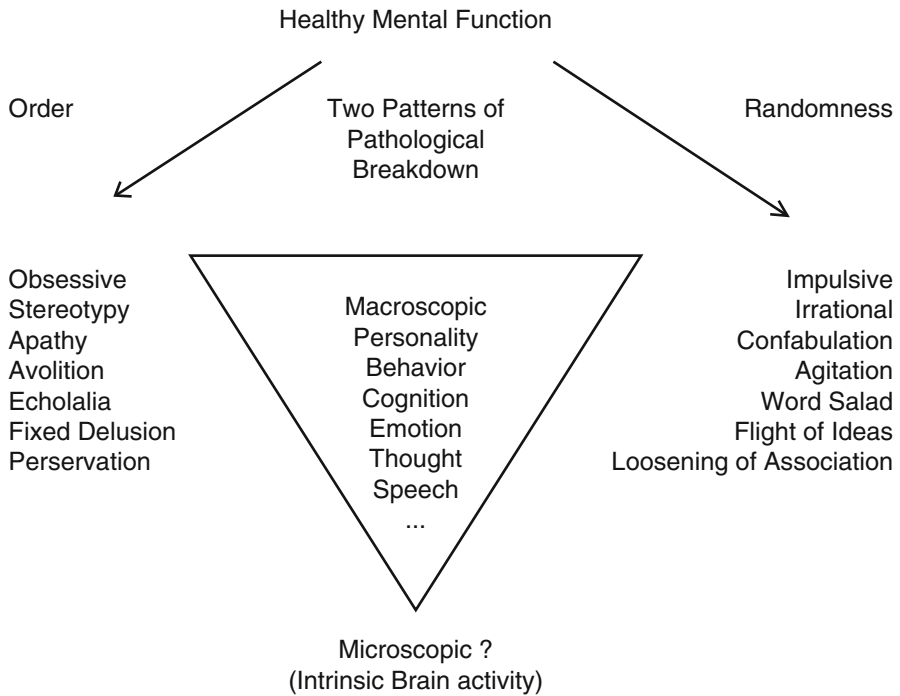


Fig. 29.1 Schematic illustration of the deterioration of healthy mental function into either an ordered or random pattern (Adapted from Yang and Tsai [41] with permission)

Future research should evaluate whether it is possible to relate pathological behaviours with microscopic changes in the neuronal dynamics of the brain. Furthermore, more studies are needed about the relationship between complexity measures and symptomatology. Implications of this line of research are of great relevance in the clinical practice. Nowadays, the diagnosis of a mental illness is based on the subjective appreciation of the clinician; despite numerous efforts, objective markers of mental diagnoses have not been found so far. The evaluation of the treatment effects also relies on the subjectivity of the clinician. Fractal measures could be a useful tool in the diagnosis, outcome prediction and treatment evaluation in affective and anxiety disorders.

References

1. Aftanas LI, Golocheikine SA. Non-linear dynamic complexity of the human EEG during meditation. *Neurosci Lett.* 2002;330:143–6.
2. Ahmadlou M, Adeli H, Adeli A. Fractality analysis of frontal brain in major depressive disorder. *Int J Psychophysiol.* 2012;85:206–11.

3. Aybek S, Ionescu A, Berney A, Chocron O, Aminian K, Vingerhoets FJG. Fractal temporal organisation of motricity is altered in major depression. *Psychiatry Res.* 2012;200:288–93.
4. Bachmann M, Lass J, Suhhova A, Hinrikus H. Spectral asymmetry and Higuchi's fractal dimension measures of depression electroencephalogram. *Comput Math Methods Med.* 2013(2013):e251638; pp-8.
5. Baer RA. Front matter. In: Baer RA, editor. *Mindfulness-based treat. Approaches.* Burlington: Academic; 2006.
6. Bahrami B, Seyedsadjadi R, Babadi B, Noroozian M. Brain complexity increases in mania. *Neuroreport.* 2005;16:187–91.
7. Chae J-H, Jeong J, Peterson BS, Kim D-J, Bahk W-M, Jun T-Y, Kim S-Y, Kim K-S. Dimensional complexity of the EEG in patients with posttraumatic stress disorder. *Psychiatry Res.* 2004;131:79–89.
8. Chouvarda I, Michail E, Kokonozi A, Staner L, Domis N, Maglaveras N. Investigation of sleepiness induced by insomnia medication treatment and sleep deprivation. In: Schmorrow DD, Estabrooke IV, Grootjen M, editors. *Foundations of augmented cognition. Neuroergonomics and operational neuroscience.* Berlin: Springer; 2009. p. 120–7.
9. Dik OE, Sviatogor IA, Ishinova VA, Nozdrachev AD. Fractal characteristics of the functional state of the brain in patients with anxious phobic disorders. *Fiziol Cheloveka.* 2012;38:30–6.
10. Fernández A, Gómez C, Hornero R, López-Ibor JJ. Complexity and schizophrenia. *Prog Neuropsychopharmacol Biol Psychiatry.* 2013;45:267–76.
11. Feshchenko VA, Veselis RA, Reinsel RA, Wronski M. Dependence of midazolam-induced beta rhythm on individual characteristics of alpha rhythm. *Electroencephalogr Clin Neurophysiol.* 1995;95:P26.
12. Fingelkurts AA, Fingelkurts AA, Kivisaari R, Pekkonen E, Ilmoniemi RJ, Kähkönen S. The interplay of lorazepam-induced brain oscillations: microstructural electromagnetic study. *Clin Neurophysiol Off J Int Fed Clin Neurophysiol.* 2004;115:674–90.
13. Gangadhar BN, Subbakrishna DK, Janakiramaiah N, Motreja S, Narayana Dutt D, Paramehwara G. Post-seizure EEG fractal dimension of first ECT predicts antidepressant response at two weeks. *J Affect Disord.* 1999;52:235–8.
14. Gentili C, Vanello N, Cristea I, David D, Ricciardi E, Pietrini P. Proneness to social anxiety modulates neural complexity in the absence of exposure: a resting state fMRI study using Hurst exponent. *Psychiatry Res Neuroimaging.* 2015;232:135–44.
15. Georgiev S, Minchev Z, Christova C, Philipova D. EEG fractal dimension measurement before and after human auditory stimulation. *Bioautomation.* 2009;12:70–81.
16. Goldberger AL, Rigney DR, West BJ. Chaos and fractals in human physiology. *Sci Am.* 1990;262:42–9.
17. Gottschalk A, Bauer MS, Whybrow PC. Evidence of chaotic mood variation in bipolar disorder. *Arch Gen Psychiatry.* 1995;52:947–59.
18. Ha TH, Yoon U, Lee KJ, Shin YW, Lee J-M, Kim IY, Ha KS, Kim SI, Kwon JS. Fractal dimension of cerebral cortical surface in schizophrenia and obsessive-compulsive disorder. *Neurosci Lett.* 2005;384:172–6.
19. Heiby EM. Assessment of behavioral chaos with a focus on transitions in depression. *Psychol Assess.* 1995;7:10.
20. Higuchi T. Approach to an irregular time series on the basis of the fractal theory. *Phys D Nonlinear Phenom.* 1998;31:277–83.
21. Hosseinifard B, Moradi MH, Rostami R. Classifying depression patients and normal subjects using machine learning techniques and nonlinear features from EEG signal. *Comput Methods Prog Biomed.* 2013;109:339–45.
22. Kantelhardt JW, Zschiegner SA, Koscielny-Bunde E, Bunde A, Havlin S, Stanley HE. Multifractal detrended fluctuation analysis of nonstationary time series. *Phys A Stat Mech Appl.* 2002;316:87–114.
23. Klonowski W, Ciszewski J, Jernajczyk W, Niedzielska K. Application of chaos theory and fractal analysis for EEG-signal processing in patients with seasonal affective disorder. In:

- Proc. 1999 Int. Symp. Nonlinear Theory Its Appl. NOLTA99 Hawaii USA. 1999. pp. 339–42. <http://www.nolta.ieice.org/index.html>
24. Kojima M, Hayano J, Fukuta H, Sakata S, Mukai S, Ohte N, Seno H, Toriyama T, Kawahara H, Furukawa TA, Tokudome S. Loss of fractal heart rate dynamics in depressive hemodialysis patients. *Psychosom Med.* 2008;70:177–85.
 25. Li Y, Tong S, Liu D, Gai Y, Wang X, Wang J, Qiu Y, Zhu Y. Abnormal EEG complexity in patients with schizophrenia and depression. *Clin Neurophysiol.* 2008;119:1232–41.
 26. Mackey MC, Milton JG. Dynamical diseases. *Ann N Y Acad Sci.* 1987;504:16–32.
 27. Mendez MA, Zuluaga P, Hornero R, Gomez C, Escudero J, Rodriguez-Palancas A, Ortiz T, Fernandez A. Complexity analysis of spontaneous brain activity: effects of depression and antidepressant treatment. *J Psychopharmacol Oxf Eng.* 2012;26:636–43.
 28. Michail E, Chouvarda I, Maglaveras N. Benzodiazepine administration effect on EEG Fractal Dimension: results and causalities. In: 2010 Annual International Conference of the IEEE Engineering in Medicine and Biology Society EMBC. Buenos Aires, Argentina, 2010. pp. 2350–53.
 29. Migliorini M, Mendez MO, Bianchi AM. Study of heart rate variability in bipolar disorder: linear and non-linear parameters during sleep. *Front Neuroengineering.* 2011;10(4):22.
 30. Montgomery GH, DuHamel KN, Redd WH. A meta-analysis of hypnotically induced analgesia: how effective is hypnosis? *Int J Clin Exp Hypn.* 2000;48:138–53.
 31. Moore PJ, Little MA, McSharry PE, Goodwin GM, Geddes JR. Mood dynamics in bipolar disorder. *Int J Bipolar Disord.* 2014;2:1–9.
 32. Schallek W, Horst WD, Schlosser W. Mechanisms of action of benzodiazepines. *Adv Pharmacol Chemother.* 1979;16:45–87.
 33. Solhjo S, Motie Nasrabadi A, Hashemi Golpayegani MR. EEG-based mental task classification in hypnotized and normal subjects. *Conf Proc Annu Int Conf IEEE Eng Med Biol Annu Conf.* 2005;2:2041–3.
 34. Sprott JC. Is chaos good for learning? *Nonlinear Dyn Psychol Life Sci.* 2013;17:223–32.
 35. Suppes T, Webb A, Carmody T, Gordon E, Gutierrez-Esteinou R, Hudson JI, Pope HG. Is postictal electrical silence a predictor of response to electroconvulsive therapy? *J Affect Disord.* 1996;41:55–8.
 36. Takahashi T, Cho RY, Murata T, Mizuno T, Kikuchi M, Mizukami K, Kosaka H, Takahashi K, Wada Y. Age-related variation in EEG complexity to photic stimulation: a multiscale entropy analysis. *Clin Neurophysiol.* 2009;120:476–83.
 37. Thomasson N, Pezard L, Allilaire J-F, Renault B, Martinerie J. Nonlinear EEG changes associated with clinical improvement in depressed patients. *Nonlinear Dyn Psychol Life Sci.* 2000;4:203–18.
 38. Vyšata O, Schätz M, Kopal J, Burian J, Procházka A, Jiřík K, Hort J, Vališ M. Non-linear EEG measures in meditation. *J Biomed Sci Eng.* 2014;07:731–8.
 39. Walsh R, Shapiro SL. The meeting of meditative disciplines and Western psychology: a mutually enriching dialogue. *Am Psychol.* 2006;61:227–39.
 40. Woyshville MJ, Lackamp JM, Eisengart JA, Gilliland JA. On the meaning and measurement of affective instability: clues from chaos theory. *Biol Psychiatry.* 1999;45:261–9.
 41. Yang AC, Tsai S-J. Is mental illness complex? From behavior to brain. *Prog Neuropsychopharmacol Biol Psychiatry.* 2013;45:253–7.
 42. Yargholi E, Nasrabadi AM. Chaotic features analysis of EEG signals during hallucination tasks of waterloo-standford standard. *J Biomed Sci Eng.* 2010;03:1175–81.
 43. Zorick T, Mandelkern MA. Multifractal detrended fluctuation analysis of human EEG: preliminary investigation and comparison with the wavelet transform modulus maxima technique. *PLoS One.* 2013;8:e68360.

Chapter 30

Fractal Fluency: An Intimate Relationship Between the Brain and Processing of Fractal Stimuli

Richard P. Taylor and Branka Spehar

Abstract Humans are continually exposed to the rich visual complexity generated by the repetition of fractal patterns at different size scales. Fractals are prevalent in natural scenery and in patterns generated by artists and mathematicians. In this chapter, we will investigate the powerful significance of fractals for the human visual system. In particular, we propose that fractals with midrange complexity ($D=1.3-1.5$ measured on a scale between $D=1.1$ for low complexity and $D=1.9$ for high complexity) play a unique role in our visual experiences because the visual system has adapted to these prevalent natural patterns. This adaption is evident at multiple stages of the visual system, ranging from data acquisition by the eye to processing of this data in the higher visual areas of the brain. For example, eye-movement studies show that the eye traces out mid- D fractal trajectories that facilitate visual searches through fractal scenery. Furthermore, quantitative electroencephalography (qEEG) and preliminary fMRI investigations demonstrate that mid- D fractals induce distinctly different neurophysiological responses than less prevalent fractals. Based on these results, we will discuss a fluency model in which the visual system processes mid- D fractals with relative ease. This fluency optimizes the observer's capabilities (such as enhanced attention and pattern recognition) and generates an aesthetic experience accompanied by a reduction in the observer's physiological stress levels. In addition to exploring the fundamental science of our visual system, the results have important practical consequences. For example, mid- D fractals have the potential to address stress-related illnesses.

Keywords Fractals • Complexity • Perception • Stress reduction • qEEG

R.P. Taylor
Department of Physics, University of Oregon, Eugene, OR, USA
e-mail: rpt@uoregon.edu

B. Spehar (✉)
School of Psychology, UNSW Australia, Sydney, NSW, Australia
e-mail: b.spehar@unsw.edu.au

30.1 Introduction: The Complexity of Biophilic Fractals

Fractal patterns are prevalent throughout nature. Examples include lightning, clouds, trees, rivers, and mountains. Furthermore, they have permeated cultures spanning across many centuries and continents, ranging from Hellenic friezes (300 BC) to Jackson Pollock’s poured paintings (1950s) [20, 21]. From the 1860s onward, their visual properties have also been explored by mathematicians. Consequently, fractals constitute a central component of our daily experiences. In Fig. 30.1, we use a coastline to demonstrate their intrinsic visual properties. As shown in the left column, fractals can be divided into two categories – “exact” (top image) and “statistical” (bottom image). Whereas exact fractals are built by repeating a pattern at different magnifications, “statistical” fractals introduce randomness into their construction. This disrupts the precise repetition so that only the pattern’s statistical

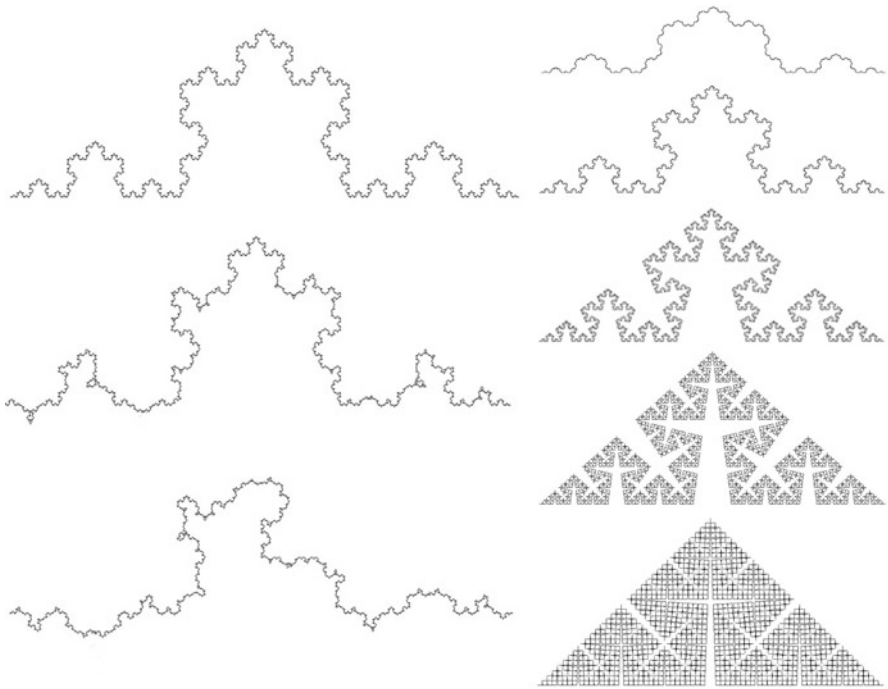


Fig. 30.1 *Left column:* A computer-generated coastline based on exact fractals (*top*) is morphed into a statistical fractal coastline (*bottom*) by introducing randomness. For the top fractal, all of the headlands point upward. For the bottom fractal, half point downward and the positions of the up and down headlands are randomized. Note the D value (1.24) is preserved for all three patterns (*top, middle, and bottom*). *Right column:* The effect of increasing D is shown for five exact coastlines. Each of the coastlines is built using the same coarse-scale pattern. Increasing the contributions of the fine-scale patterns causes the coastlines to occupy more of the two-dimensional plane, thus raising their D values: 1.1 (*top*), 1.3, 1.5, 1.7, and 1.9 (*bottom*)

qualities (e.g., density, roughness, complexity) repeat. Consequently, statistical fractals simply look similar at different size scales. Whereas exact fractals display the cleanliness of artificial shapes, statistical fractals capture the “organic” signature of natural objects.

Statistical fractals are highly topical in the field of “bio-inspiration,” in which scientists investigate the favorable functionality of natural systems and apply their findings to artificial systems. For example, the ability of fractal coastlines to efficiently disperse wave energy reduces erosion, inspiring fractal storm barriers. The growing role of fractals in art suggests that the repeating patterns might serve another bio-inspired function beyond the scientific realm – an aesthetic quality. Previous studies have shown that exposure to natural scenery can have dramatic, positive consequences for the observer [24–26]. In particular, Ulrich and colleagues showed that patients recover more rapidly from surgery in hospital rooms with windows overlooking nature. Although groundbreaking, these demonstrations of “bio-philic” (nature-loving) responses employed vague descriptions for nature’s visual properties. Our research builds on these studies by testing a highly specific hypothesis – that the statistical fractals inherent in natural objects are inducing these remarkable effects [22].

To quantify the rich visual intricacy of the statistical fractals, we adopt a traditional measure employed by mathematicians – the pattern’s fractal dimension D [4]. This parameter describes how the patterns occurring at different magnifications combine to build the resulting fractal shape. For a smooth line (containing no fractal structure), D has a value of 1, while for a completely filled area (again containing no fractal structure), its value is 2. However, the repeating patterns of the fractal line cause the line to begin to occupy space. As a consequence, its D value lies between 1 and 2. By increasing the amount of fine structure in the fractal mix of repeating patterns, the line spreads even further across the two-dimensional plane (see the right column of Fig. 30.1) and its D value therefore moves closer to 2. Figure 30.2 demonstrates how a statistical fractal’s D value has a profound effect on the visual appearance of fractal patterns found in nature, art, and mathematics. Clearly, for fractals described by low D values, the small content of fine structure builds a very smooth sparse shape. However, for fractals with D values closer to 2, the larger amount of fine structure builds a shape full of intricate, detailed structure. More specifically, because the D value charts the ratio of coarse to fine structure, it is expected that D will serve as a convenient measure of the visual complexity generated by the repeating patterns. Behavioral research by Cutting and Garvin confirms that the complexity perceived by observers does indeed increase with D [3].

Our initial investigations used three distinct categories of stimuli summarized in Fig. 30.2: natural fractals (using photographs of clouds, trees, mountains, etc.), artistic fractals (paintings generated by Jackson Pollock using his famous pouring technique), and mathematics (computer-generated images) [14]. Our current studies focus exclusively on computer-generated fractals due to their advantageous properties [15]. Firstly, the D values of the images are known precisely because they are input parameters for the computer-generation process. Secondly, the greater control

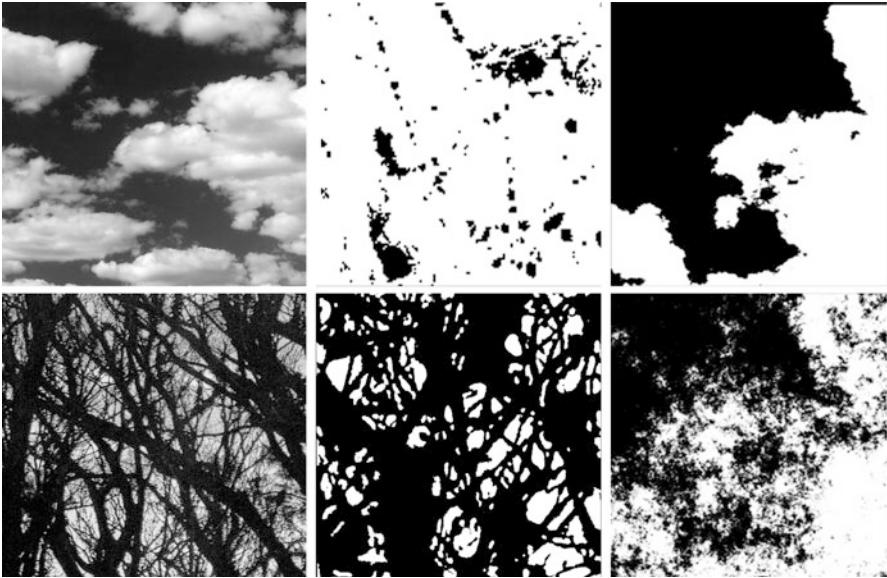


Fig. 30.2 Fractal complexity in nature, art, and mathematics. The *left column* shows clouds with $D=1.3$ (*top*) and a forest with $D=1.9$ (*bottom*). The *middle column* shows Jackson Pollock's *Untitled 1945* with $D=1.1$ (*top*) and *Untitled 1950* with $D=1.89$ (*bottom*). The *right column* shows computer-generated fractals with $D=1.2$ (*top*) and $D=1.8$ (*bottom*)

offered by computers allows the separation of different visual characteristics. For example, whereas density and D are intrinsically linked in Pollock's paintings (as seen in Fig. 30.2), he raised the painting's D value by adding more paint which in turn inevitably raised the density [20]; these two parameters can be adjusted independently using computer-generated images. Thirdly, the images are purely abstract. Consequently, responses are not contaminated by associations with recognizable objects such as trees and clouds.

Figure 30.3 shows examples of our current stimuli, which are generated by Fourier spectrum or midpoint displacement methods [4]. For the far left image, the computer has generated a geographical terrain (in this case viewed from above) and this serves as the source to generate other images. To obtain the second image, a horizontal slice is taken through the terrain at a selected height. Then all of the terrain below this height is colored black and all of the terrain above is colored white. Referred to as the coastline pattern (black being the water), this image is used to generate the third image by highlighting the coastline edges in white. The fourth image is created by taking a vertical slice through the terrain to create a mountain profile. Finally, the grayscale image is generated by assigning grayscale values (on a scale from 0 to 255) to the heights of the terrain. Taken together, these five families of fractals are powerful stimuli for examining people's responses because, although superficially quite different in appearance, they all possess identical scaling properties.

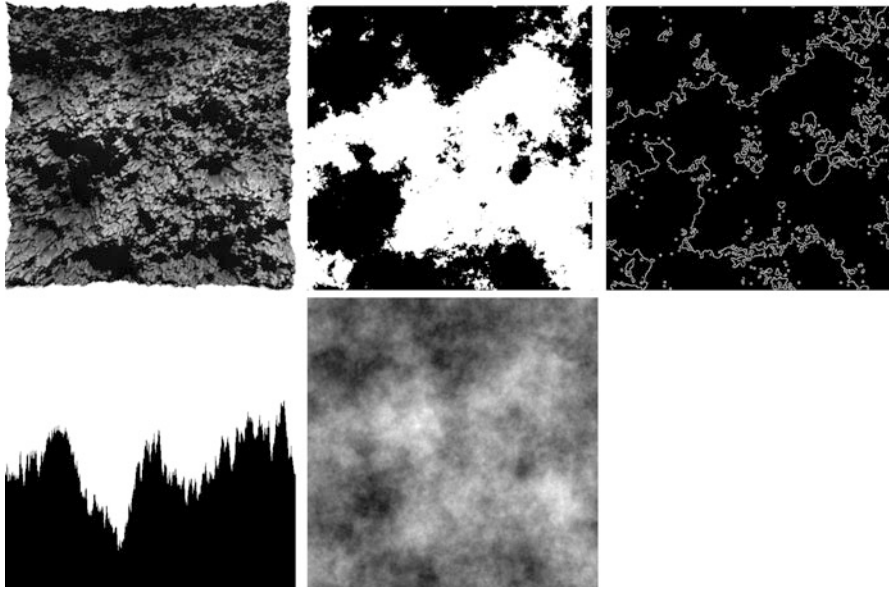


Fig. 30.3 Computer-generated fractal stimuli. From left to right: terrains, coastlines, edges, mountains, and grayscale patterns

30.2 Fractal Fluency

The physical processes that form nature's fractals determine their D values. For example, wave erosion generates the low complexity ($D=1.1$) of the Australian coastline while ice erosion results in the high complexity ($D=1.5$) of the Norwegian fiords. Significantly, although all D values between $1.1 < D < 1.9$ appear in natural scenes, the most prevalent fractals lie in the narrower range of $1.3-1.5$. For example, many examples of clouds, trees, and mountains lie in this range. We therefore proposed a fluency model in which the human visual system has adapted to efficiently process the mid-complexity patterns of these prevalent $D=1.3-1.5$ fractals [22]. We expect this adaption to be evident at multiple levels of the visual system, ranging from data acquisition by the eye to processing of this data in the higher visual areas of the brain. Based on the phenomenon of synesthesia, in which sensations are transferred between the senses, it is possible that mid-complexity fractals might also hold special significance for tactile and auditory experiences in addition to visual ones. This could be tested in the future using 3D printers to generate physical versions of the terrains shown in Fig. 30.3 and to use computers to convert visual stimuli into the sonic equivalents. This includes plans to convert the fractals in Pollock paintings into music and compare people's responses to these equivalent visual and sonic fractals.

Our studies of fractal fluency commenced with the eye-movement studies shown in Fig. 30.4 [4, 22]. The eye-tracking system (Fig. 30.4a) integrates infra-

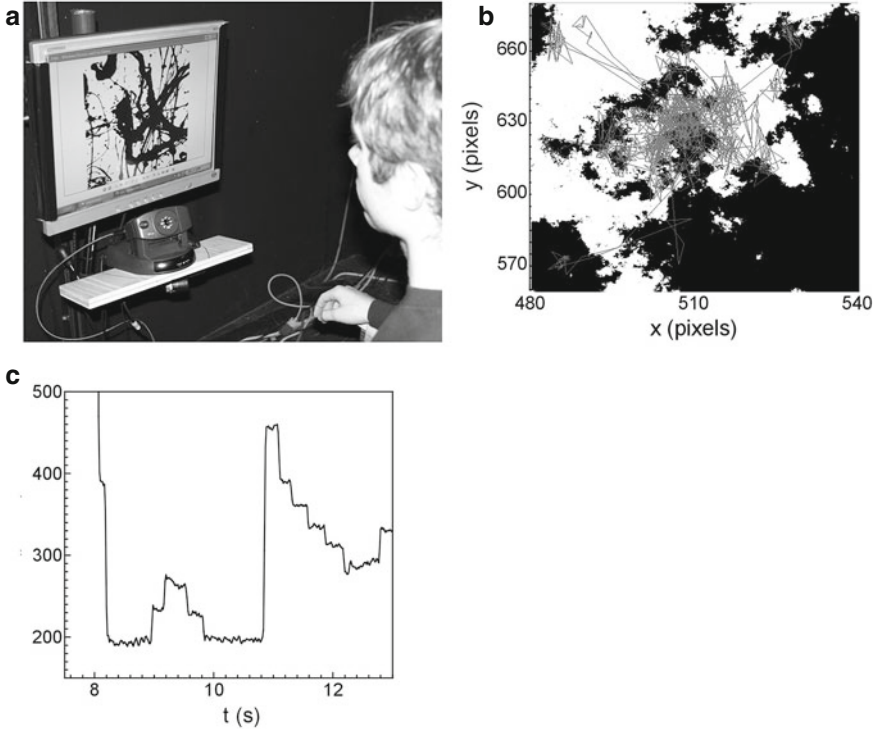


Fig. 30.4 (a) A photograph of the eye-tracking apparatus and (b) the spatial pattern of the eye tracks (*light gray*) plotted in the *x* (*horizontal*) and *y* (*vertical*) directions. The eye track is overlaid on the observed fractal pattern (*black and white*) and (c) the equivalent time series data which plots *x* versus time

red and visual camera techniques to determine the eye's gaze to an accuracy of 4 pixels when looking at a 1,024 by 1,024 pixel pattern presented on the computer monitor. During the 60 s observation period, participants were instructed to memorize the pattern in order to induce "free-viewing" activity. Figure 30.4b shows a section of the spatial pattern traced out by the eye's gaze as it moves across the monitor. As expected, the pattern is composed of long saccade trajectories as the eye jumps between the locations of interest and smaller micro-saccades that occur during the dwell periods. These periods of relative motionless can also be seen in the associated temporal trace of Fig. 30.4c. Details of the fractal measurement technique applied to the eye's spatial and temporal patterns are reported elsewhere [4, 12, 13, 22]. The results show that the saccade trajectories trace out fractal patterns with D values that are insensitive to the D value of the fractal pattern being observed: the saccade pattern is quantified by $D=1.4$, even though the underlying pattern varied over a large range from 1.1 to 1.9. This mid- D saccade pattern was confirmed for viewing computer-generated, natural, and Pollock fractals. Furthermore, participants with Alzheimer disease, frontal and anterior temporal

lobe degeneration, and progressive supranuclear palsy all exhibited the same fractal gaze dynamics as healthy participants, indicating that it is fundamental to eye-movement behavior and that it is not modified by processing in the higher levels of the visual system [12].

We propose that the purpose of the eye's search through fractal scenery is to confirm its fractal character (e.g., the ability to confirm that a forest features only fractal trees and no predators would promote survival). If the gaze is directed at just one location, the peripheral vision only has sufficient resolution to detect coarse patterns. Therefore, the gaze shifts position to allow the fovea to detect the fine-scale patterns at multiple locations. This allows the eye to experience the coarse and fine-scale patterns necessary for confirmation of fractal character. Why, though, does the eye adopt a fractal trajectory when performing this task? A possible answer can be found in the fractal motions of animals when they forage for food [27]. The short trajectories allow the animal to look for food in a small region and then to travel to neighboring regions and then onto regions even further away, allowing searches across multiple size scales. Significantly, such fractal motion has an "enhanced diffusion" compared to the equivalent random motion of Brownian motion. The amount of space covered by the fractal search is therefore larger. This might explain why it is adopted for both animal searches for food and the eye's search for visual information [4]. The mid- D saccade is optimal for this fractal search because it matches the D values found in prevalent fractal scenery – the saccades then have the same amounts of coarse and fine structure as the observed stimulus, allowing the eye to sift through the visual information efficiently.

We expect that strategies for efficiently processing mid- D fractals will also be evident at higher levels in the visual system. In the 1990s, Field and others presented a neural model featuring virtual "pathways" used for processing scenic information in the visual cortex of the brain [5, 10]. Some pathways are dedicated to analyzing large structures in nature's environment and others to small structures. He proposed that these pathways have evolved to accommodate our fractal view of nature as follows: the number of pathways dedicated to each structure size is proportional to the number of structures of that size appearing in the scene. In other words, the distribution of processing pathways matches the D values that dominate the viewed environment. In other early studies, Geake and Landini proposed that fractal processing utilizes images stored in memory [6]. Their experiments showed that people who displayed a superior ability to distinguish between fractals with different D values were found to also excel in mental tasks involving simultaneous synthesis (an ability to combine current perceptual information with data from long-term memory). Modern neurophysiological measurement techniques such as quantitative EEG (qEEG) and functional MRI (fMRI) now offer the potential for researchers to refine these preliminary ideas of how the brain processes fractal stimuli.

EEG is a well-established measure of cortical arousal. While the alpha frequencies (9–12 Hz) indicate a wakefully relaxed state, the beta frequencies (18–24 Hz) are associated with external focus, attention, and an alert state [11]. Previous recordings by Ulrich and colleagues revealed that people are more wakefully relaxed

during exposure to natural landscapes than to townscapes, and studies of wall art found that images with natural content have positive effects on anxiety and stress [24, 25]. In our studies, participants' responses were continuously monitored using a digital EEG recorder while they viewed fractal "mountain" stimuli (Fig. 30.3) with different D values [8]. The images were viewed for 1 min each and interspaced by a neutral gray picture for 30 s. This exposure period was chosen to ensure that a relaxation effect in the subjects could occur. Three regions of the brain – frontal, parietal, and temporal – were chosen because processes in these associational zones are known to be complementary [11]. The results showed that fractal images quantified by $D=1.3$ induce the largest changes in participants' alpha and beta responses [8]. Intriguingly, these responses were dampened when the images were morphed from the statistical to exact versions (Fig. 30.1), emphasizing the adaption of processing fluency to nature's biophilic fractals [7]. Our preliminary studies using the fMRI technique further indicate that mid- D fractals induce distinct responses when compared to those of low or high D equivalent images. Although requiring further study, they suggest that mid- D fractals preferentially activate specific regions such as the ventral visual stream (including the ventrolateral temporal cortex), the parahippocampal region, and the dorsolateral parietal cortex [22].

30.3 Enhanced Performance and Fractal Aesthetics

The fluency model predicts that the increased processing capabilities should result in enhanced performances of visual tasks when viewing mid- D fractals. Indeed, our recent behavioral studies demonstrate participants' heightened sensitivity to mid- D fractals [16]. Using grayscale fractal images displayed on a computer monitor (Fig. 30.3), the contrast in the patterns was gradually reduced until the monitor displayed uniform mean luminance. Participants were able to detect the mid- D fractals for much lower contrast conditions than the low and high D fractals [16]. Similarly, participants displayed a superior ability to distinguish between fractals with different D values in the mid- D range [16]. The increased beta response in the qEEG studies suggests a heightened ability to concentrate when viewing mid- D range [8]. There is also anecdotal evidence to suggest that pattern recognition capabilities increase for mid- D fractals. We are all familiar with percepts induced by cumulus clouds (Fig. 30.5, top). A possible explanation is that our pattern recognition processes are so enhanced by these $D=1.3$ clouds that the visual system becomes "trigger happy" and consequently we see patterns that aren't actually there.

Does fractal fluency create a unique aesthetic quality because we find them relatively easy to process and comprehend? Perhaps this "aesthetic resonance" for $D=1.3-1.5$ fractals induces the state of relaxation indicated by the peak in alpha response in the qEEG studies. Our earlier skin conductance measurements similarly demonstrated that mid- D fractals are stress reducing [8, 18]. The question of fractal aesthetics holds special significance for the field of experimental aesthetics. One of its early pioneers, George Birkhoff, introduced "aesthetic measure" in the 1930s – the

idea that aesthetics could be linked to measureable mathematical properties of the observed images. Visual complexity was a central parameter in his proposals [2]. In 1993, RPT conducted the first aesthetics experiments on fractals, showing that 95% of observers preferred complex fractal images over simple Euclidean ones [17]. Soon after, Sprott employed computer-generated fractals to show that mid- D fractals were preferred over low and high D fractals [1].

Over the past two decades, fractal aesthetics experiments performed by ourselves and other groups have shown that preference for mid- D fractals is universal rather than dependent on specific details of how the fractals are generated. We showed that preference for mid- D patterns occurred for fractals generated by mathematics, art, and nature [9, 14]. Whereas this experiment featured relatively simple natural images such as a tree or a cloud, this was soon broadened to include more complex natural scenes featuring many fractals [1]. Figure 30.5 shows example results for computer-generated stimuli [22]. The panels are for four different “configurations” (i.e., the computer uses four different seed patterns). The peak preference shows remarkable consistency despite superficial variations in the four families of fractals. More recently, our experiments demonstrated a direct correlation between preference and the observer’s enhanced capabilities (based on their abilities to detect and discriminate fractals) [16]. In addition to these laboratory-based behavioral experiments, a computer server has been used to send screen savers to a large audience of 5,000 people. New fractals were generated by an interactive process between the server and the audience, in which users voted electronically for the images they preferred [23]. In this way, the parameters generating the fractal screen savers evolved with time, much like a genome, to create the most aesthetically preferred fractals. The results reenforced the preference for mid- D fractals found in the laboratory-based experiments.

30.4 Conclusion: The Brave New World of Neuro-Aesthetics

Behavioral experiments, coupled with qEEG and fMRI techniques, might initially appear to be highly unusual tools for judging art and aesthetics. The history of neuro-aesthetics can be viewed as an epic battle fought between scientists and art theorists since the days of surrealism and Freudian psychology [19]. This deep clash between art and science is fueled by a fundamental concern: To what extent is art appreciation driven by the automatic responses of human neurophysiology and biology versus the intellectual and emotional deliberations of the culture-influenced observer? Consider the neurophysiological responses to Pollock’s paintings as an example. Can an appreciation of his paintings be likened to the way a frog continues to twitch when its head is cut off? After all, our results indicate that both are automatic responses. Such a comparison seems simplistic, but it does reflect the widespread fear of the “neurophysiology is destiny” approach to art. Equally, the “culture is destiny” supporters cannot distance art from neurophysiology. Pollock’s colleague, Willem de Kooning, serves as a dramatic example of how drastically his

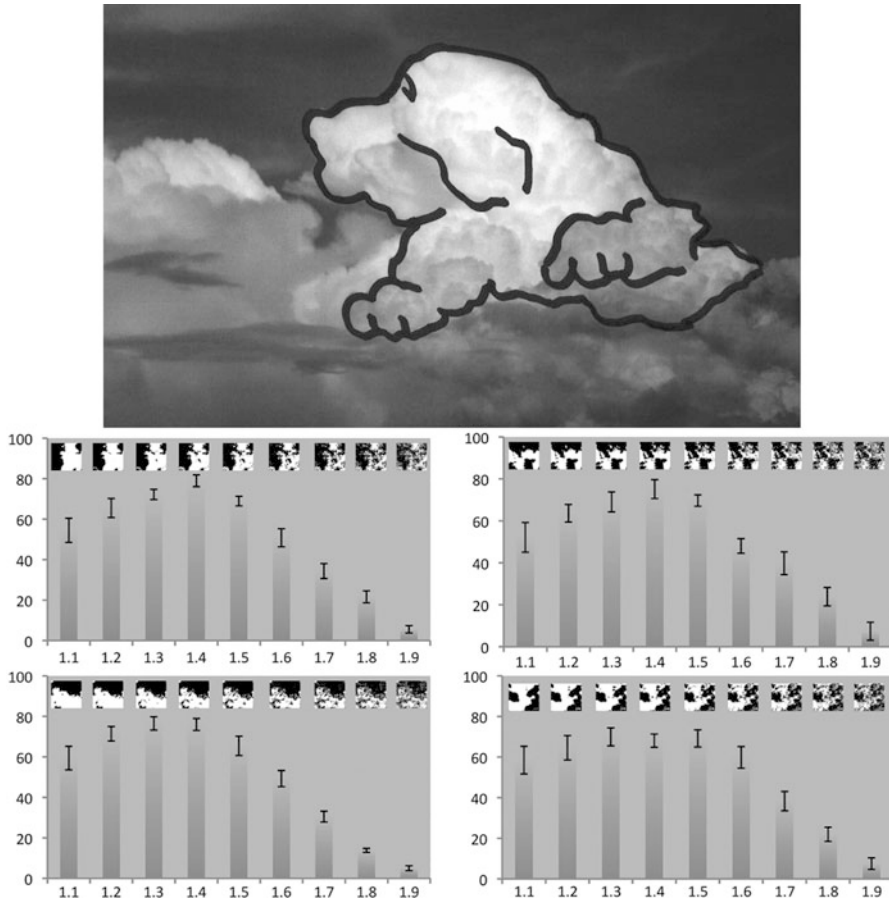


Fig. 30.5 *Top:* A perceived image of a dog drawn on a $D=1.3$ cloud. *Bottom:* Visual preference for computer-generated fractal patterns. For each of the four panels, D is plotted along the x -axis and the preference on a scale 0–100 is plotted along the y -axis. Each of the four panels uses a different fractal configuration to investigate preference. The fractal images are shown as *insets* in each panel

artistry changed as his Alzheimer’s disease progressed. The reality of aesthetics will almost certainly prove to be “neurophysiology and culture are destiny.” Its foundation is set by the observer’s neurophysiology, which is then modified by intellectual and emotional deliberations.

The neuro-aesthetics debate is also fueled by Zeki’s use of fMRI to catalog art based on the regions of the observer’s brain that are activated [28]. Imagine taking Zeki’s vision one step further – if we can identify the region that is activated when looking at a Pollock, then might we replace the original artwork with technology that allows us to stimulate this region directly? Though efficient, this radical and controversial approach would dishearten the art lovers who frequent galleries and

museums. In reality, it is doubtful that we will ever master a technology sufficiently subtle to stimulate the same fMRI pattern that a Pollock painting does.

Despite these and similar concerns, the interplay between art and the brain will be crucial for our future understanding of humanity. Novel measurement technology is destined to play an increasing role. Our results follow a long tradition of experimental aesthetics and the use of modern tools for analyzing human response to art works. They provide a fascinating insight into the impact that art might have on the observer's perceptual, physiological, and neurological condition. Our studies have only started to probe the neurophysiological origin of fractal aesthetics. It might well turn out that there is a deep resonance between the observed fractal stimuli and the fractal properties of the brain. In addition to exploring the fundamental science of our visual system, our fractal studies have important practical consequences. Mid-*D* fractals have the potential to address stress-related illnesses, which currently cost countries such as the USA over \$300 billion annually.

Acknowledgments We thank our collaborators Cooper Boydston, Colin Clifford, Caroline Hagerhall, and Margaret Sereno for their useful discussions. This work was supported by an Australian Research Council grant DP120103659 to BS and RPT.

References

1. Aks D, Sprott J. Quantifying aesthetic preference for chaotic patterns. *Empir Stud Arts*. 1996;14:1–16.
2. Birkhoff GD. *Aesthetic measure*. Cambridge: Harvard University Press; 1933.
3. Cutting JE, Garvin JJ. Fractal curves and complexity. *Percept Psychophys*. 1987;42:365–70.
4. Fairbanks MS, Taylor RP. Scaling analysis of spatial and temporal patterns: from the human eye to the foraging albatross. In: *Non-linear dynamical analysis for the behavioral sciences using real data*. Boca Raton: Taylor and Francis Group; 2011.
5. Field DJ, Brady N. Visual sensitivity, blur and the sources of variability in the amplitude spectra of natural scenes. *Vision Res*. 1997;37:3367–83.
6. Geake J, Landini G. Individual differences in the perception of fractal curves. *Fractals*. 1997;5:129–43.
7. Hagerhall CM, Laike T, Küller M, Marcheschi E, Boydston C, Taylor RP. Human physiological benefits of viewing nature: EEG response to exact and statistical fractal patterns. *J Nonlinear Dyn Psychol Life Sci*. 2015;19:1–12.
8. Hagerhall CM, Laike T, Taylor RP, Küller M, Küller R, Martin TP. Investigation of EEG response to fractal patterns. *Perception*. 2008;37:1488–94.
9. Hagerhall CM, Purcell T, Taylor RP. Fractal dimension of landscape silhouette outlines as a predictor of landscape preference. *J Environ Psychol*. 2004;24:247–55.
10. Knill DC, Field D, Kersten D. Human discrimination of fractal images. *J Opt Soc Am*. 1990;77:1113–23.
11. Kolb B, Whishaw IQ. *Fundamentals of human neuropsychology*. New York: Worth Publishers; 2003.
12. Marlow CA, Viskontas IV, Matlin A, Boydston C, Boxer A, Taylor RP. Temporal structure of human gaze dynamics is invariant during free viewing. *PLoS One*. 2015;10:e0139379.
13. Moon P, Murday J, Raynor S, Schirillo J, Fairbanks MS, Taylor RP. Fractal images induce fractal pupil dilations. *Int J Psychophysiol*. 2014;93:316–21.

14. Spehar B, Clifford C, Newell B, Taylor RP. Universal aesthetic of fractals. *Chaos Graph*. 2003;37:813–20.
15. Spehar B, Taylor RP. Fractals in art and nature: why do we like them? *SPIE Electron Imaging*. 2013;865:1–18.
16. Spehar B, Wong S, van de Klundert S, Lui J, Clifford CWG, Taylor RP. Beauty and the beholder: the role of visual sensitivity in visual preference. *Front Hum Neurosci*. 2015;9:1–12.
17. Taylor RP. Splashdown. *New Sci*. 1998;2144:30–1.
18. Taylor RP. Reduction of physiological stress using fractal art and architecture. *Leonardo*. 2006;39:245–51.
19. Taylor RP. Across the cultural divide. *Nature*. 2010;463:431.
20. Taylor RP, Guzman R, Martin TM, Hall G, Micolich AP, Jonas D, Scannell BC, Fairbanks MS, Marlow CA. Authenticating Pollock paintings with fractal geometry. *Pattern Recognit Lett*. 2007;28:695–702.
21. Taylor RP, Micolich AP, Jonas D. Fractal analysis of Pollock's drip paintings. *Nature*. 1999;399:422.
22. Taylor RP, Spehar B, von Donkelaar P, Hagerhall CM. Perceptual and physiological responses to Jackson Pollock's fractals. *Front Hum Neurosci*. 2011;5:1–13.
23. Taylor RP, Sprott JC. Biophilic fractals and the visual journey of organic screen-savers. *J Non-linear Dyn Psychol Life Sci*. 2008;12:117–29.
24. Ulrich RS. Natural versus urban scenes: some psychophysiological effects. *Environ Behav*. 1981;13:523–56.
25. Ulrich RS. Biophilia, biophobia and natural landscapes. In: *The biophilia hypothesis*. Washington, DC: Island Press; 1993.
26. Ulrich RS, Simons RF. Recovery from stress during exposure to everyday outdoor environments. *Proc EDRA*. 1986;17:115–22.
27. Viswanathan GM, Afanasyev V, Buldyrev SV, Murphy EJ, Prince PA, Stanley HE. Lévy flight search patterns of wandering albatrosses. *Nature*. 1996;381:413–5.
28. Zeki S. *Inner vision: an exploration of art and the brain*. Oxford: Oxford University Press; 1999.

Part IV
Computational Fractal-Based
Neurosciences

Chapter 31

Computational Fractal-Based Neurosciences: An Overview

Antonio Di Ieva

Abstract After the section “Fractals: What and Why?”, the last section of this book covers the software tools necessary to perform computational fractal-based analysis, with special emphasis on its applications into the neurosciences. The use of *ImageJ* and MATLAB, as well as other software packages, is reviewed. The current and future applications of fractal modelling in bioengineering and biotechnology are discussed as well. Perspectives on the translation of merging fractals with artificial intelligence-based methods with the final aim of pattern discrimination in neurological diseases by means of a unified fractal model of the brain are also given.

Keywords Artificial intelligence • Computation • Fractal • ImageJ • MATLAB • Modelling • Patterns recognition

What we observe is not nature itself, but nature exposed to our method of questioning.
(Werner Heisenberg, 1958)

From the previous chapters of this book, it is clear that computational fractal-based analysis has found and still finds large applications in the basic as well as clinical neurosciences, offering quantitative and quantitative parameters for the study of cellular and subcellular components of brain cells as well as the whole brain itself. Moreover, fractal analysis offers potential image and prognostic biomarkers useful in clinical medicine. After having reviewed such applications, the reader may be interested in the methods and software to perform computational fractal-based analysis. Part IV of this book is focused on the software tools to

A. Di Ieva, MD, PhD
Neurosurgery Unit, Faculty of Medicine and Health Sciences, Macquarie University,
Sydney, Australia

Garvan Institute of Medical Research, Sydney, NSW, Australia

Medical University of Vienna, Vienna, Austria

University of Toronto, Toronto, ON, Canada

e-mail: diieva@hotmail.com

compute the fractal dimension and other complementary parameters. This section may be of interest to the neophyte approaching computational methods as well as for the computer science expert who would like to review the state-of-the-art methods or obtain new inputs.

Moreover, some computer science and engineering-based perspectives (actual and future) are offered in the last two chapters.

31.1 How to Compute Fractals in Clinical Neurosciences

The previous sections of this book dealt with the questions “Fractals in Neurosciences: What and Why?”. The key question of this section is: “How?”

Several software packages are available for the fractal analysis of images (i.e. radiological and histological images) and times series. Many researchers use software programmed ad hoc by computer scientists for specific tasks. Nonetheless, one of the most used toolsets for computing fractal parameters in neurosciences has been, and currently is, the open-source image analysis software named *ImageJ*, which supports functions to compute the fractal dimension, lacunarity and other parameters. In Chap. 32, two pioneers of the application of *ImageJ* for fractal analysis in the neurosciences, *Audrey Karperien and Herbert Jelinek*, who also introduced the plug-in *FracLac* for *ImageJ*, illustrate its use for pattern extraction and translational research, which was aimed at translating the fractal geometry of the brain into clinical applications. MATLAB and other software platforms and tools online can be used as well, as illustrated in Chap. 33 by *Juan de Miras*. In the latter two chapters, some practical examples of applications in the neurosciences are illustrated. Moreover, in order to avoid the time-consuming process of computing the fractal dimension, a method to increase processor computational speed is presented by *Juan de Miras and Jesús Ibáñez* in Chap. 34.

31.2 Fractals in Bioengineering and Artificial Intelligence

Leaping into the realms of bio-engineering and biotechnology, in Chap. 35 *William Watterson, Saba Moslehi, Julian Smith, Rick Montgomery and Richard Taylor* introduce the reader to a fractal fabric for the construction of bio-inspired fractal interconnects to interface the body and brain elements (e.g. neurons) in order to restore damaged functions.

In the last chapter of this book, *Lorenzo Livi, Alireza Sadeghian and Antonio Di Ieva* suggest some intriguing future perspectives in the field on the merging of fractal analysis with computational intelligence methods for pattern identification and extraction.

31.3 Conclusive Remarks: Towards a Unified Fractal Model of the Brain?

The Heisenberg's quote at the beginning of this short chapter subtends a key concept of fractal analysis as well as every kind of analysis applied to scientific research, including biomedical sciences and neurosciences: that our observation of natural phenomena is filtered by the lens of the applied methodology. For example, in neuroradiology what we see is not the brain itself but pixels showing specific features of the brain. Similarly, in digital pathology, what we see of histological slides of brain tumors are two-dimensional images of the tumors as revealed by specific histological and/or immunohistochemistry techniques. Aware of such method-related limitations, we are still able to use such information to our benefit, despite the fact that we are observing the natural phenomenon filtered by a methodological "Veil of Maya". This is often forgotten by neophytes, and even by the more experienced researcher. As widely expressed in Chaps. 1 and 12, fractal geometry is a model, with its advantages and intrinsic limits. Fractal geometry represents a universal language to translate natural phenomena, but the limits of the model itself do not qualify it to be a Rosetta stone that is able to interpret every natural object, as fractals are not a panacea.

The value of fractal dimension can change according to several different factors: different computational methods, preprocessing tools, different scale windows, etc. The same structure can show different values depending upon "the angles of view". The methodological differences give rise to a heterogeneous dataset of results, and the clinical significance of the fractal dimension as biomarker becomes controversial in the absence of a well-standardized computational procedure. Being aware of such limitations of fractal geometry as a model, there are still several aspects that make this analysis such a powerful tool to analyze natural phenomena, including the complexity of the human brain in its entire physiopathologic spectrum. As introduced in Chap. 1, this book has not shown the existence of the fractal geometry of the brain as a pure mathematical model, rather it has suggested that computational fractal-based analysis be used for pattern recognition in the basic and clinical neurosciences. The fractal approach has been shown suited to automatic image analysis (e.g., in neuroradiology as well as neuropathology), extraction of features in images as well as in time series, and identification and classification of types and subtypes of states within the wide spectrum of the normal to the pathological brain. In sum, there exist a host of fractal-based morphometrics of biodata in the clinical neurosciences that are *objective, realistic, reproducible, and potentially prognostic and predictive biomarkers* with much promise for use in clinical practice.

As suggested by *Audrey Karperien and Herbert Jelinek* at the end of Chap. 32, "We hope [that this book] has further inspired the reader to continue to demystify fractal analysis, to explore new fractal possibilities, to develop pattern extraction methods for new perspectives and especially for databases, [...] to bring the multiple levels of the fractal geometry of the brain to the fore, not just as a wonder of the digital age but as a clinical reality".

As illustrated in Chap. 36, computational intelligence methods are aimed at recognition, discrimination and prediction in the analysis of complex patterns. The future of this field may be a computational fractal-artificial intelligence-based analysis, which, associated with further analyses, might offer, in a multiparametric way, a computer-aided, objective and reproducible categorization of the different pathologies. By this way, the clinicians' armamentarium will be enriched by new diagnostic, prognostic and eventually therapeutic biomarkers as well.

Chapter 32

ImageJ in Computational Fractal-Based Neuroscience: Pattern Extraction and Translational Research

Audrey L. Karperien and Herbert F. Jelinek

Abstract To explore questions asked in neuroscience, neuroscientists rely heavily on the tools available. One such toolset is *ImageJ*, open-source, free, biological digital image analysis software. Open-source software has matured alongside of fractal analysis in neuroscience, and today *ImageJ* is not a niche but a foundation relied on by a substantial number of neuroscientists for work in diverse fields including fractal analysis. This is largely owing to two features of open-source software leveraged in *ImageJ* and vital to vigorous neuroscience: customizability and collaboration. With those notions in mind, this chapter's aim is threefold: (1) it introduces *ImageJ*, (2) it outlines ways this software tool has influenced fractal analysis in neuroscience and shaped the questions researchers devote time to, and (3) it reviews a few examples of ways investigators have developed and used *ImageJ* for pattern extraction in fractal analysis. Throughout this chapter, the focus is on fostering a collaborative and creative mindset for translating knowledge of the fractal geometry of the brain into clinical reality.

Keywords Computer-assisted image processing • Fractals • Box counting • ImageJ • FracLac • Microglia • Neurons • Theoretical models

32.1 Introduction

Imagine opening the screen on a cell phone and showing a patient a fractal dimension displayed overtop of the large vessels in the vicinity of their brain tumor and then zooming in to the gross overall outline and texture of their biopsy, through microvasculature and intertwining neuronal and other brain cell processes, all the way down to that one unusually complex astrocyte, and then its nucleus, fractal dimension displaying on the screen at each level—and patient and clinician alike

A.L. Karperien (✉) • H.F. Jelinek (✉)

School of Community Health & Centre for Research in Complex Systems, Charles Sturt University, Albury, Australia

e-mail: akarperien@yahoo.com; hjelinek@csu.edu.au

© Springer Science+Business Media New York 2016

A. Di Ieva (ed.), *The Fractal Geometry of the Brain*, Springer Series in Computational Neuroscience, DOI 10.1007/978-1-4939-3995-4_32

503

understanding. This is the vision and mindset of fractal-based neuroscience for the near future that *ImageJ* supports.

The topic of fractal analysis is decades old, in its infancy within the millennia of science that human history holds, but of age in today's digital revolution. It is underlain by a set of tools developing in the context of unprecedented technological advances and global collaboration. Generally, the path any tool develops along follows the questions being asked in the workshop and world served by that workshop, and those questions in turn develop within the questioner's expectations of how well their question might even begin to be explored. This chapter delineates the place of one tool, *ImageJ* (*IJ*), in influencing the imaginations of the people asking questions in the global community of fractal-based neuroscience and in making the topic generally accessible.

First, this chapter answers two questions, "What is *IJ*?" (Sect. 32.2) and "Where does it fit in fractal-based neuroscience today?" (Sect. 32.3). As the anatomical fly-through thought exercise in the introductory paragraph suggests, this chapter's scope is limited to fractal analysis of digital images. In particular, bridging the gap between tumor and fractal dimension, vasculature and fractal dimension, neuropil and fractal dimension, etc., lies a substantial part of the realm of fractal analysis of digital images—pattern extraction. Thus, the chapter also reviews some ways investigators have used *IJ* to creatively answer questions about fractal analysis pattern extraction (Sect. 32.4).

32.2 What Is *ImageJ*?

32.2.1 *Removing Barriers with Free, Open-Source Software*

To some people, *IJ* is one of many user-friendly photo filtering "apps"—to others, a powerful lab tool. At its simplest, it is computationally powerful [33], open-source software for digital image processing and analysis. At its broadest, it was designed with a mindset to meet four freedoms of open-source software quoted below:

Freedom:

1. *To run the program, for any purpose,*
2. *To study how the program works, and change it to make it do what you wish,*
3. *To redistribute copies so you can help your neighbor,*
4. *To improve the program, and release your improvements to the public, so that the whole community benefits [67].*

IJ was created by Wayne Rasband at the US National Institutes of Health (NIH). First released in 1997, it was based on an existing computer program, *NIH Image*, but written in the then new Java programming language (hence the "J") [75]. The significance of this is that it made *IJ* independent of computer architecture, owing to Java's then revolutionary philosophy of "write once, run anywhere." *IJ* was at the outset and remains easily installed on most computer operating systems, making it a tool that diminishes barriers to collaboration that different operating systems can

pose. This is important today, but was perhaps more important when the program was first made available, a time when, more than today, having incompatible computer operating systems rendered many forms of collaboration very time consuming or impossible. *IJ* reduced other barriers, too, making it popular in many fields, by being freeware [1, 26, 75]. *IJ* was and remains available for anyone to download from the NIH's public website (<http://imagej.nih.gov/ij/download.html>).

32.2.2 *Shaping Computational Fractal-Based Neuroscience*

32.2.2.1 Making Fractal Analysis Accessible and Customizable

Among many image-processing and analysis functions, *IJ* included fractal analysis methods early on. In particular, it included a fractal dimension-determining function, a basic binary box counting tool, founded on existing code written for *NIH Image* by Tom Smith, a pioneer in determining the fractal dimensions of neurons and other brain cells [77, 78]. Making fractal analysis even easier, *IJ* also included the basic pattern extraction methods required to use that binary box counting function (see Fig. 32.1) [77, 78].

Thus, it was possible for someone with basic digital image processing skills and no computer programming knowledge to use *IJ* to open digital images, decide on the type of patterns to extract, extract them, and obtain and compare fractal dimensions. This was, albeit, a rudimentary approach (Chap. 2 discusses box counting fractal analysis in detail and highlights this approach's limitations), but the point here is that the combination of these fundamental fractal analysis tools with the features of being platform independent, available, and free offered a timely opportunity for scientists with or without programming experience to personally explore their own questions about the growing field of fractal analysis.

In addition to demystifying and helping establish fractal analysis as an accessible method for the neuroscientist or clinician, *IJ* played an important role in encouraging the field to grow. Carrying forward basics from its predecessor program, it provided:

- Built-in functions to record and save macros (sequences of commands to repeat tasks and potentially apply them to batches of stored images or the same image with multiple modifiers)
- Plug-in capability (a plug-in is software that can be shared and quickly installed to make *IJ* able to do new tasks)
- Opportunity to shape the core software [56]

These features, which are applications of the freedoms underlining the *IJ* mindset (Sect. 32.2.1), were especially relevant at the time because the methods of fractal analysis in neuroscience were just beginning to be developed [49]. They let people go beyond the basic box counting function to experiment with, customize, and hone fractal analysis methods; formulate and test questions; dynamically answer queries about multiple, changing nuances; rapidly process large numbers of images; etc.

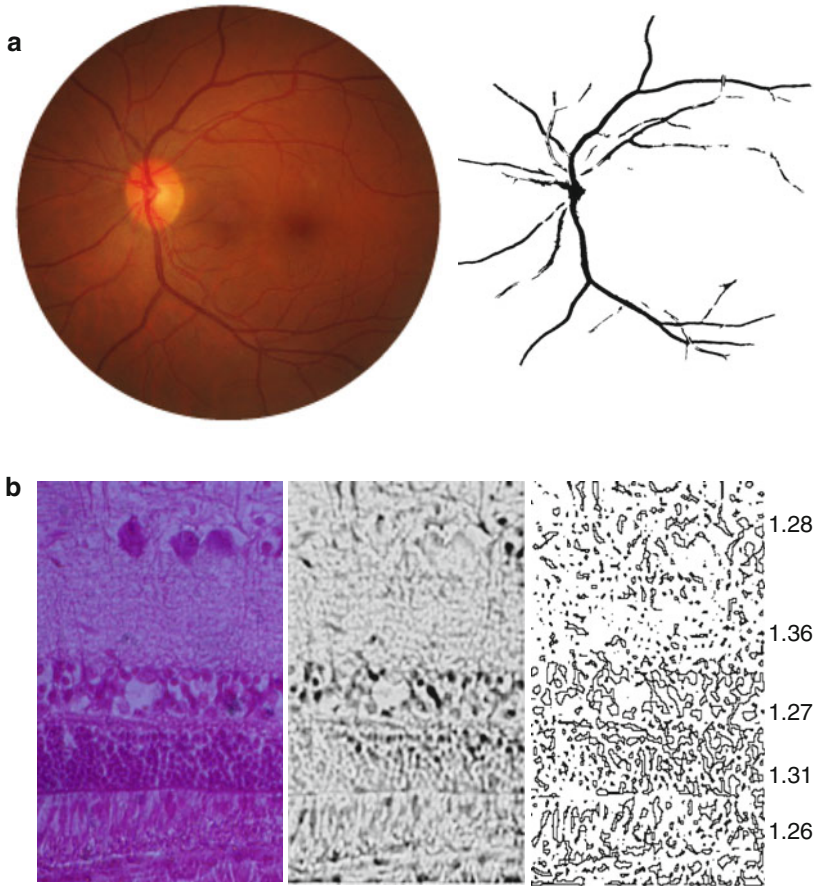


Fig. 32.1 Examples of patterns suitable for box counting fractal analysis extracted from retina using basic *IJ* functions. **(a)** A binary silhouette (*right*) showing only the pattern of the vasculature, extracted from a retinal fundus photo, using background subtraction, smoothing, auto-selection, and binarizing. **(b)** Grayscale and binary textures extracted from a digital microphotograph of retinal layers on an HE-stained histological slide of retina; extracted by converting to grayscale, using background subtraction to remove ganglion and other cell body interiors and other undesired information, binarizing, and outlining

IJ in general tapped into a growing scientific resource, and researchers and programmers soon produced a wide-ranging list of plug-ins, online guides, and tutorials in many fields (see <http://rsb.info.nih.gov/ij/plugins/>). Many of these resources supported fractal analysis to varying degrees, and many were created by or for both theoretical and clinical researchers to answer questions in fields such as microscopy, radiography, and brain morphology. They offered in one toolset a free, accessible, flexible, and user-friendly compendium of ways for non-programmers and programmers to do several types of fractal analysis (e.g., dilation, mass vs. radius [38], local connected fractal dimension [41, 45], grayscale analysis, and multifractal

analysis) as well as related required pattern extraction tasks [15, 20, 31, 39, 48, 64, 68, 70, 75]. While these were certainly not the only means available to the research community for applying fractal analysis, they did create a common ground and foster a collaborative approach.

32.3 Where Does *IJ* Fit in Fractal-Based Neuroscience Today?

IJ plays a major part in both neuroscience and fractal analysis today. As illustrated in Fig. 32.2, one outcome of the resources described in the previous section and their continued development is that *IJ* today has a presence in published work linking the two fields [1, 15, 75].

Furthermore, *IJ* has become an image-processing model itself. It is now used as an applet in webpages and is available in a limited form for the Android operating system (e.g., for tablets and cell phones) [12, 72–74]. Today, *IJ* and *Fiji*, an *IJ* distribution developed to accommodate increasingly complicated plug-ins and data formats including “Digital Imaging and Communications in Medicine” (DICOM) and complex 3-dimensional (3D) data, are neuroscience industry standards. (Still straightforward software, “Fiji” is an acronym for “Fiji is Just *ImageJ*.”) *IJ* can communicate bidirectionally with many other types of software (e.g., MatLab) and is used as a software library in many applications including commercial applications used in neuroscience. Indeed, neuroscience labs today hire dedicated *IJ* programmers [3, 5, 7, 9, 10, 14, 18, 19, 50, 57, 71, 73].

IJ is also relevant in today’s changing science education environment and plays roles in translational research. *IJ* is being used increasingly in higher education, for instance, as digital pathology is now a reality, and virtual microscopy is becoming the norm for teaching medical histology [8, 43, 60]. Moreover, it is used to teach youth in high schools, including for teaching youth participating in science fairs and at science camps, how to do and understand fractal analysis of brain cells and how to evaluate heart rate variability using fractal measures (see Fig. 32.3) [16, 36].

A key element of this widespread presence is that despite that *IJ* has evolved into a highly respected programming library and gained increasingly complex and specialized functions and uses, its main software interface has remained straightforward. *IJ* remains a potent tool that the programmer and nonprogrammer alike can easily use on its own or with other software, at home and at work, to investigate, collaborate on, and explore new questions.

In fact, in many labs, for collaborating with colleagues on digital imaging fractal analysis questions, *IJ* is a preferred tool that equalizes differences in resources because it can be shared and customized as rapidly as the questions being asked change their nuances (e.g., by emailing images, macros, plug-ins, and results). To illustrate, a regular part of our work is adding features to or customizing the plug-in *FracLac for ImageJ*, which was developed in our lab to overcome many pitfalls of fractal analysis (see Chap. 2) and has been used to publish in neuroscience and other

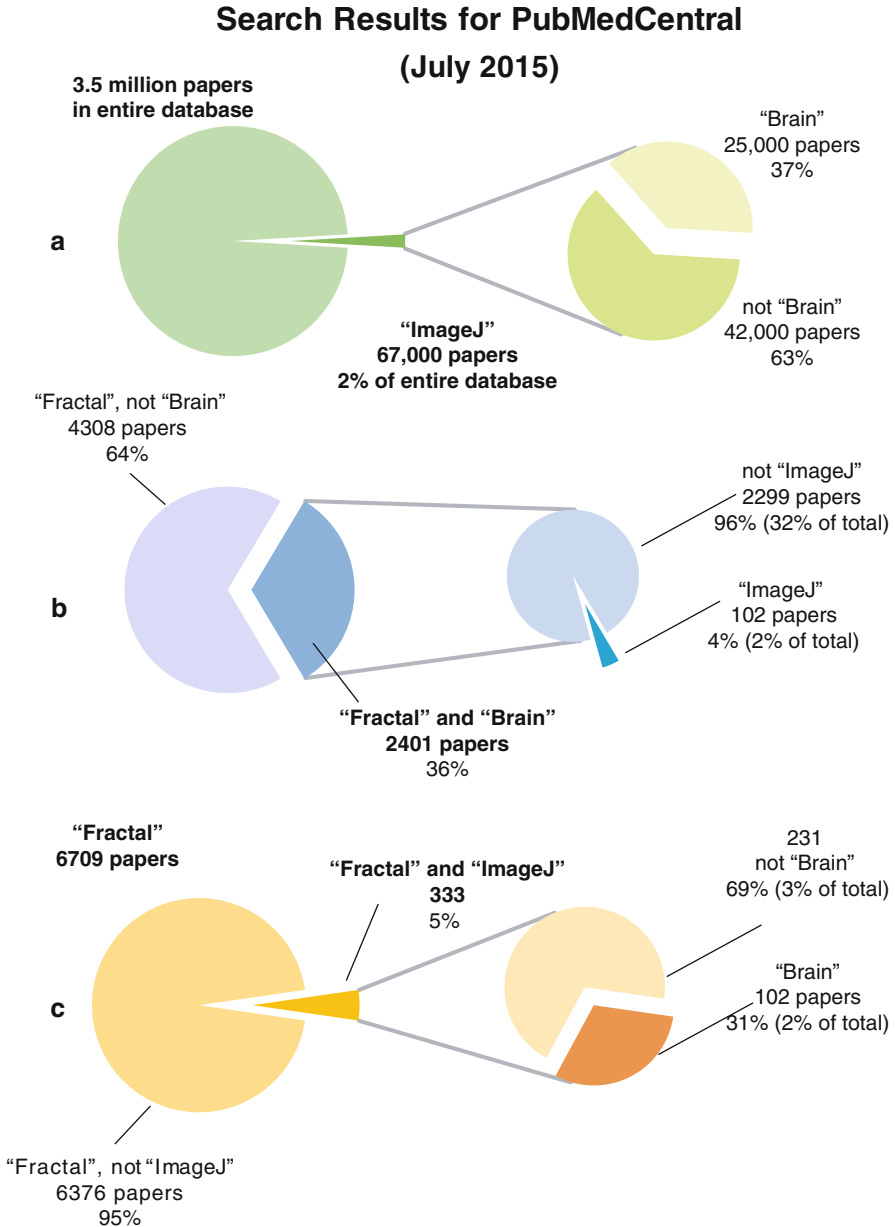


Fig. 32.2 *IJ* is referenced substantially in published articles indexed in PubMedCentral relevant to fractal analysis in neuroscience. (a) *IJ* is cited or otherwise referenced in 67,000 papers in the PubMedCentral database [57] and around a third of those are relevant to neuroscience (i.e., are also indexed under the term “brain”). (b) 36% of all articles relevant to fractal analysis (i.e., indexed under “fractal”) in the database are relevant to neuroscience and about 4% of those cite or otherwise reference *IJ*. (c) 5% of the database articles relevant to fractal analysis cite or otherwise reference *IJ*; about a third of those are relevant to neuroscience (Data based on a search of the US National Library of Medicine’s PubMedCentral in August 2015. Note that publication data generally underrepresent *IJ*’s use because authors do not always credit it when they use it for scientific publications [1, 75])

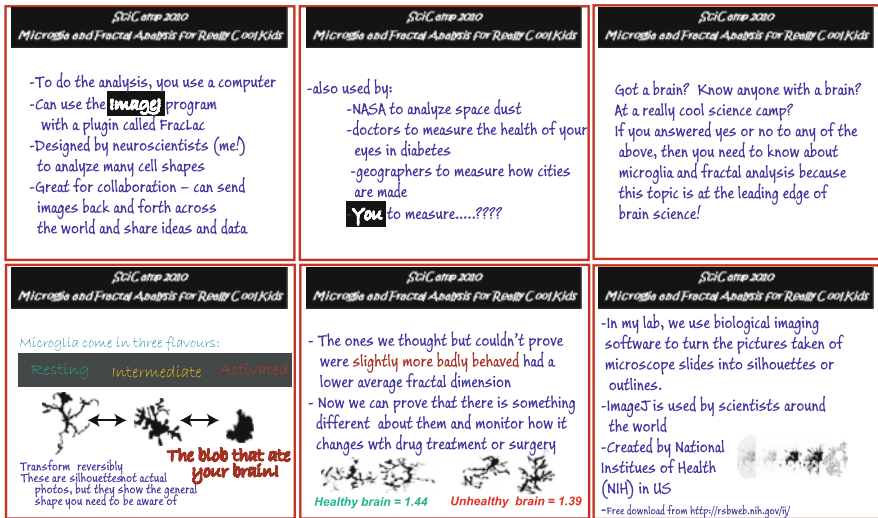


Fig. 32.3 *ImageJ* is used to teach young people about fractal analysis in neuroscience and leave them with the skills and tools (e.g., a youth-focused plug-in) to explore their own basic fractal analysis questions. (Panels are from presentations delivered to youth at a summer science camp in Bonnyville, Alberta, Canada, 2010)

fields (see <http://rsbweb.nih.gov/ij/plugins/fracLac/FLHelp/FLCitations.htm> for 73 recent publications citing it) [4, 17, 21, 28, 30, 42, 82]. *FracLac* is an ongoing collaborative freeware project including a suite of tools for fractal analysis (including monofractal, lacunarity, multifractal, mass vs. distance, and local connected dimension analyses) and fractal bio-modeling (see Sect. 32.4). It was initially developed to answer basic questions about the fractal dimension of microglial brain cells and, as an open-source plug-in adhering to the *IJ* mindset, continues to develop based on our own evolving research needs and requests from users [2, 11, 27, 29, 40, 41, 45, 51, 79, 80].

32.4 Pattern Extraction

As was discussed in conjunction with the thought exercise that started this chapter (Sect. 32.1), fractal analysis of the geometry of the brain depends on bridging the gap between digital images and structural information (i.e., numerical coordinates in space). Today, *IJ* has centralized much effort spent toward solving one well-known and vexing burr in neuroscience that is doubly vexing in fractal-based neuroscience—the information problem [54, 65]. To elaborate, the scientific and medical worlds no longer face archival problems of too little cabinet space to store every x-ray and photograph, but of inadequate methods to analyze and manage rapidly amassing 3D data sets, videos, and still digital image information. Testifying to the significance of the problem, cash rewards are being offered for innovative contributions to the solution [37, 54, 58, 65, 66].

32.4.1 *Pattern Types*

Turning original digital images into patterns for fractal analysis is called “pattern extraction,” “segmentation,” or “preprocessing” and generally entails extracting some variation or combination of binary, grayscale, and 3D (e.g., voxel-based) data. The usual product of pattern extraction is itself another digital image, generally one of three basic types:

Contour	Gross outline with no fill (e.g., the outline of a hemisphere or tumor, a cell membrane, a nuclear membrane, the outer edges of branches, and the structures they radiate from such as a vessel or microglial cell); typically for binary analysis
Skeleton	The basic path of a branching structure excluding diameter changes (e.g., the path of an axonal tree or vasculature pattern); usually one pixel wide, typically for binary analysis
Silhouette or area	The texture within an area (e.g., the mass inside a hemisphere, tumor, cell, or nucleus), which may include a branching structure that may or may not have diameter changes and has diameters greater than a single pixel (e.g., vasculature; the area within the contour of a microglial cell); for either binary (filled with one color) or grayscale (filled with multiple possible colors) analysis

32.4.2 *Extraction Methods*

In general, published fractal analysis pattern extraction methods range from simple to elaborate. In terms of *IJ*, there are numerous free, open-source segmentation plug-ins including methods that can be trained and methods that can be adapted to work with entire databases [12, 24, 31, 32, 44, 48]. This section outlines built-in functions (Sect. 32.4.2.1), tracing plug-ins (Sect. 32.4.2.2), thresholding (Sect. 32.4.2.3), and customized methods (Sect. 32.4.2.4) relevant to fractal analysis in neuroscience using *IJ*.

There is an important caveat to this section, based on two general points. First, reading a signal, such as by extracting to a binary format, choosing the part of a grayscale image to analyze, reconstructing 3D data, etc., is always idiosyncratic, and, in the end, what is considered signal and what noise, even within one image being investigated in more than one way, is limited only by the questions one chooses to ask. Second, all means of imaging are subject to confounders such as variation in lighting, contrast agent, intra- and interoperator variability, and a host of others pertinent to specific image acquisition protocols such as retinal photography, microscopy, radiography, etc. [61, 62]. These two points are common to all forms of image analysis, computer-aided or not, in science and medicine.

Accordingly, selecting a pattern extraction method requires many steps including testing that proposed methods (even automated) work in the way desired for a proposed dataset, reducing confounders, using control images, documenting anomalies and deviations, and, if the images are not in a previously acquired dataset, maximizing acquisition protocols in the first place (e.g., using staining, lighting, etc., appropriate to the question). Thus, whereas this section surveys options, it does not authoritatively prescribe how to extract patterns.

32.4.2.1 Built-in Functions

Fractal pattern extraction from images typically involves two fundamental techniques—tracing and thresholding. Tracing can be done manually, automatically, or semiautomatically and is usually the slower of the two. Thresholding means choosing for grayscale or color images a range of pixel values defining which pixels to keep (called foreground) and which to ignore (background). Sometimes pattern extraction combines the two processes. *IJ* includes a variety of functions for doing both and filters that enhance them, such as automated background subtraction, smoothing, etc. In labs with computer programming expertise, these basic methods are often modified and incorporated into macros and plug-ins to address specific issues pertinent to a set of images (discussed in Sect. 32.4.2.4). Table 32.1 outlines some basic functions for tracing and thresholding and Table 32.2 outlines some basic filters used in conjunction with those functions.

IJ's built-in functions are not necessarily original, insofar as commercial applications include many similar functions, and it is possible with some commercial applications to combine functions in macros and plug-ins as can be done with *IJ*. The unique value, however, inheres in features of *IJ* outlined in Sect. 32.2.1. From a lab perspective, for example, licensing restrictions can limit the number of people working with software at one time, giving free, open-source software an advantage for time-consuming tasks in particular. Moreover, basic extraction methods support informal or pilot level enquiry and are adequate for some images, but do not necessarily work for every type of fractal enquiry. The generally greater freedom to write macros and customized computer code with *IJ* can be essential for unusual images, large jobs with often changing parameters, and the ability to look at images creatively [23, 46, 52–54].

32.4.2.2 Tracing Plug-Ins

Although using the unaided tracing methods from Table 32.1 can be quick for some images, it often becomes labor intensive (e.g., it may take hours to manually reconstruct the most complicated branching cells in *IJ* and similar computer software). To deal with this, several *IJ* developers have created tracing plug-ins that make the process easier and potentially less subjective. Three examples of such plug-ins are *NeuronJ* [55], *Neuron_Morpho* [15], and the *Simple Neurite Tracer* [48] (see

Fig. 32.4). These plug-ins can be used to obtain branching structure information in all three of the basic pattern types from Sect. 32.4.1; *Neuron Morpho* and the *Simple Neurite Tracer* can also be used for 3D reconstructions. Although the developers

Table 32.1 Basic built-in functions for fractal analysis pattern extraction by tracing and thresholding

Pattern	Function	Implementation
Contour	Draw	Select area with selection tools or other method then: Edit>Draw
		Optionally: Image>Adjust>Line width
	Binary outline	Select area with selection tools or other method then: Process>Binary>Make Binary
		Process>Binary>Fill
	Particle analyzer	Process>Binary>Make Binary
		Analyze>Analyze Particles
		Check Show Outlines then OK To make a selection to analyze: Edit>Selection>Create Selection
	ROI manager	Analyze>Tools>ROI Manager
		Select area with selection tools or other method then: ROI Manager>Add to add each to Manager
		ROI Manager>More>Draw
Skeleton	Skeletonize	Select area with selection tools or other method then: Process>Binary>Make Binary
		Process>Binary>Skeletonize
		Select area with selection tools or other method then: Process>Binary>Make Binary
		Process>Binary>Erode (repeat)
Silhouette or area	Fill	Select area with selection tools or other method then: Edit>Fill
	Binary fill	Select area with selection tools or other method then: Process>Binary>Make Binary
		Process>Binary>Fill
	Threshold	Image>Adjust>Threshold
	Particle analyzer	Process>Binary>Make Binary
		Analyze>Analyze Particles Check Show Masks then OK
	Grayscale	Select area with selection tools or other method then: Edit>Copy
		Or Edit>Clear Outside
		Or Image>Crop
	ROI manager	Analyze>Tools>ROI Manager
Select area with selection tools or other method then: ROI Manager>Add to add each to Manager		
ROI Manager>More>Fill		

Table 32.2 Methods for filtering images

Method	Implementation
Auto-selection	Choose Wand (tracing) tool
	Click on image to select a single or shift-click for a composite area
Subtract background	Process>Subtract Background
Filter	Process>Smooth or
	Process>Filter or
	Image>Color>Adjust LUT or
	Image>Color>Split Channels
Paintbrush	Image>Overlay>Add Overlay
	Choose Paintbrush Tool from main interface
	Optionally set width (e.g., edge or branch diameter):
	Highlight edge
	Analyze>Measure then note and set size:
	Choose Image>Overlay>Overlay Options
	Or Paintbrush Tool>Brush Width
	Type in noted size
	Manually trace features of interest then:
	Image>Overlay>To ROI Manager
Reselect on original image by selecting ROI in ROI list	
Extract patterns using methods in Table 32.1	

originally created and tested these to answer questions about the structure of neurons, researchers have used them for related structures such as vasculature [81].

32.4.2.3 Thresholding

Like most segmentation methods, the tracing plug-ins described in Sect. 32.4.2.2 work better for images such as the *in silico* image illustrated in Fig. 32.4 and images from biological imaging modalities with similarly stark contrast. This can be a severe limitation for images with less contrast or significant background variation. As an example, it is much more difficult and ambiguous to extract vessel and neuronal patterns from grayscale versions of the retinal images from Fig. 32.1 than the *in silico* cell in Fig. 32.4. This is part of a broader issue. The last decade has seen mammoth effort put into developing automated pattern extraction methods, but there remain two intertwined issues computer programmers, macro writers, and generally anyone in neuroscience or any other field reliant on pattern extraction continue to spend their time on: background subtraction and auto-thresholding. These are significant barriers to pattern extraction for fractal analysis.

One major problem complicating general background subtraction and thresholding is that whatever is decided upon as “noise” or “background” is not necessarily the same over all parts of an image. Some methods have been developed that account

Tracing Branching Patterns for Fractal Analysis Simple Neurite Tracer

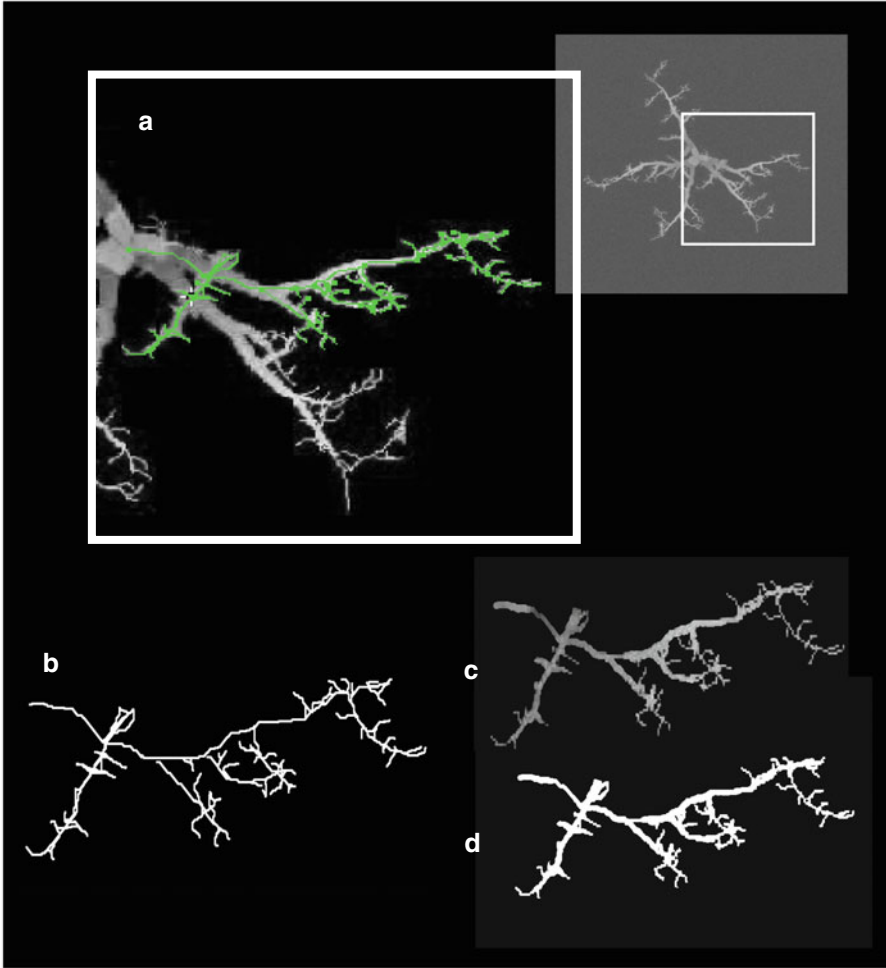


Fig. 32.4 Extracting branching patterns for fractal analysis in *IJ* (a) The green tracing is a path generated by the *Simple Neurite Tracer* [48]. The user clicks on points successively along a tortuous and branched structure (e.g., vessels or branched cells) and the plug-in automatically segments a basic skeleton. (Upper right) Original grayscale image of a modeled microglial cell. (b) Final skeleton generated by the plug-in. (c) Grayscale structure with background and unrelated cell parts removed automatically by the plug-in, based on the skeleton and parameters for filling in the area. (d) Binary silhouette generated by the plug-in from the grayscale trace and skeleton. (Cell model with stark background contrast generated with *MicroMod for IJ*, a plug-in for fractal modeling of biological cells [35])

for local variation within one image or in a stack or other set of images with the result that patterns can sometimes be extracted automatically or with very little intervention, but this is not the general case with most medical images [44]. There are many, many sophisticated segmentation algorithms available, each with its strengths and weaknesses. Recognizing this, Gabriel Landini, a researcher and *IJ* developer [44], has added to the core *IJ* software a built-in function that tests several algorithms at once and lets the investigator select a method for the work at hand.

This built-in function highlights an important point relevant to fractal analysis. If multiple patterns can be extracted from one image, that means investigation is required to test how different patterns translate to fractal dimensions [32, 44]. It also means automatic segmentation has a precarious side. To elaborate, *FracLac* and many related plug-ins such as the *Sholl Analysis* plug-in have options to automatically threshold [25, 34], but the option in *FracLac*, for instance, is a pilot testing convenience rather than a recommended strategy. It is vital to be aware that fully automatic thresholding cannot work on all original images simply because any automated segmentation method has a baseline whereby the programmer decides what is noise and what is signal, which may not agree with what the researcher decides is noise and signal. Even when looking at one image, an investigator's questions may be pertinent to different features and need two different thresholding methods to extract two different types of information (e.g., the overall tissue texture vs. individual cells in Fig. 32.1) [22].

32.4.2.4 Customized Pattern Extraction Methods

Much of the research done in fractal analysis of digital images in neuroscience involves custom pattern extraction methods involving variations on tracing and thresholding, but there are other, novel approaches. Wave data, for instance (meaning any sequence of values, such as EEG signals, sound, or other temporal data), can be converted to binary digital images for box counting analysis using the *Wave* command in *FracLac* [39]. Table 32.3 summarizes and compares some ways *IJ* has been used alone and with other means to inspire creative thinking in fractal-based neuroscience.

One particular example from Table 32.3d [13] succinctly illustrates a vital feature of *IJ* and similar open-source software in general. In that example, researchers asked how retinal microvessel complexity measured by the box-counting dimension (D_B) might be proxy for cerebral microcirculation pathology in CADASIL, a disorder having grave consequences including dementia. Working with retinal photographs obtained using a digital fundus camera, they found the mean D_B was significantly lower in patients than controls (1.426 vs. 1.506), suggesting that altered retinal vessel complexity might be a practical, noninvasive window into and early indicator of pathology in CADASIL. To come to that conclusion, they extracted patterns through the following summarized five steps using *IJ* functions:

Table 32.3 Examples of pattern extraction and fractal analysis methods implemented in *ImageJ*

Basic topic and model	Pattern extraction	Fractal dimension
(a) White matter		
<i>Texture</i> [59]		
Corpus callosum Anterior cingulum Digital micrographs Rat	Grayscale tiff of white mass	Box count: FracLac (texture) Discriminates adjacent white mass structures
<i>Multiple sclerosis</i> [22]		
Voxel-based slices Conventional MRI Human	Threshold slice, extract 2 binary patterns: 1. Skeleton of gyri within mass in IJ 2. Outline of entire mass in other software	Box count: HarFA [83] Identifies early brain changes in MS
(b) Cerebral arteries		
<i>Arteriovenous malformation</i> [69]		
Maximum intensity projections Time-of-flight MRI Human	Extract vessels and remove background with k-means clustering Binary skeleton in IJ	Box count: in-house Multifractal: FracLac Correlates with flow and size
<i>3-D reconstruction</i> [81]:		
Human Methods originally for neurons	Neuron Morpho [15]	Branching: L-Measure [63] Reconstructions now on free database
(c) Axonal architecture		
<i>Autism-related mutations</i> [29]		
Cells in culture Axon trajectories Rat	Binary network; white background; no somata or other structures; long and short, curved black lines of consistent diameter In-house software	Box count: FracLac Lacunarity: FracLac Mutations alter network architecture and synchrony
(d) Eye		
Cerebral autosomal dominant arteriopathy with subcortical infarcts and leukoencephalopathy (CADASIL) [13]		
Cerebral microcirculation Retinal fundus photographs Human	Binary contours Automated in IJ	Box count: FracLac Vessel complexity identifies early pathology
<i>Diabetic retinopathy</i> [41]		
Nonproliferative vs. proliferative Retinal digital images Fluorescein Human	Extract vasculature tree from 2 methods, then skeletonize in IJ 1. Automated continuous wavelet transform with supervised classification 2. Manual tracing	Box count: FracLac Local connected: FracLac Correlation: other Progress on automated, objective screening

Table 32.3 (continued)

Basic topic and model	Pattern extraction	Fractal dimension
<i>Choroid</i> [76]		
Neovascularization Microglial ramification Neuroprotectin D1(NPD1) Mice	3-D reconstruction from laser confocal microscopy Fiji and other	3-D: Shape and Fractal Count [6] Microglia are potential targets of NPD1

1. Split color channels using green filtering: Image>Color>Split Channels.
2. Select an ROI 3.5 times the optic disk radius and centered on it.
3. Subtract background using the mean optical density from four arbitrarily selected, vessel-free areas.
4. Convert to binary, automatically trace vessels: Process>Binary>Outline.
5. Manually remove artifacts if present [13].

The above description has pedagogical value beyond the method per se. With free, open-source software, methods such as this can be easily shared and reproduced, improved, or modified for related data sets. Being able to convey detailed steps of a method so that researchers can easily reproduce them, so that differences in lab resources are not a barrier to reproducing them, is an important feature of *IJ* that has the potential to significantly influence fractal-based neuroscience. It provides a level of continuity to enhance timely scientific development and advancement.

32.5 Conclusion

In conclusion, let us recap the answers to the questions posed at the beginning of this chapter (Sect. 32.1). The first question was “What is *IJ*?” The answer is that, substantially more than powerful, open-source image analysis software, *IJ* is both bio-tool and mindset. It removes barriers and promotes vigorous, collaborative neuroscience. It has matured alongside of and contributed to the presently materializing field of fractal-based neuroscience. It is a global project, an emergent feature of which is potential for inspiring creativity, and a platform for collaboration [15, 47, 70] especially useful now when information is amassing ahead of our ability to analyze it [40, 66]. Researchers working with *IJ* are not bound by existing methods of analysis but are instead able to rapidly customize and repeatedly hone solutions and therefore formulate questions creatively using it.

The second question was: “Where does *IJ* fit in fractal-based neuroscience today?” It occupies a prominent role in the published work of computational fractal-based neuroscience and multifarious collaborative roles in diverse areas relevant to the topic including industry and education. *IJ* has become a highly accessible avenue for researchers with and without computer programming background to join forces and fashion the tools they envision to answer questions about the fractal geometry of the brain at all levels, from gross to fine.

Moreover, despite becoming very powerful and being integrated in commercial applications, the main software itself remains practical and accessible, a bridge for sharing ideas and results with the nonexpert in many venues including the clinical picture of patient communication painted at the beginning of this chapter.

We hope this chapter has further inspired the reader to continue to demystify fractal analysis, to explore new fractal possibilities, to develop pattern extraction methods for new perspectives and especially for databases, to build that fly-through cell phone app, or to otherwise use the tools or embrace the mindset characteristic of *IJ* to bring the multiple levels of the fractal geometry of the brain to the fore, not just as a wonder of the digital age but as a clinical reality.

References

1. Abramoff M, Magalhaes P, Ram S. Image processing with ImageJ. *Biophoton Int.* 2004;11:36–42.
2. Abramyuk A, Wolf G, Shakirin G, Haberland U, Tokalov S, Koch A, Appold S, Zöphel K, Abolmaali N. Preliminary assessment of dynamic contrast-enhanced CT implementation in pretreatment FDG-PET/CT for outcome prediction in head and neck tumors. *Acta Radiol.* 2010;51(7):793–9.
3. Anderson JR, Barrett SF, Wilcox MJ. The segmentation and visualization of a neuron in the housefly's visual system. *Biomed Sci Instrum.* 2005;41:235–40.
4. Andjelkovic J, Zivic N, Reljin B, Celebic V, Salom I. Application of multifractal analysis on medical images. *WSEAS Trans Inf Sci Appl.* 2008;5(11):12.
5. Andrews S, Gilley J, Coleman MP. Difference tracker: ImageJ plugins for fully automated analysis of multiple axonal transport parameters. *J Neurosci Methods.* 2010;193(2):281–7.
6. Bache-Wiig and Per Christian Henden. "Fractal Count" 2004–2012. Haugesund, Norway. https://imagej.nih.gov/ij/plugins/download/misc/FractalCount_.java.
7. Barboriak DP, Padua AO, York GE, Macfall JR. Creation of DICOM – aware applications using ImageJ. *J Digit Imaging.* 2005;18(2):91–9.
8. Bellis M, Metias S, Naugler C, Pollett A, Jothy S, Yousef GM. Digital pathology: attitudes and practices in the Canadian pathology community. *J Pathol Informat.* 2013;4:3.
9. Bernard A, Campolmi N, He Z, Ha Thi BM, Piselli S, Forest F, Dumollard JM, Peoc'h M, Acquart S, Gain P, Thuret G. CorneaJ: an imageJ plugin for semi-automated measurement of corneal endothelial cell viability. *Cornea.* 2014;33(6):604–9.
10. Boudaoud A, Burian A, Borowska-Wykret D, Uyttewaal M, Wrzalik R, Kwiatkowska D, Hamant O. FibrilTool, an ImageJ plug-in to quantify fibrillar structures in raw microscopy images. *Nat Protoc.* 2014;9(2):457–63.
11. Captur G, Muthurangu V, Cook C, Flett AS, Wilson R, Barison A, Sado DM, Anderson S, McKenna WJ, Mohun TJ, Elliott PM, Moon JC. Quantification of left ventricular trabeculae using fractal analysis. *J Cardiovasc Magn Reson.* 2013;15:36.
12. Cardona A, Saalfeld S, Arganda I, Pereanu W, Schindelin J, Hartenstein V. Identifying neuronal lineages of *Drosophila* by sequence analysis of axon tracts. *J Neurosci.* 2010;30(22):7538–53.
13. Cavallari M, Falco T, Frontali M, Romano S, Bagnato F, Orzi F. Fractal analysis reveals reduced complexity of retinal vessels in CADASIL. *PLoS One.* 2011;6(4):e19150.
14. Chothani P, Mehta V, Stepanyants A. Automated tracing of neurites from light microscopy stacks of images. *Neuroinformatics.* 2011;9(2–3):263–78.
15. Collins TJ. ImageJ for microscopy. *Biotechniques.* 2007;43(1 Suppl):25–30.

16. Cornforth DJ, Tarvainen MP, Jelinek HF. How to calculate renyi entropy from heart rate variability, and why it matters for detecting cardiac autonomic neuropathy. *Front Bioeng Biotechnol.* 2014;34(2):1–8.
17. Davoudi B, Morrison M, Bizheva K, Yang VX, Dinniwell R, Levin W, Vitkin IA. Optical coherence tomography platform for microvascular imaging and quantification: initial experience in late oral radiation toxicity patients. *J Biomed Opt.* 2013;18(7):76008.
18. Deroulers C, Ameisen D, Badoual M, Gerin C, Granier A, Lartaud M. Analyzing huge pathology images with open source software. *Diagn Pathol.* 2013;8:92.
19. Doube M, Klosowski MM, Arganda-Carreras I, Cordelieres FP, Dougherty RP, Jackson JS, Schmid B, Hutchinson JR, Shefelbine SJ. BoneJ: free and extensible bone image analysis in ImageJ. *Bone.* 2010;47(6):1076–9.
20. Edelstein AD, Tsuchida MA, Amodaj N, Pinkard H, Vale RD, Stuurman N. Advanced methods of microscope control using muManager software. *J Biol Methods.* 2014;1(2):e10.
21. Égerházi L, Smausz T, Bari F. Inverted fractal analysis of TiOx thin layers grown by inverse pulsed laser deposition. *Appl Surf Sci.* 2013;278(0):106–10.
22. Esteban FJ, Sepulcre J, de Mendizabal NV, Goni J, Navas J, de Miras JR, Bejarano B, Masdeu JC, Villoslada P. Fractal dimension and white matter changes in multiple sclerosis. *Neuroimage.* 2007;36(3):543–9.
23. Falconer K. *Fractal geometry: mathematical foundations and applications.* Hoboken, NJ: Wiley; 2014.
24. Fanti Z, Martinez-Perez ME, De-Miguel FF. NeuronGrowth, a software for automatic quantification of neurite and filopodial dynamics from time-lapse sequences of digital images. *Dev Neurobiol.* 2011;71(10):870–81.
25. Ferreira TA, Blackman AV, Oyrer J, Jayabal S, Chung AJ, Watt AJ, Sjostrom PJ, van Meyel DJ. Neuronal morphometry directly from bitmap images. *Nat Methods.* 2014;11(10):982–4.
26. Girish V, Vijayalakshmi A. Affordable image analysis using NIH Image/ImageJ. *Indian J Cancer.* 2004;41(1):47.
27. Goni J, Sporns O, Cheng H, Aznárez-Sanado M, Wang Y, Josa S, Arrondo G, Mathews VP, Hummer TA, Kronenberger WG, Avena-Koenigsberger A, Saykin AJ, Pastor MA. Robust estimation of fractal measures for characterizing the structural complexity of the human brain: optimization and reproducibility. *Neuroimage.* 2013;83:646–57.
28. González AM, Garcia T, Samper E, Rickmann M, Vaquero EC, Molero X. Assessment of the protective effects of oral tocotrienols in arginine chronic-like pancreatitis. *Am J Physiol Gastrointest Liver Physiol.* 2011;301:G846–55.
29. Gutierrez RC, Hung J, Zhang Y, Kertesz AC, Espina FJ, Colicos MA. Altered synchrony and connectivity in neuronal networks expressing an autism-related mutation of neuroligin 3. *Neuroscience.* 2009;162(1):208–21.
30. Hamida T, Babadagli T. Fluid-fluid interaction during miscible and immiscible displacement under ultrasonic waves. *Eur Phys J B.* 2007;60(4):447–62.
31. Ho SY, Chao CY, Huang HL, Chiu TW, Charoenkwan P, Hwang E. NeurphologyJ: an automatic neuronal morphology quantification method and its application in pharmacological discovery. *BMC Bioinformatics.* 2011;12:230.
32. Ignacio Arganda-Carreras AC, Verena Kaynig, Schindelin J. Trainable Weka Segmentation. 2011.
33. ImageJ Features. National Institutes of Health. 2015. <http://rsb.info.nih.gov/ij/features.html>.
34. Jelinek H, Elston N, Zietsch B. Fractal analysis: pitfalls and revelations in neuroscience. In: *Fractals in biology and medicine.* Basel, Switzerland: Springer; 2005. p. 85–94.
35. Jelinek HF, Karperien A. Microglia modelling and analysis using L-systems grammar. In: Encarnação P, Veloso A, editors. *BIOSTEC 2008 International Joint Conference on Biomedical Engineering Systems and Technologies, Funchal, Madeira, Portugal, January 28–31, 2008. BIOSIGNALS 2008 International Conference on Bio-inspired Systems and Signal Processing.* Basel, Switzerland: Springer; 2008. p. 289–294.

36. Jelinek HF, Md Imam H, Al-Aubaidy H, Khandoker AH. Association of cardiovascular risk using non-linear heart rate variability measures with the Framingham risk score in a rural population. *Front Physiol.* 2013;186(4):1–8.
37. Karmonik C, York M, Grossman R, Kakkar E, Patel K, Haykal H, King D. An image analysis pipeline for the semi-automated analysis of clinical fMRI images based on freely available software. *Comput Biol Med.* 2010;40(3):279–87.
38. Karperien A. *FracLac for ImageJ*. Charles Sturt University. 2013.
39. Karperien A. *FracLac for ImageJ: JavaDoc, source code, and jar.* vol 7, 201501 edn. National Institutes of Health ImageJ Plugins. 2015.
40. Karperien A, Ahammer H, Jelinek HF. Quantitating the subtleties of microglial morphology with fractal analysis. *Front Cell Neurosci.* 2013;7:3.
41. Karperien A, Jelinek HF, Leandro JGG, Soares JVB, Cesar J, Roberto M, Luckie A. Automated detection of proliferative retinopathy in clinical practice. *Clin Ophthalmol.* 2008;2(1):109–22.
42. Kohn-Luque A, de Back W, Starruss J, Mattiotti A, Deutsch A, Perez-Pomares JM, Herrero MA. Early embryonic vascular patterning by matrix-mediated paracrine signalling: a mathematical model study. *PLoS One.* 2011;6(9):e24175.
43. Krippendorf BB, Lough J. Complete and rapid switch from light microscopy to virtual microscopy for teaching medical histology. *Anat Rec B New Anat.* 2005;285(1):19–25.
44. Landini G. *Auto Threshold.* v1.15 (19 Feb 2013) edn. 2013.
45. Landini G, Murray PI, Misson GP. Local connected fractal dimensions and lacunarity analyses of 60 degrees fluorescein angiograms. *Invest Ophthalmol Vis Sci.* 1995;36(13):2749–55.
46. Linkert M, Rueden CT, Allan C, Buel JM, Moore W, Patterson A, Loranger B, Moore J, Neves C, Macdonald D, Tarkowska A, Sticco C, Hill E, Rossner M, Eliceiri KW, Swedlow JR. Metadata matters: access to image data in the real world. *J Cell Biol.* 2010;189(5):777–82.
47. LISTSERV 16.0 – IMAGEJ List at LIST.NIH.GOV. Center for Information Technology, US National Institutes of Health. <https://list.nih.gov/cgi-bin/wa.exe?A0=IMAGEJ>. Accessed 23 Jan 2015.
48. Longair MH, Baker DA, Armstrong JD. Simple neurite tracer: open source software for reconstruction, visualization and analysis of neuronal processes. *Bioinformatics.* 2011;27(17):2453–4.
49. Losa GN, Theo F, Merlini D, Weibel ER, editors. *Fractals in biology and medicine, vol II. Mathematics and biosciences in interaction.* Basel: Birkhauser; 1997.
50. Mailly P, Haber SN, Groenewegen HJ, Deniau JM. A 3D multi-modal and multi-dimensional digital brain model as a framework for data sharing. *J Neurosci Methods.* 2010;194(1):56–63.
51. Mancardi D, Varetto G, Bucci E, Maniero F, Guiot C. Fractal parameters and vascular networks: facts & artifacts. *Theor Biol Med Model.* 2008;5:12.
52. Mandelbrot, Evertsz, Hayakawa. Exactly self-similar left-sided multifractal measures. *Phys Rev A.* 1990;42(8):4528–36.
53. Mandelbrot BB. *The fractal geometry of nature.* Updated and augmented. edn. New York: Freeman WH; 1983.
54. Meijering E. Neuron tracing in perspective. *Cytom Part A: J Int Soc Anal Cytol.* 2010;77(7):693–704.
55. Meijering E, Jacob M, Sarria JC, Steiner P, Hirling H, Unser M. Design and validation of a tool for neurite tracing and analysis in fluorescence microscopy images. *Cytometry Part A: J Int Soc Anal Cytol.* 2004;58(2):167–76.
56. Mutterer J, Rasband W. *ImageJ macro language programmer's reference guide* v1.46d.
57. NIH/NLM. PubMed Central. U.S. National Institutes of Health's National Library of Medicine. 2015. <http://www.ncbi.nlm.nih.gov/pmc/?term=ImageJ>. Accessed 5 Aug 2015.

58. Pani G, De Vos WH, Samari N, de Saint-Georges L, Baatout S, Van Oostveldt P, Benotmane MA. MorphoNeuroNet: an automated method for dense neurite network analysis. *Cytom Part A : J Int Soc Anal Cytol.* 2014;85(2):188–99.
59. Pantic I, Dacic S, Brkic P, Lavrnja I, Pantic S, Jovanovic T, Pekovic S. Application of fractal and grey level co-occurrence matrix analysis in evaluation of brain corpus callosum and cingulum architecture. *Microsc Microanal.* 2014;20(5):1373–81.
60. Park S, Pantanowitz L, Parwani AV. Digital imaging in pathology. *Clin Lab Med.* 2012;32(4):557–84.
61. Patton N, Aslam TM, MacGillivray T, Deary IJ, Dhillon B, Eikelboom RH, Yogesan K, Constable IJ. Retinal image analysis: concepts, applications and potential. *Prog Retin Eye Res.* 2006;25(1):99–127.
62. Peng T, Wang L, Bayer C, Conjeti S, Baust M, Nava N. Shading correction for whole slide image using low rank and sparse decomposition. *Med Image Comput Comput Assist Interv.* 2014;17(Pt 1):33–40.
63. Scorcioni R, Polavaram S, Ascoli GA. L-Measure: a web-accessible tool for the analysis, comparison and search of digital reconstructions of neuronal morphologies. *Nat Protoc.* 2008;3(5):866–76.
64. Pool M, Thiemann J, Bar-Or A, Fournier AE. NeuriteTracer: a novel ImageJ plugin for automated quantification of neurite outgrowth. *J Neurosci Methods.* 2008;168(1):134–9.
65. Prasad K, Prabhu GK. Image analysis tools for evaluation of microscopic views of immunohistochemically stained specimen in medical research—a review. *J Med Syst.* 2012;36(4):2621–31.
66. The quest for quantitative microscopy. *Nat Methods.* 2012;9(7):627.
67. Rasband W. Basic Concepts. US National Institutes of Health. 2015. <http://rsb.info.nih.gov/ij/docs/concepts.html>. Accessed 22 Jan 2015.
68. Rasband W. Plugins. U.S. National Institutes of Health. 2015. <http://rsb.info.nih.gov/ij/plugins/>.
69. Reishofer G, Koschutnig K, Enzinger C, Ebner F, Ahammer H. Fractal dimension and vessel complexity in patients with cerebral arteriovenous malformations. *PLoS One.* 2012;7(7):e41148.
70. Reuden C. ImageJ Net. <http://imagej.net/ImageJ>. 2015.
71. Rueden CT, Eliceiri KW. Visualization approaches for multidimensional biological image data. *Biotechniques.* 2007;43(1 Suppl):31, 33–36.
72. Sage D, Prodanov D, Tinevez J-Y, Schindelin J. MIJ: making interoperability between ImageJ and Matlab possible. Paper presented at the ImageJ User & Developer Conference, Luxembourg. 2012. 24–26 Oct 2012.
73. Schindelin J, Arganda-Carreras I, Frise E, Kaynig V, Longair M, Pietzsch T, Preibisch S, Rueden C, Saalfeld S, Schmid B, Tinevez JY, White DJ, Hartenstein V, Eliceiri K, Tomancak P, Cardona A. Fiji: an open-source platform for biological-image analysis. *Nat Methods.* 2012;9(7):676–82.
74. Schmid B, Schindelin J, Cardona A, Longair M, Heisenberg M. A high-level 3D visualization API for Java and ImageJ. *BMC Bioinforma.* 2010;11:274.
75. Schneider CA, Rasband WS, Eliceiri KW. NIH image to ImageJ: 25 years of image analysis. *Nat Methods.* 2012;9(7):671–5.
76. Sheets KG, Jun B, Zhou Y, Zhu M, Petasis NA, Gordon WC, Bazan NG. Microglial ramification and redistribution concomitant with the attenuation of choroidal neovascularization by neuroprotectin D1. *Mol Vis.* 2013;19:1747–59.
77. Smith Jr TG, Lange GD, Marks WB. Fractal methods and results in cellular morphology – dimensions, lacunarity and multifractals. *J Neurosci Methods.* 1996;69(2):123–36.
78. Smith Jr TG, Marks WB, Lange GD, Sheriff Jr WH, Neale EA. A fractal analysis of cell images. *J Neurosci Methods.* 1989;27(2):173–80.
79. Țălu Ș, Giovanzana S. Image analysis of the normal human retinal vasculature using fractal geometry. *Int J Bioflux Soc.* 2012;4(1):5.

80. Trevino J, Liew SF, Noh H, Cao H, Dal Negro L. Geometrical structure, multifractal spectra and localized optical modes of aperiodic Vogel spirals. *Opt Express*. 2012;20(3):3015–33.
81. Wright SN, Kochunov P, Mut F, Bergamino M, Brown KM, Mazziotta JC, Toga AW, Cebal JR, Ascoli GA. Digital reconstruction and morphometric analysis of human brain arterial vasculature from magnetic resonance angiography. *Neuroimage*. 2013;82:170–81.
82. Xu Y, Qian C, Pan L, Wang B, Lou C. Comparing monofractal and multifractal analysis of corrosion damage evolution in reinforcing bars. *PLoS One*. 2012;7(1):e29956.
83. Zmeskal O, Bzatek T, Nežadal M, Buchnec M. “HarFA: Harmonic and Fractal Image Analysis”, 2001; Brno University of Technology, Czech Republic. http://www.fch.vut.cz/lectures/imagesci/main_menu.php.

Chapter 33

Fractal Analysis in MATLAB: A Tutorial for Neuroscientists

Juan Ruiz de Miras

Abstract MATLAB is one of the software platforms most widely used for scientific computation. MATLAB includes a large set of functions, packages, and toolboxes that make it simple and fast to obtain complex mathematical and statistical computations for many applications. In this chapter, we review some tools available in MATLAB for performing fractal analyses on typical neuroscientific data in a practical way. We provide detailed examples of how to calculate the fractal dimension of 1D, 2D, and 3D data in MATLAB. Furthermore, we review other software packages and several online tools available for fractal analysis.

Keywords Fractal analysis • Fractal dimension • MATLAB

33.1 MATLAB Packages and Toolboxes for Fractal Analysis

Boxcount [19] is one of the first MATLAB scripts developed for computing the fractal dimension (FD) of 1D, 2D, or 3D sets. As its name indicates, *Boxcount* estimates the FD of a set by using the box-counting method [18]. It can be only used with binary datasets (for an RGB image, for example, a previous summation of the three components is performed) and the box sizes used to estimate the fractal dimension must be power of two. *Boxcount* is a MATLAB function that must be integrated into other MATLAB scripts in order to be executed.

FracLab [14] is veteran MATLAB software that allows fractal analysis of 1D signals and 2D images, but analysis of 3D sets is not supported. All the functionality of *FracLab* is accessible through a graphical interface, so no direct MATLAB programming is needed. *FracLab* allows the user to calculate not only the fractal dimension of the set but also parameters like the Hölder exponent or multifractal spectra.

J. Ruiz de Miras
Computer Science Department, University of Jaén, Jaén 23071, Spain
e-mail: demiras@ujaen.es

For the case of 1D signals, the FD is commonly estimated by using Higuchi's algorithm [12], and there are several MATLAB implementations of this algorithm [23, 26]. Another well-known technique for estimating the FD of a 1D signal is Katz's algorithm [17]. In [20] a MATLAB implementation of this algorithm is provided. Unlike Higuchi's algorithm, which needs a manual-set parameter in order to establish the maximum size of the intervals to consider for approximating the 1D signal, Katz's algorithm can calculate the fractal dimension automatically without needing manual-set parameters. Some studies [8] have proven that Higuchi's algorithm is more accurate but also more noise sensitive than Katz's algorithm.

The FD value is associated to static structures; nevertheless, the multifractal spectrum [1] is a useful parameter in the fractal analysis of structures that present spatial and temporal variations. A detailed description and the related MATLAB scripts used to calculate the multifractal spectrum of biomedical time series can be found in [13, 28].

33.2 MATLAB Examples: Fractal Dimension Computation for 1D, 2D, and 3D Sets

The FD is the most commonly used parameter in fractal analysis. A recent review of applications of the FD parameter in the neuroscience field can be found in [7]. In this section, we show several step-by-step practical examples of how the FD parameter can be computed in MATLAB for typical neuroscientific data in 1D, 2D, and 3D.

33.2.1 EEG Fractal Dimension

In this first example, we describe how to estimate the FD of an electroencephalograph (EEG), a unidimensional signal commonly used in neuroscience. For this purpose, we use two different MATLAB implementations of FD: Higuchi's algorithm provided in [23] and Katz's algorithm provided in [20]. Figure 33.1 shows the signals of the same electrode for two different EEGs and the results of the two FD estimations for them. The MATLAB script that generates these results is shown in Listing 33.1.

In Listing 33.1, the EEG data is provided in European Data Format (EDF), a format for the exchange and storage of multichannel biological and physical signals. EDF files in Listing 33.1 are read by using the function `edfread()`, available from [25]. It is easy to import or export EEG data to EDF format through well-known MATLAB toolboxes like EEGLAB [6]. Katz's algorithm does not have any parameter to set. However, Higuchi's function `hfd()` needs to establish the parameter `kmax`, indicating the maximum value for k in Higuchi's algorithm [12].

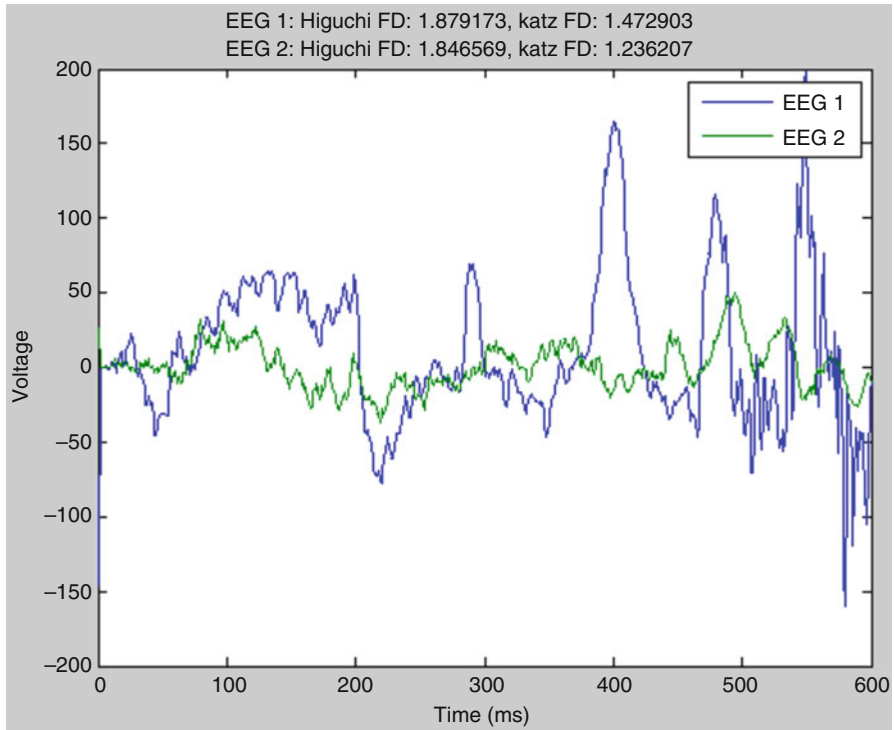


Fig. 33.1 Two EEG signals and their Higuchi's and Katz's FD values

```

% Load EEG data in EDF format
[hdr1, eeg1] = edfread('eeg1.edf');
[hdr2, eeg2] = edfread('eeg2.edf');

% Higuchi and Katz Fractal Dimension computation
maxtime = 600; % for the entire signal use maxtime = length(eeg1(1,:));
kmax = floor(maxtime / 2); % parameter needed in hfd function, set by default
elec = 1; % electrode to process

hfd1 = hfd(eeg1(elec, 1:maxtime), kmax);
kfd1 = Katz_FD(eeg1(elec, 1:maxtime));

hfd2 = hfd(eeg2(elec, 1:maxtime), kmax);
kfd2 = Katz_FD(eeg2(elec, 1:maxtime));

% Plots the results
plot(1:maxtime, [eeg1(elec, 1:maxtime); eeg2(elec, 1:maxtime)]);
tit = sprintf('EEG 1: Higuchi FD: %f, Katz FD: %f\nEEG 2: Higuchi FD: %f, Katz FD: %f',...
             hfd1, kfd1, hfd2, kfd2);
title(tit); xlabel('Time (ms)'); ylabel('Voltage'); legend('EEG 1', 'EEG 2');

```

Listing 33.1 MATLAB code used to calculate the FD of an EEG by using both Higuchi's and Katz's algorithms

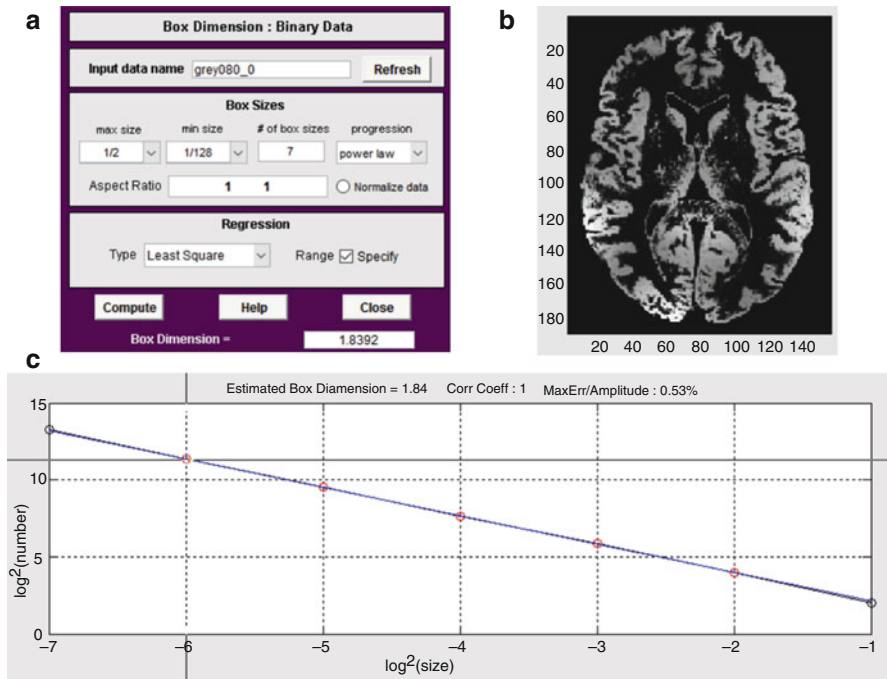


Fig. 33.2 Fractal dimension computation with *FracLab*. (a) Parameter selection for the box-counting method. (b) The gray matter slice to be processed. (c) Selection of the interval of box sizes to calculate the linear regression for estimating the fractal dimension value

33.2.2 Brain MRI Fractal Dimension of the Gray Matter with *FracLab*

In this example, it is shown how to calculate the FD value of a 2D image of the gray matter from a slice of an MR image of the human brain. First, we have to segment the original MR to extract the gray matter by using, for example, the SPM (statistical parametric mapping) toolbox [2] for MATLAB. The next step consists of selecting one slice of the segmented 3D image and extracting it to a single file in BMP format. This task can be easily performed with the software MRICron [21]. Then we load the BMP file of the slice into *FracLab* and execute the *box method* for binary data. Several parameters allow us to configure the box sizes and the type of linear regression used to estimate the FD. Figure 33.2a shows an example of the values used to calculate the fractal dimension of the gray matter slice of size 189×157 shown in Fig. 33.2b. Finally, the interval of box sizes used to perform the linear regression is manually selected (red dots) as shown in Fig. 33.2c, obtaining a fractal dimension value of 1.839 for this example.

33.2.3 *Fractal Dimension Computation of an MRI Volume of the Brain White Matter with a Boxcount-Based MATLAB Script*

In the last example, we show how to calculate the FD of a 3D volume representing the brain white matter. The main MATLAB function that we use for this process is *Boxcount*. The first step is the same as in the previous section; we have to segment the white matter of the original 3D MR image. This task can be performed with the toolbox SPM, as previously described. The segmented volume of the white matter is obtained from SPM in ANALYZE format (HDR and IMG files), although another usual file format for dealing with MRI data is the NIFTI format. We have several choices for loading this kind of 3D image into MATLAB: (1) we can extract the BMP file for each slice of the 3D image with MRICron software and then load all the individual BMPs into a single 3D MATLAB matrix through a loop where the MATLAB function `imread()` loads each individual BMP into the corresponding layer of the 3D matrix; (2) we can load an *analyze75* file directly into a MATLAB matrix by using the function `analyze75read()`; (3) NIFTI files are not directly supported by MATLAB functions, but there exist MATLAB toolboxes, such as the one in [24], allowing us to manage them. We can load a NIFTI image into MATLAB by using the function `load_nii()`. The 3D representation of the brain white matter that we use through this section is shown in Fig. 33.3.

The next step consists of performing the box counting of the 3D image. In this example, we use the *Boxcount* function introduced in Sect. 33.1. This function returns two arrays: an array (r) containing the incremental sizes of the boxes used to cover the 3D image and another array (n) containing the number of boxes of each size in r covered or partially covered by the 3D image. For our 3D white matter representation in Fig. 33.3, the arrays have these values:

- $r = [1; 2; 4; 8; 16; 32; 64; 128; 256]$
- $n = [1138742; 171868; 26976; 4141; 667; 121; 25; 7; 1]$

From these data, we can easily calculate the fractal dimension by computing the slope of the linear regression of the log-log plot of $1/r$ versus n . Least-squares linear regression in MATLAB can be obtained with the `\operator` (equivalent to the `mldivide()` function). Figure 33.4a shows the log-log plot, the regression line, and the final fractal dimension value calculated for our 3D image. In order to select the linear range of the regression line, we have selected the range of box sizes from 1 to 4. This selection was based on the plot provided by the function `boxcount(img, 'slope')`, shown in Fig. 33.4b; this plot provides us with the evolution of the exponent $D = -d \ln(n) / \ln(r)$ for all the box sizes in r . As you can see in Fig. 33.4b, this exponent (local dimension) is almost constant (around 2.7) in the range 1–4. Finally, the full MATLAB script used to obtain the fractal dimension from a 3D image is shown in Listing 33.2.

Fig. 33.3 3D MR imaging of the brain white matter (example described in the text)

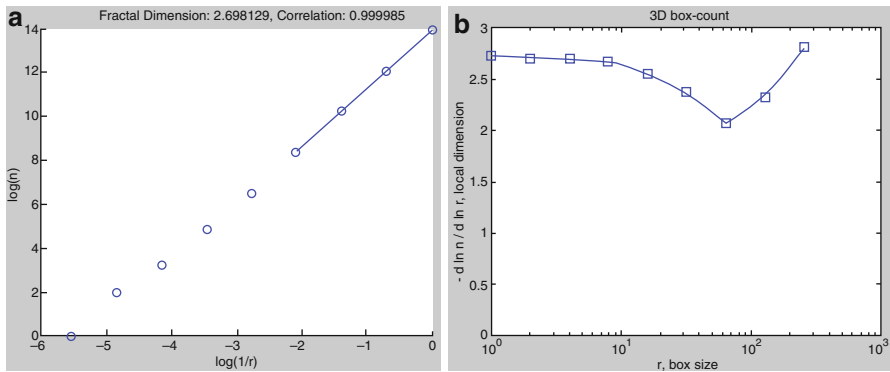
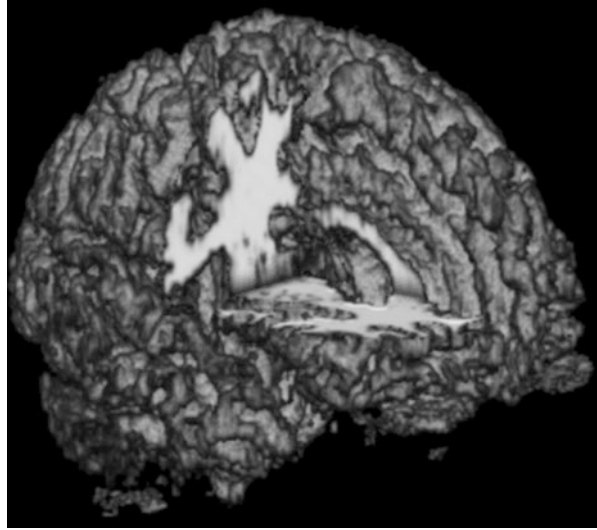


Fig. 33.4 (a) Log-log plot of box size versus number of voxels and the fractal dimension value for the 3D representation of the white matter. (b) Plot of the local dimension shows that it is almost constant in the range 1–4

33.3 Other Software and Online Resources for Fractal Analysis

If you do not have access to MATLAB software or prefer to perform fractal analysis using stand-alone software through a graphic user interface, then you have some choices on your hands: *BENOIT* [3] is paid software from TruSoft Inc that allows the FD and hurst exponent of 1D, 2D, and 3D data sets to be measured using a set of methods. *BENOIT* only runs on Windows operating systems, but a MATLAB

```

% loads the 3D image from a NIFTI file (.nii.gz)
% requires the package "Tools for NIFTI and ANALYZE image"
% http://www.mathworks.com/matlabcentral/fileexchange/8797-tools-for-nifti-and-analyze-image
image = load_nii('white.nii.gz');

% shows the image loaded
view_nii(image);

% box-counting computation
% requires the package "BoxCount"
% http://www.mathworks.com/matlabcentral/fileexchange/13063-boxcount
c = image.img; % extracts the 3D matrix of the image
[n, r] = boxcount(c); % computes the box-counting

boxcount(c, 'slope'); % plots the local dimension to select the range of box sizes

% log-log plot of the box-counting
N = log(n)';
R = log(r.^-1)';
scatter(R, N);
hold on;

% linear regression computation
ini = 1; % initial box size
fin = 4; % final box size
Rr = R(ini : fin); % R limited to the selected range of boxes
Nr = N(ini : fin); % N limited to the selected range of boxes

x = [ones(length(Rr), 1) Rr]; % adds a column of ones to Rr
b = x \ Nr; % b(1) is the y-intercept and b(2) is the slope of the line
y = x * b; % linear regression
corr = 1 - sum((Nr - y).^2) / sum((Nr - mean(Nr)).^2); % correlation

% plots the regression line and the fractal dimension results
plot(Rr, y);
xlabel('log(1/r)');
ylabel('log(n)');
title(sprintf('Fractal Dimension: %f, Correlation: %f', b(2), corr));

```

Listing 33.2 MATLAB code used to calculate the fractal dimension of a 3D image

version of BENOIT is also available. FDC [4] is another MAC OS paid software for computing the FD of a black and white image. *Fractalys* [27] is a computer program running on Windows and Linux that estimates the FD of binary images by using several algorithms. The FD value of grayscale images can be computed using the Windows program *Fdim* [9]. A Visual BASIC software for estimating the FD of grayscale objects of up to 4D on the Windows platform was presented in [10]. Two popular programs for analyzing 2D images are *ImageJ* [22] and *HarFa* [11]. Fractal analysis in *ImageJ* can be performed through the plug-in *FracLac* [16] (see Chap. 32). *ImageJ* is written in Java, so it can be executed in any platform supporting Java. *HarFa* is a Windows program specifically designed to perform harmonic and fractal analysis on images. *ImageJ* and *HarFa* estimate the fractal dimension by using the box-counting method.

There are also several online tools for performing fractal analysis on a Web browser. A Java applet that estimates the FD value of an image by means of the box-counting algorithm is available from [5]. In [15] a Web platform for calculating and visualizing the FD of MRI data is presented. This platform calculates the fractal dimension of 3D MRI volumes by using the box-counting method and allows an interactive comparison of the results obtained for a set of images.

Table 33.1 Summary of fractal analysis software

Software	Platforms	Algorithms	Data	Commercial	Reference
Boxcount ()	MATLAB	FD (box counting)	1D, 2D, 3D binary	No	[19]
FracLab	MATLAB	FD, holder exponent, multifractal analysis	1D, 2D	No	[14]
hfd ()	MATLAB	FD (Higuchi)	1D	No	[23]
HFDCALC ()	MATLAB	FD (Higuchi)	1D	No	[26]
Katz_FD ()	MATLAB	FD (Katz)	1D	No	[20]
WLBMF	MATLAB	Multifractal analysis	1D, 2D	No	[28]
BENOIT	Windows	FD, Hurst exponent	1D, 2D, 3D	Yes	[3]
FDC	MAC	FD	2D binary	Yes	[4]
Fractalyse	Windows, Linux	FD	2D binary	No	[27]
FDim	Windows	FD	2D grayscale	No	[9]
Fractal Analysis v3	Windows	FD	1D, 2D, 3D, 4D grayscale	No	[10]
ImageJ	Java	FD, multifractal analysis	2D	No	[22]
HarFa	Windows	FD (box counting)	2D	No	[11]
http://www.stevec.org/fracdim	Web	FD (box counting)	2D binary	No	[5]
http://3dfd.ujaen.es	Web	FD (box counting)	3D binary	Yes	[15]

33.4 Conclusions

In this chapter we have reviewed several MATLAB packages and toolboxes, as well as other software and online resources, used to perform fractal analysis on 1D, 2D, and 3D data sets. We have provided practical examples on how to compute the fractal dimension in MATLAB for typical neurological signals and images. To summarize, Table 33.1 shows a comparative synopsis of all the software reviewed.

Acknowledgments This work has been partially supported by the University of Jaén, the Caja Rural de Jaén, the Ministry of Economy and Competitiveness, and the European Union (via ERDF funds) through the research projects UJA2013/12/04, UJA2013/08/35, TIN2014-58218-R, and MTM2014-61312-EXP.

References

1. Abry P, Jaffard S, Wendt H. Irregularities and scaling in signal and image processing: multi-fractal analysis. In: M. Frame Ed. Benoit Mandelbrot: a life in many dimensions. World Scientific, Singapore. 2012.
2. Ashburner J. SPM: a history. *Neuroimage*. 2012;62(2):791–800. SPM software available from <http://www.fil.ion.ucl.ac.uk/spm>.
3. BENOIT. Fractal Analysis System. TruSoft Inc. Available from <http://www.trusoft-international.com>.
4. Bourke P. Fractal Dimension Calculator. 2003. Available from <http://paulbourke.net/fractals/fracdim>.
5. Crampton S. A Java Applet to Compute Fractal Dimensions. Available from <http://www.stevec.org/fracdim>.
6. Delorme A, Makeig S. EEGLAB: an open source toolbox for analysis of single-trial EEG. *J Neurosci Methods*. 2004;134:9–21. MATLAB toolbox available from <http://sccn.ucsd.edu/eeglab>.
7. Di Ieva A, Esteban FJ, Grizzi F, Klonowski W, Martín-Landrove M. Fractals in the neurosciences, part II: clinical applications and future perspectives. *Neuroscientist*. 2015;21(1):30–43.
8. Esteller R, Vachtsevanos G, Echaz J, Litt B. A comparison of waveform fractal dimension algorithms. *IEEE Trans Circuits Syst I Fund Theory Appl*. 2001;48(2):177–83.
9. FDim. Laboratory for computational longitudinal neuroimaging. Harvard Medical School. Available from <http://reuter.mit.edu/software/fdim>.
10. Grossu IV, Grossu I, Felea D, Besliu C, Jipa AL, Esanu T, Bordeianu CC, Stan E. Hyperfractal analysis: visual tool for estimating the fractal dimension of 4D objects. *Comput Phys Commun*. 2013;184(4):1344–5.
11. HarFa. Harmonic and fractal image analyzer. Available from <http://www.fch.vutbr.cz/lectures/imagesci>.
12. Higuchi T. Approach to an irregular time series on the basis of the fractal theory. *Physica D Nonlinear Phenomena*. 1988;31(2):277–83.
13. Ihnlen EAF. Introduction to multifractal detrended fluctuation analysis is in Matlab. *Front Physiol Fractal Physiol*. 2012;3(141):1–18.
14. INRIA. FracLab: a fractal analysis tool for signal and image processing. Available from <http://fraclab.saclay.inria.fr>.
15. Jiménez J, López AM, Cruz J, Esteban FJ, Navas J, Villoslada P, Ruiz de Miras J. A web platform for the interactive visualization and analysis of the 3D fractal dimension of MRI data. *J Biomed Inform*. 2014;51:176–90.
16. Karperien, A. FracLac for ImageJ. 1999–2013. Available from <http://rsbweb.nih.gov/ij/plugins/fraclac/FLHelp/Introduction.htm>.
17. Katz M. Fractals and the analysis of waveforms. *Comput Biol Med*. 1988;18(3):145–56.
18. Mandelbrot BB. *The fractal geometry of nature*. New York: Freeman; 1982.
19. Moisy F. Computing a fractal dimension with Matlab: 1D, 2D and 3D Box-counting. Available from <http://www.mathworks.com/matlabcentral/fileexchange/13063-boxcount>.
20. Monge-Álvarez J. Higuchi and Katz fractal dimension measures. Available from <http://www.mathworks.com/matlabcentral/fileexchange/50290-higuchi-and-katz-fractal-dimension-measures>.
21. MRICron software. Available from: <http://www.mccauslandcenter.sc.edu/mricro/mricron>.
22. Rasband, WS. ImageJ. Image processing and analysis in Java. 1997–2015. Available from <http://imagej.nih.gov/ij>.
23. Selvman S. Complete Higuchi fractal dimension algorithm. Available from <http://www.mathworks.com/matlabcentral/fileexchange/30119-complete-higuchi-fractal-dimension-algorithm>.
24. Shen J. Tools for NIFTI and ANALYZE image. 2005. Available from <http://www.mathworks.com/matlabcentral/fileexchange/8797-tools-for-nifti-and-analyze-image>.

25. Shoelson B. edfRead: a simple file reader for European Data Formatted (EDF-) files. Available from <http://www.mathworks.com/matlabcentral/fileexchange/31900-edfread>.
26. Sumanth. Simple Higuchi fractal dimension implementation. 2012. Available from <http://www.mathworks.com/matlabcentral/fileexchange/36027-simple-higuchi-fractal-dimension-implementation>.
27. Vuidel G. Fractalyse – fractal analysis software. Available from <http://www.fractalyse.org>.
28. Wendt H. Wavelet leader and bootstrap based MultiFractal analysis (WLBMF) toolbox. Available from <http://www.irit.fr/~Herwig.Wendt/software.html>.

Chapter 34

Methodology to Increase the Computational Speed to Obtain the Fractal Dimension Using GPU Programming

Juan Ruiz de Miras and Jesús Jiménez Ibáñez

Abstract Computing the fractal dimension (FD) can be a very time-consuming process. Nowadays, the data precision or resolution of many sensors is increasingly high (magnetic resonance, ultrasounds, microcomputed tomography, etc.) and, furthermore, some applications require 3D data post-processing. The processing of large data sets is also very common in several analyses and applications. Therefore, fast algorithms for computing the FD are required, above all for interactive applications. Graphics processing unit (GPU) programming has become a standard tool for optimizing certain sorts of time-consuming algorithms. If the problem fits the GPU programming model well, high speedups can be achieved. CUDA and OpenCL are two of the most popular GPU technologies since they do not require special knowledge of computer graphics programming. In this chapter, we present our experience optimizing the processing time of the classic box-counting algorithm to compute the FD by means of CUDA and OpenCL GPU programming. Speedups of up to 28× (CUDA) and 6.3× (OpenCL) against the single-thread CPU version of the algorithm have been obtained. CUDA results are better because the box-counting algorithm has a strong dependency on sorting, and the OpenCL implementations of the best sorting algorithms are not as efficient as the CUDA ones.

Keywords 3D fractal dimension • GPU • Box counting • CUDA • OpenCL

J. Ruiz de Miras (✉) • J. Jiménez Ibáñez
Computer Science Department, University of Jaén, 23071 Jaén, Spain
e-mail: demiras@ujaen.es

34.1 An Introduction to GPU Programming

GPU programming has become a standard technique for optimizing highly time-consuming algorithms, especially within the biomedical field. As reviewed in [9, 31], there are several applications of GPU computing used to accelerate computationally demanding algorithms for medical imaging.

Not only is GPU computing power constantly increasing, but GPUs are also much cheaper than traditional parallel computers. These are the main reasons why GPU programming is a very interesting solution for optimizing those time-consuming algorithms, which can be parallelized. However, using the GPU to code algorithms for general purposes (not related to graphics visualization) can be slightly difficult, since a deep knowledge of the graphic pipeline and its specific data structures is required. Several innovative technologies have been developed in order to overcome these difficulties, such as CUDA [24] for NVIDIA GPUs and OpenCL [17] for GPUs and multi-core CPUs. CUDA and OpenCL do not require the programmers to know the graphic pipeline of the GPU because these technologies are simple extensions of well-known programming languages like C/C++, CUDA and OpenCL are very similar technologies. Both technologies are based on providing access to hundreds of processing cores through the parallel execution of thousands of *threads*, i.e., pieces of the same code that are concurrently executed. The main difference between the two technologies is that OpenCL is cross-platform, meaning that the same OpenCL program can be executed in any GPU or multi-core CPU that supports OpenCL, regardless of their manufacturer. On the other hand, CUDA can be executed only on NVIDIA GPUs. Below we briefly show the main features of CUDA and OpenCL.

34.1.1 NVIDIA CUDA

CUDA application program interface (API) allows programmers to place data in the GPU memory and execute *kernels* to process this data. A *kernel* is a GPU program that is called as many times as threads are needed to process the data. Therefore, each kernel applies the same operations on each data element. This is known as single instruction multiple data (SIMD) processing. Threads, which execute the kernel, are grouped into 1D, 2D, or 3D structures called *thread blocks* or simply *blocks*. In the same way, these blocks can also be grouped into 1D, 2D, or, from CUDA version 4.4, 3D structures called *grids*. This hierarchy allows the programmer to set the kernel execution in the way that best fits the structure or organization of the data to process. Figure 34.1 shows the GPU execution hierarchy based on threads, blocks, and grids. The threads in each block are executed in groups of 32, called *warps*. Many blocks are simultaneously executed. The exact number of blocks executing at the same time depends on the available resources of the GPU (number of cores, amount of memory, registers, etc.).

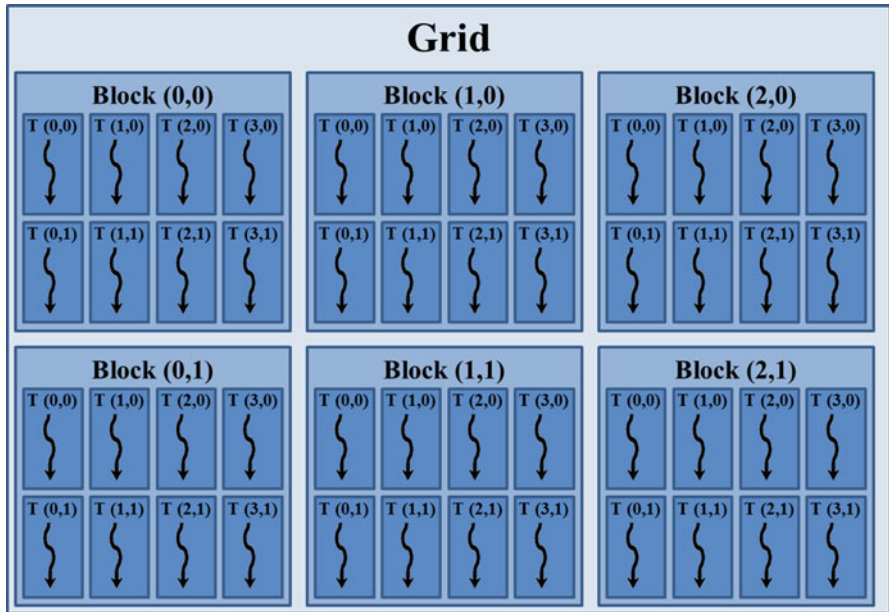


Fig. 34.1 CUDA grid-block-thread organization. A 2D grid with 3x2 blocks. Blocks have 4x2 threads each

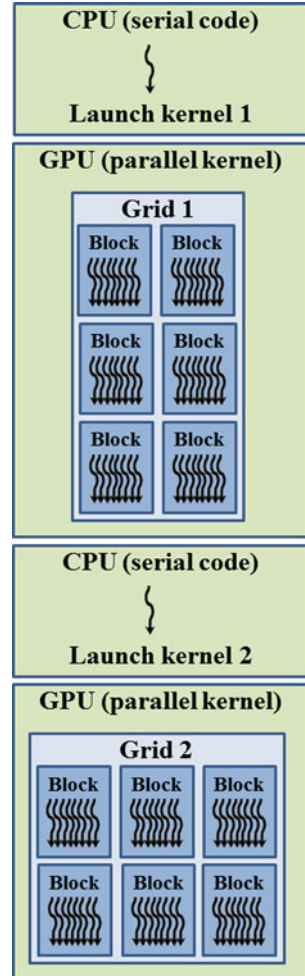
In general terms, the software architecture of CUDA consists of a single-thread *host* program, which is executed in the CPU, and a kernel launched by the host program that is executed in parallel by means of thousands of threads in the GPU. The control flow is returned to the host program (CPU) when all threads have ended their execution; and then the host program can launch other kernels into the GPU [16]. This way, the sequential parts of the algorithm are executed in CPU, while the parts of the algorithm that can be parallelized are executed as kernels in GPU. Figure 34.2 shows the graphical representation of the execution of a host program with two CUDA kernels. From version 5.0 of CUDA, and requiring NVIDIA Kepler architecture, it is also possible that a GPU kernel launches other kernels, what is called *dynamic parallelism*.

A common CUDA program usually follows the following steps:

1. Allocation of memory in GPU
2. Transferring data to be processed from CPU to GPU
3. Setting up the parameters for the execution in GPU, such as the number of threads per block, number of blocks, dimensionality in thread-block-grid structure, etc.
4. Execution of the kernel, storing the results in the GPU memory
5. Transferring of results from GPU to the RAM memory in CPU

Regarding the hardware architecture, a CUDA GPU is composed of a set of *multiprocessors* (MP) each one containing a set of *scalar processors* (SP). Each SP

Fig. 34.2 Execution of a program in CUDA



has a local memory and a set of registers. On the other hand, each MP has its own memory, called *shared memory*, which is accessible from all SPs in the same MP. MPs can access the main memory of the GPU, called *global memory*, and also two other types of memory: *constant memory* and *texture memory*.

Constant memory, texture memory, registers, and shared memory have very low access latencies, and therefore data stored in these memories can be accessed very fast. However, global and local memories have very high latencies; as a result, storing and accessing data in these types of memory must be avoided. Since the release of *Fermi* architecture [35], NVIDIA GPUs have incorporated a two-level cache hierarchy completely transparent to programmers. This cache memory considerably reduces the access time to global memory. Figure 34.3 shows a representation of the different types of memory in CUDA and their

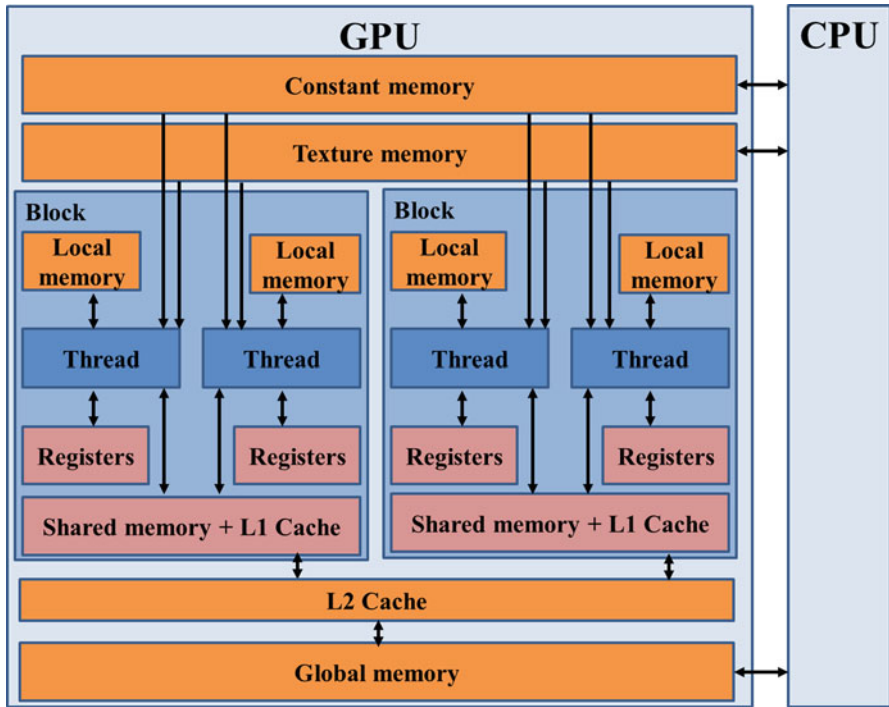


Fig. 34.3 CUDA memory architecture

relationship with threads and blocks. Note that L1 cache and shared memory share the space, and the programmer can select the amount of memory assigned for each type.

The CUDA software-programming model has a direct matching with the hardware architecture. By this way, a grid of blocks is assigned to a GPU device, each block is assigned to an MP, and each thread is assigned to an SP. Threads in the same block can share data through the shared memory of the MP. Threads in different blocks can share data only through the global memory of the device (see Fig. 34.3). The CUDA hierarchy based on grids, blocks, and threads allows the scalability of the programs and their automatic adaptation to different devices with different numbers of MPs and SPs.

34.1.2 OpenCL

CUDA and OpenCL are almost identical technologies. The CUDA concepts explained previously are exactly the same in OpenCL, with only a few changes of terminology (see Table 34.1).

Table 34.1 CUDA and OpenCL terminology correspondence

Concept	CUDA	OpenCL
Multiprocessor	Multiprocessor (MP)	Compute unit (CU)
Scalar processor	Streaming processor (SP)	Processing element (PE)
Single unit of execution	Thread	Work item
Groups	Block	Work group
Shared memory of multiprocessor	Shared memory	Local memory

Even though OpenCL is a recent technology, many studies have already been published with very good results in optimizing the computation time of different kinds of algorithms. For example, some applications in the medical imaging field have been described, such as for segmentation of blood vessels [30] or for image classification in Alzheimer's disease [27]. Unlike CUDA, OpenCL is cross-platform; therefore, an OpenCL program can be run on GPUs from different manufacturers and on multi-core CPUs. Although the same program can be run on both GPU and CPU, since GPUs and CPUs have different architectures and they present different types of parallelism, specific configurations and optimizations must be carried out in the programs to gain the best results from each platform.

34.2 Previous Work

A very efficient algorithm to estimate FD using the box-counting method was proposed by Hou et al. [11] as an optimization of the box-counting algorithm originally proposed by Liebotich et al. [19]. There are some studies addressing the problem of improving the efficiency of Hou's box-counting algorithm, like those presented in [18, 32]. However, these tried to improve the algorithm by using only a single thread of the CPU (a sequential program), and nowadays this type of implementation is no longer considered competitive against GPU or multi-core CPU algorithms, as shown in Sect. 34.5.

The first attempt to optimize the computational cost of the box-counting algorithm through parallel computing is found in [5]. In this study the authors propose a parallel implementation of the differential box-counting algorithm (DBC) presented in [28]. This approach is based on a SIMD array processor implementation, although only a theoretical computational complexity study was presented and no practical timings were shown. This study revealed that SIMD processing, the one that GPUs have, was a promising technique for improving the efficiency of the box-counting algorithm, but until now the only optimization of the DBC algorithm has been a multi-core CPU implementation presented in [34]. A recent study [22] presented two OpenCL kernels to calculate the box counting of 2D images. These algorithms obtain good results (speedups of up to 35×) comparable to the best ones we achieved, but these algorithms depend on additional GPU data structures that may cause memory overflow for large 3D data.

The emergence of Web applications [15, 20] that offer image-analysis algorithms, like FD computation, in an online environment implies the new challenge of providing the interactive computation times that these platforms require. With this goal in mind, two studies presented the first results on parallelization and optimization of Hou’s box-counting algorithm by using both GPU platforms CUDA and OpenCL [13, 14]. Here we analyze, compare, and integrate the methodologies, techniques, and results of these two previous studies.

The next section illustrates that one of the steps in the box-counting algorithm is to sort a large set of elements. In fact, as analyzed below in Sect. 34.5, this is the most time-consuming step of the algorithm. Therefore, highly optimized sorting algorithms are required to perform a fast box-counting algorithm processing. There are many studies addressing the problem of developing fast parallel sorting algorithms in GPU. According to our tests, the radix-sort algorithm [21] implemented in the thrust library [10] is the one providing the fastest performance for the CUDA platform. There are also several parallel OpenCL implementations of sorting algorithms [3, 7, 25], but some of them have limitations regarding the number of elements to be sorted [3]. This influences the final selection of the algorithm to be used, as discussed in Sect. 34.4. The OpenCL sorting algorithm presented in [25] seems to be a very promising solution comparable to the CUDA sorting algorithm present in the thrust library. Unfortunately, the code provided by the authors did not work properly in our tests, and it was impossible for us to obtain their sorting algorithm code in order to test it in our OpenCL box-counting implementation. Other recent studies have presented new advanced implementations of different sorting algorithms [4, 29]. None of these interesting and recent approaches adapt well to our problem, due to the fact that they are focused on distributed supercomputers [29] or hybrid platforms [4].

34.3 Box-Counting Algorithm

The *box-counting* algorithm [26] is one of the most widely used methods to approximate the FD value, because (a) it is quite simple; (b) it provides a good approximation; and (c) it is valid for statistically self-similar models [23].

In this part we focus on optimizing the computation time of 3D fractal dimension (3DFD). The box-counting algorithm consists of dividing the space containing the object under investigation into boxes of the same size l , where l is the size in voxels of the edge of the box. Each box of size l is classified as *black*, *gray*, or *white* depending on how the object covers the box. A box is black if the object fills all its voxels. A box is labeled gray if it is partially filled by the object. Finally, those boxes covering parts of the space where the object is not present are classified as white boxes. Once all boxes are classified, the number of boxes of each type is counted. This process of generating, classifying, and counting boxes is repeated for different box sizes (different values of l). Figure 34.4 shows this process in a graphic way. Values of 2, 4, and 8 for the box size (l) are used in Fig. 34.4b–d, respectively.

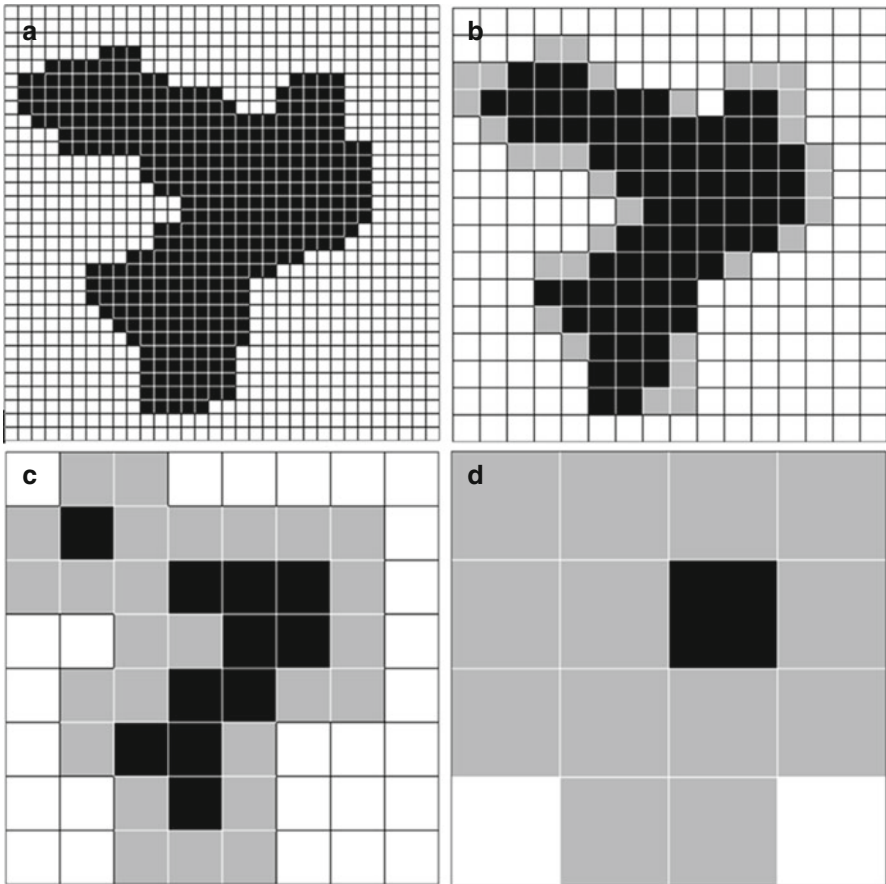


Fig. 34.4 An example of the box-counting algorithm. (a) Original image. (b–d) show different divisions of the space in boxes size 2, 4, and 8, respectively, and their classification as *black*, *gray*, or *white*

All these counts at different resolutions (box sizes) are the final result of the box-counting algorithm.

The estimation of the FD value for a selected type of voxel (white, gray, black, or black + gray) is calculated through a log-log linear regression, where the X coordinate represents the inverse of the box size ($1/l$) and the Y coordinate represents the number of boxes for that type of voxel ($N(l)$). The FD value corresponds to the slope of the linear regression: $FD = -((\ln N(l))/(\ln l))$.

As previously shown, there are two widely used box-counting algorithms. The first one is Liebotich's algorithm [19], improved later in [11] by Hou et al. This algorithm has a time complexity of $O(N \cdot \ln(N))$, is valid for binary images, and is the method that we have implemented in GPU in this study. The other box-counting

algorithm is the differential box-counting (DBC) presented in [28]. The DBC algorithm is based on grey level images, which falls outside the scope of this study.

For a 3D sample, Hou's box-counting algorithm represents the coordinates of the voxels of the object by using a binary representation of k bits. Therefore, 2^k represents the number of voxels of the edge of the box that completely covers the object. This representation allows the algorithm to directly locate the box that contains each voxel. To perform the box-counting process, the algorithm generates a set of grids of boxes with incremental edge size $l=2^m$, where $0 \leq m \leq k$. As a result, if n is the number of voxels of the object contained in a box, this box is classified as black if $n=(2^m)^3$, it is classified as gray if $0 \leq n \leq (2^m)^3$, and it is classified as white if $n=0$. Hou's algorithm follows these steps [11]:

1. Coordinates x , y , and z of each voxel are considered as binary numbers of k bits, with values from 0 to $2^k - 1$. Therefore, the position of a voxel is represented as $(x_{k-1} \dots x_2x_1x_0, y_{k-1} \dots y_2y_1y_0, z_{k-1} \dots z_2z_1z_0)$.
2. The binary coordinates of each voxel of the object are intercalated and combined in a string of 3 k bits as follows: $x_{k-1}y_{k-1}z_{k-1} \dots x_2y_2z_2x_1y_1x_0y_0z_0$. In this way, a list of bit strings is obtained. Each bit string in this list uniquely identifies a voxel of the object.
3. The list of bit strings is sorted using the value of each bit string.
4. The last step consists of masking to 0 the $3m$ bits on the right of each bit string, where 2^m is the edge size of the boxes. In this way, the resulting masked bit strings have a value of 0 in their last $3m$ bits. The key of this algorithm is that those masked bit strings with the same value are contained in the same box of edge size 2^m . Therefore, the number of boxes (black and gray boxes) that covers the object corresponds to the number of distinct values in the list of masked bit strings. A black box must have $(2^m)^3$ masked bit strings in the list, and the exact number of black and gray boxes is calculated. The number of white boxes is trivially obtained from the total number of voxels in the grid. This step is repeated with $m \leq k$.

Once these steps have been executed for all grids of box size 2^m with $0 \leq m \leq k$, the number of black, gray, and white boxes for each box size 2^m is obtained and therefore the box counting is computed. Figure 34.5 shows a graphic representation of the different steps of Hou's algorithm. For the sake of clarity, a 2D example is shown in this figure. The example represents an object composed of eight voxels whose coordinates are represented with 2 bits (k). Step 4 of the algorithm is shown only for $m=1$ (boxes with edge size of 2^1 voxels). Due to the fact that this is a 2D example, the bit strings in step 4 are masked to 0 in their $2m$ bits on the right.

As previously shown, this algorithm has several optimized implementations in CPU for 2D objects [18, 32]. In the next section, we describe our approach for obtaining two very fast GPU implementations of Hou's box-counting algorithm in 3D based on CUDA and OpenCL technologies.

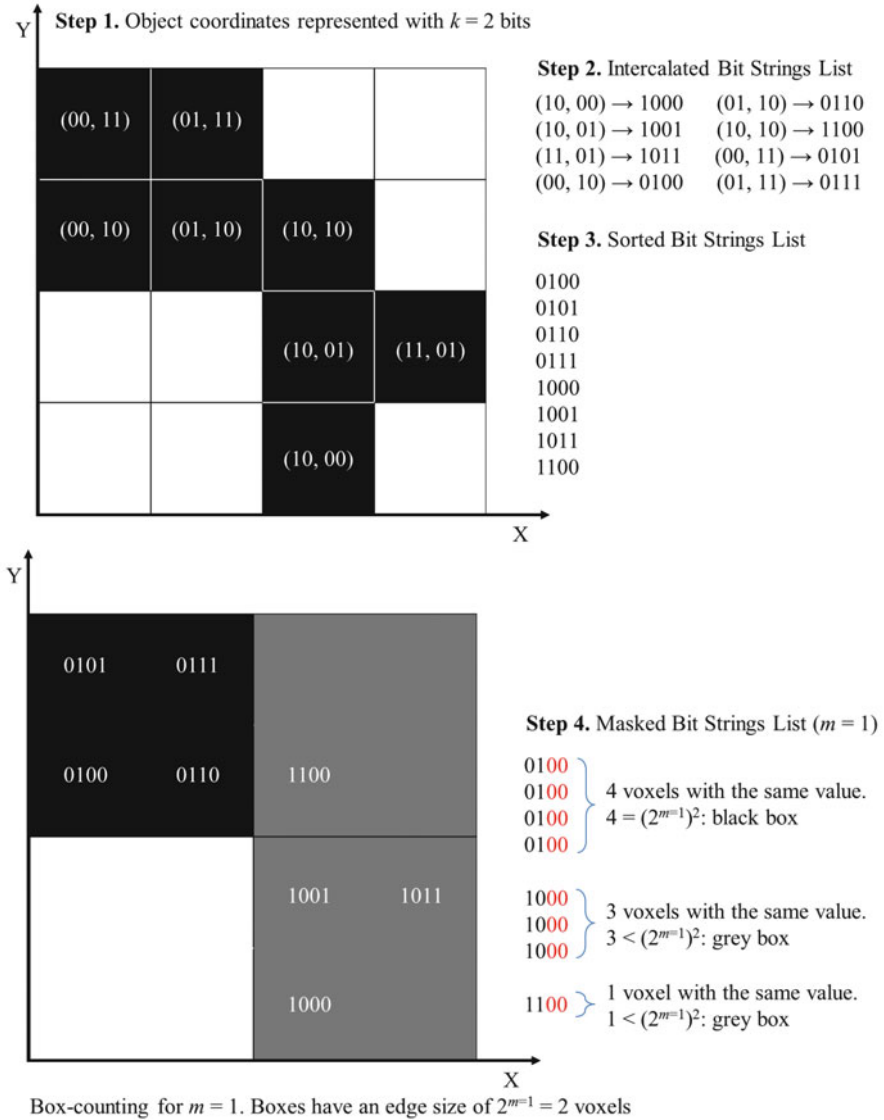


Fig. 34.5 Steps in Hou’s box-counting algorithm

34.4 GPU Implementation

We have developed two optimized GPU implementations of Hou’s box-counting algorithm: a CUDA implementation for NVIDIA GPUs and a cross-platform OpenCL implementation optimized for GPUs. Figure 34.6 shows the main modules and the data flow of both implementations. Since CUDA and OpenCL are very

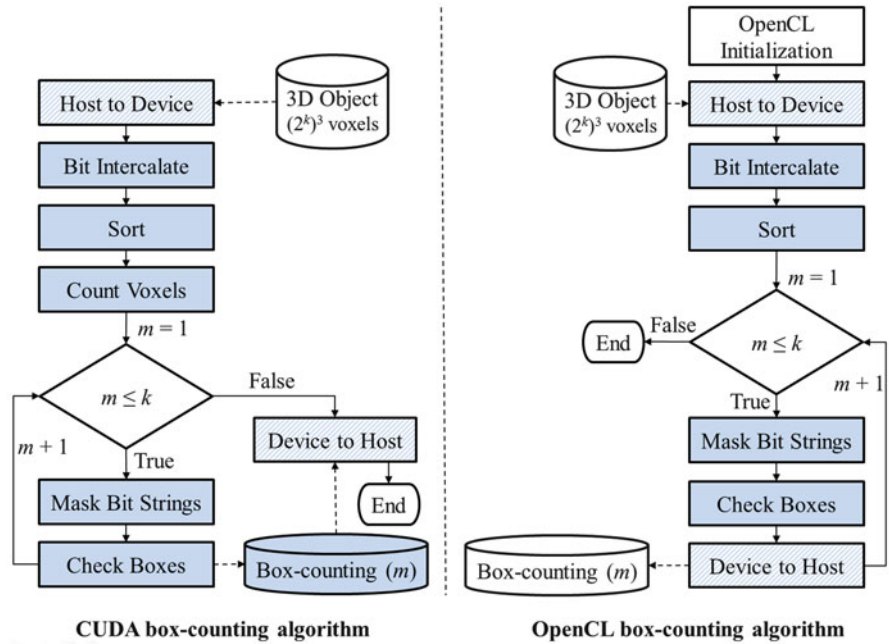


Fig. 34.6 Flow charts for CUDA and OpenCL GPU implementations of Hou’s box-counting algorithm

similar technologies, both implementations are almost the same but have important differences that affect the final speedup achieved.

Light blue shaded functions in Fig. 34.6 are executed in the GPU. As a first step, due to the cross-platform nature of OpenCL, the OpenCL context and the target device need to be initialized at runtime. Based on the target device (GPU or CPU) and its platform (NVIDIA, AMD, or Intel) the OpenCL kernels are compiled in execution time. This process is not needed for the CUDA version. As in any GPU algorithm, the first stage is transferring the data from the RAM of the CPU to the global memory of the GPU (“host to device” function in Fig. 34.6). In our case, data is composed of an array of 0s and 1s representing the 3D voxelization of the object. Note that voxels not containing the object are also stored with a 0 value. Once data is in the GPU, kernels can operate on it.

The first kernel is called *bit intercalate*. Each thread of this kernel accesses to one different voxel. If the voxel is part of the object (it has a value of 1), the thread performs steps 1 and 2 of Hou’s algorithm described in the previous section. That is, the thread creates the binary representation for the coordinates of the voxel, intercalates them, and stores a new bit string in a bit string array in the global memory. If the voxel does not belong to the object (it has a value of 0), a value of $(2^k)^3$ (the greatest possible value) is stored in the bit string array position for that voxel. This ensures that voxels not belonging to the object will be placed at the end of the bit string list when this list is sorted. After the execution of all the threads, the array

with the entire bit string list is completely generated in the global memory of the GPU. The configuration used for launching the bit intercalate kernel consists of a block size of $8 \times 8 \times 8$ threads. This 3D configuration of blocks fits the 3D structure of our data very well, which helps to improve the kernel performance.

Once the intercalated bit string list has been generated, the next step in the process consists of sorting the list by using the kernel called *sort* in Fig. 34.6. Sorting is a basic operation in computer programming, and for this reason there are many studies devoted to obtaining fast GPU implementations of several sorting algorithms. CUDA implementations are more advanced than OpenCL at the moment, and this fact has a large impact on the final speedup achieved in our GPU box-counting algorithms, as we will see in the next section. The best CUDA sorting algorithm we found was the one present in the *thrust library* [10] based on the radix-sort algorithm developed in [21]. This library is included in the CUDA toolkit since version 4.0. For the case of OpenCL, we tested three different implementations: two based on bitonic sorting, one developed by Bainville [3] and the one included in the NVIDIA OpenCL SDK, and one based on the radix-sort algorithm [7]. The performances of the two implementations of bitonic sorting are better than the radix-sort performance in [7], but they decrease for objects with a large amount of voxels. Another limitation of bitonic sort algorithms is that they only work with a number of elements to sort power of two. A key feature of our GPU box-counting implementation is that the sort kernel can be replaced in the future with any improved new GPU sorting algorithm. As we will show in the next section, the sort kernel consumes the longest time in the box-counting process; therefore, any further improvement of the sorting algorithm will have a deep impact on the overall performance of our algorithm.

After executing the sort kernel, we obtain a sorted bit string list in ascending order. The bit strings corresponding to voxels that do not belong to the object have the maximum value possible and therefore are placed at the end of the list. For the case of the CUDA implementation, an intermediate kernel is now executed, called *count voxels* in Fig. 34.6. This kernel counts the number of voxels of the object. This value corresponds to the number of black voxels of the box counting for $m=0$. This value also allows the algorithm to deal only with those voxels belonging to the object in the following steps of the process, avoiding the necessity to launch threads for empty voxels. This count is performed very efficiently through the CUDA thrust library. However, such an efficient function for the OpenCL case does not exist. This is the reason why our OpenCL implementation does not have an equivalent GPU kernel for this purpose. Instead, the OpenCL version performs this count previously in the CPU side of the algorithm.

The next step is the main loop of the algorithm, consisting of masking and counting the black, gray, and white voxels for boxes of edge size 2^m , with $1 \leq m \leq k$. These two processes are performed through the GPU kernels *mask bit strings* and *check boxes*. Both kernels use the sorted bit string list as input data. Owing to these input data, the launch configuration for both kernels is simple and consists of a 2D grid of 1D blocks with 512 threads each. The total number of threads launched equals the number of voxels of the object, and therefore the empty voxels, whose bit strings are

placed at the end of the list, do not have to be processed. The mask bit string kernel simply sets to 0 the $3m$ bits on the right of the bit string. When all threads execute this kernel, the result is a masked bit string list as shown in Fig. 34.5. The check box kernel works on this masked list in order to determine the number of black and gray boxes (see last step in Fig. 34.5). Each thread reads its corresponding bit string (v) and the previous one in the list. If these two bit strings are the same, then the bit string v is not the first occurrence of a series, and this thread does nothing else. On the contrary, if the two bit strings are different, then the bit string v is the first occurrence of a set of values, and the next step is to check if this set contains all the voxels of the box (black box) or not (gray box). To do this, the thread reads the bit string located $(2^m)^3 - 1$ positions from v (this is the maximum number of voxels for a box of size 2^m). If that bit string is the same as v , then the box is black, otherwise the box is gray. Finally, this type of box has to be counted. To avoid problems with concurrent accesses to the memory positions that store black and gray counters, the check box kernel first stores the thread result in the shared memory of the thread, and when all threads in the same block have finished their execution, the partial sum of each block is stored in the global memory of the GPU. From this point, again, a different processing is performed on our two implementations, as can be seen in Fig. 34.6. For the CUDA case, the partial sums stored in the global memory are added onto the GPU by using the CUDA thrust library. However, for the OpenCL case, since we do not have a similar function as efficient as the one provided in the CUDA thrust library, the partial sums are transferred to the host and the final sum is performed in the CPU side and the box counting for an edge size of 2^m is obtained. The whole box-counting process is finished when these two kernels, mask bit strings and check boxes, are executed for all values of m , with $1 \leq m \leq k$.

34.5 Results

In this section, we show a performance analysis of our two GPU implementations of Hou's box-counting algorithm. Both the CUDA and the OpenCL algorithms are compared against the single-thread CPU implementations of Hou's algorithm and, to make the comparison as fair as possible, against two different multi-core CPU implementations.

34.5.1 Hardware and Test Models

Our test system was composed of a NVIDIA GeForce GTX 580 GPU and a two Intel Xeon E5620 at 2.40 GHz CPU. We used the NVIDIA driver version 275.33 and the CUDA driver version 4.1 with our GPU. This GPU has GF100 architecture, called Fermi, consisting of 16 MPs with 32 SPs each; therefore, we counted on a total of 512 SPs. In this GPU, each MP can manage a total of 1,536 threads and can

allocate up to 8 thread blocks simultaneously. Each thread block can manage 1,024 threads. The memory of this GPU is composed of 32 K 32-bit registers, a shared memory of 48 KB + 16 KB of cache memory, a constant memory of 64 KB, and 1,536 MB of slow global memory. Regarding the CPU, each Intel Xeon has four cores. The RAM memory of the system has 12 GB and we use Windows 7 as our operating system.

To test the algorithms, we used a set of six standard 3D voxelized models extracted from public 3D repositories [1, 2, 33]. Each model was used with resolutions ranging from $128 \times 128 \times 128$ to $512 \times 512 \times 512$ voxels. The models were selected to have different shapes and topologies in order to test the algorithms properly.

We coded three CPU versions of Hou's algorithm to compare them with the GPU implementations: one single-thread version and two parallel multi-core versions. The first parallel implementation was coded in C language using the *process.h* library [8] for multi-threading. The second multi-core CPU algorithm was coded in OpenCL, optimizing our GPU OpenCL code to take advantage of the intrinsic characteristics of parallel processing in multi-core CPUs. Both implementations launch eight threads in order to use all the cores available in our CPU. The sort method in these two multi-core algorithms was the parallel implementation of the classic quick sort algorithm included in the Intel Threading Building Blocks library (TBB) [12]. This sort algorithm was the most efficient we found for use in multi-core CPU systems. For the single-thread codification of Hou's algorithm, we also used the quick sort method.

34.5.2 Implementation Results

Table 34.2 shows the computation times for all our implementations of Hou's box-counting algorithm. The execution times shown in this table are the average value obtained for the six test models for each different resolution. Note that computation times for the GPU algorithms include the time needed for transferring data from CPU to GPU and vice versa. Figure 34.7 shows a graphic representation of the data in Table 34.2. Average speedups of up to $28.5 \times$ (CUDA GPU) and $6.32 \times$ (OpenCL GPU) were achieved against the CPU implementation of Hou's box-counting algorithm.

We also measured the computation time of each individual kernel in the GPU algorithms. For the CUDA case, each processing element has the following percentage of the total processing time of the algorithm: sort, 42%; GPU idle waiting for CPU, 24%; CPU-GPU data transfers, 19%; check boxes, 6%; bit intercalate, 4%; mask bit strings, 3%; and count voxels, 2%. These results clearly show that the sort function is the most time-consuming process in the CUDA GPU algorithm. For the case of the OpenCL GPU algorithm, the sort kernel requires even more computation time, reaching average percentages of more than 60% of the global processing time. Therefore, if new and faster parallel sort algorithms are developed in the future, including them in our GPU box-counting implementations will imply a large improvement.

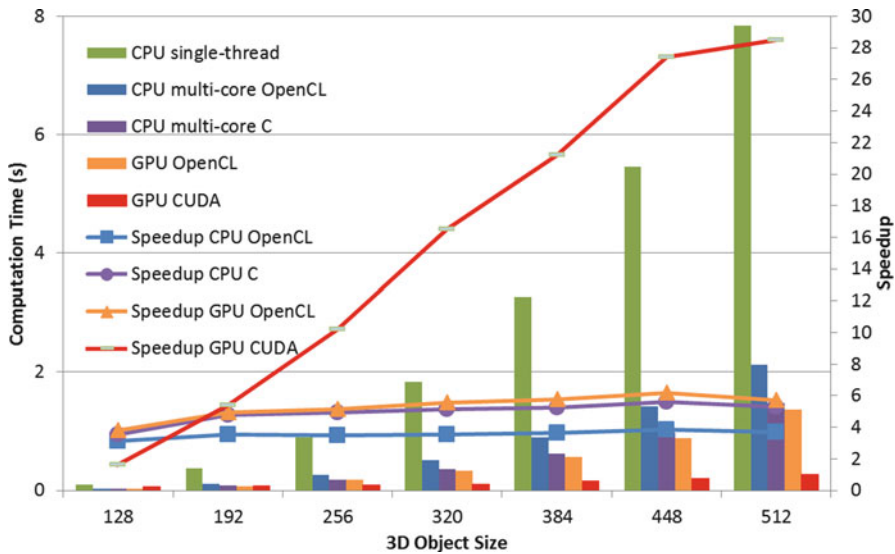


Fig. 34.7 Computation times and speedups achieved by the CPU and GPU implementations of the box-counting algorithm. Execution times and speedups are the average values for the six test objects, with sizes from $128 \times 128 \times 128$ voxels to $512 \times 512 \times 512$ voxels

Table 34.2 shows the average computation times and speedups achieved by the CPU multi-core and the GPU implementations of the box-counting algorithm against the CPU single-thread version. In the columns corresponding to GPU CUDA and GPU OpenCL, speedup 1 and speedup 2 refer to the speedup regarding the CPU single-thread and the CPU multi-core C algorithms, respectively.

Since we have not found any other GPU implementation of Hou’s box-counting algorithm, we have compared our GPU results with the most recent non-GPU implementation of that algorithm, corresponding to the Matlab program presented in [32]. In this study a computation time of 16.49 seconds was required to compute the box counting of the classic fractal called *Menger sponge* with a size of $243 \times 243 \times 243$ on an Intel Xeon 3.2 GHz CPU, a CPU very similar to ours. In our case, the CUDA algorithm needed only 0.087 s to calculate the box counting of that Menger sponge. On the other hand, this processing took our OpenCL algorithm 0.153 s. Therefore, the CUDA and OpenCL algorithms achieved impressive speedups of $189.54 \times$ and $107.77 \times$, respectively, which situate our GPU implementations as two very interesting approaches for dealing with high-resolution objects or performing repeated box-counting computations.

As a final test for our fastest GPU algorithm in the biomedical context, we performed an analysis of the 3D FD of three brain-related structures, i.e., cerebral blood vessels (cerebral veins and dural sinuses), the skull, and gray matter (including the cortex and subcortical structures). The voxel representations were constructed from 20 sets of simulated MR images obtained from [6]. The size of these models is $434 \times 362 \times 362$ voxels and the average number of nonempty voxels is 194,300 for blood vessel models, 1,473,129 for skull models, and 7,906,182 for gray matter models. Figure 34.8 shows

Table 34.2 Average computation times and speedups achieved by the CPU multi-core and the GPU implementations of the box-counting algorithm against the CPU single-thread version

Size (voxels)	CPU single-thread (s)	CPU multi-core C		CPU multi-core OpenCL		GPU CUDA		GPU OpenCL				
	Time (s)	Speedup	Time (s)	Speedup	Time (s)	Speedup	Time (s)	Speedup 1	Speedup 2			
128×128×128	0.102		0.029	3.52×	0.033	3.09×	0.062	1.64×	0.47×	0.027	3.77×	1.07×
192×192×192	0.378		0.079	4.78×	0.107	3.53×	0.071	5.40×	1.11×	0.076	4.97×	1.04×
256×256×256	0.900		0.182	4.94×	0.257	3.50×	0.088	10.22×	2.07×	0.174	5.17×	1.05×
320×320×320	1.831		0.358	5.11×	0.516	3.55×	0.111	16.49×	3.22×	0.328	5.58×	1.09×
384×384×384	3.264		0.619	5.27×	0.892	3.66×	0.154	21.19×	4.02×	0.563	5.79×	1.10×
448×448×448	5.543		0.976	5.68×	1.420	3.90×	0.202	27.44×	4.83×	0.877	6.32×	1.11×
512×512×512	7.840		1.472	5.33×	2.125	3.70×	0.275	28.50×	5.35×	1.364	5.74×	1.08×

In the columns corresponding to GPU CUDA and GPU OpenCL, Speedup 1 and Speedup 2 refer to the speedup regarding the CPU single-thread and the CPU multi-core C algorithms, respectively

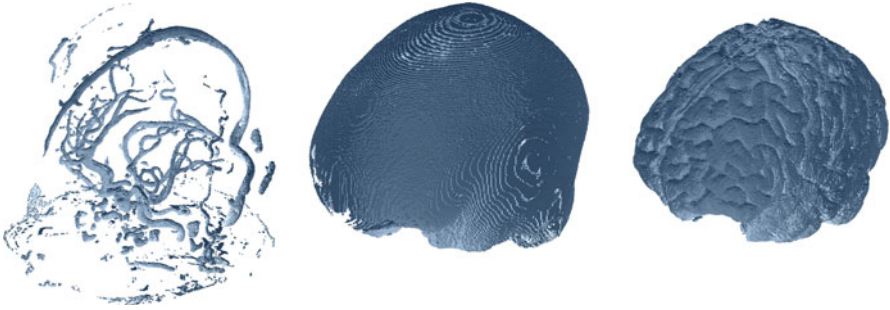


Fig. 34.8 Representation of the cerebrovascular system, skull, and gray matter at a size of $434 \times 362 \times 362$ voxels

one example of each type of model. We measured the computation time of Hou's box-counting algorithm for our implementations on CPU and CUDA. The 3D FD was also calculated for each model (obviously, the 3D FD value obtained is the same regardless of the implementation used). The results showed average speedups of $22.01\times$ (blood vessels), $22.83\times$ (skull), and $26.4\times$ (gray matter). These speedups are similar to those obtained for the six test objects. Moreover, these results manifest the characteristic of our GPU algorithm of being faster when the object has more nonempty voxels. Regarding the 3D FD values obtained, the average values were 1.530 (blood vessels), 2.008 (skull), and 2.413 (gray matter). These results are the ones expected according to how each type of brain tissue occupies the space.

34.6 Discussion, Conclusions, and Future Work

In this chapter we have presented a methodology based on GPU programming to increase the performance of Hou's box-counting algorithm, one of the most widely used algorithms to calculate the fractal dimension of an object. The box-counting computation time could be very high, especially in 3D objects with a large number of voxels or when there is a large amount of objects to be analyzed. Our approach provides two main solutions: The first one is a highly efficient solution based on CUDA technology for NVIDIA GPUs, allowing the algorithm to increase its computational performance with speedups of up to $28\times$; the second one is an efficient OpenCL cross-platform solution that achieves speedups of up to $6.32\times$ for GPUs and $3.9\times$ for multi-core CPUs. In this way our approach covers a wide range of modern computing platforms.

The most remarkable results are:

- The CUDA algorithm is the fastest one, largely outperforming not only the CPU algorithm but also the OpenCL GPU implementation. The GPU CUDA implementation is much better than the OpenCL one due to the fact that CUDA is a more established technology, having libraries with highly optimized basic algorithms. The CUDA thrust library provides very efficient algorithms for sorting

and for counting. These algorithms have a great influence on the final performance of the box-counting algorithm, and there are no similar counterparts in any OpenCL library. According to our tests, the sort algorithm of the CUDA thrust library is three to five times faster than the best one for OpenCL.

- When the object resolution increases, CPU single-thread times grow very quickly, while GPU times grow much slower, especially in the case of the CUDA version. This is a very desirable characteristic for scaling purposes: the greater the object is, the better the GPU speedup obtained.
- The multi-core CPU implementations achieve speedups of between $3\times$ and $5.7\times$ against the CPU single-thread algorithm. Taking into account that our CPU has eight cores, the speedups achieved are not close to what was expected theoretically. A detailed analysis of the computation cost of each part of the multi-core CPU algorithms was performed, and it revealed two main factors involved: (1) a relevant percentage of nonparallelizable sequential code in the algorithm and (2) an unbalanced thread workload due to the empty voxels present in the objects. The location of empty voxels is unpredictable when no prior information about the shape of the objects is available.

As future work, efforts will be focused on obtaining a fast GPU implementation of the differential box-counting algorithm. This box-counting algorithm deals with gray-scale images, and only an optimization based on multi-core CPU programming has been proposed until now. Other interesting work related to GPU programming would be to study the application of the new features of the latest NVIDIA GPU architectures in our algorithms. Dynamic parallelism and atomic operations are two of these characteristics that could improve the performance of the GPU box-counting algorithm.

Acknowledgments This work has been partially supported by the University of Jaén, the Caja Rural de Jaén, the Ministry of Economy and Competitiveness, and the European Union (via ERDF funds) through the research projects UJA2013/12/04, UJA2013/08/35, and TIN2014-58218-R.

References

1. 3DVIA repository. 2015. Available from <http://www.3dvia.com>.
2. Aim@shape repository. 2015. Available from <http://visionair.ge.imati.cnr.it>.
3. Bainville E. OpenCL sorting. 2011. Available from http://www.bealto.com/gpu-sorting_intro.html.
4. Banerjee DS, Sakurikar P, Kothapalli K. Comparison sorting on hybrid multicore architectures for fixed and variable length keys. *Int J High Perform Comput Appl*. 2014;28(3):267–84.
5. Biswas MK, Ghose T, Guha S, Biswas PK. Fractal dimension estimation for texture images: a parallel approach. *Pattern Recogn Lett*. 1998;19:309–13.
6. BrainWeb: Simulated Brain Database. 2015. Available from <http://brainweb.bic.mni.mcgill.ca/brainweb>.
7. OpenCL Data Parallel Primitives Library. 2011. Available from <http://code.google.com/p/clpp/>.
8. Digital Mars. *Process.h C Library Specification*. 2015. Available from <http://www.digitalmars.com/rtl/process.html>.

9. Eklund A, Dufort P, Forsberg D, LaConte SM. Medical image processing on the GPU – past, present and future. *Med Image Anal.* 2013;17:1073–94.
10. Hoberock J, Bell N. Thrust: a parallel template library. v1.8.0, February 2015. Available from <http://thrust.github.com/>.
11. Hou X, Gilmore R, Mindlin GB, Solari HG. An efficient algorithm for fast $O(N*\ln(N))$ box counting. *Phys Lett A.* 1990;151:43–6.
12. Intel. Intel threading building blocks reference website. 2015. Available from <http://threading-buildingblocks.org>.
13. Jiménez J, Ruiz de Miras J. Fast box-counting algorithm on GPU. *Comput Methods Progr Biomed.* 2012;108:1229–42.
14. Jiménez J, Ruiz de Miras J. Box-counting algorithm on GPU and multi-core CPU: an OpenCL cross-platform study. *J Supercomput.* 2013;65:1327–52.
15. Jiménez J, López AM, Cruz J, Esteban FJ, Navas J, Villoslada P, Ruiz de Miras J. *J Biomed Inform.* 2014;51:176–90.
16. Kirk DB, Hwu WW. Programming massively parallel processors. Hands-on approach. Burlington: Morgan Kaufmann Publishers; 2010.
17. Khronos Working Group. The OpenCL specification. 2015. <http://www.khronos.org/opencl/>
18. Kruger A. Implementation of a fast box-counting algorithm. *Comput Phys Commun.* 1996;98:224–34.
19. Liebotich LS, Toth T. A fast algorithm to determine fractal dimension by box counting. *Phys Lett A.* 1989;141:386–90.
20. Manjón JV, Coupé P. volBrain: an online MRI brain volumetry system. In: Proceeding of organization for human brain mapping; 2015 June 14–18; Honolulu. 2015.
21. Merrill D, Grimshaw A. High performance and scalable radix sorting: a case study of implementing dynamic parallelism for GPU computing. *Parallel Process Lett.* 2011;21:245–72.
22. Mukundan R. Parallel implementation of the box counting algorithm in OpenCL. *Fractals.* 2015;23(3):1–8.
23. Normant F, Tricot C. Methods for evaluating the fractal dimension of curves using convex hulls. *Phys Rev.* 1991;43:6518–25.
24. NVIDIA. NVIDIA CUDA toolkit documentation 2015. Available from <http://docs.nvidia.com/cuda/index.html>.
25. Polok L, Ila V, Smrz P. Fast radix sort for sparse linear algebra on GPU. *Simul Ser.* 2014;46(5):79–86.
26. Russell D, Hanson J, Ott E. Dimension of strange attractors. *Phys Rev Lett.* 1980;45:1175–8.
27. Shamonin DP, Bron EE, Lelieveldt BPF, Smits M, Klein S, Staring M. Fast parallel image registration on CPU and GPU for diagnostic classification of Alzheimer’s disease. *Front Neuroinforma.* 2014;7:1–15.
28. Sarkar N, Chaudhuri BB. An efficient differential box counting approach to compute fractal dimension of images. *IEEE Trans Syst Man Cybernet.* 1994;24:115–20.
29. Shamoto H, Shirahata K, Drozd A, Sato H, Matsuoka S. Large-scale distributed sorting for GPU-based heterogeneous supercomputers. In: Proceeding of the IEEE international conference on big data; 2014 October 27–30; Washington, DC: IEEE press; 2014.
30. Smistad E, Elster AC, Lindseth F. GPU accelerated segmentation and centerline extraction of tubular structures from medical images. *Int J Comput Assist Radiol Surg.* 2014;9:561–75.
31. Smistad E, Falch TL, Bozorgi M, Elster AC, Lindseth F. Medical image segmentation on GPUs – a comprehensive review. *Med Image Anal.* 2015;20:1–18.
32. de Souza J, Rostirolla SP. A fast MATLAB program to estimate the multifractal spectrum of multidimensional data: application to fractures. *Comput Geosci.* 2011;37(2):241–9.
33. Stanford University: The Stanford 3D scanning repository. 2015. Available from <http://graphics.stanford.edu/data/3Dscanrep>.
34. Tzeng YC, Fan KT, Su YJ, Chen KS. A parallel differential box counting algorithm applied to hyperspectral image classifications. In: Proceeding of the IEEE International Geoscience and Remote Sensing Symposium; 2009 July 12–17; Cape Town: IEEE press; 2009.
35. Wittenbrink CM, Kilgari E, Prabhu A. Fermi GF100 GPU architecture. *IEEE Micro.* 2011;31:50–9.

Chapter 35

Fractal Electronics as a Generic Interface to Neurons

William J. Watterson, Saba M. Moslehi, Julian H. Smith,
Rick D. Montgomery, and Richard P. Taylor

Abstract Imagine a world in which damaged parts of the body – an arm, or an eye, and ultimately a region of the brain – can be replaced by artificial implants capable of restoring or even enhancing human performance. The associated improvements in the quality of human life would revolutionise the medical world and produce sweeping changes across society. Biotechnology has the potential to transform this imagined world from science fiction into science fact. The use of implants to interface with the body is growing rapidly and represents the brave new world of electronics. However, today’s electronic implants are based on the commercial electronics employed in computers and communications technology. Consequently, their performance is limited severely by the interface between the artificial and biological systems. In this chapter, we will discuss the optimal solution of establishing a bio-inspired interface using ‘interconnects’ that mimic the biological circuitry employed by the body – neurons. Neurons are fractal, featuring dendritic branches that repeat at increasingly fine sizes. We will discuss the construction of fractal interconnects and their fundamental functions – inducing and detecting electrical signals in the neurons. We will outline their enhanced performance, which includes their electrical, optical and physical properties.

Keywords Fractals • Bio-inspiration • Human implants • Electronics • Neurons

35.1 Introduction

In 1752, Benjamin Franklin attached a metal key to the bottom of a dampened kite string and then flew the kite in a storm. It didn’t take long to go from his simple demonstration of harnessing electricity to applying it to living bodies. In 1764, physician Charles Le Roy applied electricity to patients’ eyes, causing them to see

W.J. Watterson • S.M. Moslehi • J.H. Smith • R.D. Montgomery • R.P. Taylor (✉)
Physics Department, University of Oregon, Eugene, OR 97403, USA
e-mail: rpt@uoregon.edu

flashes of light. In 1791, **Luigi Galvani** did the same to the muscles of frog legs, causing them to twitch. Since then, two centuries of rapid development have led to today's commercial electronics industry. Miniaturisation has been the main driver of improvements. In addition to faster operation, the evolution from microelectronics to nano-electronics facilitates novel methods for manipulating the flow of electricity. For example, our research group has investigated ballistic electronics [33], quantum electronics [26], spin electronics [31] and coulomb blockade [37]. However, developments such as these target the computing and communications industry rather than electronic interfaces with biological systems.

Miniaturisation offers surgeons the opportunity to implant devices in humans rather than relying on the crude external wires used by Le Roy and Galvani. For example, electronic devices have been implanted into human retinas in the hope of restoring vision to victims of retinitis pigmentosa and macular degeneration [39]. More than 80,000 Americans have brain implants designed to combat neurological disorders such as Parkinson's disease [23]. However, in each case the implant's functionality is limited by conventional designs inherited from the commercial electronics industry. For example, today's retinal implants could in principle deliver 20/80 vision and yet they only achieve 20/1260 vision, suggesting that they communicate effectively with less than 10% of the targeted neurons [36]. Similarly, although research programmes such as the White House BRAIN Initiative call for future electronics that simultaneously measure at least 10,000 neuronal signals, today's implants typically track less than 100 at a time [1].

Figure 35.1 highlights the fundamental mismatch between today's implants and the neurons that they interact with. Neurons are described by fractal geometry, featuring dendritic branches that repeat at increasingly fine size scales (Fig. 35.1a, b). In contrast, the active area of the implant is based on the smooth lines inherent in Euclidean geometry (e.g., the grey square shape shown in Fig. 35.1c). Adopting the principle of bio-inspiration, we will describe the use of fractal interconnects to establish a 'biophilic' interface for the implants (Fig. 35.1d). In effect, the biophilic interface convinces nearby neurons that they are interacting with other neurons rather than an artificial device. We will consider implants with two distinct functions – stimulators (which induce electrical signals in the neurons) and sensors (which then detect and track these signals as they pass through the body's neural network). The superior electrical, optical and physical properties of the fractal interconnects are expected to be generic. Future applications could therefore include interaction with neurons in the brain, retina and limbs.

35.2 Fabrication of the Fractal Interconnects

When neurons interact with each other, they do so by exploiting both their physical and chemical environments. Our interconnects will do the same. In addition to adopting the physical geometry of the neurons, our project builds on previous investigations of materials known to establish favourable chemical environments for the neurons. Accordingly, our fabrication methods exploit two established

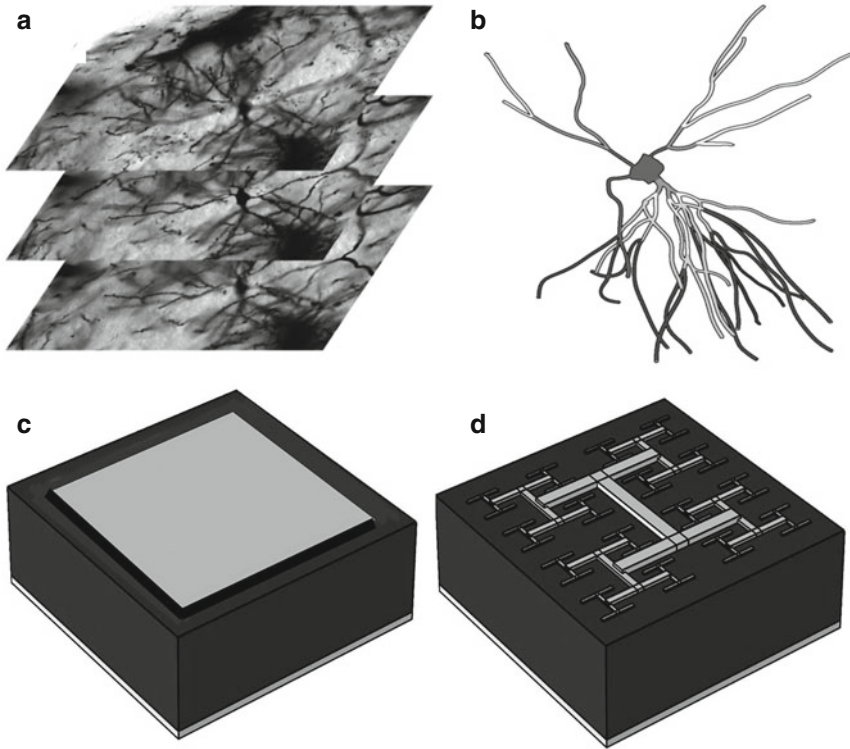


Fig. 35.1 (a) In collaboration with B. Harland and J. Dalrymple-Alford (University of Canterbury, New Zealand), we use scanning confocal microscopy to image a stack of $200\ \mu\text{m}$ by $200\ \mu\text{m}$ horizontal sections (with vertical separations of $2\ \mu\text{m}$) of Golgi-Cox-stained neurons. (b) These sections are then computer assembled into three-dimensional images for pattern analysis. A neuron's basal dendrites from a rat's hippocampus are shown for demonstration. (c) A schematic showing the square-shaped active area (grey) of a conventional implant. (d) For our bio-inspired implants, the active area features branched patterns that repeat at different size scales

materials – TiN and carbon nanotubes (CNTs). TiN research demonstrates its stability over long periods of electronic operation both *in vitro* and *in vivo* [18]. *In vitro* neuron cultures on TiN reveal that it is also non-cytotoxic [16]. Furthermore, TiN retinal implants have been implanted in human patients for more than a year without negative reaction [34]. Similarly, the unique properties of CNTs make them ideal for bioelectronics. They have excellent electrical current capacity (1,000 times greater than copper) and superior electron mobilities to silicon. They are also incredibly strong (100 times stronger than steel) yet mechanically flexible [20]. Furthermore, CNTs adhere well to substrates (with binding energies of a few $\text{eV}/\text{\AA}$) [19] and living cells [12] and can be synthesised to be nontoxic [22]. For both material systems, we will adapt their surfaces to improve adhesion and the survival rate of the neurons. These procedures include using nanowire textures [17], homopolymer poly-L-lysine for TiN [18] and pyrene for the nanotubes [5].

Two novel fabrication techniques are being developed, each designed to match the fractal characteristics of the interconnects to those of the neurons. For each technique, the interconnects' smallest branches measure down to 50 nm, and the largest branches are designed to match the spread of the neuron branches – approximately 500 μm for the brain and 20 μm for the retina. Whereas all fractals exhibit repetition of patterns at multiple size scales, fractals can be grouped into two categories based on how the patterns repeat. For fractals prevalent in the body (e.g. neurons, veins and bronchial trees), the statistical qualities of the patterns repeat at different scales. In contrast, the patterns of mathematically generated 'exact' fractals repeat exactly at different scales. Consequently, whereas exact fractals look precisely the same at increasingly fine scales, 'statistical' fractals simply look similar at different scales [9]. One of our fabrication techniques exploits the precision and control associated with the clean geometry of exact fractals. The other harnesses natural growth processes to generate statistical fractals similar to neurons. Fractal dimension D is a central parameter for quantifying both types of fractal. This describes how the patterns occurring at different scales combine to build the resulting fractal shape [9]. For Euclidean shapes, dimension is described by familiar integer values – for a smooth line $D=1$, while for a completely filled area $D=2$. However, the repeating patterns of a fractal line cause the line to begin to occupy more space. Consequently, its D value lies between 1 and 2. Figure 35.2a, b shows the result of adjusting D for the branches of our fractal interconnects. For each fabrication method, D can be adjusted along with the number of repeating iterations I to investigate the impact of these fractal parameters on the interconnects' properties.

The exact fractal interconnects (Fig. 35.2) are fabricated using electron-beam lithography [35] to generate patterns in two biocompatible resists (SU-8 and HafSOx). For the SU-8 method, this pattern can then be transferred to a TiN pattern using electron-beam evaporation and a 'lift-off' technique. For the HafSOx method, the exposed HafSOx acts as a mask for an electron milling process that defines the pattern in an underlying TiN layer.

Fabricated using novel self-assembly growth processes, the statistical fractal interconnects look strikingly similar to neurons (Fig. 35.3). Using this technique, a beam of metallic clusters (each with a diameter of ~ 50 nm) is deposited on a substrate in an ultrahigh vacuum chamber. These clusters then grow into fractal islands called nanoflowers by diffusion-limited aggregation [8]. Figure 35.3a charts this growth process, showing the small ellipsoidal islands that initially form (plotted on the graph's left side) and the islands with fractal branches that they grow into (right side). The islands' fractal morphology can be adjusted by varying deposition conditions such as temperature, deposition rate and flux (Fig. 35.5b–d). Fortuitously, neighbouring islands naturally self-avoid rather than merge (Fig. 35.5c), allowing arrays of fractal interconnects to be grown efficiently.

Figure 35.3e shows statistical fractals formed from CNTs that spread both parallel and perpendicular to the implant's surface with thicknesses of ~ 1 μm . Both single and multiwalled varieties of the nanotubes are synthesised using

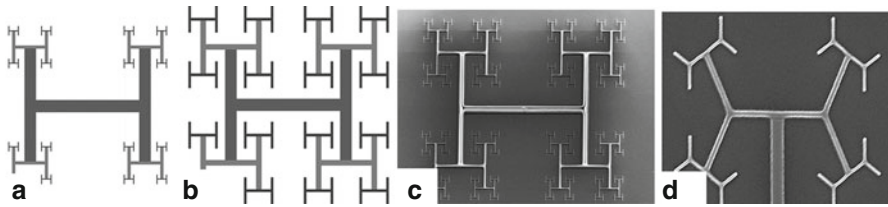


Fig. 35.2 (a, b) Schematic demonstrations of D 's impact on the scaling properties of an exact interconnect in which an 'H' pattern repeats. Three iterations of repetition are shown. Note how the H's size decreases at a higher rate between iterations for $D=1.1$ (shown in a) than for $D=1.9$ (shown in b). (c, d) Scanning electron micrographs (SEMs) of interconnects featuring $D=1.5$ branches made in collaboration with K. Fairley and D. Johnson (University of Oregon, USA). The branches span from $500\ \mu\text{m}$ down to $2\ \mu\text{m}$ in (c). In (d), the widths of the smallest branches are $\sim 10\ \text{nm}$

chemical vapour deposition. In this process, substrates are metallised with thin (a few Å) layers of a catalyst (e.g. Fe, Co) that form a network of metallic islands. These islands then serve as seeds for nanotube growth, allowing them to connect to multiple catalyst islands and form a large network called a CNT 'mat'. These growth conditions are being manipulated to generate statistical fractal interconnects. To achieve higher degrees of fractal quality of the CNT networks, the catalyst islands can be patterned using optical or electron-beam lithography, or the mat can be patterned post-synthesis by etching away selected regions. An alternative approach for etching will be pursued using atomic force microscopy (AFM). The sharp tip of the AFM will be scanned across the nanotube network while applying an electrical bias to the probe tip, which will cut the network into the desired fractal pattern. Both approaches can achieve features with 10 nm resolution.

35.3 Functionality of the Fractal Interconnects

Our implants are designed to serve two distinct electronic functions – inducing and detecting electrical signals in the neurons. For both functionalities, it is crucial to consider the impact of the fractal design on the mechanical, optical, electrical and physical (adhesive) properties of the neuron-implant interface. Adopting the philosophy that the implant is only as strong as its weakest link, we are targeting the fundamental science that emerges when all of these properties are considered in unison. In terms of their mechanical properties, fractal circuits were recently proposed for stretchable electronics [11] – the associated flexibility will therefore allow our interconnects to be conformal to the regions in which they are implanted. In terms of optics, the surface coverage of the fractal interconnects is considerably less than the equivalent squares due to the multitude of gaps between the branches (Fig. 35.1c, d). This suggests that light can be easily transmitted through the fractal

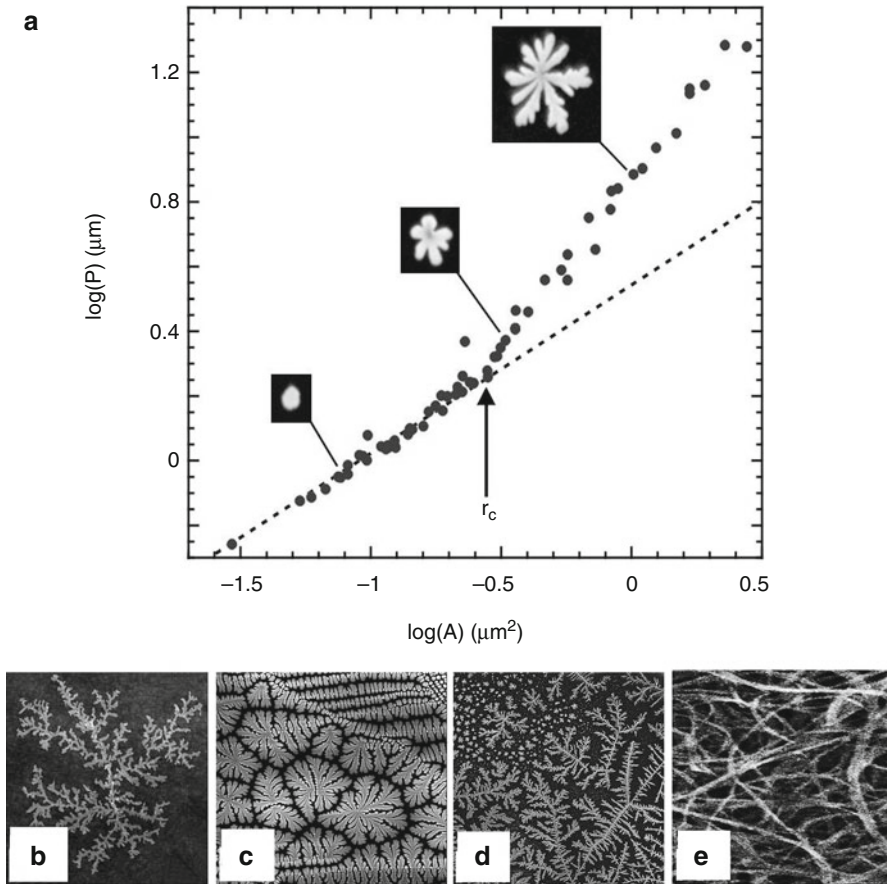


Fig. 35.3 (a) A plot of \log (island perimeter P) versus \log (island area A), as measured from a digital SEM image. Each data point represents an individual island. The dotted line is a guide to the eye, showing the behaviour expected for purely ellipsoidal (i.e. non-fractal) islands. The critical radius (r_c) represents the point at which the data deviates from this behaviour, indicating the formation of fractal branches. (b, c) Images of fractal interconnects demonstrating that their fractal morphology can be controlled by the growth conditions. The interconnects in (b, c) are $10\ \mu\text{m}$ wide. In (d), fractal features span a remarkable 2.5 orders of magnitude down to $90\ \text{nm}$. The interconnects shown in (a–d) are fabricated in collaboration with S. Brown (University of Canterbury, New Zealand). (e) A SEM showing a $5\ \mu\text{m}$ section of a network of CNT branches fabricated in collaboration with B. Alemán (University of Oregon, USA)

interconnect. This will be advantageous for future brain implants that utilise both optical and electrical stimulation [38]. Furthermore, the ability to shine light through the interconnects is crucial for the operation of retinal implants [39]. In addition to minimising coverage, some of the fractal branches are comparable to, or smaller than, the light's wavelength. This raises the possibility of manipulating feature sizes to tune the light transmission using diffractive and plasmonic effects. This idea is inspired by recent experiments (unrelated to implants) demonstrating that fractal

branches efficiently filter light based on its wavelength [2]. The fractal interconnects could therefore potentially serve as colour filters, allowing them to receive white light and then selectively transmit red, green and blue light. As an example of applications, this ‘RGB’ sensitivity could be used to build the first colour vision implants (today’s retinal implants generate monochromatic vision).

The interconnects’ electrical properties are crucial to the operation of both stimulators and sensors. Electronic stimulation dates back to the pioneering *in vivo* studies of Le Roy and Galvani. The electrical fields from their electrodes set up potential differences across the neuron membrane, inducing ion flows that triggered a signal along the axon [6]. In Le Roy’s experiment, for example, this process induced signals in the retinal neurons that the brain interpreted as originating from the retina’s photoreceptors. The positive impact of adopting the fractal geometry becomes clear by returning to the schematic of Fig. 35.1c, d in which the grey interconnect serves as the stimulating electrode. For the same surface coverage, the fractal geometry spreads out further across the implant’s surface than for the conventional square design (i.e. its bounding perimeter is larger). Consequently, the voltages induced by the interconnect extend further from the implant surface into the neural layer, and these larger distances rapidly increase the likelihood of stimulation. The precise extent to which the fractal interconnect outperforms the square will depend on its D value (Fig. 35.2a, b).

In terms of electronic sensors, today’s conventional implants employ either multiple electrode arrays (MEAs) or multiple transistor arrays (MTAs) to measure the electrical potentials generated by neuron signals. However, the simultaneous occurrence of many neuronal signals makes tracking individual signals extremely difficult. This problem is analogous to the ‘cocktail party problem’ when the listener tries to focus on a specific conversation among the background ‘chatter’ from many guests. To accomplish this task, recordings from the conventional sensors are analysed using waveform analysis or triangulation to determine signal location. Waveform analysis relies on a priori information about signals’ temporal characteristics (their waveforms) to identify unique signatures of individual neurons. *In vivo*, this is limited by (1) isolating thousands of signals, (2) waveform variability within each neuron and (3) electrode drift with time [7]. Triangulation works by measuring the waveform variation between different sensors in the array. However, errors in uniquely identifying thousands of signals present critical problems for triangulation algorithms [4]. Despite the clear need to develop nonsubjective measures of signals with quantified errors, different laboratories still can’t objectively compare data. Our fractal sensor avoids all of the above limitations by uniquely identifying neuronal signals without post-measurement analysis and its reliance on a *priori* information about waveforms. Our probe achieves this by adopting the MTA approach but taking the vital step of incorporating a fractal conduction network.

For the conventional MTA, each field effect transistor (FET) in the array features a silicon channel (light grey) which conducts electricity between source (white) and drain (dark grey) terminals (Fig. 35.4a, b). The electric potential generated by neuron signals depletes electrons in the channel, leading to a measurable resistance change. Unfortunately, this traditional design offers little flexibility for improvement. For

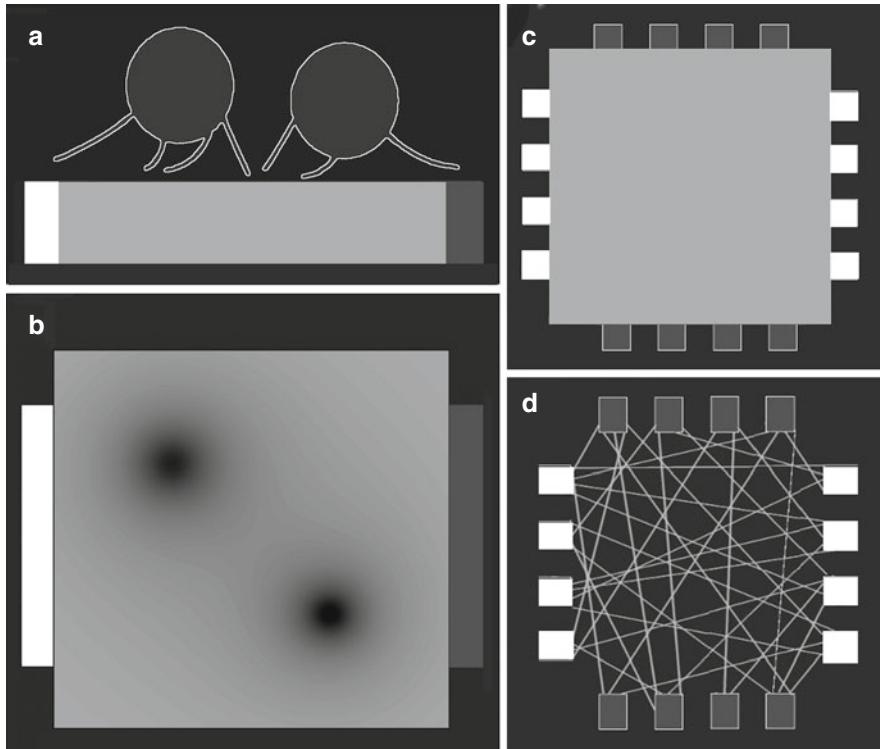


Fig. 35.4 (a) A side view of a FET sensor. The neurons (outlined in white) generate signals that are detected by measuring the electricity flowing through the channel (light grey) between the source (white) and drain (dark grey) terminals. (b) A top view of the FET. The neuron signal depletes electrons in the channel regions (dark) directly below the neurons, thus reducing the measured current flow. (c) A modified FET using multiple (16) source and drain terminals. (d) A FET based on a statistical fractal network of CNTs (light grey lines)

example, gains in measurement resolution by reducing device size are inevitably coupled with larger measurement noise due to increased resistance. Our bio-inspired design is shown in Fig. 35.4d. Current is passed from each of the source terminals (white) to each of the drains (dark grey) through a fractal distribution of conducting channels (light grey lines). Depletion of a local region of this network will induce a rearrangement of current through the network. The non-linear signature of this rearrangement produces an exponential sensitivity of the measured resistance to the location of the depletion region [8] and hence to the neuronal signal. To detect the non-linear signature, the number of measurement terminals per transistor is increased from 2 for the conventional FET (Fig. 35.4a, b) to 16 (Fig. 35.4d). These combine to create an emergent knowledge greater than the sum of the individual measurements. This is achieved through a calibration library that, in real time, converts the multiple resistance values into unique values for position and size of each signal's depletion pattern. The library is generated by a systematic series of tests which establish the

unique multi-resistance signatures of different neuron signal positions. Returning to the cocktail party analogy, the resulting enhanced sensitivity is equivalent to giving the party guests hearing aids. The calibration library is equivalent to the guests working as a team, comparing notes about previous parties.

35.4 The Biophilic Interface

Building on the advantageous mechanical, optical and electrical properties outlined so far, the fractal network also provides a crucial bio-inspired function by establishing a physical fractal pattern in the implant surface. This encourages neurons to stay close to the surface, enhancing stimulation and detection of their signals. This is analogous to attracting the party guests that you want to listen and talk to. Previous experiments have shown that surface topologies that are not smooth encourage neuron adhesion, e.g. [10, 14, 17, 25, 30], and that topological factors are more important than the chemical environment established by the materials used [15]. Only 10% of neurons adhere to smooth metallic interconnects [34], while experiments on textured metallic interconnects indicate 50% [32]. None of the previous studies took the vital step of introducing surface patterns that match the neurons' fractal branches to improve adhesion.

In addition, smooth surfaces are known to trigger an accumulation of glial cells into a protective layer called a glial scar [3]. Whereas the presence of individual glial cells is a signature of health (because they serve as the neuron's life-support system), the scar pushes the neurons away from the smooth surface of conventional implants reducing their ability to stimulate or sense the neurons. Based on these findings, our *in vitro* experiments (Fig. 35.5) are designed to test our hypothesis that (1) neurons will adhere to the physical patterns established by the fractal distribution of channels (i.e. the pattern of lines in Fig. 35.4d); (2) to maintain health, these neurons might be accompanied by individual glial cells; and (3) glial cells will accumulate in the smooth regions established by the larger gaps (i.e. black regions) in Fig. 35.4d. Thus, even if this accumulation eventually forms a scar, it will not form on the lines (conducting channels).

In the *in vitro* experiments, implants are lowered into a retinal culture and fluorescence microscopy is used to image cells as they interact with the interconnects [27]. To prepare the culture, the retina is first removed from the outer epithelium of neonatal mice and placed in a culture medium, which is then mechanically agitated to separate the retinal cells. Staining allows the various retinal cells to be analysed separately. DAPI (blue) fixes to both glial and neuron cell nuclei (allowing a total cell count), GFAP (green) attaches to glial cells and β -tubulin III (red) binds to neuron microtubules. A simple test geometry, consisting of rows of 100 μm -wide textured regions separated by rows of smooth surface, confirmed expectations that neurons predominantly adhere to the textured regions and glial cells accumulate in the smooth gaps [28]. Furthermore, immunohistochemistry confirmed that markers expressed by healthy neurons were present. The microscopy was performed after

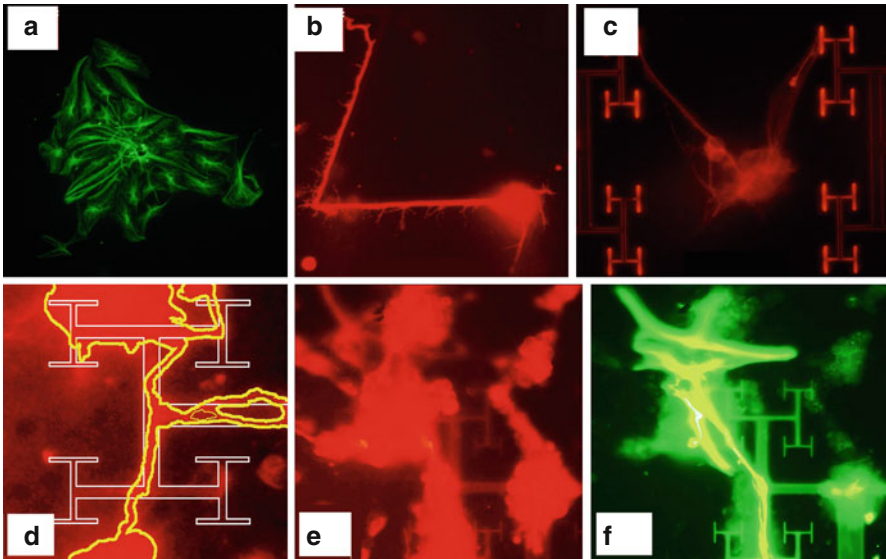


Fig. 35.5 Images from the *in vitro* fluorescence microscopy experiments. (a) A 300 μm -wide glial scar (*green*) forming on a smooth surface. (b) A neuron (*red*) extending along a test interconnect with a 200 μm long ‘zigzag’ shape. (c) A neuron (*red*) located in a 100 μm gap within one of our fractal ‘H-tree’ designs. (d) Individual neuron dendrites (highlighted with *yellow* edges) attach to fractal interconnect branches (*white* edges) (image width = 60 μm). The images in (e) and (f) demonstrate how individual neurons (*red*) and glial cells (*green*) adhere to the same interconnect region (image widths = 150 μm) (All images are taken in collaboration with M.T. Perez (Lund University, Sweden))

18 days (this is close to the maximum period for *in vitro* studies). This time frame is significantly longer than on-sets of scar formation in previous *in vitro* experiments (2 days) [21] and is of the order of scar formation in *in vivo* experiments (2–3 weeks) [29]. Thus, any detrimental developments would have emerged by day 18. Furthermore, there were no significant changes between days 8 and 18, suggesting that the experiment captured long-term behaviour and that the observed positive effects will persist indefinitely.

Figure 35.5a shows an image of glial cells (*green*) accumulating on a smooth surface and forming a scar. We are developing novel pattern analysis techniques to characterise this process and to quantify the scar’s growth rate and size. The image in Fig. 35.5b shows a neuron (*red*) extending along a test interconnect with a zigzag shape. These test patterns show that neurons can follow interconnect branches for more than 200 μm and can turn through angles sharper than 90° . The image in Fig. 35.5c shows a neuron located in a gap within one of our fractal ‘H-tree’ designs. Images such as this are being used to quantify how far neuron dendrites can extend in order to adhere to the interconnect branches. The interconnect’s fractal geometry amplifies the effects revealed in Fig. 35.5a–c because it maximises the combination of patterned lines and smooth gaps within a given region. Indeed, positive effects

are already evident after 3 days in culture: the zoom-in of Fig. 35.5d shows adhesion of neural dendrites to the fractal lines of the interconnect. This picture is further supported by Fig. 35.5e, f which shows that an attached neuron is accompanied by an individual glial cell.

Based on the above preliminary research, our long-term aim is for each neuron dendrite to automatically seek out and adhere to a fractal branch of the interconnect. Consequently, this ‘one-to-one’ adhesion could generate unprecedented stimulation and sensing. We also aim for ‘selective’ adhesion, whereby targeted types of neuron will adhere to specific interconnects. We hope to achieve selective adhesion (and consequently selective stimulation and sensing) by matching the specific fractal properties of the interconnects to those of the target neurons. Analysing the neuron shapes is vital for understanding the neuron-interconnect interface. Previous research of neuron geometry used fractal analysis simply as a tool for quantifying their structural complexity. In contrast, we are using confocal microscopy to construct three-dimensional images of neurons, allowing the first investigation of the origin of neurons’ fractal character (Fig. 35.1a, b). Strikingly, this character originates from the way dendrites ‘weave’ through space. This has crucial consequences because adhesion experiments reveal that this weave is forced to change as neurons interact with surfaces. Our hypothesis predicts superior adhesion when the fractal characteristics (in particular D and branch orientation (Fig. 35.2)) of the interconnect and neuron are matched. This will occur because the dendrites can connect without having to adjust their fractal characteristics. This effect is an example of ‘fractal geometric resonance’ in which interface properties are enhanced by matching the geometric properties of two fractals. Because different neuron types are expected to have specific weaves [24], selective adhesion should be possible – whereby specific neurons adhere to targeted interconnects based on their precise fractal characteristics. This novel capability offers the possibility of revolutionising applications of human implants. Considering the eye as an example, the retina features five types of neuron. Successful implants will need to select which neuron types to stimulate and sense. Similarly, brain implants will also be able to target selected neuron types.

35.5 Conclusions

Fractal implants that stimulate or sense neuronal signals in the brain could be used to address a number of pathological conditions including Parkinson’s disease. In addition, they could also radically improve other stimulation techniques to improve learning and cognition, visual perception, working memory and motor control [13]. The long-term potential impact of fractal interconnects stretches well beyond improving implants designed to interact with the human brain, retina and limbs. In addition to stimulating and sensing naturally occurring neurons, they could be applied to retinal stem cells in *in vitro* and *in vivo* investigations.

Acknowledgements We thank our collaborators S. Brown, J. Dalrymple-Alford and B. Harland (University of Canterbury, New Zealand); B. Alemán, K. Fairley and D. Johnson (University of Oregon, USA); and M. Perez (Lund University, Sweden). We also thank the Research Corporation for Science Advancement (RCSA), the ONR-ONAMI N3 programme and the W.M. Keck Foundation for funding.

References

1. Abbot A. Neuroscience: solving the brain. *Nature*. 2013;499:272–4.
2. Afshinmanesh F, Curto AG, Milaninia KM, van Hulst NF, Brongersma ML. Transparent metallic fractal electrodes for semiconductor devices. *Nano Lett*. 2014;14:5068–74.
3. Butterwick A, Huie P, Jones BW, Marc RE, Marmor M, Palanker D. Effect of shape and coating of a subretinal prosthesis on its integration with the retina. *Exp Eye Res*. 2009;88:22–9.
4. Buzsáki G. Large-scale recording of neuronal ensembles. *Nat Neurosci*. 2004;7:446–51.
5. Chen X, Kis A, Zettl A, Bertozzi CR. A cell nanoinjector based on carbon nanotubes. *Proc Natl Acad Sci*. 2007;104:8218–22.
6. Cogan SF. Neural stimulation and recording electrodes. *Annu Rev Biomed Eng*. 2008;10:275–309.
7. Einevoll GT, Franke F, Hagen E, Pouzat C, Harris KD. Towards reliable spike-train recordings from thousands of neurons with multielectrodes. *Curr Opin Neurobiol*. 2012;22:11–7.
8. Fairbanks MS, McCarthy DN, Scott SA, Brown SA, Taylor RP. Fractal electronic devices: simulation and implementation. *Nanotechnology*. 2011;22:365304.
9. Fairbanks MS, Taylor RP. Measuring the scaling properties of temporal and spatial patterns: from the human eye to the foraging albatross. In: *Nonlinear dynamical systems analysis for the behavioral sciences using real data*. Boca Raton: CRC Press; 2011: p. 341–66.
10. Fan YW, Cui FZ, Hou SP, Xu QY, Chen LN, Lee IS. Culture of neural cells on silicon wafers with nano-scale surface topograph. *J Neurosci Methods*. 2002;120:17–23.
11. Fan JA, Yeo WH, Su Y, Hattori Y, Lee W, Jung SY, Zhang Y, Liu Z, Cheng H, Falgout L, Bajema M. Fractal design concepts for stretchable electronics. *Nat Commun*. 2014;5:1–8.
12. Fischer KE, Alemán BJ, Tao SL, Daniels RH, Li EM, Bünger MD, Nagaraj G, Singh P, Zettl A, Desai TA. Biomimetic nanowire coatings for next generation adhesive drug delivery systems. *Nano Lett*. 2009;9:716–20.
13. Fox D. Neuroscience: brain buzz. *Nat News*. 2011;472:156–9.
14. Gentile F, Medda R, Cheng L, Battista E, Scopelliti PE, Milani P, Cavalcanti-Adam EA, Decuzzi P. Selective modulation of cell response on engineered fractal silicon substrates. *Sci Rep*. 2013;3:1461–71.
15. Gomez N, Chen S, Schmidt CE. Polarization of hippocampal neurons with competitive surface stimuli: contact guidance cues are preferred over chemical ligands. *J R Soc Interface*. 2007;4:223–33.
16. Guenther E, Tröger B, Schlosshauer B, Zrenner E. Long-term survival of retinal cell cultures on retinal implant materials. *Vis Res*. 1999;39:3988–94.
17. Hällström W, Mårtensson T, Prinz C, Gustavsson P, Montelius L, Samuelson L, Kanje M. Gallium phosphide nanowires as a substrate for cultured neurons. *Nano Lett*. 2007;7:2960–5.
18. Hämmerle H, Kobuch K, Kohler K, Nisch W, Sachs H, Stelzle M. Biostability of micro-phodiode arrays for subretinal implantation. *Biomaterials*. 2002;23:797–804.
19. Hertel T, Walkup RE, Avouris P. Deformation of carbon nanotubes by surface van der Waals forces. *Phys Rev B*. 1998;58:13870.
20. Jensen K, Mickelson W, Kis A, Zettl A. Buckling and kinking force measurements on individual multiwalled carbon nanotubes. *Phys Rev B*. 2007;76:195436.
21. Lewis GP, Fisher SK. Muller cell outgrowth after retinal detachment: association with cone photoreceptors. *Injury*. 2000;1542:1545.

22. Liu Y, Zhao Y, Sun B, Chen C. Understanding the toxicity of carbon nanotubes. *Acc Chem Res.* 2012;46:702–13.
23. Lozano A. Tuning the brain. *The Scientist.* 2013; 27. Available from: <http://www.the-scientist.com/?articles.view/articleNo/38047/title/Tuning-the-Brain/>.
24. MacNeil MA, Heussy JK, Dacheux RF, Raviola E, Masland RH. The population of bipolar cells in the rabbit retina. *J Comp Neurol.* 2004;472:73–86.
25. Mattson MP, Haddon RC, Rao AM. Molecular functionalization of carbon nanotubes and use as substrates for neuronal growth. *J Mol Neurosci.* 2000;14:175–82.
26. Micolich AP, Taylor RP, Davies AG, Bird JP, Newbury R, Fromhold TM, Ehlert A, Linke H, Macks LD, Tribe WR, Linfield EH, Ritchie DA, Cooper J, Aoyagi Y, Wilkinson PB. The evolution of fractal patterns during a classical-quantum transition. *Phys Rev Lett.* 2001;87:036802–5.
27. Piret G, Perez MT, Prinz CN. Neurite outgrowth and synaptophysin expression of postnatal CNS neurons on GaP nanowire arrays in long-term retinal cell culture. *Biomaterials.* 2013;34:875–87.
28. Piret G, Perez MT, Prinz CN. Support of neuronal growth over glial growth and guidance of optic nerve axons by vertical nanowire arrays. *ACS Appl Mater Interfaces.* 2015;7:18944–8.
29. Polikov VS, Tresco PA, Reichert WM. Response of brain tissue to chronically implanted neural electrodes. *J Neurosci Methods.* 2005;148:1–8.
30. Rajniecek A, Britland S, McCaig C. Contact guidance of CNS neurites on grooved quartz: influence of groove dimensions, neuronal age and cell type. *J Cell Sci.* 1997;110:2905–13.
31. Sachrajda AS, Taylor RP, Dharmawardana D, Zawadzki P, Adams JA, Coleridge PT. Spin-controlled resonances in the magneto-transport in quantum dots. *Phys Rev B Rapid Commun.* 1993;47:6811–4.
32. Schlie-Wolter S, Deiwick A, Fadeeva E, Paasche G, Lenarz T, Chichkov BN. Topography and coating of platinum improve the electrochemical properties and neuronal guidance. *ACS Appl Mater Interfaces.* 2013;5:1070–7.
33. See AM, Pilgrim I, Scannell BC, Montgomery R, Klochan O, Aagesen M, Lindelof P, Farrer I, Ritchie DA, Taylor RP, Hamilton AR, Micolich AP. Impact of small-angle scattering on ballistic transport in quantum dots. *Phys Rev Lett.* 2012;108:196807–10.
34. Stingl K, Bartz-Schmidt KU, Besch D, Chee CK, Cotttriall CL, Gekeler F, Groppe M, Jackson TL, MacLaren RE, Koitschev A, Kusnyerik A. Subretinal visual implant alpha IMS—clinical trial interim report. *Vis Res.* 2015;111:149–60.
35. Taylor RP. The role of surface-gate technology for AlGaAs/GaAs nanostructures. *Nanotechnology.* 1994;5:183.
36. Taylor RP. Artificial vision: vision of beauty. *Phys World.* 2011;24:22–7.
37. Taylor RP, Sachrajda AS, Zawadzki P, Coleridge PT, Adams JA. Aharonov-Bohm oscillations in the coulomb blockade regime. *Phys Rev Lett.* 1992;69:1989–92.
38. Zhang J, Laiwalla F, Kim JA, Urabe H, Van Wagenen R, Song YK, Connors BW, Zhang F, Deisseroth K, Nurmikko AV. Integrated device for optical stimulation and spatiotemporal electrical recording of neural activity in light-sensitized brain tissue. *J Neural Eng.* 2009;6:055007.
39. Zrenner E. Will retinal implants restore vision? *Science.* 2002;295:1022–5.

Chapter 36

Fractal Geometry Meets Computational Intelligence: Future Perspectives

Lorenzo Livi, Alireza Sadeghian, and Antonio Di Ieva

Abstract Characterizations in terms of fractals are typically employed for systems with complex and multi-scale descriptions. A prominent example of such systems is provided by the human brain, which can be idealized as a complex dynamical system made of many interacting subunits. The human brain can be modeled in terms of observable variables together with their spatio-temporal-functional relations. Computational Intelligence is a research field bridging many nature-inspired computational methods, such as artificial neural networks, fuzzy systems, and evolutionary and swarm intelligence optimization techniques. Typical problems faced by means of Computational Intelligence methods include those of recognition, such as classification and prediction. Although historically conceived to operate in some vector space, such methods have been recently extended to the so-called non-geometric spaces, considering labeled graphs as the most general example of such patterns. Here we suggest that fractal analysis and Computational Intelligence methods can be exploited together in neuroscience research. Fractal characterizations can be used to (i) assess scale-invariant properties and to (ii) offer numeric, feature-based representations to complement the usually more complex pattern structures encountered in neurosciences. Computational Intelligence methods could be used to exploit

L. Livi, PhD (✉) • A. Sadeghian, PhD
Department of Computer Science, Ryerson University,
350 Victoria Street, Toronto, ON M5B 2K3, Canada
e-mail: llivi@scs.ryerson.ca; asadeghi@ryerson.ca

A. Di Ieva, MD, PhD
Neurosurgery Unit, Faculty of Medicine and Health Sciences, Macquarie University,
Sydney, NSW, Australia

Garvan Institute of Medical Research, Sydney, NSW, Australia

Medical University of Vienna, Vienna, Austria

University of Toronto, Toronto, ON, Canada
e-mail: diieva@hotmail.com; antonio.diieva@mq.edu.au

such fractal characterizations, considering also the possibility to perform data-driven analysis of non-geometric input spaces, hence overcoming the intrinsic limits related to Euclidean geometry.

Keywords Computational intelligence • Complex systems • Analysis of non-geometric input spaces • Fractal analysis • Brain research

36.1 Introduction

The analysis of complex systems [16, 31, 43] is rapidly expanding with the development of novel theoretical and computational tools designed to tackle the problem of disentangling the interactions among different parts of a complex process/system. The human brain is a natural and important example of complex systems made of many interacting parts. The rich complexity of the brain along with its multilevel, time-varying, and intricate topological organization of neurons suggests to look beyond explanations driven by classical Euclidean geometry and linear dynamics [21–23]. Mathematical tools from fractal geometry offer a means to perform quantitative analysis and description of the complexity of natural, social, and artificial systems. It is a fact that modern neurosciences admit the prevalence of fractal properties in the brain at various levels of observation and in different contexts. In general, the brain can be analytically or computationally studied by (i) focusing on a specific subunit (i.e., a specific aspect) and/or (ii) by taking into account (time-dependent) interactions between such units. In the first case, usually one resorts to the study of a series of suitable observable variable recorder over some time span – usually named time series. In the literature, there are many approaches to study the peculiarities of the systems underlying the observed time series. Such methods include causality analysis [1] and directional transfer of information [41, 68, 69], memory effects and predictability in stochastic systems [17, 55], clustering [91], and recurrence plots [57]. In the latter case, instead, the graph-theoretic framework and its modern revival as the science of complex networks play a pivotal role in the characterization of brain structures along with its dynamical and functional aspects [9, 19, 27, 35, 64, 78, 85, 89]. Graph characterizations, in terms of both static and dynamic measures of complexity, are also popular in describing complex systems and their functions [3, 15, 20, 24, 26, 34, 47, 51, 54, 72, 94].

The field of Computational Intelligence (CI) is founded on data-driven methods, which take inspiration from natural systems. Examples of such systems include artificial neural networks, kernel methods, fuzzy systems, and evolutionary and swarm intelligence optimization techniques as well [25]. Typical tasks tackled by means of Computational Intelligence methods include recognition problems (e.g., classification, clustering, and function approximation) and those of adaptive control (e.g., fuzzy control and data-driven optimization via neural networks). Intelligent systems operating through data analysis come with various connotations and usually imply different interpretations. In spite of the existing diversities, it is possible to recognize several features that are profoundly visible across a broad spectrum of those systems.

An intelligent system should be adaptable, meaning that it should come with a parametric mathematical model. Adaptation is typically implemented via the learning-from-examples paradigm by using suitably error criteria and update mechanisms. Another important aspect characterizing intelligent systems is the capability to generalize with accuracy under uncertainty or when dealing with unseen data. The spectrum of successful applications of Computational Intelligence methods is rapidly expanding. Far from being exhaustive, it is worth to cite few related applications in biomedical and particularly in the brain science context: classification of brain injury [67], seizure recognition in intracranial EEG [97], feature transformation and clustering on fMRI data [96], and data selection for EEG signal classification [88].

Here in this chapter we hypothesize that an interplay between fractal analysis and Computational Intelligence methods could offer a compelling tool of analysis in neuroscience. Fractal characterizations can be used to (i) assess scale-invariant properties and to (ii) offer numeric, feature-based representations to complement the usually more complex pattern structures encountered in brain research. Computational Intelligence methods could be used to exploit such fractal characterizations, considering also the possibility to perform data-driven analysis of non-geometric input spaces, hence overcoming the limits related to Euclidean geometry-based approaches.

The remainder of this chapter is structured as follows. Section 36.2 offers a brief overview of fractal analysis and its impact in neuroscience. In Sect. 36.3, we introduce the Computational Intelligence research context; we discuss also the more recent research endeavor in processing non-geometric data by using conventional Computational Intelligence methods. Section 36.4 provides a conceptual bridge between fractal analysis and Computational Intelligence methods, highlighting their possible interplay in future researches. Finally, Sect. 36.5 concludes this chapter offering future perspectives for interdisciplinary research in brain science.

36.2 Fractal Analysis and Brain Complexity

Fractal and multifractal analysis play a pivotal role in several scientific fields. Notably, neuroscience [28, 29, 63] and physiology in general [92, 93] are two important examples. Characterizations in terms of fractal scaling are typically used for the purpose of describing the complexity of systems following a multiscale paradigm. Fractal analysis formalisms have been developed for image analysis, discrete-time signals (i.e., time series), and complex networks analysis as well. Considering the former, a large body of applications exists, including neuronal spike trains [70], background neuronal noise-like activity underlying epileptiform transitions in human and mouse hippocampus [82], and EEG signals analysis [6, 42, 81, 95], for instance. The application of fractal geometry to the analysis of complex networks is a novel research approach [18, 33, 44, 46, 56, 76, 84]. As suggested by Song et al. [84], fractal scaling in complex networks emerges as a particular combination of a disassortative degree mixing – repulsion between hub and weakly connected vertices. The renormalization group approach [76] is a well-known approach to evaluate the fractality of a network

underlying dynamical changes. The method consists in compressing the network in clusters by considering a characteristic (topological) length scale. If the network compression adheres to a specific power-law scaling, then the network can be considered as fractal. It is worth stressing that the renormalization group approach provided a way to explain the coexistence of otherwise conflicting features, such as fractal and small-world properties of networks. Li et al. [44] recently proposed a generalization of the box-counting method in order to perform multifractal analysis on complex networks. A novel perspective for multifractal analysis of complex networks has been recently proposed by Maiorino et al. [56]. Time series of vertex observables, such as degree, clustering coefficient, and closeness centrality, can be formed via (stationary) random walks on the network. Fractal and multifractal analysis can then be performed by making use of the more consolidated time series framework. The fractal structure of brain networks is typically related to its highly modular topology [32, 65], which contributes the compartmentalization of brain functions. However, brain networks, as well as other complex biophysical systems, exhibit also the celebrated small-world feature [9], implying that efficiency of long-range connections is something that is optimized taking care of the related (energetic) costs.

36.3 Computational Intelligence Methods and the Challenge of Processing Non-geometric Input Spaces

Computational Intelligence (CI) is a research field bringing together many nature-inspired computational methods, such as artificial neural networks, fuzzy systems, and evolutionary and swarm intelligence optimization techniques [25]. In Table 36.1 we report some of the most common terminology, methods, and techniques that are encountered in the CI research field. It is worth noting that CI is closely related to soft computing, which is a toolbox of techniques, conceived to provide solutions for modeling and computational problems casted in an intrinsically uncertain and complex setting. Bonissone [7] defines the boundary of the soft computing context by stating “The term Soft Computing (SC) represents the combination of emerging problem-solving technologies such as Fuzzy Logic, Probabilistic Reasoning, Neural Networks, and Genetic Algorithms. Each of these technologies provide us with complementary reasoning and searching methods to solve complex, real-world problems.”

Typical problems faced by means of CI methods include recognition problems (e.g., classification, clustering, and function approximation [12, 39, 45, 50, 58, 59, 61, 62, 86, 90, 98]) and those of adaptive control (e.g., fuzzy control and data-driven optimization via neural networks [40, 60]). Focusing on recognition problems [38, 87], the concept of pattern, plays an important role. Patterns can be discovered virtually everywhere: in climate science, geophysics, rare catastrophic events, complex biochemical processes in living beings and ecosystems, clinical diagnostics, financial market trends, and social network evolution. Formally

Table 36.1 Typical terminology and methods used in the Computational Intelligence field (sorted in alphabetic order)

Terminology	Definition
Artificial neural networks	Adaptive system comprised of nodes and connections in an organization similar to the central nervous system. Neural networks are capable of dealing with complex systems by adapting the model during the learning phase
Back propagation algorithm	Learning algorithm for neural networks
Data mining	Techniques used to analyze and discover knowledge and relationships in data
Evolutionary algorithm	Global optimization method inspired by evolution biological systems. Important concepts include fitness function, natural selection, mutation, recombination, and crossover
Expert system	Computer technique that aims to simulate a human expert in order to provide support and advices to humans
Fuzzy logic	A multivalued logic in which the degree of truth of statement ranges in the unit interval
Hidden Markov model	Statistical model used to characterize and predict sequences of observable variables without inspecting directly the underlying system's state
K-nearest neighbor	Classification method that categorizes data according to their proximity in a given representation space
Machine learning	Computer algorithms designed to learn complex relationships, rules, and patterns from empirical data in order to perform inductive inference
Representation space	Mathematical formalization of the input space where the data is represented
Self-organizing feature map	Unsupervised learning mechanism that can be used for either clustering and classification
Supervised learning	Methods of machine learning that requires knowledge of the classes during the training of the model
Support vector machines	Flexible method for linear and nonlinear classification based on the concept of separating hyperplane and convex optimization
Unsupervised learning	Machine learning techniques that do not require knowledge of the classes during the training

speaking, a pattern is a form of experimental evidence gathered from a data-generating process, P . A process $P: X \rightarrow Y$ is the idealization of a system, either abstract or physical, which generates outputs according to input patterns. X is referred to as the input space (or data domain, representation space), where the patterns are represented according to some suitable formalism. Y , instead, is the output space, providing a way to learn how to recognize patterns according to their description. In pattern recognition the closed-form, analytical expression of P is unknown. The problem typically is reduced to determine the parameters of a suitable mathematical model of P , e.g., M , by analyzing a finite dataset S . The

objective is to obtain a model that is able to generalize over pattern instances different from those in S . Three categories of problems in pattern recognition can then be distinguished:

1. *Classification*. In classification, Y is finite set of classes (a finite nominal set of labels) that is completely – or, in some variations, partially – known a priori. X contains pattern instances that are (correctly) labeled with respect to Y . Classification is also referred to as discrimination, since in fact the problem consists of learning a model that is able to correctly label patterns.
2. *Clustering*. In clustering, X contains unlabeled pattern instances, and therefore the definition of Y is not available a priori; there is no supervision. The goal is to determine the hidden structure of the data by relying on some measure of similarity among the patterns.
3. *Function approximation*. In function approximation (also known as regression), Y is a normed space, usually a continuous interval in \mathbb{R} . As the name suggests, the goal is learn a (nonlinear) function by using labeled training patterns in X . In the case of multidimensional outputs, i.e., when the problem is generalized to learning a mapping.

Practically, a mathematical model M must be tuned to the problem at hand. Learning (or synthesizing) a model M from the available dataset S consists in optimizing some criterion, i.e., a performance measure that allows adjusting the model parameters according to suitable training dataset. Two principal schools of pattern recognition exist: the one including discriminative methods (such as support vector machines [80] and many neural network models [38]) and the one exploiting generative models (such as the well-known hidden Markov model [5] and several versions of the recently developed deep convolutional neural network model [79]).

CI methods are typically designed based on the assumption that the input space, X , is essentially a subset of \mathbb{R}^d . When departing from the \mathbb{R}^d vector-based pattern representation, many theoretical and practical problems arise, which are mostly due to the absence of an intuitive geometric interpretation of the data. Notwithstanding, the availability of datasets of non-geometric data motivated the development of pattern recognition and soft computing techniques on such domains [2, 4, 14, 30, 49, 52, 53, 66, 73–75, 99, 100]. Non-geometric patterns include data which are characterized by pairwise dissimilarities that are not metric; therefore, they cannot be straightforwardly represented in a Euclidean space [36, 52, 66]. A particularly interesting instance of such non-geometric data is constituted by structured patterns. A structured pattern is conceived to include in the structure the information regarding the relations and, at the same time, attributes describing the pattern itself. A labeled graph is the most prominent example of structured pattern that is conceivable. In fact, a graph can be used to characterize a pattern by describing the topological structure of its constituting elements (by means of the vertices) through their relations (the edges) [11, 37, 48]. Both vertices and edges can be equipped with suitable labels, i.e., the specific attributes characterizing the elements and their relations. Sequences of generic objects, trees, and automata can be thought of as particular instances of labeled graphs. Labeled graphs are used to represent data and systems in many different contexts, such as document analysis [10],

solubility of the *Escherichia coli* proteome [54], brain functional networks [71], biomolecule recognition [13, 77], digital images [83], and scene understanding [8].

Figure 36.1 offers a schematic, visual representation of the typical stages involved in the use of CI methods to address recognition problems. By means of a training set (Tr in the figures), a model is synthesized and then used during the testing stage using unseen data (denoted as Ts). This high-level overview is valid for both \mathbb{R}^d (1(a)) and non-geometric (1(b)) data. However, in order to make proper use of CI methods, in the case of non-geometric data, the input space must be processed with particular care. Notably, three mainstream approaches can be pursued [52, 66]: (i) using a suitable dissimilarity measure operating in the input space, (ii) using positive definite (PD) kernel functions, and (iii) designing an embedding to map the input in \mathbb{R}^n . The choice depends on the particular data-driven system adopted for the task at hand and on other factors, typically related to the particular application context. The first case is the most straightforward one, but its use is legitimate only if the data-driven system does not require a specific geometrical structure of the input space. In fact, a dissimilarity measure might not be metric, therefore not Euclidean either. A first example in this direction could be provided by citing the well-known k -nearest neighbor rule, which process the input patterns by relying only on their topological similarity. The second scenario is a typical choice in the case of kernel methods. However, positive definite kernels can be obtained only if the underlying geometry is Euclidean. Nonetheless, if such a requirement is not satisfied at first, correction techniques could

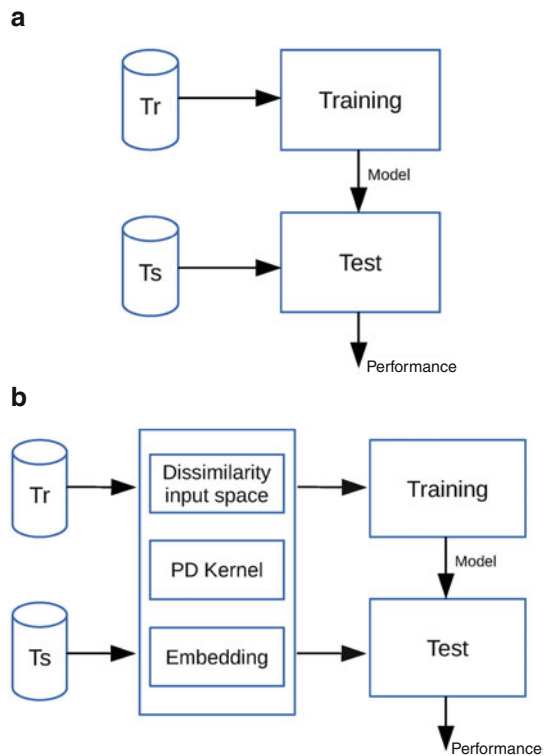


Fig. 36.1 Schematic representations of a data-driven inference system operating in \mathbb{R}^d (a) and considering non-geometric data (b), respectively

be used for this purpose to “rectify” the data domain [52]. The last approach consists of mapping (i.e., embedding) the input space to a vector space, typically \mathbb{R}^n . By this way, conventional CI methods can be used without alterations since in fact the problem is reduced to processing conventional patterns represented as numeric vectors.

36.4 On the Interplay Between Fractal Analysis and CI Methods

As mentioned before, from a computational viewpoint, the human brain can be studied by considering measurements targeted to specific regions together with their spatial, temporal, and functional relations. A systemic view of such measurements gives rise to complex data patterns, providing structured and potentially heterogeneous dataset of information to be processed. CI techniques, with particular interest in those for non-geometric data, could be used to tackle data-driven problems in such a context [71].

Let us elaborate further on this idea by describing a hypothetical case study. Let us assume that we are interested in modeling each particular state of the conscious mind as a graph – a network of activated brain regions. Furthermore, typically we would be interested in correlating such states with the execution of task; therefore, we assume to have collected such states during the execution of a specific task over time. A graph would provide a way to encode the time-varying relations among the active brain regions, together with suitable, problem-dependent descriptive attributes. Such attributes can be associated to both vertices and edges, describing in principles any type of data (signals, vectors, sequences). In order to infer insights on structure–function relationships from the experiment, the collection of graphs recorded over time could be analyzed with conventional graph-theoretical methods. For example, it could be beneficial to study the variation of structural and dynamical properties elaborated from such graphs, including their fractal dimension – for instance, as a measure of complexity. However, it could also be interesting to conceive problems of automatic classification (discrimination) of such states, dealing with the classification problem directly in the space of graphs, i.e., states of the conscious mind in our example. This might be of interest to a neuroscientist, since representing a neurological state as a graph has significantly more representational power than using a vector of numeric values. Notably, it could be interpreted more easily, and hence the discrimination process could be explained in a language closer to human reasoning. The interpretability issue of CI methods is a well-known research endeavor; researchers usually refer to such a problem with the expression “opening the black-box.” In fact, most the CI methods operate without providing information intelligible to humans. Of course, this is not an issue when the task at hand is purely technological – problem-solving oriented. However, when scientific knowledge has to be extracted from a data-driven process, then interpretability of the data and the inference mechanism itself assumes critical importance.

We hypothesize here that the interplay of fractal analysis and Computational Intelligence methods could offer a compelling tool of analysis in the context of brain research. Fractal characterizations can be used to assess scale-invariant

properties and offer numeric, feature-based representations to complement the otherwise more complex patterns usually encountered in brain research. Computational Intelligence methods, especially those for non-geometric spaces, could be used to face specific recognition problems exploiting such information, without limiting the problem definition to conventional Euclidean spaces.

36.5 Future Perspectives and Concluding Remarks

The human brain is a complex dynamical system made of many units (neurons) that interact over time, space, and/or by considering specific functions. The hierarchical organization of the brain connections calls for advanced computational techniques of analysis, including those based on graph-theoretical methods and time series analysis. The intricate shape of the brain is better described in terms of fractal geometry and related mathematical and computational tools. The field of Computational Intelligence research is founded on data-driven methods, which take inspiration from natural systems. Examples of such systems include artificial neural networks, fuzzy systems, and evolutionary and swarm intelligence optimization techniques. We discussed also the more recently developed methods for analyzing non-geometric spaces, which allow to depart from the assumption of an underlying Euclidean geometry for the input space.

In this chapter, we first described graph-based and time series analysis methods exploiting fractal analysis concepts. Such methods play an important role in neurosciences, since in fact the types of data that are encountered in such a context require complex characterizations that typically go beyond the usual vector-based representation. Successively, we suggested a possible interplay between fractal analysis and Computational Intelligence methods, especially considering methods for non-geometric spaces. Computational Intelligence methods (such as classifiers and prediction systems) are already highly exploited in related contexts, such as biomedical signals and diagnostic medicine. However, the full potential of an interplay between the two disciplines still needs to be discovered.

In the following, we provide a list of possible applications in which Computational Intelligence methods and fractal analysis could be used by neuroscientists:

- Time series in physiological as well as pathological states, e.g., intracranial pressure trends to predict patients' outcome following traumatic brain injury and/or bleeding
- EEG analysis for seizure prediction, MEG (magnetoencephalography) time series analysis for analysis of cognitive states, EMG (electromyography) time series analysis for the study of neuromuscular disorders, fMRI analysis of brain oscillation in physiopathological states
- Image analysis for characterization of brain tumor features (e.g., distribution of the microvessels, roughness of the tumors' edges, architectural pattern, etc.) for automatic classification (histotype and/or grading) and follow-up. Machine learning algorithms for the classification of brain diseases according to neuro-radiological features (e.g., spectroscopy) and for the connectomics analysis

- Training machines for automatic segmentation of region of interests, such as brain tumors and/or arteriovenous malformations, for surgical and/or radiosurgical planning
- Neural networks and similar CI methods for the analysis of gene expression patterns in neurological diseases
- Computational quantitative analysis for the study of brain cells and receptors.

References

1. Amblard P-O, Michel OJJ. The relation between granger causality and directed information theory: a review. *Entropy*. 2012;15(1):113–43.
2. Bai L, Rossi L, Torsello A, Hancock ER. A quantum Jensen–Shannon graph kernel for unattributed graphs. *Pattern Recog*. 2015;48(2):344–55.
3. Banerji CRS, Severini S, Teschendorff AE. Network transfer entropy and metric space for causality inference. *Phys Rev E*. 2013;87(5):052814.
4. Bianchi FM, Livi L, Rizzi A, Sadeghian A. A granular computing approach to the design of optimized graph classification systems. *Soft Comput*. 2014;18(2):393–412.
5. Bicego M, Murino V, Figueiredo MAT. Similarity-based classification of sequences using hidden Markov models. *Pattern Recog*. 2004;37(12):2281–91.
6. Blythe DAJ, Haufe S, Müller K-R, Nikulin VV. The effect of linear mixing in the EEG on hurst exponent estimation. *Neuroimage*. 2014;99:377–87.
7. Bonissone PP. Soft computing: the convergence of emerging reasoning technologies. *Soft Comp*. 1997;1(1):6–18.
8. Brun L, Saggese A, Vento M. Dynamic scene understanding for behavior analysis based on string kernels. *IEEE Trans Circ Syst Video Technol*. 2014;24(10):1669–81.
9. Bullmore ET, Sporns O. The economy of brain network organization. *Nat Rev Neurosci*. 2012;13(5):336–49.
10. Bunke H, Riesen K. Recent advances in graph-based pattern recognition with applications in document analysis. *Pattern Recog*. 2011;44(5):1057–67.
11. Bunke H, Riesen K. Towards the unification of structural and statistical pattern recognition. *Pattern Recog Lett*. 2012;33(7):811–25.
12. Castillo O, Melin P, Pedrycz W. Design of interval type-2 fuzzy models through optimal granularity allocation. *Appl Soft Comput*. 2011;11(8):5590–601.
13. Ceroni A, Costa F, Frasconi P. Classification of small molecules by two- and three-dimensional decomposition kernels. *Bioinformatics*. 2007;23(16):2038–45.
14. Chen Y, Garcia EK, Gupta MR, Rahimi A, Cazzanti L. Similarity-based classification: concepts and algorithms. *J Mach Learn Res*. 2009;10:747–76.
15. Costa F, Rodrigues FA, Traverso G, Villas Boas PR. Characterization of complex networks: a survey of measurements. *Adv Phys*. 2007;56(1):167–242.
16. Crutchfield JP. Between order and chaos. *Nat Phys*. 2012;8(1):17–24.
17. Crutchfield JP, Feldman DP. Regularities unseen, randomness observed: levels of entropy convergence. *Chaos: An Interdisc J Nonlinear Sci*. 2003;13(1):25–54.
18. Daqing L, Kosmidis K, Bunde A, Havlin S. Dimension of spatially embedded networks. *Nat Phys*. 2011;7(6):481–4.
19. de Lange SC, de Reus MA, van den Heuvel MP. The Laplacian spectrum of neural networks. *Front Comput Neurosci*. 2013;7.
20. Dehmer M, Varnuza K, Borgert S, Emmert-Streib F. On entropy-based molecular descriptors: statistical analysis of real and synthetic chemical structures. *J Chem Inf Model*. 2009;49(7):1655–63.

21. Di Ieva A, Schmitz EM, Cusimano MD. Analysis of intracranial pressure: past, present, and future. *Neuroscientist*. 2013;19(6):592–603.
22. Di Ieva A, Grizzi F, Jelinek H, Pellionisz AJ, Losa GA. Fractals in the neurosciences, part I general principles and basic neurosciences. *Neuroscientist*. 2014;20(4):403–17.
23. Di Ieva A, Esteban FJ, Grizzi F, Klonowski W, Martín-Landrove M. Fractals in the neurosciences, part II clinical applications and future perspectives. *Neuroscientist*. 2015;21(1):30–43.
24. Duardo-Sánchez A, Munteanu CR, Riera-Fernández P, López-Díaz A, Pazos A, González-Díaz H. Modeling complex metabolic reactions, ecological systems, and financial and legal networks with MIANN models based on Markov-Wiener node descriptors. *J Chem Inf Model*. 2013;54(1):16–29.
25. Engelbrecht AP. *Computational intelligence: an introduction*. Hoboken: Wiley; 2007.
26. Escolano F, Hancock ER, Lozano MA. Heat diffusion: thermodynamic depth complexity of networks. *Phys Rev E*. 2012;85(3):036206.
27. Fallani FDV, Richiardi J, Chavez M, Achard S. Graph analysis of functional brain networks: practical issues in translational neuroscience. *Philos Trans R Soc B: Biol Sci*. 2014;369(1653):20130521.
28. Fernández E, Jelinek HF. Use of fractal theory in neuroscience: methods, advantages, and potential problems. *Methods*. 2001;24(4):309–21.
29. Fernández E, Bolea JA, Ortega G, Louis E. Are neurons multifractals? *J Neurosci Methods*. 1999;89(2):151–7.
30. Fischer A, Suen CY, Frinken V, Riesen K, Bunke H. Approximation of graph edit distance based on Hausdorff matching. *Pattern Recog*. 2015;48(2):331–43.
31. Friedrich R, Peinke J, Sahimi M, Tabar MRR. Approaching complexity by stochastic methods: from biological systems to turbulence. *Phys Rep*. 2011;506(5):87–162.
32. Gallos LK, Makse HA, Sigman M. A small world of weak ties provides optimal global integration of self-similar modules in functional brain networks. *Proc Natl Acad Sci*. 2012;109(8):2825–30.
33. Gallos LK, Potiguar FQ, Andrade Jr JS, Makse HA. IMDB network revisited: unveiling fractal and modular properties from a typical small-world network. *PLoS One*. 2013;8(6):e66443.
34. Giuliani A, Krishnan A, Zbilut JP, Tomita M. Proteins as networks: usefulness of graph theory in protein science. *Curr Protein Pept Sci*. 2008;9(1):28–38.
35. Godwin D, Barry RL, Marois R. Breakdown of the brain's functional network modularity with awareness. *Proc Natl Acad Sci*. 2015;201414466.
36. Hammer B, Hasenfuss A. Topographic mapping of large dissimilarity data sets. *Neural Comput*. 2010;22(9):2229–84.
37. Hancock ER, Wilson RC. Pattern analysis with graphs: parallel work at Bern and York. *Pattern Recog Lett*. 2012;33(7):833–41.
38. Haykin S. *Neural networks: a comprehensive foundation*. Upper Saddle River: Prentice Hall PTR; 2007.
39. Izakian H, Pedrycz W, Jamal I. Fuzzy clustering of time series data using dynamic time warping distance. *Eng Appl Artif Intel*. 2015;39:235–44.
40. Jang JSR. ANFIS: adaptive-network-based fuzzy inference system. *IEEE Trans Syst Man Cybern*. 1993;23:665–85.
41. Jizba P, Kleinert H, Shefaat M. R'enyi's information transfer between financial time series. *Phys A: Stat Mech Appl*. 2012;391(10):2971–89.
42. Karkare S, Saha G, Bhattacharya J. Investigating long-range correlation properties in EEG during complex cognitive tasks. *Chaos Solitons Fractals*. 2009;42(4):2067–73.
43. Kwapien J, Drożdż S. Physical approach to complex systems. *Phys Rep*. 2012;515(3):115–226.
44. Li B-G, Yu Z-G, Zhou Y. Fractal and multifractal properties of a family of fractal networks. *J Stat Mech: Theory Exp*. 2014;2014(2):P02020.

45. Liang Q, Karnik NN, Mendel JM. Connection admission control in ATM networks using survey-based type-2 fuzzy logic systems. *IEEE Trans Syst Man Cybern.* 2000;30:329–39.
46. Liu J-L, Yu Z-G, Anh V. Determination of multifractal dimensions of complex networks by means of the sandbox algorithm. *Chaos: An Interdiscip J Nonlinear Sci.* 2015;25(2):023103.
47. Livi L, Rizzi A. Graph ambiguity. *Fuzzy Set Syst.* 2013;221:24–47.
48. Livi L, Rizzi A. The graph matching problem. *Pattern Anal Appl.* 2013;16(3):253–83.
49. Livi L, Rizzi A, Sadeghian A. Optimized dissimilarity space embedding for labeled graphs. *Inform Sci.* 2014;266:47–64.
50. Livi L, Tahayori H, Sadeghian A, Rizzi A. Distinguishability of interval type-2 fuzzy sets data by analyzing upper and lower membership functions. *Appl Soft Comput.* 2014;17:79–89.
51. Livi L, Maiorino E, Pinna A, Sadeghian A, Rizzi A, Giuliani A. Analysis of heat kernel highlights the strongly modular and heat-preserving structure of proteins. *Phys A: Stat Mech Appl.* 2016;441:199–214.
52. Livi L, Rizzi A, Sadeghian A. Granular modeling and computing approaches for intelligent analysis of non-geometric data. *Appl Soft Comput.* 2015;27:567–74.
53. Livi L, Sadeghian A, Pedrycz W. Entropic one-class classifiers. *IEEE Trans Neural Netw Learn Syst.* 2015.
54. Livi L, Giuliani A, Sadeghian A. Characterization of graphs for protein structure modeling and recognition of solubility. *Curr Bioinforma.* 2016;11(1):106–14.
55. Lizier JT, Prokopenko M, Zomaya AY. Local measures of information storage in complex distributed computation. *Inform Sci.* 2012;208:39–54.
56. Maiorino E, Livi L, Giuliani A, Sadeghian A, Rizzi A. Multifractal characterization of protein contact networks. *Phys A: Stat Mech Appl.* 2015;428:302–13.
57. Marwan N, Carmen Romano M, Thiel M, Kurths J. Recurrence plots for the analysis of complex systems. *Phys Rep.* 2007;438(5):237–329.
58. Melin P, Castillo O. A review on the applications of type-2 fuzzy logic in classification and pattern recognition. *Expert Syst Appl.* 2013;40(13):5413–23.
59. Mendel JM. General type-2 fuzzy logic systems made simple: a tutorial. *IEEE Trans Fuzzy Syst.* 2014;22(5):1162–82.
60. Nauck D, Klawonn F, Kruse R. *Foundations of Neuro-Fuzzy systems.* New York: Wiley; 1997.
61. Oh S-K, Kim W-D, Pedrycz W, Seo K. Fuzzy radial basis function neural networks with information granulation and its parallel genetic optimization. *Fuzzy Set Syst.* 2014;237:96–117.
62. Pagola M, Lopez-Molina C, Fernandez J, Barrenechea E, Bustince H. Interval type-2 fuzzy sets constructed from several membership functions: application to the fuzzy thresholding algorithm. *IEEE Trans Fuzzy Syst.* 2013;21(2):230–44.
63. Pantic I, Dacic S, Brkic P, Lavrnja I, Jovanovic T, Pantic S, Pekovic S. Discriminatory ability of fractal and grey level co-occurrence matrix methods in structural analysis of hippocampus layers. *J Theor Biol.* 2015;370:151–6.
64. Papo D, Zanin M, Pineda-Pardo JA, Boccaletti S, Buldó JM. Functional brain networks: great expectations, hard times and the big leap forward. *Philos Trans R Soc Lond B: Biol Sci.* 2014;369(1653):20130525.
65. Park H-J, Friston K. Structural and functional brain networks: from connections to cognition. *Science.* 2013;342(6158):1238411.
66. Pełalska E, Duin RPW. *The dissimilarity representation for pattern recognition: foundations and applications.* Singapore: World Scientific; 2005.
67. Prichep LS, Jacquin A, Filipenko J, Dastidar SG, Zabele S, Vodencarevic A, Rothman NS. Classification of traumatic brain injury severity using informed data reduction in a series of binary classifier algorithms. *IEEE Trans Neural Syst Rehabil Eng.* 2012;20(6):806–22.
68. Prokopenko M, Lizier JT. Transfer entropy and transient limits of computation. *Sci Rep.* 2014;4:5394.

69. Prokopenko M, Lizier JT, Price DC. On thermodynamic interpretation of transfer entropy. *Entropy*. 2013;15(2):524–43.
70. Rasouli G, Rasouli M, Lenz FA, Verhagen L, Borrett DS, Kwan HC. Fractal characteristics of human Parkinsonian neuronal spike trains. *Neuroscience*. 2006;139(3):1153–8.
71. Richiardi J, Achard S, Bunke H, Van De Ville D. Machine learning with brain graphs: predictive modeling approaches for functional imaging in systems neuroscience. *IEEE Signal Proc Mag*. 2013;30(3):58–70.
72. Riera-Fernandez P, Munteanu CR, Escobar M, Prado-Prado F, Martín-Romalde R, Pereira D, Villalba K, Duardo-Sanchez A, González-Díaz H. New Markov–Shannon entropy models to assess connectivity quality in complex networks: from molecular to cellular pathway, parasite–host, neural, industry, and legal–social networks. *J Theor Biol*. 2012;293:174–88.
73. Riesen K, Bunke H. Improving bipartite graph edit distance approximation using various search strategies. *Pattern Recog*. 2015;48(4):1349–63.
74. Rossi L, Torsello A, Hancock ER. Unfolding kernel embeddings of graphs: enhancing class separation through manifold learning. *Pattern Recog*. 2015;48(11):3357–70.
75. Rossi L, Torsello A, Hancock ER. Measuring graph similarity through continuous-time quantum walks and the quantum Jensen-Shannon divergence. *Phys Rev E*. 2015;91(2):022815.
76. Rozenfeld HD, Song C, Makse HA. Small-world to fractal transition in complex networks: a renormalization group approach. *Phys Rev Lett*. 2010;104:025701.
77. Rupp M, Schneider G. Graph kernels for molecular similarity. *Mol Inform*. 2010;29(4):266–73.
78. Russo R, Herrmann HJ, de Arcangelis L. Brain modularity controls the critical behavior of spontaneous activity. *Sci Rep*. 2014;4.
79. Sainath TN, Kingsbury B, Saon G, Soltau H, Mohamed A-r, Dahl G, Ramabhadran B. Deep convolutional neural networks for large-scale speech tasks. *Neural Netw*. 2014;64:39–48.
80. Schölkopf B, Smola AJ. *Learning with kernels: support vector machines, regularization, optimization, and beyond*. Cambridge, MA: MIT Press; 2002.
81. Seely AJE, Newman KD, Herry CL. Fractal structure and entropy production within the central nervous system. *Entropy*. 2014;16(8):4497–520.
82. Serletis D, Bardakjian BL, Valiante TA, Carlen PL. Complexity and multifractality of neuronal noise in mouse and human hippocampal epileptiform dynamics. *J Neural Eng*. 2012;9(5):056008.
83. Serratos F, Cortés X, Solé-Ribalta A. Component retrieval based on a database of graphs for hand-written electronic-scheme digitalisation. *Exp Syst Appl*. 2013;40(7):2493–502.
84. Song C, Havlin S, Makse HA. Origins of fractality in the growth of complex networks. *Nat Phys*. 2006;2(4):275–81.
85. Stoop R, Saase V, Wagner C, Stoop B, Stoop R. Beyond scale-free small-world networks: cortical columns for quick brains. *Phys Rev Lett*. 2013;110(10):108105.
86. Tahayori H, Livi L, Sadeghian A, Rizzi A. Interval type-2 fuzzy sets reconstruction based on fuzzy information-theoretic kernels. *IEEE Trans Fuzzy Syst*. 2014.
87. Theodoridis S, Koutroumbas K. *Pattern recognition*. 4th ed. Waltham: Elsevier/Academic; 2008.
88. Tomida N, Tanaka T, Ono S, Yamagishi M, Higashi H. Active data selection for motor imagery EEG classification. *IEEE Trans Biomed Eng*. 2015;62(2):458–67.
89. van den Heuvel MP, Fornito A. Brain networks in schizophrenia. *Neuropsychol Rev*. 2014;24(1):32–48.
90. Wagner C, Hagrais H. Toward general type-2 fuzzy logic systems based on zSlices. *IEEE Trans Fuzzy Syst*. 2010;18(4):637–60.
91. Warren Liao T. Clustering of time series data—a survey. *Pattern Recog*. 2005;38(11):1857–74.
92. West BJ. *Fractal physiology*, vol. 2. Oxford: Oxford University Press; 1994.
93. West BJ. *Fractal physiology and chaos in medicine*, vol. 16. Singapore: World Scientific; 2012.

94. Xiao B, Hancock ER, Wilson RC. Geometric characterization and clustering of graphs using heat kernel embeddings. *Image Vision Comput.* 2010;28(6):1003–21.
95. Zappasodi F, Olejarczyk E, Marzetti L, Assenza G, Pizzella V, Tecchio F. Fractal dimension of EEG activity senses neuronal impairment in acute stroke. *PLoS One.* 2014;9(6):e100199.
96. Zhang J, Tuo X, Yuan Z, Liao W, Chen H. Analysis of fMRI data using an integrated principal component analysis and supervised affinity propagation clustering approach. *IEEE Trans Biomed Eng.* 2011;58(11):3184–96.
97. Zhang Y, Zhou W, Yuan S. Multifractal analysis and relevance vector machine-based automatic seizure detection in intracranial EEG. *Int J Neural Syst.* 2015;0(0):1550020.
98. Zhou S-M, Garibaldi JM, John RI, Chiclana F. On constructing parsimonious type-2 fuzzy logic systems via influential rule selection. *IEEE Trans Fuzzy Syst.* 2009;17(3):654–67.
99. Zhu X, Gisbrecht A, Schleif F-M, Hammer B. Approximation techniques for clustering dissimilarity data. *Neurocomputing.* 2012;90:72–84.
100. Zhu X, Schleif F-M, Hammer B. Adaptive conformal semi-supervised vector quantization for dissimilarity data. *Pattern Recog Lett.* 2014;49:138–45.

Erratum to: The Fractal Geometry of the Brain

Antonio Di Ieva

A. Di Ieva (ed.), *The Fractal Geometry of the Brain*, Springer Series in Computational Neuroscience, DOI 10.1007/978-1-4939-3995-4

One of the affiliations of the editor was incorrect. The correct affiliation should read as given below:

Garvan Institute of Medical Research
Sydney
Australia

The updated original online version for this book can be found at
DOI 10.1007/978-1-4939-3995-4

Index

- A**
Affective disorder, 420, 421, 472–474, 480
Aging, 37, 40, 141, 190, 200, 206, 213–229, 238, 241
ALS. *See* Amyotrophic lateral sclerosis (ALS)
Alzheimer's disease, 34, 37, 100, 200, 204–206, 214, 216, 222, 227, 234–236, 241, 296, 297, 299, 303, 494, 538
Amyloid plaques, 222, 234, 236–239
Amyotrophic lateral sclerosis (ALS), 94, 214, 216, 222–224, 227, 303, 304, 312
Analysis of non-geometric input spaces, 567–572
Aneurysm, 191, 255, 263–275, 288, 305, 458
Angioarchitecture, 196, 280, 282–283, 287, 290–292, 322, 377, 394, 395, 397, 405
Anxiety, 193, 471–481, 492
ARFIMA. *See* Autoregressive fractionally integrated moving average (ARFIMA)
Arteriovenous malformation (AVM), 34, 191, 201, 279–292, 305, 327, 516, 574
Artificial intelligence, 195, 500
Autoregressive fractionally integrated moving average (ARFIMA), 55, 57–61, 63
AVM. *See* Arteriovenous malformation (AVM)
- B**
Bio-inspiration, 487, 500, 552, 558, 559
Biomarker, 190, 194–196, 201, 204, 208, 224, 284, 287, 289, 290, 292, 305, 314, 319, 324, 327, 365, 372, 394, 397, 400, 402, 407, 409, 501, 502
Biosignal, 191, 193, 416, 427, 445, 448
Box counting, 5–7, 9, 10, 13–38, 70, 71, 73, 77, 94, 95, 97, 98, 100, 101, 103, 109–125, 138, 195, 200, 202, 203, 216–219, 241, 280, 284–286, 288, 289, 297–299, 302, 318, 319, 352–355, 357, 359, 365, 374, 375, 382, 397, 398, 403, 404, 406, 407, 465, 505, 506, 526, 527, 529, 538–549, 568
Box dimension (D_B), 20, 22–25, 27–29, 34–37, 95–98, 102, 112, 113, 122–124
Brain
 design, 9, 86, 87, 169, 179, 183
 evolution, 169–174, 179, 183
 histopathology, 388
 imaging, 74–76, 191, 236, 301, 305
 research, 272, 566, 573
 tumor, 66, 86, 190–192, 195, 205, 207, 208, 287, 296, 301, 302, 312–324, 327, 333–335, 341, 346, 352–356, 359, 361–365, 371–388, 393–409, 501, 503, 573, 574
- C**
CADASIL. *See* Cerebral autosomal dominant arteriopathy with subcortical infarcts and leukoencephalopathy (CADASIL)
Cancer, 6, 190, 192, 314, 322, 324, 352, 355–357, 365, 394, 395, 478
Capacity dimension, 32, 352–355, 365
CBF. *See* Cerebral blood flow (CBF)
CBFV. *See* Cerebral blood flow velocity (CBFV)
Cell networks, 148, 151

- Cerebral aneurysm, 268, 275
- Cerebral autosomal dominant arteriopathy with subcortical infarcts and leukoencephalopathy (CADASIL), 458, 515, 516
- Cerebral blood flow (CBF), 236, 242, 243, 252–255, 257–260
- Cerebral blood flow velocity (CBFV), 253–255, 257–260
- Cerebral cortex, 86, 94, 101, 169–173, 175, 177, 178, 181–183, 200, 216, 220, 222, 227, 241, 303, 457
- Chaotic advection, 266, 272, 274
- Classification, 29, 75, 93, 96, 101, 173, 191, 192, 204, 206, 208, 257, 260, 280, 282, 284, 291, 296, 297, 299, 302, 305, 314, 334, 340–342, 344, 352, 361, 366, 371–388, 394, 397, 408, 422, 423, 431–441, 474, 501, 516, 538, 540, 566–570, 572, 573
- Classifier, 203, 204, 206, 208, 236–241, 245, 298, 299, 334, 338, 341, 342, 344, 347, 370, 380, 440, 479, 573
- Clinical neurosciences, 10, 189–196, 204, 208, 283, 312, 499–501
- Cognitive neurosciences, 193
- Complexity, 5, 14, 50, 66, 84, 101, 110, 138, 164, 176, 190, 200, 214, 236, 252–255, 274, 280, 296, 317, 351, 373, 394, 417, 432, 445, 458, 473, 486, 501, 515, 538, 561
- Complex networks, 46, 192, 352, 361–366, 566–568
- Complex systems, 9, 45, 91, 150, 151, 416, 566, 569
- Computation, 70–72, 87, 194, 206–208, 241, 255, 256, 271, 288, 289, 314, 318, 326, 338, 362, 399, 449–450, 524, 526–528, 538, 539, 546–549
- Computational fluid dynamics (CFD), 264–266
- Computational intelligence (CI), 500, 502, 565–574
- Computed tomography (CT), 26, 75, 191, 195, 266, 280, 282, 296, 305
- Correlation dimension, 32, 361, 418, 427, 438, 473–475, 479
- Cortical atrophy, 241, 242
- Cortical folding, 86, 171–173, 178, 182, 201, 302
- CUDA, 534–539, 541–545, 547–549
- D**
- Decomplexification, 259
- Deep brain stimulation, 72
- Demyelination, 229, 244
- Dendritic arbors, 92–95, 99, 103
- Detrended fluctuation analysis (DFA), 52, 57, 71, 72, 139, 193, 195, 256, 258, 291, 296, 297, 305–308, 361, 432–436, 474
- Differential diagnosis, 312, 314, 320, 407, 458–460
- Differentiation, 85, 133, 141, 161, 164, 240, 282, 313, 321, 381, 396
- Diffusion-limited aggregation (DLA), 159, 163, 458, 467, 554
- Digital Imaging and Communications in Medicine (DICOM), 265, 507
- Dynamics, 15, 26, 37, 45, 46, 63, 66, 74–76, 84, 85, 92, 101, 102, 127–135, 143, 144, 146, 147, 150, 151, 170, 191–193, 200, 203–204, 244, 245, 267, 282–284, 286, 352, 355–357, 359–361, 363, 365, 379, 395, 408, 416, 417, 449, 472, 478–481, 491, 535, 549, 566
- E**
- Eden fronts, 158–160
- Electroencephalogram (EEG), 13, 46, 74, 75, 77, 193, 195, 203, 204, 206, 207, 242, 413–426, 432, 448, 472–480, 491, 492, 515, 524, 525, 567, 573
- Electronics, 551–561
- Electron microscopy, 20, 30, 141, 402
- Entropy, 32, 75, 131, 133–135, 228, 397, 460–463, 467, 477–479
- Epilepsy, 7, 66, 74, 190, 203, 205–207, 216, 224, 227–229, 415
- Euclidean dimension, 6, 111, 175, 176, 178, 194, 337, 355, 357, 417
- F**
- Fluctuation analysis, 52, 57, 71, 72, 139, 193, 195, 256, 258, 291, 296, 297, 305–308, 361, 432–434, 474
- 1/f* noise, 45–63
- FracLac, 20, 21, 24, 25, 28, 33, 35, 98, 114, 115, 500, 507, 509, 515, 516, 529
- Fractals, 3–10, 14, 50, 66, 84, 101, 110, 138, 164, 176, 190, 200, 214, 236, 255, 274, 280, 296, 317, 351, 373, 394, 417, 432, 445, 458, 473, 486, 501, 515, 538, 561

- analysis, 4–5, 13–38, 50, 66, 84, 101, 110, 138, 164, 176, 190, 200, 214, 236, 255, 274, 280, 296, 317, 351, 373, 394, 417, 432, 445, 458, 473, 486, 501, 515, 538, 561
- in biomedicine, 4
- Brownian motion, 256, 257, 336–337
- geometry, 3–10, 13, 20, 38, 66, 84–87, 93, 109–111, 124, 125, 131, 138–141, 159, 169–183, 192, 194, 196, 214, 296, 318, 352, 354, 355, 373, 374, 377, 399, 400, 408, 458, 501, 503, 517, 552, 557, 560–574
- parameters, 51, 55–58, 60, 61, 63, 98, 257, 260, 407, 408, 467, 500, 554
- time-space, 130–135
- Fractal dimension (FD), 6, 14, 50, 66, 84, 101, 110, 138, 164, 176, 190, 200, 214, 236, 255, 274, 280, 296, 317, 351, 373, 394, 417, 432, 445, 458, 473, 486, 501, 515, 538, 561
- Fractional differencing parameter, 10, 51, 61
- G**
- Gait analysis, 432
- Gamma Knife radiosurgery, 201, 290, 312
- Geometrical complexity, 5–7, 85, 190, 192, 280, 282–284, 286, 290, 317, 318, 373, 374, 394, 400, 404, 405
- Glioblastoma multiforme (GBM), 314, 316, 320, 321, 342, 353–355, 358–360, 363–365, 395, 401, 403, 406, 407
- Glioma, 192, 208, 296–298, 314, 315, 317–322, 324, 334, 335, 342, 346, 353, 355–359, 361, 377, 395, 398, 404, 406, 407
- Gompertz growth, 131, 132, 134
- GPU. *See* Graphics processing unit (GPU)
- Graphics processing unit (GPU), 533–549
- H**
- Henon Map, 27, 34
- Higuchi's algorithm, 418, 427, 449–450, 473, 524
- Human brain, 5, 8, 9, 45, 84, 86, 169–183, 241, 302, 400, 416, 423, 425, 501, 526, 561, 566, 572, 573
- Human implants, 561
- Hurst coefficient, 10, 51–52, 55, 75, 139, 254–256, 259
- Hurst exponent, 52, 191, 291, 296, 298, 299, 305–308, 364, 397, 432, 435, 440, 476, 528
- I**
- ImageJ, 15, 17, 21, 28, 36, 98, 114, 285, 500, 503–518, 529, 530
- Image preprocessing, 109, 110
- Information dimension, 32, 201, 272, 460, 461, 463
- Information processing, 87, 151, 170, 179, 182–183, 227
- K**
- Katz's algorithm, 449, 524, 525
- Koch curve, 9, 15, 16, 18, 20–22, 158, 159, 161–162
- L**
- Lacunarity, 10, 14, 22, 24, 26–29, 32, 85, 101, 102, 129, 139, 141, 240, 283, 292, 382, 384, 385, 388, 397, 401, 402, 458, 500, 509, 516
- Lesion, 86, 202, 224–226, 228, 280, 315–317, 320, 322, 324–326, 333, 334, 344, 346, 353, 355, 356, 362, 365, 395
- Long memory, 47–48, 50, 53, 55, 58, 61, 62, 308
- M**
- Magnetic resonance imaging (MRI), 75, 87, 179, 191, 195, 214, 280, 296, 303, 312, 352, 353, 355, 459, 460
- MATLAB, 434, 500, 507, 523–530, 547
- Memory, 45, 47–53, 55, 58, 61, 63, 147, 221, 222, 227, 234, 259, 308, 325, 388, 415, 431, 432, 434, 491, 534–538, 543–546, 561, 566
- Meningioma, 192, 208, 317, 319, 320, 355, 356, 359, 360, 363–365, 375, 378, 381–388, 395
- Microglia, 19, 20, 24, 25, 28, 34, 35, 37, 84–85, 91–103, 142, 203, 229, 238, 244, 509, 510, 514, 516

- Microscopy, 20, 30, 36, 94, 141, 165, 402, 464, 465, 506, 507, 510, 553, 555, 559–561
- Microvasculature, 192, 323, 324, 353, 377, 395–398, 404, 407, 409, 458–462, 467
- Minkowski dimension, 285, 286
- Modelling, 477
- Molecular networks, 140, 145, 148, 162
- Monofractal, 31, 34, 46, 66, 68, 72, 74, 75, 110, 257, 288, 298, 404, 406, 435, 509
- MRI. *See* Magnetic resonance imaging (MRI)
- MS. *See* Multiple sclerosis (MS)
- MSA. *See* Multiple system atrophy (MSA)
- Multifractal analysis, 33–35, 38, 66–77, 102, 197, 219, 352, 361, 366, 432, 435, 530, 567, 568
- Multifractality, 14, 35, 38, 66, 76, 77, 102, 191, 400, 409, 432, 433, 435, 438, 440, 476
- Multifractal spectrum, 60, 72–76, 298, 432, 435, 440, 524
- Multifractal systems, 66, 355, 361
- Multi-modal magnetic resonance, 208, 302, 335
- Multiple sclerosis (MS), 202, 207, 214, 224–225, 228, 244, 296, 303, 312, 334, 459, 460, 516
- Multiple system atrophy (MSA), 202, 214, 217, 225, 228
- N**
- NAION. *See* Nonarteritic anterior ischemic optic neuropathy (NAION)
- Neural networks, 87, 131, 146–148, 178, 180–182, 191, 244, 297, 302, 305, 327, 341, 355, 378, 432, 433, 552, 566, 568–570, 573, 574
- Neural wiring, 179–183
- Neuroanatomy, 83–87, 100, 140
- Neurodegeneration, 101, 215–229
- Neurodegenerative disease, 66, 190, 202, 213–229, 233–245
- Neurodynamics, 425
- Neuroimaging, 148, 190–192, 280–283, 287, 289, 291, 292, 295–308, 313, 314, 319, 327, 409
- Neurological diseases, 87, 190, 199–208, 214, 296, 312, 419, 460, 574
- Neurology, 190–191, 200, 203–204, 208, 312
- Neuronal morphology, 92, 94, 99, 103, 123
- Neuronal networks, 84, 87, 143, 145, 183
- Neurons, 9, 18, 29, 46, 84, 101, 110, 138, 164, 176, 190, 200, 214, 236, 255, 274, 280, 296, 317, 351, 373, 394, 417, 432, 445, 458, 473, 486, 501, 515, 538, 561
- Neuro-ophthalmology, 190, 457–467
- Neurosciences, 4–6, 8, 10, 18, 26, 34, 35, 37, 38, 41, 58, 65–77, 84–87, 91, 93, 150, 189–196, 199–208, 432, 499–518, 524, 566, 567, 573
- Noise, 10, 45–63, 66, 74, 75, 164, 304, 305, 313, 334, 385, 417–419, 427, 432, 433, 435, 447, 510, 513, 515, 524, 558, 567
- Nonarteritic anterior ischemic optic neuropathy (NAION), 459, 461, 464, 467
- O**
- OpenCL, 534, 537–539, 541–548
- Optic neuritis (ON), 459, 460, 462–464, 467
- Outcome, 26, 60, 194, 208, 273, 280, 282, 287–291, 324–326, 372, 388, 397, 480, 481, 507, 573
- P**
- Parkinsonian rest tremors, 431–441
- Passive tracers, 263
- Patterns
 - classification, 372, 373
 - extraction, 500, 501, 503–518
 - recognition, 502, 505
- Perception, 46, 180, 372, 476, 561
- Power exponent, 10, 47, 51, 53, 55
- Power spectra, 49, 52–53, 56, 58, 253, 254, 256–260, 433, 473, 479
- Primate neocortex, 173–174, 178, 181
- Primates, 170–174, 178–182, 354, 403
- Prognosis, 208, 255, 290, 312, 317, 324, 352, 395, 397, 467
- Psychiatry, 191, 193, 425
- Q**
- Quantitative electroencephalography (qEEG), 491–493
- R**
- Radiography, 20, 506, 510
- Retinal photography, 20, 510
- Richardson's method, 97, 112

S

SAH. *See* Subarachnoid hemorrhage (SAH)
 Sandbox method, 70, 71
 Scaling, 6, 7, 9, 10, 14–21, 23, 25, 26, 32, 35, 37, 38, 47, 52–55, 62, 66, 72, 74–76, 95, 97, 99, 110–113, 124, 125, 132, 133, 162, 164, 169, 171, 173–176, 178, 193, 199, 256, 291, 298, 306, 307, 319, 320, 337, 339, 352, 355, 357–359, 365, 366, 398, 406, 408, 431–441, 476, 549, 555, 567, 568
 Scaling exponent, 10, 51, 52, 55, 72, 73, 75, 76, 111, 256, 291, 307, 432, 435, 476
 Segmentation, 72, 206, 207, 241, 285, 288, 289, 291, 292, 302, 320, 333–347, 352, 353, 355, 361, 362, 379, 399, 406, 510, 513, 515, 538, 574
 Self-similarity, 6, 7, 9, 10, 14, 17–19, 47–48, 51–53, 61, 66, 75, 86, 87, 110–112, 125, 137–151, 158, 176, 219, 236, 252, 255, 257, 355, 373, 374, 382, 432, 434, 435, 445, 446, 448–449, 472, 2602
 sEMG. *See* Surface electromyogram (sEMG)
 Shannon entropy, 32
 Shape complexity, 214, 215, 218, 220–226, 228, 229, 302
 Sjogren's syndrome, 459, 462–464, 466, 467
 Spectral exponent, 256, 258, 376
 Spectral index, 254, 256–260, 425
 Stationarity, 49–51, 54, 59, 416, 418
 Statistical tests, 299, 380, 467
 Stress reduction, 492
 Subarachnoid hemorrhage (SAH), 191, 253, 255, 257–259

Subscanning analysis, 35
 Surface electromyogram (sEMG), 193, 445–450, 452, 453
 Susceptibility-weighted imaging (SWI), 191, 208, 311–326
 Suture fractal, 161, 162
 SWI. *See* Susceptibility-weighted imaging (SWI)
 Synapse, 84, 85, 102, 127–135, 143, 145, 147, 149, 181, 229

T

TBI. *See* Traumatic brain injury (TBI)
 Texture analysis, 192, 244, 334, 352, 377, 378, 381, 386, 387
 Texture feature, 302, 335, 337, 338, 340, 341, 344, 346, 377
 Thresholding, 379, 510, 511, 513, 515
 Time series, 5, 6, 8, 10, 46, 48, 49, 51–61, 66, 67, 72, 190, 191, 193, 195, 203, 204, 252–260, 292, 361, 362, 364, 413–427, 431–440, 446, 448, 450, 473, 474, 476, 490, 501, 524, 566–568, 573
 Tissue characterization, 365, 372, 378, 388
 Topological dimension, 6, 110, 176
 Traumatic brain injury (TBI), 259, 312, 324, 573
 Tumor growth, 192, 351–366, 400
 Two-dimensional (2D) images, 22, 37, 110, 113–114, 122, 337, 501, 523, 526, 529, 538
 3D fractal dimension (3DFD), 319, 539